WHOI-96-09

"Rotating Convection"
1995 Summer Study Program in Geophysical Fluid Dynamics

by

Rick Salmon and Glen Flierl, Directors
and
Lee Anne Campbell, Staff Assistant

Woods Hole Oceanographic Institution
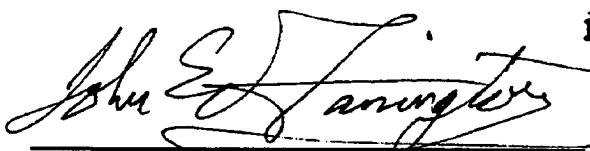Woods Hole, Massachusetts 02543

July 1996

Technical Report

Approved for Distribution:

DTIC QUALITY INSPECTED 2

John W. Farrington
Associate Director for Education
Dean of Graduate Studies

19970421 293

Course Lectures
Abstracts of Participants
Fellows Project Reports

WHOI-96-09

"Rotating Convection"
1995 Summer Study Program in Geophysical Fluid Dynamics

by

Rick Salmon and Glen Flierl, Directors
and
Lee Anne Campbell, Staff Assistant

Woods Hole Oceanographic Institution
Woods Hole, Massachusetts 02543

July 1996

Technical Report

Approved for public release; distribution unlimited.

Approved for Distribution:

DTIC QUALITY INSPECTED 2

John W. Farrington
Associate Director for Education
Dean of Graduate Studies

Contents

Other Lectures

Standing (l-r): E. Spiegel, J. Fernando, J. Wylie, R. Ford, W. Young, J. Whitehead, K. Julien, J. Marshall, V. Putkaradze, K. Helfrich, O. Esenkov, P. Dellar, L. Howard, S. Zatman, J. Noyes Jr., G. Flierl, R. Salmon

Seated on porch: S. Legg, M. Visbeck, A. Stamp, R. Kerswell, D. del-Castillo, L. Campbell, G. Veronis, R. Krishnamurti, J. Aurnou, P. Cessi, F. Straneo, H. Banks, C. Rooth, E. Chassignet

Seated on ground: N. Balmforth, S. Meacham

Not pictured: J. Anderson, P. Berloff, E. D'Asaro, S. Fauve, A. Gnanadesikan, T. Haine, J. Hammack, D. Henderson, J. Herring, S. Hood, J. Keller, R.M. Kerr, O. Kerr, R. Kerswell, E. Knobloch, A. Mahadevan, W. Malkus, O. Metais, P. Morrison, Y. Park, B. Plapp, T. Rossby, E. Schucking, U. Send, V. Steinberg, M. Stern, R. Thieberger, G. Veitch, J. Werne, R. Worthing, A. Woods

Preface

The 1995 program in Geophysical Fluid Dynamics addressed "Rotating Convection," with particular emphasis on high-Rayleigh-number convection and on convection in the ocean. Principal lecturers Ruby Krishnamurti, Joe Fernando and John Marshall were our guides. Ruby's courageous laboratory experiments with a rotating table proved so sensitive to small disturbances that her listeners were required to sit still and be quiet — a feat never before accomplished in Walsh Cottage. Joe Fernando offered us a panoramic survey of convection theory, and John Marshall challenged our theoretical impulses with a chilling account of real-ocean convection. John has very generously edited his lecture notes into a substantial review of ocean convection appearing in this volume. Sonya Legg, Keith Julien, Joe Werne and Bob Kerr presented sophisticated numerical studies of convection at high Rayleigh numbers. Martin Visbeck and Uwe Send described field measurements of convection in the ocean. These stimulating lectures were followed by many others, too numerous to mention. As usual, the subjects sometimes strayed quite far from the summer's official topic — to anything and everything of interest in the broad and rapidly developing field of geophysical fluid dynamics. Our eight graduate-student fellows seemed to thrive in this atmosphere, making up in their research for what can only be described as a character-building season on the softball field.

Once again, participants were discouraged from submitting lecture summaries to this volume if the results would soon be published in a regular journal. Therefore, readers should be sure to scan the "1995 Lecture Schedule" for a fair impression of the spectrum of our activities.

In August, the staff faced an unusual challenge when the director decided to spend a week relaxing in Falmouth Hospital and two more weeks malingering at home. While it would be impossible for me to thank all of the people at GFD and WHOI who showed kindness and offered help, I especially want to thank stalwart Neil Balmforth and the new Iron Man of GFD, Rupert Ford, for their generosity and skill in rescuing abandoned fellows.

Just as the current directors seem to be wearing out, reinforcements have arrived: We are very proud to announce that Steve Meacham and Stephan Fauve have joined the GFD steering committee. These two Steves have contributed to the program in numerous past summers, and Steve Meacham (assisted by George Veronis) will direct the 1996 session on "Double-Diffusive Processes."

Once again it is a pleasure to thank the Woods Hole Oceanographic Institution for its hospitality. Jake Peirson and his staff at the Education Office provided indispensable support. This year, we were very fortunate to have Lee Campbell — a newcomer to GFD — as our administrator in the cottage. Lee kept things running smoothly despite everything we could do. We gratefully acknowledge the support of the National Science Foundation and the Office of Naval Research. Finally, very special thanks to my co-director Glenn Flierl for his help, patience, and unfailing good spirit.

Rick Salmon
1995 co-director

1995 GFD Participants

The Fellows

Jonathan Aurnou	Johns Hopkins University
Helene Banks	Southampton University
Paul Dellar	Cambridge University
Oleg Esenkov	University of Miami
Jim Noyes	University of California at San Diego
Vakhtang Putkaradze	Niels Bohr Institute, Copenhagen
Fiammetta Straneo	University of Washington
Stephen Zatman	Harvard University

The Staff and Visitors

James Anderson	Stevens Institute of Technology
Neil Balmforth	University of Texas
Pavel Berloff	Florida State University
Paola Cessi	University of California at San Diego
Eric Chassignet	University of Miami
Eric D'Asaro	Applied Physics Laboratory, Seattle
Diego del-Castillo	University of California at San Diego
Stephan Fauve	Ecole Normale Superieure de Lyon
Joe Fernando	Arizona State University
Glenn Flierl	Massachusetts Institute of Technology
Rupert Ford	Imperial College
Anand Gnanadesikan	Woods Hole Oceanographic Institution
Thomas Haine	Massachusetts Institute of Technology
Joseph Hammack	Warriors Mark, Pennsylvania
Diane Henderson	Pennsylvania State University
Jackson Herring	National Center for Atmospheric Research
Simon Hood	University of Liverpool
Louis Howard	Florida State University
Keith Julien	National Center for Atmospheric Research
Joseph B. Keller	Stanford University
Robert M. Kerr	National Center for Atmospheric Research
Oliver Kerr	City University, London
Richard Kerswell	University of Newcastle
Edgar Knobloch	University of California at Berkeley
Ruby Krishnamurti	Florida State University
Sonya Legg	University of California at Los Angeles
Amala Mahadevan	University of Chicago
Willem Malkus	Massachusetts Institute of Technology
John Marshall	Massachusetts Institute of Technology

Steven Meacham	Florida State University
Olivier Metais	LEGI/ING, France
Philip J. Morrison	University of Texas
Young-Gyu Park	Woods Hole Oceanographic Institution
Brendan Plapp	Cornell University
Claes Rooth	University of Miami
Thomas Rossby	University of Rhode Island
Richard Salmon	University of California at San Diego
Engelbert Schucking	New York University
Uwe Send	Kiel University
Edward A. Spiegel	Columbia University
Andrew Stamp	University of Washington
Victor Steinberg	Weizmann Institute of Science
Melvin Stern	Florida State University
Reuben Thieberger	Columbia University
George Veronis	Yale University
Graham Veitch	Wolfson College
Martin Visbeck	Massachusetts Institute of Technology
Joseph Werne	National Center for Atmospheric Research
Jack Whitehead	Woods Hole Oceanographic Institution
Rodney Worthing	Massachusetts Institute of Technology
Andy Woods	University of Cambridge
Jonathan Wylie	University of Cambridge
William Young	University of California at San Diego

1995 Lecture Schedule

Mon. June 19, 10 am
> **Convection without rotation**
> Ruby Krishnamurti

Tues. June 20, 10 am
> **Rotation without convection**
> Ruby Krishnamurti

Tues. June 20, 2 pm
> **Tutorial on convection**
> George Veronis

Wed., June 21, 10 am
> **Rotating convection**
> Ruby Krishnamurti

Wed. June 21, 2 pm
> **Turbulent rotating Rayleigh-Benard convection**
> Joe Werne

Thurs. June 22, 10 am
> **Turbulent thermal convection in non-rotating fluids**
> Joe Fernando

Thurs. June 22, 2 pm
> **Two- and two and one-half- dimensional rotating convection**
> Keith Julien

Fri. June 23, 10 am
> **Turbulent thermal convection in rotating fluids**
> Joe Fernando

Fri. June 23, 2 pm
> **Tutorial on spin-up**
> Lou Howard

Mon. June 26, 10 am
> **Convection from isolated and finite-size sources in the presence of rotation**
> Joe Fernando

Mon. June 26, 2 pm
>   **Rotating, penetrative convection**
>   Sonya Legg

Tues. June 27, 10 am
>   **Oceanic convection**
>   John Marshall

Wed. June 28, 10 am
>   **Convection and baroclinic instability**
>   John Marshall

Wed. June 28, 2 pm
>   **Observations of small-scale oceanic convection**
>   Martin Visbeck

Thurs. June 29, 10 am
>   **Convection and oceanic circulation**
>   John Marshall

Thurs. June 29, 2 pm
>   **The organization of turbulent convection by waves**
>   Andrew Stamp

Fri. June 30, 10 am
>   **Convection and oceanic circulation**
>   John Marshall

Fri. June 30, 2 pm
>   **Rotating convection with differential bottom heating**
>   Young-Gyu Park

Wed. July 5, 10 am
>   **Shear flow stability and critical layers**
>   Diego del Castillo

Thurs. July 6, 10 am
>   **Some unexpected consequences of the interaction of convective
>   adjustment and diffusion**
>   Paola Cessi

Fri. July 7, 10 am
>   **Baroclinic instability of the mixed layer**
>   Tom Haine

Mon. July 10, 10 am
Is the thermocline a front?
Simon Hood

Mon. July 10, 2 pm
Modeling mesoscale flow
Amala Mahadevan

Tues. July 11, 10 am
Measuring mixing and convection in the ocean
Eric D'Asaro

Wed. July 12, 10 am
Spin-offs of the North Atlantic Current
Tom Rossby

Wed. July 12, 2 pm
Velocity and thermal boundary layer scaling in Rayleigh-Benard convection
Robert Kerr

Thurs. July 13, 10 am
Langmuir cells: General background, physics, evidence for wave-current interaction
Anand Gnanadesikan

Fri. July 14, 10 am
Baroclinic instability and the mixed-layer T-S relation
Bill Young

Mon. July 17, 10 am
Rotating Rayleigh-Benard convection: asymmetric modes and vortex states
Victor Steinberg

Tues. July 18, 10 am
Vortex evolution in non-axisymmetric spin-up
Diane Henderson

Wed. July 19, 10 am
Coherent vortices in rotating shear flows
Olivier Metais

Thurs. July 20, 10 am
Three-dimensional waves in shallow water
Joe Hammack

Thurs. July 20, 2 pm
Inverse cascade in stably stratified rotating turbulence
Olivier Metais

Fri. July 21, 10 am
Boundary layers in rotating flow; a little more than you wanted to know ...
Lou Howard

Mon. July 24, 10 am
Large-scale fluctuations in swirling turbulent flows
Stephan Fauve

Tues. July 25, 10 am
Turbulent diffusion
Joe Keller

Wed. July 26, 10 am
Deep water formation and thermohaline circulation in ocean general circulation models
Eric Chassignet

Thurs. July 27, 10 am
Effect of rotation on double-diffusive interleaving
Oliver Kerr

Fri. July 28, 10 am
Bifurcations, chaos and structures
Ed Spiegel

Mon. July 31, 10 am
Bifurcations in rotating systems
Edgar Knobloch

Tues. August 1, 10 am
Spectral theory of the ideal vortex
Neil Balmforth

Wed. August 2, 10 am
Hamiltonian discription of linear ideal-fluid problems with continuous spectra
Phil Morrison

Wed. August 2, 8 pm, *Special Evening Lecture*
The world viewed from outside
Engelbert Schucking

Thurs. August 3, 10 am
> **The wall jet in a rotating fluid**
> Melvin Stern

Fri. August 4, 10 am
> **The use of eddy viscosity in turbulence and the statistical theory of turbulence**
> Jack Herring

Sun. August 6, 6:45 am
> **An introduction to the renal calculus: flow stoppage by a solid body in a thin elastic tube**
> Rick Salmon

Mon. August 7, 10 am
> **Flow regimes in a small barotropic ocean**
> Steve Meacham

Thurs. August 10, 10 am
> **Diffusion by intelligent movements**
> Glenn Flierl

Fri. August 11, 10 am
> **Rayleigh-Benard convection in compressed gases**
> Brendan Plapp

Tues. August 15, 10 am
> **Large-scale aspects of convection: observations, vertical transports and implications**
> Uwe Send

Thurs. August 17, 10 am
> **Some thoughts on simplified ocean models with topography**
> Rupert Ford

Fri. August 18, 10 am
> **Energy theory, upper bound theory and diamonds in rotating convection**
> Rodney Worthing

Tues. August 22, 10 am
> **The effects of cooling on a baroclinic current**
> Jim Noyes

Tues. August 22, 11:30 am
> **Stretching of passive vector fields**
> Vakhtang Poutkaradze

Wed. August 23, 10 am
> **A single Fourier mode model of frontogenesis**
> Paul Dellar

Wed. August 23, 11:30 am
> **Kelvin waves in a semigeostrophic model**
> Helene Banks

Wed. August 23, 1:30 pm
> **Circulation in a two-D convective chimney**
> Fiammetta Straneo

Thurs. August 24, 10 am
> **Unstable convective modes in a two-layer system**
> Oleg Esenkov

Thurs. August 24, 11:30 am
> **Instability at a general latitude**
> Stephen Zatman

Thurs. August 24, 1:30 pm
> **Magnetic buoyancy effects in convection**
> Jonathan Aurnou

August & September, 1995
> **A diabetic invariant of the Islets of Langerhans: depletion of the beta-effect**
> Phil Morrison

Principal Lecturers (l-r): Ruby Krishnamurti, John Marshall
and Joe Fernando

Lectures by Ruby Krishnamurti

Lecture 1   Rayleigh - Bénard Convection

by Ruby Krishnamurti

1) Cellular Convection:

1.1.1 Theoretical Background

A layer of fluid lies between two plates of infinite horizontal extent. The temperature on the lower plate is $T_0 + \Delta T$, and the temperature on the upper plate is T_0. The governing equations in the Boussinesq approximation(Spiegel and Veronis, 1960) are:

Momentum
$$\left(\partial_t + u_j \partial_j\right) u_i = -\frac{1}{\rho_0}\partial_i p - g\frac{\rho}{\rho_0}\lambda_i + \nu_0 \nabla^2 u_i \tag{1}$$

where $i = 1, 2, 3$ and $\lambda_i = (0, 0, 1)$

Mass
$$\partial_j u_j = 0 \tag{2}$$

Energy
$$\left(\partial_t + u_j \partial_j\right) T = \kappa_0 \nabla^2 T \tag{3}$$

State
$$\rho = \rho_0\left[1 - \alpha\left(T - T_0\right)\right] \tag{4}$$

1.2 Basic State Solution

The basic state of the system is one of no motion, hydrostatic balance and steady heat conduction.

$$u_{i,B} = 0 \tag{5}$$

$$\frac{\partial p_B}{\partial z} = -g\rho \tag{6}$$

$$T_B = -\frac{\Delta T}{d}z + (T_0 + \Delta T) \tag{7}$$

1.1.2 Linear Stability of Basic State

The system is perturbed with an infinitesimal amplitude disturbance u_i, θ, π so that $T = T_B + \theta$, $p = p_B + \pi$ and $u_i = u_i$, and linearised about the basic state(see Chandrasekhar, 1960). The dimensionless equations governing the perturbations are:

$$\frac{1}{Pr}\partial_t u_i = -\partial_i \pi + \lambda_i \theta + \nabla^2 u_i \tag{8}$$

$$\partial_j u_j = 0 \tag{9}$$

$$\partial_t \theta = \nabla^2 \theta + R u_j \lambda_j \tag{10}$$

where $Pr = \frac{\nu_0}{\kappa_0}$ is the Prandtl number and $R = \frac{g\alpha}{\kappa_0 \nu_0}\Delta T d^3$ is the Rayleigh number. The boundary conditions at $z = 0, 1$ are $w = 0$, $\theta = 0$, and $u = v = 0$ for rigid boundaries or $\partial_z u = \partial_z v = 0$ for stress free boundaries.

We may separate out the time dependence of u_i and θ as $e^{\sigma t}$ and consider the marginal state, i.e. where $\sigma_R = 0$ (σ_I turns out to be zero for $\sigma_R \geq 0$):

$$\nabla^2 u_i + \lambda_i \theta - \partial_i \pi = 0 \tag{11}$$

$$\nabla^2 \theta + R u_j \lambda_i = 0 \tag{12}$$

$$\partial_j u_j = 0 \tag{13}$$

This is an eigenvalue problem for R. We can combine (11), (12), and (13), and obtain an equation solely in terms of the vertical velocity w:

$$\nabla^6 w - R\nabla_h^2 w = 0 \tag{14}$$

where $\nabla_h^2 = \partial_{xx}^2 + \partial_{yy}^2$. We can look for solutions of the form $\nabla_h^2 w = -k^2 w$, in which case:

$$\left[(\partial_z^2 - k^2)^3 + Rk^2\right] w = 0 \tag{15}$$

For the stress-free case, $w(x, y, z) = e^{i\mathbf{k}\cdot\mathbf{r}} \sin n\pi z$ where $\mathbf{r} = (x, y)$, $n = 1, 2, 3, \ldots$ so:

$$R = \frac{(n^2\pi^2 + k^2)^3}{k^2} \qquad (16)$$

The mininum value of R occurs for $n = 1$ and $k^2 = \frac{\pi^2}{2}$ giving $R_{min} \equiv R_c = \frac{27}{4}\pi^4$. The eigenfunctions are infinitely degenerate: $k^2 = k_x^2 + k_y^2 = \frac{\pi^2}{2}$ at $R = R_c$, i.e. rectangles of any k_x/k_y including squares, rolls, triangles and hexagons are all marginally stable at $R = R_c$, so an experiment in which R is increased through R_c may contain a superposition of many eigenfunctions.

1.2 Demonstration

The lecturer demonstrated the degeneracy of the eigenfuctions using a tank of fishscale-laced water $\simeq$ 1cm deep on top of an overhead projector. The lecturer slipped sheets of acetate with dark stripes or clear dots under the tank for a while and then removed them, after which convection along rolls or in hexagons appeared. The lecturer then excited a more complicated pattern using a cutout snowflake swiped from her departmental Christmas decorations.

1.3 Steady Finite Amplitude Flow

(See Malkus and Veronis, or notes on Veronis' talk on steady finite amplitude convection)

For $R > R_c$ there are steady finite amplitude solutions for a modified perturbation expansion as follows:

$$X = \sum_{}^{\infty} \epsilon^n X^{(n)} \qquad (17)$$

$$R = R_c + \epsilon R^{(1)} + \epsilon^2 R^{(2)} + \ldots \qquad (18)$$

where $X = u_i$, θ or π. The resulting equations at each order of ϵ can be solved. The result is that $R^{(1)} = 0$, $R^{(2)} > 0$ (i.e. $R - R_c > 0$ for real ϵ), and $R^{(2)}$ is smallest for rolls. There are still an infinite number of "solutions" (i.e. orientation of rolls) unless boundaries are considered. Viscous dissipation on boundaries will break this degeneracy.

1.4 Stability of Steady Finite Amplitude Flows

(See Schlüter, Lortz and Busse, 1965)

Each of the steady finite amplitude solutions is perturbed with infinitesimal amplitude disturbance $(\tilde{u}_i, \tilde{\theta}, \tilde{\pi})$, with growth rate σ. Then:

$$\frac{1}{Pr}\left[\partial_t \tilde{u}_i + u_j \partial_j \tilde{u}_i + \tilde{u}_j \partial_j u_i\right] = -\partial_i \tilde{\pi} + \lambda_i \tilde{\theta} + \nabla^2 \tilde{u}_i \tag{19}$$

$$\partial_j \tilde{u}_j = 0 \tag{20}$$

$$\left[\partial_t \tilde{\theta} + u_j \partial_j \tilde{\theta}_j + \tilde{u}_j \partial_j \theta\right] = \nabla^2 \tilde{\theta} + R\tilde{u}_j \lambda_j \tag{21}$$

Note that ϵ now occurs as a **given** small parameter and as $\epsilon \to 0$, we recover the linear stability problem. $\tilde{u}_i, \tilde{\theta}$ and $\tilde{\pi}$ can be expaned in a perturbation expansion in powers of ϵ, along with

$$\sigma = \sigma^{(0)} + \epsilon \sigma^{(1)} + \epsilon^2 \sigma^{(2)} + \dots \tag{22}$$

The results are that $\sigma^{(1)} = 0$ and $\sigma^{(2)} > 0$ for all three dimensional solutions - hence the only stable solutions are rolls. The observations are of rolls with a heat flux $\overline{w\theta} \sim \epsilon^2$.

2) Laboratory Experiments

2.1 Generation of Steady Mean Flows

Laboratory experimental data was shown in which steady finite amplitude rolls become unstable. After a number of transitions, cellular structure disappears completely and is replaced by transient randomly occurring plumes. This happens at $R \simeq 10^6$ for $Pr = 7$. When R is increased to 2×10^6, the randomly occurring plumes all develop a non-random tilt. If they tilt from lower left to upper right, hot plumes near the bottom boundary drift to the left and cold plumes near the top boundary drift to the right. If they tilt from lower right to upper left, hot plumes drift to the right, cold to the left. This is shown schematically in Figure 1. With tilted plumes, the Reynolds stress uw does not vanish upon horizontal averaging (as it would for upright cells). The turbulent velocity components were measured with a laser-velocity technique, and it was shown that the divergence of the Reynolds stress $\frac{\partial}{\partial z}\overline{uw}$ balances the viscous deceleration of a mean flow $\overline{u}$:

$$\frac{\partial}{\partial z}\overline{uw} = \nu \frac{\partial^2 \overline{u}}{\partial z^2} \tag{23}$$

Thus a large scale shearing flow $\overline{u}(z)$ has spontaneously formed. The only external forcing is still uniform and steady heating below, uniform and steady cooling above. This organized mean flow $\overline{u}(z)$ results from the Reynolds stress of the turbulent velocity transporting horizontal momentum up the mean velocity gradient. That such a phenomena can occur has been shown in a low order mathematical model which shows symmetry breaking bifurcations to tilted flows.

2.2 Laboratory Experiments: generation of low frequency oscillations

At $R > 10^7$ and $Pr = 7$ there is a new kind of organization in the form of travelling clusters of tilted plumes that results locally in long-period oscillations. The lecturer observed (i) space-time portraits of the flow, (ii) analyses of internal temperature time-series, and (iii) heat flux measurements, all in the Rayleigh number range $10^6 - 10^8$, with Prandtl number of 7. The first two types of observations give quantitative information about the frequencies, length scales, and speeds of the clusters. These observations showed that there are typically 5 to 10 transient tilted plumes in a cluster. Along a direction of travel of these clusters we see at any instant of time an alternating pattern of clusters of plumes, next to a quiescent region with almost no plumes, next to another cluster of plumes, etc. Along a 4 ft. line spanning the layer, there may be at any instant 3 to 4 clusters of plumes, each separated from the next by quiescent zones. At a fixed point near the bottom boundary, there is a high frequency (with periods on the order of 10 seconds) variation in temperature as the plumes within the cluster pass. The cluster passes in order 10^2 seconds. The quiescent epoch also lasts on the order of 10^2 seconds. Thus at a fixed point there is the high frequency variability associated with plumed passage and the low frequency variability associated with cluster passage. The data showed how these periods vary with Rayleigh and Nusselt numbers. Tests also were described to convince us that this low frequency oscillation was not inadvertently forced.

Finally, comparison is made with previous high Rayleigh number and small aspect ratio studies. In recent years there has been much discussion of "soft" and "hard" turbulence. For cells (i.e. containers) with aspect ratio $A = 1.0$ and $Pr \simeq 1$, there is a transition at $R \simeq 10^7$. Above this Rayleigh number it is found that:
    (i) there is a quasi-steady large scale flow;
    (ii) the probability density function of the mid-cell temperature is a double exponential;
    (iii) the scaling law for $N \propto R^\alpha$ has $\alpha = \frac{2}{7}$.
These constitute hard turbulence. Siggia(1994), however, points out that for other cells these three criteria do not onset together but occur singly, and that furthermore "the hard

regime is unlikely to be asymptotic." To add to the confusion, we are reporting here for our apparatus aspect ratio $A = 12$, $Pr = 7$, that:

(i) steady large flow sets in at $R = 2 \times 10^6$;

(ii) the probability density function approaches a double exponential at $R \simeq 7 \times 10^7$;

(iii) α is never $\frac{2}{7}$ for $R < 10^8$ (unless the $A = 12$ tank is partitioned into 144 cells each with $A = 1$).

The $N - R$ relationship with 144 cells of $A = 1$, $Pr = 7$ is

$$N = 0.148 \ R^{0.28} \tag{24}$$

in good agreement with previous investigations at $A \simeq 1$.

3) Scavenging Plume Model

Clusters of travelling tilted plumes have been observed moving past a fixed point in nearly periodic repetition. Although such regularity seemed strange in a turbulent flow, a "scavenging plume model" was presented which has such a periodic behavior. In this model, prior passage of a plume or cluster of plumes has depleted the thermal boundary layer in a history-dependent way: the boundary layer is very thin where the plume has just passed, but has had time to thicken where the plume passed some time ago. Thus at any moment there is a thermal boundary layer of varying thickness, and the pressure gradient in it drives a flow towards the thicker regions. Taking this to be slow viscous flow, there is then a shear and a down-gradient momentum flux at the wall. This boundary layer is supposed to erupt when and where its thickness reaches some critical value. Then, assuming that the interior momentum flux is entirely by Reynolds stresses, we can, by matching interior and boundary layer heat and momentum fluxes, show that plumes move away from regions of thick boundary layer at just such a rate that the ever-thickening boundary layer keeps the plume "fed" with buoyant fluid. The periodic recurrence at a fixed position is from the successive passage of clusters of plumes. The predicted period is shown to be in reasonable agreement with that obtained from the x,t photographs and the power spectra shown in (Krishnamurti, 1995).

A Galilean transformation is applied to the boundary layer shown in Figure 2:

$$x^* = x + U_0 t \tag{25}$$

$$z^* = z \tag{26}$$

$$t^* = t \tag{27}$$

$$u^* = u + U_0 \tag{28}$$

$$w^* = w \tag{29}$$

yielding:

$$\gamma w \partial_z u = r \partial_x h + \partial_{zz}^2 u \tag{30}$$

$$\partial_z w = 0 \tag{31}$$

for $\delta = h_c/l << 1$ and $\partial_t = 0$, and where $\gamma = w_o h_c/\nu$ (the Peclet number), $r/\delta = [g\Delta\rho h_c^3/\rho_0\nu^2]$ (the Rayleigh number), and h_c is the critical value of the height of the boundary layer for which it explodes into a plume. The boundary conditions on $z = 0$ are:

$$\partial_z u = M_0 + \gamma U_0 \tag{32}$$

$$w = 1 \tag{33}$$

where M_0 is the momentum in the rest frame. In the laboratory frame, $\partial_t h = w_0$. In the Galilean frame, $\partial_{t^*} h = w_0 - U_0 \partial_{x^*} h$. For $\partial_{t^*} = 0$:

$$\partial_{x^*} h = \frac{w_0}{U_0} \tag{34}$$

The interior of the flow is assumed to be homogeneous, incompressible, effectively inviscid but **not** necessarily irrotational. Vorticity ω is constant following material particles, so in a two dimensional flow $\omega = -\nabla^2\phi$. If this flow is steady, particle paths coincide with streamlines, and ω is constant on streamlines, i.e. $\nabla^2\phi = f(\phi)$. For an inviscid flow the vorticity distribution is arbitrary, so we can chose it to be proportional to ϕ:

$$\nabla^2\phi = -\beta^2\phi \tag{35}$$

The interior is then rotated and distorted so that the spaces between the plumes have right angles. This is shown in figure 3. Then the heat and momentum fluxes are matched between the boundary layer and the interior:

$$\frac{\tau^2}{4(sinh\beta l)^2}\left[\frac{\frac{1}{2}sinh(2^{1/2}\beta l)}{2^{1/2}\beta l} - 1\right] + \frac{\tau^2}{2} = U_0 w_0 + \mu M_0 \tag{36}$$

$$l = \left(\frac{g^* h_c^3}{\nu}\right)\frac{1}{w_0} \tag{37}$$

$$U_0 = \left(\frac{g^* h_c^2}{\nu}\right) \tag{38}$$

$$\tan\alpha = 1 \tag{39}$$

$$\text{Period} = \frac{l}{U_0} = \frac{h_c}{w_0} \tag{40}$$

α is the angle the plume makes with horizontal. μ is simply $\rho\nu$. τ is the mean velocity at which fluid flows up the plume.

Experimental evidence supports this model. Figure 4 shows how plumes move to the left (in the case shown) whilst growing upwards. At the bottom of the figure, the evolution of the boundary layer with time is depicted. Each box in the figure represents a parcel of fluid. The first number in each box represents the box's intial position. The second number records the time. At time 1, the box on the lower right has just moved out of the boundary layer because the height boundary layer just reached a value of h_c. At subsequent times, it moves up and slightly to the right in this frame of reference while other boxes to its left also come out of the boundary layer. By time 5, it is apparent that the boxes have formed a tilted plume.

4) References:

Chandrasekhar, S., 1961. *Hydrodynamic and hydromagnetic stability.* Claredon Press, 652pp.

Howard, L., and R. Krishnamurti, 1986. Large-scale flow in turbulent convection: a mathematical model. *J. Fluid Mech.*, **170**, 385-410.

Krishnamurti, R., and L. Howard, 1981. Large-scale flow generation in turbulent convection. *Proc. Natl. Acad. Sci. USA*, **78**, 4: 1981–1985.

Krishnamurti, R., 1995. Low frequency oscillations in turbulent Rayleigh-Benard convection. *Fluid Dynamics Research*, **16**, 87–108.

Malkus, W. and G. Veronis, 1960. Finite amplitude cellular convection. *J. Fluid Mech.*, **4**, 225–260.

Schlüter, A., Lortz, D., and F. Busse, 1965. On the stability of steady finite amplitude convection. *J. Fluid Mech.*, **23**, 129–144.

Spiegel, E. and G. Veronis, 1960. On the Boussinesq approximation for a compressible fluid. *Astrophysical Journal*, **131**, 442-447.

Notes submitted by Stephen Zatman and Jim Noyes

Figure 1

RAYLEIGH-BENARD CONVECTION

With no imposed shear, it develops its own shear via the Reynolds stress of tilted plumes

Hot

↓g

↓g

Hot

Upright Cells

$$\overline{uw} = 0$$

$\overline{u}$

Hot

Tilted Plumes

$$\overline{uw} \neq 0$$
(negative)
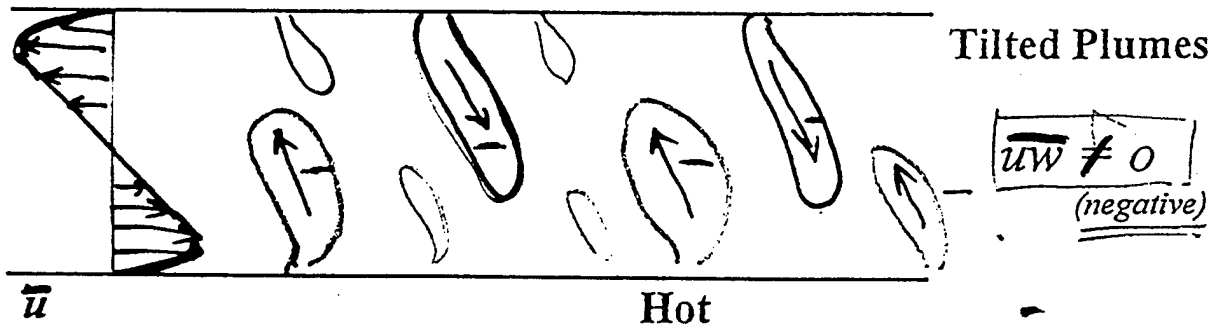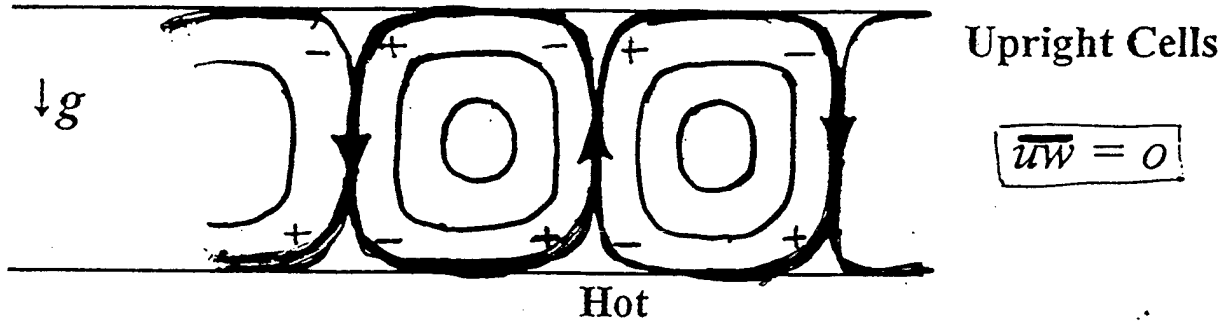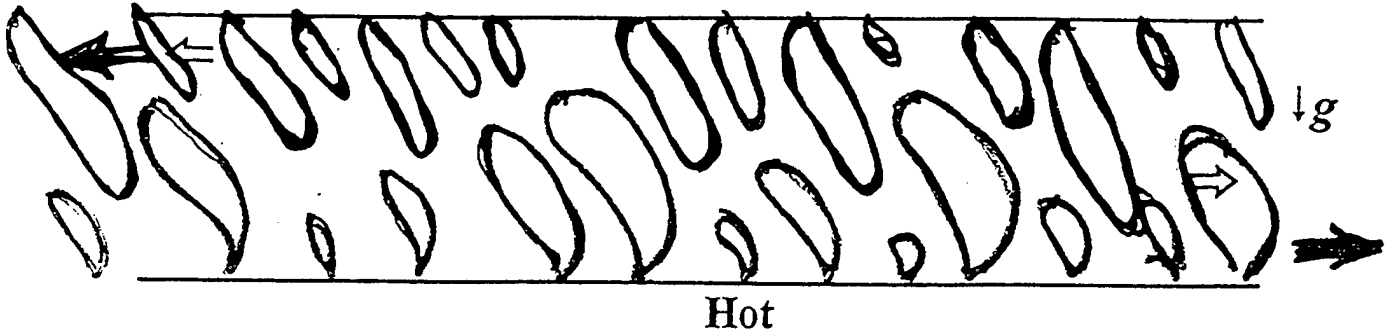
When Steady

First integral

$$\frac{\partial \overline{u}}{\partial t} + \frac{\partial \overline{uw}}{\partial z} = \upsilon \frac{\partial^2 \overline{u}}{\partial z^2}$$

$$\overline{uw} - \upsilon \frac{\partial \overline{u}}{\partial z} = M_o$$

Figure 2

$W_0, \rho_o - \Delta\rho$

$h(x, t_o + \Delta t)$

$h(x, t_o)$

PLUME 2
AT $t = t_o + \Delta t$

PLUME 2
AT $t = t_o$

PLUME 1
AT $t = t_o + \Delta t$

PLUME 1
AT $t = t_o$

Figure 3

AFTER GALILEAN TRANSFORMATION

INTERIOR $\nabla^2 \Psi = \beta^2 \Psi$

$z = h(x)$

BOUNDARY LAYER

PLUME L

R PLUME

α

Z

X, U$_0$

AFTER ROTATION

INTERIOR $\nabla^2 \Psi = \beta^2 \Psi$

L'

R'

h'

y'

X'

AFTER DISTORTION

INTERIOR

$$\left[\frac{\delta^2}{\delta\xi^2} + A\frac{\delta^2}{\delta\eta^2} + C\frac{\delta^2}{\delta\xi\delta\eta} - \beta^2 \right] \Psi = 0$$

L''

R''

h''

η

ξ
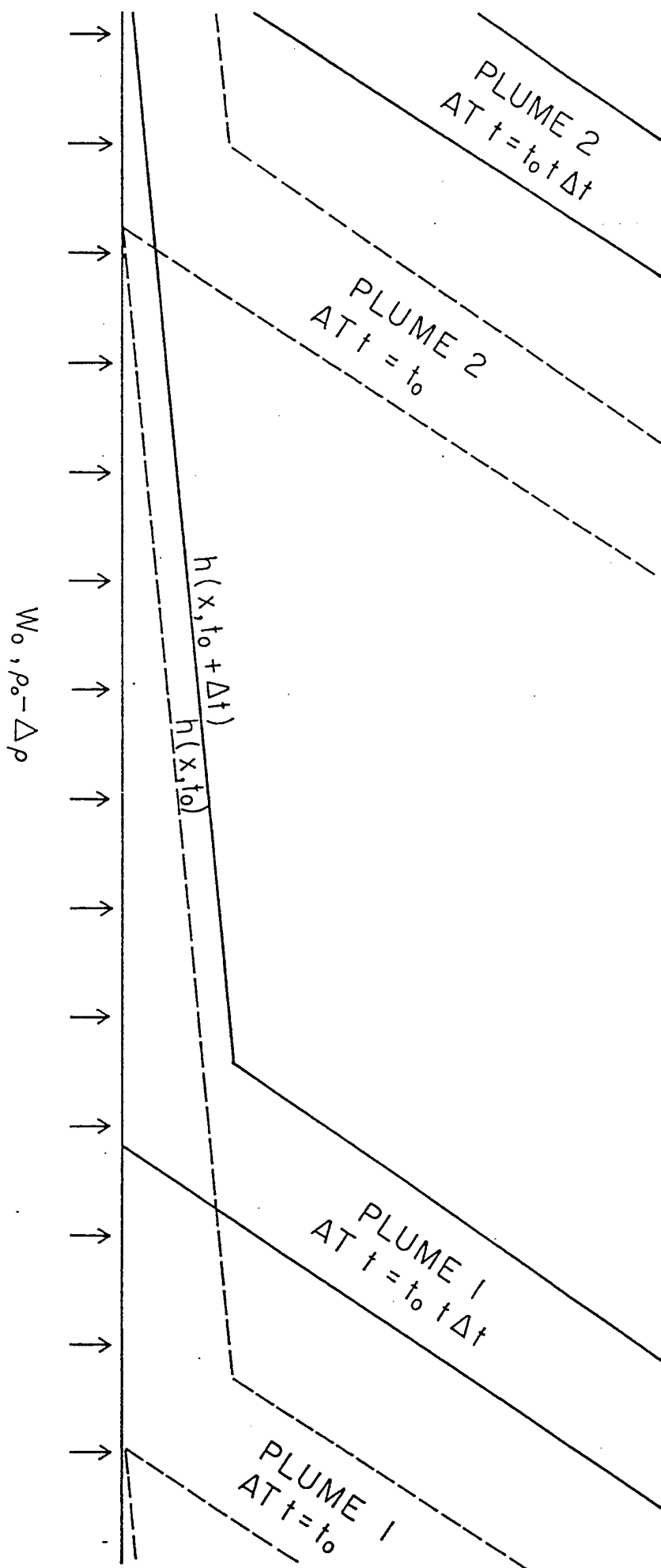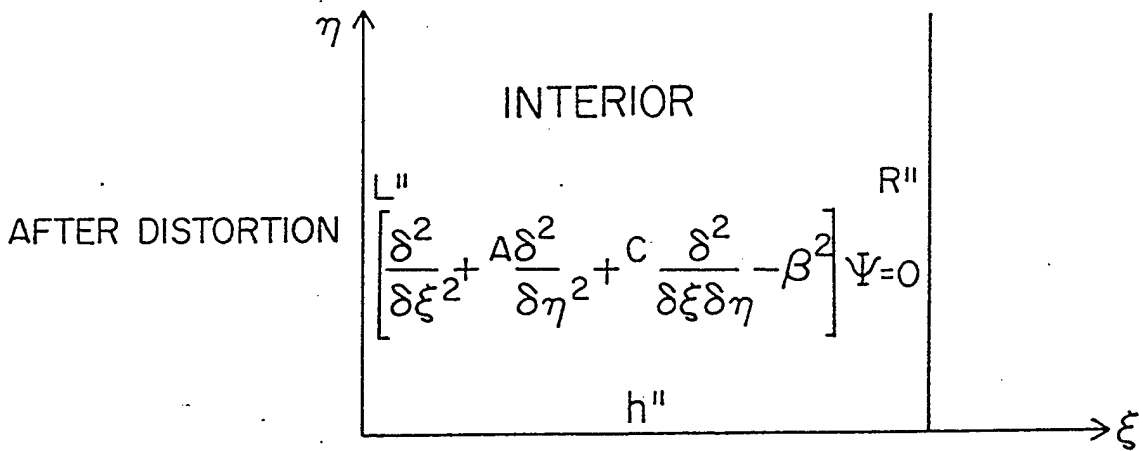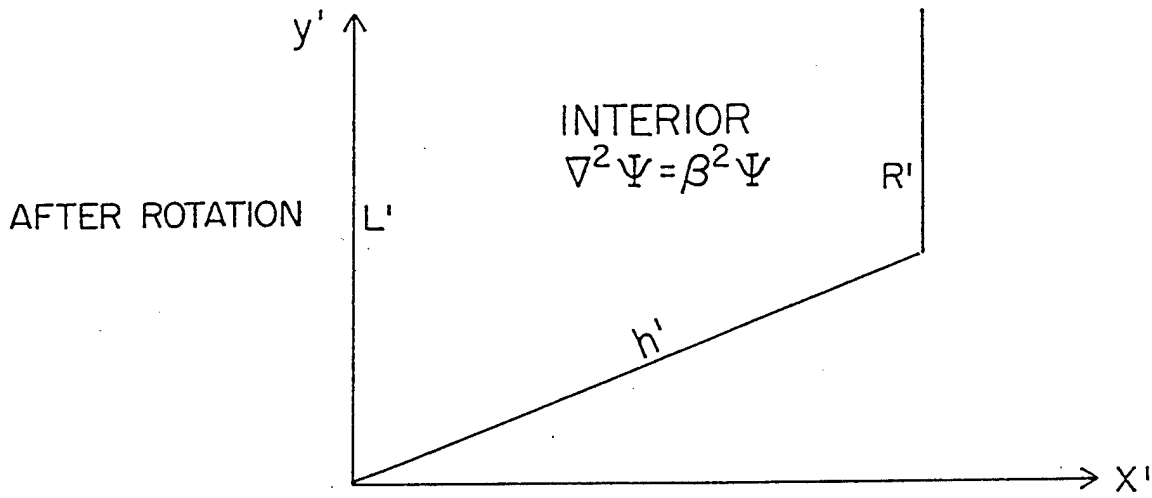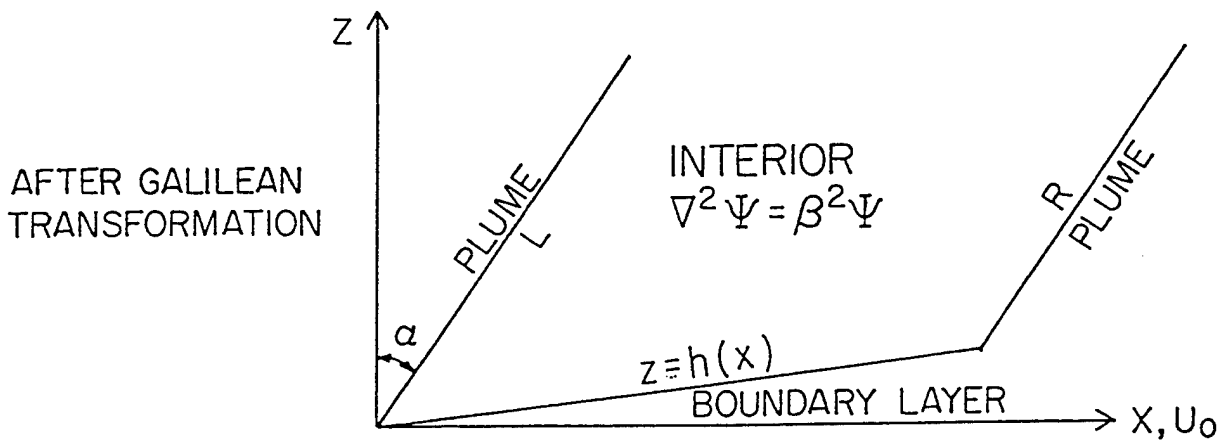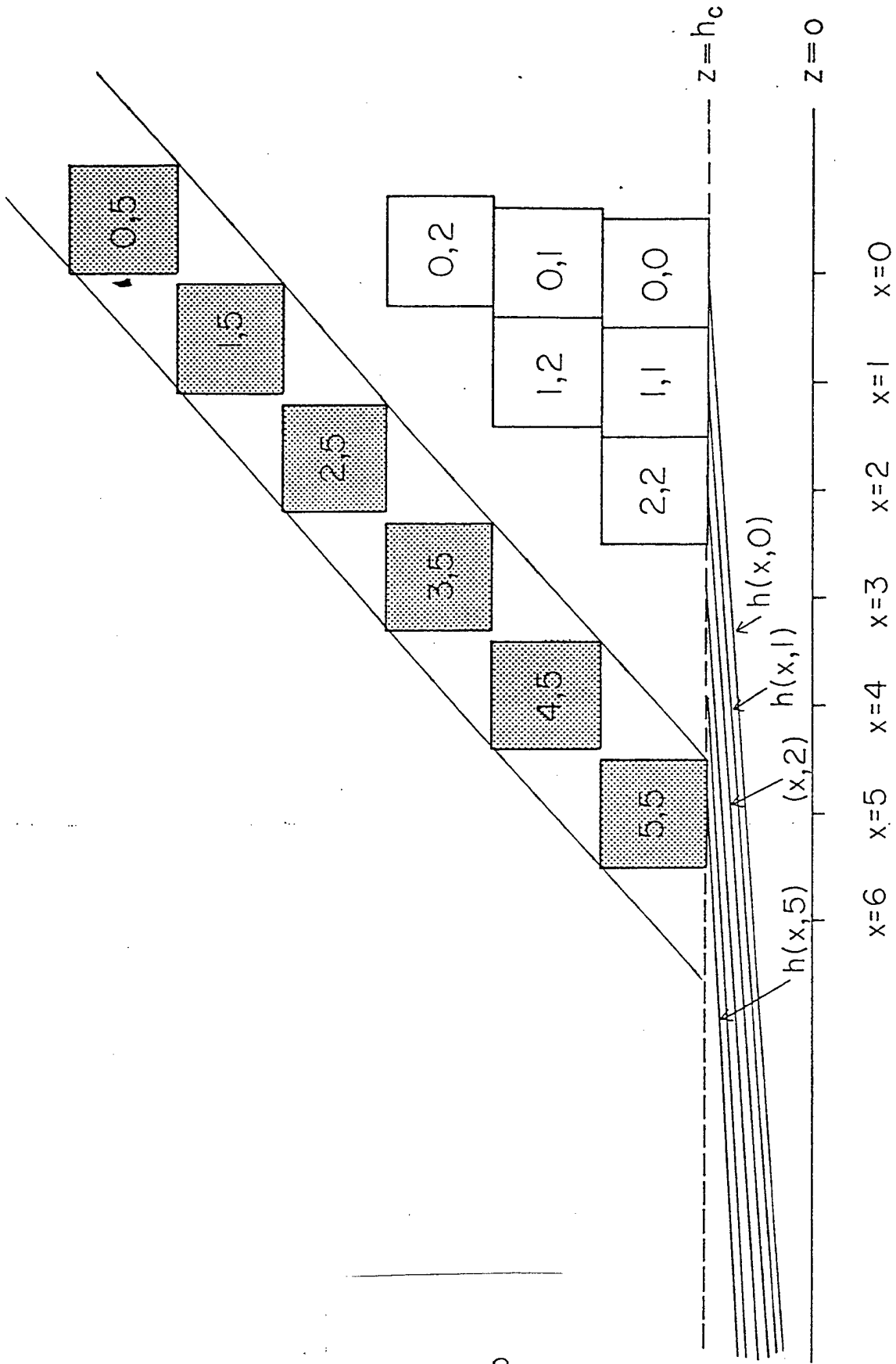
Figure 4

Lecture 2 : Rotation without Convection

1   Theoretical Background

In a rotating frame, the equation of motion is

$$\frac{\partial \mathbf{u}}{\partial t} + \mathbf{u} \cdot \nabla \mathbf{u} + 2\Omega \times \mathbf{u} = -\frac{\nabla p}{\rho} + \nu \nabla^2 \mathbf{u} \tag{1}$$

where $\mathbf{u}$ is the velocity, 2Ω is the planetary vorticity, p is the generalized pressure, ν is the kinematic viscosity and ρ is the fluid density. If the equations are scaled, one arrives at the non-dimensional equation

$$\frac{U}{\tau}\frac{\partial \mathbf{u}^*}{\partial t^*} + \frac{U^2}{L}\mathbf{u}^* \cdot \nabla^* \mathbf{u}^* + 2\omega U \Omega^* \times \mathbf{u}^* = -2\omega U \frac{\nabla^* p^*}{\rho} + \nu \frac{U}{L^2}\nabla^{*\,2}\mathbf{u}^* \tag{2}$$

Defining the frequency number, $F = \frac{1}{2\omega\tau}$, the Rossby number, $R_0 = \frac{U}{2\omega L}$, and the Ekman number, $E = \frac{\nu}{2\omega L^2}$, it is found for

$$F << 1, \ R_0 << 1, \ E << 1$$

that the equation of motion may be approximated by the geostrophic balance :

$$2\Omega \times \mathbf{u} = -\frac{\nabla p}{\rho} \tag{3}$$

Taking the curl of equation (3) gives the geostrophic vorticity equation:

$$\nabla \times (2\Omega \times \mathbf{u}) = -\nabla \times \left(\frac{\nabla p}{\rho}\right) \tag{4}$$

which expands to:

$$2\Omega \frac{\partial u}{\partial z} = -\frac{1}{\rho^2}\left[\frac{\partial p}{\partial z}\frac{\partial \rho}{\partial y} - \frac{\partial p}{\partial y}\frac{\partial \rho}{\partial z}\right] \tag{5}$$

$$2\Omega \frac{\partial v}{\partial z} = \frac{1}{\rho^2}\left[\frac{\partial p}{\partial z}\frac{\partial \rho}{\partial x} - \frac{\partial p}{\partial x}\frac{\partial \rho}{\partial z}\right] \tag{6}$$

$$2\Omega \frac{\partial w}{\partial z} = -\frac{1}{\rho^2}\left[\frac{\partial p}{\partial y}\frac{\partial \rho}{\partial x} - \frac{\partial p}{\partial x}\frac{\partial \rho}{\partial y}\right] \tag{7}$$

If the vertical pressure balance is hydrostatic then equations (5)-(7) can be rewritten as:

$$2\Omega\frac{\partial u}{\partial z} = \frac{g}{\rho}[\frac{\partial \rho}{\partial y} - \frac{\partial h}{\partial y}\frac{\partial \rho}{\partial z}] \tag{8}$$

$$2\Omega\frac{\partial v}{\partial z} = \frac{g}{\rho}[-\frac{\partial \rho}{\partial x} + \frac{\partial h}{\partial x}\frac{\partial \rho}{\partial z}] \tag{9}$$

$$2\Omega\frac{\partial w}{\partial z} = \frac{g}{\rho}[\frac{\partial h}{\partial y}\frac{\partial \rho}{\partial x} - \frac{\partial h}{\partial x}\frac{\partial \rho}{\partial y}] \tag{10}$$

where h describes the height to a density interface. Equations (8)-(10) are one formulation of the thermal wind equations.

For a homogeneous fluid, $\rho =$ constant everywhere, the thermal wind equations yield:

$$\frac{\partial u}{\partial z} = \frac{\partial v}{\partial z} = \frac{\partial w}{\partial z} = 0 \tag{11}$$

and using the boussinesq continuity equation, $\nabla.\underline{u} = 0$, gives :

$$\frac{\partial u}{\partial x} + \frac{\partial v}{\partial y} = 0 \tag{12}$$

These results are known as the Taylor-Proudman theorem and are interpreted to mean that for a slow, steady, inviscid flow of a barotropic fluid there are no variations in the velocity field parallel to the rotation vector. Equation (12) expresses that the flow is solenoidal in planes perpendicular to the rotation vector.

2   Experiments

Four experiments were performed to demonstrate rotational effects on fluid flows. The experiments were done in a cylindrical tank having a 20 cm diameter. The working fluid was water with a layer depth close to 20 cm. The tank revolved about a vertical axis once every 5 seconds so that the spin-up time, which is of the order of $E^{-\frac{1}{2}}$, was 100 seconds. Three spin-up times were allowed for the fluid to approach solid body rotation.

2.1   Experiment 1: Taylor Columns

The first experiment was an attempt to show Taylor columns. These columns occur in flow regimes where the Taylor-Proudman theorem is valid and a volume in the flow field is given a velocity perturbation. Because the Taylor-Proudman theorem allows no velocity deviations along the axis of rotation, a fluid volume that is perturbed will drag with it a column of fluid that spans the depth of the fluid layer. The reason for this phenomenon is that for slow, steady, nearly inviscid flows of a barotropic fluid there is no available mechanism to apply a torque to a fluid column. Therefore, the angular momentum of each fluid column will be preserved for all time. When a localized velocity perturbation is introduced to the fluid, the angular momentum

vectors in that fluid column will change unless the entire column moves with the perturbed region. Therefore, the vortex lines are fixed parallel to the rotation axis for Taylor-Proudman flows.

To visualize the columns, ground-up fish scales were placed in the water. The fish scales tend to mechanically align with shears in the flow, while, optically, the individual fish scales act as reflectors. Fish Scales randomly scatter light in a well mixed, calm fluid. The fluid appears a silver color and has an optical depth of approximately 5 cm. Local shears in the fluid align the scales, changing the optical properties radically in these regions to reveal the flow. The fish scales will either strongly reflect light or let all the light pass depending on the angle between the observer and the light source.

A slightly buoyant float with a characteristic length scale of 2 cm was placed in the solid body flow. If the float is in very slow relative motion with the fluid in the tank, a Taylor column will be visible in light reflected off the fish scales. This did not occur in the experiment. Instead, curtains of sheared fluid were seen to extend to the bottom of the tank and these curtains did not form a cylinder around the float. This result occurred because the float was introduced into the water at a relative velocity too large for Taylor columns to form. Even though the Rossby number was not small enough for Taylor columns to form, the formation of full layer depth curtains revealed the two dimensionality of the rotation dominated flow.

2.2 Experiment 2: Taylor Columns Revisited

The second experiment also looked for Taylor column formation. In this set-up a small cylinder of diameter and height of about 4 cm was placed on the bottom of the tank. Wires were placed above each other at three different heights in the layer. The plane of the wires did not intersect the cylinder and the lowest of the wires was situated well above the top of the cylinder.

The water in the tank contained thymol blue, a pH indicator, which changes to a deep blue color when the pH of the fluid is increased (D.J. Baker, *JFM* (1966), **26**). By passing a current through the wires the local pH changed enough for the surrounding fluid to turn blue.

After allowing for spin-up, the speed of the tank was slightly decreased. This caused the fluid to rotate faster than the wires and the cylinder. When the blue fluid was advected through the region above the cylinder, it wrapped around the region instead of passing through it. This effectively demonstrated the existence of Taylor columns.

2.3 Experiment 3: Geostrophic Adjustment

The third experiment involved geostrophic adjustment of a baroclinic vortex (P.M. Saunders, *JPO* (1973)). The apparatus consisted of a 5 cm diameter, open-ended cylinder being placed in the center of the tank. The tank was filled with fresh water while the cylinder was filled with salt water with a 2 percent density jump.

After solid body rotation had been established, the inner cylinder was pulled out of the tank. In a non-rotating fluid layer the denser fluid would all settle to the bottom of the tank. Here, the settling is resisted by the Coriolis force. At the bottom of the tank, the dense fluid pushes outward and is deflected into a clockwise rotation as it spreads outwards. Lighter fluid flows inwards to replace denser fluid at the top of the tank and is deflected into a counterclockwise rotation. This thermal wind flow is able to restore the sloping interface so that the cone of denser fluid is supported by the rotation.

The radius that the fluid flows out to is approximated by the Rossby radius of deformation, L_ρ, which describes the inner length scale at which rotational effects become relevant with respect to stratification. In this experiment the Rossby radius is defined as

$$L_\rho = \frac{\sqrt{g'H}}{f}$$

where g' is the effective gravity in the two layer system, H is the depth of the layer and f is the Coriolis parameter. For a fluid depth of 15 cm and a rotational period of 5 seconds the Rossby radius is about 6 cm. Upon removing the inner cylinder, two cones formed with radii approximating the Rossby radius. The break up of the vortex into two cones may have been due to baroclinic instability or this could have been caused by perturbations to the system upon removing the cylinder.

2.4 Experiment 4: Rotating Convection

The final experiment featured the same apparatus as the previous one except that the two fluids were different. The outer fluid was salt water while the inner cylinder was filled with a starch suspension in water.

Ideally, the well mixed starch suspension initially slumps into a thermal wind supported cone because its density is greater than that of the surrounding salt water. The starch slowly settles out of suspension leaving buoyant fresh water at the top of the cone. The fresh water layer becomes buoyantly unstable and plumes ascend through salt layer. These ascending plumes will generate vorticity as they accelerate upwards via vortex stretching as

$$\frac{\partial \omega}{\partial t} = \Omega . \nabla \mathbf{u}$$

where ω represents the vorticity vector of the parcel. Therefore, the plume will rise in a right-handed helix up through the layer.

When the experiment was performed, the starch settled in the time it took to spin-up the fluids. An attempt was made to stir the starch back into suspension prior to removing the cylinder, but this proved ineffective. The starch and the water remained separated and the fresh water layer rose en masse. The helical motions of the outermost plumes were still easily visible.

Lecture written-up by Jonathan Aurnou and Helene Banks.

Lecture 3: Stability of Rotating Convection

Introduction

This lecture will consider the stability of rotating convection. As an introduction, a simple laboratory experiment is performed showing the effect of rotation on convection. A theoretical model of the transition to turbulence in a rotating fluid layer is then discussed. Finally, recent laboratories experiments are presented, illustrating the transition to turbulence.

1 Convection with and without rotation

A simple introduction to the effects of rotation on convection was given by considering different convective mechanisms in the rotating and non-rotating case. Warm water was poured in a cylindrical tank which had an aluminum plate, which had been preheated, at the bottom overlaying an insulating one. Evaporation at the surface of the tank causes a net heat flux out, thus cooling the surface water and causing convection to take place. The experiment was performed both in the rotating and in the non-rotating case. In the non rotating case, the convective processes occur in the form of large convective cells as well as small scale turbulence. In the rotating case, on the other hand, the blue-dye emphasized the smaller scale convective spirals that formed all the way to the bottom of the tank.

In this simple experiment, scaling of the parameters shows that given a tank with a diameter, $d \sim 20cm$, a difference in temperature, $\Delta T \sim 10^{\circ}C$ then the Rayleigh number, $Ra = \frac{g\alpha\Delta T d^3}{\kappa\nu} \sim 1.1 \times 10^9$. The Taylor number for this experiment is given by $\tau^2 = \frac{4\Omega^2 d^4}{\nu^2} \sim 6 \times 10^9$.

2 Stability of Rotating Convection

2.1 Stability of non-rotating convection

The stability of convection in a non-rotating regime and the transition to turbulence have received a great deal of attention in the fluid dynamics literature. It may be worth mentioning a few works that are of relevance to this lecture. Schlüter et al.(1965) present a theory for the stability of finite amplitude solutions in the infinite Prandtl number regime for the case of an infinite layer of unstably stratified fluid, due to either cooling at the surface or heating at the bottom. They find that all three dimensional flows are unstable to infinitesimal disturbances, whereas the stability of two-dimensional flows depends both on the convection cells' wavelength and on the wavelength of the disturbance. Laboratory experiments confirm these results, introducing a dependence on the Prandtl number, (see, for example, Krishnamurti,1970a,1970b), as well as the recognized Rayleigh number dependence. More complex forms of instabilities at high Prandtl number are identified by Busse and Whitehead (1971) who study the stability of convective rolls with varying wavenumber. Two regimes are found which involve the bending of rolls and the cross-roll instability, where rolls develop at right angles to the original rolls.

2.2 Stability of rotating convection Küppers-Lortz Instability

The stability analysis of Schlüter *et al.*(1965) mentioned above was expanded by Küppers and Lortz(1969) to include the effects of rotation. The equations can be rewritten in terms of three non-dimensional parameters: the Rayleigh, Prandtl and Taylor numbers. The stability calculation yields the following results:

1. There exist stable small-amplitude rolls for the slightly super-critical Rayleigh number regime, provided $\tau^2 < \tau_c^2$ where $\tau = \frac{2\Omega d^2}{\nu}$. All three-dimensional flows are unstable.

2. For $\tau^2 > \tau_c^2$, no stable convective flow exists for slightly supercritical Rayleigh number, i.e. all flows are necessarily time-dependent.

Figure 1 from Küppers-Lortz shows these results. For the case studied, $Pr = \infty$, they show that given a Taylor number, there are no steady-state solutions in Rayleigh sub-critical regime $(R_c = R_c(\tau))$. Thus for a given $\tau > \tau_c$, if the Rayleigh number is increased from a subcritical value, then there is a transition from pure conduction to a time-dependent convective flow. For $\tau < \tau_c$, the only stable flow in the form of rolls has maximum amplitude for a certain Rayleigh number.

3 Unsteady Turbulent Convection

In the ocean, convective turbulent plumes may develop as a consequence of brine-rejection during ice-formation or of intensive cooling at the surface. Different scenarios arise depending on whether the plumes sense rotation before or after they reach the bottom (for example in the open-ocean in contrast with the shelf regions). A laboratory experiment result is presented to illustrate unsteady turbulent convection in a homogeneous rotating fluid (Maxworthy and Narimousa, 1994). Two different cases are presented: a laterally confined experiment and an unconfined one. A source of saltier, denser water is placed at the surface of a water column that is in solid body rotation with the tank. This results in a 3D turbulent front propagating downward. At a depth $z = z_c$, the front starts sensing rotational effects and many quasi-2D vortices develop.

Confined experiment

In this experiment the source covers the whole surface of the tank. The 2D vortex structures described above, penetrate downward (below the mixed layer) to produce vortex columns that eventually fill up the rest of the tank. Measurements for the transition layer depth, the mean-diameter, the downward propagation speed and the maximum swirl velocity of the vortex columns agree with scaling presented in previous papers, see for example Maxworthy and Narimousa (1994).

Unconfined experiment

In this experiment the buoyancy source covers only a small portion of the tank. Initially the flow develops in the same manner as in the above experiment. The vortex columns 'fill out' after reaching the bottom and begin to tilt until the whole column becomes baroclinically unstable. Baroclinic vortices form and propagate away. Evidence is also provided for the spreading of the convective layer near the bottom of

the tank. Figure 2 shows a schematic of the process.

Two cases were considered in the 'closed boundary experiment: $z_c < H$ and $z_c > H$, where H is the depth of the tank. In the first case, quasi-2D vortices develop at the base of the 3D turbulence region, and propagate downward until they reach the bottom of the tank. As the vortex columns begin to fill out, they form this truncated-cone which is shown in the diagram. This is the structure that then becomes baroclinically unstable, forming eddies which propagate away from the region. In the case $z_c > H$, the turbulent mixed layer reaches the bottom. It then forms a gravity current which spreads on the bottom and is then deflected by rotation.

In Maxworthy and Narimousa's scaling laws, a determinant parameter is the *natural* Rossby number (a Rossby number where the velocity is taken to be the swirling velocity of the plumes), $R_o^* = [B_o/f^3 H^2]^{1/2}$, where B_o is the surface buoyancy flux. In the unconfined experiment, the vortex columns scaled according to the law $D/H \sim R_o^{*1/2}$, where D is the diameter, and the columns extended throughout the depth of the tank (case $H < z_c$). In the case $z_c > H$, the baroclinic vortices formed at the edge of the of the spreading front scaled according to $D/H \sim R_o^{*2/3}$. The transition depth z_c is experimentally found to be $\approx (12.7 \pm 1.5)(B_o/f^3)^{1/2}$.

There are a number of numerical experiments which illustrate the process of convection in the presence of rotation. Amongst these, Jones and Marshall, 1993, use a non-hydrostatic numerical model to study the convective overturning of a homogeneous rotating ocean. The numerical results show a fairly good agreement with the laboratory case, for small values of R_o^*, together with an overall qualitative agreement. For a discussion of the discrepancies see Maxworthy and Narimousa (1994).

NOTES SUBMITTED BY FIAMMA STRANEO + PAUL DELLAR

References

Busse, F.H., Whitehead, J.A. 1971: Instability of convection rolls in a high Prandtl number fluid. J. Fluid Mech., 47, 305-320.

Jones, H., Marshall, J. 1993, Convection with rotation in a neutral ocean: A study of open-ocean convection, J. Phys. Ocean., 23, 1009-1039.

Krishnamurti, R. 1970a: On the transition to turbulent convection. Part I. Transition from two to three-dimensional flow. J. Fluid Mech., 42, 295-307.

Krishnamurti, R. 1970b: On the transition to turbulent convection. Part II. Transition to time-dependent flow. J. Fluid Mech., 42, 309-320.

Küppers, G., Lortz, D. 1969: Transition from laminar convection to thermal turbulence in a rotating fluid layer. J. Fluid Mech., 35, 609-620.

Maxworthy, T., Narimousa, S. 1994: Unsteady, turbulent convection into a homogeneous, rotating fluid, with oceanographic applications. J. Phys. Ocean., 24, 865-887.

Schluter, A., Lortz, D., Busse, F.H. 1965: On the stability of finite amplitude convection. J. Fluid Mech., 23, 129-144.

τ^2

10^4

$5 \cdot 10^3$

τ_c^2

10^3

NO
STABLE
STEADY
ROLLS

0   45° α_c 90°

$\rightarrow \alpha$
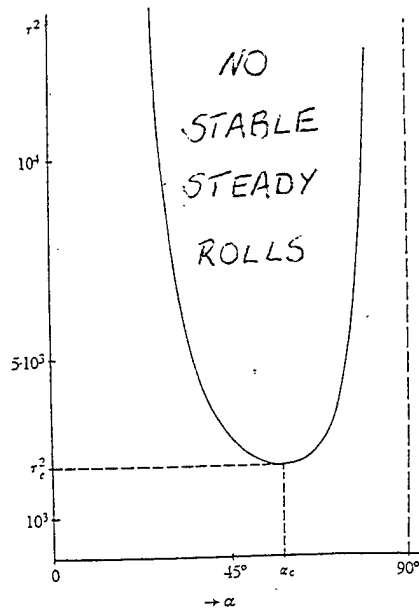
FIGURE 1. τ^2, Taylor number; α, angle between the two k-vectors. In the convex domain rectangles do not exist and rolls are unstable.

$u_f \sim (B_0 z_f)^{1/3}$

$q_f' \sim \left(\dfrac{B_0^2}{z_f}\right)^{1/3}$

$t < \dfrac{1}{f}$

Entrainment

$\dfrac{H}{u_v} > t > \dfrac{1}{f}$

$D_v \sim \left(\dfrac{B_0}{f^3}\right)^{1/2}$ $u_v \sim \left(\dfrac{B_0}{f}\right)^{1/2}$

Ambient entrainment

a)

b)

$g' \sim (B_0 f)^{1/2}$

$t > \dfrac{H}{u_v}$

R

Cyclonic

Anticyclonic

c)

d)
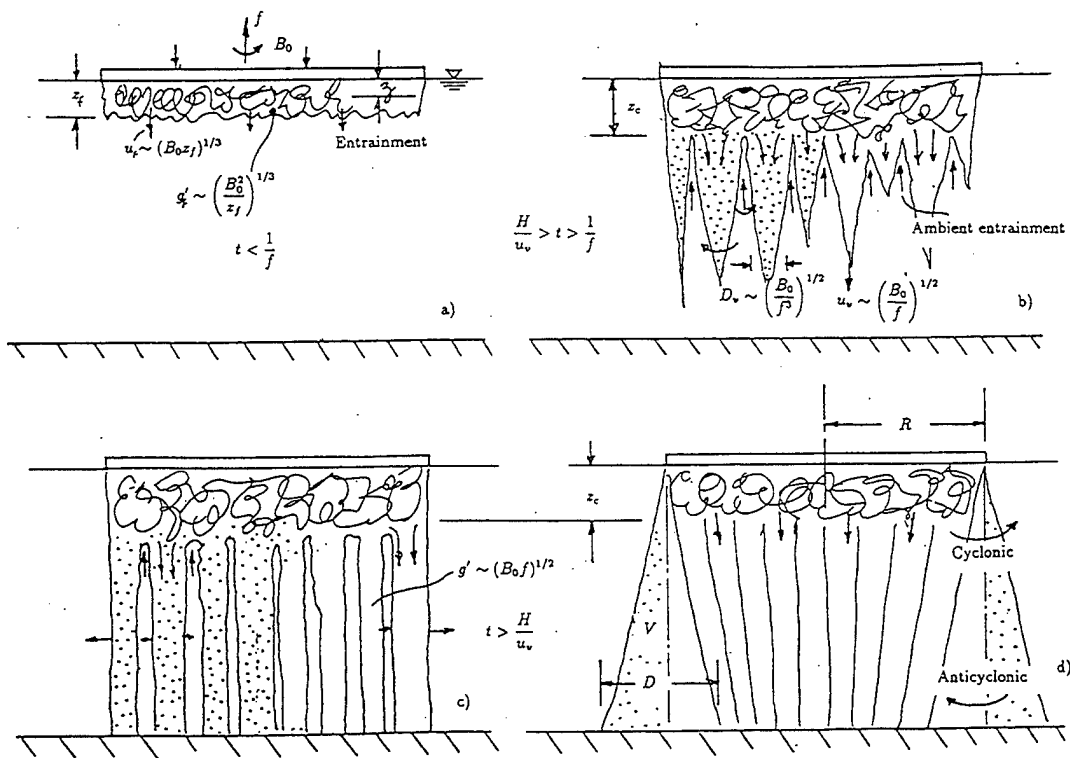
FIG. 10. Schematic of the sequence of events that occurs after a negative buoyancy flux is started into a rotating fluid, for the case when rotation influences the turbulence during its evolution under the source. The indicated scaling of the various parameters is explained in the text (section 4). (a) For time t less than $1/f$. (b) After rotation influence the turbulence but before the latter reaches the bottom. (c) Filling and tilting of the vortex structures after interaction with the bottom. (d) Generation of baroclinically, unstable eddies from the conical density field under the source.

MAXWORTHY AND NARIMOUSA (1994)

Finite amplitude cellular convection in a rotating fluid

George Veronis,   21st June 1995

We consider a layer of fluid confined between two horizontal parallel plates in a rotating frame. The governing equations for the Boussinesq limit and a linear equation of state are

$$\frac{\partial T}{\partial t} + \mathbf{v}\cdot\nabla T = \kappa\nabla^2 T$$

$$\frac{\partial \mathbf{v}}{\partial t} + \mathbf{v}\cdot\nabla\mathbf{v} + 2\Omega\times\mathbf{v} = -\frac{1}{\rho_m}\nabla p - g\frac{\rho}{\rho_m}\hat{\mathbf{z}} + \nu\nabla^2\mathbf{v}$$

$$\rho = \rho_m(1 - \alpha T) \quad \text{and} \quad \nabla\cdot\mathbf{v} = 0$$

We adopt boundary conditions in which the temperature T is specified on the upper and lower boundaries, on which the normal velocity w also vanishes. For simplicity, we assume 'slippery' or stress-free boundaries on which the normal stresses νu_z and νv_z vanish. With these boundary conditions the equations admit a basic state solution characterised by no motion, hydrostatic equilibrium and a linear temperature field

$$\mathbf{v} = 0, \quad \frac{\partial p}{\partial x} = \frac{\partial p}{\partial y} = 0, \quad \frac{\partial p}{\partial z} = -g\rho, \quad T = T_b + \Delta T(1 - z/d)$$

It is convenient to separate the temperature field into this basic linear profile plus a perturbation, and to rescale the equations based on the layer depth d, applied temperature difference ΔT, and diffusion timescale d^2/κ

$$T = T_b + \Delta T(1 - z/d) + \theta(x, y, z, t)$$

$$\nabla = (1/d)\nabla', \qquad t = (d^2/\kappa)t', \qquad \theta = \Delta T\theta'. \qquad \mathbf{v} = (\kappa/d)\mathbf{v}'. \qquad p = (\nu\kappa\rho_m/d^2)p'$$

In these new variables the equations take the form

$$\sigma^{-1}(\frac{\partial \mathbf{v}'}{\partial t'} + \mathbf{v}'\cdot\nabla'\mathbf{v}') + \mathcal{T}\hat{\mathbf{z}}\times\mathbf{v}' = -\nabla'p' + R\theta'\hat{\mathbf{z}} + \nabla'^2\mathbf{v}'$$

$$\frac{\partial \theta'}{\partial t'} - w' + \mathbf{v}'\cdot\nabla'\theta' = \nabla'^2\theta'$$

$$\nabla\cdot\mathbf{v}' = 0$$

where we have introduced three dimensionless parameters, the Prandtl number σ, the Taylor number $\mathcal{T}$, and the Rayleigh number R.

$$\sigma = \nu/\kappa, \qquad \mathcal{T}^{1/2} = (2\Omega d^2)/\nu, \qquad R = (g\alpha\Delta T d^3)/(\nu\kappa)$$

We now eliminate the pressure term by taking the curl of the momentum equation twice. Introducing the vertical vorticity ζ and collecting nonlinear terms on the right hand side we obtain

$$(\frac{1}{\sigma}\frac{\partial}{\partial t} - \nabla'^2)\nabla'^2 w + \mathcal{T}\zeta_z - R\nabla_1^2\theta = \mathcal{L}/\sigma$$

$$(\frac{1}{\sigma}\frac{\partial}{\partial t} - \nabla'^2)\zeta + \mathcal{T}w_z = -\mathcal{Z}/\sigma$$

$$\zeta = (\nabla\times\mathbf{v})\cdot\hat{\mathbf{z}} = v_x - u_y, \qquad \nabla_h^2 = \partial_x^2 + \partial_y^2$$

$$\mathcal{L} = \partial_x(\mathbf{v}\cdot\nabla u) + \partial_y(\mathbf{v}\cdot\nabla v) - \nabla_h^2(\mathbf{v}\cdot\nabla w), \qquad \mathcal{Z} = \partial_x(\mathbf{v}\cdot\nabla v) - \partial_y(\mathbf{v}\cdot\nabla u)$$

Linear Stability

Assuming solutions of the form $w_o = e^{\lambda t}f(x,y)g(z)$ where $f(x,y)$ satisfies $\nabla_h{}^2 f = -\pi^2\alpha^2$, and discarding the nonlinear terms $\mathcal{L}$ and $\mathcal{Z}$ on the assumption that w_o is small, we can obtain a single linear equation for w_o

$$(\frac{1}{\sigma}\frac{\partial}{\partial t} - \nabla^2)^2(\frac{\partial}{\partial t} - \nabla^2)\nabla^2 w_o + \mathcal{T}^2(\frac{\partial}{\partial t} - \nabla^2)w_{ozz} - (\frac{1}{\sigma}\frac{\partial}{\partial t} - \nabla^2)R_o\nabla_h{}^2 w_o = 0$$

where R_o denotes the Rayleigh number for the linear stability problem. The boundary conditions $\theta_o = 0, w_o = 0$ and $u_{oz} = v_{oz} = 0$ imply all even derivatives $w_{ozz} = w_{ozzzz} = \dots = 0$ on the boundaries. Thus we may take $g(z) = \sin(n\pi z)$ as a solution, giving the following cubic dispersion relation for the growth rate λ

$$(\alpha^2 + n^2)[\lambda + \pi^2(\alpha^2 + n^2)]\left[\frac{\lambda}{\sigma} + \pi^2(\alpha^2 + n^2)\right]^2 + \mathcal{T}^2 n^2[\lambda + \pi^2(\alpha^2 + n^2)]$$

$$- \alpha^2 R_o\left[\frac{\lambda}{\sigma} + \pi^2(\alpha^2 + n^2)\right] = 0.$$

Exchange of stability

When the growth rate $\lambda = 0$ we obtain

$$\frac{R_o}{\pi^4} = \frac{(\alpha^2 + n^2)^3 + \mathcal{T}_1{}^2 n^2}{\alpha^2} \qquad \text{where } \mathcal{T}_1{}^2 = \mathcal{T}^2/\pi^4$$

The critical Rayleigh number R_{min} occurs when $\frac{\partial R_o}{\partial\alpha} = 0$, at the roots of the cubic

$$2\alpha^6 + 3\alpha^4 n^2 - n^2 - \mathcal{T}_1{}^2 n^2 = 0.$$

In the limit $\mathcal{T} \to \infty$, corresponding to strong rotation,

$$\alpha^2 \sim (\frac{1}{2}\mathcal{T}_1{}^2 n^2)^{1/3} \qquad R_{min} \sim 3\pi^4(\frac{1}{2}\mathcal{T}_1{}^2 n^2)^{2/3} \qquad (*)$$

As $\mathcal{T}$ increases the horizontal wavenumber α increases so the cellular diameter decreases. Note, however, that the wavelength in the direction of fluid flow remains unchanged (see figure 2) but the cells become tilted so the projected wavelength becomes shorter (corresponding to larger α). The smallest value of R_{min} occurs when $n = 1$. Notice that since $\mathcal{T}_1{}^2 \propto \nu^{-2}$, both R_{min} and the corresponding ΔT decrease as ν increases. Thus *viscosity is destabilising* in the asymptotic limit of strong rotation ($\mathcal{T} \to \infty$) !

Time dependent solution (overstability)

In a rotating system ($\mathcal{T} > 0$) the cubic equation for λ may have complex roots. The cubic's coefficients are all real so the roots must be of the form λ' and $\lambda_r \pm i\lambda_i$. Overstability occurs when $\lambda_r = 0$, for which the cubic takes the form

$$\lambda^3 - \lambda'\lambda^2 + \lambda_i^2\lambda - \lambda'\lambda_i^2 = 0$$

Notice that the constant term equals the product of the coefficients in the λ and λ^2 term. Thus

$$\frac{R_o}{\pi^4} = 2(\sigma + 1)\frac{[(\alpha^2 + 1)^3 + \frac{\sigma^2}{(\sigma+1)^2}\mathcal{T}_1^2]}{\alpha^2}$$

and the minimum Rayleigh number is attained when

$$2\alpha^6 + 3\alpha^4 = 1 + \frac{\sigma^2}{(\sigma + 1)^2}\mathcal{T}_1^2$$

A necessary condition for real λ_i is

$$\mathcal{T}_1^2 \geq \frac{\sigma + 1}{1 - \sigma}(\alpha^2 + 1)^3$$

Notice also that $\alpha \to \infty$ as $\sigma \to \sqrt{2/3}$ so overstability, at least in this horizontally infinite system, can only occur when the Prandtl number $\sigma < \sqrt{2/3}$. As $\mathcal{T}_1 \to \infty$,

$$\alpha^2 \sim 2^{-1/3}\left[\frac{\sigma\mathcal{T}_1}{1 + \sigma}\right]^{2/3} \qquad \text{and} \qquad \frac{R_{\min}}{\pi^4} \sim 2^{1/3} \cdot 3\frac{(\nu + \kappa)^{1/3}}{\kappa}\left[\frac{2\Omega d^2}{\pi^2}\right]^{2/3}$$

Thus κ is destabilising but ν is now stabilising.

Strongly rotating convection

In this section we rederive the conclusion of the section 'Exchange of stabilities' using an entirely different approach. Rescaling the governing equations based on the layer depth d and an arbitrary velocity scale V,

$$\mathbf{v} = V\mathbf{v}', \qquad p = d\rho_m\Omega V p', \qquad t = (d^2/\nu)t', \qquad \nabla = (1/d)\nabla', \qquad T = (d\Delta T/\kappa)VT'$$

and introducing the Ekman number, $E = \nu/(\Omega d^2) = (2\mathcal{T})^{-1}$, we obtain

$$E\frac{\partial\mathbf{v}'}{\partial t} + 2\hat{\mathbf{z}}\times\mathbf{v}' = -\nabla'p' + RET'\hat{\mathbf{z}} + E\nabla'^2\mathbf{v}', \qquad \sigma\frac{\partial T'}{\partial t} - w' = \nabla'^2 T', \qquad \nabla\cdot\mathbf{v}' = 0$$

As the Ekman number $E \to 0$ the momentum equation reduces to the thermal wind equations for geostrophic balance. Guided by the existence of Stewartson layers of width $O(E^{1/3})$ we assume a horizontal wavenumber $k \sim E^{-1/3}$ and an $O(1)$ vertical lengthscale and perform an expansion in powers of $E^{1/3}$.

$$R \sim E^{-4/3}R_0, \qquad k \sim E^{-1/3}k_0, \qquad u', v' \sim E^0, \qquad T' \sim E^{2/3}$$

$$(u', v', w') = \sum_{n=0}^{\infty} E^{n/3}(u_n, v_n, w_n), \qquad p' = E^{1/3}\sum_{n=0}^{\infty} E^{n/3}p_n, \qquad T' = E^{2/3}\sum_{n=0}^{\infty} E^{n/3}T_n$$

At leading order we recover the geostrophic balance equations

$$-2v_o = -\frac{\partial p_o}{\partial x}, \qquad 2u_o = -\frac{\partial p_o}{\partial y}, \qquad \frac{\partial u_o}{\partial x} + \frac{\partial v_o}{\partial y} = 0 \qquad (1a,b,c)$$

together with

$$\frac{\partial p_o}{\partial z} = R_o T_o - k_o^2 w_o, \qquad w_o = k_o^2 T_o \qquad (2a,b)$$

At next order, $O(E^{1/3})$, we obtain

$$-2v_1 = -\frac{\partial p_1}{\partial x} + \nabla_h^2 u_o, \qquad 2u_1 = -\frac{\partial p_1}{\partial y} + \nabla_h^2 v_o, \qquad \frac{\partial u_1}{\partial x} + \frac{\partial v_1}{\partial y} + \frac{\partial w_o}{\partial z} = 0 \quad (3a,b,c)$$

Eliminating p_1 between the horizontal momentum equations $(3a, b)$ and substituting into the continuity equation $(3c)$ yields

$$2\left(\frac{\partial u_1}{\partial x} + \frac{\partial v_1}{\partial y}\right) = \nabla_h^4 p_o = k^4 p_o, \qquad w_{oz} = -\frac{1}{4}k_o^4 p_o$$

Substituting these equations into the leading order heat equation $(2a, b)$ we finally obtain,

$$-\frac{4}{k_o^2}T_{ozz} = (R_o - k_o^4)T_o$$

Assuming solutions of the form $T_o \propto \cos(k_o x)\cos(\pi z)$ and minimising over wavenumbers k_o we obtain

$$R_{\min} = 3 \cdot 2^{2/3}\pi^{4/3}\left(\frac{\Omega d^2}{\nu}\right)^{4/3}$$

which is precisely the same as $(*)$ at the end of the earlier section 'Exchange of stabilities'. Thus we can successfully treat convection as a perturbation to a rotating system, as well as vice versa.

References

VERONIS, G. 1959, *Finite amplitude cellular convection in a rotating fluid*, J. Fluid Mech. **5** pp 401-435

STEWARTSON, K. 1957, *On almost rigid rotations*, J. Fluid Mech. **3** pp 17-26

CHANDRASEKHAR, S. 1953, *The instability of a layer of fluid heated from below and subject to Coriolis forces*, Proc. Roy. Soc. A **217** pp 307-327

Notes submitted by Paul Dellar, University of Cambridge
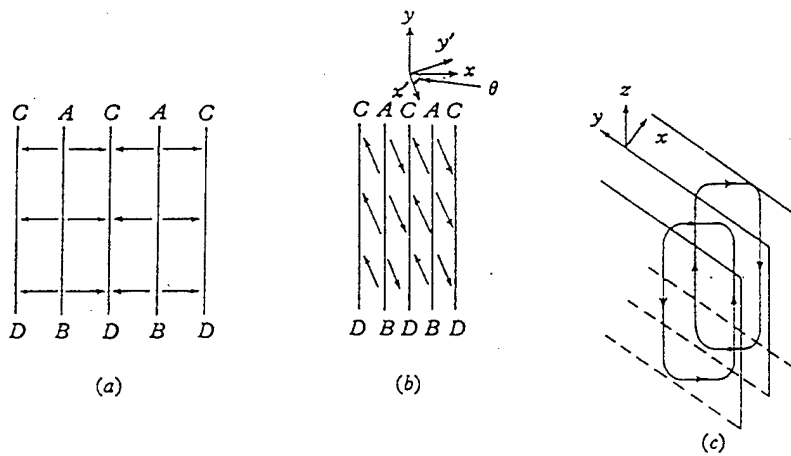
FIGURE 2. (a) A top view of two-dimensional rolls in a non-rotating fluid. The arrows indicate the direction of motion of the fluid. (b) The same in a system rotating counter-clockwise. (c) A perspective view of fluid particle motions in a role when the fluid is rotated.

Some examples of linear convective flow patterns

Figure 2 illustrates the tilting of convective cells in the rotating system as mentioned earlier. The lengths BD and AC measured along the direction of flow (arrows) are the same in 2(a) and 2(b). Figure (3) and (4) illustrate rolls combined into square and hexagonal planforms, the latter being preferred in most real experiments. The change in direction of rotation seen in 3 is due to the horizontal divergence changing sign halfway down. Diverging fluid spirals clockwise when deflected to the right, and converging fluid spirals anticlockwise.
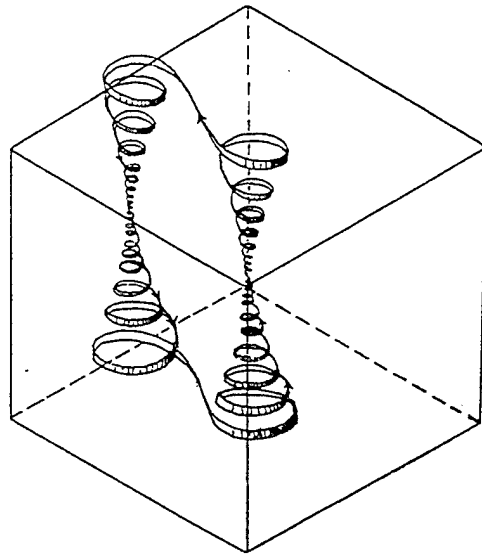
FIGURE 3c. A perspective sketch of a fluid particle motion in the square cell.
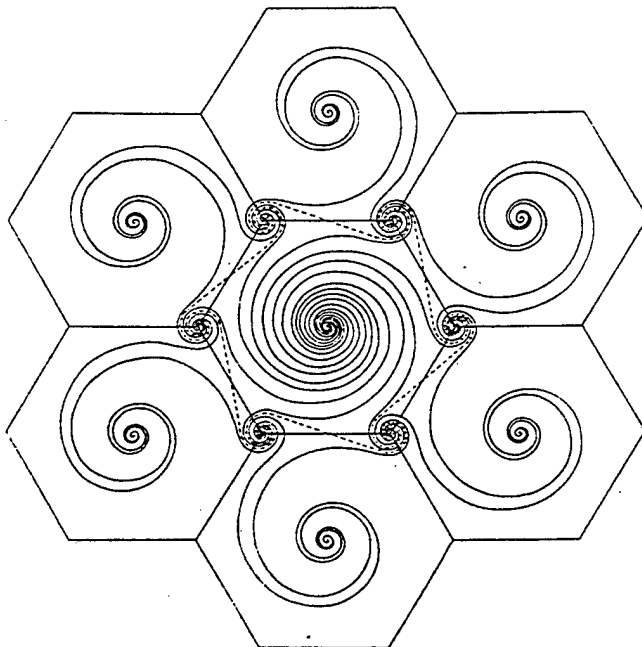
FIGURE 4b. A top view of seven rotating hexagonal cells. The fluid particles follow spiral paths from the centre toward the corners. The dashed lines form the boundaries of the centre cell.

Lectures by Joe Fernando

Lecture 4   Turbulent Convection in Fluids

Convection occurs in flows in which buoyancy forces are major contributors to the motion field. The phenomena of convection can be broken into two broad classes, forced convection and free convection. Forced convection occurs in situations where buoyancy forces compete with other driving forces to influence the flow. For example, in a turbulent pipe flow with heat addition, buoyancy forces may compete with pressure gradient forces in transporting heat and momentum. Free convection takes place when buoyancy forces dominate over all other forces.

Convection occurs when regions of fluid become lighter or heavier than their surroundings. When the temperature is responsible for convection, the fluid parcels feel a buoyancy force of $g\alpha\Delta T$ where g is gravity, α is the thermal expansion coefficient, and ΔT is the temperature difference between the blob and its surroundings. During the slow motion of fluid parcels, the buoyancy force is mainly balanced by the frictional drag force $\nu u/\delta^2$ where u is the velocity and δ is the length scale of the fluid parcels. Thus, the time scale of motion $t_c \simeq \delta/u$ is approximately $\frac{\nu}{g\alpha\Delta T\delta}$ whereas the timescale of diffusion is $t_d \simeq \delta^2/\kappa$. For convection to occur, the motion time scale must be much smaller than the diffusive time scale, $t_c \gg t_d$. With some rearrangement this inequality can be expressed in term of the Rayleigh number $Ra = \frac{g\alpha\Delta T\delta^3}{\kappa\nu} \gg 1$. Thus, convection occurs when the Raleigh number $Ra \gg 1$ and the exact value of this critical parameter Ra can be obtained by considering the equations of motion. For small amplitude motions, the critical Ra is given by linear stability theory.

Convection can be driven in many ways. Figure 1 contains Turner(1969)'s sketch of several convective phenomena. The term 'plume' is generally used to describe flows which develop when buoyancy is supplied continuously by a point source. The buoyant fluid of turbulent plumes is separated from the surrounding fluid by sharp boundaries. They increase their width by entraining fluid (by large eddies) and mixing at small scales in their interior. This entrainment mechanism is described in detail by Townsend(1976). 'Thermal' denotes a flow generated by a buoyancy source which appears impulsively at a point. In a rising thermal, like those which generate and maintain clouds, upward flow occurs in the center and downward flow at the edges. Entrainment is also common in such flows. However, it appears that when the mean flow velocity becomes of the same order as the turbulent fluctuations in the thermal, the entrainment becomes vanishingly small.

The source of buoyancy could also be horizontally homogenerous as it was in the Rayleigh-Bérnard problem which was examined in earlier lectures by R. Krishnamurti and G. Veronis. Linear stability theory was applied to the problem. Nonlinearities were delt with using perturbation theory and mutiple scales analysis to obtain some results for finite amplitude convection. However, these methods do not predict transitions to new regimes at high Rayleigh numbers. Most of the current interest is focused on high Ra regimes, the realm of hard turbulence. Hard turbulence is defined to occur for $Ra \gg 4 \times 10^7$. The properties of hard turbulence are described in Castaing et al.(1989).

Suppose the boundary conditions were changed in the previously examined Rayleigh-Bérnard problem in which constant temperatures were imposed at the top and bottom

boundaries. If instead of constant temperature, a constant heat flux $Q = -\kappa \rho_0 C_p \frac{\partial T}{\partial z}$ is now imposed at $z = 0$ and $z = 1$, the bottom and top respectively, one can solve the previously derived equations using essentially the same steps and obtain the critical value of the so called flux Raleigh number:

$$Ra_f = \frac{g \alpha Q d^4}{\rho_0 C_p \kappa^2 \nu} = \frac{q_0 d^4}{\kappa^2 \nu}$$

for which instability occurs; here q_0 is the buoyancy flux. Foster(1971) looked at the problem of two dimensional finite amplitude thermal convection at infinite Prandtl number in which a constant negative heat flux was imposed at the top boundary and the bottom boundary was completely insulated. For $Ra_f > 10^7$, Foster found that convection occurred intermittently, switching on and off for certain periods of time. These observations generally agreed with a phenomenological model put forth by Howard(1964). Figure 2 outlines Howard's conception of the stages of development of a thermal boundary layer. Howard argued that at first the thermal boundary layer forms by diffusion. The boundary layer becomes unstable when it is sufficiently thick and blobs of fluid breaks off from the bottom and rises. The departed fluid is replenished by cooler fluid and the process repeats.

In an experiment designed to simulate the nature of the planetary boundary layer, Deardorff and Willis(1974) described the horizontal structure of a convecting region. Figure 3 contains a figure from their paper. In the regime they looked at, an irregular pattern of open cells developed. Smaller scale dendritic convergence lines appeared along the edges of the cells. The most energetic plumes tended to occur where several of these convergence lines intersect. The lines were short lived and often got swept into plumes. Thermals or plumes of this kind may dominate the flow initially at high Ra. However, Adrian et. al.(1986) found that the thermals or plumes may set up a large scale circulation composed of large eddies which disrupt the ability of the boundary layer to eject isolated thermals.

Scaling laws are used to parameterize various convective turbulent flows. In high Rayleigh/Reynolds number convection, there are two separate regions in which the flow behaves very differently. There is a small conduction region near the bottom boundary where d, the height of the fluid layer, is irrelevant. When the bottom buoyancy flux is prescribed at this boundary, the important governing parameters near the boundary are ν, κ, and q_0; dimensional analysis implies the following scalings:

$$w_b = (q_0 \kappa)^{\frac{1}{4}} \quad ; \quad b_b = \frac{q_0}{w_b} \quad ; \quad z_b = \frac{\kappa}{w_b}$$

where w is the vertical velocity scale, b is the buoyancy scale, and z is the height scale. In the interior region away from the boundary the molecular parameters are unimportant and the scaling is

$$w_i = (q_0 d)^{\frac{1}{3}} \quad ; \quad b_i = \frac{q_0}{w_i} \quad ; \quad z_i = d$$

Using an open-topped box, heated from below, Townsend(1959) investigated thermal convection and checked the scaling w_b, b_b, and z_b. The differences between z_b scalings and

measurements was attributed to the variation of the molecular parameters ν and κ with temperature.

Early attempts to describe the atmospheric boundary layer using simple parameterizations were not very successful. For example, Sutton (1953) proposed that a single value of eddy diffusivity K_m can be representative of the whole atmosphere. He assumed that wind stress (τ_0) is constant in the lower 50–100 m, and geostrophy is achieved above the height $z_h = (K_m/f)^{1/2}$.

Tennekes (1981) using different scaling arguments obtained a value of the height of the boundary layer surprisingly close to the value measured (which may be quite fortuitous) for the daytime boundary layer, even though heat flux (q_0) was considered unimportant: $z_h = 0.25u_*/f$.

According to the current point of view, the atmospheric convection boundary layer (CBL) consists of four layers, each governed by different physics.
1) In the thin molecular sublayer [O(1 cm)] at the surface molecular processes dominate.
2) Wind stress becomes important in the unstable superadiabatic surface layer, and the important parameters are z, τ_0/ρ_0 and q_0. Then the scales for velocity and buoyancy are $u_* = (\tau_0/\rho)^{1/2}$ and $b_* = q_0/u_*$. Heat in the SAL is transported by small-scale turbulent eddies and mixing is forced by convection that has the scale of the Monin–Obukhov length scale $L_{mo} = u_*^3/q_0$, and $\frac{dU}{dz} = \frac{u_*}{\kappa z} f(z/L_{mo})$.
3) In the free–convection layer wind stress is not important, so from the remaining parameters z and q_0 the following scales of motion can be constructed: $u_f = (q_0 z)^{1/3}$ and $b_f = q_0/u_f$.
4) Turbulence is insensitive to z and τ_0 in the mixed layer, so $w_* = (q_0 d)^{1/3}$, $z_* = d$ and $b_* = q_0/w_*$

The convection boundary layer in the ocean as described by Anis and Moum (1994) has certain similarities to the atmospheric boundary layer.

On the top of the atmospheric boundary layer is the entrainment interface and the inversion layer. The entrainment zone is considered to lie at heights of 0.8–1.2 d. Processes such as entrainment and mixing dominate there. How fast the atmospheric boundary layer grows is important from a practical viewpoint — the pollutants are confined to the region below the entrainment interface. Due to the interaction of convective elements with the inversion layer, internal waves can be radiated to the outer stably stratified layer.

Experimental results show that the dissipation rate ϵ is independent of z in the interior of the domain. Thus, one can analyze shear–free CBL and stable layers using the techniques of the rapid distortion theory (Hunt 1984).

Carruthers and Hunt (1986) calculated velocity fluctuations near an interface between a turbulent region and a stably stratified layer in the absence of mean shear. They showed that the stratification has least effect on eddies with frequency close to the buoyancy frequency N. In the inviscid stratified region waves with frequency $\omega < N$ propagate without attenuation while the evanescent waves with $\omega > N$ decay rapidly with distance z from the boundary.

If a density interface is introduced in a domain of homogeneous turbulence, then far away from it $d\varepsilon/dz \to 0$, as before. Observations show that $d\varepsilon/dz \to 0$ near the interface also, and hence $\varepsilon = \nu \langle \omega_i \omega_i \rangle$ is unchanged. Thus we can conclude that the effect of the interface on the turbulent layer is to produce irrotational fluctuations. The velocity field can be decomposed into $\mathbf{u}(\mathbf{x},t) = \mathbf{u}^h(\mathbf{x},t) + \nabla\phi$, where ϕ is a velocity potential ($\nabla^2\phi = 0$). If $\mathbf{u}^h(\mathbf{x},t)$ is specified, then $\mathbf{u}(\mathbf{x},t)$ can be calculated by using the appropriate matching conditions.

One of the direct effects of stratification–turbulence interaction is the entrainment due to turbulent mixing. In convective boundary layers this mixing may occur due to several mechanisms, namely, (i)the impingement of thermals or buoyant elements on the interface and subsequent splashing of fluid into the non–turbulent layer. (ii)The impinging eddies on the interface cause sloshing motions on the interface, and cause Kelvin–Helmholtz type instabilities (Kaimal et al.,1976), and (iii) The pressure fluctuations of turbulence cause waves to develop, grow and break at the interface thus causing mixing. Of course, if shear is present various other mixing mechanisms such as critical-layer absorption appear. Laboratory and field observations indicate that these different mechanisms take place at different Richardson number ranges. Parameterizations of mixing rates have been proposed and tested in the laboratory (Deardorff et al., 1980; Fernando 1991).

References

Adrian, R.J., and R. Kumar, 1986. Higher order moments in the entrainment zone of turbulent penetrative thermal convection. *Transactions of the ASME. Journal of Heat Transfer*, **108**, 2:323–329.

Anis, A., and J. N. Moum 1992. The superadiabatic surface layer of the ocean during convection. *J. Phys. Oceanogr.*, **22**, 1221–1228.

Carruthers, D. J., and J. C. Hunt 1986. Velocity fluctuations near an interface between turbulent region and a stably stratified layer. *J. Fluid Mech.*, **165**, 475–501.

Castaing, B., Gunaratne, G., Heslot, F., Kadanoff, L., Libchaber, A., Thomae, S., Wu, X., Zalesk, S., and G. Zanetti, 1989. Scaling of hard thermal turbulence in Rayleigh-Bèrnard convection. *J. Fluid Mech.*, **204**, 1–30.

Deardorff, J. W., G. E. Willis, and B. H. Stockton 1980. Laboratory studies of the entrainment zone of a convective mixed layer. *J. Fluid Mech.*, **100**, 41–64.

Fernando, H.J.S. 1991. Turbulent mixing in stratified fluids. *Ann. Rev. Fluid Mech.*, **23**, 455–493.

Foster, T.D., 1971. Intermittent Convection. *Geophysical Fluid Dynamics*, **2**, 3: 210–217.

Howard, L.N., 1966. "Convection at high Rayleigh numbers," in *Proceedings of the Eleventh International Congress of Applied Mechanics, Munich(Germany) 1964*, edited by H. Görtler. Berlin: Springer-Verlag.

Hunt, J.C.R. 1984. Turbulence structure in thermal convection and shear-free boundary layers. *J. Fluid Mech.*, **138**, 161–184.

Kaimal, J. C., J. C. Wyngaard, D. A. Haugen, O. R. Cote, Y. Izumi, S. J. Caughey, and C. J. Reddings 1976. Turbulence structure in the convective boundary layer. *J. Atmos. Sci.*, **33**, 2153–2169.

Townsend, A., 1959. Temperature Fluctuations over a heated, horizontal surface, *J. Fluid Mech.*, **5**, 209–241.

Townsend, A., 1976. *The Structure of Turbulent Shear Flow*. Cambridge University Press, 315pp.

Turner, J.S., 1969. Buoyant plumes and thermals. *Annual Review of Fluid Mechanics*, **1**, 29–44.

Willis, G.E., and J.W. Deardorff, 1979. Laboratory Observations of Turbulent Penetrative-Convection Planforms. *J. Geophys. Res.*, **84**, C1:295–302.

Notes submitted by: JIM NOYES AND OLEG ESENKOV

H.J.S. Fernando
Arizona State University
Tempe, Arizona

PLUME   THERMAL   STARTING PLUME
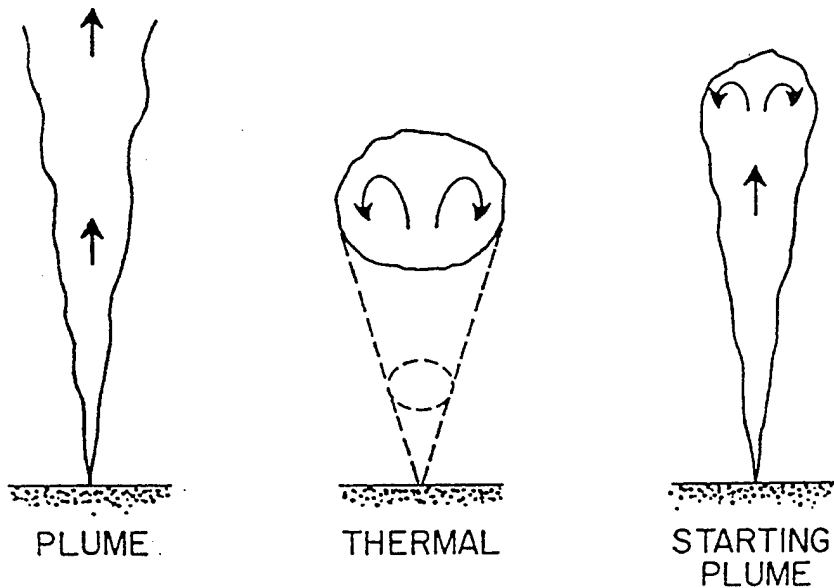
Figure 1. Sketches of the various stages of convection phenomena described in the text. The arrows indicate the direction of mean motion.

Figure 2. Stages in the development of the transient thermal boundary layer. The cycle is repeated upon departure of the thermal burst.
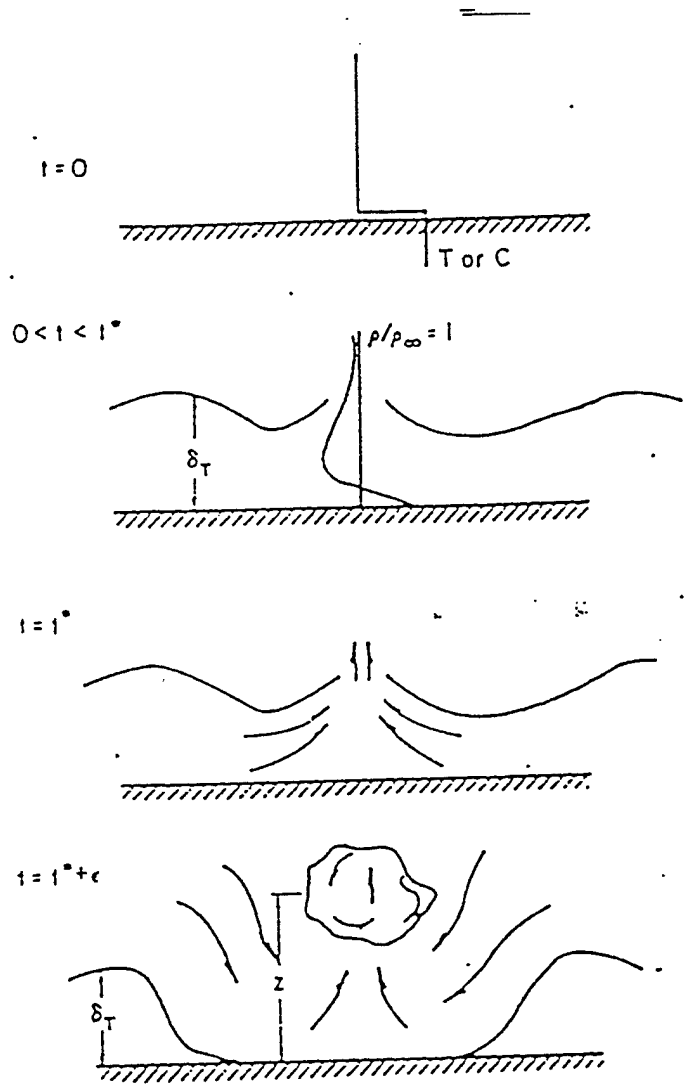
Figure 3. Simultaneously occurring patterns near the surface(solid lines) and near the inversion base (shaded areas), based upon a pair of photographs of the milk tracer in plan view.
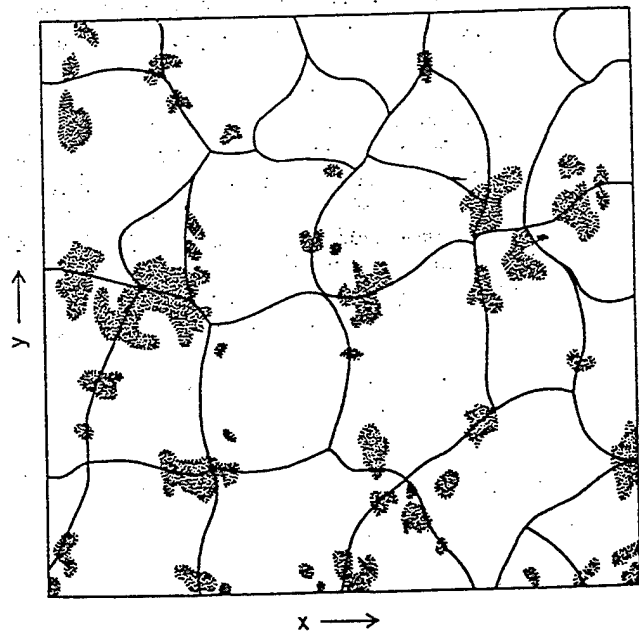
Lecture 5 : Motion in Rotating Fluids

In rotating fluids, small amplitude motions lead to linear internal waves while finite amplitude motion lead to turbulence.

1   Small Amplitude Motions

$$\rho\frac{\partial \underline{u}}{\partial t} + \rho 2\underline{\Omega} \times \underline{u} + \nabla p^{'} = 0 \tag{1}$$

Taking the curl of this equation gives

$$\rho\frac{\partial \omega_i}{\partial t} - 2\Omega_m\frac{\partial u_i}{\partial x_m} = 0 \tag{2}$$

and the curl of (2) gives

$$\frac{\partial^2\nabla^2 u_i}{\partial t^2} - 2\Omega_m.\nabla\omega_i = 0 \tag{3}$$

Eliminating ω_i from (2) and (3) gives

$$\frac{\partial^2\nabla^2 u_i}{\partial t^2} + (2\Omega.\nabla)^2 u_i = 0 \tag{4}$$

This has solutions

$$u_i = A_i e^{i(\underline{k}.\underline{x}-\omega t)}$$

where

$$\omega = 2\Omega.l = 2\Omega cos\theta$$

ie, anticyclonic motion is induced.

2   Viscous effects

When viscous effects are included, the solution now becomes:

$$\underline{u}(x,t) = Re\ u_o(k)e^{-i(\underline{k}.\underline{x}-\omega t)}e^{-\nu k^2 t} \tag{5}$$

$$c(\mathbf{k}) = \frac{2\Omega\cdot\mathbf{l}}{|\mathbf{k}|}\mathbf{l} \tag{6}$$

If the motion is spatially homogeneous s.t.

$$\hat{u}(\underline{k}, t) = \frac{1}{(2\pi)^3} \int_\infty^\infty \int \int \underline{u}(\underline{x}, t) e^{-i\underline{k}\cdot\underline{x}} d\underline{x} \qquad (7)$$

then

$$\hat{u}(\underline{k}, t) = R(\underline{l}, 2\underline{\Omega}\cdot\underline{l}t) e^{-\nu k^2 t} \hat{u}(k, t = 0) \qquad (8)$$

where R is the rotational matrix.

So the anisotropic propogation of inertial waves in physical space corresponds in spectral space to a differential rotation of the initial spectrum, $\hat{u}(k, t = 0)$ in a plane normal to $\underline{k}$ with a rate of rotation $2\underline{\Omega}\cdot\underline{l}$.

3   Finite Amplitude Motions

When the amplitude of fluid motions is large, $\underline{u}.\nabla\underline{u}$ is important and the motions become turbulent   In three dimensions, the non-linear terms dominate over other body forces. This transition to 3D turbulent motions in rotating fluids has been studied mainly experimentally.

The maximum scale transverse to the rotational axis should be given by a balance between the Coriolis force and the inertial forces.

$$\frac{u^2}{L_\Omega} \sim 2\Omega u \rightarrow L_\Omega = \frac{u}{2\Omega}$$

This is known as the Coriolis scale. The dissipation scale, ϵ is given by

$$\epsilon \propto \frac{u^3}{l}$$

This gives the   Coriolis scale

$$L_\Omega \propto \left(\frac{\epsilon}{\Omega^3}\right)^{\frac{1}{2}}$$

If we define the integral lengthscale

$$L_{ij,k} = \int_0^\infty \frac{\overline{u_i(\underline{x})u_j(\underline{x} + r\underline{i}_k)}dr}{\overline{u_i(\underline{x})u_j(\underline{x})}}$$

and Ω is parallel to the x_1 axis, then we expect $L_{11,1}$ to be least affected by the rotation.

4 Statistical Theory

The instantaneous equations for buoyancy-driven rotating turbulent flow are:

$$\frac{\partial \hat{u}_i}{\partial t} + \hat{u}_j \frac{\partial \hat{u}_i}{\partial x_j} + 2\epsilon_{ijk}\Omega_j u_k = -\frac{1}{\rho}\frac{\partial p}{\partial x_i} + \nu \frac{\partial^2 \hat{u}_i}{\partial x_j \partial x_j} + \hat{b}\delta_{i3} \qquad (9)$$

If we write the instantaneous velocity $\hat{u}_i$ in terms of a mean and a fluctuation, ie $\hat{u}_i = \overline{U_i} + u_i$, then the mean equations are

$$\frac{\partial \overline{U_i}}{\partial t} + \overline{U_k}\frac{\partial \overline{U_i}}{\partial x_k} + 2\epsilon_{ilk}\Omega_l \overline{U_k} = -\frac{1}{\rho}\frac{\partial \overline{P}}{\partial x_k} + \nu \frac{\partial}{\partial x_k}(\nu \frac{\partial \overline{U_i}}{\partial x_k} - \overline{u_i u_k}) + \overline{B}\delta_{i3} \qquad (10)$$

Subtracting equation (10) from (9) gives an equation for u_i and an equation for u_j. Multiplying these by u_j and u_i respecitively gives

$$\frac{\partial}{\partial t}(\overline{u_i u_j}) + \overline{u_j u_k}\frac{\partial \overline{U_i}}{\partial x_k} + \overline{u_i u_k}\frac{\partial \overline{U_j}}{\partial x_k} + \overline{U_k}\frac{\partial}{\partial x_k}\overline{u_i u_j}$$

$$\qquad (11)$$

$$+2[\epsilon_{ilk}\Omega_l \overline{u_k u_j} + \epsilon_{jpm}\Omega_p \overline{u_m u_i}]$$

$$\qquad (12)$$

$$= -\frac{\partial}{\partial x_k}\overline{u_i u_j u_k} - \frac{1}{\rho}(\frac{\partial}{\partial x_i}\overline{p u_j} + \frac{\partial}{\partial x_j}\overline{p u_i}) + \frac{1}{\rho}\overline{p(\frac{\partial u_j}{\partial x_i} + \frac{\partial u_i}{\partial x_j})}$$

$$\qquad (13)$$

$$+(\overline{u_j b}\delta_{i3} + \overline{u_i b}\delta_{j3}) + \nu \frac{\partial^2 \overline{u_i u_j}}{\partial x_l \partial x_l} - 2\nu \overline{\frac{\partial u_i}{\partial x_l}\frac{\partial u_j}{\partial x_l}}$$

$$\qquad (14)$$

There are three interesting features of turbulent flows which can be illustrated by these equations:

- Taking i=j and contracting gives the turbulent kinetic energy equation

$$\frac{\partial}{\partial t}\frac{\overline{q^2}}{2} + \overline{U_k}\frac{\partial}{\partial x_k}\frac{\overline{q^2}}{2} + \overline{u_i u_k}\frac{\partial \overline{U_i}}{\partial x_k} = -\frac{\partial}{\partial x_k}\overline{(\frac{p}{\rho} + \frac{q^2}{2})u_k} + \overline{b u_3} + \nu \frac{\partial^2}{\partial x_l \partial x_l}\frac{\overline{q^2}}{2} - \nu\overline{\frac{\partial u_i}{\partial x_l}\frac{\partial u_i}{\partial x_l}} \quad (15)$$

where $q^2 = u^2 + v^2 + w^2$. There is no dependence on Ω, which implies that rotation has NO importance for the overall energy budget.

- Consider homogeneous turbulence with $\underline{\Omega}$ parallel to the x_1 axis. In this case the equations reduce to:

$$\frac{\partial}{\partial t}\overline{u_1^2} = \frac{2}{\rho}\overline{p\frac{\partial u_1}{\partial x_1}} - 2\nu\overline{\frac{\partial u_1}{\partial x_k}\frac{\partial u_1}{\partial x_k}} \qquad (16)$$

$$\frac{\partial}{\partial t}\overline{u_2^2} = -4\Omega\overline{u_2 u_3} + \frac{2}{\rho}\overline{p\frac{\partial u_2}{\partial x_2}} - 2\nu\overline{\frac{\partial u_2}{\partial x_k}\frac{\partial u_2}{\partial x_k}} \qquad (17)$$

$$\frac{\partial}{\partial t}\overline{u_3^2} = 4\Omega\overline{u_2u_3} + \frac{2}{\rho}\overline{p\frac{\partial u_3}{\partial x_3}} - 2\nu\overline{\frac{\partial u_3}{\partial x_k}\frac{\partial u_3}{\partial x_k}} \tag{18}$$

$$\tag{19}$$

So $\overline{p\frac{\partial u_i}{\partial x_i}}$ does the redistributing among all three components and Ω terms does the redistributing among u_2 and u_3.

- If the flow starts with a isotropic state, $\overline{u_1^2} = \overline{u_2^2} = \overline{u_3^2}$ and $\overline{u_iu_j} = 0, i \neq j$, then the isotropy is preserved.

$$\frac{\partial}{\partial x_k}\overline{u_2u_3} = 2\Omega(\overline{u_2^2} - \overline{u_3^2}) - \frac{1}{\rho}\overline{p\frac{\partial u_2}{\partial x_3}} - \frac{1}{\rho}\overline{p\frac{\partial u_3}{\partial x_2}} - 2\nu\overline{\frac{\partial u_2}{\partial x_k}\frac{\partial u_3}{\partial x_k}} \tag{20}$$

5 2-D Turbulence

A review of such flows has been given by Salmon (1982). $Ro \to 0$ and $\Omega\frac{\partial u}{\partial z} = 0$ yields two dimensionality. This should be discerned from two dimensional component turbulence where one component vanishes. The vorticity equation is:

$$\frac{D\underline{\omega}_a}{Dt} = \underline{\omega}_a \cdot \nabla\underline{u} + \nu\nabla^2\underline{\omega} \tag{21}$$

where $\underline{\omega}_a = \underline{\omega} + \underline{\Omega}$. If $\underline{\Omega}$ is parallel to the z-axis, then since $\underline{\omega} = \nabla \times \underline{u}$ and hence $\underline{\omega}_a$ will also be parallel to the z axis, the first term of the right hand side is zero and in the inviscid limit $\nu \to 0$:

$$\frac{D\underline{\omega}_a}{Dt} = 0 \tag{22}$$

and hence $\overline{\omega^2}$ is conserved. Also, in such a two dimensional case, we may write $u = -\frac{\partial\phi}{\partial y}$ and $v = \frac{\partial\phi}{\partial x}$. Then we have:

$$\overline{|\nabla\phi|^2} = \int_0^\infty E(k,t)dk \to \text{Conserved} \tag{23}$$

$$\overline{\omega^2} = \int_0^\infty k^2 E(k,t)dk \to \text{Conserved} \tag{24}$$

If we define:

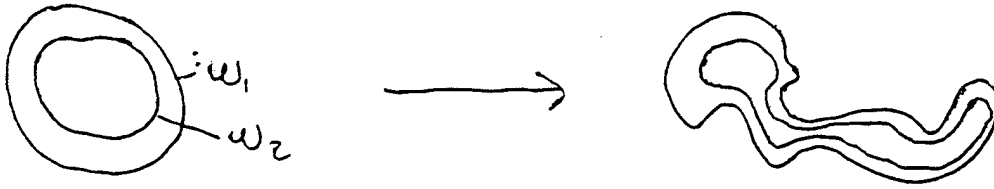$$k_\epsilon = \frac{\int_0^\infty kE(k)dk}{\int_0^\infty E(k)dk} \tag{25}$$

then one can use $(k - k_1)^2 = k^2 - 2k_1k + k_1^2$ to show that:

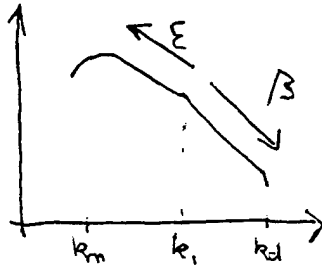$$\frac{dk_\epsilon}{dt} = -\frac{1}{2k_1}\frac{\frac{d}{dt}\left(\int_0^\infty (k-k_1)E(k)dk\right)}{\int_0^\infty E(k)dk} < 0 \tag{26}$$

Hence k_ϵ becomes smaller with time. Energy is transferred toward smaller wave numbers, and the dissipation is reduced.

Also, vortex lines are material lines (implied by $\frac{D\omega_a}{Dt} = 0$).

Hence, as these lines get more convoluted, the mean square vorticity gradients $|\nabla\underline{\omega}| \cdot |\nabla\underline{\omega}| = \int_0^\infty k^4 E(k,t)\,dk$ increase.

If $\overline{\omega^2}$ is injected at rate β and $\overline{\omega^2}$ is injected at rate ϵ at some wavenumber k_1, then:

$$E(k,t) = f(\beta, k) \sim \beta^{\frac{2}{3}} k^{-3} \quad \text{for} \quad k_1 < k < k_d \tag{27}$$

$$E(k,t) = f(\epsilon, k) \sim \epsilon^{\frac{2}{3}} k^{-\frac{5}{3}} \quad \text{for} \quad k_m < k < k_1 \tag{28}$$

where $k_m = f(\epsilon, t) \sim \epsilon^{-\frac{1}{2}} t^{-\frac{3}{2}}$ and $k_d = f(\beta, \nu) \sim \left(\frac{\beta}{\nu^2}\right)^{\frac{1}{6}}$. There is some observational evidence for such scalings. There are other scaling arguments for 2-D turbulence.
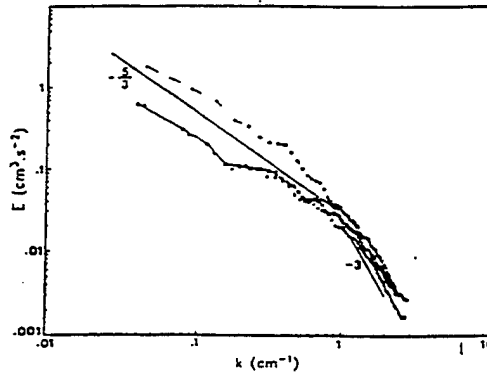
Saffman (1971) describes "vorticity shocks" with vorticity spectra $k^2 E(k) \sim k^{-2}$ and hence $E(k) \sim k^{-4}$

Experimentally, $E(k) \sim k^{-2}$ to k^{-3} (Hopfinger's group) or $E(k) \sim k^{-3}$ (certain other groups).

NOTES SUBMITTED BY STEVE ZATMAN
AND HELENE BANKS

Lecture 6: Effects of Rotation on Simple Convective and Turbulent Flows

This lecture considers how simple convective processes are affected by background rotation. Here we focus attention to turbulent plumes and thermals and entrainment across interfaces. For studies of rotating turbulent convection in horizontally homogeneous fluid layers see Fernando, Chen and Boyer (1991) or Boubnov and Golitsyn (1990).

6.1 Turbulent Thermals in Rotating Fluids

The initial buoyancy, q_T, contained in a thermal is

$$q_T = \left(\frac{\rho' - \rho_o}{\rho_o} g \right) V_o \tag{1}$$

where ρ' is the density of the thermal, ρ_o is the density of the background fluid, g is the gravitational acceleration and V_o is the initial volume of the thermal. The dimensions of q_T are $\left[\frac{m^4}{s^2} \right]$.

It has been shown that prior to the onset of rotational effects the buoyancy is the dominant parameter that controls the motion of the thermal and that the evolution of the thermal in time is self similar. According to this scaling the entraining thermal will travel as

$$h = c_1 (q_T)^{\frac{1}{4}} t^{\frac{1}{2}} \tag{2}$$

where h is the vertical distance travelled by the thermal, t is time measured after an initial transient acceleration and c_1 is a constant. The width of the thermal, b, is found to be a linear function of h:

$$b = c_2 h \tag{3}$$

where c_2 is a second constant. The thermal velocity, u, is scaled as

$$u = c_3 \left(\frac{q_T}{h^2} \right)^{\frac{1}{2}} \tag{4}$$

When the effects of rotation are felt by the thermal, at time $\simeq \frac{1}{2\Omega}$, the Coriolis forces will try to constrain the flow to a cylinder aligned with the rotation axis. The

thermal will cease to grow laterally and the entrainment rate will be greatly reduced. These effects should manifest in the turbulence of the flow when the Coriolis forces become of the order of the inertial forces in the thermal such that

$$2\Omega u \sim \frac{u^2}{l} \tag{5}$$

where Ω is the rate of rotation, u is the rms velocity in the thermal and l is the lengthscale. Applying this last relation to equation (4) for values of h and b when rotational effects first become relevant yields

$$h_c = c_3 \left(\frac{q_T}{\Omega^2}\right)^{\frac{1}{4}} \tag{6}$$

and

$$b_c = c_4 \left(\frac{q_T}{\Omega^2}\right)^{\frac{1}{4}} \tag{7}$$

where c_3 and c_4 are further constants that have been determined experimentally by Ayotte and Fernando (1994).

An idealized calculation of h_c in the earth's atmosphere gives $h_c \sim 6.5\ km$ where parameter values of $c_3 = 2.3$, $q_T = 3.0\ \frac{m^4}{s^2}$ and $\Omega = 7.1 \times 10^{-5}\ \frac{rad}{s}$ have been used. $h_c \sim 6.5 km$ is a significant fraction of the height of the troposphere and, therefore, this estimate suggests that rotation only affects very deep convection in the atmosphere.

6.2 Turbulent Plumes in Rotating Fluids

A plume is created by a source region that inputs a buoyancy flux, q_o, into the fluid layer

$$q_o = \frac{\pi d_o^2}{4}\left(\frac{\rho' - \rho_o}{\rho_o}g\right)u_o \tag{8}$$

where d_o is the diameter of the source region and u_o is the flow rate from the source region into the surrounding fluid. Therefore, the dimensions of the buoyancy flux are $\left[\frac{m^4}{s^3}\right]$. If the same reasoning is employed as was used for the analysis of thermals, that at times smaller than $(2\Omega)^{-1}$ the flow cannot be affected by the rotation and, therefore, q_o is the controlling parameter of the flow, then self-similar temporal evolution of the flow leads to scales

$$u = \alpha_1 (\frac{q_o}{z})^{\frac{1}{3}} \tag{9}$$

$$l \propto z \propto b \implies l = \alpha_2 z \tag{10}$$

where u is the characteristic plume velocity, z is the vertical distance the plume has travelled, b is the plume head width, l is an integral length- scale of the turbulence in the plume, and α denotes a constant in this section.

Balancing the inertial forces of the turbulent motion in the plume with the Coriolis force as in equation (5) gives the relation

$$z_c = \left(\frac{\alpha_1}{\alpha_2\alpha_3}\right)^{\frac{3}{4}} \left(\frac{q_o}{\Omega^3}\right)^{\frac{1}{4}} \tag{11}$$

The rotational effects become important at z_c and a critical plume width, b_c is proportional to z_c as

$$b_c = \alpha_4 \left(\frac{\alpha_1}{\alpha_2\alpha_3}\right)^{\frac{3}{4}} \left(\frac{q_o}{\Omega^3}\right)^{\frac{1}{4}} \tag{12}$$

Data from Fernando et. al. (1995-in preparation) give laboratory determinations of these α values.

6.3 Effects of Rotation on Entrainment

Fleury et al.(1991) devised a number of experiments to determine the effect of rotation on the entrainment rate by looking at turbulent mixing across a 2-layer stratified fluid. They observed a decrease in the entrainment rate, E, together with an increase in the low-frequency oscillations of the density interface across which turbulent mixing is occurring. The high frequency oscillations are unaffected by the rotation. From their experiments two laws for E are derived as a function of Ri, the Richardson number, and Ro, the Rossby number:

$$E = 0.5R_0 Ri^{-1} \text{ - with rotation}$$
$$E = 1.6Ri^{-\frac{3}{2}} \text{ - without rotation}$$

A model for turbulent mixing in the presence of rotation was proposed by Mory(1991) which provides an explanation for the laboratory results. Mory(1991) proposes mixing by small turbulent eddies of $Ri = \frac{g\partial\rho/\partial z}{\rho(\partial u/\partial z)^2} \sim O(1)$ or less. The eddies are responsible for the conversion of kinetic energy of the motions into potential energy increase associated with interfacial mixing.

6.4 Polar Leads

A lead is a long, thin break in the polar ice cap. Leads may be hundreds of kilometers long and hundreds of meters wide. The break in the ice exposes water to the cold winter atmosphere which causes the ice to refreeze. Salt is rejected back into the water during the refreezing process which leads to a sinking line plume forming below the lead. Rotation affects the plume in two ways. The first involves the arrest of the turbulent diffusion, which occurs when the plume's Rossby number becomes of order one, i.e. $R_0 = \frac{q_o^{\frac{1}{3}}}{fl} \sim O(1)$, where l is the length scale of the plume. Secondly rotation affects the entrainment flow by deflecting it sideways, thus generating a background

mean flow in the direction of the long-axis of the lead. The critical height at which the line plume is affected by rotational forces is given as

$$z_c = \phi_1 \left(\frac{q_o}{\Omega^3} \right)^{\frac{1}{3}} \tag{13}$$

where q_o is now the buoyancy flux per unit length. The constant $\phi_1 = 3.2$ has been experimentally determined by Fernando and Ching (1993a). Coriolis forces will then tend to bend the plane of the plume. Line plumes that are much longer than the critical width, b_c, of the plume head should break up into smaller sheets analogous to the formation of smaller chimneys inside of a larger oceanic downwelling region. Simple calculations give that a plume from a lead will fall to roughly 3500 m before reaching z_c. If the thermocline resides at a level well above this height then the plume will fall to this interface and spread to some size on the order of the Rossby deformation radius before coming to be affected by the background rotation. This implies that for a plume descending in polar regions, rotation will come into effect only after the plume has started spreading out horizontally as a gravity current, by inducing baroclinic instability and break-up into eddies. Fernando and Ching(1993b) show the development of a pair of stacked vortices in their laboratory experiments simulating convection in a lead.

6.5 Effects of Stratification and Boundaries

In many geophysical settings, fluid layers have an appreciable stratification or a physical boundary, such as a finite layer depth, that will change the flow field considerably from the case of a homogeneous rotating fluid. Examples of these types of flows found in the oceans are chimney formation (Jones and Marshall, 1993), thermal and plume flows from hydrothermal vents (Helfrich,1994) and Arctic lead flows. Deep convection in the earth's atmosphere must take stratification effects into account as well as the finite height of the tropopause. In planetary studies, the effects of rotating convection interacting with the unknown stratification of the earth's outer core fluid is of vital interest to dynamo theorists for the determination of the type of flow regime that is dominant at different radii through the core (Bergman, 1993). The strength of the stable stratification of Jupiter's upper atmosphere may hold the key to whether it is deep convection or insolation that drives the banded structure of the Jovian cloud layer (Condie and Rhines, 1994). Current numerical work on rotating and penetrative convection can be found in Julien, Legg, McWilliams and Werne (in press).

References

Ayotte, B.A. and H.J.S. Fernando, 1994: The Motion of a Turbulent Thermal in the Presence of Background Rotation, J. Atmos. Sci. **51**: 1989-1994.

Bergman, M.I., 1993: Magnetic Rossby Waves in a Stably Stratified Layer Near the Surface of the Earth's Outer Core, Geophys. Astrophys. Fluid Dynamics. **68**: 151-176.

Boubnov, B.M. and G.S. Golitsyn, 1986: Experimental Study of Convective Structures in Rotating fluids, J. Fluid Mech. **167**: 503-531.

Condie, S. and P. Rhines, 1994: A Convective Model for the Zonal Jets in the Atmosphere of Jupiter and Saturn, Nature. **367**: 711-713.

Fernando, H.J.S., R.-R. Chen and D.L. Boyer, 1991: Effects of Rotation on Convective Turbulence, J. Fluid Mech. **228**: 513-548.

Fernando, H.J.S., and C.Y. Ching, 1993a: Effects of Background Rotation on Turbulent Line Plumes. J. Phys. Oceanogr, **23**: 2125-2129.

Fernando, H.J.S., and C.Y. Ching, 1993b: Lead-induced convection: a laboratory perspective. J. Mar. Syst. **4**: 217-230.

Fleury M., Mory, M., Hopfinger E.J. and Auchere D. 1991: Effects of rotation on turbulent mixing across a density interface. J. Fluid Mech. **223**: 165-191.

Helfrich, K.R., 1994: Thermals with Background Rotation and Stratification, J. Fluid Mech. **259**: 265-280.

Jones, H. and J. Marshall, 1993: Convection with Rotation in a Neutral Ocean: A Study of Open-Ocean Deep Convection, J. Phys. Oceanogr. **23**: 1009-1039.

Julien, K., S. Legg, J. McWilliams and J. Werne, in press: Dyn. Atmos. Oceans.

Mory, M., 1991: A model of turbulent mixing across a density interface including the effect of rotation. J. Fluid Mech. **223**: 193-207.

Lecture written by Jonathan Aurnou and Fiammetta Straneo

Lectures by John Marshall

Lecture 1: OCEAN CONVECTION

Background

In recent years there has been much progress in our understanding of the kinematics and dynamics of ocean convection through new results from field experiments, through focused laboratory experiments and through numerical simulation. The observations suggest a complex interplay of scales, ranging from plumes at scales of less than a kilometer, through eddies on and above the Rossby radius of deformation, right up to the scale of the general circulation. These key elements appear to be common to all the open-ocean convection sites that have been studied. In these lectures we draw together and review results of laboratory and numerical experiments, and summarize our current understanding of the underlying hydrodynamical processes at work at the convection site and the interplay between the convective and geostrophic scales. A more detailed account of much of the material presented in these lectures can be found in Marshall et.al. (1994) and Marshall and Schott (1996). This latter study includes a comprehensive discussion of the observations presented in the context of relevant theory.

Formation of deep water in 50 km wide convective `chimneys', occurs in the Labrador, Greenland, Weddell, and Mediterranean Seas - see the observational review by Schott, Visbeck and Send (1993). These are the principal source regions for deep and intermediate waters of the world's oceans; processes local to these seas set the volume and temperature/salinity properties of the thermohaline circulation. Observations of open-ocean deep convection in the weakly stratified waters of the Western Mediterranean, the most intensively studied site - (the MEDOC Group, 1971; Stommel, 1972; Schott and Leaman, 1991), suggested that three successive phases can be identified; `preconditioning', on the large-scale (of order 100 km), `violent-mixing' occurring in localized, intense plumes (on scales of order 1km) and `sinking and spreading' of the convectively tainted water, on a scale of 5 to 10km.

During **preconditioning**, the gyre-scale circulation and buoyancy forcing combine to predispose a particular site to overturn. With the onset of strong surface forcing the near-surface stratification, over an area up to 100 km across, can be readily erased exposing the very weakly stratified water-mass beneath to the surface (Swallow and Caston, 1973). Subsequent cooling events can then initiate **violent mixing** in which the whole of the fluid column may overturn in numerous plumes which distribute cooled surface water in the vertical. The plumes have a horizontal scale of order 1 km with vertical velocities in excess of 10 cm s^{-1} (Voorhis and Webb, 1970). In concert the plumes are thought to rapidly mix properties over the preconditioned site forming a `chimney' of

homogeneous fluid. Chimneys ranging in scale from several to many tens of kilometers in diameter have been observed. With the cessation of strong forcing there follows a sharp decline in convective overturning; the predominantly vertical heat transfer of the mixing phase giving way to horizontal transfer associated with eddying on geostrophic scales (Swallow and Caston, 1973). Individual eddies tend to organize the convected water in to cone-like features. The mixed fluid slumps under gravity, **spreading** out at middle depths, leading, on a timescale of days, to the disintegration of the chimney. The descent of the dense fluid in the weeks and months after mixing, draws in water from outside the chimney, restratifying near surface layers (Stommel, 1972).

Such observations have inspired theoretical, laboratory and numerical studies of rotating convection which are the focus here. Two aspects make ocean convection interesting from a theoretical point of view. First the convective process in the ocean may be modified by rotation; second the convective and geostrophic scales are not very disparate in the ocean and so the water-mass transformation process involves a fascinating interplay between upright convection and baroclinic instability. Laboratory and numerical studies of rotating convection motivated by this specific geophysical application has led to advances in our understanding of the general problem. We present numerical experiments here in the same spirit as those in the laboratory, except a numerical fluid is used rather than a real one. Both approaches have their limitations - unless extraordinary measures are taken only Rayleigh numbers in the range 10^9 to 10^{16} are attainable compared to 10^{26} in the ocean - but when laboratory and numerical experiments are used in concert, and in the light of the observations, they lead to great insight.

It is interesting to note how little the developments described here have been influenced by 'classical convection studies'[1] which trace their lineage back to 'Rayleigh-Benard' convection. In the ocean the Rayleigh number in convecting regions is many orders of magnitude greater than the critical value, and the convection is fully turbulent with transfer properties that do not, we believe, depend on molecular viscosities and diffusivities. Even more importantly the convective process in the ocean is *localized in space* (horizontally non-uniform) making it distinct from the myriad classical studies of convection rooted in the Rayleigh problem (convection between two plates extending to $\pm \infty$ induced by uniform cooling/heating induced by uniform cooling/heating); as one might anticipate edge effects and baroclinic instability ultimately come to dominate the evolving flow fields in the oceanic context.

---

[1] Many of these studies were brought together in an excellent compendium edited by Barry Saltzman; Theory of Thermal Convection.

1. Plume Dynamics; the 'violent mixing' phase

In this lecture we explore the underlying hydrodynamics of the convective process in the absence of horizontal inhomogeneities, whereby a column of ocean is overturned by convection induced by widespread and uniform buoyancy loss at its surface. The details of the process are interesting, inherently complicated, but may not be of paramount importance for the large-scale. We thus emphasize the benefit of thinking about the *ensemble* properties of convection rather than (as one is often tempted to do) exclusively about the individual elements themselves. We argue that the gross transfer properties of the plumes are dictated by demands placed upon them by the large-scale; that they draw buoyancy from depth at a rate to offset the loss imposed by the meteorology at the surface. This leads to simple scaling laws and the identification of key non-dimensional parameters, independent of molecular diffusivity and conductivity, and which have been very successful in bringing order to observations, and laboratory/numerical experiments.

1.1 Gravitational instability; upright convection

Consider a resting ocean of constant stratification N_{th} (subscript 'th' for thermocline) which is subject to uniform and wide-spread buoyancy loss from its upper surface as shown in Fig. 1.1.1. The thermodynamic equation is:

$$\frac{Db}{Dt} = B \tag{1.1.1}$$

where $b = -(g/\rho_o)\sigma$ is the buoyancy with σ is the potential density, ρ_o a constant reference density, g is the acceleration due to gravity and $B = \partial \mathcal{B} / \partial z$ is the buoyancy forcing, the divergence of the flux $\mathcal{B}$.[2] Because of rotational constraints the fluid cannot simultaneously overturn on the large scale; rather the qualitative description must be that the response to wide-spread cooling is one in which relatively small convection cells (plumes) develop. Fluid parcels at the surface will become dense and sink under gravity displacing less dense parcels from below. The continual exchange of fluid parcels in this way creates a layer which, as we show below, is very close to neutral with respect to its thermodynamic properties. However, as long as the buoyancy loss persists there will be, on the average, an adverse buoyancy gradient:

---

[2] The buoyancy flux is related to the heat and fresh water flux by:

$$\mathcal{B} = \frac{g}{\rho_o}\left(\frac{\alpha}{c_w}\mathcal{H} + \beta S(E - P)\right)$$

$$N_{mix}^2 = \frac{\partial b}{\partial z} < 0 \qquad (1.1.2)$$

If $N_{mix}^2 < 0$ then exchange of parcels vertically must release gravitational potential energy. Since horizontal motion does not affect potential energy one need consider only vertical overturning; 'parcel theory' (see Appendix I) then yields an upper limit to the growth rate ω:

$$\omega^2 \le -N_{mix}^2 \qquad (1.1.3)$$

For a prescribed N_{mix}^2, and applying appropriate boundary conditions, it is straightforward to obtain complete solutions through linear stability analysis (see, for example Rayleigh, 1916; Veronis, 1958; Chandresakhar 1961); these show that ω^2 is nearly attained when the convection cells are tall and thin, for which little energy is 'wasted' in horizontal motion. Laboratory simulations, however, suggest that the aspect ratio of fully developed turbulent convection approaches unity such that horizontal and vertical scales are of the same order.

Many competing effects collude together to control the detailed dynamics on the plume-scale. However, it is important to realize that, irrespective of these details, the gross transfer properties of the population of convective cells must be controlled by the large scale; the *raison d'être* for the overturning is to flux buoyancy vertically to offset buoyancy loss at the surface. As shown in the appendix, the following 'law' of vertical heat transfer for the plume-scale can be developed using the same parcel theory that leads to Eq.1.1.3.

$$\mathcal{B}_p = w\Delta b = \Delta z^{1/2} \Delta b^{3/2} \qquad (1.1.4)$$

where w is the vertical velocity in the plume and Δb is the difference in buoyancy of the rising and sinking fluid.

Now if the plumes, acting in concert, achieve a vertical buoyancy flux sufficient to balance loss from the surface, then $\mathcal{B}_p = \mathcal{B}_o$, and choosing a deep mixed layer exposed to a heat loss of ~ 500 W/m^2 typical of the Labrador Sea:

---

where g denotes the acceleration due to gravity, ρ_o a reference density, c_w the heat capacity of water and α the thermal and β the haline expansion coefficient; typically $\alpha = 2 \times 10^{-4}$ K^{-1} and $\beta = 7 \times 10^{-4}$ psu^{-1} see the appendix in Gill, 1982. $\mathcal{H}$ is the surface heat loss and E - P represent the net fresh water flux. The buoyancy flux $\mathcal{B}$ plays an important role in the dynamical ideas presented here; it has units of m^{2}s^{-3}, that of a velocity times an acceleration.

$$\Delta z = 1000 \text{ m}; \ \mathcal{B}_o = 10^7 \text{ m}^2 \text{ s}^{-3}$$

then we deduce that $\Delta T \sim 0.001°C$, typical vertical velocities are (using A2 of the appendix) a few cm/s with time-scales of perhaps 8 hours or so. Here we have assumed that the buoyancy loss is all due to heat and the thermal expansion coefficient of water is $\alpha \sim 10^{-4} \text{ K}^{-1}$. It is notable that such a tiny temperature difference between rising and sinking fluid parcels can achieve a very large heat (and buoyancy) flux. We conclude, then, that the vertical column within the convecting layer is indeed very well mixed; N_{mix}^2 in Eq. (1.1.3) is very small relative to typical thermocline stratifications. In the limit that $N_{mix}/N_{th} \ll 1$, and to the extent that entrainment of stratified fluid from the base of the mixed layer can be neglected[3], Eq(1.1.1) tells us that the depth of the mixed layer, H, must increase according to:

$$H = \frac{\sqrt{2\mathcal{B}_o t}}{N_{th}} \tag{1.1.5}$$

where $\mathcal{B}_o$ is the buoyancy forcing at the sea surface and N_{th} is the stratification of the underlying fluid.

The erosion of a resting stratified fluid by convection can readily be studied in 2D using a numerical model in the absence of rotation (rotation will be added to this model later). Convection is induced by a steady, constant, buoyancy loss of $\mathcal{B}_o = 10^7 \text{ m}^2\text{s}^{-3}$ from the surface of the stratified fluid with $N/f \sim 10$. Results after 9 days are shown in fig.1.1.2. Energetic vertical overturning is occurring in a convecting layer several hundred meters thick, with much weaker flow below. The streamfunction of the overturning circulation shows vertical convection cells. A very small adverse vertical temperature gradient is evident in the body of the convective layer, with a pronounced inversion close to the surface. The interior of this mixed layer is unstable with a temperature contrast of a few hundredths of a degree over its depth agreeing well with the above prediction from parcel theory. Using the mean temperature profile (fig.1.1.2b) we estimate a depth for the mixed layer and plot its timeseries in fig.1.1.2c along with the

---

[3]At sufficiently high Peclet numbers (ie long diffusive timescale compared to advective timescale) convective plumes impinging on stable stratification may overshoot their neutral buoyancy level, and penetrate into the stably stratified region, resulting in entrainment of fluid from below and a reverse buoyancy flux at the base of the convective zone (Deardorff et al 1980). This reverse flux can lead to a sharpening of the pycnocline at the base of the mixed layer, a faster rate of deepening of the convective layer, and a transfer of properties between the stable layer and convective layer. However, there is no observational evidence (such as a large density jump) that such entrainment is prevalent at the base of deep mixed layers - see Marshall and Schott (1996). Moreover numerical simulations of rotating convection by Julien et al, 1996 suggest one possible explanation; they show that rotation significantly decreases entrainment and reduces reverse buoyancy fluxes.

prediction from the simple law (Eq. 1.1.5). Evidently the mixed layer is deepening in a 1-d fashion.

We will return to this example in lecture 3 when we consider the influence of angular momentum and rotational constraints on convection and the 'switch-over' from convection to baroclinic instability.

1.2 Convection modified by rotation

Once a mixed layer is established subsequent convection occurs in to fluid in which $N^2 \approx 0$. We thus now consider convection in a neutral, rotating ocean. One of the more interesting aspects of the convective scale in the ocean is that, much more so than its atmospheric counterpart, it can be modified by the earth's rotation. The possible effect of rotation on convection can be illustrated by considering a single dense plume sinking in to an initially unstratified rotating ocean, as sketched schematically in fig 1.2.1. As it sinks the plume will fold in (entrain) fluid from the surroundings leading to expansion in the lateral scale of the plume as it reaches further down. However if the neutral layer is sufficiently deep the entraining plume will attain a lateral scale at which it becomes aware of the earth's rotation, *before* it strikes the bottom. This inhibition of lateral growth in the presence of rotation is a consequence of the existence of Taylor columns which impart rigidity to the fluid column and which resist lateral displacement. Let us call this scale, to which the entraining plume expands, both laterally and vertically, 'l'. As shown below, and as is clear on dimensional grounds, this scale 'l depends on the external parameters, the buoyancy flux $\mathcal{B}_o$ (m^{2}s^{-3}) and the rotation rate f (s^{-1}) thus:

$$l \approx l_{rot} = \left(\frac{\mathcal{B}_o}{f^3}\right)^{\frac{1}{2}} \qquad (1.2.1)$$

The constant of proportionality between l and l_{rot} depends on the nature of the entrainment process and must be determined experimentally; it is of order unity. (The entrainment process is difficult to model in detail - see section 1.5). Now if l_{rot}/H is very small, where H is the total fluid depth, one might expect rotation to have a controlling influence on the convective process; if l_{rot}/H is very large then H limits the scale of the convection and rotational effects will play a secondary role. This rotational constraint has recently been vividly illustrated in the laboratory by Helfrich (1994). Figure 1.2.2 shows a sequence of photographs from an experiment in which a salt solution, dyed for flow visualization, was introduced into a rotating, 45 cm deep volume of fresh water. The buoyancy flux and rotation rate were such that l_{rot} = 1.98 cm, much less than the water depth. The first three frames show the early evolution before rotation becomes important. The effects of rotation are evident in frames (d), (e) and (f). The radius remains nearly constant and the front falls to form a columnar structure

which ultimately undergoes geostrophic adjustment to form an anticyclonic, conical eddy of convected fluid on the tank bottom. The radius of the column is found to scale very closely with an appropriately defined l_{rot}.

Such experiments suggest that if l_{rot}/H is small one might expect to see a surface 'convective layer' beneath which plumes, under rotational control, extend down to the bottom, as shown schematically in fig 1.2.1. It turns out that deep convection in the ocean lies in the transitional regime where rotation begins to be felt even on the plume-scale. But, as we shall go on to discuss, the plume scale in the ocean does not seem to be *controlled* by rotation, but rotation plays an important role.

1.3 Controlling non-dimensional parameters

The natural Rossby number

$$R_o^* = \frac{l_{rot}}{H} = \left(\frac{\mathcal{B}_o}{f^3 H^2}\right)^{\frac{1}{2}} \tag{1.3.1}$$

(Maxworthy and Narimousa, 1994; Jones and Marshall, 1993), is the ratio discussed above which compares the scale l_{rot} at which convection comes under the influence of the Earth's rotation, to the total depth of the convective layer H. This non-dimensional number has played a central role in the development of our ideas about the plume-scale and chimney-scale dynamics. It turns out that Ro* is *large* in the atmosphere but *small* in the ocean.

In atmospheric and oceanic convection typical vertical heat fluxes achieved by a population of convective elements are comparable---indeed they have to be because heat loss to the atmosphere drives convection in the ocean. But the buoyancy fluxes are very different, the vertical buoyancy flux in the atmosphere exceeding that in the ocean by many orders of magnitude. If the two fluids achieve the same heat flux, the ratio of the buoyancy flux is

$$\frac{\mathcal{B}_{atmos}}{\mathcal{B}_{ocean}} = \frac{\rho_w c_w}{\rho_a \alpha c_a \vartheta_a} \approx 10^5$$

where ρ is the density, c is the specific heat, and α is the coefficient of thermal expansion of water, with ϑ_a^{-1} the analogous quantity for air (where ϑ_a is a typical air temperature). Subscripts 'w' and 'a' represent water and air respectively.

Inserting typical values (ρ_w= 1000 kg/m^3, ρ_a=1 kg/m^3, α = 2x10^{-4} K^{-1}, c$_w$=4000 J kg^{-1} K^{-1}, c$_a$=1000 J kg^{-1} K^{-1} and θ_a=300 K) we find that atmospheric buoyancy fluxes are

some 10^5 times greater than oceanic buoyancy fluxes, giving an l_{rot} of 100 ~ km or more in the atmosphere compared to 100 m or so in the ocean. Typical vertical scales in the atmosphere are set by the depth of the troposphere, H = 10 km, giving Ro* ≈ 10; the convection ``hits the ceiling'' before it feels the effect of rotation; see table 1.3.1.

Contrast this with the ocean. At the site of deep convection in the western Mediterranean Sea, from example, where H ≈ 2000 m, f ≈10^{-4} s⁻¹, and heat fluxes in excess of 800 W m⁻² have been observed, $\mathcal{B}_o$ ≈ 4×10^7 m²/s³ (Leaman and Schott, 1991) then Ro* =0.1. If we take ``deep'' convection to encompass regimes from Labrador Sea convection to Weddell Sea deep water formation, then relevant values for H range from about 1000 m to 4000 m, $\mathcal{B}_o$ from perhaps 10^7 m²/s³ to perhaps 5×10^7 m²/s³ and f from its Mediterranean value up to 1.5 x 10^{-4} s⁻¹ in polar oceans. Consequently values of Ro* from about .01 to 1 are most relevant to oceanic deep convection suggesting that rotation cannot be ignored even on the plume-scale.

Table 1.3.1 presents velocity, buoyancy and space scalings, together with Ro* as a function of $\mathcal{B}_o$ (corresponding to a heat loss ranging from 100 to 1500 W m⁻²) typical of open-ocean convection sites. We have assumed that H = 2 km and f = 10^{-4} s⁻¹.

$H = 2 km$, $f = 10^{-4} s^{-1}$ Scaling		$\mathcal{H}$ (W m⁻²)			
		100	500	1000	1500
		B_o (m² s⁻³)			
		5.00×10^{-8}	2.25×10^{-7}	5.00×10^{-7}	7.25×10^{-7}
l_{rot} (km)	$\left(\frac{B_o}{f^3}\right)^{1/2}$	0.22	0.47	0.71	0.85
u_{rot} (m s⁻¹)	$\left(\frac{B_o}{f}\right)^{1/2}$	0.02	0.05	0.07	0.09
U_{norot}	$(BH)^{1/3}$	0.04	0.08	0.09	0.12
l_p (km)	$\frac{B_o^{1/4}H^{1/2}}{f^{3/4}}$	0.67	0.97	1.19	1.31
Ro*$^{1/3}$		0.48	0.62	0.705	0.755
Ro*	$\frac{B_o^{1/2}}{f^{3/2}H}$	0.11	0.24	0.35	0.43
Ro*$^{1/2}$	$\frac{B_o^{1/4}}{f^{3/4}H^{1/2}}$	0.33	0.49	0.59	0.65

Table 1.3.1 Velocity, buoyancy and space scalings in the open-ocean deep convection regime.

It is perhaps useful to consider other interpretations of Ro*. Using the rotational scaling outlined below, it is a measure of the fraction of the total depth that a particle reaches in a rotation period; alternatively one can think of Ro* as a measure of the number of vertical excursions a particle makes in a rotation period - strong forcing makes the particle undergo many circuits in a day and rotation is felt little. The square of Ro* is a non-dimensional measure of the strength of the forcing, comparing $\mathcal{B}_0$ to f^3H^2 - a velocity scale, fH, times a measure of acceleration, f^2H. Finally we shall find that its square root is a measure of the radius of deformation relative to the depth of the ocean, pertaining after the convective overturning of an initially unstratified ocean has ceased.

In addition to Ro* there are a variety of other nondimensional parameters which can be employed to completely define the external parameters. The influence of diffusion of momentum and buoyancy may be characterized by the flux Rayleigh number (which is independent of f),

$$Ra_f = \frac{\mathcal{B}H^4}{k^2 v} \tag{1.3.2}$$

where v and κ are viscosity and thermal diffusivities respectively, or by the Taylor or Ekman numbers,

$$Ta = \frac{1}{E_k^2} = \left(\frac{fH^2}{v}\right)^2 \tag{1.3.3}$$

Appropriate values of Ra_f and Ta for oceanic deep convection are not known with any certainty because the turbulent processes are represented by `eddy' viscosities and diffusivities which are not distinct from the convective process itself. For this reason Klinger and Marshall (1994) attempt to characterize the flow in terms of (Ra_f, Ro*), rather than the more common choice (Ra_f, T_a), because the former pairing produces a tidy division of the external parameters between a viscous/diffusive parameter independent of f - Ra_f - and a rotational parameter independent of diffusion - Ro*. Such a division is especially useful for application to the ocean because Ro* is rather readily calculated for convection in the ocean (see table 1.3.1), but Ra_f, which depends on poorly-known values of `eddy' diffusivities, is not.

For all the above reasons it also seems appropriate to set $v = \kappa$ i.e. the Prandtl number is set to unity:

$$P_r = \frac{v}{k} \tag{1.3.4}$$

1.4 Scaling ideas

Imagine that loss of buoyancy, associated with a sustained flux of magnitude $\mathcal{B}_o$, at the surface of a homogeneous ocean of depth H, drives a convective layer of depth l_z as illustrated schematically in fig.1.2.1. The convective layer will deepen as the plumes that make it up evolve in time, penetrating into the fluid below. Ultimately the layer will extend down to the bottom of the ocean. If Ro* becomes sufficiently small then the convective layer will come under the influence of the earth's rotation.

Let us suppose that in the initial stages, plumes extending into the convective layer are so small in scale that they cannot feel the finite depth of the ocean H. Furthermore if $t << f^1$, then rotation is unimportant; only $\mathcal{B}_o$ remains as the controlling parameter. It is then not possible to construct scales for the depth, buoyancy or velocity of the plumes. The convective process must evolve in time, and we suppose that it proceeds in a self-similar way. Remembering that the units of buoyancy flux $\mathcal{B}_o$ are m^2s^{-3}, the following scales can be formed from $\mathcal{B}_o$ and t :

$$l \sim \left(\mathcal{B}_o t^3\right)^{\frac{1}{2}}$$

$$u \sim w \sim \left(\mathcal{B}_o t\right)^{\frac{1}{2}} \tag{1.4.1}$$

$$g' \sim \left(\frac{\mathcal{B}_o}{t}\right)^{\frac{1}{2}}$$

Scale constrained by the depth of ocean; Ro* >>1

If it is the depth of the ocean that ultimately limits the scale of the cells then putting $l = H$ in Eq. 1.4.1a, above, the following scalings are suggested (Deardorff and Willis, 1967), independent of rotation:

$$l \sim l_{norot} = H$$

$$u \sim u_{norot} = \left(\mathcal{B}_o H\right)^{\frac{1}{3}} \tag{1.4.2}$$

$$g' \sim g'_{norot} = \left(\frac{\mathcal{B}_o{}^2}{H}\right)^{\frac{1}{3}}$$

The subscript 'norot' indicates that these are the scales adopted in the absence of rotation. They are the velocity scales that are implicit in the flux law Eq.1.1.4.

Scale constrained by the Earth's rotation; Ro* << 1

If the ocean is sufficiently deep then the evolving convective layer will come under geostrophic control *before* it strikes the ocean bottom as described in section 1.2. The transition from 3-d thermally driven plumes to quasi-2-d, rotationally dominated motions (represented schematically in Fig. 1.2.1 and evident in figs. 1.2.2) will occur as t approaches f^{-1} at which point, replacing t by f^{-1} in Eq.1.4.1 the following scales pertain (see Fernando et.al, 1991):

$$l \sim l_{rot} = \left(\frac{\mathcal{B}_o}{f^3} \right)^{\frac{1}{2}}$$

$$u \sim u_{rot} = \left(\frac{\mathcal{B}_o}{f} \right)^{\frac{1}{2}} \tag{1.4.3}$$

and

$$g' \sim g'_{rot} = \left(\mathcal{B}_o f \right)^{\frac{1}{2}}$$

where the subscript `rot', for `rotation', has been used to denote the scales at which rotation begins to be important.

At these scales the plume Rossby number is unity:

$$R_o^* = \frac{u}{fl} \approx \frac{u_{rot}}{fl_{rot}} = 1$$

It should be noted that the scales identified above are independent of assumptions concerning eddy viscosity and diffusivities; they are the velocity, space and buoyancy scales that can be constructed from the `external' parameters $\mathcal{B}_o$, f and H. However the constants of proportionality in Eq. 1.4.2 and 1.4.3 *will* be dependent on viscous/diffusive processes.

Velocity and length scales implied by Eq 1.4.2 and Eq.1.4.3 are tabulated in table 1.3.1. for typical oceanographic parameters. Note that when Ro* ≡ 1 (and Ro* never becomes very small in the ocean) rotating and non-rotating scales are the same.

1.5 Numerical studies of plumes

Numerical studies of rotating convection clearly demonstrate the features schematized in Fig. 1.2.1 and observed in the laboratory, fig. 1.2.2. Fig. 1.5.1. shows currents and temperatures in a very high resolution numerical experiment (50x50x50m) 24 hours after vigorous cooling (800 W/m²) was applied at the surface of an initially resting unstratified, rotating ocean in which

Ro*=0.1 and Ra_f= 10^9. As the cooling persists, plumes penetrate progressively deeper into the interior, lowering the mean base of the convective layer and, in time, distributing the influence of intense surface heat loss over the whole depth of the ocean. A linear equation of state was used (but see Sander et.al.1995 where a more realistic equation of state is considered).

In Fig. 1.5.2a we plot the horizontal velocity variance $\sqrt{u'^2 + v'^2}$ at day 2 as a function of depth for a series of experiments, normalized with respect to the non-rotating scaling u_{norot}, Eq. 1.4.2. Velocities in the (essentially) non-rotating experiment f = 10^{-6} s^{-1} do indeed scale as u_{norot} - the curve is centered on unity in fig. 1.5.2a. However, we see that in the `high-rotation' regime typical eddy velocities decrease as the rotation rate increases, as suggested by the scaling 1.4.2. Fig. 1.5.2b again plots $\sqrt{u'^2 + v'^2}$ against depth but now normalized with respect to u_{rot}, Eq. 1.4.3. The normalized velocities from all the high rotation experiments collapse on to the same line centered around unity; u_{rot} is indeed the velocity scale adopted by the plumes. Note that it is only the f = 10^{-6} s^{-1} velocities that appear anomalous when scaled with respect to the rotational velocity u_{rot}.

Laboratory experiments reported by, for example, Maxworthy and Narimousa (1994) and Coates et. al. (1995), suggest that the numerical experiments presented above, and in Jones and Marshall (1993), over-emphasize the role played by rotation in oceanic plume-scale dynamics. The consensus of the laboratory experimentalists is that rotational affects are only felt when Ro* < 0.1, rather than Ro* < 0.7 or so in these numerical experiments. This issue can only be resolved through the careful design of further numerical experiments, but the way forward is not clear.

The approach of Jones and Marshall (1993) is that of a Large Eddy Simulation (LES) and uses very crude closure assumptions (laplacian diffusion of heat and momentum with constant diffusivities); it has been criticized by Sander et al (1995) and Coates et.al (1995). More sophisticated closure schemes exist (but more often than not tuned to *atmospheric* observations), but even the most sophisticated LES assumes the turbulence to be isotropic and homogeneous and thus make gross assumptions about the nature of the small scale turbulence (a critical review of the method in the atmospheric context is given by Mason; 1994 - see Garwood et.al. 1994 and Denbo et.al. 1994 for examples of LES applied to ocean convection). However rotating convection is strongly anisotropic - both because of the nature of the plumes, which are stiffened by rotation, and because of the organization of the flow by rotation. The advantage of LES is that simulations with Reynolds numbers approaching realistic values can be made; its disadvantage is that results obtained using the method may depend on assumptions implicit in the assumed closure hypotheses.

An alternative approach - that of Direct Numerical Simulation (DNS) - is one in which all the dynamically active scales of motion, down to the Kolmogorov scale, are resolved; it is being pursued by Julien et al (1996a) and Kerr et al (1995) but, because of the enormous computational costs is limited in the range of Re it can study. However, anisotropies in mixing properties, and boundary layer processes, can be examined without any pre-imposed bias in DNS. Since realistic Re cannot be examined, instead the DNS approach searches for scaling behavior in the solutions, and then extrapolates to realistic values, assuming that the flow remains in the same dynamical regime.

Studies of Raleigh-Benard convection using DNS by Julien et al, 1996b, although not in a parameter regime directly applicable to the ocean, reveal an important influence of rotation on the dynamics of convective plumes. The localized cyclonic vortices associated with low Rossby number convective plumes lead to a quasi-2-dimensional vortex dynamics, stirring the fluid in horizontal planes. This enhanced lateral mixing inhibits the vertical transports of density anomalies, and leads to the establishment of a finite negative temperature gradient (rather than the homogeneous mixed layer seen in non-rotating convection). This was also observed in the numerical study of Klinger and Marshall (1994); the magnitude of the adverse temperature gradient, although enhanced over that seen in the non-rotating case, is rather small, however, for typical oceanographic parameters and conditions; in the field it would be very difficult to isolate from other effects.

The underlying hydrodynamics explored in the above numerical experiments, can be modified, but not fundamentally changed, by thermobaric effects[4]. Gill(1973) and Killworth (1979) first recognized the role of thermobaric enhancement of thermal expansion in their calculations/models of hydrostatic stability in the water column in the Weddell Sea. The thermobaric effect on Greenland Sea convection was studied in LES simulations by Garwood et.al.(1994), Denbo et al (1995) and Sander, Wolf-Gladrow and Olbers, 1995, and was shown to effect plume development and convection depth; see also the review by Paluszkiewicz et al (1994).

---

[4] The stability of a water parcel in a column is determined entirely by the buoyancy force acting on it. Complications arise because the density of sea-water can depend on T, S and p in subtle ways. Often in theoretical study a simplified equation of state is adopted of the form:

$\rho = \rho_o (1 - \alpha T + \beta S)$ where α and β are thermal expansion and haline contraction coefficients respectively. To the extent that they can be taken as constant, the dynamical equations can be entirely reformulated in terms of a buoyancy variable and buoyancy forcing. But particularly at low temperatures the thermal expansion coefficient varies strongly with T and p; it becomes smaller at lower temperatures but increases with depth. The excess acceleration of a parcel due to the increase in α with depth, the *thermobaric effect*, can result in a destabilization of the water column if the displacement of a fluid parcel (as a result of gravity waves, turbulence or convection from above) is sufficiently large.

Lecture 2; CHIMNEY DYNAMICS

The most unrealistic feature of the convective process discussed in the first lecture, is that there were no *lateral* inhomogeneities. In nature convection acts to homogenize a patch of ocean which is confined in space. In this lecture we go on to review what is understood of the dynamics of the mixed patch as a whole. The mixed patch has become known as a chimney (although we shall see that this is not an ideal name). The defining feature of chimneys is that properties (such as T and S) are mixed by convection *locally* leading to a diminution of property gradients interior to the chimney, but an enhancement of gradients around the periphery. From a theoretical point of view this localization in space makes the chimney problem distinct from the myriad studies of convection rooted in the Rayleigh problem (convection between two plates extending to ±∞); as one might anticipate edge effects ultimately come to dominate the evolving flow fields in the chimney problem. Large horizontal buoyancy gradients on the edge of the convection patch support strong horizontal currents in thermal-wind balance with them - the 'rim-current'. If the chimney has a lateral scale greater than the radius of deformation, then instability theory (see lecture 3) tells us that it must break up in to Rossby-radius-scale fragments. This instability plays a dominant role in the dynamics and thermodynamics of the chimney, orchestrating the exchange of fluid and buoyancy to and from it.

To introduce some of the important ideas we first consider the overturning of a neutral, rotating fluid to an extended, but localized loss of buoyancy. We then go on to consider the same problem but in a stratified rotating fluid.

2.1 *Chimneys in initially unstratified rotating fluids*

Studies of the convective overturning of *neutral* fluids are of importance because they enable one to focus on the role of rotation in isolation from other effects. They also have some practical oceanographic relevance because deep convection sites are (almost by definition) very weakly stratified - see the observations of Leaman and Schott (1991), for example. We shall see that Ro* emerges again as a key non-dimensional parameter; its square root is a measure of the radius of deformation relative to the depth of the ocean, pertaining after the convective process has ceased.

2.1.1 Laboratory analogues

<u>Melting ice-disc</u>

Laboratory `chimney' experiments have been carried out in Woods Hole to observe the flow produced by an extended patch of cooling in the presence of

rotation. One particularly instructive (and simple) series of experiments was carried out by Jack Whitehead and Brian Racine in 1991; they are described in more detail in Marshall et.al. 1994.

A 1 cm thick ice disc (molded in a cylindrical metal film canister) was gently inserted at the top center of the rotating water, as sketched schematically in Fig. 2.1.1. The ice also contained a dye so that water that was originally ice was tagged with a tracer. The ice disc melted in 300 seconds extracting its latent heat of fusion from the water implying a cooling rate of 1.2×10^4 Wm^{-2} (taking the latent heat of ice to be 363 J cm^{-3}). This gives $\mathcal{B}_0 = 6 \times 10^{-6}$ m^{2}s^{-3} and hence an Ro* = 0.03 for the shortest rotation period of 15 seconds (f=0.84). Three other rotation rates were also used with periods of 30, 60, and 120 seconds (that is Ro*'s of 0.09, 0.25, and 0.72, respectively, spanning the oceanographic range).

After the ice was placed on the water, convection cells were observed to extend to the bottom beneath the ice; see fig. 2.1.2a. As the ice melted, small eddies migrated away from the edge of the ice. By the time the ice was completely melted, at roughly 360 seconds or 24 rotation periods, the cooled fluid had broken up into about half a dozen eddies that continued to spread apart with time. A side view of the dyed water is shown in figure 2.1.2b for the largest rate of rotation. The eddies are conical in shape with cold water (tagged with dye) spreading out over the bottom, but 'contained' by rotation. Above each conical eddy clear water can be seen. Injected dye showed that there was pronounced counterclockwise (cyclonic) circulation there. Dye injected directly into the convected fluid revealed little circulation. This picture is consistent with the upper cyclonic circulation being associated with a low pressure that 'holds up' the placid lens of dense fluid.

Pellets of potassium permanganate were also dropped next to the outer edge of the ice disc to produce a vertical column of dyed fluid. Cyclonic circulation built up around the periphery of the ice in the early part of the experiment. Simultaneously, near the bottom at the same radius, anticyclonic circulation started to develop. This is easily understood from a consideration of angular momentum and its conservation since fluid flows inward near the top and consequently outward near the bottom. Finally, after all the ice had melted, cyclonic circulation was found to extend over the full depth of each eddy, presumably due to the persistent action of bottom friction.

An important message to be taken from this experiment is that 'chimney' is a misleading name; the convection site does not act as a 'pipe' down which material flows to thence spread laterally away. Rather the plumes act as 'mixing agents' churning the column vertically. But on scales somewhat (but not much) larger than the plume-scale, rotation has a controlling influence and the dense gravity current emanating from the convection site is constrained almost

immediately by the earth's rotation. The 'spreading phase' in which convectively modified fluid is carried to sites many Rossby radii away from the formation region, is a geostrophic process in which eddies formed by baroclinic instability play a central role.

Shower-head

In an important study by Maxworthy and Narimousa (1994) laboratory experiments were combined with scaling arguments to determine the size and velocity scales of newly formed baroclinic vortices - the cones we see in Fig 2.1.2b - generated by surface cooling. They used both laterally confined and unconfined apparatus. In the confined experiments saline water was introduced over the entire top surface of a rotating tank. In the unconfined experiments salty water was introduced only over a central circular region using a shower head. These latter experiments are of particular interest because the buoyancy is extracted in a localized region (as in Whitehead's ice-disk experiment) and so the convectively processed water can escape the forcing and geostrophically adjust under rotation and gravity, mimicking the fate of convected fluid in the open ocean.

Maxworthy and Narimousa argued that after convection has ceased convectively modified fluid would be found in geostrophically adjusted cones, the remnants of the chimney broken up by baroclinic instability into radius-of-deformation-scale fragments. The cones of convected water, have a scale controlled by a radius of deformation:

$$l_{cone} \approx l_\rho = \frac{\sqrt{g'_{rot} H}}{f} = \frac{B_o^{\frac{1}{4}}}{H^{\frac{1}{2}} f^{\frac{3}{4}}}$$

The aspect ratio of the cones of dense fluid, l_{cone}/H, scales with the (square-root of the) natural Rossby number of the system because:

$$\frac{l_{cone}}{H} \approx \frac{l_\rho}{H} = \frac{1}{f}\sqrt{g'H} = \frac{B_o^{\frac{1}{4}}}{f^{\frac{3}{4}} H^{\frac{1}{2}}} = \sqrt{R_o^*} \qquad (2.1.1)$$

where Ro*, depending only on `external' parameters, is the `natural Rossby number' discussed in lecture 1.

Their experiments ranged Ro* from .08 to 1. In both confined and unconfined experiments, the slope of the experimental data could be rationalized in terms of the scaling arguments reviewed in lecture 1 (section 1.4); in particular it was found that the velocity and space scale of the eddies shed by the baroclinically unstable, convectively driven vortex, could be expressed as a function of Ro*,

consistent with predictions of baroclinic instability theory and the numerical experiments of Jones and Marshall (1993) - see below. The experiment also provided constants of proportionality which depend on the nature of the (rotationally influenced) entrainment process.

These laboratory experiments have been followed up and extended by Brickman (1995) and Coates et.al. (1995)

2.1.2 Numerical analogues

Extensive numerical simulations of chimneys in neutral ambient conditions have been carried out using ocean models which solve the incompressible Navier Stokes equations - see, for example, Jones and Marshall, 1993; Send and Marshall, 1995. The implied flux Rayleigh number Ra_f is 8×10^8 and the Taylor number, Ta, ranges between 4×10^2 and 10^8, placing these experiments in the fully developed turbulence/geostrophic turbulence regime - regions 3 and 4 of fig.1 in Fernando et.al (1991). The grid-spacing of the model is small enough that gross aspects of convective plumes themselves can be resolved, yet the domain of integration is sufficiently large to permit a study of both the influence of the plumes on the large-scale and the geostrophic adjustment/baroclinic instability of the convected water. An example is presented in fig.2.1.3 simulating the overturning and break-up of a chimney. A buoyancy loss of $\mathcal{B}_o =$ 4×10^{-7} m^{2}s^{-3} (corresponding to a heat-loss of 800 Wm^{-2}) was applied over a 16 km disc centered at the surface of a 32 km, doubly periodic, 2 km deep ocean. The implied Ro* is 0.1. The water was initially homogeneous with a linear equation of state dependent on temperature alone.

The sequence of events - sinking in plumes and subsequent spreading of convected fluid in baroclinic structures - can be readily seen in fig. 2.1.3 where the temperature is rendered in three dimensions at various stages in the developing chimney, resulting in images reminiscent of those obtained in the laboratory using dye. The darker patches correspond to colder fluid.

As in the laboratory, the combined effect of the plume-scale convection is to drive an increasingly strong, large-scale rim-current around the disk of cooling, cyclonic at the surface, anticyclonic beneath. This rim-current serves to confine the convected fluid to the volume defined by the disk of cooling. Fluid outside the chimney is unmodified and initially there is little lateral transfer of fluid between the overturning and the non-overturning regions. By day two, however, there is evidence of the growth of meanders in the rim-current as it becomes baroclinically unstable, an instability which eventually leads to the break-up of the patch of convected water and lateral exchange of fluid with the surroundings. By day four the chimney of homogenized cold water has broken

up into a number of distinct conical structures extending through the depth of the model ocean. These cones have a definite space and velocity scale.

The ratio l_{cone}/H is plotted in fig.2.1.4, obtained from a series of such numerical experiments, as a function of Ro*, along with data obtained by Maxworthy and Narimousa (1993) in their laboratory. It is very pleasing to find that the laboratory and numerical experiments collapse on a very similar line; taken together they are strongly supportive of the scaling Eq.2.1.1. From the slope of the line drawn through the data in fig.2.1.4 we deduce that:

$$\frac{l_{cone}}{H} \approx 5\sqrt{R_o^*} \qquad\qquad (2.1.2)$$

This formula can be used to predict, with a reasonable measure of success, the scale of the cones produced by the melting ice experiment described above.

The scale $l_\rho = H\sqrt{R_o^*}$, is tabulated in table 1.3.1 as a function of the buoyancy flux $\mathcal{B}_o$.

2.2 Chimneys in stratified, rotating fluids

Laboratory and numerical experiments

Jack Whitehead designed a set of laboratory experiments which prescribed a constant buoyancy loss at the surface of rotating *stratified* fluid; they are reported in Hufford, Marshall and Whitehead (1996). Filter paper was attached to the bottom of a cylinder and placed in contact with the free surface of a linearly stratified body of water in a rotating (1 m^2) tank. The porosity of the filter paper was selected so that the flux of brine through it was of the desired rate if the standing water depth in the cylinder was 2 or 3 cm; typical buoyancy fluxes of $\mathcal{B}_o$ = 10^{-5} m^{2}s^{-3} can be obtained in this way and, with judicious choice of porosity, it can be reduced further by two orders of magnitude. A camera was used to obtain a top view of the evolving convection, together with a side view through a 45°mirror. The cylinder obscured the central area in the top view, so only intrusive fluid that spread laterally could be seen from the top. The side view in the mirror was visible for the entire duration of the experiment, however - see fig.2.2.1.

The convective layer penetrated rapidly downward in the early part of the experiment. The dye would typically collect under the source as a rapidly - deepening mixed region. After a time, however, the rate of advance of the layer slowed markedly but generally never entirely ceased for the duration of a run. Usually when the advance slowed, the side view revealed considerable lateral

slumping of the sides of the dyed region. As time progressed the patch of dense dyed fluid broke in to a number of eddies thus arresting the deepening of chimney - see fig.2.2.1. Much quantitative information was obtained from dozens of such experiments and interpreted in terms of the theoretical ideas set out in section 2.3 below. First, however, we mention parallel numerical studies that have used to help us understand the problem.

The deepening of a mixed layer in to an initially stratified, resting fluid, has also been studied numerically, as illustrated in Fig.2.2.2. As in the laboratory buoyancy is extracted from the surface of the fluid over a disc of radius r at a rate $\mathcal{B}_o$. In the figure cooling at a rate of 500 W/m^2 was imposed over a disc of radius 30 km. Initially the mixed layer deepens by the action of plumes at a rate close to that given by a non-penetrative convection model (eq.1.1.5), but as rotation takes over and baroclinic instability sets in, and just as in the laboratory experiments, the deepening of the mixed layer is arrested as baroclinic eddies sweep the convected fluid away sideways and draw stratified waters in from the side. The developing eddies can be seen in fig. 2.2.2.

Much as outlined in lecture 1, in section 2.3.2 we develop scaling laws, guided by our understanding of the underlying hydro-dynamics, for the stratified problem also. In addition to Ro*, two other non-dimensional number play an important role; N/f, measures the Rossby radius $(NH)/f$ to the depth of the ocean H, and r/H measures the aspect ratio of the convection patch. Here N is the Brunt-Vaissala frequency of the ambient fluid. But first let us consider important integral properties of the chimney.

2.3 Theoretical interpretation

2.3.1 Vertical mass transport and deep water formation rates

What are the integral properties of a population of plumes working in concert over a local area to form a chimney? A law of vertical heat transport for such a collection of plumes was outlined in appendix (i) and applied in lecture 1. We consider here the role of plumes in the net vertical mass transport and deep water formation rate.

On the large-scale stretching/compression of Taylor columns generates horizontal circulation, thus enabling one to relate the *net* vertical velocity over a patch of ocean to the rate of change with time of the circulation around the patch:

$$\frac{\partial}{\partial t} \oint \mathbf{u}.\, dl = f_o \frac{\overline{\frac{\partial w}{\partial z}}^{area}}{\partial z}$$

where $\overline{w}^{area}$ is the vertical velocity averaged over the patch. Observations in the Gulf of Lyons (Send, personal communication) do not reveal any systematic tendency in rim-current speeds and neither do they appear to be correlated with convective events, suggesting that during convection $\overline{w}^{area}$ is not significantly different from zero. Indeed horizontal currents observed on the periphery of convection sites rarely exceed 20-30 cm s^{-1}. Even if one supposed that such currents were set up rapidly, in only a few days, then the above formula yields a net w of a fraction of a mm/sec, over a patch 50 km in diameter and 1 km deep. This is a very small vertical velocity, tiny compared to those associated with individual plumes, and so small as to be insignificant in the context of deep water formation. We conclude (the arguments are developed in more detail in Send and Marshall, 1995) that the plume-scale does not play a significant role in vertical mass transport - downwelling in a plume is almost entirely compensated by upwelling *local* to that plume - but they are very efficient mixers of properties. This has important implications for the way in which plumes are parameterized in numerical models (see Marshall and Schott, 1996). Evidently the sinking of the homogenized column occurs on much longer timescales and, we believe, is associated with geostrophic eddy dynamics. A further implication is that the volumes of fluid created (for example, the number of Sverdrups of Labrador Sea Water) cannot be computed directly from measurements (or deductions) of vertical velocity w which are vanishingly small integrated over the chimney. Instead it is best to relate them directly to the volumes of homogenized fluid created in the mixing phase - see Send et.al 1995.

For example, suppose that convection has created dense water over an area A down to a depth h. The volume created is A x h. Taking, for example, $A = \pi(60km)^2$ and h = 1 km, typical of the Mediterranean (see Send et.al. 1995), we obtain a deep water formation rate of 1.1x10^{13} m^3 per year, or approximately 0.3 Sv, just from one event; this is in approximate agreement with the observed outflow of deep water at Gibralter.

2.3.2 Equilibrium depth and timescales

Visbeck, Marshall and Jones (1995) study and quantify the equilibrium state of the convective chimney in a linearly stratified ocean which would ultimately be set up if buoyancy loss through the sea surface $\mathcal{B}_o$ over the chimney, were *entirely* balanced by lateral buoyancy flux due to eddies around the periphery of the chimney *across* the rim-current $\overline{v'b'}$:

$$\int \mathcal{B}dA = \int_{-h_{equil}}^{o} \oint \overline{v'b'} dl dz \qquad (2.3.1)$$

where $b' = -g\dfrac{\sigma}{\rho_o}$ and the overbar denotes a time-average long compared to a typical eddy lifetime. Of course, such an equilibrium state may not always be achieved in nature - see below - but it is an interesting limit state and one which is amenable to analysis.

We now solve (2.3.1) for the equilibrium depth, h_{equil}. Parcel theory is applied to close for the eddy flux $\overline{v'b'}$ following Green (1970). The eddy velocity is:

$$v' = \frac{y}{t_{eddy}} \qquad (2.3.2)$$

where $t_{eddy} = \dfrac{\sqrt{R_i}}{f}$ is assumed to be the inverse of the Eady(1949) growth-rate (see lecture 3 and appendix (ii)), y is the lateral scale of the eddy transfer process and R_i is the Richardson number of the mean flow given by:

$$R_i = \frac{N^2 f^2}{M^4} \qquad (2.3.3)$$

Here $M^2 = \dfrac{\partial b}{\partial y}$ is a measure of the stratification in the horizontal, entirely analogous to N^2, the measure of the vertical stratification.

Furthermore the buoyancy perturbation associated with the eddy is

$$b' = M^2 y \qquad (2.3.4)$$

and so, combining (2.3.2), (2.3.3) and (2.3.4), we arrive at an expression for the lateral buoyancy flux (written down by Green (1970) in the context of lateral heat flux by baroclinic eddies in the atmosphere):

$$\overline{v'b'} = \alpha \frac{f}{\sqrt{Ri}} M^2 y^2 \qquad (2.3.5)$$

where α is a constant of proportionality and 'y' is a transfer scale, both of which need to be determined.

Now, if the vertically mixed region joins smoothly on to the ambient stratification below, with no jumps in buoyancy at its base so that

$$M^2 y = N^2 h_{equil} \qquad (2.3.6)$$

then, solving (2.3.1) for h_{equil} using (2.3.5) and (2.3.6), we deduce that:

$$h_{equil} = \gamma \frac{(Br)^{\frac{1}{3}}}{N} \qquad (2.3.7)$$

where r is the radius of the rim-current and $\gamma = \dfrac{1}{(2\alpha)^{1/3}}$.

It is interesting that the prediction (2.3.7) is independent of the Coriolis parameter f. However, this should not be interpreted as implying that geostrophic dynamics are not important - on the contrary, the energy supply for the eddies seen in Figs. 2.2.1 and 2.2.2 which make equilibration possible is the potential energy stored in the thermal wind.

In an exhaustive evaluation of many numerical and laboratory experiments on baroclinically unstable chimneys, including the ones shown in the figures here, Visbeck et. al. (1996) confirm the parameter dependence of h_{equil} on B, r and N suggested by Eq.(2.3.7) and find that (a fit from experimental data):

$$\gamma = 3.9 \pm 0.9$$

implying that α in Eq.(2.3.5)

$$\alpha = .008 \pm .002 \qquad (2.3.8)$$

remarkably close to 0.005, the value obtained by Green in his study of heat transport by baroclinic eddies.

Eq.(2.3.7) can be succinctly expressed in terms of our three controlling non-dimensional numbers; dividing through by H, the depth of the ocean, Eq.(2.3.7) can be written thus:

$$\frac{h_{equil}}{H} = \gamma \frac{f}{N} \left(\frac{r}{H}\right)^{\frac{1}{3}} R_o^{*\frac{2}{3}} \qquad (2.3.9a)$$

and the implied eddy scale of the equilibrated state is $L_\rho = \dfrac{N}{f} h_{equil}$, or

$$\frac{L_\rho}{H} = \gamma \left(\frac{r}{H}\right)^{\frac{1}{3}} R_o^{*\frac{2}{3}} \qquad (2.3.9\ b)$$

independent of N!

Typically, in chimney convection, N/f ~ 10 (of the ambient fluid), Ro* ~ 0.1 $\rightarrow$ 1 and r/H ~ 50, giving h_{equil}/H ~ 0.1 $\rightarrow$ 1 if γ ~ 4 (we present more numbers in section 2.3.3 below).

Time-scales

Let us now ask the questions; is it likely that the chimney will reach the depth predicted by (2.3.7), and, if so, how long will it take? If the mixed-layer deepens in a 1-d fashion according to (1.1.5) it will take a time t_{one-d} given by:

$$t_{one-d} = \frac{N^2 h^2}{2B} \qquad (2.3.10)$$

to reach the depth h if N^2 is constant. However, if, as the mixed-layer deepens, baroclinic eddies have time to grow to finite amplitude, then our one-dimensional assumption will break down as lateral fluxes of buoyancy begin to contribute to the buoyancy budget of the evolving mixed layer. Suppose that the time required for the chimney to equilibrate through baroclinic instability is t_{equil} and

$$t_{equil} < t_{one-d}$$

then the deepening of the mixed-layer at the center of the gyre will be slowed and possibly arrested. In the limit that the deepening is halted completely, buoyancy loss from the surface over the gyre is offset entirely by lateral flux in eddies setting up a quasi-steady state (as hypothesized in 2.3.2).

The time t_{equil} to reach the depth h_{equil} cannot be greater than the time it takes a one-dimensional mixed layer deepening as in (1.1.5) to arrive there. Thus, combining (2.3.10) and (2.3.7) we find that:

$$t_{equil} < \gamma^2 \left(\frac{r^2}{\mathcal{B}} \right)^{\frac{1}{3}} \qquad (2.3.11)$$

Fig. (2.3.1b) plots t_{equil} as deduced by inspection of laboratory and numerical experiments reported in Visbeck et.al (1996) and Hufford et.al.(1996); t_{equil} scales thus:

$$t_{equil} = \beta \left(\frac{r^2}{\mathcal{B}} \right)^{\frac{1}{3}} \qquad (2.3.12)$$

$$\beta = 12 \pm 1.2$$

as suggested by (2.3.11) and β (which is plausibly somewhat smaller than the $\gamma^2 \approx 16$ of 2.3.8) has been determined empirically from the data.

We now go on to discuss the implications of these results for the dynamics of chimneys in the ocean.

2.3.3 Oceanographic parameters

In fig.(2.3.2) we plot t_{equil}, Eq(2.3.12) and t_{one-d}, Eq(2.3.10), as a function of the cooling rate for h = 100 m, N = 10^{-2} s^{-1} and r = 50 km. We see that for persistent cooling rates in excess of 300 W/m², the mixed layer will reach a depth of 100 m *before* it is arrested by baroclinic instability. Choosing somewhat different, but not untypical values; - $N_{surface} \sim 5 \times 10^{-3}$ s^{-1}, $\mathcal{B}_o = 7.5 \times 10^{-8}$ m^2s^{-3} (corresponding to a heat flux of 150 W/m²), H = 200m - we find that $t_{one-d} = 60$ days. This is long compared to typical baroclinic instability times-scales (see lecture 3). Thus for lower cooling rates perhaps more typical of the climatology, baroclinic instability may indeed control the ultimate depth to which the mixed layer reaches. But if buoyancy is extracted rapidly, in one or two violent events, baroclinic instability will not have sufficient time to limit the depth - one-dimensional ideas ought to be adequate to determine the depth to which rapid deepening reaches. The patch of homogeneous fluid will nevertheless subsequently break up by baroclinic instability and the eddies will disperse and play a role in restratifying the convection site.

In the winter of 1969 (MEDOC) and 1992 (Schott et.al, 1994) convection did not reach the bottom but stopped at intermediate levels. Perhaps the deepening of the chimney was arrested due to lateral, eddy induced buoyancy flux offsetting the surface cooling. For a Mediterranean chimney of width ~ 60 km and a typical Mistral heat loss (600 W/m²), Eq.2.3.12 gives t_{equil} ~ 30 days. Therefore, it seems unlikely that baroclinic eddies played a central role in arresting the deepening chimney because the period of strong heat loss lasted only 10 days. However, close to the rim-current significant lateral heat and tracer fluxes must have occurred associated with geostrophic eddies. Our prediction for a typical eddy size, given by the final Rossby radius, are close to the observations; Eq.2.3.9 suggests a Rossby radius of 8 km which is roughly in accord with the eddy scales observed by Gascard (1978).

Baroclinic eddy fluxes are likely to be of great importance, however, on the seasonal (preconditioning) time-scale because the geostrophic eddy instability time is then considerably shorter than that of the forcing. If the heat loss is ~ 200 W/m² and the diameter of the convecting region ~ 200 km, parameters perhaps more typical of the Labrador Sea gyre, then eq.2.3.12 yields a breakup time scale of ~ 60 days. This suggests that by the end of winter baroclinic eddies can influence the mixed-layer budget significantly, even at the center of the gyre.

If conditions are such that the chimney *does* reach its equilibrium depth, then characteristic scales of the equilibrium state are summarized in fig.2.3.3.

Lecture 3 :*A potential vorticity perspective*

In this third lecture we present a generalized view of the convective process which has been helpful to us in crystallizing ideas. It is couched in terms of potential vorticity (Q). Potential vorticity acts as a wonderful bridge between theoretical ideas (which are almost invariably most succinctly expressed in terms of Q), models and, most importantly, the observations, because it gets to the heart of the dynamics in the most succinct, and hence profound way (see, for example the review by Hoskins et.al., 1984).

Potential vorticity Q is defined thus:

$$Q = \frac{1}{g} \eta . \nabla b \qquad (3.1a)$$

and so is a measure of the stratification in the direction of η, the absolute vorticity vector:

$$\eta = \nabla x \, \mathbf{v} + f \mathbf{k} \qquad (3.1b)$$

where k is a unit vector in the vertical.

We have a particular interest in the distribution, transformation and transport of potential vorticity through the ocean because:

- Q is conserved in adiabatic, frictionless motion and hence marks a fluid particle just like any other fixed feature of a particle of fluid.
- given suitable boundary conditions any Q field can be 'inverted' subject to boundary conditions, to yield the balanced velocity and buoyancy field - the 'invertibility principle'.
- all of our basic theoretical constructs - Rossby waves, baroclinic instability etc. etc. - have their simplest expression when couched in terms of Q. Potential vorticity is the focus of theoretical models of the oceanic thermocline and, in an approximated form, is the basis of quasi-geostrophic theory.

If our primary interest is in the large-scale (geostrophically and hydrostatically balanced) component of the flow, then the above three aspects suggest that Q ought to be the central focus of attention in any parameterization of smaller-scale processes that drive large-scale flow (such as baroclinic eddies and/or convection, for example). In the convection problem in particular, Q does indeed act as this bridge between theory/observations and small/large-scale

processes. The simple notion on which we wish to elaborate here is the following:

- convection rapidly sets (transforms) the Q of the convection region to zero:

$$\text{transformation: } Q \xrightarrow{\text{convection}} 0 \tag{3.2}$$

- the effect of convection on the large-scale flow can be deduced by inversion of the Q field thus transformed, subject to balance and boundary conditions:

$$\text{inversion: } Q \xrightarrow{\text{inversion}} \left\{ \frac{\text{balanced}}{\text{v and b}} \right. \tag{3.3}$$

Eq.(3.2) is discussed in section 3.1, Eq.(3.3) in section 3.2.

3.1 Convection sets PV to zero

Let us again consider overturning in the vertical plane, as in lecture 1, section 1.1, but now in the presence of more generalized potential vorticity (rotational/angular momentum, as well as stratification) constraints. The normal state of affairs in mixed layers - drawn schematically in Fig. 1.1.1b - is one in which the density varies in the horizontal *across* the mixed layer (because of more vigorous convection on one side of it than the other, for example). On the large-scale a zonal current u(y,z), in thermal wind balance with lateral mixed-layer density gradients, will develop given by:

$$u_z = -\frac{b_y}{f} \tag{3.1.1}$$

Suppose that there are no variations in x. Then a consideration of the zonal momentum equation (assumed inviscid) on an f-plane tells us that:

$$\frac{Dm}{Dt} = 0 \tag{3.1.2}$$

where

$$\frac{D}{Dt} = \frac{\partial}{\partial t} + v\frac{\partial}{\partial y} + w\frac{\partial}{\partial z}$$

is the total derivative, $v = Dy/Dt$ is the meridional and $w = Dz/Dt$ the vertical velocity and

$$m = u - fy \tag{3.1.3}$$

is the absolute momentum with f the Coriolis parameter and u the zonal velocity.

The presence of rotation and a zonal flow in thermal wind balance with a lateral density gradient, place, through Eq.(3.1.2), important rotational and angular momentum constraints on the convective process. Because the m surfaces are material surfaces, they will induce fluid particles to move along slanting, rather then vertical paths. The stability of the layer will depend on the sign of ∇b measured in the m surface, or the sign of the absolute vorticity normal to the b surface (corresponding to a centrifugal instability). Both viewpoints are complementary and entirely equivalent. *Emanuel* (1994) calls this more general mixed instability 'slantwise convection'. The stability depends on the sign of the potential vorticity:

$$Q = \frac{1}{g}\eta.\nabla b \qquad (3.1.4)$$

a measure the stratification in the direction of η, the absolute vorticity vector or, equivalently, a measure of η normal to b surfaces. If, as in our thought experiment, there are no variations in x, then the absolute vorticity vector lies in a surface of constant absolute momentum and Q is just the Jacobian of b and m:

$$Q = \frac{1}{g}J_{yz}(m,b) \qquad (3.1.5)$$

If Q is negative then the flow is unstable to symmetric instabilies and slantwise convection might be expected to return the Q of the layer to zero, the state of marginal stability. The sign of Q depends on the slope of the m surfaces relative to the b surfaces and is zero when they are exactly coincident; in the limit of zero Q there is no stratification in an m surface and the component of η normal to the b surface is zero. The magnitude of the absolute vorticity, resolved perpendicular to the b surfaces, is simply $|\eta| = gQ/|\nabla b|$. For small slopes $|\nabla b| \sim N^2_{mix}$ and

$$Q = \frac{fN^2_{mix}}{g}\left(\frac{\zeta}{f} - \frac{1}{Ri}\right) \qquad (3.1.6)$$

where $\zeta = f - u_y$ is the vertical component of the absolute vorticity and $Ri = N^2_{mix}/u_z^2$ is the Richardson number.

Parcel theory can be readily employed to analyze the stability of a zonal flow in thermal wind balance to overturning in a vertical plane. The method is outlined in Appendix II - see also chapter 12 of Emanual, 1994. Maximum release of

energy occurs when fluid parcels are exchanged along surfaces which are coincident with the b surfaces. Then parcel theory yields:

$$\omega^2 \le f^2\left(\frac{\zeta}{f} - \frac{1}{Ri}\right) \qquad (3.1.7)$$

and the flow will be unstable when Q < 0 or, equivalently,

$$Ri < f/\zeta \qquad (3.1.8)$$

(see Eq.B6, Appendix (ii))

Theoretically, then, one has compelling arguments which strongly suggest that:

- if Q < 0, convection will occur and
- the end-state of the convective process will be one in which $Q \equiv 0$.

These ideas are readily borne out in numerical experiments.

Numerical illustration

Consider again the numerical experiment presented in fig 1.1.2 and discussed in lecture 1. We now repeat it but make two changes: (1) introduce the possibility of rotational control by including f and making the model 2.5 dimensional - (y,z) with no x variations and (2) introduce a meridional gradient in the cooling to induce lateral buoyancy gradients and so support a zonal wind.

In Figure 3.1.1 a resting, stratified fluid (N/f=10) is subject to a steady buoyancy loss through the sea surface; no variations in down-channel (x) coordinate are allowed (further details can be found in Haine and Marshall, 1996). The cooling is independent of x but increases across the channel following a hyperbolic tangent variation. Thus in the southern third of the channel there is weak surface forcing, in the northern third fairly constant densification equivalent to a heat loss of 800 Wm^{-2}, and a sharp transition in between. A linear equation of state is specified dependent on temperature alone and the resolution is sufficient to represent gross aspects of the convective process. The figure shows the fields from the central portion of the channel after 9 days of cooling. It is clear from the isotherms and streamfunction that the overturning motions cause fluid to move systematically in slanting paths, and maintain a non-vanishing stratification in the region which is being actively mixed. Here the contours of absolute momentum, m, are closely aligned with the isotherms indicating that the PV is close to zero. The temperature field alone is ambiguous at highlighting the regions of active overturning. Rather, potential vorticity is the key

dynamical variable as shown by Figure 3.1.1b. There are distinct plumes, of negative PV, draining the surface source of negative PV into the interior.

The integration was carried on for another 24 hours, but now with the surface cooling switched off. Figure 3.1.2 shows that within this period almost all of the turbulent flow has ceased, leaving a layer with non-vanishing vertical stratification, but very small potential vorticity (around 1% of the undisturbed value). The plumes of negative PV have been mixed away by the symmetric instability, erasing density gradients along absolute momentum surfaces.

Such numerical experiments, then, give a measure of support to the notion that convection sets PV to zero i.e. stratification measured in a very special direction; indeed it is possible to show rigorously that Q=0 is the state of marginal stability for the symmetric instability problem for which strips of fluid are assumed to conserve absolute momentum. One expects that the same result pertains in 3-dimensions; but *no such proof exists*. Nevertheless we will adopt the notion as a working hypothesis and enquire in to its consequences.

3.2 Influence of convection on the large-scale; PV inversions

If on the small-scale, the convective process sets (in a violent mixing process) the potential vorticity to zero, and, in the aftermath of convection, fluid now 'tagged' with zero Q evolves quasi-adiabatically, what are the consequences for the large-scale? To answer that question we invoke the 'invertibility principle'.

Fig.3.2.1a shows the expected Q distribution schematically, just after convection has ceased. The chimney, made up of convected fluid, is imagined to have Q = 0, and the sea-surface is dense; the ambient fluid has $Q=Q_{ref}$ and the sea-surface is at its ambient density.

If the large-scale flow is in geostrophic and hydrostatic balance, then on entering the geostrophic and hydrostatic relation in to Q, eq.(3.1), it can be expressed as an elliptic problem for the perturbation pressure ' $\tilde{p}$ ' with (the perturbation) Q as the source function:

$$\frac{N^2}{f^2}\nabla_h^2\tilde{p} + \frac{\partial^2\tilde{p}}{\partial z^2} = g\tilde{Q} + \nabla\cdot\left(\eta\tilde{b}\right) \qquad (3.2.1)$$

and the ˜ represents the deviation from a conveniently chosen reference state. In the above $\tilde{p}$ is the pressure perturbation (divided by ρ_o) and b the buoyancy perturbation related through the hydrostatic relation:

$$\text{hydrostatic} \qquad \frac{\partial\tilde{p}}{\partial z} = \tilde{b} \qquad (3.2.2)$$

The balanced currents can be deduced from $\tilde{p}$ using the geostrophic relation:

$$\text{geostrophic} \quad \mathbf{v}_g = fkx\nabla\tilde{p} \qquad (3.2.3)$$

Eq.3.2.1 is an elliptic equation for $\tilde{p}$ subject to Neumann/Dirichlet boundary conditions; it can readily be solved numerically by iterating on the non-linear term which is Rossby number smaller than the other terms. The inverted b and vg implied by the PV distribution shown in fig.3.2.1a, is plotted in fig.3.2.1b; one section is shown through the 3-dimensional solution. The Q field was inverted subject to the following boundary conditions:

(i) $\tilde{p} = 0$ on all lateral boundaries which are placed far away from the cylinder of zero Q in the center of the domain

(ii) $\dfrac{\partial \tilde{p}}{\partial z} = \tilde{b}_{surface}$ at the sea surface, with $\tilde{b}_{surface} < 0$ within the disc of the chimney and $\tilde{b}_{surface} = 0$ outside; $\dfrac{\partial \tilde{p}}{\partial z} = 0$ at the bottom where we assume $\tilde{b} = 0$.

We see that the highly idealized Q distribution does indeed induce a large-scale flow that has many of the characteristic features of observed chimneys: a rim-current, strong and cyclonic toward the surface, somewhat weaker and anticyclonic below, circumscribing a large, mixed pool of fluid. On the edge of the homogenized pool, isopycnals arch upwards to the surface. By invoking the 'invertibility principle', then, we see that the convective process is bound to drive a large-scale flow much as is observed if it mixes Q away to zero in the mixed layer.

We can take 'PV thinking' forward to consider the hydrodynamical stability of the chimney by making use of a 'mathematical trick' due to Bretherton (1966).

In the inversion of Fig.3.2.1a we employed inhomogeneous Neumann boundary conditions at the surface [(ii) above] because we prescribed the density there. But a well-known result of 'potential theory' is that any such inhomogeneous boundary condition can be replaced by a homogeneous one provided that the source function is modified. Thus in the (numerically obtained) solution shown in Fig.3.2.1b we employ homogeneous boundary conditions $\dfrac{\partial \tilde{p}}{\partial z} = 0$ in conjunction with an appropriately modified source function; to the r.h.s. of 3.2.1 we add a delta-function sheet of positive potential vorticity anomaly just underneath the surface to represent the cold surface. The strength of the sheet, $\delta_{surface}$, is just

that required to ensure that the vertical integral of $(\tilde{Q} + \delta_{surface})$ over each column of ocean vanishes; the Q can be imagined to have been 'evacuated' by convection in the interior (Q=0 there) and concentrated in to the sheet of Q just beneath the surface; the positive source at the surface induces cyclonic flow, the negative source anticyclonic. In the interior of the fluid the solutions shown in Fig 3.2.1(a) and (b) are *identical* to one another. It is to be appreciated (and sometimes this takes some time!) that this is not *just* mathematical trickery because in (b) boundary conditions and interior sources are given an equal footing - they are just potential vorticity distributions which can be inverted subject to homogeneous boundary conditions.

Thus we can now easily see why a cold surface (positive PV sheet) induces cyclonic circulation and the low PV of the interior induces anticyclonic circulation. Bretherton sheet concepts also clearly indicate that the chimney will be subject to baroclinic instability, discussed now in section 3.3, and suggest highly instructive idealized models of chimneys based on point vortices.

3.3 Hydrodynamical instability of chimneys

The convective process resets and redistributes the PV of the ambient fluid resulting in chimneys which, as we have seen in laboratory and numerical experiments, are highly susceptible to, and strongly modified by, baroclinic instability. The homogeneous column of water is cold and dense at the surface relative to its surroundings and so ∇Q points *inwards* to the δ-function disc of high PV at the surface. The interior of the chimney has very low (essentially zero) PV and so below ∇Q points *outwards* from the chimney - see fig.3.2.1b. Thus the necessary conditions for baroclinic instability (reversal in sign of ∇Q somewhere within the fluid) are manifestly satisfied. Analytical study of the stability of such structures using 'the method of perturbations' can readily be carried out within the confines of quasi-geostrophic theory - see, for example, Killworth, 1976; Pedlosky 1985 and Helfrich and Send (1988). If the radius of the chimney is large relative to the Rossby radius of deformation, then the results of such analysis asymptote to that of Eady (1949); a growth rate for the fastest growing mode proportional to $f / \sqrt{R_i}$ (see appendix (ii)) on a scale close to NH / f, where H is the depth of the chimney and R_i the Richardson number of the ambient fluid. Because the ambient N is relatively small in deep convection sites ($N / f \sim 5 \rightarrow 10$), the growth rates are rapid (a few days) and the scales small (a few kilometers).

Laboratory and numerical experiments suggest that linear theory is a useful guide in the early growth of instabilities but non-linear processes soon take hold; eddies mature and merge as the chimney disintegrates. Legg and Marshall

(1993) exploit Bretherton sheets to model the chimney as a collection of paired point vortices (called 'hetons' by Hogg and Stommel) and so are able to address non-linearities. In numerical experiments using Green's function techniques in a two-layer model, they pepper the convection site with paired point vortices, one (of strength q+) in the upper layer to represent the cold surface and one (strength q-) in the lower layer to represent low PV. The rate of introduction of vortices can be directly related to the rate at which buoyancy is lost from the sea surface. In the experiment shown in Fig.3.2.2 a constant cooling of 800 W m^{-2} over a disk of diameter 16 km (about 10 times the Rossby radius of deformation) is assumed, consistent with the explicit calculations of Jones and Marshall (1993). Cooling at this rate creates hetons of strength 0.6 f at a rate of 33 per day. They are introduced with random initial (Cartesian) coordinates. During the first 2 days, most of the hetons remain within the patch of cooling (see fig.3.2.2a and 3.2.2b). As the number of hetons within the patch increases, a sheared current develops around the rim, cyclonic above, anticyclonic below, reaching a magnitude of ~ 20 cm s^{-1}. This rim-current effectively constrains the vortices within the disc. Initially they are prevented from forming self-propelling pairs by this strong shear current - any pairs are torn apart before they can `escape'. However, over time, the rim current develops waves of mode number 4 - 5, - see fig.3.2.2b and c - through the mechanism of baroclinic instability. After about 2 days we see tilted clusters containing several hetons which burst out of the main cloud, breaking through the sheared rim current (fig.3.2.2c). The convection site therefore breaks up into several smaller tilted clusters which propagate outwards. The heton clusters continue to travel outwards (fig.3.2.2d), carrying cold water far from the area of cooling. These extended hetons, clumping together on the radius of deformation scale, are very efficient at fluxing heat laterally into the cooling area; they are the point-vortex model's attempt to represent the eddies seen in figs. 2.2.1. and 2.2.2. The linear theory of Pedlosky, 1985, is very successful in predicting the scale of the clumping.

As time progresses and the hetons disperse, the magnitude of the rim current diminishes, so that it is easier for subsequent groupings to move outwards. Ultimately a steady-state is reached in which the flux of hetons out of the area of cooling, in the form of tilted clusters, approximately balances the rate at which hetons are generated and so the number of hetons in the area of cooling remains approximately constant.

Hetons have been used to help in the interpretation of the mean temperature attained over warm discs in laboratory models of convection by Brickman (1995). The equilibrium limit in which heat input (or output) is entirely balanced by lateral flux, the one discussed in lecture 2, can also be addressed using heton models - see Legg et.al.1996.

Appendix I

'Law of vertical heat transfer for deep convective plumes in the ocean'

Suppose that a weakly stratified ocean is subject to vigorous cooling at the surface over some hundreds of kilometers producing a density inversion and the possibility of overturning. The fluid cannot simultaneously overturn on this scale; rather the qualitative description must be that the response to wide-spread cooling is one in which relative small convection cells (plumes) develop. The detailed physics setting the plume-scale is as yet unclear. But irrespective of these details the gross transfer properties of the population of convective cells must be controlled by the large scale; the *raison d'etre* for the overturning is to flux heat vertically to offset the cooling at the surface. A law of vertical heat transfer for the plume-scale can be developed using parcel theory as follows.

Suppose that the net effect of overturning is to exchange particles of fluid, of density ρ_1 and ρ_2, over a depth Δz. Dense water sinks displacing lighter water below, and releases potential energy to power the plume and flux heat vertically.

The change in potential energy ΔP consequent on the idealized rearrangement of particles shown in the figure, is given by:

$$\Delta P = P_{final} - P_{initial} = -g\Delta\rho\Delta z = \rho_o \Delta b \Delta z \tag{A1}$$

where Δb is the buoyancy difference of the exchanged particles, g is the acceleration due to gravity, and ρ_o is a representative value of the density.

Equating the released potential energy, to the acquired kinetic energy of the ensuing convective motion $K = 2 \times \frac{1}{2}\rho_o w^2$ (where w is the vertical velocity scale and there is a factor of 2 because there are two particles) then:

$$w^2 = \Delta b \Delta z \tag{A2}$$

Now if heavy fluid lies above light fluid an unstable disturbance with growth-rate ω will develop. Thus $z \propto e^{\omega t}; \frac{d}{dt} = \omega; w = \frac{dz}{dt} = \omega z$ and hence from (A2):

$$\omega^2 z^2 = |N^2| z^2$$

and so

$$\omega^2 = |N^2| \tag{A3}$$

which is the 'correct' answer for the growth rate of the fastest growing mode, as determined by linear stability analysis (in the inviscid limit, the lateral scale of the fastest growing convective mode collapses to zero, no energy is 'wasted' in lateral motion, and the limit (A3) is achieved).

The implied "law" of vertical heat flux on this the plume-scale is then, using (1),

$$\boxed{\mathcal{B}_p = w\Delta b = \Delta z^{1/2}\Delta b^{3/2}}$$ (A4)

which is Eq.1.1.4.

Appendix II
Energy analysis of the thermal wind

We now consider parcels of incompressible fluid at positions (y_1,z_1) and (y_2,z_2) in thermal wind balance with a meridional density gradient. The parcels are then interchanged 'adiabatically' (ie with conservation of buoyancy).

The change in potential energy (per unit volume) is again (A1):

$$\Delta P = \rho_o(z_2 - z_1)(b_2 - b_1)$$ (B1)

We also have:

$$\delta b = \frac{\partial b}{\partial y}\delta y + \frac{\partial b}{\partial z}\delta z$$

so that

$$(b_2 - b_1) = M^2(y_2 - y_1) + N^2(z_2 - z_1)$$

if, for simplicity, N^2 and M^2 are assumed constant and quantify the strength of the vertical and horizontal density gradients, respectively.

For the slope, s_1, of a buoyancy surface we have, since $b_2 = b_1$:

$$s_1 = \frac{dy}{dz} = -\frac{M^2}{N^2}$$

Hence if $s = \dfrac{z_2 - z_1}{y_2 - y_1}$ is the slope of the surface of interchange, then we may write:

$$(b_2 - b_1) = N^2(y_2 - y_1)[s - s_1]$$

and so (B1) becomes

$$\Delta P = \rho_o N^2(y_2 - y_1)^2 s(s - s_1)$$

In convectively stable conditions $N^2 > 0$. Hence the sign of ΔP is the same as that of the factor s(s-s₁) and that it will be negative, corresponding to the possibility of instability, if s<s₁ ie if the slope of the exchange surface has a smaller slope than the isopycnals. That this corresponds to actual instability has to be confirmed by carrying out a stability analysis, but it (almost) invariably does - the fluid always finds a way to release the potential energy if there is lots of it available in the mean flow.

For a given exchange distance $(y_2 - y_1)$ the release of potential energy will be a maximum (-ΔP a maximum) when $s(s - s_1)$ is a maximum ie when:

$$s = \frac{1}{2} s_1$$

Then

$$(\Delta P)_{min} = \frac{1}{4} \rho_o N^2 (y_2 - y_1)^2 s_1^2$$

$$= \frac{1}{4} \rho_o (y_2 - y_1)^2 \frac{M^4}{N^2}$$

$$= \frac{1}{4} \rho_o (y_2 - y_1)^2 \frac{f^2}{Ri} \tag{B2}$$

where Ri is the Richardson number of the large-scale flow defined by:

$$Ri = \frac{f^2 N^2}{M^4} \tag{B3}$$

where use has been made of the thermal wind relation.

We see that in any region where a thermal wind exists it is always possible to release potential energy for eddy growth provided an appropriate re-arrangement of particles takes place.

Instability at high Richardson number; Baroclinic instability

If the Richardson number of the mean flow is large , then only changes in its potential energy need be taken in to account. If an unstable disturbance grows then $y \propto e^{\omega t}; \frac{d}{dt} = \omega; v = \frac{dy}{dt} = \omega y$ and equating released potential energy to

acquired kinetic energy of the eddying motion ($\rho_o v^2$) we find, in direct analogy with the upright convection problem outlined in Appendix (i):

$$\omega^2 \approx \frac{f^2}{R_i} \tag{B4}$$

which is a heuristic derivation of the growth-rate of an Eady wave. Eq.(B4) is in effect just A3 but with the $\left|N^2\right|$ measured along a slope that has one half that of the isopycnals. Again it is the 'correct answer', but one must also demonstrate that the hypothesized re-arrangement of particles does indeed occur. This can only be done by a 'stability analysis', of which many exist in the literature.

Instability at low Richardson; symmetric instability

If the Ri of the large-scale flow is not large, then one must also consider the change in kinetic energy of the mean motion. Let us assume a zonal motion U = U(y,z) of complete rings of fluid independent of x (rather than just parcels). Then we have:

$$\frac{Dm}{Dt} = 0$$

where $m = U - fy$ is the absolute momentum.

For any small displacement in the 'y' direction we must have:

$$\delta U = f\delta y$$

as the change following the motion.

Now consider the change in kinetic energy resulting from the exchange of rings of fluid with zonal motion U_1 at (y_1, z_1) and U_2 at (y_2, z_2). Then

$$\Delta K = \frac{1}{2}\rho_o\left[\{U_1 + f(y_2 - y_1)\}^2 + \{U_2 - f(y_2 - y_1)\}^2 - U_1^2 - U_2^2\right]$$

$$= \rho_o(y_2 - y_1)^2 f\left[f - \frac{(U_2 - U_1)}{(y_2 - y_1)}\right]$$

Since

$$(U_2 - U_1) = \frac{\partial U}{\partial y}(y_2 - y_1) + \frac{\partial U}{\partial z}(z_2 - z_1)$$

this may be written:

$$\Delta K = \rho_o(y_2 - y_1)^2 f \left[f - \frac{\partial U}{\partial y} - s\frac{\partial U}{\partial z} \right]$$

or, since $f\frac{\partial U}{\partial z} = -M^2 = N^2 s_1$, then

$$\Delta K = \rho_o(y_2 - y_1)^2 \left[f\left(f - \frac{\partial U}{\partial y}\right) - N^2 ss_1 \right]$$

and

$$\Delta P = \rho_o(y_2 - y_1)^2 N^2 (s^2 - ss_1)$$

as before.

Hence the change in total energy of the mean motion ΔE_m is, after a little rearranging:

$$\Delta E_m = \rho_o(y_2 - y_1)^2 \left[f\left(f - \frac{\partial U}{\partial y}\right) - \frac{f^2\left(\frac{\partial U}{\partial z}\right)^2}{N^2} + N^2(s - s_1)^2 \right]$$

Regarding s, the direction of exchange as a variable, ΔE_m has a minimum when $s = s_1$ ie when the exchange is in the initial isopycnal surface. Then:

$$(\Delta E_m)_{min} = \rho_o(y_2 - y_1)^2 f^2 \left[\frac{\zeta}{f} - \frac{1}{Ri} \right] \tag{B5}$$

will be negative if:

$$\boxed{Ri < \frac{f}{\zeta}} \tag{B6}$$

giving the possibility of instability. Here ζ is the 'absolute vorticity'.

From (B5) we may again deduce the growth rate:

$$\omega^2 \le f^2 \left[\frac{\zeta}{f} - \frac{1}{Ri} \right] \tag{B7}$$

Acknowledgments

References

Bretherton, F. P., 1966
      Critical layer instability in baroclinic flows.
      Quart.J. R. Meteorol. Soc., 92, 325-334.
Brickman, D, 1995
      Heat flux partitioning in open-ocean deep convection
      J. Phys. Oceangr. 2609-2623
Chandrasekhar,S, 1961
      Hydrodynamic stability,
      Dover.
Coates, M.J., G.V. Ivey and J.R. Taylor, 1995
      Unsteady, turbulent convection in to a rotating linearly
      stratified fluid: modeling deep ocean convection.
      J. Phys. Oceanogr., 25, 3032-3050.
Deardorff, J.W. and G.E. Willis, 1967
      Investigation of turbulent, thermal convection between
      horizontal plates.
      J. Fluid. Mechs.,28, 675-704.
Deardorff, J.W, G.E.Willis, and B.H.Stockton, 1980
      Laboratory studies of the entrainment zone of a convectively mixed
      layer. J. fluid Mech. v 100, 41-64.
Denbo D.W. and E.D.Skyllingstad, 1994
      An ocean large eddy model with application to deep
      convection in the Greenland Sea.
      J. Geophys. Res.
Eady, E. T., 1949.
      Long waves and cyclone waves.
      Tellus,1, 33--52.
Emanuel, K, 1994
      Atmospheric convection.
      Oxford University Press, pp $\mathcal{B}_0$ 580.
Fernando, J. S. F., R, Chen, D. L. Boyer, 1991.
      Effects of rotation on convection turbulence
      J. Fluid Mech, 228, 513--48.
Garwood, Isakari and Gallacher, 1994
      Thermobaric convection
      In AGU Monograph for Nansen Centennial.
Gascard, J.-C., 1978
      Mediterranean deep water formation, baroclinic instability and oceanic eddies.
      Oceanol. Acta, 1, 315-330.

Gill, A.E. Atmosphere-Ocean Dynamics 1982
    Academic Press
Gill, A.E. 1973)
    DSR 20, 111.
Green, J. S. A., 1970.
    Transfer properties of the large--scale eddies and the general circulation of the
    atmosphere.
    Quart. J. Roy. Meteor. Soc., 96, 157--185.
Haine, T.W.N. and J.C. Marshall, 1996
    Gravitational, symmetric and baroclinic instability of the ocean mixed layer.
    submitted to J. Phys. Oceanogr.
Helfrich, K. R., 1994.
    Thermals with background rotation and stratification.
    Journal of Fluid Mechanics, 259, 265--280.
Helfrich, C. and U. Send 1988
    Finite-amplitude evolution of two-layer geostrophic vortices
    J.Fluid Mech, 197, 331-348.
Hogg, N, and H. Stommel, 1985
    Hetonic explosions: the breakup and spread of warm pools as explained by baroclinic
    point vortices.
    J.Atmos.Sci.,42, 1465-1476
Hoskins, B; McIntyre, M. and A. Robertson, 1985
    On the use and significance of isentropic potential vorticity maps.
    Quart. J. Roy. Meteorol. Soc., 111, 877-946 - also 113, 402-404
Hufford, G., J.C. Marshall and J.Whitehead, 1996
    Convection in a rotating, stratified fluid.
    submitted to J. Geophys. Res.
Jones, H.L. and J.C. Marshall, 1993
    Convection with rotation in a neutral ocean: A study of open-ocean deep convection.
    J. Phys. Oceanogr., 23, 1009-1039.
Julien, K. S. Legg, J. McWilliams, and J. Werne, 1996b:
    Penetrative convection in rapidly rotating flows:
    preliminary results from numerical simulation.
    In press, Dynamics of Atmospheres and Oceans.
Julien, K., S. Legg, J. McWilliams and J. Werne, 1996
    Rapidly rotating turbulent Raleigh-Benard convection.
    submitted to J. Fluid. Mech.
Kerr, R.M., J.R. Herring and A. Brandenburg, 1995
    Large-scale structure in Rayleigh-Benard convection with impenetrable sidewalls.
    Chaos, Solitons and Fractals, 5, 2047.
Killworth, P. D., 1976
    The mixing and spreading phases of MEDOC 1.
    Progress in Oceanography, 7, 59-90.
Killworth (79)
    JPO 9, 531.
Klinger, B.A. and J.C. Marshall, 1995
    Regimes and scaling laws for rotating deep convection in the ocean.
    Dynamics of Atmospheres and Oceans, 21, 227-256.
Leaman, K.D. and F. Schott, 1991:
    Hydrographic structure of the convection
    regime in the Golfe du Lion. J. Phys. Oceanogr., 21, 575-598.

Legg, S.A., H.L. Jones and M. Visbeck, 1996
    The role of baroclinic instability in open ocean deep convection: a heton perspective.
    submitted to J. Phys. Oceanogr.
Legg, S.A. and J.C. Marshall, 1993
    A heton model of open ocean convection.
    J. Phys. Oceanogr., 23, 1040-1056.
Marshall, J.C., J.A. Whitehead and T. Yates, 1994
    Laboratory and numerical experiments in oceanic convection.
    Ocean Processes in climate Dynamics: Global and Mediterranean Examples, Malanotte-
    Rizzoli and Robinson (editors), Kleuver Academic Publishers, pp.~437.
Marshall, J.C. and F. Schott, 1996
    Open-ocean convection; Observations, theory and models.
    to be submitted to Reviews of Geophys.
Mason, P.J., 1994
    Large eddy simulation: A critical review of technique.
    Quarterly J. Royal Meteorological Soc., 120, 1.
Maxworthy, T. and S. Narimousa, 1994
    Unsteady, turbulent convection in to a homogeneous, rotating fluid, with oceanographic
    applications.
    J. Phys. Oceanogr., 24, 865-887.
MEDOC Group, 1970
    Observations of formation of deep water in the Mediterranean Sea, 1969.
    Nature, 227, 1037-1040.
Paluszkiewicz, Garwood and Denbo (94)
    Deep convective plumes in the ocean.
    Oceanography 7, 37.
Pedlosky, J., 1985
    The instability of a continuous heton cloud.
    J.Atmos.Sci., 42, 1477-1486
Rayleigh, O.M. 1916
    On convection currents in a horizontal layer of fluid, when the higher temperature is on
    the lower side.
    Phil. Mag. Ser. 6, 32, 529-546.
Sander, J., D. Wolf-Gladrow and D. Olbers, 1995
    Numerical studies of open-ocean deep convection.
    J. Geophys. Res., 100, No. C10, 20579-20600.
Saunders, P.M.,1973
    The instability of a baroclinic vortex
    J. Phys. Oceanogr., 3, 61-65
Schott, F. and K.D. Leaman, 1991
    Observations with moored acoustic Doppler
    current profilers in the convection regime in the Golfe du Lion.
    J. Phys. Oceanogr., 21, 558-574.
Schott, F., M. Visbeck and J. Fischer, 1993:
    Observations of vertical currents and convection in the central Greenland Sea during the
    winter of 1988/89.
    J. Geophys. Res., 98 (C8), 14401- 14421.
Schott, F., M. Visbeck und U. Send, 1994:
    Open ocean deep convection, Mediterranean and Greenland Seas.
    In Malanotte- Rizzoli, P. and A.R. Robinson (eds.): Ocean Processes on Climate
    Dynamics: Global and Mediterranean Examples, 203-225. Kluwer Academic Publishers,
    Netherlands

Send, U. and J.C. Marshall, 1995
    Integral effects of deep convection.
    J. Phys. Oceanogr, 25, 5, 855-872.
Send, U., F.Schott, F. Gaillard and Y. Desaubies, 1994
    Observation of a deep convection regime with acoustic tomography.
    G. Geophys. Res., 100, 6927-6941.
Stommel, H., 1972
    Deep winter-time convection in the Western Mediterranean Sea.
    Studies in Physical Oceanography, A Tribute to Georg Wust on his 80th Birthday,
    A. L. Gordon and Breach Science, 207-218.
Swallow, J. C., and G. F. Caston, 1973
    The preconditioning phase of MEDOC 69. Part I: Observations.
    Deep-Sea Res., 20, 429-448.
Veronis. G, 1958
    Cellular convection with finite-amplitude in a rotating fluid.
    J. Fluid. Mech., 5, 410-435
Visbeck, M., J.C. Marshall and H.L. Jones, 1996
    On the dynamics of convective `chimneys' in the ocean.
    to appear in J. Phys. Oceanogr.
Voorhis, A.D., and D.C. Webb, 1970
    Large vertical currents observed in a winter sinking region of the northwestern
    Mediterranean.
    Cah. Oceanogr.,22, 571-580.

—.
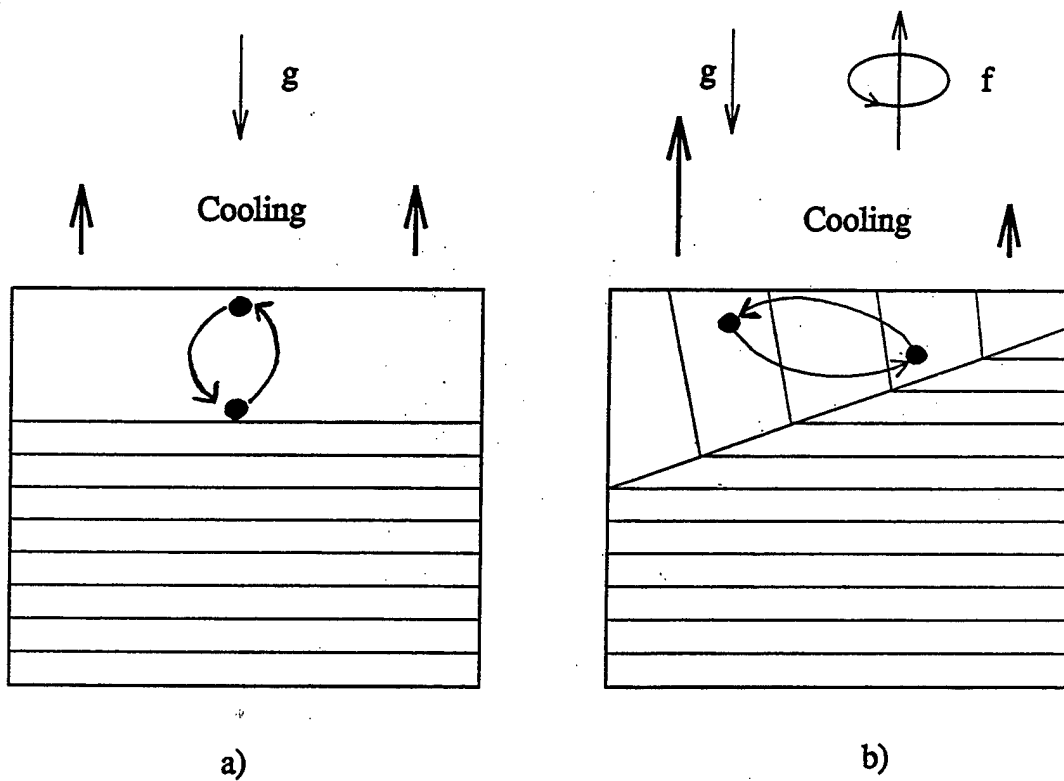
Fig.1.1.1 Schematic diagram showing the convective deepening of a mixed layer. In (a) an initially resting stratified fluid is subject to widespread and uniform buoyancy loss from the surface; the layer deepens by drawing buoyancy from depth through upright convection which exchange parcels of fluid in the vertical. In (b) we suppose that there are spatial inhomogeneities which induce lateral gradients in mixed-layer depth and density. Now the mode of buoyancy transfer through the mixed layer can change to one in which fluid parcels are exchanged laterally in, for example, baroclinic instability.

(a) Temperature(-), streamfunction (--) and flow

(b)

(c)
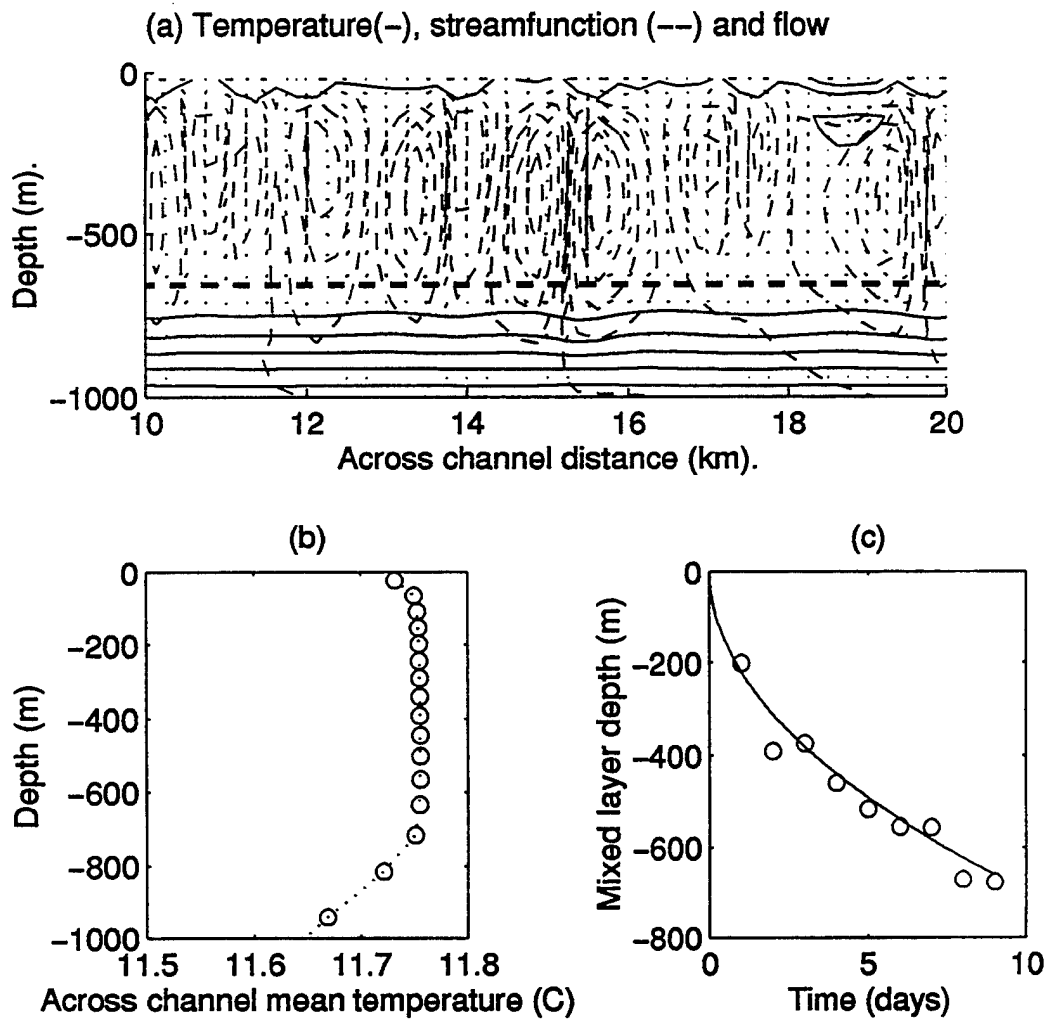
Fig.1.1.2 Deepening by upright convection in a numerical simulation. Vertical section at day 9 showing isotherms (solid), overturning streamfunction (dashed) and flow. The flow is shown by the small dashes which indicate equivalent displacements after 30mins. The peak speeds are (0.069,0.024) ms^{-1} in the (y,z) directions. The thick dashed line is the prediction of the one-dimensional law for the depth of the mixed layer (Eq.1.1.5) (b) Across channel mean temperature profile at day 9. (c) Timeseries of mixed layer depth. Full line is 1D prediction - circles are model results. From Haine and Marshall (1996).
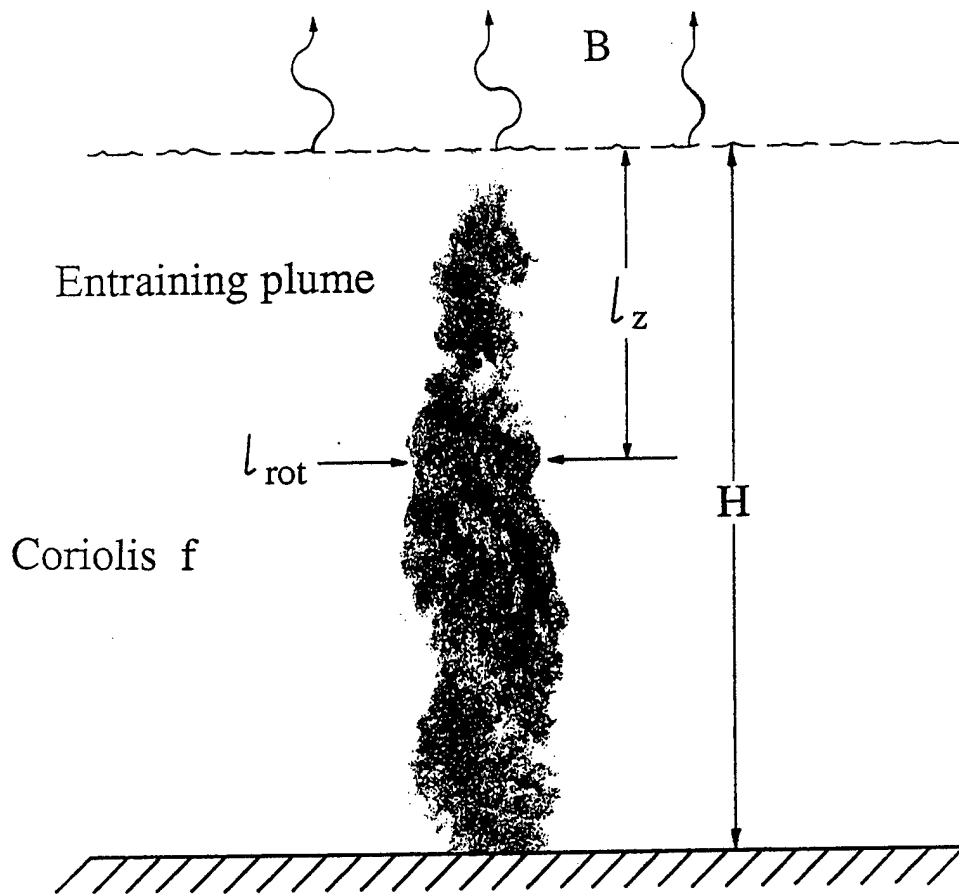
Fig.1.2.1
A schematic representation of an entraining plume sinking in to a homogeneous ocean of depth H, at a latitude where the Coriolis parameter is f, triggered by buoyancy loss $\mathcal{B}_0$. If the ocean is sufficiently deep (as drawn here) the plumes that make up the convective layer of depth l_z will come under rotational control on the scale l_{rot}.
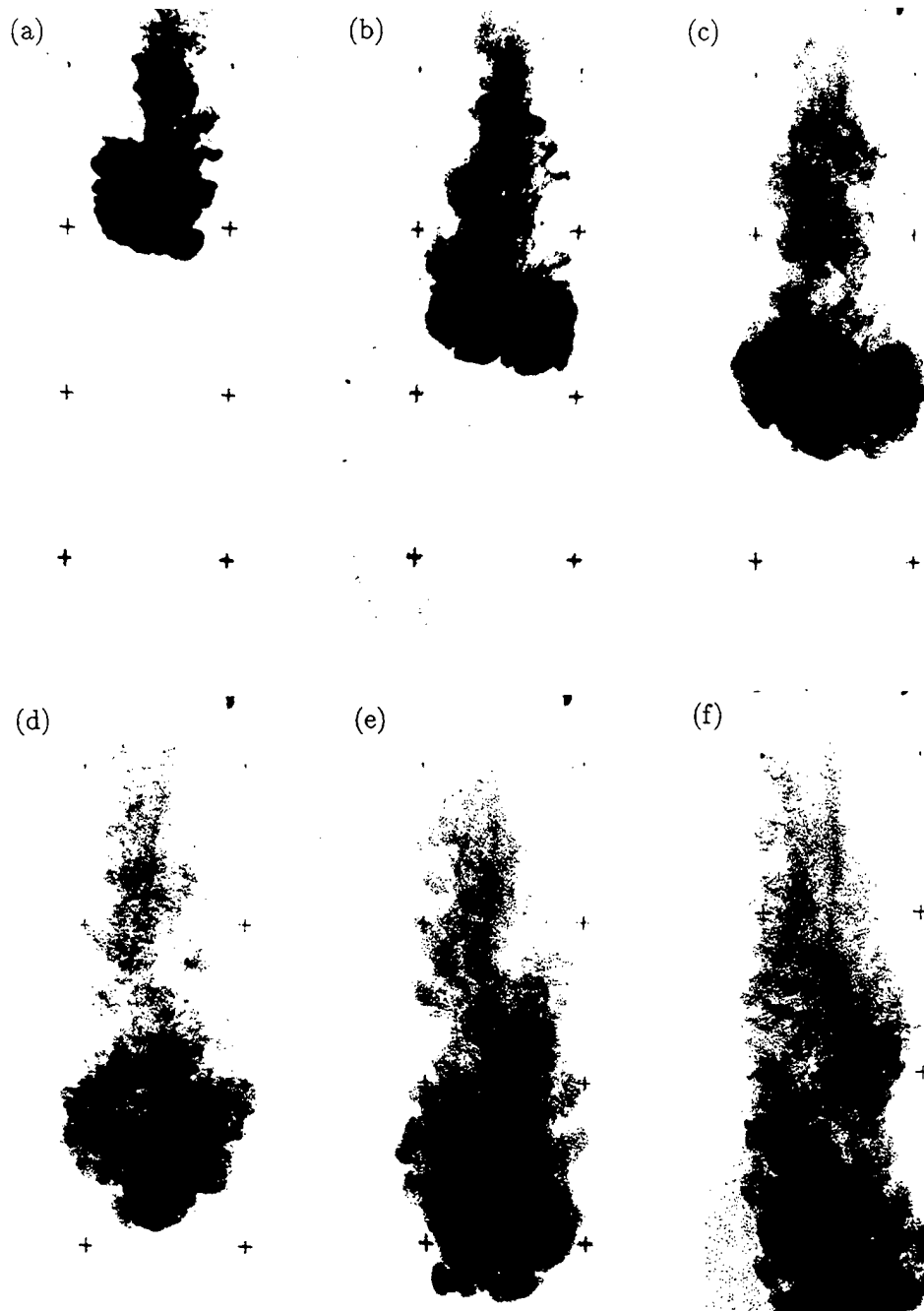
Fig. 1.2.2 A sequence of photographs from a laboratory experiment carried out by Helfrich (1994) in which a salt solution, dyed for flow visualization, was introduced into a rotating, 45 cm deep volume of fresh water. The buoyancy flux and rotation rate were such that $lrot$ = 1.98 cm, much less than the water depth. The first three frames show the early evolution before rotation becomes important. The effects of rotation are evident in frames (d), (e) and (f). The radius remains nearly constant and the front falls to form a columnar structure which ultimately undergoes geostrophic adjustment to form an anticyclonic conical eddy of dense fluid on the tank bottom. The crosses map out a square grid of side 5 cm.

(a) w(m/s) (NS,x=120)

(b) w (m/s) (z=-1km)

(c) T (NS,x=120)

(d) T (z=-1km)
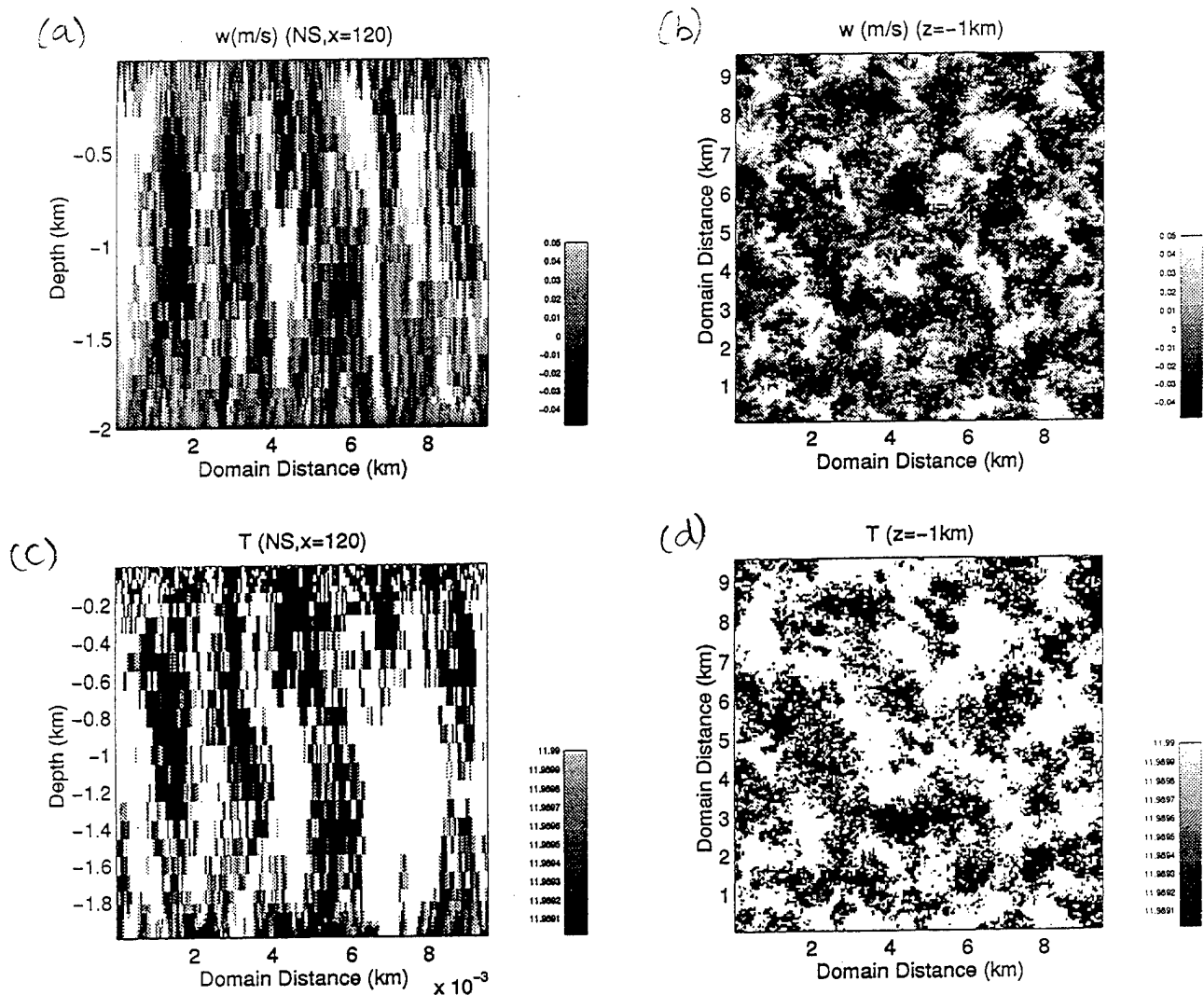
Fig. 1.5.1

Numerical simulation of convection induced by surface cooling of $800W/m^2$ in an initially neutral, unstratified rotating fluid in a $10 \times 10 \times 2$ km doubly periodic box. Fields are plotted after one day of integration. The horizontal resolution is 50m while the vertical resolution varies from 6m at the surface to 100m at mid-depths.

(a) north-south section of vertical velocity, 6.25 km east of the origin.

(b) horizontal section of vertical velocity, at mid-depths z=-1km.

(c) north-south section of in-situ temperature (corresponding to (a)).

(d) horizontal section of in-situ temperature (corresponding to (b)).
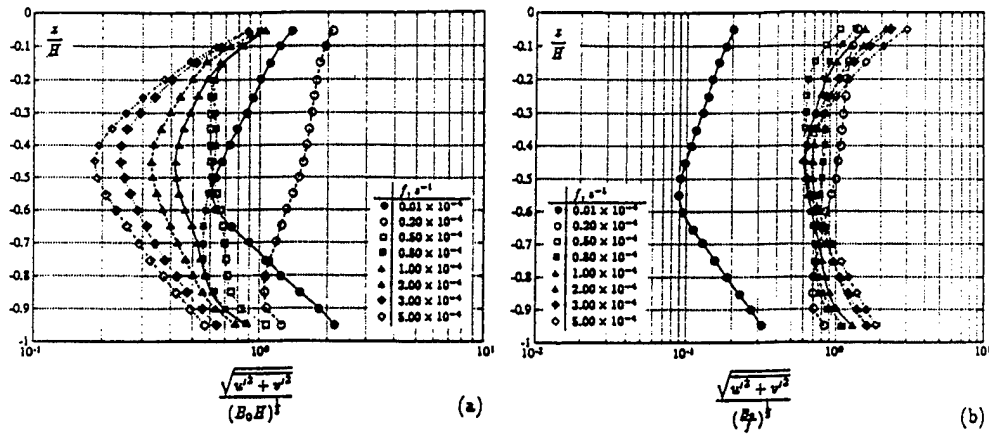
Fig. 1.5.2 Horizontal velocity variance (a) normalized with respect to the non-rotating scaling u_{norot}, plotted as a function of depth (b) normalized with respect to u_{rot} and plotted as a function of depth.
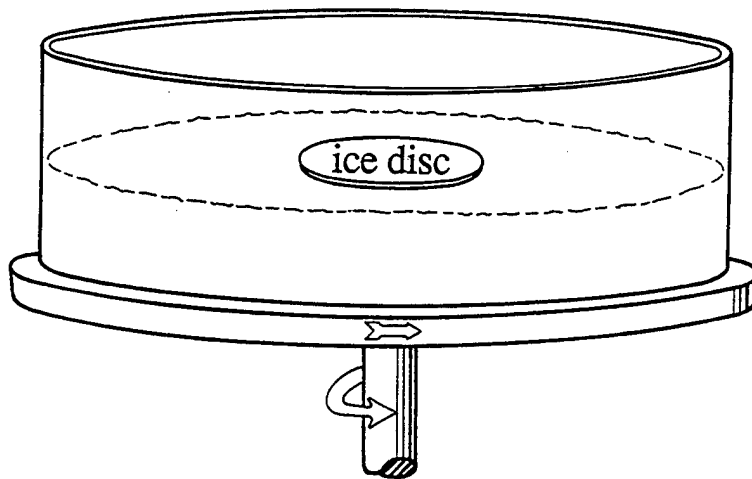
Fig.2.1.1

Sketch of the apparatus for observing cooling under melting ice. The tank, mounted on a turntable, was 120 cm in diameter and filled to a depth of 10 cm with fresh water at room temperature. The period of rotation ranged from 15 secs up to 120 secs. Convection was instigated and visualized by placing a 1 cm thick disc of ice containing food coloring at the axis of rotation at the surface.

(a)
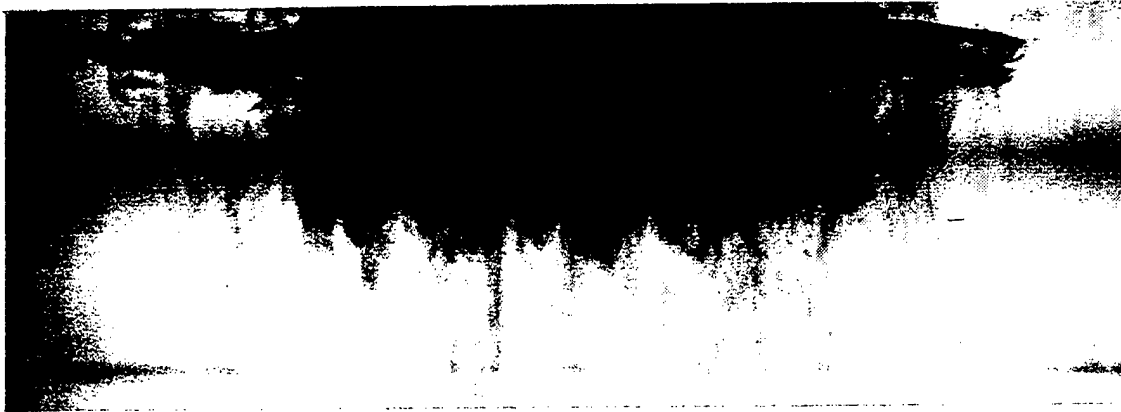
(b)

Fig.2.1.2
(a) Side view of plumes descending from the disc at the surface under rotational control; this is the most rapidly rotating melting-ice experiment with Ro* = 0.03 and a 15 second rotation period.
(b) Eddies marking by dye showing the geostrophically adjusted end-state of the convective process after ice has melted and hence cooling has ended; the convected fluid resides in Rossby-radius-scale eddies.
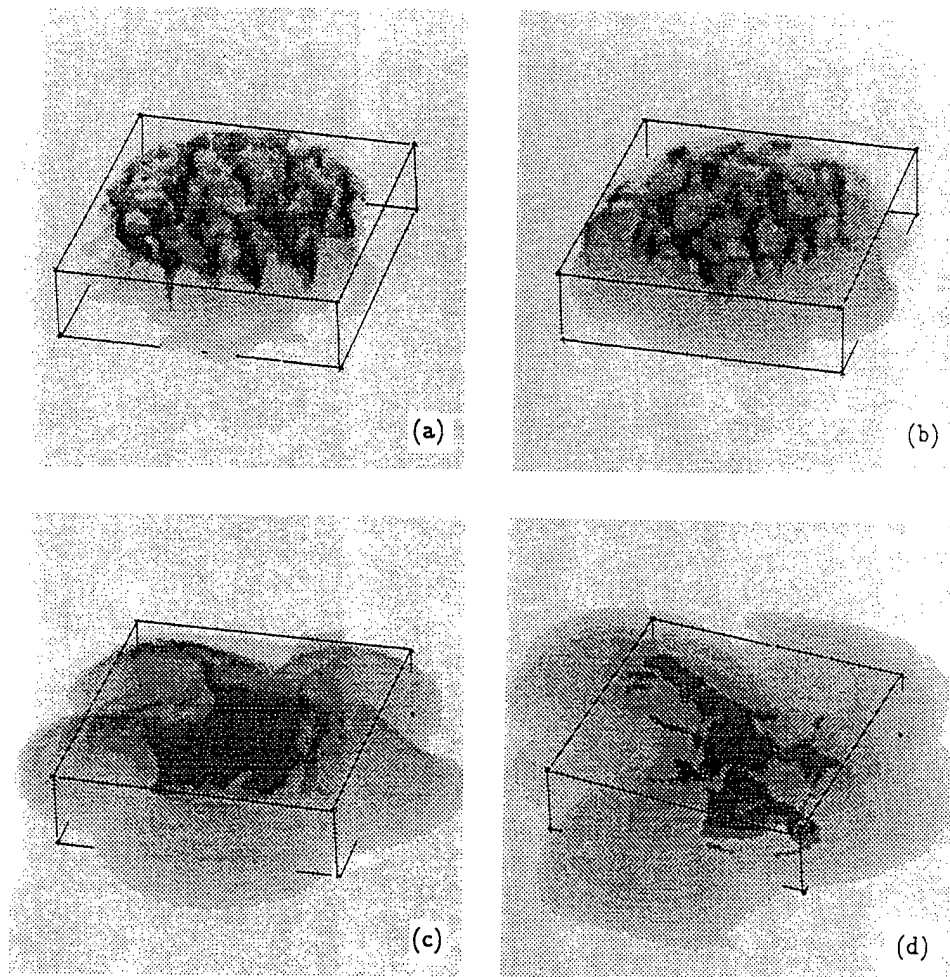
Fig.2.1.3
The temperature field in a numerical simulation of chimney convection rendered in three-dimensions at (a) 1 day, (b) 2 days, (c) 4 days and (d) 6 days. Cold water is dark, warmer water lighter. As an aid to perspective a box, 16 km on the side and 2 km deep, has been outlined.
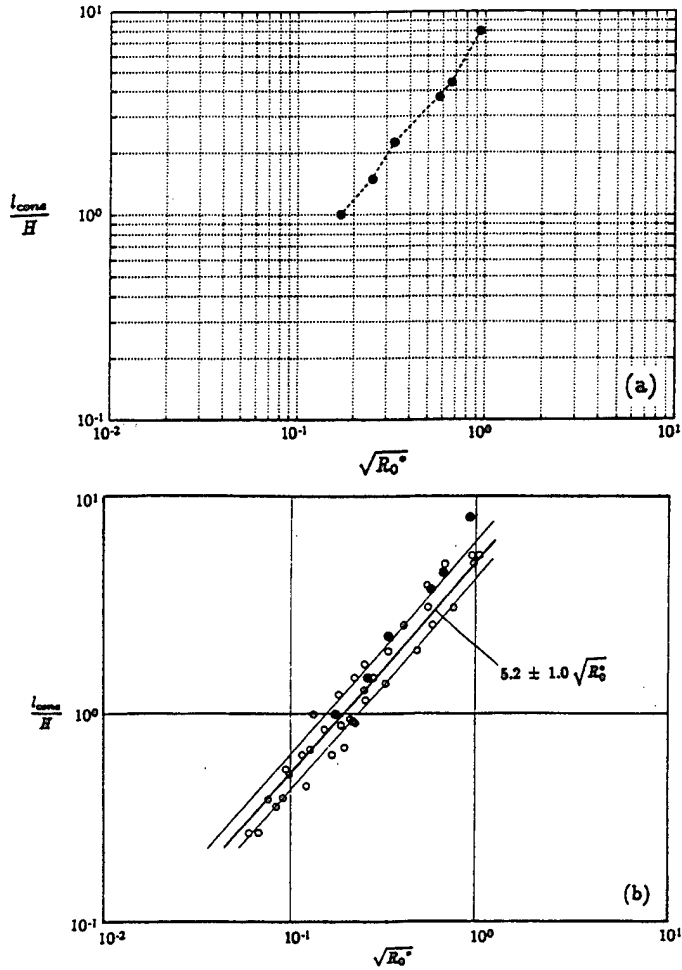
Fig.2.1.4. The aspect ratio of the cones, l_{cone}/H, plotted against $\sqrt{R_o^{\,*}}$ for six numerical experiments (black dots) superimposed on data (open circles) obtained by Maxworthy and Narimousa (1994) in their laboratory.
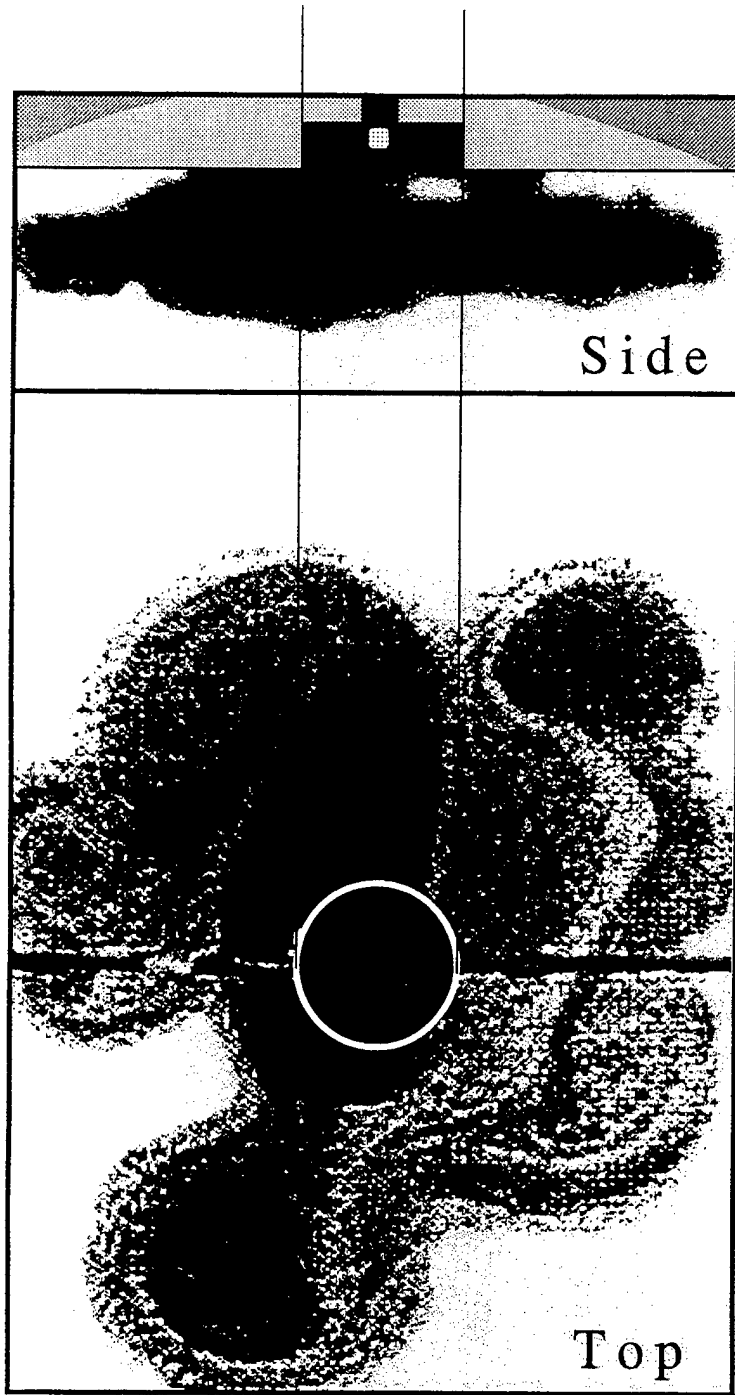
Fig.2.2.1 Top and side photographs of the dispersal of convected fluid away from an evolving mixed patch in a linearly stratified fluid.

a) Vertical Vorticity x 10^4 s^{-1}
z=-165m t= 3 days

b) Vertical Vorticity x 10^4 s^{-1}
z=-165m t= 4 days

c) Vertical Vorticity x 10^4 s^{-1}
z=-165m t= 5 days

d) Vertical Vorticity x 10^4 s^{-1}
z=-165m t= 7 days

e) Temperature °C
x=15km t= 6 days
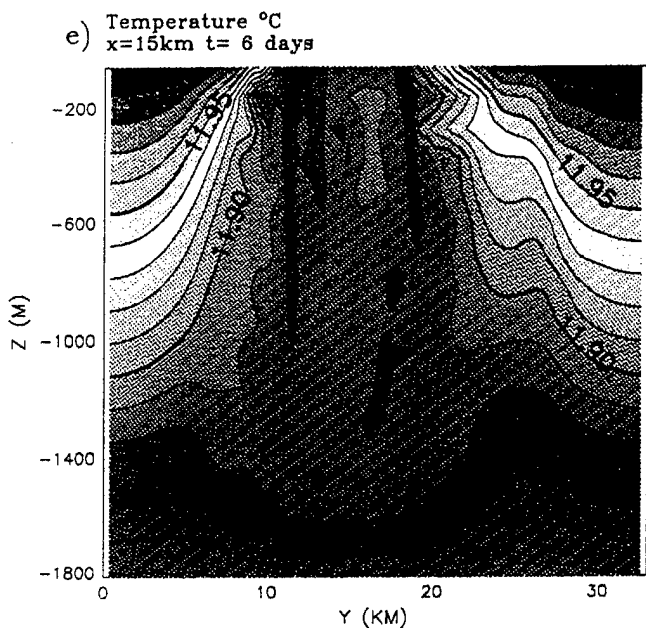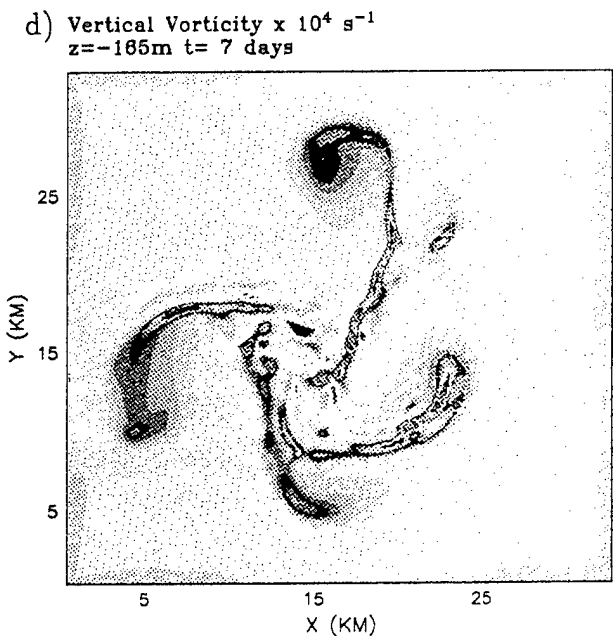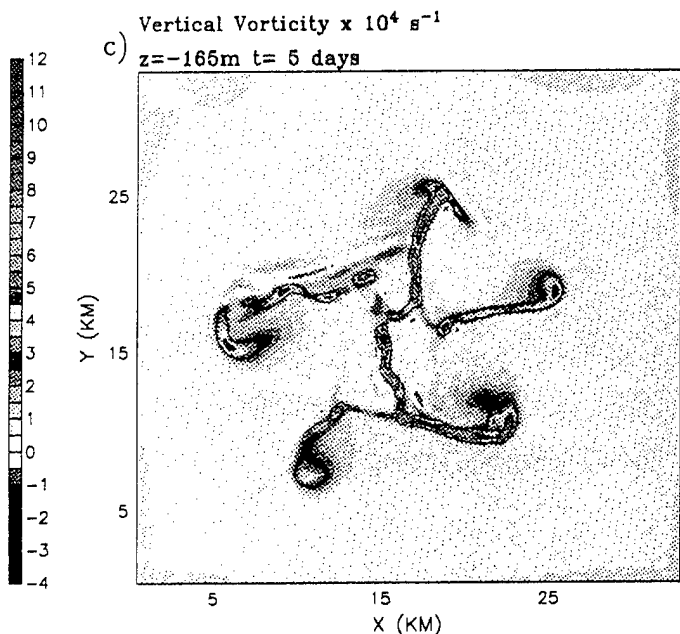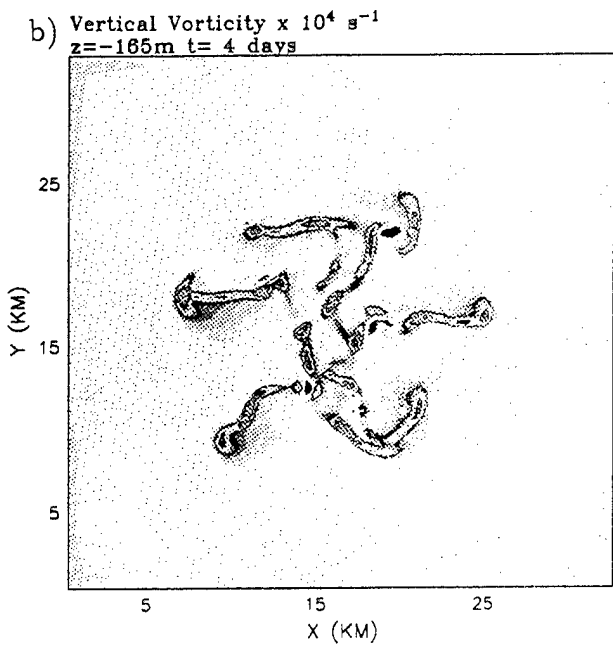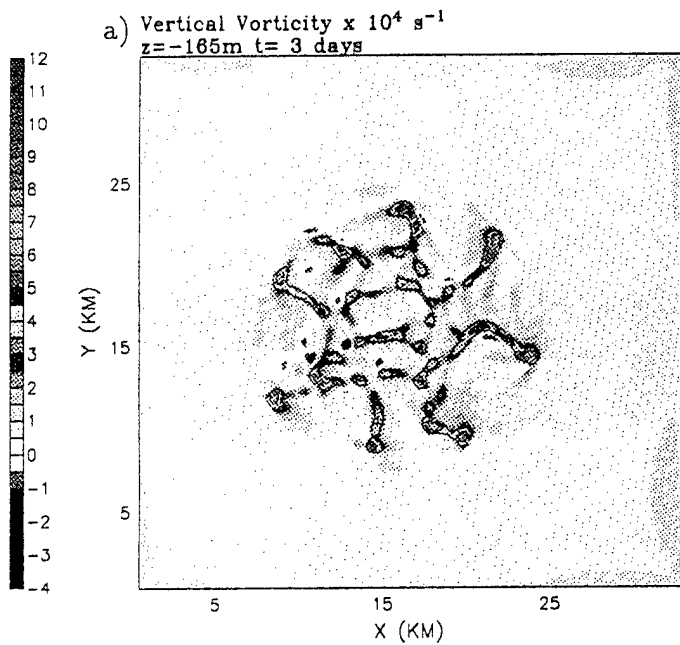
Fig.2.2.2 Numerical simulation of a chimney induced by a localized, but extended patch of cooling applied to the surface of a resting, stratified ocean. In (a), (b), (c) and (d) the vertical component of absolute vorticity is plotted at a depth of 200 m after 3, 4, 5 and 7 days respectively. In (e) we show a vertical section of temperature through the middle of the chimney at day 6. Again we see that plume-scale convection (evident at day 3) gives way to finite amplitude baroclinic instability (from day 4 onwards).
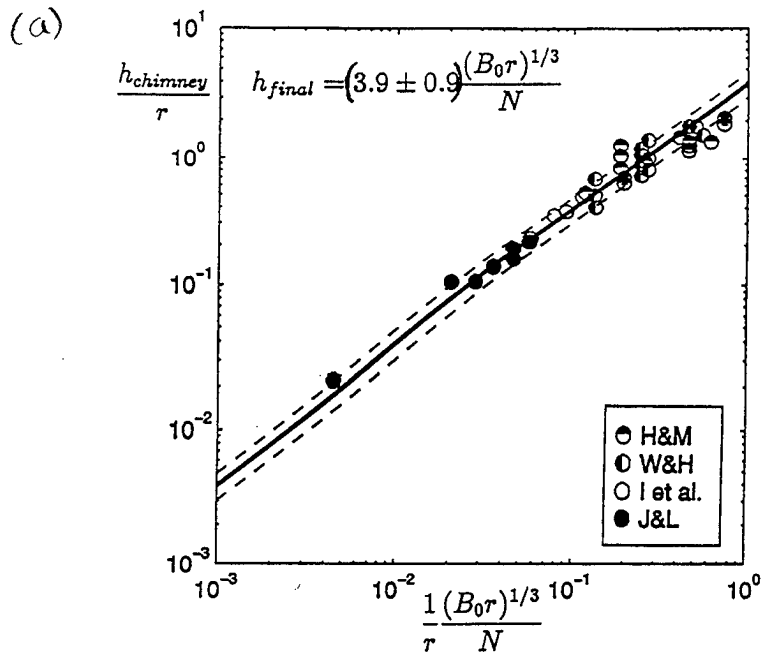
-108-
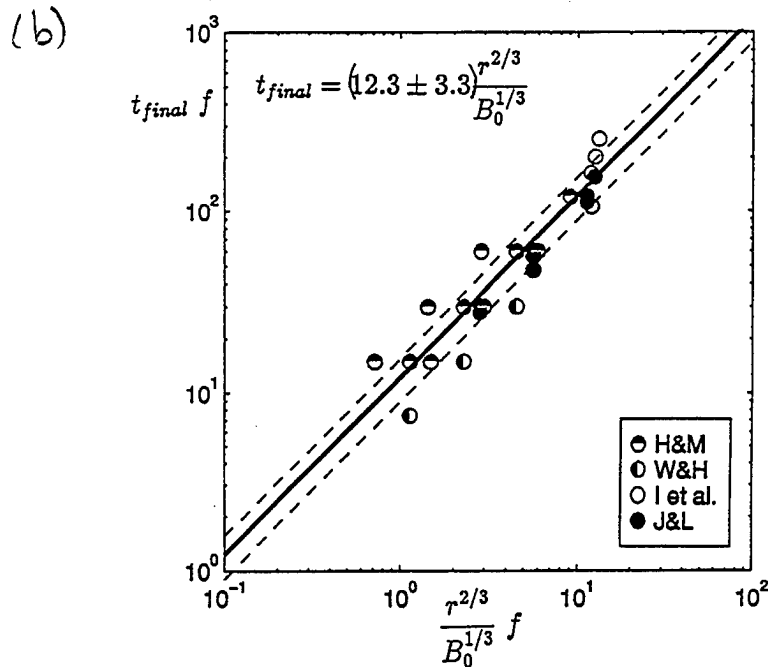
Fig. 2.3.1 - taken from Visbeck, Marshall and Jones (1996)
(a)Regression of the final observed chimney depth versus the prediction, eq(2.3.7), both normalized by the radius of the chimney. H&M indicate numerical simulations by Hufford and Marshall, W&H laboratory experiments by Hufford and Whitehead, I et.al. laboratory work by Ivey and collaborators, J&L numerical experiments by Jones and Lascaratos.
 (b) Regression of the observed final time-scale versus the prediction, eq(2.3.11). Both axes are normalized wrt the rotation rate f.
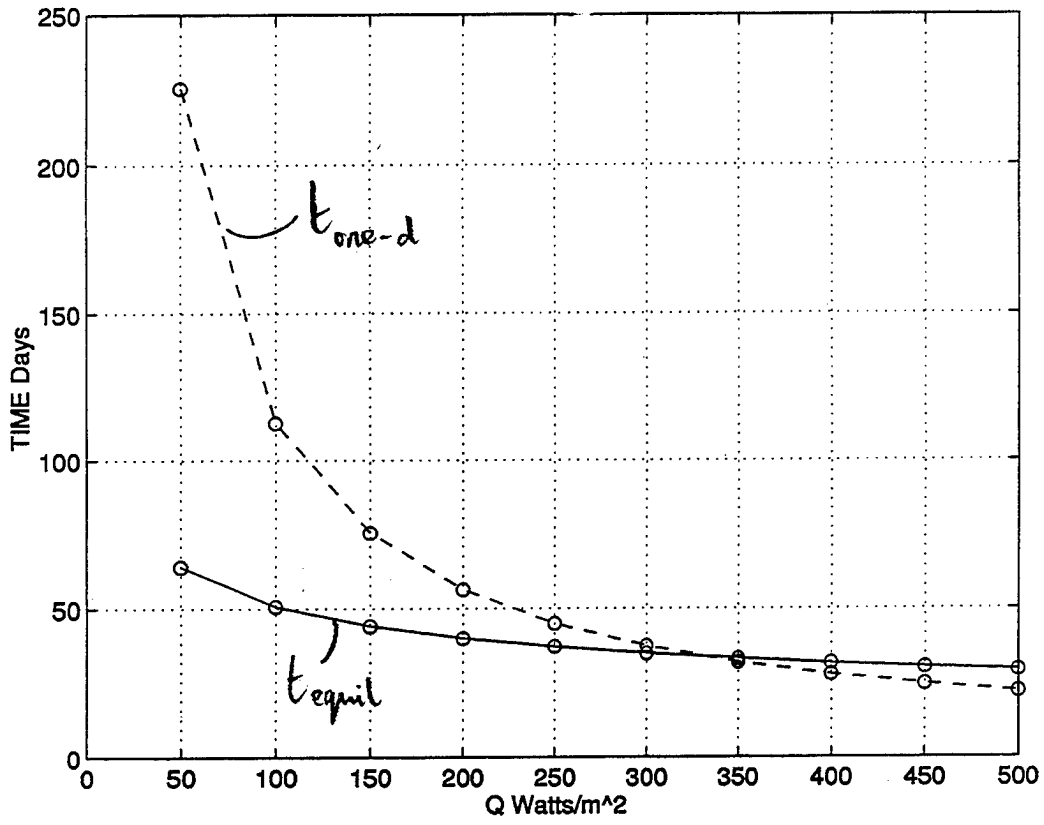
Fig.2.3.2 The curve of t_{one-d} , Eq (2.3.10) and t_{equil} Eq.(2.3.12) as a function of the cooling rate if H = 100 m and N = 10^{-2} s^{-1}.
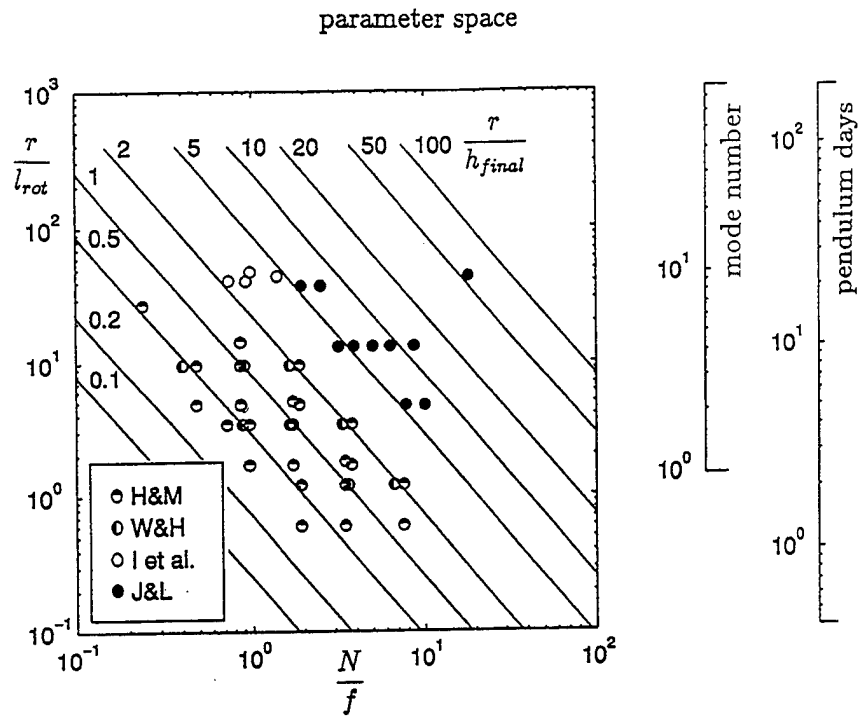
Fig.(2.3.3)

The parameter space covered by all chimney experiments, both laboratory and numerical. Solid slanting lines represent constant chimney aspect ratios r/h_{equil} (Eq.2.3.7) Axes representing the final mode number of baroclinic instability and the predicted time (in pendulum days) to reach the steady-state are also included. Axes and lines are enumerated making use of our best estimate of the constants of proportionality $\gamma = 3.9$ and $\beta = 12$. l_{rot} can be found in table 1.3.1 as a function of $\mathcal{B}_o$.

(a) Temperature and flow
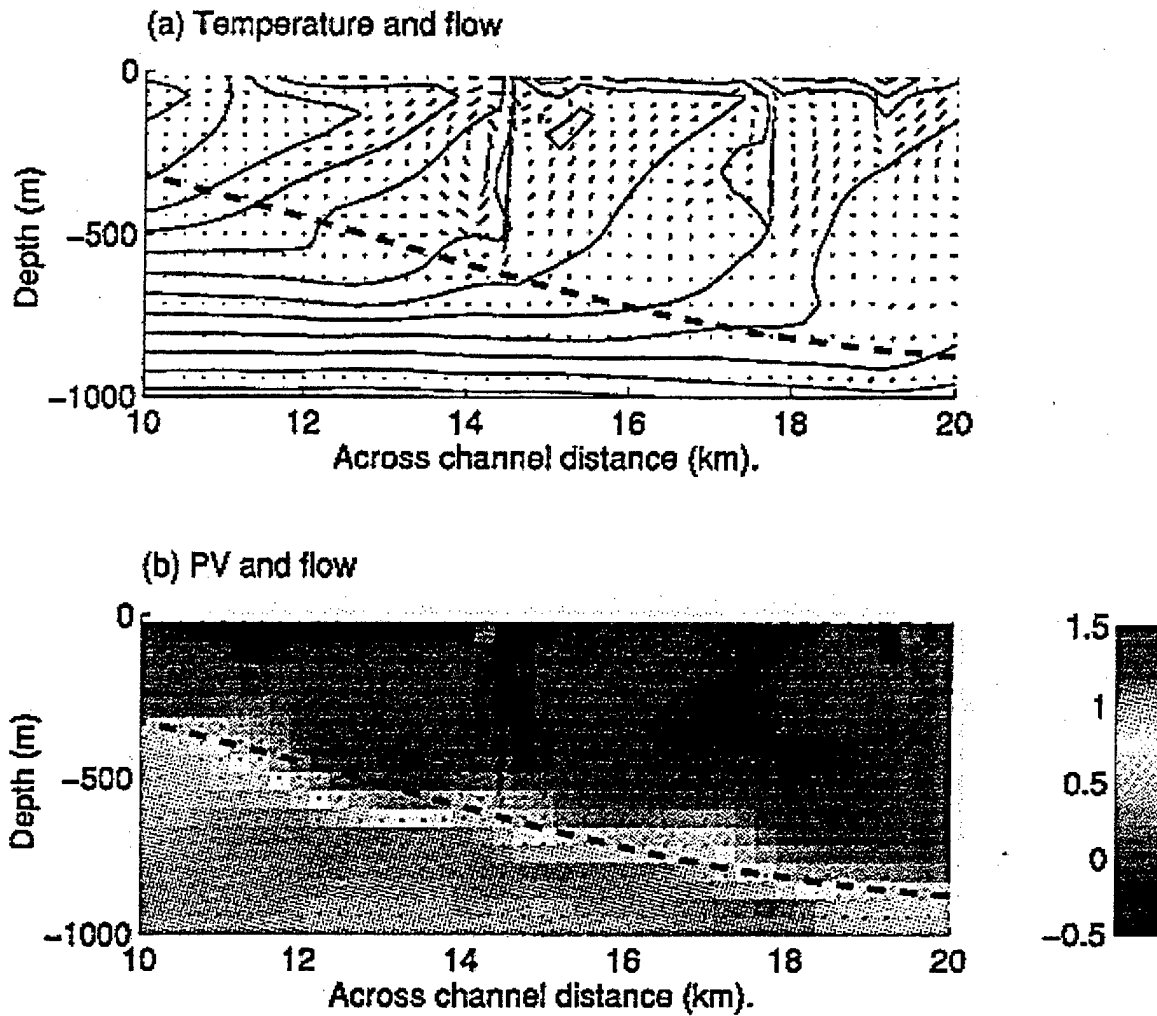
(b) PV and flow

Figure 3.1.1 Vertical sections from the 2D integration at day 9, for the central part of the channel. a) Temperature, b) Ertel potential vorticity normalized by the PV of the initial condition. In each figure the flow and 1D mixed layer depth are shown as in Figure 1.1.2 Peak speeds (v,w) are (0.11,0.050) m s⁻¹.

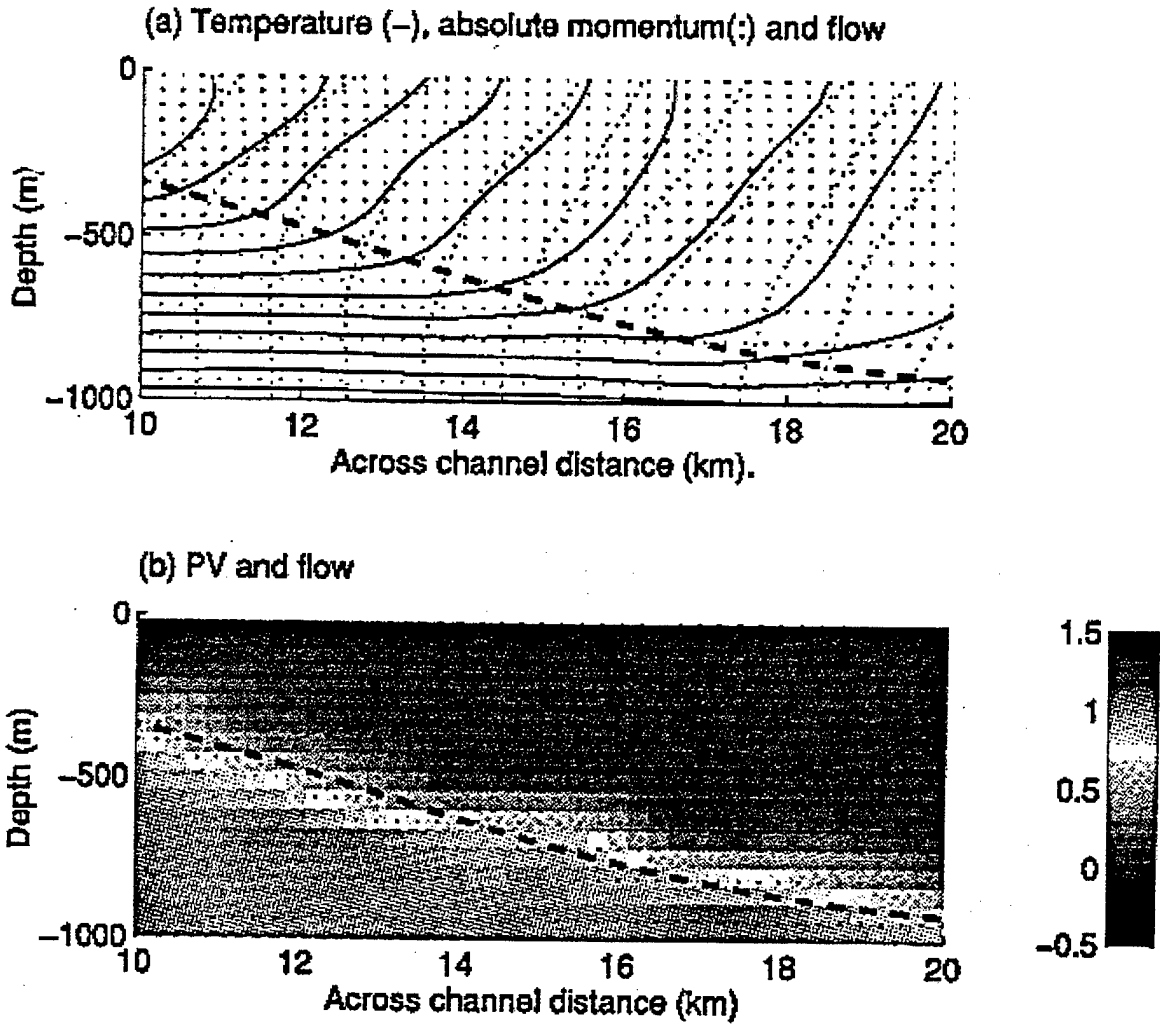(a) Temperature (–), absolute momentum(:) and flow

(b) PV and flow

Figure 3.1.2 Fields at day 10, after the surface cooling has ceased for 24 hours. Peak speeds are (0.030, 0.0045) m s^{-1} in the (y,z) directions at this time. (a) temperature and absolute momentum (b) Ertel potential vorticity. From Haine and Marshall (1996).

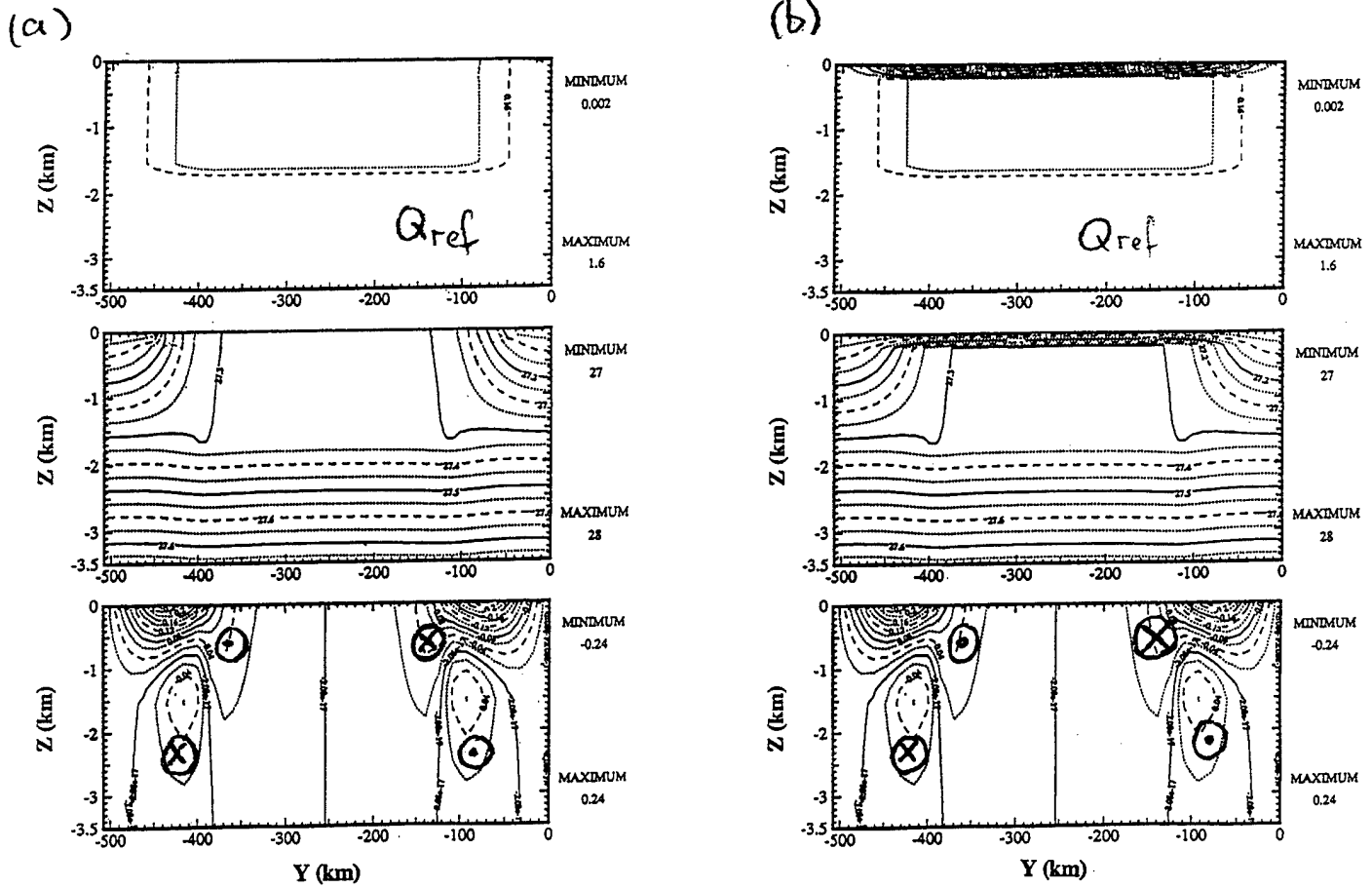(a)   (b)

Fig.3.2.1. PV chimney inversion with (a) inhomogeneous and (b) homogenous boundary conditions at the surface. The top panel shows the PV distribution that was inverted to yield the potential density (middle) and currents (bottom panel). In (b) the cold surface is represented as a delta-function sheet of high PV. Isopycnals and currents and plotted. In (a) the potential density at the sea-surface is specified and an idealized interior PV anomaly inverted to give the hydrography and azimuthal velocity of a baroclinic vortex. In (b), an interior PV field identical to that of (a) is used, but now the cold surface is represented by a sheet of high PV just beneath the upper boundary, which is prescribed to be an isopycnal surface. Note that in (b), unlike (a), the isopycnals cannot cut the upper surface which is itself an isopycnal.
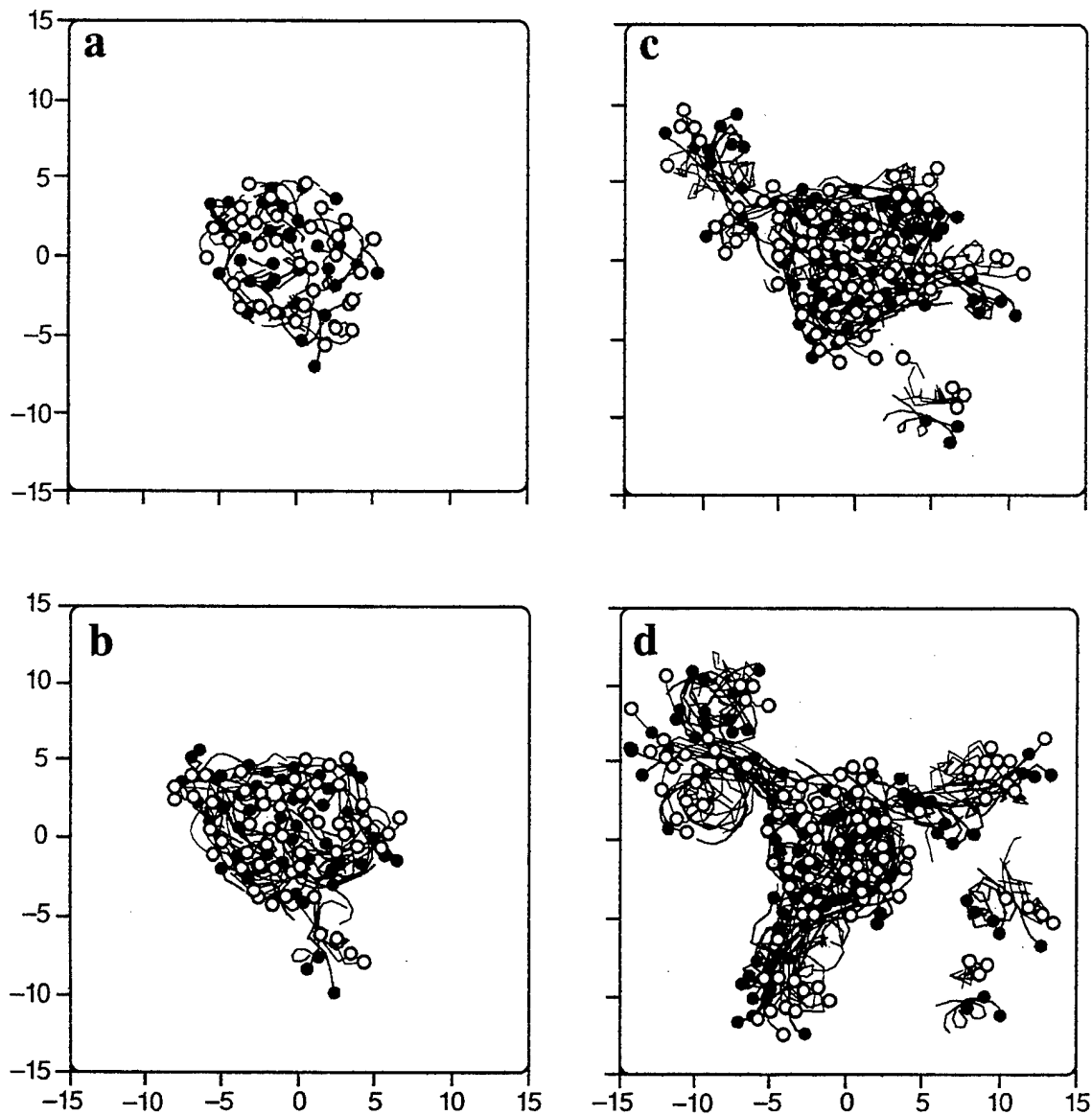
Fig.3.2.2 Four pictures charting the development of a chimney comprising an evolving cluster of hetons . Each picture shows the trajectories of the hetons over a period of 0.6 days: (a) .6 to 1.2 days , (b) 1.2 to 1.8 days, (c) 1.8 to 2.4 days, (d) 2.4 to 1.0 days. The trajectories of the upper layer vortices are shown in green, while those of the lower layer vortices are shown in red. The horizontal scale is presented in units of the deformation radius and the hetons are introduced over a disc of diameter of 5 Rossby radii. From Legg and Marshall (1993).

Magnetic versus Rotational Effects in Fluids and Magnetic Buoyancy

Jonathan Aurnou

Abstract

Magnetic fields can interact with conducting fluids in similar ways to the interaction of rotation on fluid flow. This is evident from the existence of the magnetic Taylor- Proudman theorem, the magnetic Kelvin's theorem and the symmetry between the vorticity equation and the magnetic induction equation (Chandrasekhar, 1961). The effects of a uniform rotation on a connectively unstable nondiffusive fluid layer are studied and an alternative derivation of the Rossby deformation radius is found. When the rotation is replaced by a uniform magnetic field the flow is found to be absolutely stable against convective motions for finite field strengths. A problem similar to the Rossby adjustment problem is solved with a magnetic field in the place of rotation. Perfect shape preservation of the initial surface occurs. Purely magnetically supported Rossby waves are not found to exist. Lastly, the governing equations of the magneto-Boussinesq approximation are derived and summarized.

1 Magnetic Deformation Radius

T.G. Cowling (1951) studied how rotation can affect convection in stellar systems. By performing a linear perturbation analysis on the equations of motion, the onset of convection with rotation was found to have a critical wavenumber equivalent to the reciprocal of the Rossby deformation radius. Convection may occur for inverse wavenumbers smaller than the Rossby radius while inertial waves are produced for larger length scale perturbations.

The present analysis develops Cowling's problem with and without rotation and then considers a magnetic field in place of the rotation. The scales are assumed to be of astrophysical proportions and, therefore, the diffusivities are assumed to have negligible effects on the large scale motions of the fluid.

1.1 Basic Equations

The basic equations governing a Boussinesq fluid with zero-valued diffusivities are

$$\frac{\partial \mathbf{u}'}{\partial t} + \mathbf{u}' \cdot \nabla \mathbf{u}' = -\frac{1}{\rho_o} \nabla p' - \frac{\rho}{\rho_o} g \hat{\mathbf{k}} \tag{1}$$

$$\frac{\partial T'}{\partial t} + \mathbf{u}' \cdot \nabla T' = 0 \tag{2}$$

$$\nabla . \mathbf{u}' = 0 \tag{3}$$

with the density as $\rho = \rho_o(1 - \alpha(T' - T_o))$. The velocity, pressure and temperature are defined as

$$\mathbf{u}' = 0 + \mathbf{u}$$

$$p' = p_o(z) + p$$

$$T' = T_o - \beta z + \theta$$

where $\mathbf{u}$, p and θ are the perturbations quantities and $\beta = -\frac{\partial T(z)}{\partial z}$ is the adverse temperature gradient.

Linearizing the equations and subtracting out the hydrostatic background pressure yields

$$\frac{\partial \mathbf{u}}{\partial t} = -\frac{1}{\rho_o}\nabla p + g\alpha\theta\hat{\mathbf{k}} \tag{4}$$

$$\frac{\partial \theta}{\partial t} = \beta w \tag{5}$$

$$\nabla \cdot \mathbf{u} = 0 \tag{6}$$

The vertical component of the second curl of equation (4) is

$$-\frac{\partial}{\partial t}\nabla^2 w = -g\alpha\nabla_H^2\theta \tag{7}$$

Solving equations (5) and (7) for the vertical velocity gives

$$\frac{\partial^2}{\partial t^2}\nabla^2 w = g\alpha\beta\nabla_H^2 w \tag{8}$$

where ∇_H^2 is the horizontal Laplacian.

Free boundary solutions that are periodic in the x and y directions are

$$w = C\sin(\frac{n\pi}{d}z)exp[ik_x x + ik_y y + \sigma t] \tag{9}$$

where C is a constant, d is the layer depth, σ is the growth rate, and a total horizontal wavenumber, k, is defined as $k^2 = k_x^2 + k_y^2$.

Substituting (9) into (8) gives the dispersion relation for this system

$$\sigma^2 = g\alpha\beta\frac{k^2}{k^2 + \frac{n^2\pi^2}{d^2}} \tag{10}$$

Defining the buoyancy frequency, N, as

$$N^2 = -\frac{g}{\rho}\frac{\partial \rho}{\partial z} = -g\alpha\beta \tag{11}$$

allows equation (10) to be written as

$$\sigma^2 = -N^2 \frac{k^2}{k^2 + \frac{n^2\pi^2}{d^2}} \qquad (12)$$

where $-N^2$ is a positive number corresponding to an unstable density gradient. It can be seen from equation (12) that the fluid layer is unstable for all positive wavenumbers. The growth rate goes to zero as k tends to zero and approaches $|N|$ as k grows large. The convective motions become harder to excite as the aspect ratio gets larger because no gravitational work is done on the parcels moving along equipotential surfaces. It is only the fluid travelling vertically upwards and downwards that powers the convection; the fluid travelling horizontally is being passively driven.

1.2 Effects of Rotation

If the layer is subjected to a vertical rotation, Ωk, equation (1) becomes

$$\frac{\partial u}{\partial t} + u \cdot \nabla u + f\hat{k} \times u = -\frac{1}{\rho_o}\nabla p - \frac{\rho}{\rho_o}g\hat{k} \qquad (13)$$

where $f = 2\Omega$. Linearizing the governing equations for instability of this system gives

$$\sigma^2 = \frac{-N^2 k^2 - f^2 \frac{n^2\pi^2}{d^2}}{k^2 + \frac{n^2\pi^2}{d^2}} \qquad (14)$$

This system acts the same as the fluid layer without rotation when the horizontal wavenumber is large. At small k values the growth rate becomes imaginary and instability is replaced by inertial oscillations in the fluid. The boundary between oscillations and convection is found by solving for k at $\sigma = 0$, leading to

$$k_o = \left(\frac{-N^2 d^2}{f^2 n^2\pi^2}\right)^{-\frac{1}{2}} \qquad (15)$$

The only differences between the critical wavenumber, k_o, and the reciprocal of the Rossby deformation radius found in the oceanographic literature is the unstable stratification of the fluid layer. Convection will be found to occur on length scales smaller than the Rossby radius; inertial oscillations will occur at length scales greater than the Rossby radius.

For the case when the rotation axis is aligned parallel to the x-axis, the growth rate is

$$\sigma^2 = \frac{-N^2 k^2 - f^2 k_x^2}{k^2 + \frac{n^2\pi^2}{d^2}} \qquad (16)$$

Convection occurring in rolls aligned with the x-axis, with $k_x = 0$, is unaffected by the rotation. This is because the motion is two-dimensional in planes perpendicular to the rotation axis such that all the convective motions perfectly satisfy the Taylor-

Proudman theorem. For convection aligned perpendicular to the rotation axis, $k_y = 0$, and

$$\sigma_x^2 = (-N^2 - f^2)\frac{k_x^2}{k_x^2 + \frac{n^2\pi^2}{d^2}} \tag{17}$$

The x-direction growth rate is stifled by the rotation and becomes imaginary for all positive k_x when $f^2 > -N^2$. Thus, no critical wavenumber may be defined.

1.3 Magnetic Effects

If the fluid layer has a vertical magnetic field, $B_o\hat{\mathbf{k}}$, imposed across it and the fluid is assumed to have a very high electrical conductivity then the governing equations become

$$\frac{\partial \mathbf{u}}{\partial t} + \mathbf{u} \cdot \nabla\mathbf{u} = -\frac{1}{\rho_o}\nabla p - \frac{\rho}{\rho_o}g\hat{\mathbf{k}} + \frac{1}{\rho_o\mu}(\nabla \times \mathbf{B}) \times \mathbf{B} \tag{18}$$

$$\frac{\partial \mathbf{B}}{\partial t} + \mathbf{u} \cdot \nabla\mathbf{B} = \mathbf{B} \cdot \nabla\mathbf{u} \tag{19}$$

$$\frac{\partial T}{\partial t} + \mathbf{u} \cdot \nabla T = 0 \tag{20}$$

$$\nabla \cdot \mathbf{u} = \nabla \cdot \mathbf{B} = 0 \tag{21}$$

where μ is the magnetic permeability of the fluid.

Using the same analysis as before, the growth rate of instabilities is given by

$$\sigma^2 = \frac{-N^2 k^2}{k^2 + \frac{n^2\pi^2}{d^2}} - V_A^2\frac{n^2\pi^2}{d^2} \tag{22}$$

where $V_A = \frac{1}{(\rho_o\mu)^{\frac{1}{2}}}B_o$ is the the Alfven velocity. At $\sigma = 0$ the critical wavenumber is

$$k_o = \frac{n\pi}{d}\frac{1}{\sqrt{Q-1}} \tag{23}$$

where

$$Q = \frac{-N^2 d^2}{V_A^2 n^2\pi^2}$$

Q is the ratio of convective velocities to the Alfven velocity and is known as the Chandrasekhar number.

The critical magnetic wavenumber is singular when Q is of order unity. Therefore, convection is completely inhibited at finite field strengths. Complete inhibition of convective motions occurs in the rotational case only for infinite rotation rates. This effect results mathematically from an extra Laplacian that comes into the term involving $\mathbf{B}$. Physically, this amounts to $\mathbf{B}$ acting back on itself even in the linear case.

An imposed horizontal field, $B_o\hat{\mathbf{x}}$, leads to the dispersion relation

$$\sigma^2 = -N^2\frac{k^2}{k^2 + \frac{n^2\pi^2}{d^2}} - V_A^2 k_x^2 \tag{24}$$

As with horizontal rotation, convection rolls aligned with the axis of the magnetic field are unaffected by the field's presence. For rolls transverse to the field the critical wavenumber is given as

$$k_{x_o} = \frac{n\pi}{d}\sqrt{Q-1} \qquad (25)$$

The horizontal field is very different than the vertical field in that the critical wavenumber tends to zero, not infinity, as $Q \to 1$ because the Lorentz force tries to keep the field lines unbent. It is this magnetic tension inherent in the Lorentz force that resists motions occurring at high k_x values and consequently the critical wavenumber becomes smaller.

Thermal convection in the presence of a 4500 gauss horizontal magnetic field was experimentally studied by Lehnert and Little (1957). Rolls were not observed to form parallel to the field lines. Instead elongated convective cells were seen with streamlines parallel to the field. This may have been caused by ungovernable horizontal temperature gradients in the experiment or due to the surface visualization technique employed. This experiment is currently being set-up in order to better examine these results.

2 The Linear Adjustment Problem with Magnetic Pressure

In a rotating fluid layer an initial discontinuity of the surface will reach equilibrium with non-zero surface slope. This slope is upheld because potential vorticity conservation sets up currents which geostrophically balance the gravitational forces.

For a shallow fluid layer that has an initial step function surface displacement, $\eta(x,0) = -\eta_o sgn(x)$, the equilibrium surface relaxes to

$$\eta = \eta_o(1 - exp\frac{x}{R})$$

for $x < 0$ and

$$\eta = \eta_o(-1 + exp\frac{-x}{R})$$

for $x > 0$ where $R = \sqrt{\frac{gH}{f^2}}$ is another form of the Rossby deformation radius (Gill, 1982).

If rotation is removed from this problem and a vertical magnetic field, $B_o\hat{k}$, is imposed across the layer a completely different stationary solution is found. The shape of the initial displacement is unaltered and the height of this preserved structure goes from η_o to zero as B_o ranges from infinity to zero.

The two dimensional governing equations are

$$\frac{\partial \mathbf{u}}{\partial t} + \mathbf{u} \cdot \nabla \mathbf{u} = -\frac{1}{\rho_o}\nabla p - g\hat{\mathbf{k}} + \frac{1}{\rho_o\mu}(\nabla \times \mathbf{B}) \times \mathbf{B} \qquad (26)$$

$$\frac{\partial \mathbf{B}}{\partial t} + \mathbf{u} \cdot \nabla \mathbf{B} = \mathbf{B} \cdot \nabla \mathbf{u} \qquad (27)$$

$$\nabla \cdot \mathbf{B} = 0 \tag{28}$$

$$\frac{\partial \eta}{\partial t} + H \frac{\partial u}{\partial x} = 0 \tag{29}$$

with non-permeable, free-slip boundary conditions at $z = 0$

$$w = \frac{\partial u}{\partial z} = 0 \tag{30}$$

and a free-surface, free-slip condition at $z = \eta + H$

$$\frac{D\eta}{Dt} = w \tag{31}$$

$$\frac{\partial u}{\partial z} = 0 \tag{32}$$

A non-conducting medium is found above and below the fluid layer so that the external perturbation to the magnetic field is continuous at the interface (Chandrasekhar, 1961).

Applying equation (32) to the induction equation results in the x-component of the magnetic field perturbation, b_x, being equal to zero on the boundaries. If the fluid layer is very shallow, then the mean value theorem and the boundary conditions on b_x allow one to assume that $b_x \sim 0$ throughout the fluid layer. Alternatively, the small vertical gradients assumed in the shallow water equations causes the field lines to be advected by the flow field but not bent.

The linearized x-momentum equation then becomes

$$\frac{\partial u}{\partial t} = -g \frac{\partial \eta}{\partial x} - \frac{B_o}{\mu \rho_o} \frac{\partial b_z}{\partial x} \tag{33}$$

where $p = -\rho_o g(z - (\eta + H))$ for a hydrostatic layer and $p = 0$ for a free surface boundary. The steady form of equation (33) used to solve for the equilibrium surface, $\eta(x, t)$, is

$$g \frac{\partial \eta}{\partial x} = -\frac{B_o}{\mu \rho_o} \frac{\partial b_z}{\partial x} \tag{34}$$

Integrating the z-component of the linearized induction equation

$$\frac{\partial}{\partial t} \int_0^{\eta + H} b_z dz = B_o \int_0^{\eta + H} \frac{\partial w}{\partial z} dz \tag{35}$$

Because $b_x \sim 0$ in the layer, $\nabla \cdot \underline{b} = 0$ reduces to $\frac{\partial b_z}{\partial z} = 0$ and, therefore, b_z can be removed from the left-hand integral giving the result

$$H \frac{\partial b_z}{\partial t} = B_o \frac{\partial \eta}{\partial t} \tag{36}$$

where the the boundary condition in equation (31) has been used. Integrating in time gives the relationship between the induced field and the surface displacement:

$$\frac{b_z}{B_o} = \frac{\eta(x, t) - \eta(x, 0)}{H} \tag{37}$$

This result is the magnetic analogue to shallow water potential vorticity conservation. Substituting equation (37) into equation (34):

$$g\frac{\partial \eta}{\partial x} = -\frac{B_o^2}{\rho_o \mu}\frac{\partial}{\partial x}\left(\frac{\eta - \eta(0)}{H}\right) \tag{38}$$

Using $c = \sqrt{gH}$, equation(38) may be rewritten as

$$\frac{\partial \eta}{\partial x} = \left(\frac{V_A^2}{V_A^2 + c^2}\right)\frac{\partial \eta(0)}{\partial x} \tag{39}$$

and integrating in x leads to

$$\eta = \left(\frac{V_A^2}{V_A^2 + c^2}\right)\eta(0) \tag{40}$$

The linear theory preserves the shape of the initial surface displacement with the amplitude modulated by the factor $V_A^2/(V_A^2 + c^2)$. For Alfven velocities approaching infinity, the surface displacement is exactly preserved. For vanishing Alfven velocities, η must go to zero.

No analogue to the Rossby radius exists in the linear magnetic pressure problem. This shape preservation is not so unexpected when one considers how different the magnetic deformation radius is compared to the rotational case. Even though a precise magnetic analogue exists for shallow water potential vorticity conservation, the force balance in equation (34) is very different from the rotational case. The magnetic and gravitational forces balance each other by having gradients in the same direction. This does not occur in the geostrophic force balance and it is this difference that leads to the shape preservation.

3 Magnetic Rossby Waves

The dispersion relation for motions in a shallow conducting fluid layer with a vertical magnetic field and a slanting bottom boundary and the relation for a vertical magnetic field that varied along a β-plane were studied. No analogue to Rossby waves were found to exist because perturbations to the magnetic field do not feedback into the velocity field as occurs with vorticity. Though magnetic fields alone will not support planetary waves, they will affect planetary wave propagation in a conducting rotating fluid (Malkus, 1967; Bergman, 1993).

4 Magnetic Buoyancy Effects in Convection

Horizontal magnetic fields with vertical gradients may stabilize or destabilize a fluid layer by way of magnetic buoyancy. The Lorentz force can be broken up into two terms: a magnetic pressure term, $\frac{1}{2\mu}|\mathbf{B}|^2$, and a term that resists any curvature of the field lines, $\frac{1}{\mu}\mathbf{B}\cdot\nabla\mathbf{B}$. The magnetic pressure may be placed together with the

thermodynamic pressure to form a total pressure term. In the magneto-Boussinesq approximation (Spiegel and Weiss, 1982) variations in the total pressure are shown to be small. When this criterion is fulfilled, the positive buoyancy of fluid parcels is caused by positive temperature or magnetic field perturbations. Therefore, a horizontal field that decreases (increases) with height can destabilize (stabilize) a fluid layer. Instabilities that do not bend the field lines are appropriately called interchange instabilities while instabilities that do involve bending the field lines are called undular instabilities. Undular instabilities are usually more complex than the interchange instabilities due to the addition of the curvature force.

4.1 Magneto-Boussinesq Equations

The governing equations are

$$\rho(\frac{\partial \mathbf{u}'}{\partial t} + \mathbf{u}' \cdot \nabla \mathbf{u}') = -\nabla p' - \rho g \hat{\mathbf{k}} + \rho \nu \nabla^2 \mathbf{u}' + \frac{1}{\mu}(\nabla \times \mathbf{B}') \times \mathbf{B}' \tag{41}$$

$$\frac{\partial \mathbf{B}'}{\partial t} + \mathbf{u}' \cdot \nabla \mathbf{B}' = \mathbf{B}' \cdot \nabla \mathbf{u}' - \mathbf{B}'(\nabla \cdot \mathbf{u}') + \eta \nabla^2 \mathbf{B}' \tag{42}$$

$$\rho C_v \frac{DT'}{Dt} + p(\nabla \cdot \mathbf{u}') = K' \nabla^2 T' \tag{43}$$

$$\nabla \cdot \mathbf{u}' = 0 \,, \qquad \nabla \cdot \mathbf{B}' = 0 \tag{44}$$

where all the primed variables are defined in section 2.1 except the magnetic field which is defined as $\mathbf{B}' = \mathbf{B}(z) + \mathbf{b}$. ν is the viscosity, η is the magnetic diffusivity, C_v is the specific heat at constant volume, and K' is the thermal conductivity. The dissipation terms have been thrown out of the entropy equation because they will be small in the Boussinesq limit of $d/H_i \ll 1$ and $u/c \ll 1$ where d is the layer depth, $H_i = -\frac{\partial ln i}{\partial z}$ is the scale height of the ith state variable of the system, u is the velocity and c is the sound speed in the fluid(Spiegel and Veronis,1960; Veronis, 1961).

The linearized magneto-Boussinesq approximation yields

$$\frac{\partial \mathbf{u}}{\partial t} = -\frac{1}{\rho_o} \nabla \Pi + (g \alpha \theta + g K p_m) \hat{\mathbf{k}} + \nu \nabla^2 \mathbf{u} + \frac{1}{\mu \rho_o} \mathbf{B} \cdot \nabla \mathbf{B} \tag{45}$$

$$\frac{\partial \mathbf{b}}{\partial t} = -w \left[\frac{\partial \mathbf{B}(z)}{\partial z} + \frac{\mathbf{B}(z)}{H_\rho} \right] \hat{\mathbf{y}} + \mathbf{B} \cdot \nabla \mathbf{u} + \eta \nabla^2 \mathbf{b} \tag{46}$$

$$\frac{\partial \theta}{\partial t} + \frac{1}{\rho_o C_p} \frac{\partial p_m}{\partial t} = -w \left[\frac{\partial T(z)}{\partial z} + \frac{g}{C_p} \right] + \kappa \nabla^2 \theta \tag{47}$$

$$\nabla \cdot \mathbf{u} = 0 \,, \qquad \nabla \cdot \mathbf{b} = 0 \tag{48}$$

where Π is the total pressure perturbation and p_m is the magnetic pressure perturbation such that $\Pi = p + p_m$. The thermal expansion coefficient is α, K is the compressibility and C_p is the specific heat at constant pressure.

The magnetic buoyancy term in equation (45) results from setting the variation in total pressure to zero:

$$\delta\Pi = \delta\left(p + \frac{|\mathbf{B}|^2}{2\mu}\right) = 0$$

This expression can be expanded to

$$\frac{\partial p}{\partial \rho}\delta\rho + \frac{\partial p}{\partial T}\delta T + \frac{\mathbf{B_o} \cdot \delta\mathbf{B}}{\mu} = 0$$

If the fluid is treated as an ideal gas then

$$\frac{\delta\rho}{\rho_o} = -\alpha\,\delta T - K\,\frac{\mathbf{B_o} \cdot \delta\mathbf{B}}{\mu}$$

The magnetic pressure term in equation (47) comes from a similar expansion of $p(\nabla.\mathbf{u})$ in equation (43).

When the diffusivities κ and η are different in value one would expect that double convection might exist within this system. The only difference between interchange mode double convection and thermohaline convection results from the magnetic pressure term in the entropy equation. Spiegel and Weiss (1982) have given a non-trivial transformation whereby these interchange modes can be cast into a form equivalent to the equations governing thermohaline circulation (Hughes, 1985; Hughes and Proctor, 1988).

In the absence of diffusion the interchange instability occurs for $(\mathbf{B}(z)/\rho(z))$ decreasing with height while the undular instability can occur when $\mathbf{B}(z)$ decreases with height. This discrepancy between the stability criteria can be explained by the differences in the energy release mechanisms (Hughes and Proctor, 1988). The interchange instability generates density fluctuations that must do work against the thermodynamic and the magnetic pressure while the undular instability can generate fluctuations by motions along the field lines that do not require doing any work against the magnetic pressure. For very short wavenumber instabilities the curvature forces become negligible and, therefore, the undular instability may go unstable even when the interchange processes are stable.

D.W. Hughes (1987) uses normal form analysis (Coullet and Spiegel, 1983) to analyze interchange instabilities in the finite amplitude regime. Finite amplitude analysis of undular instabilities began this summer but no results have yet been obtained.

5   Future Experiments

This work has lead to many ideas for magnetoconvection experiments in liquid Gallium. Besides a re-evaluation of Lehnert and Little's experiment, convection will be studied using stacked rare-earth "hockey puck" magnets (radius $\sim$ 4 cm, height $\sim$ 1.5 cm) to produce a strong magnetic flux tube (3000 gauss). By putting two separate stacks of magnets with opposed polarities below the fluid layer it may also be possible to simulate a magnetic bipolar pair. We have not yet devised a way to create a

strong vertical gradient in a horizontal magnetic field in the laboratory and, therefore, cannot experimentally study the rich spectrum of magnetic buoyancy phenomena.

Acknowledgements

References

Bergman, M.I., 1993: Magnetic Rossby Waves in a Stably Stratified Layer Near the Surface of the Earth's Outer Core, Geophys. Astrophys. Fluid Dynamics. **68**: 151-176.

Coullet, P.H. and E.A. Spiegel, 1983: Amplitude Equations for Systems with Competing Instabilities, SIAM J. Appl. Math. **43**: 776-821.

Cowling, T.G., 1951: The Condition for Turbulence in Rotating Stars, Ap. J. **114**: 272-286.

Chandrasekhar, S., 1961: Hydrodynamic and Hydromagnetic Stability. Oxford: Clarendon Press. 652 pp.

Gill, A.E., 1982: Atmosphere- Ocean Dynamics. Academic Press. 662 pp.

Hughes, D.W., 1985: Magnetic Buoyancy Instabilities for a Static Plane Layer, Geophys. Astrophys. Fluid Dynamics. **32**: 273-316.

Hughes, D.W., 1987: Finite Amplitude Solutions for Interchange Instabilities Driven by Magnetic Buoyancy, Geophys. Astrophys. Fluid Dynamics. **37**: 297-343.

Hughes, D.W. and M.R.E. Proctor, 1988: Magnetic Fields in the Solar Convection Zone: Magnetoconvection and Magnetic Buoyancy, Ann. Rev. Fluid Mech. **20**: 187-223.

Lehnert, B. and N.C. Little, 1957: Experiments on the Effect of Inhomogeneity and Obliquity of a Magnetic Field in Inhibiting Convection, Tellus. **9**: 97-103.

Malkus, W.V.R., 1967: Hydromagnetic Planetary Waves, J. Fluid Mech. **28**: 793-802.

Spiegel, E.A. and N.O. Weiss, 1982: Magnetic Buoyancy and the Boussinesq Approximation, Geophys. Astrophys. Fluid Dynamics. **22**: 219-234.

Spiegel, E.A. and G. Veronis, 1960: On the Boussinesq Approximation for a Compressible Fluid, Astrophys. J. **131**: 442-447.

Veronis, G., 1962: The Magnitude of the Dissipation Terms in the Boussinesq Approximation, Astrophys. J. **135**: 655-656.

A Semigeostrophic Model in a Closed Basin: Linear Waves and Normal Modes

Helene Banks

Dept. of Oceanography, University of Southampton

1   Introduction

The dynamics in closed basins are described exactly by the shallow water equations. However, in many situations we are interested only in low frequency dynamics (ie, motions on a longer timescale than the inertial scale). Balanced models are approximations to the shallow water equations, which filter the high frequency motions, and allow us to restrict our attention to the low frequency dynamics.

The most popular of the balanced models is the quasi-geostrophic approximation. The dynamics of the quasi-geostrophic approximation includes Rossby waves but not Kelvin waves, which are ageostrophic boundary trapped waves and also exist at low frequencies. Here we develop a formulation of the semigeostrophic approximation for the purposes of examining the interaction between Kelvin waves and Rossby waves. With this objective, we study two classic problems; Rossby wave reflection from boundaries and the basin modes of the model.

2   Kelvin wave in shallow-water equations

The linear shallow water equations (SWE) are:

$$\frac{\partial u}{\partial t} - fv = -g\frac{\partial h}{\partial x} \tag{1}$$

$$\frac{\partial v}{\partial t} + fu = -g\frac{\partial h}{\partial y} \tag{2}$$

$$\frac{\partial h}{\partial t} + \left\{\frac{\partial(Hu)}{\partial x} + \frac{\partial(Hv)}{\partial y}\right\} = 0 \tag{3}$$

where H is the total depth of the fluid. The exact boundary condition is given by:

$$\underline{u}.\underline{n} = 0 \tag{4}$$

Now we will look at the Kelvin wave propogating along a zonal boundary. The boundary condition is $v = 0$. Substituting in equations (1-3) we see that the Kelvin wave is geostrophic in the cross-stream direction. Choosing a solution which decays as y increases, gives

$$h(x, y, t) = e^{\frac{-y}{R_d}} F(x - ct) \tag{5}$$

where $R_d = (gH)^{\frac{1}{2}}/f$ is the Rossby radius of deformation. The Kelvin wave travels cyclonically around the basin.

3 Quasi-geostrophic approximation

Formally, the quasi-geostrophic approximation is a small Rossby number expansion (Pedlosky(1987)), where the Rossby number is given by $R_o = U/f_o L$, where U is the characteristic velocity, f_o is the Coriolis parameter (to leading order) and L is the characteristic length scale.

The diagnostic equation for the streamfunction ψ is given by:

$$\frac{\partial}{\partial t}\{\nabla^2 \psi - \frac{1}{R_d^2}\psi\} + J(\psi, f) = 0 \tag{6}$$

where $u_g = -\frac{\partial \psi}{\partial y}$ and $v_g = \frac{\partial \psi}{\partial x}$. The boundary condition, that the normal geostrophic velocity is equal to zero on a boundary, implies

$$\psi = \gamma(t) \tag{7}$$

where $\gamma(t)$ is any function of time.

In a closed domain, integral constraints must be imposed which close the balances of mass, energy and circulation.

$$\frac{\partial}{\partial t}\oint_C \underline{u}.d\underline{r} = 0. \tag{8}$$

Applied to lowest order, this implies that

$$\frac{\partial}{\partial t}\oint_C \nabla\psi.\hat{\underline{n}}ds = 0. \tag{9}$$

This constraint requires that the normal velocity vanishes at the boundary at both zero order and first order in Rossby number.

In particular, imposing equation (7) by requiring $\psi = 0$ on C implies that no free surface elevation is allowed on the boundary. Imposing constraints (7) and (8) allows for boundary adjustment, but since there are no variations along the boundary Kelvin waves are not permitted.

For a complete description of the low-frequency dynamics in a closed basin, it is necessary to include Kelvin waves. A model which allows us to include the Kelvin wave dynamics is the semigeostrophic approximation, which we will now examine.

4 Semigeostrophic approximation

In obtaining the quasi-geostrophic approximation we assumed that $R_o = U/f_o L < 1$. To obtain the semigeostrophic approximation we define a Rossby number:

$$R_o = \frac{|\frac{\partial u}{\partial t}|}{|fu|}$$

and assume that $R_o < 1$ (Hoskins(1975)). For wave motions, ie $u(t) \approx cos(\omega t)$ this implies that $\omega/f < 1$.

Given R_o defined in this manner, we approximate the acceleration in SWE by the geostrophic velocity, $u_g = \frac{g}{f}\underline{k} \times \nabla h$, while retaining the true velocity elsewhere in the equations (the geostrophic momentum approximation).

$$-\frac{g}{f}\frac{\partial^2 h}{\partial y \partial t} - fv = -g\frac{\partial h}{\partial x} \tag{10}$$

$$\frac{g}{f}\frac{\partial^2 h}{\partial x \partial t} + fu = -g\frac{\partial h}{\partial y} \tag{11}$$

$$\frac{\partial h}{\partial t} + \{\frac{\partial(Hu)}{\partial x} + \frac{\partial(Hv)}{\partial y}\} = 0 \tag{12}$$

These equations may also be obtained by linearizing Salmon's (1985) generalised semigeostrophic equations. From these equations we see that the exact boundary condition, equation (4) in semigeostrophy is:

$$h_{nt} = -fh_s \tag{13}$$

where n and s are defined as the normal and the tangential direction, respectively and (s, n) is a right-handed system.

Now we can derive a diagnostic equation for h. Taking $\frac{\partial}{\partial x}$ (11) subtracting $\frac{\partial}{\partial y}$ (10) and substituting in (12) gives:

$$\frac{\partial}{\partial t}\{h - \nabla.(\frac{gH}{f^2}\nabla h)\} + J(h, \frac{gH}{f}) = 0. \tag{14}$$

It should be noted that f is variable throughout equation (14) and in the boundary condition (13).

In a closed basin, this set of equations conserves energy:

$$\frac{\partial}{\partial t}\int\int\frac{H}{2}\{(\frac{g\nabla h}{f})^2 + \frac{gh^2}{H}\}dA = 0 \tag{15}$$

and also mass:

$$\frac{\partial}{\partial t}\int\int hdA = 0. \tag{16}$$

If, after expansion of the Jacobian, f is approximated by f_o in (13) and (14), then neither mass nor energy are conserved. If f is kept variable in the boundary condition then energy is

conserved but not mass. In both of these cases the diagnostic equation reduces to equation (6). However, if $R_d{}^2$ is held constant then energy and mass conservation is retained. This formulation of the model will be discussed in section 6.

The linearized form of potential vorticity is conserved:

$$\frac{\partial}{\partial t}\{\zeta_g - \frac{fH}{h}\} = 0 \tag{17}$$

where $\zeta_g = \frac{\partial v_g}{\partial x} - \frac{\partial u_g}{\partial y}$. This is another way of expressing equation (14).

5 Kelvin wave dynamics

Here we will examine the Kelvin wave in the semigeostrophic model; firstly, for the f-plane case ($f = $ constant) and secondly, for the case of variable f.

Case 1 : f-plane (see also Allen et al(1990))
Look for solutions of equation (14), proportional to $e^{-kx+i(ly-\omega t)}$ with the boundary condition: $h_{xt} = -fh_y$ (ie, a meridional boundary).

The boundary condition gives $l = \frac{\omega k}{f}$. Equation (14) $\Rightarrow$

$$\omega = \frac{flR_d}{(1 + l^2 R_d{}^2)^{\frac{1}{2}}}.$$

The phase speed $c = \frac{\omega}{l} = fR_d(1 - \frac{1}{2}l^2 R_d{}^2 + ...)$. If we compare this with the result in shallow water, $c = fR_d$, we see that in the semigeostrophic model the Kelvin wave phase speed is slower than in SWE. The error is small for $lR_d < 1$, which implies that the along-stream wavelength is larger than that in the cross-stream direction (the Rossby radius of deformation). It is this anisotropic wave which is precisely the low-frequency Kelvin wave which we wish to include in the dynamics (since $lR_d < 1 \Rightarrow \omega < f$).

Case 2 : f slowly-varying
Look for solutions to equation (14) s.t.

$$h \propto \tilde{h}(x, y)e^{-i\omega t}.$$

$$\tilde{h}_{xx} + \tilde{h}_{yy} - 2\frac{\beta}{f}\tilde{h}_y + i\frac{\beta}{\omega}\tilde{h}_x - \frac{f^2}{gH}\tilde{h} = 0 \tag{18}$$

and

$$-i\omega\tilde{h}_x = -f\tilde{h}_y.$$

Now if we non-dimensionalise:
$\omega = \epsilon f; f = \beta R; x = L_x x'; y = L_y y'$.

Then since the Kelvin wave has anisotropic scales and the coriolis parameter varies slowly over one wavelength

$$L_x < L_y < R$$

and we let $\epsilon L_y = L_x$; $\epsilon^2 R = L_x$, then equation (21) (dropping the primes) becomes

$$\frac{1}{L_x^2}\tilde{h}_{xx} + \frac{\epsilon^2}{L_x^2}\tilde{h}_{yy} - \frac{2\beta\epsilon}{fRL_x}\tilde{h}_y + i\frac{\beta}{\omega}\frac{1}{ReL_x}\tilde{h}_x - \frac{f^2}{gH}\tilde{h} = 0.$$

Now if we look for solutions to this equation, which satisfy the boundary condition, of the form:

$$\tilde{h} = G(x, X, y, Y)$$

where $X = \epsilon x$, $Y = \epsilon y$, balancing terms at each order we find:

$$h(x,y,t) = f^{\frac{1}{2}}exp\{-\frac{f}{\sqrt{(gH)}}x - i\frac{\beta}{2\omega}X - i\frac{\omega}{\sqrt{(gH)}}y - i\omega t\}.$$

So we see that the cross-stream scale is that of the Rossby radius of deformation, R_d and the equatorward propogation speed is given by $c = \sqrt{(gH)}$. The amplitude of the Kelvin wave is proportional to $f^{\frac{1}{2}}$ which is a consequence of conservation of energy (Gill(1982)). The final term in the expression for h, represents a westward phase propogation of the Kelvin wave. By construction this Kelvin wave does not leak energy to the interior.

Now we have seen that the Kelvin wave appears in a natural form in the semigeostrophic dynamics, let us explore how the Rossby wave dynamics are influenced by the boundary condition.

6 Rossby wave reflection

In order to make the problem tractable, without appealing to WKB theory but retaining the same qualitative results, we consider a modified version of the semigeostrophic model; a basin where $R_d^2 = gH/f^2 = $ constant. Equation (14) becomes

$$\frac{\partial}{\partial t}\{h - R_d^2\nabla^2 h\} + J(h, R_d^2 f) = 0 \qquad (19)$$

and the boundary condition is unchanged (equation (13)).

It is important to note that the effect of making this assumption is to reverse the sign of 'beta'. We can think of this as a topographic effect. It does imply however that Rossby waves will now have an eastward phase propogation rather than westward.

Let us first consider a plane wave incident on a zonal boundary.

Incident wave : $\Re e A_I exp\{i(kx + l_i y - \omega t)\}$.

Reflected wave : $\Re e A_R exp\{i(kx + l_r y - \omega t)\}$.

and $l_r = -l_i$. Applying the boundary condition:

$$\frac{\partial}{\partial t}h_y = f_o h_x$$

we find that

$$A_R = A_I e^{i\phi}$$

where ϕ is given by

$$\phi = \tan^{-1}\left(\frac{2f_o k\omega l}{(\omega l)^2 - (f_o k)^2}\right).$$

So although the Rossby wave undergoes pure reflection from a zonal boundary (as the quasi-geostrophic result), it is subject to a phase-shift in amplitude.

Let us now consider a plane wave incident on a meridional boundary (in this case an eastern boundary).

Incident wave : $\Re e A_I exp\{i(k_i x + ly - \omega t)\}.$

Reflected wave : $\Re e A_R exp\{i(k_r x + ly - \omega t)\}.$

and $k_r = -k_i + \beta/\omega$. Applying the boundary condition:

$$\frac{\partial}{\partial t}h_x = fh_y$$

we find that there is a change in amplitude of the reflected wave:

$$|A_R|^2 = |A_I|^2\left\{\frac{[(\omega k)^2 + (fl)^2]}{[(\omega k - \beta)^2 + (fl)^2]}\right\}$$

where $k = k_i$, but unlike the quasi-geostrophic case this does not imply a change in energy.

7   Normal modes

Here we calculate the semigeostrophic normal modes. It is instructive to do this since any disturbance in the basin can be described as a linear superposition of the normal modes. The normal modes have been calculated for the quasi-geostrophic equations (Larichev (1974) , Flierl(1977)). How are the normal modes different from those calculated for quasi-geostrophy? Do we observe any coupling between the Kelvin wave and the Rossby wave?

Using the constant $R_d{}^2$ model we proceed in the manner of Larichev and Flierl and consider the normal modes in a circular basin of radius a.

If we substitute $h(x, y, t) = \phi(x, y)e^{i\frac{\beta x}{2\omega}}e^{-i\omega t}$ in equation (14), then we find

$$\nabla^2\phi + \left\{\frac{\beta^2}{4\omega^2} - \frac{1}{R_d{}^2}\right\}\phi = 0 \tag{20}$$

and the boundary condition

$$i\frac{\omega}{f}\frac{\partial}{\partial r}[\phi e^{i\frac{\beta x}{2\omega}}] = \frac{1}{r}\frac{\partial}{\partial\theta}[\phi e^{i\frac{\beta x}{2\omega}}] \tag{21}$$

on $r = a$.

The solution to equation (20) is given by

$\phi(r, \theta) = \sum_{n=-\infty}^{\infty}\{a_n J_n(kr) + b_n Y_n(kr)\}e^{in\theta}$

where

$$k^2 = \frac{\beta^2}{4\omega^2} - \frac{1}{R_d^2}.$$

Then we choose $b_n \equiv 0 \forall n$, since we want a solution which is bounded at $r = 0$.

Then the exact solution to the interior equation, is

$$\phi(r, \theta) = \sum_{n=-\infty}^{\infty} a_n J_n(kr) e^{in\theta}.$$

Substituting into the boundary condition, making the beta-plane approximation (ie, $f = f_o + \beta r \sin\theta$) and taking the Fourier integral (ie, $\int_0^{2\pi} e^{im\theta}$), the boundary condition becomes

$$
\frac{\omega}{f_o} \frac{\beta a}{4\omega} [\tilde{a}_{m+1} J_{m+1}(ka) + \tilde{a}_{m-1} J_{m-1}(ka)] + i\frac{\omega ka}{f_o} \tilde{a}_m J'_m(ka)
$$

$$
= \frac{\beta a}{4\omega} [\tilde{a}_{m+1} J_{m+1}(ka) - \tilde{a}_{m-1} J_{m-1}(ka)] + i\tilde{a}_m m J_m(ka)
$$

$$
-i\frac{\beta^2 a^2}{8\omega f_o} [\tilde{a}_{m+2} J_{m+2}(ka) - 2\tilde{a}_m J_m(ka) + \tilde{a}_{m-2} J_{m-2}(ka)]
$$

$$
+\frac{\beta a}{2 f_o} [\tilde{a}_{m+1} J_{m+1}(ka) - \tilde{a}_{m-1} J_{m-1}(ka)]. \tag{22}
$$

where $\tilde{a}_n = r_n a_n$, where $r_n = 2$ if $n = 0$ and $r_n = 1$ otherwise.

7.1 Rossby modes

Let us first consider the case $\omega/f_o \ll 1$. Then at leading order, (22) becomes

$$L\psi_m = 0$$

where ψ_m is defined

$$\psi_m = \frac{\beta a}{2\omega}(b_{m+1} + b_{m-1}) - 2mb_m \tag{23}$$

where $b_m = i^{-m}\tilde{a}_m J_m(ka)$
and L is the operator defined s.t.

$$\psi_m - i\frac{\beta a}{2 f_o}(\psi_{m-1} + \psi_{m+1}) = 0.$$

This has the solution

$$\psi_m = As_1^m + Bs_2^m$$

where

$$s_{1,2} = -i\frac{f_o}{\beta a} \pm \sqrt{\left(-\frac{f_o^2}{\beta^2 a^2} - 1\right)}.$$

$-132-$

Here we consider the special case, $A \equiv B \equiv 0$. The solution to equation (21), with $\psi_m = 0$, is

$$b_m = C J_m(\frac{\beta a}{2\omega}) + D Y_m(\frac{\beta a}{2\omega}).$$

For a bounded solution at $\beta a/2\omega = 0$ we set $D \equiv 0$. We consider the case, $J_m(ka) \neq 0 \forall m$. Then

$$\phi(r, \theta) = \sum_{n=-\infty}^{\infty} C i^n \frac{J_n(\frac{\beta a}{2\omega})}{r_n J_n(ka)} J_n(kr) e^{in\theta}.$$

Now we impose conservation of circulation, since at leading order the circulation balance is not closed,

$$i\omega \oint \{i\frac{\beta}{2\omega}cos\theta\phi + \frac{\partial \phi}{\partial r}\} e^{i\frac{\beta}{2\omega}x} dS = \frac{1}{a} \oint (f_o + \beta a sin\theta)\frac{\partial}{\partial \theta}\{\phi e^{i\frac{\beta}{2\omega}x}\} dS.$$

Integrating the right-hand side by parts, gives

$$\oint \{\frac{\beta}{2}acos\theta\phi + i\omega\frac{\partial \phi}{\partial r}\} e^{i\frac{\beta}{2\omega}acos\theta} dS = 0.$$

After some manipulation and using

$$\int_0^\pi e^{izcos\theta} cos n\theta d\theta = J_n(z)\pi e^{i\frac{\pi n}{2}},$$

we arrive at an eigenvalue relationship for ω

$$\sum_{m=-\infty}^{\infty} \frac{1}{r_n}\{\beta J_m(\frac{\beta a}{2\omega}) J_m'(\frac{\beta a}{2\omega}) + 2\omega k \frac{J_m^2(\frac{\beta a}{2\omega})}{J_m(ka)} J_m'(ka)\} = 0. \tag{24}$$

The result obtained by Larichev and Flierl for the quasi-geostrophic modes, consists of a sum over the second term in the equation only, since ϕ is a constant on the boundary in quasi-geostrophy. We see that the boundary condition in the semigeostrophic model may alter the eigenvalue of the mode but will not change the structure of this mode at leading order.

7.2 Kelvin mode

Now let us consider the asymptotic limit which corresponds to the Kelvin wave. Choose $m \gg 1, k \gg 1$ and $k^2 < 1$, which implies that the Rossby radius R_d is small, k is imaginary and $\beta a/\omega < 1$.

The boundary condition to leading order is:

$$\frac{\omega \hat{k} a}{f_o} J_m'(i\hat{k}a) = im J_m(i\hat{k}a).$$

where $\hat{k} = ik$.

Then using

$$J_m(z) = e^{i\frac{m\pi}{2}} I_n(ze^{-i\frac{\pi i}{2}}),$$

we find

$$\frac{\omega}{f_o} = \frac{m}{\hat{k}a}\frac{I_m(\hat{k}a)}{I'_m(\hat{k}a)}.$$

This is simply a Kelvin wave of wavenumber m. The mode is virtually stationary, since $\beta a/\omega \to 0$ (the westward propogation is small).

8   Discussion

The semigeostrophic model in a closed basin includes the dynamics of Kelvin waves in their natural form. This should be contrasted with the quasi-geostrophic approximation which merely parameterises the effect of Kelvin waves. The semigeostrophic model in a closed basin conserves energy and mass.

We examined the reflection of Rossby waves from boundaries and found that the boundary condition changed the nature of the reflection. The normal modes were calculated and contrasted with the quasi-geostrophic approximation. The modified (constant R_d^2) model shows that the boundary condition changes the eigenvalue of the Rossby modes as calculated in quasi-geostrophy. There is a stationary mode which represents the Kelvin mode. We did not find a mode which exhibited coupling between the Rossby wave and the Kelvin wave. In retrospect we may have anticipated this result. As shown by Grimshaw and Allen (1988), the critical frequency, above which waves remain trapped and below which waves propogate into the interior, is given by

$$\omega_{crit} = -\frac{\beta}{2}R_d.$$

Obviously in the constant R_d model the critical frequency is fixed and we will only observe either Kelvin waves or Rossby waves at a given frequency.

The semigeostrophic model provides a simple means of studying the interaction of the Kelvin wave and Rossby wave. It is only by understanding the process that we can interprete oceanographic data and numerical simulations.

References

[1] J. S. Allen, J. A. Barth, and P. A. Newberger. On intermediate models for barotropic continental shelf and slope flow fields. part i: formulation and comparison of exact solutions. *J. Phys. Oceanogr.*, 20:1017–1042, 1990.

[2] G. R. Flierl. Simple applications of mcwilliams's "a note on the consistent quasi-geostrophic model in a multiply connected domain". *Dyn. Atmos. Oceans*, 1:443–454, 1977.

[3] A. E. Gill. *Atmosphere-Ocean Dynamics*. Academic Press, 1982.

[4] R. Grimshaw and J. S. Allen. Low-frequency baroclinic motions off coastal boundaries. *J. Phys. Oceanogr.*, 18:1124–1143, 1988.

[5] B. J. Hoskins. The geostrophic momentum approximation and the semi-geostrophic approximation. *J. Atmos. Sci*, 32:233–242, 1975.

[6] V. D. Larichev. Statement of an internal boundary-value problem for the rossby-wave equation (registration of waves by coastal wave recorders). *Izv. Atmos. Ocean. Phys.*, 10:470–473, 1974.

[7] J. Pedlosky. *Geophysical Fluid Dynamics*. Springer-Verlag, 1987.

[8] R. Salmon. New equations for nearly geostrophic flow. *J. Fluid Mech.*, 153:461–477, 1985.

A Single Fourier-mode Model of Frontogenesis

Paul J. Dellar

Department of Applied Mathematics and Theoretical Physics,
University of Cambridge, Silver Street, Cambridge, CB3 9EW, UK

We investigate a simple model of atmospheric front formation based on a baroclinic instability of a rotating fluid layer with a horizontal temperature gradient. The growing instability produces steep horizontal gradients in the direction perpendicular to the original temperature gradient. We expect that such steep gradients will induce secondary baroclinic instabilities which tend to mix fluid across the front. Assuming the mixing can be represented by weak horizontal diffusion, we shall show that this is sufficient to halt the growth of the primary instability. The end result is a steady front characterised by a horizontal shear with vorticity comparable to the planetary vorticity. In the purely inviscid, diffusionless theory the primary instability grows indefinitely, with the vorticity becoming infinite within finite time. The work presented is based on a paper by Hoskins & Bretherton (1972) who studied the purely inviscid problem.

We consider a rotating layer of Boussinesq fluid confined between rigid horizontal boundaries at $z = 0, H$. We shall assume that the Coriolis parameter f is uniform, ignoring the Earth's sphericity entirely, and adopt Cartesian coordinates with the y-axis pointing North, and the x-axis pointing East. We assume the fluid to be initially stably stratified with a uniform temperature gradient in the vertical, and a linear variation of temperature in the y-direction. This is a simple model of a piece of northern hemisphere atmosphere, which is warmer in the south and cooler in the north. The rigid lid approximates the tropopause, the boundary between the lower troposphere and the overlying stratosphere. Being strongly stably stratified, the stratosphere resists vertical displacements of the tropopause.
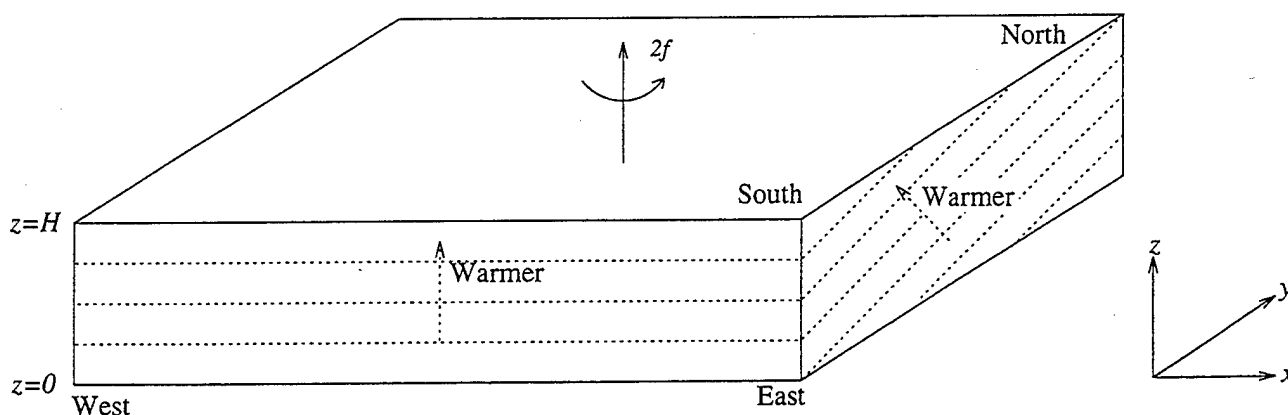
If we perturb this basic state by introducing a small horizontal shear in the y-velocity, the warm southerly wind ($v > 0$) and cold northerly wind ($v < 0$) will produce a horizontal temperature gradient in the eastward (x) direction. The eastward temperature gradient,

combined with the eastward geostrophic shear, produces a larger shear in the y-velocity in phase with the original perturbation. We shall refer to y as the along-front coordinate, and x as the cross-front coordinate.

Mathematical formulation

The governing equations for the problem described above, in the absence of viscosity and diffusion are

$$\theta = -(\frac{\theta_0}{g})s^2 y + \theta', \qquad \phi = -s^2 y(z - \tfrac{1}{2}H) + \phi' \qquad (1a,b)$$

$$\frac{Du}{Dt} - fv + \frac{\partial \phi}{\partial x} = 0 \qquad (2a)$$

$$\frac{Dv}{Dt} + fu + \frac{\partial \phi}{\partial y} = 0 \qquad (2b)$$

$$\frac{D\theta}{Dt} = 0, \qquad \nabla \cdot \mathbf{v} = 0, \qquad \theta' = \frac{\theta_0}{g}\frac{\partial \phi'}{\partial z} \qquad (2c,d,e)$$

Here u, v, w are the velocity components, θ and ϕ denote the (potential) temperature and geopotential, with the horizontal temperature gradient included explicitly. f is the Coriolis parameter (assumed constant) and s^2 is the imposed temperature gradient. We have used a pressure-based coordinate z instead of the physical height h, where z satisfied $\theta\,dz = \theta_0\,dh$. For an adiabatic atmosphere h and z are identical. Equation (2e) is the hydrostatic relation $\frac{\partial p}{\partial h} = -\rho g$ written in terms of z and the geopotential $\phi = gh$.

Following Hoskins & Bretherton we make two further simplifying assumptions.

(i) The along-front (y) lengthscale is much larger than the cross-front (x) lengthscale, so we may make a boundary-layer approximation and neglect the variation in y of θ', ϕ' and all other dependent variables except for the variation of θ and ϕ as stated explicity in (1).

(ii) Geostrophic balance is maintained in the cross-front (x) direction. Thus we may discard the cross-front acceleration term Du/Dt in (2a). This approximation, a form of the 'semigeostrophic approximation', is supported by three-dimensional numerical experiments (Williams, 1967) and the scaling arguments presented in Hoskins & Bretherton.

Having made these approximations, the equations (2) can be rewritten as conservation laws for the absolute momentum $M = fx + v$, temperature deviation θ', and potential vorticity q. Treating the $v\frac{\partial}{\partial y}$ part of the advection operator as a source term, we may write the conservation equations in terms of a two-dimensional advection operator $\mathcal{D}$ as

$$\mathcal{D}M = s^2(z - \tfrac{1}{2}H), \qquad \mathcal{D}\theta' = s^2 v, \qquad \mathcal{D}q = 0 \qquad (3a,b,c)$$

where

$$\mathcal{D} \equiv \frac{\partial}{\partial t} + u\frac{\partial}{\partial x} + w\frac{\partial}{\partial z}, \qquad M = fx + v, \qquad q \equiv \frac{\partial(M, \theta')}{\partial(x, z)} \qquad (4a,b,c)$$

These equations may be drastically simplified by introducing a 'geostrophic coordinate' X,

$$X = x + v/f, \qquad \frac{DX}{Dt} = u_g = -\frac{1}{f}\frac{\partial \phi}{\partial y} \qquad (5a,b)$$

Although M and X differ only by f, the Coriolis parameter, it is helpful to consider M always as a dependent variable, while X will be used as a new independent variable. ($5b$) shows that a fluid parcel with constant X moves with the geostrophic velocity u_g.

We now adopt X together with $Z = z$ and $T = t$ as new independent variables. The Jacobian of the coordinate transformation $(x, z, t) \to (X, Z, T)$ is

$$J = \frac{\partial X}{\partial x} = 1 + \frac{\partial v}{\partial x} = (1 - \frac{1}{f}\frac{\partial v}{\partial X})^{-1}. \qquad (6)$$

$J = \zeta/f$ is also the vertical component of the dimensionless absolute vorticity (where $\zeta = f + \partial v/\partial x$). Thus the transformation remains invertible provided the absolute vorticity remains finite. We shall see later that J also denotes the tilt of the initially horizontal isotherms in the xz plane.

We may retain the form of the geostrophic and hydrostatic balances $(2a, e)$ in the new coordinates by defining a modified geopotential Φ',

$$\Phi' = \phi' + \frac{1}{2}v^2, \qquad fv = \phi'_x = \Phi'_X, \qquad \theta' = (\frac{\theta_0}{g})\phi'_z = (\frac{\theta_0}{g})\Phi'_z. \qquad (7a,b,c)$$

The advection operator in (X, Z, T) coordinates becomes

$$\mathcal{D} \equiv \frac{\partial}{\partial T} + \frac{s^2}{f}(Z - H/2)\frac{\partial}{\partial X} + w\frac{\partial}{\partial Z}, \qquad (8)$$

which is now linear on horizontal boundaries (where $w = 0$). The conservation equation ($3a$) is now satisfied identically, and ($3b, c$) become

$$(\frac{\partial}{\partial T} + \frac{s^2}{f}(Z - \tfrac{1}{2}H)\frac{\partial}{\partial X} + w\frac{\partial}{\partial Z})\Phi'_z = \frac{s^2}{f}\Phi'_X \qquad (9)$$

and

$$q \equiv f\frac{\theta_0}{g}\frac{\Phi'_{ZZ}}{1 - f^{-2}\Phi'_{XX}} = N^2 f\frac{\theta_0}{g} \qquad (10)$$

We have made use of the fact that the potential vorticity retains its original value $q = N^2 f\theta_0/g$ from the initial state of uniform stratification and no motion in the along-front direction. N^2 is the Brunt Väisälä or buoyancy frequency of the initial stratification.

We may rearrange (9) into the more familiar form

$$\Phi'_{XX} + \frac{f^2}{N^2}\Phi'_{ZZ} = f^2. \qquad (11)$$

This elliptic equation (11) has a unique solution for suitable boundary conditions. In particular, specifying $\theta' = (\theta_0/g)\Phi'_Z$ on the upper and lower boundaries is sufficient to determine Φ' uniquely in the interior. This is just an example of a far more general result, namely that the temperature and velocity distribution everywhere in a fluid can be determined from the potential vorticity distribution in the interior, and the temperature distribution on the boundaries by a process called potential vorticity inversion. In conclusion we need only apply (9) on the upper and lower boundaries to determine the time evolution of the whole fluid. In addition, the theory of potential vorticity inversion tells us that any singularities must form initially on the boundaries.

The effects of diffusion

At this point we depart from the formulation presented in Hoskins & Bretherton in order to incorporate diffusion. We replace the temperature equation on the boundaries by

$$\mathcal{D}\theta' = s^2 v + \kappa\theta'_{xx} \qquad (z = 0, H) \qquad (12)$$

and insist that the potential vorticity remains conserved. In specifying diffusion only on the boundaries in (12) we are not saying that diffusion does not take place in the interior, but merely that the form of the diffusion in the interior need not be specified explicitly. We have already established (in the previous discussion about potential vorticity inversion) that the time evolution of the whole fluid can be determined solely from the boundaries, so it is sufficient to specify the effect of diffusion solely on the boundaries. Furthermore we have already assumed that the x (cross-front) lengthscale is the smallest, so it is consistent to include only θ'_{xx} in (12). In geostrophic coordinates (12) becomes

$$\left(\frac{\partial}{\partial T} + \frac{s^2}{f}\left(Z - \frac{H}{2}\right)\frac{\partial}{\partial X}\right)\Phi'_Z = \frac{s^2}{f}\Phi'_X + \kappa J\frac{\partial}{\partial X}(J\Phi'_{ZX}) \qquad (Z = 0, H) \qquad (13)$$

where we have used the condition $w = 0$ on the boundaries to remove the nonlinear $w\partial_Z$ term from the advection operator. In Hoskins & Bretherton's formulation, where $\kappa = 0$, (13) is a purely linear equation whose exact solutions are the Eady waves of inviscid theory. Without diffusion the Eady waves can grow indefinitely in geostrophic coordinates, but the coordinate transformation back to physical space $x = X - f^{-2}\Phi'_{XX}$ will become multi-valued after a finite time. As the horizontal lengthscales remain $O(1)$ in geostrophic coordinates, the diffusion term becomes significant only when the Jacobian J becomes large, corresponding to a near singularity in the reverse coordinate transformation.

Dimensionless equations

By rescaling the coordinates X, Z, T and Φ' we may eliminate the parameters f, N, H, s from (6),(11) and (13) to obtain a generic system of three equations.

$$\tilde{\Phi}'_{\tilde{X}\tilde{X}} + \tilde{\Phi}'_{\tilde{Z}\tilde{Z}} = \tfrac{1}{4} \qquad (14a)$$

$$(\partial_{\tilde{T}} + \tilde{Z}\partial_{\tilde{X}})\tilde{\Phi}'_{\tilde{Z}} = \tilde{\Phi}'_{\tilde{X}} + \epsilon(J^2\tilde{\Phi}'_{\tilde{Z}\tilde{X}\tilde{X}} + 4J^3\tilde{\Phi}'_{\tilde{X}\tilde{Z}}\tilde{\Phi}'_{\tilde{X}\tilde{X}\tilde{X}}) \qquad (\tilde{Z} = \pm 1) \qquad (14b)$$

$$J = (1 - 4\tilde{\Phi}'_{\tilde{X}\tilde{X}})^{-1} = (4\tilde{\Phi}'_{\tilde{Z}\tilde{Z}})^{-1} \qquad (14c)$$

$$\tilde{Z} = \frac{2}{H}Z - 1, \quad \tilde{X} = \frac{2f}{NH}X, \quad \tilde{T} = \frac{s^2}{N}T, \quad \tilde{\Phi}' = \frac{\Phi'}{(NH)^2}, \quad \epsilon = \frac{4f^2\kappa}{s^2NH^2} \qquad (15)$$

The elliptic equation (14a) holds in the interior of the fluid at each instant. The time evolution is determined by (14b) which holds only on the horizontal boundaries $\tilde{Z} = \pm 1$. The symmetric upper and lower boundary conditions admit solutions to (14a, b, c) which are invariant under coordinate inversion ($\tilde{Z} \to -\tilde{Z}, \tilde{X} \to -\tilde{X}$). We consider periodic solutions of (14a) satisfying this symmetry,

$$\tilde{\Phi}' = \frac{1}{8}\tilde{Z}^2 + \sum_{n=1}^{N} a_n(\tilde{T})\cosh(n\beta\tilde{Z})\cos(n\beta\tilde{X}) + b_n(\tilde{T})\sinh(n\beta\tilde{Z})\sin(n\beta\tilde{X}) \qquad (16)$$

where we choose β to be the wavenumber of the fastest growing Eady wave in the inviscid theory ($\epsilon = 0$) (see next section). We emphasise that (16) describes an exact solution of the inviscid equations for any N.

A single Fourier mode model

As the simplest possible model we consider a solution in the form (16) for $N = 1$. We obtain two coupled ordinary differential equations for $a(\tilde{T})$ and $b(\tilde{T})$ by substituting into (14b, c) and projecting the nonlinear right hand side of (14b) onto the two Fourier components. We include two terms because the choice of symmetry in (16), and the differing vertical structure of the two components, determine a preferred phase for the Eady wave. The projection integrals can be performed analytically, yielding the coupled equations

$$\frac{da}{dt} = (1 - \beta\coth\beta)b - \frac{\epsilon\beta^2}{(1-R^2)^{3/2}}a, \qquad \frac{db}{dt} = (\beta\tanh\beta - 1)a - \frac{\epsilon\beta^2}{(1-R^2)^{3/2}}b, \quad (17)$$

where $R = 4\beta^2\sqrt{a^2\cosh^2\beta + b^2\sinh^2\beta}$, so that $4\tilde{\Phi}'_{\tilde{X}\tilde{X}} = R\cos(\beta(\tilde{X} + \tilde{X}_0))$. The linear eigensolutions to (17) when $\epsilon = 0$ are $(a_0, b_0)e^{\sigma t}$ where

$$a_0 = \mp\sqrt{\frac{\beta\coth\beta - 1}{1 - \beta\tanh\beta}}b_0, \qquad \sigma = \pm\sqrt{(\beta\coth\beta - 1)(1 - \beta\tanh\beta)}. \qquad (18)$$

In what follows we choose $\beta = 0.8031$ to give the maximum growth rate $\sigma = 0.3098$. The results of integrating (17) numerically are shown in the figure overleaf. Solutions for arbitrary initial conditions are rapidly attracted to the growing linear eigensolution, whose ratio a/b is preserved in the nonlinear regime. Thus we may consider the single equation

$$\frac{dR}{dt} = \sigma R - (\epsilon\beta^2)\frac{R}{(1-R^2)^{3/2}}, \qquad (19)$$

which can be tackled by matched asymptotics as described in the appendix. The figure below shows plots of $b(T)$ for various diffusivities ϵ. For the moment, we need only note the final steady solution,

$$R^2 = 1 - \left(\frac{\epsilon\beta^2}{\sigma}\right)^{2/3}. \qquad (20)$$

Growth of b(T) for different values of epsilon
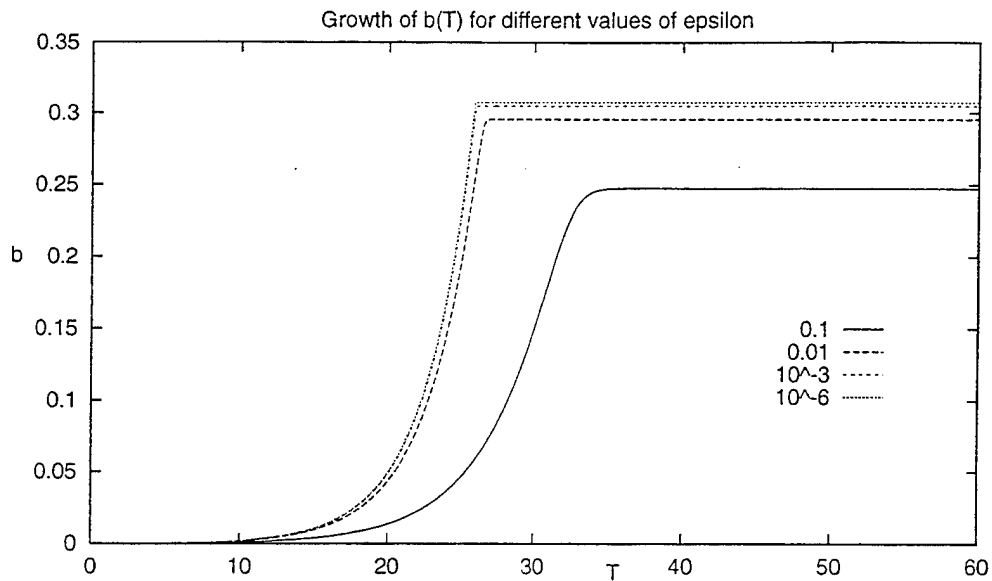
Plotting the final steady states in physical space, using the transformation $\tilde{x} = \tilde{X} - 4\tilde{\Phi}'_{\tilde{X}}$ shows a respectable front forming even in this simple model (see figures below). The limiting shape of the front as the diffusivity becomes small is constrained by the assumed sinusoidal form of the solution in geostrophic coordinates. This limits the range of geostrophic space in which the Jacobian can be large. We expect that including more Fourier modes would produce yet steeper fronts.

theta(x,z=0) for single-mode solutions

v(x,z=0) for single-mode solutions
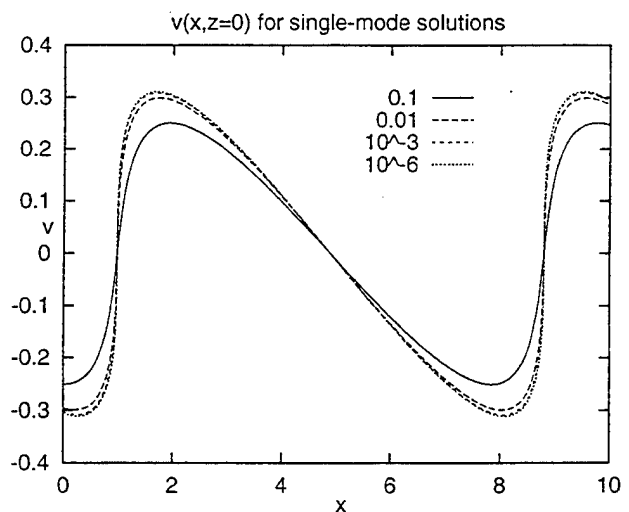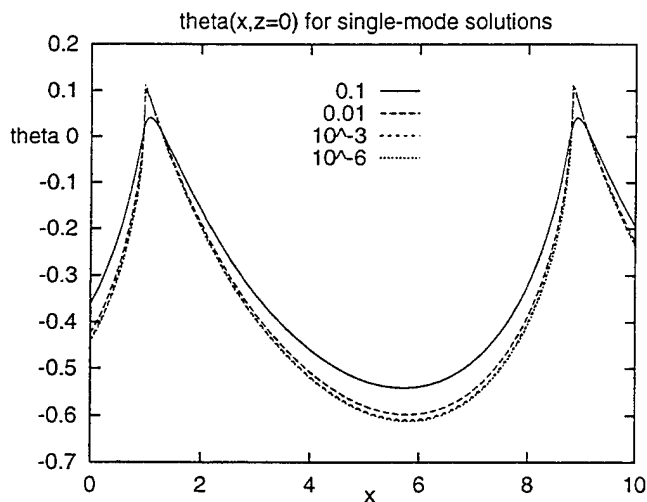
Models with more modes

For solutions comprising more Fourier modes the projection integrals have to be computed numerically. The diffusion terms become sharply peaked in the region of geostrophic coordinates corresponding to the front. We tried using an adaptive integration routine to calculate the integrals at each timestep but it proved prohibitively slow for more than four modes. A standard pseudo-spectral method also proved useless, because the nonlinear term involves division and so formally requires infinite padding to remove aliasing errors.

Instead, we adopted what might be described as a 'backwards pseudo-spectral' algorithm. The important difference is that the nonlinear terms are calculated directly on a grid, and the solution is timestepped on the same grid. Fast Fourier transforms are only used to compute the linear terms, by projecting the gridded data on the lower boundary onto the general Fourier series solution (18) and solving for a_n and b_n. The difference is that the total solution remains reasonably well behaved, so in practice it can be fast Fourier transformed more easily than the diffusion terms alone.

Final steady states for 1,2,4 and 16 modes, plotting v(x,z=0)
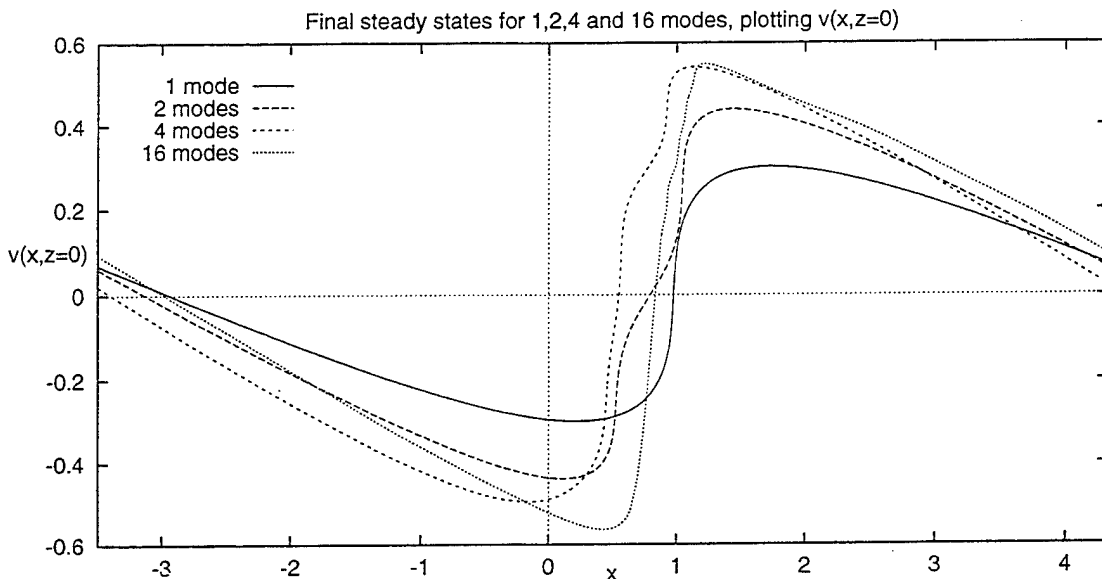
As expected, the front becomes steeper as more modes are included. Below we show the growth of a 4 mode front in physical space, plotting the shear on the lower boundary as a function of both x and time. Notice the regions of strong shear (near vertical gradients) which develop.

Growth of along-front shear for a 4 mode solution
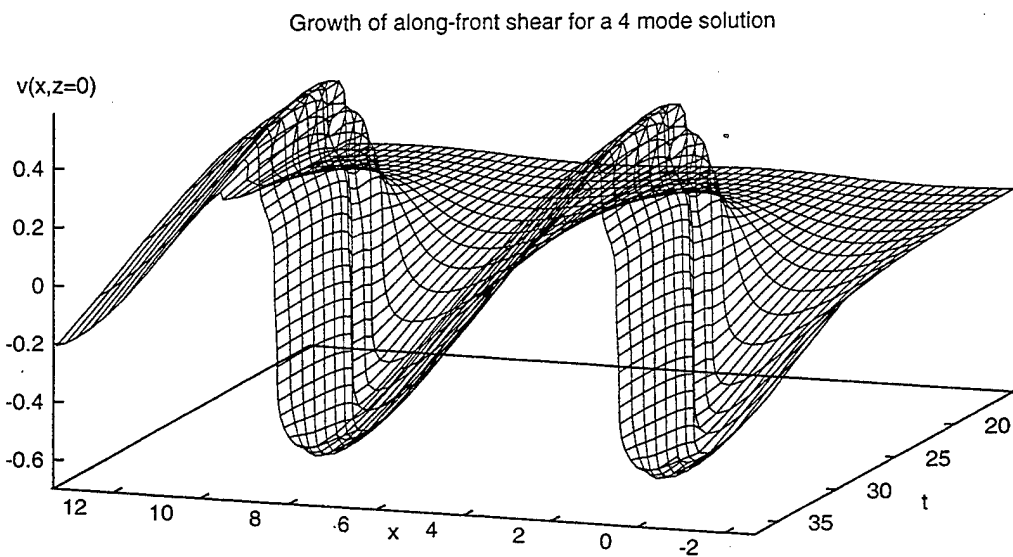
More pictures, including streamfunctions of typical solutions, are presented in Hoskins & Bretherton.

The spectrum of a front

When the fronts seen in the above solutions becomes steep, a substantial fraction of geostrophic space is compressed into a small region of physical space. To study the growth of small horizontal lengthscales we consider the evolution of the Fourier series $\hat{v}(n)$ of the along-front shear $v(x, z = 0)$.

Time-evolution of the spectrum $\hat{v}(n)$ for a single-mode solution
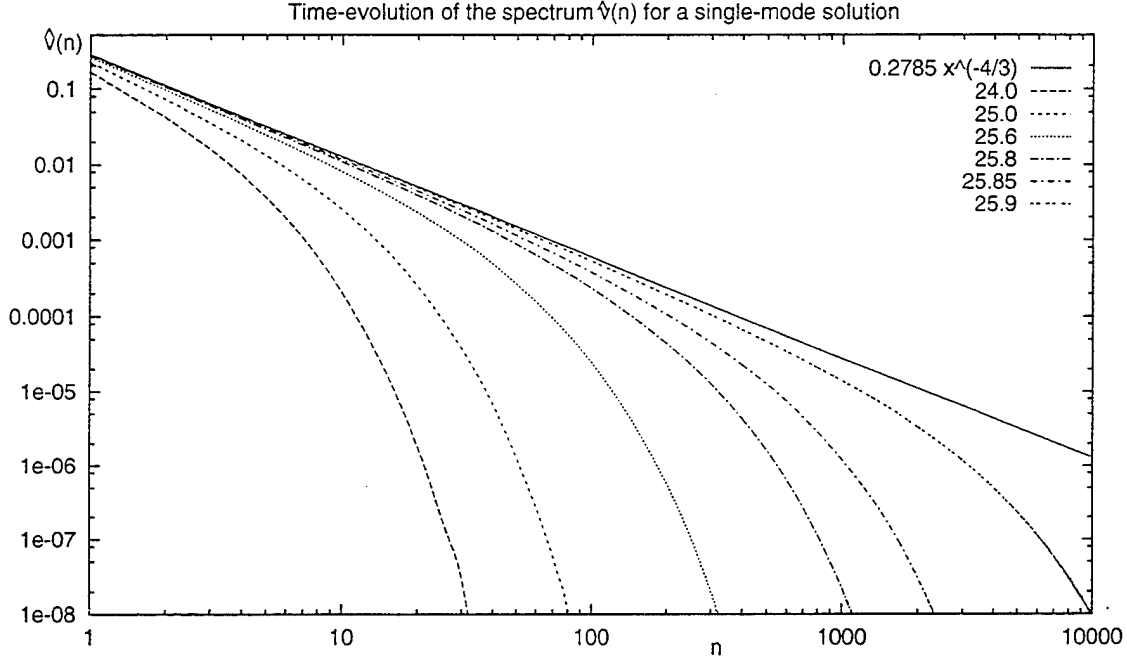
We find $\hat{v}(n) \sim n^{-4/3}$ in an 'inertial range' which extends as the front steepens, being limited eventually by diffusion. For the simple solutions comprising single Fourier modes in geostrophic space we may calculate the spectrum analytically. In dimensionless variables,

$$\hat{v}(n) = \frac{\beta}{\pi} \int_0^{\frac{2\pi}{\beta}} \tilde{v}(\tilde{x})\, e^{in\beta\tilde{x}}\, d\tilde{x} = \frac{\beta}{\pi} \int_0^{\frac{2\pi}{\beta}} \tilde{\Phi}'_{\tilde{X}}\, e^{in\beta(\tilde{X} - 4\tilde{\Phi}'_{\tilde{X}})} \left(1 - 4\tilde{\Phi}'_{\tilde{X}\tilde{X}}\right) d\tilde{X}$$

$$= \frac{i}{n\pi} \int_0^{\frac{2\pi}{\beta}} \tilde{\Phi}'_{\tilde{X}\tilde{X}}\, e^{in\beta F(\tilde{X})}\, d\tilde{X} \qquad \text{where } \tilde{x} = F(\tilde{X}) = \tilde{X} - 4\tilde{\Phi}'_{\tilde{X}}. \qquad (21)$$

Following the method of stationary phase, the dominant contributions for large n come from the region where F' is smallest. This is precisely where the Jacobian $J = (F')^{-1}$ is largest, the front is steepest and the lengthscales are shortest. Expanding around this point ($\tilde{X}_0$ in geostrophic space)

$$F(\tilde{X}) \approx (1 - R)(\tilde{X} - \tilde{X}_0) + \frac{1}{6} R\beta^2 (\tilde{X} - \tilde{X}_0)^3,$$

$$\hat{v}(n) \sim \frac{iR}{4n\pi} \int_{-\tilde{X}_0}^{\frac{2\pi}{\beta} - \tilde{X}_0} e^{in\beta\left((1-R)\tilde{Y} + \frac{1}{6}R\beta^2\tilde{Y}^3\right)} d\tilde{Y} \qquad \text{where } \tilde{Y} = \tilde{X} - \tilde{X}_0. \qquad (22)$$

If we may neglect the $(1 - R)\tilde{Y}$ term, because $1 - R$ is $O(\epsilon^{2/3})$ when the front is fully developed, then the integral can be evaluated as

$$\hat{v}(n) \sim \frac{1}{4\pi} \cos \frac{2\pi}{3} \frac{2}{3} \Gamma(\tfrac{1}{3}) 6^{1/3} \frac{R}{\beta} n^{-4/3} = 0.2785 n^{-4/3}, \tag{23}$$

which is the asymptote plotted in the diagram. The diffusive cutoff occurs when $n \sim (1 - R)^{-2/3} \sim \epsilon^{-4/3}$ and the two terms in the exponent become the same order.

We may also obtain the $n^{-4/3}$ scaling by a dimensional argument. In terms of the two-dimensional advection operator $\mathcal{D}$, conservation of semigeostrophic energy takes the form

$$\mathcal{D}E = -\tfrac{1}{2} s^2 H v, \quad \text{where} \quad E = \tfrac{1}{2}(u_g^2 + v^2) - \frac{g}{\theta_0} z\theta. \tag{24}$$

where the kinetic energy is calculated from the geostrophic velocities $u_g = (s^2/f)(z - \tfrac{1}{2}H)$ and $v_g = v$. u_g has no short scales so we ignore it in the following analysis. We observe that the energy flux into a plane $y = cst$ is the rate of advection of the along-front potential energy (temperature) gradient, which is proportional to the along-front velocity v. The total energy flux scales as $\mathcal{E} = s^2 N H^2$ since $v = 2N H \tilde{\Phi}'_{\tilde{X}}$ in dimensional variables. If we assume that the Fourier coefficients $\hat{v}(k_n)$ depend only on $\mathcal{E}$ and the wavenumber k_n then the only possibility is

$$\hat{v}(k_n) \sim \mathcal{E}^{1/3} k_n^{-4/3}. \tag{25}$$

The energy spectrum $E(k)$ is conventionally defined so that the average kinetic energy $\tfrac{1}{2} < v^2 > = \int_0^\infty E(k)\, dk$. The velocities are all independent of the along-front coordinate y so the k_y dependence of their Fourier transforms is simply $2\pi\delta(k_y)$. Using Parseval's theorem, $\tfrac{1}{2} < v^2 > = \frac{1}{4\pi^2} \int |\hat{v}^2|\, dk_x\, dk_z \sim \int (\mathcal{E}^{1/3} k^{-4/3})^2 k\, dk$ if we assume $dk_x\, dk_z \to k\, dk$. Thus we obtain a Kolmogorov-type result

$$E(k) \sim 6.17 \times 10^{-3}\, \mathcal{E}^{2/3} k^{-5/3}. \tag{26}$$

The 'universal' constant is much smaller than the usual estimates (between 1 and 1.5). This is presumably because the front is confined to a small region in physical space. For solutions with N modes it appears that the constant is proportional to $\sqrt{N}$ (see figure below) presumably because for moderate N the various regions in which a particular scale is present contribute independently. The total spectrum is thus the modulus of a sum of random phases, which scales with $\sqrt{N}$ like the variance of the random phases. We would expect the constant to tend to a finite limit, hopefully around 1, for large N.

Spectra of final steady states for 1, 2 & 4 modes (scaled by N^(1/2))
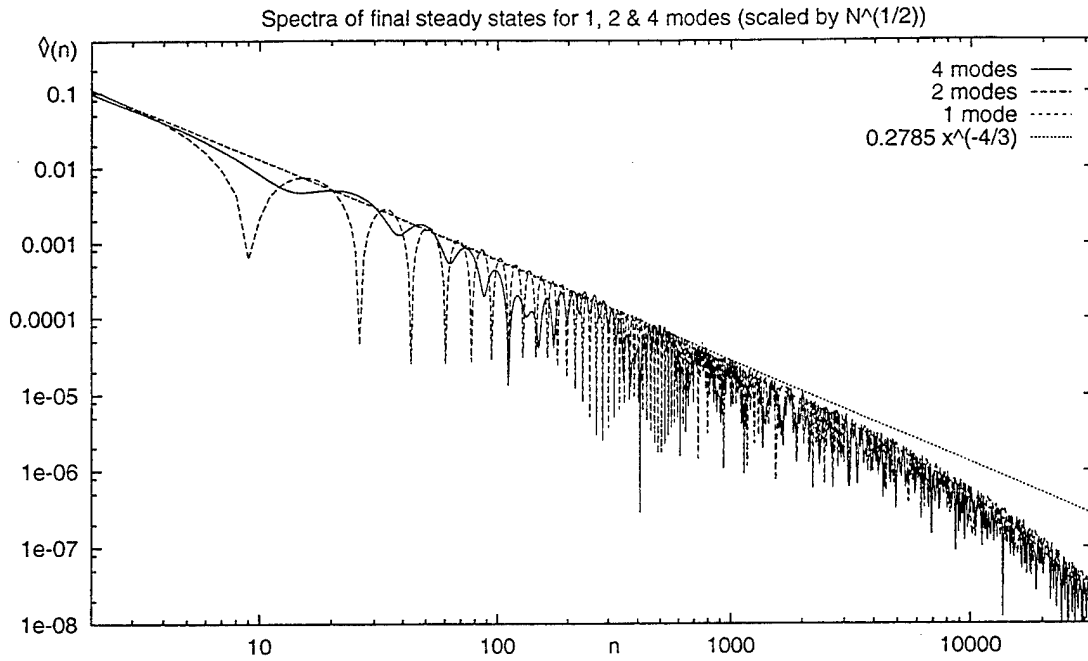
Some thoughts on interior diffusion

We have assumed that

$$\mathcal{D}\theta = s^2 v + G(x,z,t), \qquad \mathcal{D}M = s^2(z - \tfrac{1}{2}H) + H(x,z,t) \qquad (27a,b)$$

and imposed $G = \epsilon\theta_{xx}$, $H = 0$ on horizontal boundaries. The plots overleaf show G for a 4-mode solution, before and after it has reached its equilibrium steady state. Notice how diffusive effects are concentrated in narrows regions, which shrink as the front steepens. The condition for potential vorticity conservation in the presence of diffusion is

$$0 = \mathcal{D}q = \mathcal{D}\mathcal{J}(M,\theta) = \mathcal{J}(\mathcal{D}M,\theta) + \mathcal{J}(M,\mathcal{D}\theta) = \mathcal{J}(H,\theta) + \mathcal{J}(M,G) \qquad (28)$$

where $\mathcal{J}(f,g) = \frac{\partial(f,g)}{\partial(x,z)}$. If we adopt M,θ as independent variables, following more advanced forms of the semigeostrophic formalism, we conclude from (28) that 'diffusion is incompressible', in other words

$$\frac{\partial G}{\partial \theta} + \frac{\partial H}{\partial M} = 0 \qquad (29)$$

However, G is not a function of M alone, since G is localised near the horizontal boundaries. Thus diffusion of potential temperature, together with conservation of potential vorticity, induces diffusion of momentum. Finally, there exists a 'diffusion streamfunction' $\chi(M,\theta)$ such that

$$G = \chi_M, \qquad H = -\chi_\theta. \qquad (30)$$

The conditions which such a 'streamfunction' must satisfy remain mysterious. The apparently non-local nature of the diffusion is characteristic of a balanced model such as semigeostrophic theory.

G(x,z,t=28) for a 4 mode solution

G(x,z,t=35) for a 4 mode solution
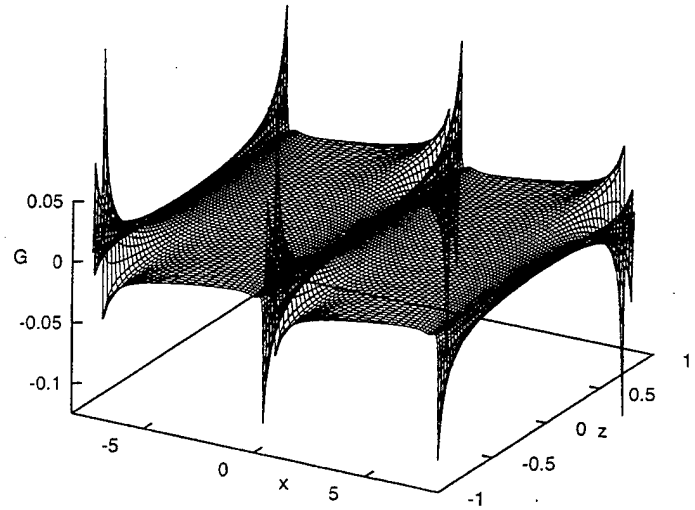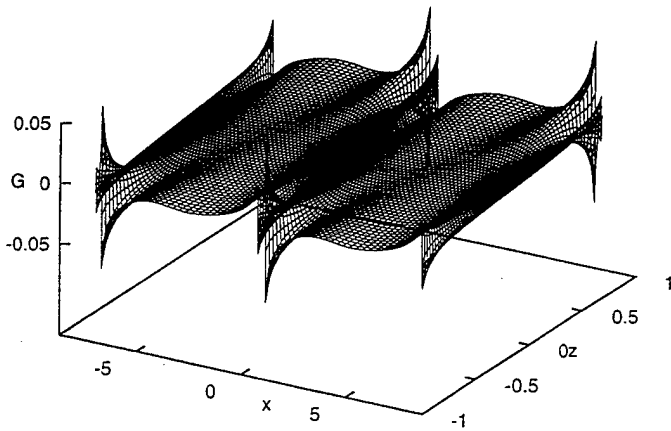
Conclusions

We have established that a simple baroclinic instability can be regularised by the inclusion of weak horizontal diffusion. In particular, realistic looking steady fronts can be constructed from simple low-order models using the semi-geostrophic formalism. We have shown that the need to conserve potential vorticity imposes a consistency requirement on the diffusion of temperature and momentum, to the extent that only the form of diffusion on the boundaries can be specified independently. As an added bonus, these simple models exhibit intriguing similarities to the properties of fully three-dimensional turbulent flows.

Acknowledgements

References

HOSKINS, B.J. & BRETHERTON, F.P., *Atmospheric frontogenesis models, mathematical formulation and solution*, 1972, J. Atmos Sci., **29** pp 11-37

WILLIAMS, R.T., *Atmospheric frontogenesis, a numerical experiment*, 1967, J. Atmos Sci., **24** pp 627-641

UNSTABLE CONVECTIVE MODES IN A 2-LAYER SYSTEM

Oleg E. Esenkov

1   Introduction.

Convective instability of a layer of fluid with positive density gradient located between horizontal boundaries is considered a classical problem. In this work we use nonhydrostatic Boussinesq Navier–Stokes equations with linear friction and cooling instead of diffusion and viscosity, which sets the problem apart from more conventional approaches. We shall try to answer the question of how addition of a convectively stable layer can change dynamics of the unstable region. The problem is important because a situation where an unstable layer, bordered on one or both sides by stable layers, occurs is not uncommon in many physical systems. Thus, in oceanography, under favorable wind conditions, Ekman transport brings colder, denser waters above the convectively stable layer (Figure 1). In A-class stars convectively unstable ionization zones are bounded by layers with stable temperature gradients.

Two illustrative experiments can be mentioned (Veronis, 1963). In the first, a layer of water with temperatures of $0°C$ and $> 4°C$ at the lower and upper boundaries, respectively has a constant static state temperature gradient. Thus, the fluid below the $4°C$ level is gravitationally unstable, while the fluid above is stable. Convection in the lower region penetrates into the fluid above.

The second is an experiment with a layer of air whose horizontal boundaries are maintained at uniform temperatures, which are steadily increased or decreased with time. The interior air temperature lags behind the boundary value due to the finite conductivity of gas, and two layers — one convectively unstable and one stable — are formed.

The problem described above was studied extensively and stability criteria were derived for different system configurations and density distributions. Thus, in their early analysis Gribov and Gurevich (1957) considered a piecewise-linear density profile with semi-infinite statically stable regions above and below the central layer. They showed that when density gradients in these stable layers are equal and tend to zero, both the minimum Rayleigh number and the horizontal wavenumber (α_m) of the neutral disturbance corresponding to it tend to zero and that the depth of penetration of the convective rolls is inversely proportional to α_m and therefore increases without bound.

Another case of a piecewise-linear density profile was studied by Souffrin and Spiegel: a finite in vertical system consisting of two layers with subadiabatic temperature gradient above a superadiabatic gradient. They derived conditions for instability and showed that overstability occurs when conductivity in a layer differs from that in the other one.

What happens if the density variation is periodic in vertical? This question arises in the theory of sedimentation waves in dispersions of small particles. Batchelor and Nitsche (1991) studied a sinusoidal density variation with height among other density distributions and showed that the fluid is unstable to small disturbances with large horizontal

wavelength.

In all of the aforementioned studies only linear cases are considered. We shall try to answer the question of how the nonlinear terms can change behavior of the system in this work.

2 Unstable Convective Modes.

2.1 Linear Problem: Governing Equations.

We consider a situation when a layer with positive density gradient lies above a convectively stable layer (Figure 1). Motions in each layer can be described by Boussinesq nonhydrostatic Navier-Stokes equations:

$$\frac{du}{dt} - fv = -p_x - \epsilon u \tag{1}$$

$$\frac{dv}{dt} + fu = -p_y - \epsilon v \tag{2}$$

$$\frac{dw}{dt} = -p_z + \theta - \lambda w \tag{3}$$

$$u_x + v_y + w_z = 0 \tag{4}$$

$$\theta_t + (u \cdot \nabla)\theta + wN^2 = -\mu\theta, \tag{5}$$

where u, v, w are velocity components in a layer, θ is the temperature perturbation, p is pressure, ϵ and λ are horizontal and vertical drag coefficients, respectively, μ is a Newtonian cooling coefficient and N is a Brunt-Väisälä frequency. Subscripts 1 and 2 will always refer to the upper and lower layers, respectively.

In our model ϵ, λ and μ are nonzero in the upper layer, and $N_1^2 = -\frac{g}{\rho_m}\frac{d\rho}{dz} = -M^2 < 0$. In the lower layer $N_2^2 = N^2 > 0$, $\epsilon_2 = \lambda_2 = \mu_2 = 0$.

Linearization of (1–5) about the basic state of no flow and with stratification shown in Figure 1 leads to:

$$u_t - fv = -p_x - \epsilon u \tag{6}$$

$$v_t + fu = -p_y - \epsilon v \tag{7}$$

$$w_t = -p_z + \theta - \lambda w \tag{8}$$

$$u_x + v_y + w_z = 0 \tag{9}$$

$$\theta_t + wN^2 = -\mu\theta, \tag{10}$$

We are looking for a solution of the form:

$$(u, v, w, p, \theta) = (U, V, W, P, \Theta)\exp[st + i(kx + ly)], \tag{11}$$

where U, V, W, P, Θ are all functions of z. After substituting these expressions in (6–10) and eliminating U, V, P and Θ, we obtain an equation for W in layer i, where $i = 1, 2$:

$$W_i'' = R_i W_i, \tag{12}$$

with

$$R_1 = \frac{s + \epsilon}{s + \mu} \left(\frac{(s + \lambda)(s + \mu) - M^2}{f^2 + (s + \epsilon)^2} \right) K^2, \tag{13}$$

$$R_2 = \frac{s^2 + N^2}{s^2 + f^2} K^2. \tag{14}$$

Boundary conditions for a system with two layers will be discussed in section 2.4.

2.2 One Layer: Linear Theory.

We consider a one-layer case first, *i. e.* only the upper layer in Figure 1 is present, which is bounded by horizontal planes. Vertical velocity in the layer is governed by (12–13) with boundary conditions $W(z = 0) = W(z = 1) = 0$.

When s is real, existence of a non-zero solution requires

$$(s + \lambda)(s + \mu) - M^2 < 0, \tag{15}$$

so that when the left-hand side of (15) is zero

$$s_{1,2} = -(\lambda + \mu)/2 \pm \left((\lambda + \mu)^2 - 4\lambda\mu + 4M^2 \right)^{1/2} /2, \tag{16}$$

and to have growing modes we must satisfy condition for instability

$$M^2 > \lambda\mu, \tag{17}$$

which is essentially the requirement for the 'free-fall' time to be shorter than damping time.

The solution to our problem is:

$$W = a \sin(\alpha z), \alpha = \pi n \tag{18}$$

Substitution of (18) into (12) after use of (13) gives:

$$\frac{s + \epsilon}{s + \mu} \left(\frac{(s + \lambda)(s + \mu) - M^2}{f^2 + (s + \epsilon)^2} \right) K^2 = -n^2\pi^2, \tag{19}$$

what may be written as

$$a_3 s^3 + a_2 s^2 + a_1 s + a_0 = 0, \tag{20}$$

where

$$a_3 = 1 + n^2\pi^2/K^2, \tag{21}$$

$$a_2 = \epsilon + \lambda + \mu + n^2\pi^2(\mu + 2\epsilon)/K^2, \tag{22}$$

$$a_1 = \epsilon(\mu + \lambda) + \mu\lambda - M^2 + n^2\pi^2(2\epsilon\mu + f^2 + \epsilon^2)/K^2, \tag{23}$$

$$a_0 = \epsilon(\mu\lambda - M^2) + n^2\pi^2\mu(f^2 + \epsilon^2)/K^2. \tag{24}$$

2.2.1 Direct Instability.

At the onset of direct instability $s = 0$, hence $a_0 = 0$ from (20) and using (24), we obtain:

$$K_c^2 = \frac{n^2\pi^2(f^2 + \epsilon^2)}{\epsilon(M^2 - \lambda\mu)}, \tag{25}$$

where K_c^2 is a critical wavenumber. Near K_c^2: $a_1 s + a_0 \approx 0$. Expanding a_0 about K_c^2 we can get an estimate for the growth rate:

$$s = -\frac{\partial a_0(K_c^2)}{\partial K^2}(K^2 - K_c^2)/a_1(K_c^2). \tag{26}$$

We can show that $a_1(K_c^2) > 0$ and $\frac{\partial a_0(K_c^2)}{\partial K^2} = -n^2\pi^2\mu(f^2 + \epsilon^2)/K_c^4 < 0$, so s grows with K^2 near K_c^2. Our numerical results show that it continues growing for larger values of $K^2 - K_c^2$. Thus, the result is the ultraviolet catastrophe: the most unstable mode is that with the shortest wavelength. This is unphysical, typically signifies strongly unstable situations, and is not suited to nonlinear analysis (section 2.3). To avoid the UV catastrophe, we can try different parameterizations of friction and temperature diffusion.

Replacing μ by μK^2 leads to

$$K_c^2 = (M^2 - n^2\pi^2\mu(f^2 + \epsilon^2)/\epsilon)/\mu\lambda \tag{27}$$

$$\frac{\partial a_0(K_c^2)}{\partial K^2} = \epsilon\mu\lambda > 0, \tag{28}$$

and $s \propto -(K^2 - K_c^2)$, as desired. Other cases (redefining ϵ or λ) still give growth of s with K^2. Using $\mu = \tilde{\mu}K^2 + \mu_0$ gives a similar result, and as we shall see in Section 2.3.1, this representation of temperature diffusion and cooling is preferential for the problem we are solving.

Note that the largest K_c^2 occurs when $n = 1$. When $M^2 - n^2\pi^2\mu(f^2 + \epsilon^2)/\epsilon \to 0$, $K_c^2 \to 0$.

Expansion of (21–24) near $K^2 = 0$ leads to an expression:

$$(f^2 + \epsilon^2)s \sim -a_0 K^2, \tag{29}$$

so that $s \sim O(K^4)$ for small K^2. This sets the stage for a long-wave theory.

2.2.2 Overstability.

Now let us investigate the onset of overstability: substituting $s = i\omega$ in (20) gives:

$$-ia_3\omega^3 - a_2\omega^2 + ia_1\omega + a_0 = 0. \tag{30}$$

Taking real and imaginary parts of the expression above, we can show that $a_3 a_0 = a_1 a_2$. Use of (21–24) gives a rather complicated expression; however, when $\epsilon = 0$ we can get a condition for the onset of overstability:

$$M_c^2 = \mu\lambda + n^2\pi^2 f^2\lambda/K^2[\mu(1 + n^2\pi^2/K^2) + \lambda]. \tag{31}$$

Another interesting case is when two of the roots coalesce. We can rewrite our polynomial in the form:

$$a_3(s - s_1)(s - s_2)(s - s_3) = a_3 s^3 + a_2 s^2 + a_1 s + a_0 \tag{32}$$

When $s_1 = s_2$, it is easy to show that

$$(a_0/a_3 - s_1^3)/s_1 = a_1/a_3. \tag{33}$$

We can plot solutions of (20–24) with s as a function of M^2. Our numerical results demonstrate that ϵ is a controlling parameter. For $\epsilon = 3$ we can see (Figure 2) that direct instability starts near $M_c^2 = 140$. A and B are the points where two roots coalesce in Figures 2–4: when $M^2 < M_A^2$ we have two complex conjugate roots for $n = 1$ (their real part is shown only) and one real root. Three real roots exist for M^2 higher than the critical value M_A^2. In the case when $\epsilon = 0.5$ $M_c^2 = 70$ is a critical value for overstability (Figure 3). Our results show that changing ϵ is essentially equivalent to a vertical shift of the $s = 0$ axis. For higher values of the parameter ($\epsilon = 5$) the picture changes (Figure 4) with complex conjugate roots lying below the real one.

2.3   One Layer: Weakly Nonlinear Theory.

After examining what happens in the linear case, we can consider the nonlinear problem (1–5), which can be reformulated in terms of relative vorticity $\zeta = v_x - u_y$, w and θ:

$$\zeta_t + \epsilon\zeta - fw_z = I_1 = -[(\mathbf{u} \cdot \nabla)v]_y + [(\mathbf{u} \cdot \nabla)u]_x \tag{34}$$

$$\nabla^2 w_t + \epsilon w_{zz} + \lambda\nabla_h^2 w - \nabla_h^2\theta + f\zeta_z = I_2 = \nabla_h \cdot [(\mathbf{u} \cdot \nabla)w]_z - \nabla_h^2 \cdot [(\mathbf{u} \cdot \nabla)w] \tag{35}$$

$$\theta_t + \mu\theta + N^2 w = I_3 = -(\mathbf{u} \cdot \nabla)\theta. \tag{36}$$

We define a linear operator $\mathcal{L} = \mathcal{L}(\partial_t, \nabla_h^2, \partial_z, M^2)$ such that

$$\mathcal{L}\xi = \mathbf{N}, \tag{37}$$

where

$$\xi = \begin{pmatrix} \zeta \\ w \\ \theta \end{pmatrix} \quad , \quad \mathcal{L} = \begin{pmatrix} \partial_t + \epsilon & -f\partial_z & 0 \\ f\partial_z & \partial_t(\partial_z^2 + \nabla_h^2) + \epsilon\partial_z^2 + \lambda\nabla_h^2 & -\nabla_h^2 \\ 0 & -M^2 & \partial_t + \mu \end{pmatrix}$$

and $\mathbf{N}$ is a vector of nonlinear terms. Eigenfunctions of the linear problem satisfy $\mathcal{L}\Psi = 0$, where

$$\Psi = \begin{pmatrix} a\cos(kz) \\ b\sin(kz) \\ c\sin(kz) \end{pmatrix} \exp[st + i(k_x x + k_y y)] \tag{38}$$

For convenience we shall use the algebraic linear operator $L(s, K^2, k, M^2)$:

$$L\Phi = 0, \tag{39}$$

where

$$\Phi = \begin{pmatrix} a \\ b \\ c \end{pmatrix} \quad , \quad L = \begin{pmatrix} s + \epsilon & -fk & 0 \\ -fk & -s(k^2 + K^2) - \epsilon k^2 - \lambda K^2 & K^2 \\ 0 & -M^2 & s + \mu \end{pmatrix} \tag{40}$$

2.3.1 Direct instability.

Assume we have the critical state $s = 0$, $M^2 = M_c^2$. Then we may write

$$M^2 = M_c^2 + \nu^2 m \tag{41}$$

$$\partial_t = \nu^2 \partial_\tau \tag{42}$$

$$\xi = \nu \xi_1 + \nu^2 \xi_2 + \ldots \tag{43}$$

$$\mathcal{L} = \mathcal{L}_c + \nu^2 \mathcal{L}_2, \tag{44}$$

where ν is a small parameter, τ is a 'slow' time, $\mathcal{L}_c = \mathcal{L}(0, \nabla_h^2, \partial_z, -M_c^2)$, $\mathcal{L}_2 = \mathcal{L}(\partial_\tau, \nabla_h^2, \partial_z, -M_c^2/\nu^2 - m) - \mathcal{L}_c/\nu^2$, such that

$$\mathcal{L}_2 = \begin{pmatrix} \partial_\tau & 0 & 0 \\ 0 & \partial_\tau(\partial_z^2 + \nabla_h^2) & 0 \\ 0 & -m & \partial_\tau \end{pmatrix} \tag{45}$$

In the first order we shall obtain a linear solution of the problem: $\mathcal{L}_c \xi_1 = 0$, $O(\nu)$; in the second order we shall find ξ_2: $\mathcal{L}_c \xi_2 = \mathbf{N}_1(\xi_1)$; and $\mathcal{L}_c \xi_3 = \mathbf{N}_2(\xi_1, \xi_2) - \mathcal{L}_2 \xi_1$, $O(\nu^3)$. We shall apply the solvability condition to the last expression to get an amplitude equation.

$O(\nu)$: $\mathcal{L}_c \xi_1 = 0$, $\xi_1 = A(\tau)\Psi(x, y, z)$.

We shall neglect the nonlinear terms I_1 and I_2 in (34–35), keeping advection of θ only. It will simplify the derivations considerably, while still retaining the important physics of the problem. Then, for the next order:

$$O(\nu^2) : I_3^{(2)} = -(u_1 \partial_x + v_1 \partial_y + w_1 \partial_z)\theta_1 = -2kbc \sin(2kz)|A|^2, \tag{46}$$

with a, b and c determined in (41–42) when $s = 0$.

$$\xi_2 = \begin{pmatrix} a_2 \cos(2kz) \\ b_2 \sin(2kz) \\ c_2 \sin(2kz) \end{pmatrix} \quad, \quad \xi_2 = L_0^{-1} \begin{pmatrix} 0 \\ 0 \\ I_3 \end{pmatrix}, \tag{47}$$

where

$$L_0 = \begin{pmatrix} \epsilon & -2fk & 0 \\ -2fk & -4\epsilon k^2 & 0 \\ 0 & -M_c^2 & \mu_0 \end{pmatrix} \tag{48}$$

and the solution

$$\xi_2 = \begin{pmatrix} 0 \\ 0 \\ -1 \end{pmatrix} \frac{2bkc}{\mu_0} \sin(2kz)|A|^2 \tag{49}$$

is used to calculate nonlinear terms of $O(\nu^3)$.

$$O(\nu^3) : I_3^{(3)} = -\frac{2cb^2 k}{\mu_0} \sin(kz)|A|^2 A \exp[i\phi] + c.c. + Q, \tag{50}$$

where Q corresponds to the non-secular terms and $\phi = k_x x + k_y y$. The equation for ξ_3 is:

$$L_c \begin{pmatrix} a_3 \\ b_3 \\ c_3 \end{pmatrix} = \begin{pmatrix} -\partial_\tau A a \\ \partial_\tau A b (k^2 + K^2) \\ m A b - \partial_\tau A c \end{pmatrix} + \begin{pmatrix} 0 \\ 0 \\ -2cb^2 k |A|^2 A / \mu_0 \end{pmatrix} \qquad (51)$$

Matrix L_c has a null vector (solution of the linear problem), and we can multiply (51) by the adjoint vector $\Phi^\dagger = (a^\dagger, b^\dagger, c^\dagger)$: $\Phi^\dagger L_c = 0$. The result is the amplitude equation:

$$\partial_\tau A + \alpha A + \beta |A|^2 A = 0, \qquad (52)$$

with

$$\alpha = mbc^\dagger / G \quad , \quad \beta = -2kb^2 cc^\dagger / G, \qquad (53)$$

and $G = bb^\dagger (k^2 + K^2) - aa^\dagger - cc^\dagger$. Substitution of values for a, b, c and $a^\dagger, b^\dagger, c^\dagger$ in (53) gives:

$$\alpha = -\frac{mK^2}{\mu G} \quad , \quad \beta = \frac{2k^2 K^2 M^2}{\mu_0 \mu^2 G}, \qquad (54)$$

where $G = k^2 + K^2 + M^2 K^2 / \mu^2 - f^2 k^2 / \epsilon^2$. For $G > 0$ we have $\beta > 0$. Therefore, we can conclude that direct instability occurs through a supercritical bifurcation (Figure 5a).

2.3.2 Direct Instability: Two Modes.

We proceed with investigation of properties of the system by considering a bimodal case. A linear solution has the form:

$$\xi_1 = A(\tau)\psi \exp[i(k_x x + k_y y)] + B(\tau)\psi \exp[i(k_x x - k_y y)] \quad , \quad \psi = \begin{pmatrix} a \cos(kz) \\ b \sin(kz) \\ c \sin(kz) \end{pmatrix}$$

with a, b and c determined in (39–40). $O(\nu^2)$ nonlinear terms are:

$$I_3^{(2)} = -bck \sin(2kz)(2|A|^2 + 2|B|^2 + AB \exp[i(\phi_+ + \phi_-)] + A^* B \exp[i(\phi_- - \phi_+)] + c.c.), \qquad (55)$$

with $\phi_+ = k_x x + k_y y$ and $\phi_- = k_x x - k_y y$. Then for ξ_2 we get:

$$\xi_2 = \begin{pmatrix} 0 \\ 0 \\ \nu_0 \end{pmatrix} (|A|^2 + |B|^2) \sin(2kz)$$

$$+ \begin{pmatrix} \nu_1 \cos(2kz) \\ \nu_2 \sin(2kz) \\ \nu_3 \sin(2kz) \end{pmatrix} (AB \exp[i(\phi_+ + \phi_-)] + A^* B \exp[i(\phi_- - \phi_+)] + c.c.), \qquad (56)$$

with $\nu_0 = -2cbk/\mu_0$, $\nu_1 = -4cbk^2 f/q$, $\nu_3 = -2bck(\epsilon^2 k^2 + \epsilon\lambda K^2 + f^2 k^2)/(K^2 q)$, and $q = \mu\epsilon^2 k^2 + \mu\epsilon\lambda K^2 + \epsilon N^2 + f^2 k^2$. Using ξ_2, we calculate:

$$I_3^{(3)} = -\sin(kz)\left[\frac{2cb^2 k^2}{\mu_0}(|A|^2 A\exp[i\phi_+] + |B|^2 B\exp[i\phi_-])\right.$$
$$\left. -k(\nu_3' b + \nu_0' b + \nu_2' c)(|A|^2 B\exp[i\phi_-] + |B|^2 A\exp[i\phi_+]) + c.c. + Q,\right.$$

where $\nu_i' = -2bck\nu_i$. In the third order we obtain two equations for A and B and using the solvability condition, we find:

$$\partial_\tau A + \alpha A + \beta|A|^2 A + \gamma|B|^2 A = 0 \tag{57}$$

$$\partial_\tau B + \alpha B + \beta|B|^2 B + \gamma|A|^2 B = 0 \tag{58}$$

with $\alpha = mbc^\dagger/G$, $\beta = 2k^2 b^2 cc^\dagger/(\mu_0 G)$, $\gamma = 2k^2 b^2 cc^\dagger(\nu_3 b + b/\mu_0 + \nu_2 c)/G$ and $G = k^2 + K^2 + M^2 K^2/\mu^2 - f^2 k^2/\epsilon^2$. After substituting values for a, b and c we find that $\beta = 2k^2 M^2 K^2/(\mu_0\mu^2 G)$ and that $\beta > |\gamma|$ is not satisfied. Therefore, the squares ($|A|^2 = |B|^2$) are not stable, and the roll pattern is a solution. Figure 5b is a phase portrait of this situation.

Matthews (1988) obtained rolls for a stratification with density represented by a cubic polynomial in z when studying solar heating of the surface layers of a lake.

2.3.3 Overstability.

We look for the solution of the linear problem of the form:

$$\xi_1 = A(\tau)\begin{pmatrix} a\cos(kz) \\ b\sin(kz) \\ c\sin(kz) \end{pmatrix}\exp[i(\omega t + k_x x + k_y y)] + c.c., \tag{59}$$

and define a linear operator L_ω:

$$L_\omega\begin{pmatrix} a \\ b \\ c \end{pmatrix} = 0 \quad , \quad L_\omega = \begin{pmatrix} \epsilon + i\omega & -fk & 0 \\ -fk & -i\omega(k^2 + K^2) - \epsilon k^2 - \lambda K^2 & K^2 \\ 0 & -M^2 & \mu + i\omega \end{pmatrix}$$

For the second order we find $I_3^{(2)} = -2bck\sin(2kz)|A|^2$ and

$$\xi_2 = \begin{pmatrix} 0 \\ 0 \\ -1 \end{pmatrix} 2bck\sin(2kz)|A|^2(\mu - i\omega)/(\mu^2 + \omega^2) \tag{60}$$

We can calculate now: $I_3^{(3)} = -2b^2 k^2 c\sin(kz)|A|^2 A\exp[i\phi](\mu - i\omega)/(\mu^2 + \omega^2) + c.c..$ The solvability condition leads to an amplitude equation of the same form as for the one-mode case of direct instability but with

$$\alpha = -mK^2(\mu + i\omega)/G(\mu^2 + \omega^2) \quad , \quad \beta = 2k^2 M^2 K^2/G(\mu^2 + \omega^2), \tag{61}$$

and $G = k^2 + K^2 + M^2 K^2/(\mu^2 + \omega^2) - f^2 k^2/(\epsilon^2 + \omega^2)$. It follows that $\beta > 0$ for $G > 0$, and as in the case of direct instability for a single mode, overstability occurs through a supercritical bifurcation.

2.4 Two Layers.

2.4.1 Boundary Conditions.

Now we consider a situation where the layer of the previous sections lies above a stably stratified layer. The equation for the vertical velocity in layer i is $W_i'' = RW_i$ with R_1 and R_2 defined in (13) and (14). We specify the boundary conditions: $W_1 = 0$ at $z = h$, $W_2 = 0$ at $z = -H$ (or at infinity).

The transition across the interface between the layers must be physically correct. The vertical velocity at the interface must be the same in the two regions what gives $W_1 = W_2$ at $z = 0$. We must also ensure continuity of pressure: $p_1 = p_2$ at $z = 0$. In the general case, this condition leads to $W_1'(f^2 + (s + \epsilon)^2)/(s + \epsilon) = W_2'(f^2 + s^2)/s$ at $z = 0$. Only when $\epsilon = 0$, is W' continuous at $z = 0$.

2.4.2 Infinitely Deep Lower Layer.

First, we examine the situation where $\epsilon = 0$ (no horizontal drag) and the lower layer is infinitely deep. We are interested in amplification of internal gravity waves in the lower layer (overreflection). Consider an incident wave (with positive group velocity) with amplitude 1, which after reflection at $z = 0$ has an amplitude A (and negative group velocity); $s = i\omega$ and $W_2(z) = A\exp[i\alpha z] + \exp[-i\alpha z]$, where $\alpha^2 = K^2(N^2 - \omega^2)/(\omega^2 - f^2)$.

If we multiply(12) by W^*, subtract from it the complex conjugate of (12) multiplied by W and integrate from $z < 0$ to h: $\int_z^h [(12) \cdot W^* - (12)^* \cdot W]dz$, then, after some algebra we get:

$$|A|^2 - 1 = -C R_{im}, \qquad (62)$$

where C is a positive constant and R_{im} is the imaginary part of R_1. Thus, if we can show that $R_{im} < 0$ for some values of the parameters, overreflection of gravity waves is possible, i. e. $|A|^2 > 1$. For the case when $\epsilon = 0$ and λ and μ have different nonzero values, we find that

$$R_{im} = \frac{\omega(\lambda\mu^2 - \mu M^2 + \lambda\omega^2)K^2}{(\omega^2 - f^2)(\omega^2 + \mu^2)}, \qquad (63)$$

so that a threshold value for overreflection is

$$M_c^2 = \frac{\lambda(\mu^2 + \omega^2)}{\mu} \qquad (64)$$

and for larger M^2 reflection coefficient is larger than one.

However, one can notice from the dispersion relation for internal gravity waves:

$$\omega^2 = \frac{N^2 + f^2 n^2 \pi^2 / K^2}{1 + n^2 \pi^2 / K^2} \qquad (65)$$

that $\omega \to f$ as n becomes larger. Therefore, the highest vertical overtone goes unstable first and to avoid this we need to reconsider this part of the problem in our future work.

In general it is rather complicated to examine when $|A|^2 > 1$, but the examples above prove that overreflection in our system is possible. Mechanism of amplification of internal gravity waves was explained by Souffrin and Spiegel (1967).

We suggest that on either side of the interface the mode has a different sense of a conserved quantity, potential energy in particular. Thus, the mode induces a change in the available potential energy (APE) in the upper layer of the opposite sign to that in the lower one, and to conserve APE, the reflected wave in the lower region has to be amplified.

For real s (direct instability) the solution which satisfies the boundary conditions at $z = h$ and $z = -\infty$ is $W_1 = a \sin[\alpha(z - h)]$ and $W_2 = b \exp(mz)$ where $m^2 = R_2$ and $\alpha^2 = -R_1$, a and b are constants. Matching W and W' at $z = 0$ gives the relation

$$m = -\alpha \cot(\alpha h), \tag{66}$$

only when $M^2 > \lambda \mu$, i. e. the same condition that we found for instability in the one-layer case must be satisfied.

2.4.3 Lower Layer of Finite Depth.

When the depth of the lower layer H is finite and $\epsilon \neq 0$ in the upper layer, the solution to the problem is $W_1 = a \sin[k(z - h)]$, $W_2 = b \sin[\kappa(z + H)]$ with $k^2 = -R_1$ and $\kappa^2 = -R_2$.

Using matching conditions at $z = 0$, we get an expression:

$$-\frac{\tan(kh)}{k} \frac{s + \epsilon}{f^2 + (s + \epsilon)^2} = \frac{\tan(\kappa H)}{\kappa} \frac{s}{s^2 + f^2} \tag{67}$$

Then the marginality condition for direct instability requires $\tan(k_0 h) = 0$, where $k_0 = k(s = 0)$. After expanding (67) for small s, we may specify a condition on ϵ to make the mode marginal:

$$\epsilon = \frac{2 k_0^2 \tan(\kappa_0 H)}{\frac{\partial k_0^2}{\partial s} f^2 \kappa_0 H} (f^2 + \epsilon^2), \tag{68}$$

where $\frac{\partial k_0^2}{\partial s} = \frac{M^2 - \lambda \mu}{f^2 + \epsilon^2} \left[\frac{1}{\epsilon} - \frac{1}{\mu} - \frac{2\epsilon}{f^2 + \epsilon^2} - \frac{\lambda + \mu}{M^2 - \lambda \mu} \right] \frac{\epsilon K^2}{\mu}$ and $\kappa_0^2 = -K^2 N^2 / f^2$.

Perturbing about M_c^2, we can get an expression for the growth rate near the marginality point:

$$s = -\frac{\frac{\partial k_0^2}{\partial M^2}(M^2 - M_c^2)}{\frac{\partial k_0^2}{\partial s} + \frac{f^2 + \epsilon^2}{n \epsilon \kappa_0 f^2} 2 k_0^2 \tanh(\kappa_0 H)} \tag{69}$$

with $\frac{\partial k_0^2}{\partial M^2} = \frac{\epsilon K^2}{\mu(f^2 + \epsilon^2)}$ and $\frac{\partial k_0^2}{\partial s}$ given above.

In the case when $s = i\omega$, $k = k_r + i k_i$ and taking the imaginary part of (67) for $\epsilon = 0$ gives the marginality condition for overstability which is exactly the same as criterion for overreflection (64) derived in the previous section.

Our further analysis of the system with finite-depth lower layer (solution of the eigenvalue problem) is numerical. As was expected, the controlling parameters are M^2 and ϵ for the upper layer and M^2, λ for the lower. By changing them different scenarios of instability occuring in the system can be achieved.

We consider modes corresponding to the upper or lower layer which are extended over the entire depth of the system by the use of matching conditions at $z = 0$. Figures 6a and

b show the eigenvalues of oscillatory (real parts) and direct modes associated with the upper layer as functions of M^2 for $\epsilon = 0, f = 1, \mu = 4, \lambda = 4, N^2 = 200$, i. e. very stable lower layer. Eigenfunctions associated with the upper layer are presented in Figure 7 for the same parameters values and $M^2 = 20$.

Figures 8 and 9 show eigenvalues and eigenfunctions related to the lower layer. Our choice of $\epsilon = 0$ makes both W and W' continuous at $z = 0$ (see Figures 7 and 9).

An interesting case is the mode that is not associated with any particular layer but is the mode of the entire system (we call it the hybrid mode). It is shown in Figure 10 and is generally heavily damped.

The linear theory for a one-layer case can be applied to two layers: $\epsilon = \lambda = \mu = 0$ in the lower layer and from (6–10) one can get a solution when $s = 0$: $w_2 = 0$, $\theta_2 = 0$ and $\zeta_2 = const$. Thus, in this situation the lower layer is stagnant and does not influence dynamics in the upper layer. Hence, the results of section 2.2 are valid in this case. However, inclusion of nonlinear terms requires analysis of the full system of equations for both layers.

3 Summary.

The goal of this work was to study stability of a layer of fluid bordered by horizontal planes or by a boundary and a layer with stable density gradient. The former case was studied using the nonhydrostatic Boussinesq equations with drag friction and diffusion of temperature. Criteria for the onset of direct instability and overstability were derived in linear theory. The necessary condition for direct instability is that free-fall time is shorter than damping time.

Analysis of the problem in weakly nonlinear theory when the temperature advection term was included showed that supercritical bifurcation leads to direct instability. A qualitatively similar result was obtained for overstability.

When considering a bimodal case, it was shown that squares are not stable and rolls are the preferred pattern.

Inclusion of a stable layer below the one discussed previously does not change stability of the upper layer in linear theory, and we obtain a similar condition for the onset of instability as in the one-layer case. However, this analogy between one- and two-layer cases disappears when nonlinear terms are included. Future work may consider fully nonlinear problems for both situations.

Amplification of gravity waves (overreflection) in the lower layer is demonstrated for some specific choices of parameters. More work can be done in this direction to obtain general criteria for overreflection in the two-layer system.

It was shown that for increasing mode number, the critical wavenumber K_c^2 decreases. In the long-wave limit we expect to obtain an amplitude equation similar to that derived by Depassier and Spiegel (1982) which has solitary waves as a solution. Thus, in the case of finite vertical extent of the system we can have coherent structures propagating in the lower layer.

4 Acknowledgements.

5 References.

Batchelor, G. K., and Nitsche, J. M. 1991. Instability of stationary unbounded stratified fluid. *J. Fluid Mech.*, **227**, 357–391.

Chandrasekhar, S. 1961. *Hydrodynamic and Hydromagnetic Stability*. Oxford University Press.

Depassier, M. C., and Spiegel, E. A. 1982. Convection with heat flux prescribed on the boundaries of the system. I. The effect of the temperature dependence of material properties. *Geophys. Astrophys. Fluid Dyn.*, **21**, 167–188.

Gribov, V. N., and Gurevich, L. E. 1957. On the theory of the stability of a layer located at a superadiabatic temperature gradient in a gravitational field. *Sov. Phys. JETP*, **4**, 720–729.

Matthews, P. C. 1988. A model for the onset of penetrative convection. *J. Fluid Mech.*, **188**, 571–583.

Souffrin, P., and Spiegel, E. A. 1967. An instability of gravity waves. *Ann. d'Astr.*, **30**, 985–994.

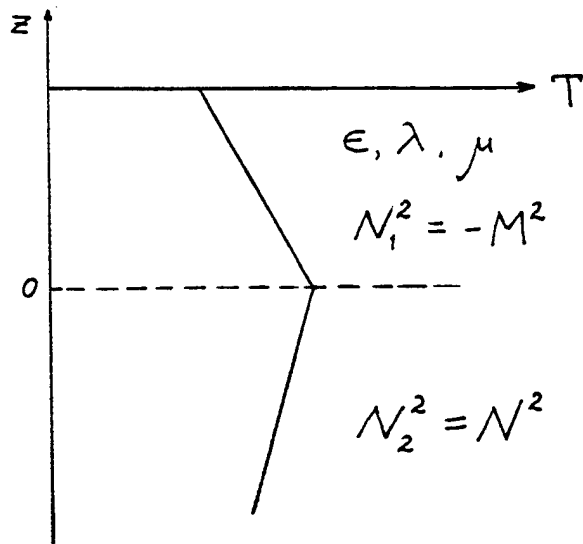Veronis, G. 1963. Penetrative convection. *Astrophys. J.*. **137**, 640–664.
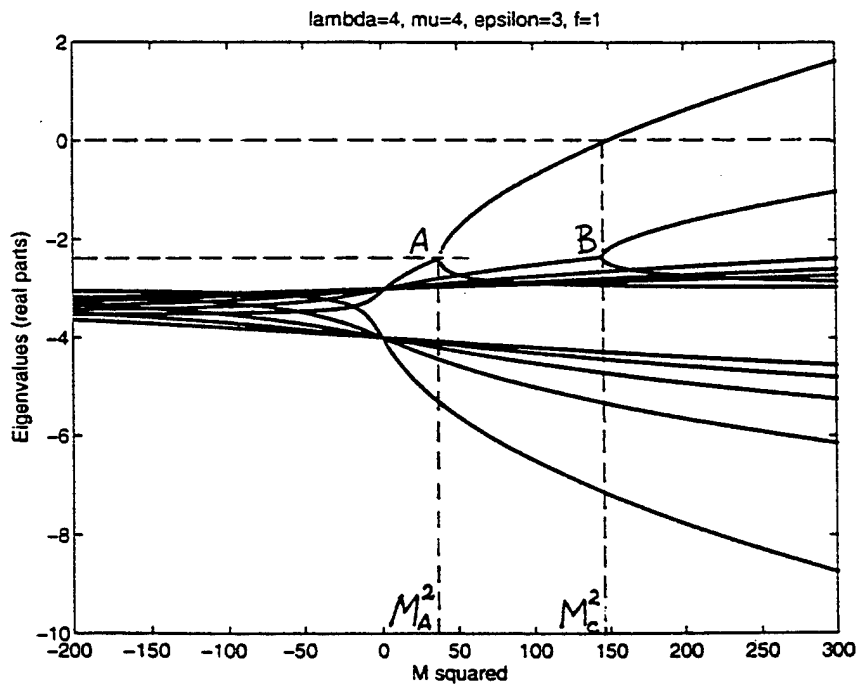
Figure 1 Basic state temperature profile.

Figure 2 Numerical solution of (20–24) for $\epsilon = 3, \mu = 4, \lambda = 4, f = 1$. Only real parts of the roots are shown. M_c^2 indicates a critical point of direct instability for the first mode.

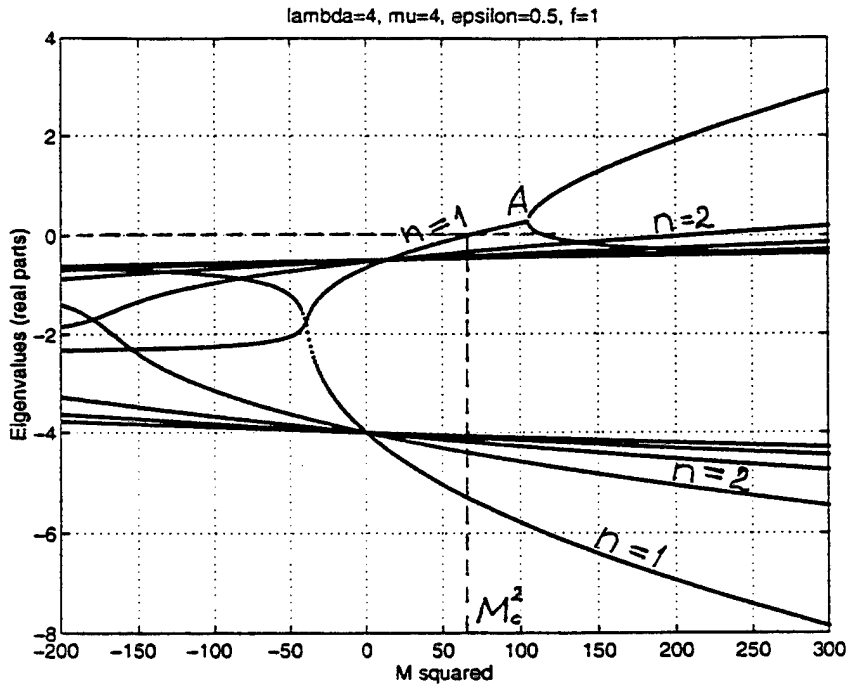**Figure 3** As Figure 2 but for $\epsilon = 0.5$. Onset of overstability occurs at M_c^2 for the first mode.
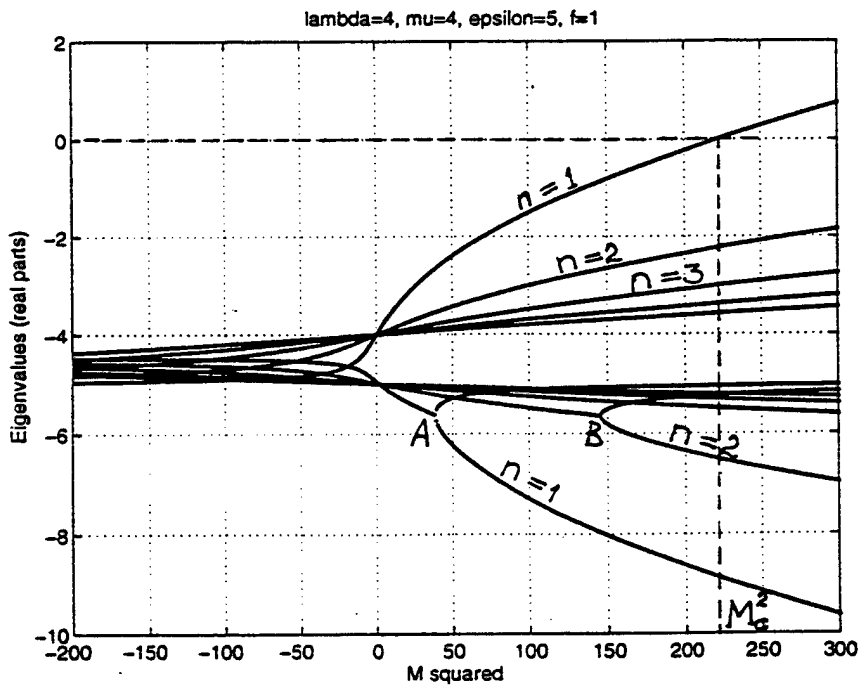

Figure 4 As Figure 2 but for $\epsilon = 5$. Note that complex conjugate roots lie below the real one now.
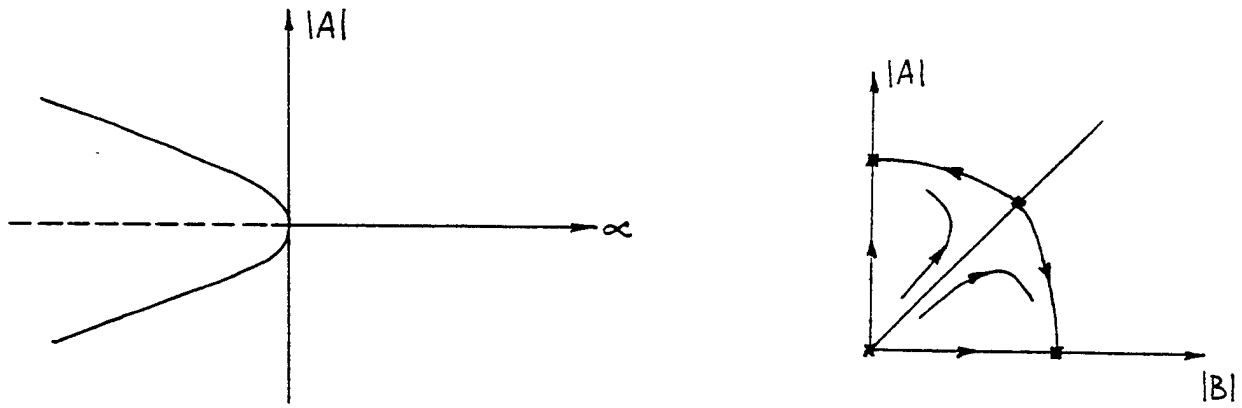
Figure 5a $|A|$ as a function of α for a supercritical bifurcation ($\beta > 0$ in (52)).

Figure 5b Phase portrait of (57–58). Roll pattern is a solution because $\beta < |\gamma|$.
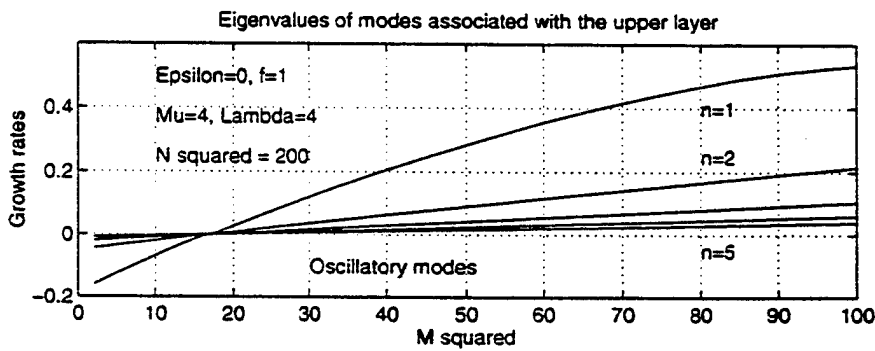

Figure 6a The real parts of eigenvalues of oscillatory modes associated with the upper layer for $\epsilon = 0$, $f = 1$, $\mu = 4$, $\lambda = 4$ and $N^2 = 200$ as functions of M^2.
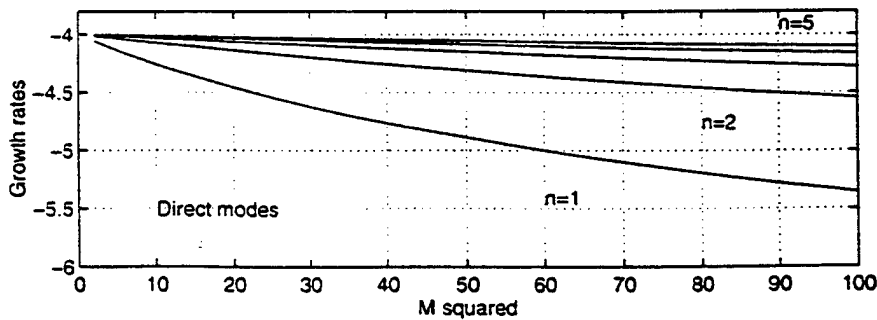

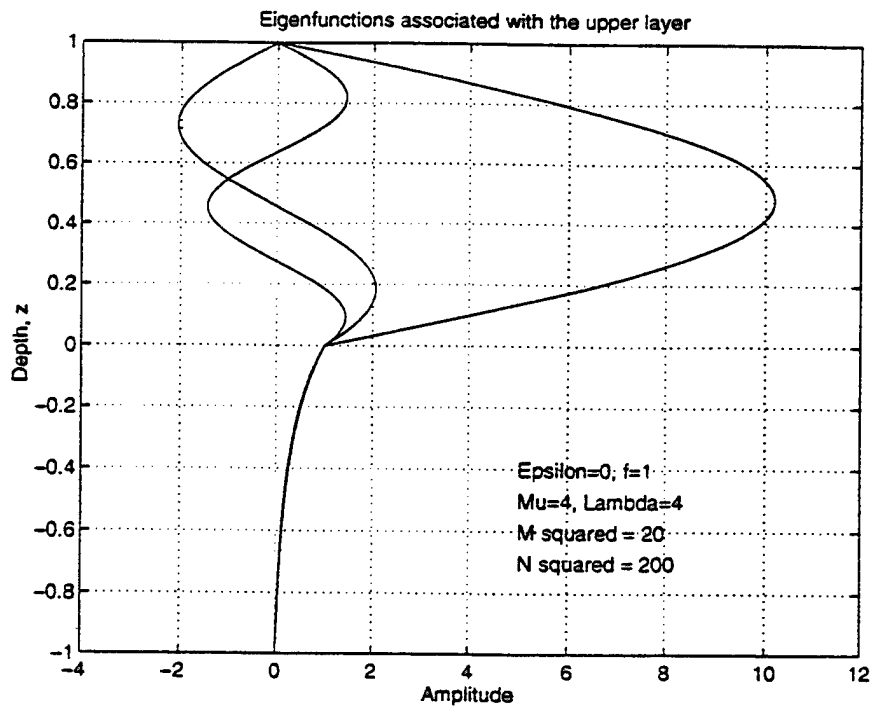**Figure 6b** As Figure 6a but for direct modes.

Figure 7 Eigenfunctions (n=1–3) associated with the upper layer for the same parameters values as in Figure 6a.
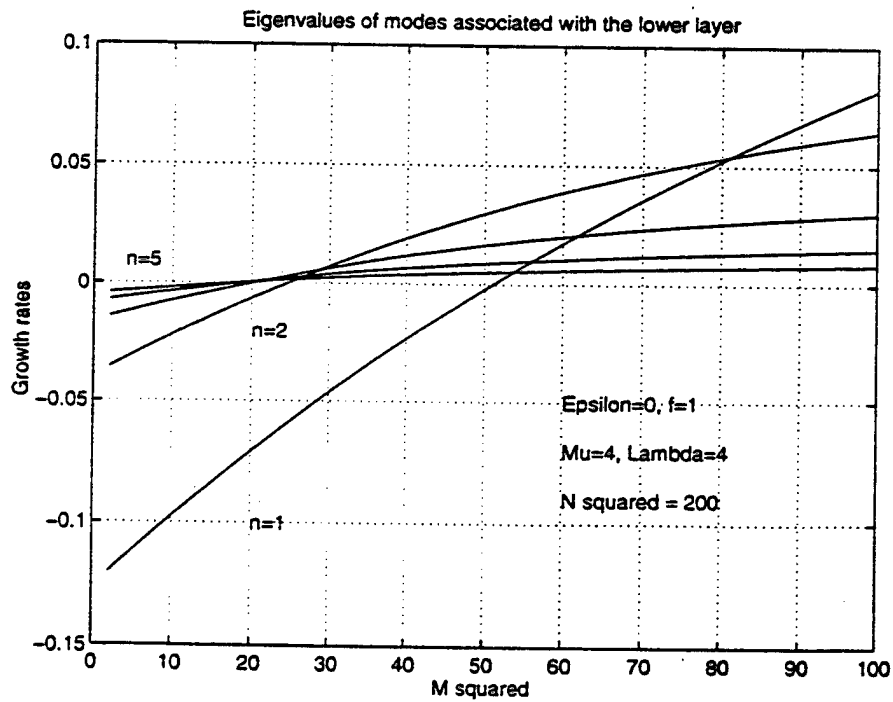

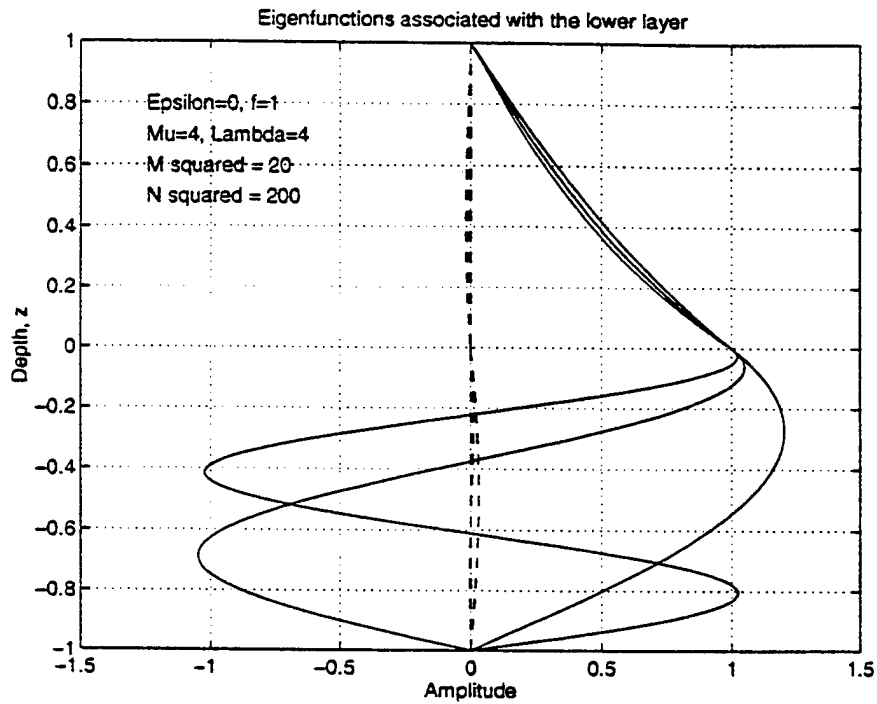**Figure 8** As Figure 6b but for the modes associated with the lower layer.

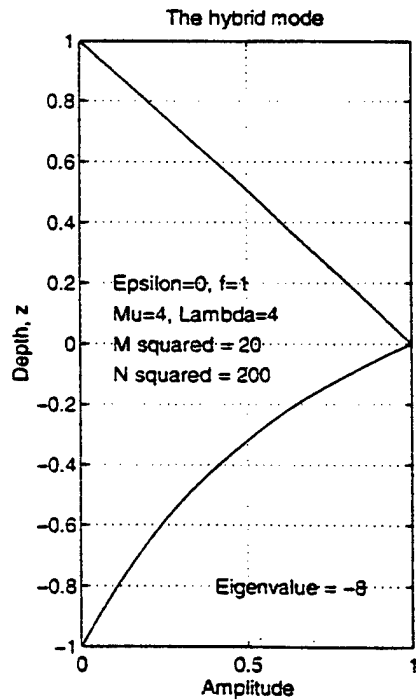**Figure 9** As Figure 7 but for the eigenfunctions associated with the lower layer.

Figure 10 The hybrid mode. Note that its eigenvalue ($s = -8$) shows that the mode is heavily damped.

The Effects of Cooling on a Shallow, Baroclinic Current

T. James Noyes

1. Introduction

In a rotating system, fluids in a geostrophically unbalanced state achieve equilibrium by undergoing a process known as geostrophic adjustment. By assuming that potential vorticity is conserved during the adjustment process, Rossby(1937) was able to analytically determine the final equilibrium state resulting from an initial momentum imbalance. In Rossby's problem, the momentum imbalance was the result of momentum injected into the ocean by wind stress. In more recent work, authors like Stommel and Veronis(1980), Ou(1984), and Blumen and Wu(1995) have investigated the adjustment of a mass imbalance caused by cooling an initially motionless ocean's surface. Cooling subtracts buoyancy and causes convective overturning which homogenizes density vertically. In this paper, the adjustment of a mass and momentum imbalance generated by cooling a shallow baroclinic current is examined. The results may serve as a rough approximation to the effects of cooling on a shallow ocean current. They illustrate the influence of cooling on the structure and energy contained in currents.

We examine a y-indepedent baroclinic current modeled with the shallow water equations. This model is sketched in figure 1. The ρ_3 layer is infinitely deep, and the condition that the interfaces between the layers must adjust so that there is no flow in this layer is enforced. Layers 1 and 2 share an interface which slopes down to the right over a height scale H_0 and a length scale equal to L_0. To maintain geostrophic equilibrium, the fluid in layer 1 has velocity $v_i = \frac{\Delta \rho g H_0}{\rho_1 f L_0}$ for $-L_0 < x < 0$, where $\Delta \rho = \rho_2 - \rho_1$ and f is the Coriolis parameter. The velocity in layer 2 is zero. The interface between layer 1 and layer 3 exponentially decays to $H_0(1 + \delta)$ over the length scale $L_{31} = \sqrt{\frac{(\rho_3 - \rho_1)g H_0}{\rho_1 f^2}}$, i.e. the internal Rossby radius of deformation. We choose $\delta = \frac{H_0}{L_0} L_{31}$ so that the velocity is continuous at $x = 0$. The velocity in layer 1 decays to zero as the interface becomes constant for $x \to \infty$.

Cooling at the surface causes overturning which mixes momentum and density vertically. The cooling is too weak to enable convective mixing to penetrate into the lower layer of density ρ_3. Mixing is assumed to occur so quickly that momentum and density are both vertically homogeneous before any adjustment takes place. The effect of cooling, shown in figure 2, is that the region which previously contained the interface between layers 1 and 2, $-L_0 < x < 0$, subsequently contains horizontal gradients in density and momentum. If no buoyancy is taken out, there is no density gradient for $x > 0$ and the momentum gradient remains unaffected. For $x < -L_0$, the fluid remains homogeneous and has suffered no change in density or momentum.

Analytical determination of the state of geostrophic equilibrium resulting from the adjustment of the density and momentum distribution described above only proved possible in the limit of $\Delta^{\frac{1}{2}} \ll 1$ where $\Delta = \frac{\rho_2 - \rho_1}{\rho_3 - \rho_2}$. In this case, the density difference between the lower layer and the upper layers is much greater than the density difference between the two upper layers. Essentially, the lower boundary is "stiff.". For a perturbation expansion in $\Delta^{\frac{1}{2}}$, the zeroth order solution corresponds to the limit in which the interface between

the upper and lower layers is rigid and flat. The model in this limit is displayed in figures 3 and 4. Note that layer 1 now has velocity v_i everywhere. If the same amount of buoyancy is removed everywhere at the surface in this model, the density would increase by the same amount everywhere as well. Since this uninteresting result would be buoyancy loss' only effect, it will be neglected. The zeroth order solution in which the interface between the lower and upper layers is rigid and flat will be discussed in this paper.

2. Rigid Bottom Solution

The dynamics of the homogeneous layers are simply determined by the shallow water potential vorticity equation.

$$v_{jx} + f = \frac{f}{H_0} h_j \quad (j = 1, 2), \tag{2.1}$$

h_j is the depth of layer j, and v_j is the velocity in layer j. Dynamical equations in the stratified middle region are obtained from the conservation of density, potential vorticity, and absolute momentum M $(= v + fx)$ on parcels in the region. Thus, each parcel in the stratified region retains the density, potential vorticity, and absolute momentum it had prior to adjustment. The conservation of absolute momentum M comes from the horizontal momentum equation.

$$\frac{Dv}{Dt} + fu = \frac{D}{Dt}(v + fx) = \frac{DM}{Dt} = 0.$$

In terms of the density and velocity fields ρ_0 and v_0 which result from convective mixing, the potential vorticity is

$$(v_{0x} + f)\rho_{0z} - \rho_{0x}v_{0z} = 0$$

since the stratification and the vertical shear are zero in the postconvection state. Not only is potential vorticity conserved on parcels in this region, but the vertical mixing sets their potential voriticity to zero. An important result follows immediately from these conservation principles and the fact that the thermal wind relation will hold in the adjusted state. The potential vorticity equation,

$$(v_x + f)\rho_z - \rho_x v_z = 0, \tag{2.2}$$

may be rewritten as the ratio of the horizontal and vertical density gradients.

$$\frac{\rho_x}{\rho_z} = \frac{(v_x + f)}{v_z} = \frac{M_x}{v_z}. \tag{2.3}$$

The conservation of both M and ρ on parcels implies that the initial functional relationship between M and ρ will be maintained. Thus, M_x may be rewritten as $M_\rho \rho_x$. The substitution of $M_x = M_\rho \rho_x$, $\frac{\rho_x}{\rho_z} = -(\frac{\partial z}{\partial x})_\rho$, and the thermal wind relationship $v_z = -\frac{g}{\rho_1 f}\rho_x$ into (2.3) reveals that

$$\left(\frac{\partial z}{\partial x}\right)_\rho = \left(\frac{\rho_1 f}{g}\right)\frac{M_x}{\rho_x} = \left(\frac{\rho_1 f}{g}\right)M_\rho \tag{2.4}$$

The slope of the isopycnals is proportional to M_ρ. Ou(1984) points out that when $M_0 = fx$, that is, when there is no northward velocity intially, $\left(\frac{\partial z}{\partial x}\right)_\rho = \left(\frac{\rho_1 f^2}{g}\right)\frac{1}{\rho_{0x}}$. The slope of the isopycnals will be proportional to the inverse of the initial lateral density gradient. The presence of a velocity gradient adds $\left(\frac{\rho_1 f}{g}\right)\frac{v_{0x}}{\rho_{0x}}$ to the slope of the isopycnals.

The postconvection distributions of density and velocity in the stratified region $-L < x < 0$ are linear in x.

$$v_0 = v_i(1 + \frac{x}{L_0}), \tag{2.5a}$$

$$\rho_0 = \rho_1 - \Delta\rho(\frac{x}{L_0}), \tag{2.5b}$$

(recall $v_i = \frac{\Delta\rho g H_0}{\rho_1 f L_0}$). This implies that M_0 $(= v_0 + fx)$ is a linear function of ρ_0. The elimination of x between (2.5a) and (2.5b) shows that the functional relationship between M and ρ is

$$M = v_i\left[1 - \left(1 + \frac{L_0^2}{L_D^2}\right)\frac{(\rho - \rho_1)}{\Delta\rho}\right], \tag{2.6}$$

where $L_D = \sqrt{\frac{\Delta\rho g H_0}{\rho_1 f^2}}$ is the internal Rossby radius of deformation. The fact that M is a linear function of ρ yields the important result that the slopes of the isopycnals are constant.

$$\left(\frac{\partial z}{\partial x}\right)_\rho = -\left(\frac{H_0}{L_0}\right)\left(1 + \frac{L_0^2}{L_D^2}\right) = -\alpha. \tag{2.7}$$

The slope of the isopycnals, which will henceforward be represented by $-\alpha$, is proportional to the slope of the preconvection interface between the homogenous layers, $\frac{H_0}{L_0}$. It is multiplied by $(1 + \epsilon^2)$ where $\epsilon = \frac{L_0}{L_D}$ is the ratio of the width of the initial interface to the internal Rossby radius. The isopycnals' slope will always be $-2\frac{H_0}{L_D}$ or steeper, so the isopycnals will always be steeper than the initial interface. For $\epsilon \ll 1$, the slope of the isopycnals approaches that of the original interface. For $\epsilon \gg 1$, the isopycnals are almost vertical.

Armed with the knowledge that the isopycnals all have the slope given in (2.7), we expect the internal structure of the stratified region will resemble figure 5a after adjustment. Columns of fluid, initially vertical, will tilt during adjustment. An infinitesimally thin column of a particular density must have the same volume prior to and after adjustment has taken place. The application of this version of the conservation of mass to the column shown in figure 5a yields the equation

$$H_0 dx_0 = H_0\sqrt{1 + \alpha^{-2}}dw, \tag{2.8}$$

where w is the width of the tilted column of fluid. Let $s = z + \alpha x$. s is a variable proportional to the width of the column. Specifically, $w_s = \frac{1}{\alpha\sqrt{1+\alpha^{-2}}}$. s is constant on

isopycnals which makes it a convenient independent variable in which to determine the distribution of density in the stratified region. (2.8) can be rewritten as

$$\frac{d\rho}{\rho_{0x}} = \sqrt{1 + \alpha^{-2}}\frac{d\rho}{\rho_w} = \sqrt{1 + \alpha^{-2}}w_s\frac{d\rho}{\rho_s}. \qquad (2.9)$$

Therefore,

$$\rho_s = -\beta H_0, \qquad (2.10)$$

where

$$\beta = \frac{\Delta\rho}{\alpha H_0 L_0} = \frac{\Delta\rho}{H_0^2(1 + \epsilon^2)}.$$

It can be shown that application of both shallow water conservation(equations (2.1)) and M and ρ conservation(equation (2.6)) is not possible if the interfaces between the stratified and homogeneous fluid are assumed to be isopycnals. This is not merely a consequence of having both a rigid top and bottom. If we allow density to vary along the interfaces, the contradiction disappears. In this case, then some columns of fluid will intersect an interface as shown in figure 5b. The proper equation for mass conservation for this column is $\rho_s = -\beta(H_0 - h)$ where h is the depth of the interface and ρ_s is evaluated along the interface. The issue of whether this is appropriate or not and what other alternatives may exist will be discussed briefly in the concluding section of the paper.

Figure 6 contains a sketch of what we expect the final state to look like. The fact that the lengths of columns of stratified fluid can be related to the interfaces divides the figure into several regions separated by dotted lines in which different equations apply. The solutions in these various regions are to be matched at their boundaries. The shallow water potential vorticity equations (2.1) reveal that the flow in regions I and V is unchanged from the initial state. Conservation of mass, equation (2.10), defines the density and momentum fields in region III to within a constant. The regions which contain the interfaces between the stratified and homogeneous fluid, labeled regions II and IV in figure 6, have modified versions of (2.10) which depend of the location of the interfaces. The fields in these regions are strongly influenced by the shape of the interfaces.

In the region II the applicable equations are,

$$v(x, z) + fx = v_i\left[1 - \left(1 + \epsilon^2\right)\frac{(\rho - \rho_1)}{\Delta\rho}\right], \qquad (2.11a)$$

$$v_{2x} + f = \frac{f}{H_0}(H_0 - h), \qquad (2.11b)$$

$$\rho_s = -\beta(H_0 - h), \qquad (2.11c)$$

corresponding to M and ρ conservation, shallow water potential vorticity conservation in layer 2, and mass conservation respectively. v_2 is the velocity in the homogeneous layer, and v is the velocity in the stratified region. h designates the distance from the rigid top to the interface between homogeneous and stratified fluid. In (2.11c), ρ_s is evaluated along the interface, that is, for $s = -h(x) + \alpha x$.

A similar set of equations holds in region IV, and the steps for solving the set of equations for each region are essentially the same. We will now solve the equations for region II. First, the velocities are eliminated from (2.11) by calculating their relationship with h, ρ, and the barotropic pressure $p_0(x)$.

$$
\begin{aligned}
v &= \frac{1}{\rho_1 f}\Big[p_{ox} + \partial_x \int_z^0 \rho(x, z')g\,dz'\Big], \\
&= \frac{1}{\rho_1 f}\Big[p_{ox} - \alpha g\big(\rho(x, z) - \rho(x, 0)\big)\Big], \tag{2.12}
\end{aligned}
$$

$$
\begin{aligned}
v_2 &= \frac{1}{\rho_1 f}\Big[p_{ox} - \rho_2 g h_x + \partial_x \int_{-h}^0 \rho(x, z')g\,dz'\Big], \\
&= \frac{1}{\rho_1 f}\Big[p_{ox} - h_x g\big(\rho_2 - \rho(x, -h)\big) - \alpha g\big(\rho(x, -h) - \rho(x, 0)\big)\Big], \tag{2.13}
\end{aligned}
$$

A version of (2.7) has been used: $\rho_x = \alpha \rho_z$. Substitution of (2.12) and (2.13) into (2.11a) and (2.11b) followed by taking the difference of the resulting equations yields

$$
\frac{d}{dx}\Big[\big(\rho_2 - \rho(x, -h)\big)\Big(\frac{g}{\rho_1 f}\Big)h_x\Big] = -\Big(\frac{g\alpha}{\rho_1 f}\Big)\frac{d}{dx}\big[\rho(x, -h(x))\big] + \frac{f}{H_0}(h - H_0). \tag{2.14}
$$

Notice that now ρ is solely a function evaluated along the interface, that is, $s = -h(x) + \alpha x$. Using mass conservation (2.11c) to eliminate h in this equation and converting to s coordinates gives

$$
\frac{\beta^{-1}(\rho_2 - \rho)\rho_{sss}}{1 + \beta^{-1}\rho_{ss}} + \rho_s\Big(1 - \Big(\frac{\epsilon^2}{1 + \epsilon^2}\Big)\big(1 + \beta^{-1}\rho_{ss}\big)^2\Big) = 0. \tag{2.15}
$$

We can integrate (2.15). At point O in Figure 6, the application of the boundary conditions $\rho = \rho_2$ and $\rho_s = 0$ yields

$$
\rho = -\frac{1}{2}\beta(1 + \sqrt{1 + \epsilon^{-2}})(s + H_0 - \alpha x_b)^2. \tag{2.16}
$$

The boundary condition $\rho = \rho_2$ comes from the assumption that the column of density ρ_2 which was adjacent to the interface between the stratified and homogeneous regions in the postconvection state is squashed into the corner denoted by O. The second comes from evaluating (2.11c) at $h = H_0$.

Substitution of (2.16) and $s = -h + \alpha x$ into (2.11c) reveals that the interface between the homogeneous and stratified regions is the straight line

$$
h = \alpha\Big(1 + \frac{\epsilon}{\sqrt{1 + \epsilon^2}}\Big)(x - x_b) + H_0 \tag{2.17}
$$

Thus, the interface will be steeper than the isopycnals. Even though the interface will always be steeper than the isopycnals, the interface is never more than twice as steep.

The following boundary condition determines x_b. The amount of homogenous fluid which has moved to the right during the adjustment process must be balanced by an equal amount of stratified fluid moving left.

$$\int_{x_t}^{-L_0} h\,dx = \int_{-L_0}^{x_b} (H_0 - h)\,dx. \qquad (2.18)$$

The dashed line on the left in figure 6 indicates the preadjustment position of the interface, and the arrows denote the fluid motion which takes place during adjustment. This constraint relates the x positions where the interface hits the top and bottom boundaries, x_t and x_b. The exact x positions can then determined using (2.17). The interface is found to be symmetric about $x = -L_0$.

At this point, equations for the interface, density, and velocities can be obtained for region II. These can be patched at the boundaries with the other regions. Figure 7 displays the resulting distributions of density and velocity for for three values of ϵ, $\epsilon = 10^{-4}$, 1, and 10^4. Several interesting features are revealed. As discussed previously, the isopycnals have slopes only slightly greater than $\frac{H_0}{L_0}$, the slope of the initial interface, for $\epsilon \ll 1$. They become progressively steeper as ϵ increases until they are nearly vertical for $\epsilon \gg 1$. In both of these limits, regions II and IV in the stratified fluid are compressed and occupy little area. Also note that velocities out of the page, that is, flow opposed to the preconvection motion of the current, occur in the lower lefthand portion of the figures. Velocities greater than v_i, the preconvection velocity of layer 1 fluid, are present in the upper righthand portion of the figures. The strength of both of these effects increases with increasing ϵ. For $\epsilon = 10^{-4}$, columns of fluid simply tilt over and keep their momentum. The result of cooling and adjustment is a frontal region spread out over L_0 instead of the sharp jump in density from ρ_2 to ρ_1 that existed prior to cooling. The current has a lateral extent of $2L_0$, twice as large as before. For $\epsilon = 10^4$, columns of fluid need only tilt a small amount to be in equilibrium. Both the current and the frontal region have a lateral extent of L_0. The only clear indication that adjustment has occured is in the velocity field.

Fronts, corresponding to discontinuities in density and velocity, occur along the interfaces between the stratified and homogenous regions. The difference in velocity across the front, $\Delta v = v - v_2$, is small for $\epsilon \ll 1$. Δv is not more than $5 \times 10^{-5} v_i$ when $\epsilon = 10^{-4}$. However, the velocity jump Δv increases with ϵ. The velocity jump along the interface in region II increases with height and reaches its maximum at the surface where $v_2 \to 0$. For $\epsilon = 1$, $\Delta v = 0.35 v_i$ at the surface. For $\epsilon = 10^4$, this increases to $\Delta v = 0.5 v_i$.

Only regions II, III, and IV are altered during the processes of convective mixing and geostrophic adjustment. Consider the energy stored in these regions, henceforward called "the system." Energy is present in two forms, kinetic energy(KE) and available potential energy(APE). The APE is given by

$$APE = \int_{-L_0 - \frac{H_0}{2h_x}}^{\frac{H_0}{2h_x}} dx \int_{-\frac{H_0}{2}}^{0} dz(\rho - \rho_1)gz + \int_{-L_0 - \frac{H_0}{2h_x}}^{\frac{H_0}{2h_x}} dx \int_{-H_0}^{\frac{-H_0}{2}} dz(\rho - \rho_2)gz \qquad (2.19)$$

The total energy(TE) in the system is the sum of KE and APE. The processes of convective mixing and geostrophic adjustment can not only change the TE, but can also shift energy from one form to another. In geostrophic adjustment problems, for example, typically APE is converted into KE during adjustment.

We'll begin this discussion of the energy in the system with the energy lost during the process of geostrophic adjustment. Let $\mathcal{E}$ be the TE of the system prior to cooling. Figure 8 contains a plot of the energy lost during adjustment in units of $\mathcal{E}$ as a function of ϵ. The peak in figure 8 corresponds to $\epsilon = 1.8$ and has a value of $0.0676\mathcal{E}$. The figure shows that currents with a length scale of the order of the internal Rossby radius radiate the most energy, about $0.05\mathcal{E}$. Generally energy lost from a system is attributed to energy carried away by gravity waves in geostrophic adjustment problems. Gravity waves do not exist in this problem because of the rigid top and bottom. However, gravity waves do exist at higher orders in the pertubation expansion to the problem discussed in the introduction. The fact that the energy lost is a small fraction of that present in the current leads me to suspect that the mechanism of energy loss is a higher order effect.

It is at the important scale of $\epsilon = O(1)$ that we shall examine qualitatively how energy is distributed within the system. Let $\epsilon = 1$. Convective mixing raises denser fluid and lowers lighter fluid. It increases APE by $0.20\mathcal{E}$. KE suffers a corresponding decrease of about $0.20\mathcal{E}$. No net energy is lost or gained. Since it is the momentum and density that are mixed and conserved during the mixing process, the system could have gained or lost energy at this stage. In fact, the system will gain energy when $\epsilon > 1$ and lose energy when $\epsilon < 1$. During adjustment for $\epsilon = 1$, about $0.10\mathcal{E}$ APE is lost; of this, $0.05\mathcal{E}$ is converted into KE and $0.05\mathcal{E}$ is lost as gravity wave radiation. The combination of both processes shows that the overall effect of cooling on the system is to increase APE by $0.10\mathcal{E}$, decrease KE by $0.15\mathcal{E}$, and thus decrease the TE by $0.05\mathcal{E}$. Geostrophic adjustment causes the system to lose energy. Convective mixing dominates how energy is redistributed within the system and transforms KE into APE.

3. Conclusions

In this paper, the effects of cooling a shallow baroclinic current were examined. For the model of a current depicted in figure 3, the final state will consist of a region of stratified fluid sandwiched between the two homogeneous layers. The isopycnals in the stratified region will have slopes given by (2.7). Their slopes are proportional to the slope of the initial interface between the two upper layers, $\frac{H_0}{L_0}$, and become progressively steeper as $\epsilon = \frac{L_0}{L_D}$ increases. The interfaces between the stratified region and the homogeneous regions are straight lines with slopes given by (2.17). They are always steeper than the isopycnals but never more than twice as steep. Fronts exist across the interfaces and are only sizable for $\epsilon \not\ll 1$. Velocities in excess of v_i occur near the surface on both sides of the front along the right hand interface. Negative velocities are present near the bottom interface on both sides of the front along the left hand interface. Both of these effects grow stronger as ϵ increases.

Little energy is lost by the current if its initial length scale is not of the order of the internal Rossby radius. The greatest amount of energy will be lost by the current if

$\epsilon = 1.8$. In that case, about 6.8% of the total available energy present in the current will be lost. Even though kinetic energy is gained and available potential energy is lost through adjustment, for $\epsilon = 1$ the kinetic energy of the final state is less than that initially present in the current. There is a proportional gain in availible potential energy. The effect of convective mixing in this model is to convert kinetic energy to potential energy. Convective mixing, and not geostrophic adjustment, dominates the way energy is redistributed within the current.

At this point there is still much work that can be done with this model. The asymptotic expansion in terms of $\Delta^{\frac{1}{2}}$ remains to be completed. In addition, the equations for the flexible bottom boundary case can be numerically integrated to find the solution in instances where $\Delta^{\frac{1}{2}} \not\ll 1$. There is still some question as to whether density can vary along the interfaces since, prior to adjustment, the interfaces were material surfaces. However, perhaps we should question whether the interfaces really are material surfaces because of the discontinuities in density and momentum gradients which existed prior to adjustment. If this is true, careful investigation of the frontal region needs to be done and matching of solutions will need to take place between it and the interior of the stratified region. On the other hand, suppose we insisted that the interfaces are isopycnals. One must then choose between discarding either shallow water potential vorticity conservation or M and ρ conservation. It has been suggested that shallow water potential vorticity conservation does not hold during the adjustment process. For example, perhaps the horizontal velocities becomes z dependent during adjustment. Whether or not this is true and what relation might replace shallow water potential vorticity conservation are presently under investigation. Shallow water potential voricity has been frequently used to consider adjustment problems in the past, but the curious nature of the model presented in this paper, one in which homogeneous and stratified regions of fluid are interacting, may render it invalid.

References

Blumen, W., and R. Wu, 1995. Geostrophic adjustment: Frontogenesis and energy conversion. *J. Phys. Oceanogr.*, **25**, 428-438.

Gill, A., 1982. *Atmosphere-Ocean Dynamics.* Academic Press, 662pp.

Ou, H.W., 1984. Geostrophic adjustment: A mechanism for frontogenesis. *J. Phys. Oceanogr.*, **14**, 994-1000.

Rossby, C.G., 1937. On the mutual adjustment of pressure and velocity distribution in simple current systems, 1. *J. Mar. Res.*, **1**, 15-28.

Rossby, C.G., 1938. On the mutual adjustment of pressure and velocity distribution in simple current systems, 2. *J. Mar. Res.*, **1**, 239-263.

Stommel, H. and G. Veronis, 1980. Barotropic response to cooling. *J. Geophys. Res.*, **85**, 6661-6666.

Wu, R. and W. Blumen, 1995. Geostrophic adjustment of a zero potential vorticity flow initiated by a mass imbalance. *J. Phys. Oceanogr.*, **25**, 439-445.
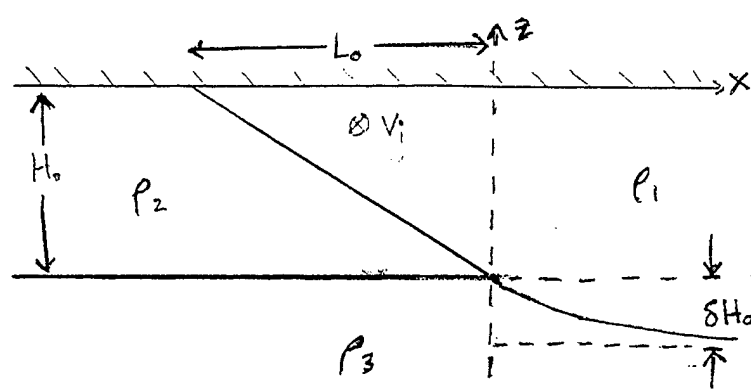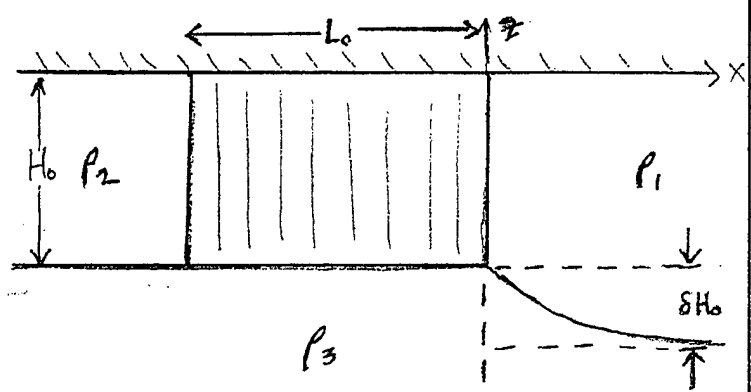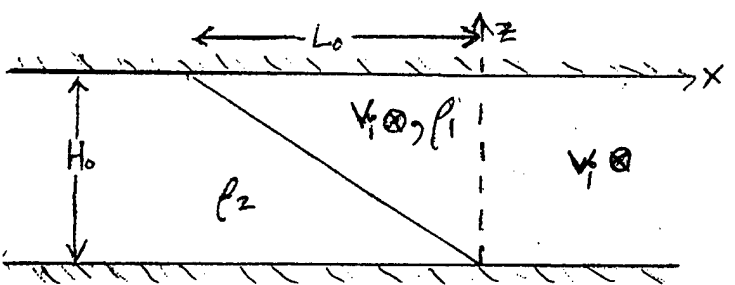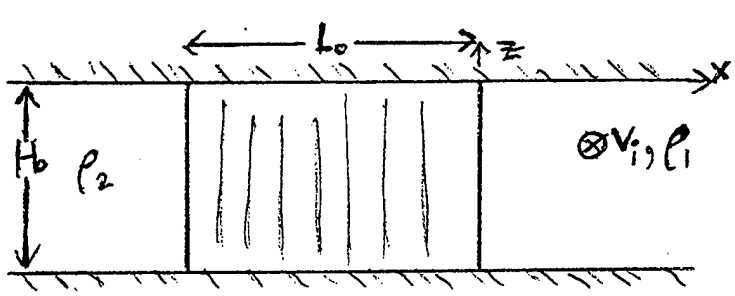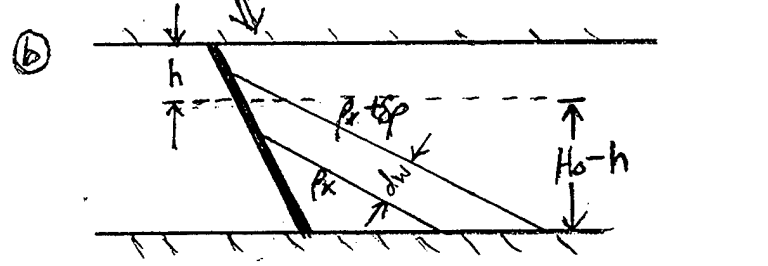
FIGURE #1

FIGURE #2

FIGURE #3

FIGURE #4

FIGURE #5

FIGURE #6

total energy lost during adjustment
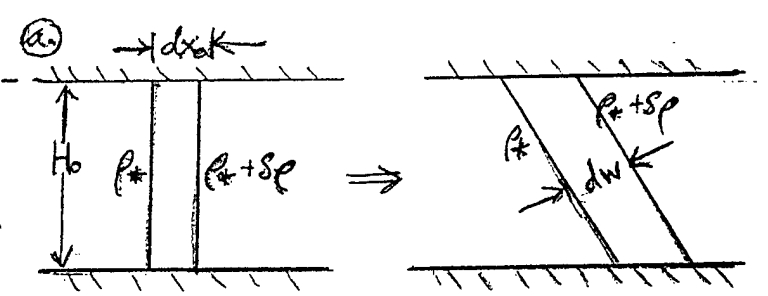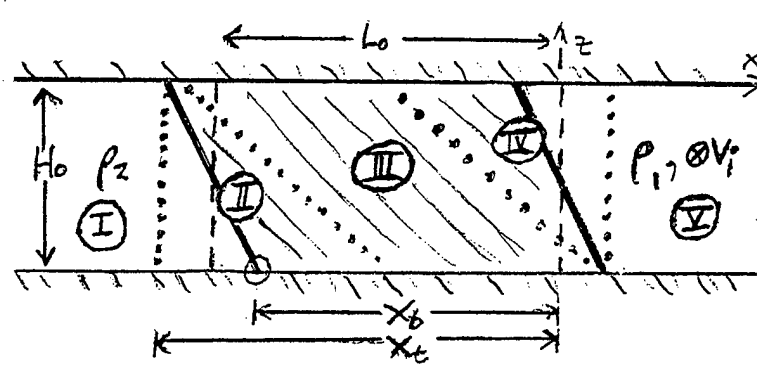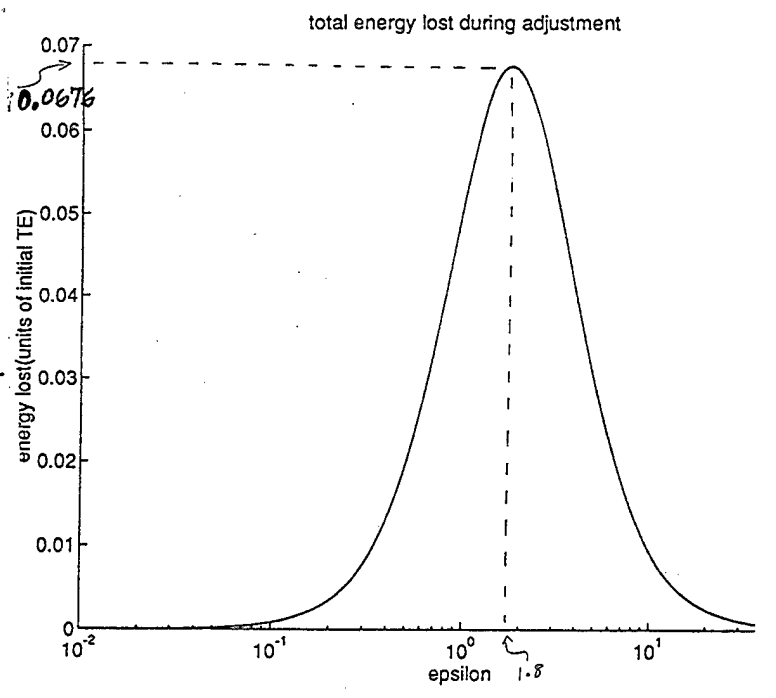
FIGURE #8

DENSITY: $\rho_1 + \Delta\rho\,\rho'$
CONTOURS OF ρ' ARE PLOTTED
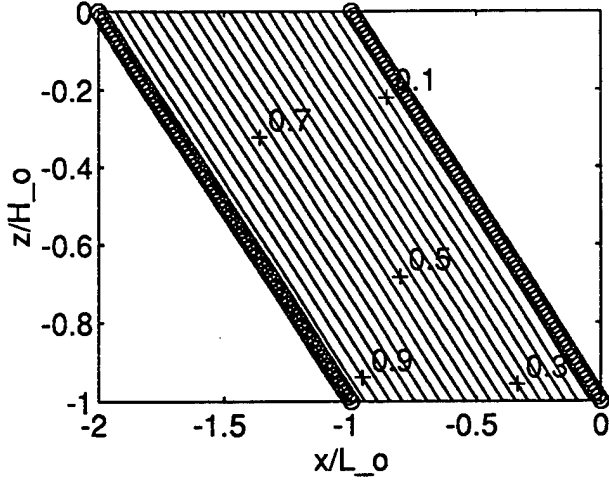
VELOCITY: $V = V_0\,v'$
CONTOURS OF v' ARE PLOTTED
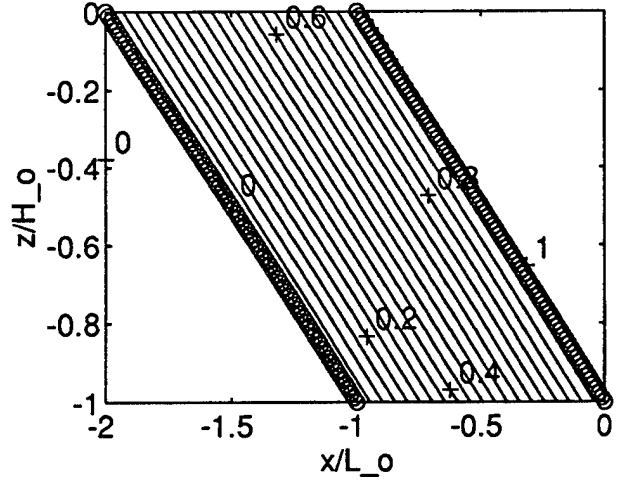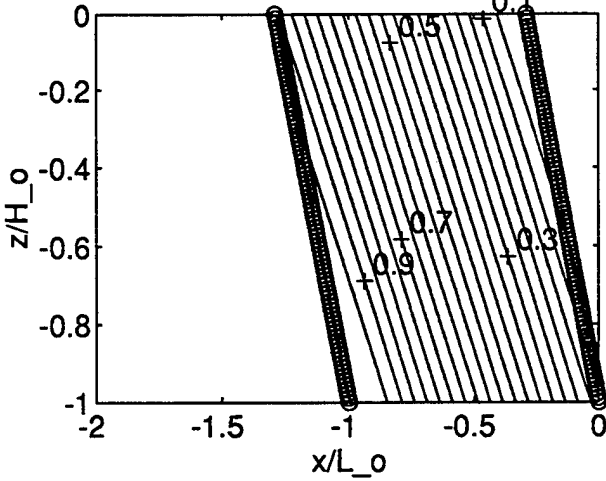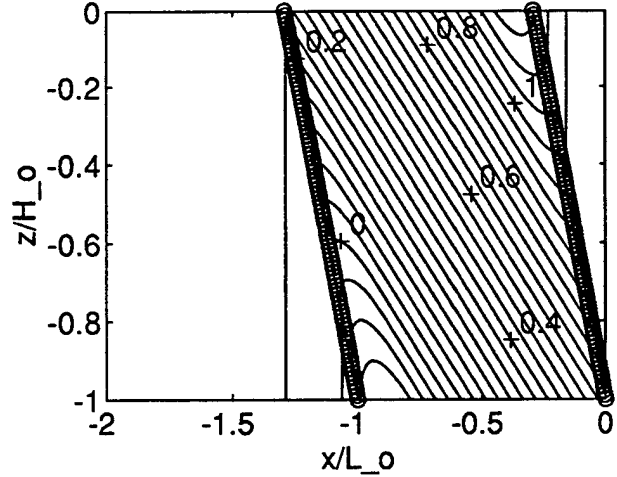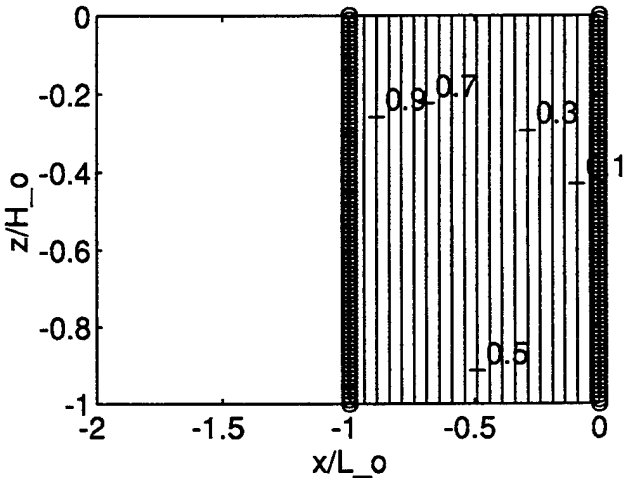
FIGURE #7

INDICATE INTERFACES BETWEEN STRATIFIED AND HOMOGENEOUS FLUID

Maximizing Passive Vector Stretching

Vachtang Putkaradze

Edward A. Spiegel

I. INTRODUCTION

G. I. Taylor claimed that the most important characteristic of turbulence is the stretching of the vortex lines. Hence, one can perceive the exponential stretching rate λ_{str} of the vortex lines as the "measure" of turbulence. Batchelor's hypothesis [1] assumes that the average length of the vortex lines increases exponentially with time:

$$< \mathcal{L}_\omega > \sim e^{\lambda_{str}t} \tag{1}$$

where $< \cdot >$ means a space average. Cocke [2] has proved that for isotropic turbulence the length of the vortex lines increases with time, but the question of the validity of (1) is still open.

One can imagine that, the larger the stretching rate λ_{str}, the more turbulent the fluid motion becomes in the "G. I. Taylor sense". The vorticity stretching rate λ_{str} is, of course, a functional of the velocity field $v(x,t)$: $\lambda_{str} = \lambda_{str}(v)$. We can try to maximize $\lambda_{str}(v)$ with respect to some class of vector fields v, say, with respect to all fluid motions. The condition $\delta\lambda_{str}(v) = 0(+$ constraints$)$ on the vector field v will give us an equation (in general, an evolution equation) for v. This will be "the most turbulent equation" in the aforementioned sense. If we can find a solution v satisfying $\delta\lambda_{str}(v) = 0$ and the constraints corresponding to a maximum, we shall be able to put an upper estimate on the stretching rate $\lambda_{str} \leq \lambda_{max} = \lambda(v_{max})$.

One should note, however, that it is difficult (perhaps impossible) to compute the functional $\lambda_{str}(v)$ analytically. However, if we simplify the pro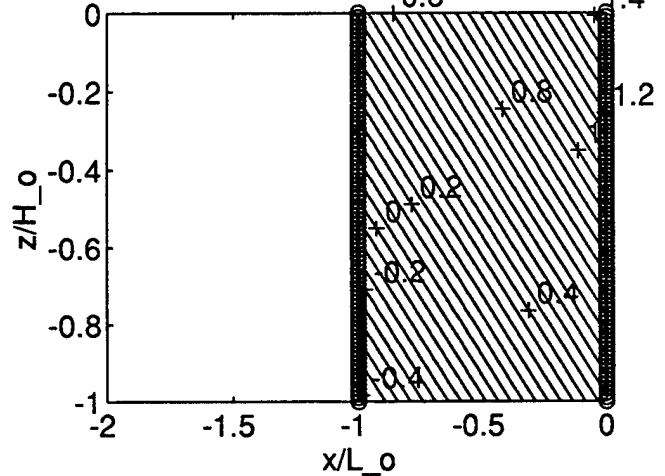blem, it will be possible to find the solution v of the variational problem $\delta\lambda_{str}(v) = 0(+$constraints$)$. Namely, we consider the case when the velocity field v is evolving independently of the vorticity field ω. In such a case, the vorticity ω is a "passive vector" which evolves according to the equation (the Lie derivative)

$$\omega_t + [v, \omega] = 0 \tag{2}$$

where the subscript t denotes the time derivative and

$$[v, \omega] = (v \cdot \nabla)\omega - (\omega \cdot \nabla)v$$

is the commutator of the vector fields ω and v. The velocity field v is a solution of some evolution equation, where ω is not present. One can say that v "does not know" that ω exists.

We would like to compute the stretching of the vortex lines of ω. However, the length of the vortex lines is a cumbersome functional. A more easily tractable function which is still connected with the vorticity is the "enstrophy"

$$I(t) = \int \omega(x,t)^2 dx. \tag{3}$$

The functional $I(t)$ will, in general, grow exponentially on average:

$$< I(t) > \sim I_0 e^{\lambda t} \tag{4}$$

where I_0 depends on the initial conditions for ω, but the growth rate λ depends only on v. In a real fluid, v and ω are connected by

$$\omega = \nabla \times v. \tag{5}$$

Equation (5) connects the evolution equations for v and ω. That means that v is no longer independent of ω and the latter becomes an *active* vector.

Our goal will be to find a vector field $v(x, t)$ such that it generates large ω according to the evolution equation (2). However, without imposing any constraints on the vector field v, the maximum growth rate in (4) will be infinite. Therefore, we will try to impose "good" constraints on the vector field v. If the constraints imposed are too weak, the maximum value will be infinite. If the constraints are too strong, there can be no extremal solution at all, except for the trivial one $v = 0$. Therefore, we shall attempt to find a sort of "golden mean" for the constraints.

Now we can formulate the problem in precise terms.

Problem 1 *Maximize the functional (3) or the growth rate $\lambda(v)$ subject to the evolution equation (2), given that ω is an active vector, i.e. (5). Find the relevant constraints.*

The solution of problem 1 was the ultimate goal of our study. However, we were not able to make substantial progress without the "passive vector" simplification, i.e., dropping the requirement (5) and thus decoupling v from ω. Problem 1 will be subject to further investigations.

The rest of this report will be devoted to:

Problem 2 *Maximize the functional (3) or the growth rate $\lambda(v)$ subject to the evolution equation (2), given that ω is a passive vector, i.e., (5) is absent. Find the relevant constraints.*

Problem 2 will be the main subject of the paper. We shall reduce it to a sequence of smaller sub-problems, which will build a ladder towards the solution of problem 2.

II. POINCARE MAP

Suppose we perform a convection experiment in a rectangular box of height h. The velocity field is v and it generates a *passive* vector according to (2).

Let us mark a horizontal plane at $z = h/2$ and follow the lagrangian trajectories starting from this plane with the coordinates (x_0, y_0). Suppose the flow is stationary. After some time t_1 this lagrangian trajectory will cross the plane $z = h/2$ at the point (x_1, y_1), then at time t_2 at the point (x_2, y_2) and so on. Therefore, we have a map (Poincare map):

$$(x_0, y_0) \to (x_1, y_1) \to (x_2, y_2) \to \dots$$

or, in short notation,

$$(x_{n+1}, y_{n+1}) = P(x_n, y_n), \tag{6}$$

where P denotes the Poincare map. Usually, the precise form of the map P is difficult to determine analytically.

The map (6) is two-dimensional if the flow is 3-dimensional. However, in the case when there is strong contraction in one dimension, the long-term trajectories for the system (6) will collapse onto some one-dimensional curves. In fact, let us suppose that the map (6) looks like

$$x_{n+1} = f(x_n, y_n)$$

$$y_{n+1} = \lambda y_n.$$

(7)

The function $f(x_n, y_n)$ is some nonlinear function of both arguments and $|\lambda| < 1$. The second equation of (7) is readily solved: $y_n = y_0 \lambda^n$. As $n \to \infty$, the y-component will become exponentially small and then, with exponentially good accuracy, the first equation of (7) reduces to a one-dimensional map

$$x_{n+1} = f(x_n, 0) = f(x_n).$$

(8)

In this case the two-dimensional dynamics has collapsed onto the line $y = 0$. However, the resulting collapsed set ("attractor") may not be that simple and the appearing curves may be arranged in a complicated way. As an example of the sophisticated geometry of an attractor, one can consider the Henon map [6].

III. TOPOLOGICAL ENTROPY FOR ONE-DIMENSIONAL MAPS

For one-dimensional maps, there is a characteristic which is closely connected with the growth rate we are interested in, namely, the topological entropy. Suppose we consider a one-dimensional map $x_{n+1} = f(x_n)$. There are several equivalent definitions for the topological entropy:

Definition 1 *The topological entropy h of the map $x_{n+1} = f(x_n)$ is the growth rate of the length of the graph of the n-th iterate of f as $n \to \infty$.*

That is, $\mathcal{L}(f^n) \sim e^{hn}$ for large n, where $\mathcal{L}(f)$ is the length of the graph.

Definition 2 *The topological entropy h of the map $x_{n+1} = f(x_n)$ is the growth rate of the number of periodic orbits of the n-th iterate of f as $n \to \infty$.*

That means $\mathcal{N}(f^n) \sim e^{hn}$ for large n, where $\mathcal{N}(f^n)$ is the number of periodic points. (Note: everywhere f^n will mean the n-th iterate of the map f, i.e $f(f(f(\ldots)))$ and *not* the n-th power of f^n.)

For example, consider the map $x_{n+1} = (x_n) \bmod \Lambda$, Λ being some positive number. The graph of the n-th iterate consists of the broken pieces of the line with the slope Λ^n. The length of the graph of the function $y = y(x)$ is $\mathcal{L}(y) = \int \sqrt{1 + y'^2(x)} dx$. In the case of the map $x_{n+1} = (x_n) \bmod \Lambda$, the length of the graph of the n-th iterate $y = f^n(x)$ is $\mathcal{L}(f^n) = \sqrt{1 + \Lambda^{2n}}$. We see that $h(f) = \log \Lambda$ for $\Lambda > 1$ (hence h is positive) and $h = 0$ for $0 < \Lambda < 1$. In general, if the topological entropy is positive, the system is chaotic.

A very important property of the topological entropy of a flow is that it bounds the exponential growth rate of the passively advected vector field (4). If the Poincare map of a flow v has an entropy h, then the growth rate of ω according to (2) will not exceed h (see [3]).

The topological entropies for a flow and for the resulting Poincare map are the same (for sufficiently nice flows). This is true when all the return times for the Poincare maps have more or less the same order of magnitude. In this case taking the limit $t \to \infty$ for the flow will be equivalent to taking the limit $n \to \infty$ for the map. We shall assume that this is the case and consider the entropies for the Poincare maps.

IV. TIME-DEPENDENT PERIODIC MAPS

From a magnetodynamo example [3], we know that the time-dependent flows are much more efficient as dynamos then the time-independent flows. We shall try to investigate this phenomenon in terms of maps by including the periodic time-dependence.

If the flow is time-periodic, one can "strobe" the flow. That is, if the flow has a period T, we follow the lagrangian trajectories for the time T. That will generate a map from a point in space to some other point in space. However, contrary to the Poincare map, the iterates will not lie in the same plane $z = h/2$ as before, but will be scattered all over the physical space. Thus, the resulting map S will be three-dimensional:

$$(x_{n+1}, y_{n+1}, z_{n+1}) = S(x_n, y_n, z_n). \tag{9}$$

We can think of modeling such a map with a time-dependent low-dimensional map. For example, the lagrangian trajectories for the convective solutions found by G. Veronis [5] go up and down in time periodically. Then, the evolution z coordinate of the lagrangian trajectory can be approximated by the periodic motion. Say, for the stroboscope map we put $z_n = z(n \bmod N)$, N being the period. Then, (9) becomes a two-dimensional time-dependent map

$$(x_{n+1}, y_{n+1}) = S(n \bmod N, x_n, y_n). \tag{10}$$

In the limit of strong contraction we obtain the one-dimensional time-dependent map

$$x_{n+1} = f(x_n, n \bmod N) \tag{11}$$

where n is an integer. To construct a visual representation of such a system, we shall apply the checkerboard technique derived in [4]. Let us say f_i is defined on the interval $(0,1)$ for each i. Then, the phase space of the system (11) consists, so to speak, of N intervals. Hence, we can then represent the system (11) by drawing a square $(0,N) \times (0,N)$. Then we divide the x and the y-axis into N intervals. Next, we draw the graph of $f_1(x)$ in the first column and the second row. We shall denote this square $(2,1)$. Next, we draw the graph of the function f_2 in square $(2,3)$, the graph of f_i in square $(i, i+1)$ for $1 \le i \le N-1$, and the graph of f_N in $(N,1)$ square $(N,1)$. We then get the function $F(x)$ defined on the interval $(0,N)$. If we iterate $F(x)$ and take $x \bmod 1$, we obtain the correct dynamics. This construction is illustrated in figure 1.
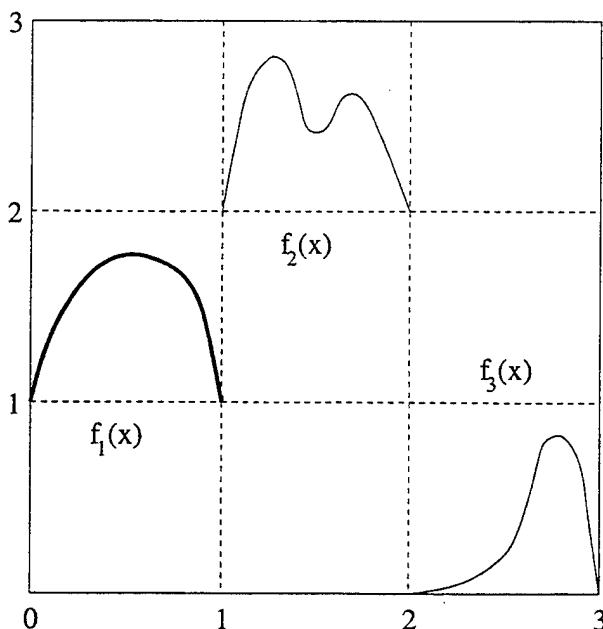
FIG. 1. Checkerboarding of a time-dependent map

One can see that the N th iterate of F splits into N diagonal squares. In the i-th window we will have the function $f_i \circ f_{i+1} \circ \cdots \circ f_n \circ f_1 \circ f_{i-1}$. Since the topological entropy is the growth rate of the length of the graph, the topological entropy of the function f (and, therefore, the time-dependent map itself) will coincide with the maximum of the topological entropies of these compositions. One can show, however, that all these compositions obtained by the cyclic permutations, have the same topological entropy, hence

$$h(f) = h(f_1 \circ f_2 \circ \cdots \circ f_N).\tag{12}$$

V. TURBULENCE ENHANCEMENT BY TIME-DEPENDENCE

We want to study why the time-dependent maps are more efficient in generating entropy then the time-independent ones. Suppose we take $N = 2$ in (12). That is, we first apply the map f_1, then f_2, then f_1 and so on. Suppose the maps f_1 and f_2 are non-chaotic: $h(f_1) = h(f_2) = 0$. Now, we want to study the following problem:

Problem 3 *What is the maximum entropy of $h(f_1 \circ f_2)$ one can obtain by composing the two maps f_1 and f_2 subject to the constraint $h(f_1) = h(f_2) = 0$? Is this constraint sufficient for the variational problem to be well-posed? If it is not, find the relevant constraints.*

We shall show now that the constraint $h(f_1) = h(f_2) = 0$ is not enough for solving this variational problem: the maximum is infinite.

The following functions f_1 and f_2 on the interval $(0, 1)$ are considered:

$$f_1 = \begin{cases} \frac{1}{2} + \frac{x}{\Lambda_1}, & 0 < x < \frac{1}{2} \\ (\Lambda_1 x - \frac{1}{2}) \bmod \frac{1}{2}, & \frac{1}{2} < x < 1 \end{cases}\tag{13}$$

and

$$f_1 = \begin{cases} \frac{1}{2} + (\Lambda_2 x - \frac{1}{2}) \bmod \frac{1}{2} & 0 < x < \frac{1}{2} \\ \frac{x}{\Lambda_2} & \frac{1}{2} < x < 1 \end{cases}\tag{14}$$

for arbitrary numbers $\lambda_1 > 1$ and $\lambda_2 > 1$. The graphs of the functions in question are drawn in figure 2.
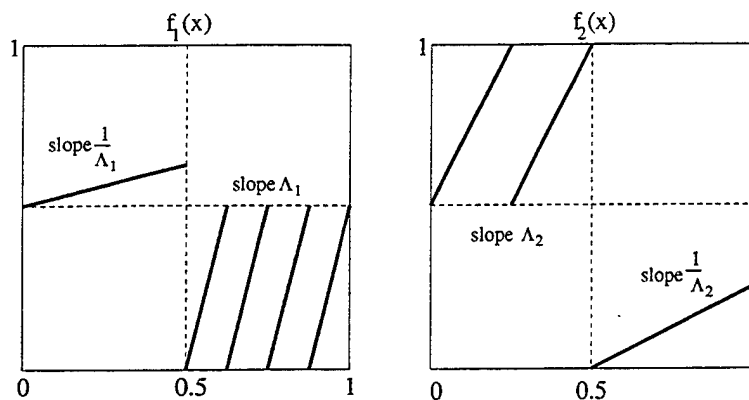

FIG. 2. The maps f_1 and f_2 which are the solutions to problem 3

One can verify that both these functions have zero entropy since they generate pieces of the line with the slope 1. Hence, for any even iterate of these functions the length of the graph will be $\sqrt{2}$ and the entropy is, therefore, zero. However, after taking the composition of these maps, the two "active" regions (i.e the regions with slopes larger than 1) will interact independently. Hence, there will be a region in the space of size $1/2$ where for the n-th iterate the slope will be $(\Lambda_1 \Lambda_2)^n$. Hence, for large n the length of the graph of the n-th iterate of $f_1 \circ f_2$ will be $(\Lambda_1 \Lambda_2)^n / 2$ (with exponentially good accuracy in n) and the entropy of the composite map $f_1 \circ f_2$ is therefore

$$h(f_1 \circ f_2) = \frac{\log \Lambda_1 + \log \Lambda_2}{2}. \tag{15}$$

Since the numbers Λ_1 and Λ_2 are arbitrary, the resulting entropy $h(f_1 \circ f_2)$ can be arbitrary large.

We see that a constraint stronger then $h(f_1) = h(f_2) = 0$ is necessary to obtain a meaningful result.

So far, we have allowed any functions f_i. However, these function have to emerge as Poincare maps of some physical flow. Therefore, the gradients of these functions have to be bounded. A relevant constraint is, therefore,

$$\max_x |f_i'(x)| \leq K. \tag{16}$$

We can show that with the constraint (16) the entropy $h(f_1 \circ f_2)$ can be maximized, and the functions f_1 and f_2 defined by (13-14) then define the exact maximum.

In fact, in this case we can put $\Lambda_1 = \Lambda_2 = K$, and $h(f_1 \circ f_2) = \log K$. on the other hand, the length of the graph of $(f_1 \circ f_2)^n$ (n-th iterate) is given by the chain rule:

$$\mathcal{L}((f_1 \circ f_2)^n) = \int \sqrt{1 + f_1'^2(x_{2n}) f_2'^2(x_{2n-1}) f_1'^2(x_{2n-2}) \cdots f_1'^2(x_1) f_2'^2(x_0)} \, dx$$

and due to the constraint (16) this length is estimated from above as

$$\mathcal{L}((f_1 \circ f_2)^n) \leq \int \sqrt{1 + K^{2n}} \leq 2K^n$$

and therefore, $h(f_1 \circ f_2) \leq lnK$. Hence, we have found functions providing the exact maximum for problem 3 with the constraint (16).

Suppose now our Poincare map comes from a vector field v, which oscillates very little around some stationary vector field. In this case, the two succesive maps maps f_1 and f_2 cannot differ by more than some small number ϵ:

$$\max_{0 \leq x \leq 1} |f_1(x) - f_2(x)| \leq \epsilon. \tag{17}$$

This will impose a constraint on the time derivative of the vector field.

Will imposing the constraint (17) improve the result? The answer is no. Of course, if $\epsilon = 0$, the maps f_1 and f_2 have to be the same and, hence, $h(f_1 \circ f_2) = h(f_1) = 0$. However, as soon as $\epsilon > 0$, we can construct the maps such that $h(f_1) = h(f_2) = 0$, $max_x |f_1(x) - f_2(x)| \leq \epsilon$ but the entropy of the composite map $f_1 \circ f_2$ can be arbitrarily large. Again, with the constraint (16), the maximum of the entropy of $f_1 \circ f_2$ is $h = \log K$.

The maps in question appear as in figure 3 (we only show the picture, since we find the formulas to be hardly illustrative).
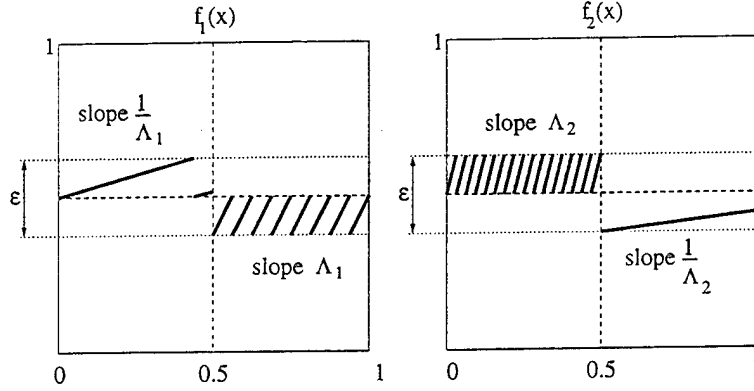
FIG. 3. The maps f_1 and f_2 differ by no more then ϵ

The length of the graph of the n-th iterate of the composition $f_1 \circ f_2$ is

$$\mathcal{L}(f_1 \circ f_2)^n \simeq \epsilon (\Lambda_1 \Lambda_2)^n.$$

Therefore, however small the value of ϵ, the entropy is still given by (15). One should notice that the "active" region has a size proportional to ϵ. Hence, restrictions of the type (16) are needed to obtain a maximum for the entropy.

The examples given in this chapter also explain why one can get more entropy by introducing the time-dependence. For example, the famous stretch-twist-fold [3] consists of simple non-chaotic transformations. The entropy is generated in the process of succesive compositions of stretch, twist and fold.

VI. THE FORMAL SOLUTION OF PROBLEM 2

The examples of the previous chapter have taught us that the only relevant constraint is the bound on the spatial gradient $\|\nabla v\| \leq K$. We shall use this constraint together with the incompressibility condition $\nabla \cdot v = 0$ to obtain a formal solution for problem 2. In fact, incompressibility is not essential for an answer, but we include it in order to remain close to the original problem.

Problem 4 *(Problem 2 modernized) Maximize the functional (3) and the growth rate $\lambda(v)$ subject to the evolution equation (2), given that ω is a passive vector, i.e., (5) is absent. Use the constraints:*

$$\|\nabla v\| \leq K \tag{18}$$

together with

$$\nabla \cdot v = 0. \tag{19}$$

Multiply equation (2) by ω and integrate with respect to the space coordinates. Then, the following equation holds:

$$\frac{d}{dt} \int \omega^2 dx = \int \omega^t \cdot \nabla v \cdot \omega \tag{20}$$

where ω^t is the transposed vector ω. Then, since the norm of a matrix is K, we have $\|\nabla v \cdot \omega\| \leq K\omega$, and from (20) follows the inequality:

$$\frac{d}{dt} \int \omega^2 dx \le K \int \omega^2 dx. \tag{21}$$

Therefore the exponential growth rate of enstrophy is no more than K. We wish to find the vector field v which generates a growth rate equal to K.

We consider the vector field v, which generates the area-preserving "baker's transformation" with coefficient K after $t = 1$ sec in the lagrangian coordinates (x, y) if $-1 \le x, y \le 1$ and does not change the coordinates z and x, y for $|x|, |y| \ge A$ for some $A > 1$ (for the description of the baker's transformation and its properties, see [6]). The transformation is shown in figure 4
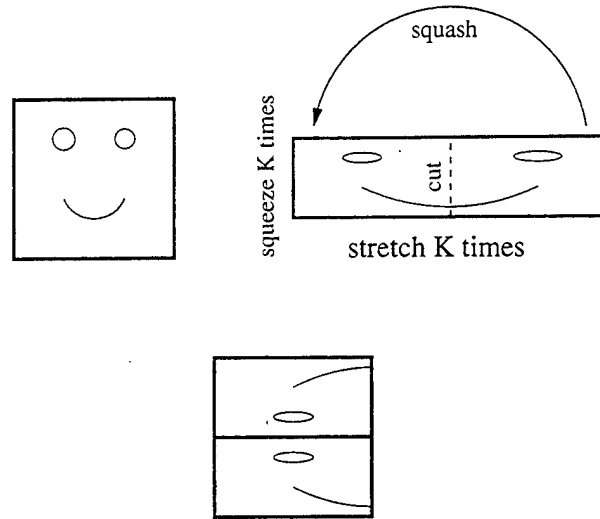
FIG. 4. The area-preserving baker map with coefficient K

Equation (2) can be integrated exactly if the transformation from the old to the new lagrangian coordinates is known. If $\mathbf{x(t)}$ is the solution of the equation $\dot{\mathbf{x}} = \mathbf{v}$ with the initial condition $\mathbf{x}(0) = \mathbf{x_0}$, and $\mathbf{j} = \frac{\partial \mathbf{x}}{\partial \mathbf{x_0}}$ is the jacobian, the solution of (2) is given by

$$\omega(\mathbf{x}, \mathbf{t}) = \omega(\mathbf{x}, \mathbf{t}) = \mathbf{j}\omega(\mathbf{x_0}, \mathbf{0}). \tag{22}$$

From (22) it follows that the x- component of the vorticity evolves according to

$$\omega_x(x, y, z, t) = e^{Kt}\omega_x(x_0, y_0, z, 0)$$

Assuming that the initial distribution is uniform within the rectangle $-1 \le x, y \le 1$, the x-component of the initial vector grows with the exponent K. Therefore, the flow v generating a baker map with the coefficient K is a solution of the variational problem 4.

VII. CONCLUSIONS

Our solution allows us to draw some conclusions about Batchelor's hypothesis. Namely, we have maximized the dynamic exponent with respect to the constraint $\|\nabla v\| \le K$. The interesting point would be, of course, to maximize the "enstrophy" with respect to the equation of fluid motion, that is, the Navier-Stokes equation. However, the Navier-Stokes equation implies that the velocity gradients remain bounded (this has at least been proved for two-dimensional flows; for three-dimensional flows the proof is still missing). The rigorous

bound is $\|\nabla v\| \leq R^2 \log R$ [7], where R is the Reynold's number. Therefore, the upper bound for the exponent in Batchelor's hypothesis is $\lambda \leq R^2 \log R$. Of course, this estimate is much too large due to the fact that the rigorous estimates are usually too far from the truth.

We are now undertaking investigation of Problem 1, when the vorticity is the "active vector". It is our hope that maximizing a functional of the type (4) with respect to the constraints which are moments of the Navier-Stokes equation and the coupling equation (5), will define a reasonably good evolution equation for the vector field v.

VIII. ACKNOWLEDGEMENTS

[1] Batchelor, G., K., The Effect of Homogenious Turbulence on Material Lines and Surfaces, *Proc. Roy. Soc. (London)*, **A213**, 349-366 (1952).

[2] Cocke W. Y., Turbulent Hydrodynamic Line Stretcing: Consequnces of Isotropy *Phys. Fluids*, **12**, Part 1, 2488-2492 (1969)

[3] Childress S. and Gilbert A., Turbulent Dynamos: Stretch-Twist-Fold *Springer*, in press.

[4] Balmforth N. J., Tresser C., Spiegel E. A., Checkerboard maps *Chaos* 5(1), (1995)

[5] Veronis G., Cellurar convection with finite amplitude in a rotating fluid *J. Fluid Mech.*, **5** 401-35 (1959)

[6] Ott E., Chaos in Dynamical Systems *Cambridge Univ. Press,* (1993).

[7] Rose H.A and Sulem P.L, *J. de Physique*, **39** p.441 (1978).

Circulation in a 2D convective chimney   F. Straneo

Introduction

Deep convection is thought to occur in the ocean via various mechanisms. Amongst these, convective chimneys have been observed in several regions including the Gulf of Lyons and the Labrador Sea. Convection within a chimney occurs via plumes whose horizontal scales are on the order of 1 km and timescales of a few hours (Schott and Leaman, 1991, and J. Marshall, in this volume). Whereas the chimney can measure 10-100km in diameter, reach depths on the order of thousands of metres and persist for periods on the order of days to weeks.

The evolution of a chimney involves preconditioning phase, where the large scale circulation sets the horizontal scale of the chimney, a violent mixing phase and the subsequent sinking collapse of the whole structure through baroclinic instability mechanisms (see John Marshall's lectures). A number of numerical and laboratory experiments confirm these hypothesis (see, for example, Jones and Marshall, 1993, and Maxworthy and Narimousa, 1994).

In this study, an attempt is made to determine the circulation inside and around a chimney which is slowly growing due to surface heat loss. The convective scales, such as the plumes, are not resolved; instead, the mixing processes are parametrized by introducing a vertical eddy diffusivity which is dependent on the stratification. When the water column is unstably stratified, the action of the plumes (i.e. the mixing of both momentum and buoyancy) is represented through an artificially high diffusivity and viscosity. Typical eddy-diffusivity values are retained for regions of stable stratification.

A discussion of this parametrization is presented in section 1, together with a solution for a one-dimensional chimney model. Scaling of the equations is described in section 2; this includes presenting a balance model and actual values for a typical oceanic chimney. Section 3 illustrates a number of approximate solutions for the chimney problem, amongst these the extension of the 1D solution to the 2D problem. In the last section, the validity of the assumptions and the results are discussed.

1   A chimney parametrization

1.1   An introduction to a variable diffusivity

Observations of temperature and salinity profiles within a chimney show an almost vertically homogeneous water mass, with slight gradients in the horizontal (U. Send personal communication). The horizontal scale of the chimney is thought to be set by pre-existing large scale circulation features, typically a cyclonic gyre that causes doming of the isopycnals. The depth to which the chimney extends mainly depends on the stratification and the cooling rate.

In this study, the horizontal scale of the chimney is set by the scale of the surface

heat-flux. In the case of linear stratification, which will be used throughout this work, this is equivalent to applying a constant heat flux to a non-uniform (in the horizontal) initial stratification, i.e. the preconditioning. The action of the plumes, the mixing of momentum and buoyancy, is obtained through a large value of the diffusivity and viscosity.

Figure 1a shows a qualitative description of the diffusivity, $\kappa = \kappa(b_z)$, as a function of the buoyancy, b. This allows us to identify three different regions depending on the value of $\kappa(b_z)$, which are schematically shown in figure 1b.

- *Interior Region:* This is a region of unstable stratification where the plumes are active. κ is assumed to be large and constant, $\kappa \approx \kappa_1$. The isotherms are almost vertical due to the mixing.

- *Transition zone:* This corresponds to the region of varying κ, and it describes the edge of the chimney. Here the isotherms bend: from the almost homogeneously vertically-mixed chimney to the horizontally stratified surroundings.

- *Exterior Region:* In this region κ resumes its low eddy diffusivity value, as used in models which do not resolve the eddies' scales. It represents the surroundings of the chimney which are vertically stratified.

This physical argument only provides a qualitative description of κ, and there is *a priori* no reason for choosing one particular form with respect to another. The criterion used in this work was to find a form of the diffusivity that would make the problem solvable analytically.

1.2   One-dimensional Problem

As an introduction to the problem, a simple 1D column of water is considered with a step function diffusivity. The column is initially stably stratified (linear stratification) when a constant heat flux (cooling) is applied at the surface. As the water columnn becomes unstably stratified, convection begins to take place. The depth to which convection penetrates increases as the cooling persists. The evolution of the system is given by a one-dimensional diffusion equation with variable diffusivity coefficient.

$$b_t = \partial_z(\kappa b_z) \tag{1}$$

In this preliminary analysis, a simple form of κ is assumed:

$$\kappa = \begin{cases} \kappa_1 & \text{for } b_z \leq 0 \\ \kappa_0 & \text{for } b_z > 0 \end{cases}$$

where $\kappa_1 \gg \kappa_0$. Let $z = -h(t)$ describe the depth of the quasi-mixed layer (the depth to which convection takes place), i.e. $b_z > 0$ for $z < -h(t)$. The two regions, corresponding to different values of κ may then be solved separately and $h(t)$ may be

determined by imposing the continuity of b at the interface.

Region 1: $b_t = \kappa_1 b_{zz}$, with $b_z = Q/\kappa_1$ at $z = 0$ and $b_z = 0$ at $z = -h(t)$

Region 2: $b_t = \kappa_0 b_{zz}$, with $b_z = 0$ at $z = -h(t)$ and $b_z = N^2$ as $z \to -\infty$

1.3 Non-dimensional form of the equations

Let $t = T\bar{t}$, $b = N^2 H\bar{b}$ and $h = H\bar{h}$, where the bars indicate the non-dimensional fields. The buoyancy has been scaled by the initial stratification.
Region 1: The equation in can be written as

$$\epsilon \bar{b}_{\bar{t}} = \bar{b}_{\bar{z}\bar{z}}$$

where $\epsilon = \frac{H^2}{T\kappa_1}$ is the ratio of the mixing time to the time over which b varies. Let κ_1 be chosen such that $\epsilon \ll 1$, and a solution found by expanding in powers of ϵ. The flux boundary condition is written as $q = \kappa_1 N^2 \epsilon \bar{q}$, which implies that if Q is the scale for q then $Q/(\kappa_1 N^2) \ll 1$. The solution of the diffusion equation in powers of ϵ, having dropped the bars, is :

$$b(z,t) = b_0(t) + \epsilon(\frac{b_{0t}z^2}{2} + qz), \text{ and } b_{0t} = \frac{q}{h}$$

Region 2: The fluid is initially stably stratified, $b = N^2 z$, and as long as convection does not take place all the way to the bottom, it is reasonable to look for a solution of the form: $b(z,t) = N^2 z + \beta(z,t)$ where $\beta(z,t)$ represents the variation of b due to small diffusion in the bottom layer. The non-zero diffusivity in the bottom layer is necessary to ensure the continuity of b_z at the interface. Let $\tilde{\kappa} = \frac{\kappa_0}{\kappa_1}$, the ratio of the diffusivities of the lower layer to the upper layer, $\tilde{\kappa} \ll 1$, and $\eta = z + h(t)$, the moving boundary coordinate. A solution of the form $\beta = \beta(\eta, t)$ can be found for the non-dimensional equation:

$$\epsilon \beta_t + \epsilon \beta_\eta h_t = \tilde{\kappa} \beta_{\eta\eta}$$

given by:

$$b(z,t) = z - \frac{\tilde{\kappa}}{\epsilon h_t} \exp(\frac{\eta h_t \epsilon}{\tilde{\kappa}})$$

Imposing the continuity of b at the interface:

$$b_{top}[z = -h(t), t] = b_{bottom}[z = -h(t), t]$$
$$\Rightarrow h(t) = -b_0(t)$$

thus a full solution to the problem is given by:

$$b(z,t) = \begin{cases} -h(t) + \epsilon zq(\frac{z}{2h} + 1) & \text{for } z \geq -h(t) \\ z - \frac{\tilde{\kappa}}{\epsilon h_t} \exp(\frac{\eta h_t \epsilon}{\tilde{\kappa}}) & \text{for } z < -h(t) \end{cases} \tag{2}$$

where $h(t) = \sqrt{-2qt}$.

Figure 2 shows $b(z,t)$ as a function of depth at different times. The solution has a quasi-mixed layer at the surface, which does, however, support an order ϵ gradient in the vertical. The depth $z = -h(t)$ describes the base of the chimney which, given a steady heat flux, deepens as $t^{1/2}$. The dimensional timescale for the formation of a chimney of depth H given a constant heat flux Q and initial linear stratification is $T = N^2 H^2/(2Q)$.

2   The 2-D chimney

A two-dimensional vertical section across the chimney is considered by assuming no-variations in the y-direction (i.e. $\partial_y = 0$). Though this assumption is made in order to simplify the problem, it is equivalent to considering the chimney in cylindrical coordinates in the limit of infinite radius.

Consider the Boussinesq equations where the convective processes are parametrized by introducing vertical diffusion and viscosity. Only the vertical terms are retained since the vertical diffusivity and viscosity terms are assumed to be much larger than the horizontal ones. Furthermore horizontal gradients of the vertical mixing terms are scaled out because of the chimney's small aspect ratio. The equations, in the usual notation, reduce to :

$$\frac{Du}{Dt} - fv = -p_x + \partial_z(\nu u_z)$$
$$\frac{Dv}{Dt} + fu = \partial_z(\nu v_z)$$
$$\frac{Dw}{Dt} = -p_z + b + \partial_z(\nu w_z)$$
$$0 = u_x + w_z$$
$$\frac{Db}{Dt} = \partial_z(\kappa b_z)$$

Rewriting the equations in terms of the streamfunction, ψ, the y-component of the vorticity, ξ, and the geostrophic momentum, m:

$$u = -\psi_z, \qquad w = \psi_x, \qquad \xi = \nabla^2\psi, \qquad m = v + fx$$

$$\frac{Dm}{Dt} = \partial_z(\nu m_z) \tag{3}$$

$$\frac{Db}{Dt} = \partial_z(\kappa b_z) \tag{4}$$

$$\frac{D\xi}{Dt} = -fm_z + b_x + \partial_z(\nu\xi_z) + \partial_z(\nabla\nu \cdot (\nabla\psi)_z) \tag{5}$$

Taking $\partial_z[f \times (3)] - \partial_x(4)$ gives:

$$(fm_z - b_x)_t + \partial_z J(\psi, fm) - \partial_x J(\psi, b) = \partial^2_{zz}(\nu fm_z) - \partial^2_{zx}(\kappa b_z) \tag{6}$$

where J is the Jacobian. A balance form of these equations has been used by Flierl and Mied (1985) to study the spin down and circulation of a warm core ring due to viscosity. By assuming thermal wind in the y-direction, i.e. $fm_z = b_x$, (6) reduces to:

$$J(\psi_z, fm) - J(\psi_x, b) = \partial_z((\nu - \kappa)b_{xz} + \nu_z b_x - \kappa_x b_z)$$

Moreover for the case of Prandtl number equal to one, $\nu = \kappa$, the equation simplifies to:

$$J(\psi_z, fm) - J(\psi_x, b) = \partial_z J(b, \kappa) \tag{7}$$

Prandtl number, $Pr = 1$, will be assumed from now. Physically it implies that momentum and buoyancy are mixed at the same rate, so that if the buoyancy and v-velocity field are in balance initially, then the balance is retained throughout the time evolution.

2.1 Non-dimensional equations

Equations (3)-(6) are non-dimensionalized in a similar way as was done for the one dimensional case. Let the bars indicate the non-dimensional quantities and the capitals the actual dimensional scales:

$$b = N^2 H \bar{b}, \qquad t = T\bar{t}, \qquad \psi = \Psi \bar{\psi}$$

$$x = L\bar{x}, \qquad \kappa = \boldsymbol{\kappa} \bar{\kappa}, \qquad v = V\bar{v}$$

then equations (1)-(3) become:

$$\frac{\bar{b}_{\bar{t}}}{T} + \frac{\Psi}{LH}J(\bar{\psi}, \bar{b}) = \frac{\boldsymbol{\kappa}}{H^2}\partial_{\bar{z}}(\bar{\kappa}\bar{b}_{\bar{z}})$$

$$\frac{\bar{v}_{\bar{t}}}{T} + \frac{\Psi}{LH}J(\bar{\psi}, \bar{v}) - \frac{f\Psi}{VH}\bar{\psi}_{\bar{z}} = \frac{\boldsymbol{\kappa}}{H^2}\partial_{\bar{z}}(\bar{\kappa}\bar{v}_{\bar{z}})$$

$$\frac{\Psi}{H^2 T}\bar{\xi}_{\bar{t}} + \frac{\Psi^2}{H^3 L}J(\bar{\psi}, \nabla^2\bar{\psi}) = -\frac{fV}{H}\bar{v}_{\bar{z}} + \frac{N^2 H}{L}\bar{b}_{\bar{x}} + \frac{\boldsymbol{\kappa}\Psi}{H^4}(\partial_{\bar{z}}(\bar{\kappa}\bar{\xi}_{\bar{z}}) + \nabla\bar{\kappa} \cdot \nabla\bar{\psi}_{\bar{z}})$$

The leading order balance in the v-equation is assumed to be:

$$-\frac{f\Psi}{VH}\bar{\psi}_{\bar{z}} = \frac{\boldsymbol{\kappa}}{H^2}\partial_{\bar{z}}(\bar{\kappa}\bar{v}_{\bar{z}})$$

then the scale for Ψ is given by $\frac{\boldsymbol{\kappa}V}{fH}$, where f is the Coriolis parameter. Similarly, from thermal wind balance the scale for the geostrophic velocity v is $\frac{N^2 H^2}{Lf}$. Three non-dimensional parameters may be introduced:

$$\epsilon = \frac{H^2}{\boldsymbol{\kappa}T}, \text{ ratio of the mixing time to the growth time of the chimney}$$

$$R_0 = \frac{V}{fL} = \frac{N^2 H^2}{f^2 L^2}, \text{ the Rossby number}$$

$$\gamma = \frac{\boldsymbol{\kappa}}{H^2 f}, \text{ the Ekman number}$$

The equations may then be rewritten, having dropped the bars as:

$$\epsilon b_t + R_0 J(\psi, b) = \partial_z(\kappa b_z) \tag{8}$$

$$\epsilon v_t + R_0 J(\psi, v) - \psi_z = \partial_z(\kappa v_z) \tag{9}$$

$$\epsilon \gamma^2 \xi_t + \gamma^2 R_0 J(\psi, \xi) = -v_z + b_x + \gamma^2 \partial_z(\kappa \xi_z) + \gamma^2 \partial_z(\nabla \kappa \cdot \nabla \psi_z) \tag{10}$$

and (6) takes the form:

$$\epsilon(b_x - v_z)_t + R_0 \partial_z J(\psi, v) - \psi_{zz} - R_0 \partial_x J(\psi, b) = \partial_z(\partial_z(\kappa v_z) - \partial_x(\kappa b_z)) \tag{11}$$

2.2   Top-Ekman Layer

A different scaling is introduced for the surface boundary layer. This is necessary to satisfy a no-stress boundary condition at $z = 0$, since thermal wind in the interior causes a shear in the geostrophic velocity at the surface. The diffusivity is considered to be constant in the thin region at the surface. Let η be the vertical coordinate in this layer and $\eta = \delta \bar{\eta}$, where δ is the Ekman layer thickness, $\delta = (\frac{\kappa}{2f})^{\frac{1}{2}}$, in the surface layer the equations reduce to:

$$\epsilon \gamma^2 b_t + R_0 \gamma J(\psi, b) = b_{\eta\eta} \tag{12}$$

$$\epsilon \gamma^2 v_t + R_0 \gamma J(\psi, v) - \psi_\eta = v_{\eta\eta} \tag{13}$$

$$\epsilon \gamma^2 \xi_t + R_0 \gamma J(\psi, \xi) = -v_\eta + b_x + \psi_{\eta\eta\eta\eta} \tag{14}$$

where the streamfunction has the same scaling as in the above formulation.

2.3   Scaling in the ocean

In deriving a scaling argument for this model it must be stressed that there is *a priori* no reason to choose one particular value for κ. The choice is can only be justified once the circulation pattern has been determined; the validity of the solution that will justify the assumptions made. The values for the following fixed parameters are chosen to represent typical oceanic convective conditions:
heat flux = $100 W m^{-2}$ which gives a buoyancy flux, $Q = 5 \times 10^{-8} m^2 s^{-3}$
$f \sim 10^{-4} s^{-1}$, $N \sim 10^{-3} s^{-1}$
horizontal and vertical scales for a chimney are
$L \sim 50 km$, and $H \sim 500 m$.
The diffusivity is chosen to be: $\kappa \sim 0.5 m^2 s^{-1}$
The non-dimensional parameters introduced in section 2.1 become:

$$\epsilon = \frac{Q}{\kappa N^2} = 0.1, \qquad R_0 = \frac{N^2 H^2}{f^2 L^2} = 0.01, \qquad \gamma = \frac{\kappa}{H^2 f} = 0.02$$

Three time scales should be considered for the problem:
T is the time needed for the chimney to grow to a depth H given a constant heat flux Q. The scaling is given by the solution to the 1D case: $T = N^2 H^2/(2Q)$.

T_{mix} is the time needed to diffuse over a depth H given a diffusivity κ, $T = H^2/\kappa$, and T_f is the period of the earth.

With this choice of variables the different timescales introduced above are:

$$T = 2.5 \times 10^6 s, \qquad T_{mix} = 5 \times 10^5 s, \qquad T_f = 10^4 s$$

With these values: $T \gg T_{mix} \gg T_{rot}$ and in terms of the non-dimensional parameters:

$$R_0 \ll \epsilon \ll 1 \text{ and } \gamma \ll 1$$

Physically, this choice of parameters implies that the mixing time is long compared to a rotational period but short compared to the time it takes for the *mixed layer* to descend a certain depth H. The fact that T is greater than T_f is consistent with the timescales of the chimney. It also implies that the chimney will be continuously adjusting to the effects of the Coriolis force. The Ekman layer thickness given by this scaling is $\delta = 50m$.

2.4   Linear Equations

Given the scaling introduced above, approximate solutions may be found by expanding in powers of ϵ. To a first order in ϵ, (8)-(10) become:

$$\epsilon b_t = \partial_z(\kappa b_z) \tag{15}$$

$$\epsilon v_t - \psi_z = \partial_z(\kappa v_z) \tag{16}$$

$$0 = -v_z + b_x \tag{17}$$

Thus the equations reduce to a simple diffusive equation for the buoyancy field, a diffusive equation plus the Coriolis term for the v-field, and thermal wind is a result of the scaling on the horizontal vorticity equation. The linearity assumption is justified for small Rossby number flows, the extent to which this approximation is valid can be assessed once a solution is found. Substituting (17) in (11) gives:

$$\psi_{zz} = \partial_z J(\kappa, b) \tag{18}$$

In principle then, any three of the above four equations constitute a closed set of equations for the description of the chimney under the scaling assumptions defined above. Thus once a certain form of κ is specified and with the following boundary conditions, one may obtain the flow field in the chimney. The non-dimensional boundary conditions can be written as:

$z = 0$ heat flux: $\kappa(b_z) \cdot b_z = q(x)$
    no stress $v_z = u_z = 0$

$t = 0$ initial values - $\psi = 0$, $b = z$, $v = 0$.

$z \to \infty$ $b_z \to 1$

Similarly the Ekman layer first order equations are:

$$0 = b_{\eta\eta} \tag{19}$$

$$-\psi_\eta = v_{\eta\eta} \tag{20}$$

$$0 = -v_\eta + b_x + \psi_{\eta\eta\eta\eta} \tag{21}$$

The full solution can then be obtained by summing the Ekman layer solution to the interior solution.

3 Approximate Solution

3.1 Analytical solution

To gain a qualitative understanding of the fluid circulation within the chimney given a x-dependent heat flux, Q, consider, as for the one-dimensional case, the case where κ is a step-function.

Interior and surface Ekman layer

If the advective terms are assumed to be negligible, then in the interior and surface layer of the chimney (where $\kappa = \kappa_1$) a solution can be found which is just the 2D extension of the 1D solution. In this case the chimney is represented as a series of independent one-dimensional columns, where x is just a parameter that enters the problem through the boundary condition, $\kappa_1 b_z = q(x)$ at $z = 0$. Given the $b(z,t)$ solution to the 1D problem, (2), extended to the 2D case by making q a function of x, then (16) and (17) can be used to evaluate the ψ and v fields (both expanded in powers of ϵ). The full solution is obtained by adding the interior solution to the surface Ekman layer solution:

$$\psi = h_x(1 - e^{z/\gamma}\cos(z/\gamma)) - \epsilon q_x z + O(\epsilon^2)$$
$$b = -h + \epsilon q z(\frac{z}{2h} + 1) + O(\epsilon^2)$$
$$u = -\frac{1}{\gamma}h_x e^{z/\gamma}(\cos(z/\gamma) - \sin(z/\gamma)) + O(\epsilon^2) \tag{22}$$
$$w = h_{xx}(1 - e^{z/\gamma}\cos(z/\gamma)) - \epsilon q_{xx} + O(\epsilon^2)$$
$$v = -h_x z + \frac{\gamma}{2}e^{z/\gamma}h_x(\cos(z/\gamma) - \sin(z/\gamma)) + \epsilon q_x(\frac{z^2}{2} - \frac{z^3}{12h}) + O(\epsilon^2)$$

where h is now a function of x as well as t, $h(x,t) = (-2q(x)t)^{1/2}$.

Exterior Region

Away from the chimney there will be no circulation and the stratification will be the same as in the initial condition, i.e. $\psi = 0$ and $b_z = 1$.

Transition region

Though the exact behaviour in this region depends on the actual choice of $\kappa(b_z)$, the general behaviour of the solutions can be deduced by matching the interior solution with the exterior region.

<u>Discussion</u>

Figure 4 shows the circulation described by solution (22) given a Gaussian-shaped heat flux (greatest cooling at the centre). The surface Ekman-layer has been expanded in the vertical and the transition region at the base of the chimney is intended only as a qualitative description. In particular, behaviour in the transition region is obtained by considering a κ such as the one proposed in figure 1a, equations (15)-(18) and by matching the interior solution to the exterior conditions. However, it should be pointed out that the thickness of this region will strongly depend on the choice of κ.

Figure 4 shows downwelling throughout the interior of the chimney and upwelling in the transition region. To balance the stress due to thermal wind balance in the interior, the Ekman layer is convergent at the surface, whereas the edge of the chimney show a divergent flow pattern.

The interior of the chimney is in thermal wind balance and the evolving chimney is in continuous geostrophic adjustment. This is consistent with the space and time scales of the chimney: $O(10 - 100km)$ and up to a few weeks.

The horizontal and vertical gradients supported by the chimney structure are the driving forces for the circulation. The more homogeneous the chimney, (the smaller ϵ) the more the circulation is confined to surface Ekman layer and to the boundary of the chimney. In this case it seems likely that the contribution of the advective terms should not be neglected.

Since the diffusivity in the outer region is chosen to be small, as the cooling persists there is no steady state solution for the chimney (i.e. the chimney has to grow, albeit slowly). The point at which, according to John Marshall's lecture, the chimney arrests its growth and the lateral eddy heat fluxes balance the heat flux at the surface is not accounted for in this parametrization. Neither is the baroclinic instability that causes the collapse of the whole structure.

3.2   Numerical Solution

Given the non-linearity of equation (1), once a certain form of κ was chosen, it was useful to evaluate a full numerical solution that included the as yet unresolved transition area. Figure 3 show the solution for the case where κ is chosen to be:

$$\kappa = \frac{\kappa_0 + \kappa_1}{2} + \frac{\kappa_1 - \kappa_0}{2} \tanh(\gamma b_z) \text{ where } \gamma = 100.$$

The numerical solution of (1) agrees, at least qualitatively, with the step-function case shown in figure 2. The chimney can support a small gradient in the vertical which tends to zero as one approaches the chimney's boundary. Linear stratification persists below the base of the quasi-mixed layer. Like the analytical case, the numerical case can be seen as a *continuum* of 1D columns in the analytic case, figures 5a-d show the same approach for the numerical solution. The solutions are calculated for different values of $q = q(x)$, having discretized the fields in the horizontal. By considering these 1D solutions *next* to each other in the x-direction one may compute the velocity and streamfunction fields from a finite difference from of equations (15)-(18). A portion

of the chimney is shown in figure 5a, where contours of b_z are shown in the x-z plane. 5b-d show the profiles of b_z, u, ψ in the vertical calculated for a given x. b_z is slightly negative in the top 200m; below it the water column rapidly becomes stably stratified tending asymptotically to N^2. The u-velocity profile is in agreement with that calculated analytically in (22), the large increase in the transition layer is is partially due to the finite difference approximation but also to the fact that the streamfunction is rapidly tending to zero (figure 5d).

These results are in good agreement with the qualitative description given above (§3.1). However, they also show that the magnitude of the terms in the transition region depends on the choice of $\kappa(b_z)$. In particular, the magnitude of the advection terms may depend on the thickness of the transition layer which is the region of varying κ. Thus this region may vary from being a boundary layer region to a region of slowly varying gradients. Though this does not affect the pattern of the flow field, it affects the magnitude of the single variables. Hopefully observations will provide some indication as to which choice of κ yields more realistic chimney structures.

3.3   Similarity Solution

The diffusion equation can be differentiated with respect to z to yield:

$$\phi_t = \partial_{zz}^2(\kappa(\phi)\phi) \text{ where } \phi = b_z$$

Let $\eta = \frac{z}{h}$ where $h = \sqrt{2qt}$ as given by the one-dimensional case , and let $\phi = \phi(\eta)$. The diffusion equation can then be rewritten as:

$$\partial_{\eta\eta}^2(\kappa(\phi)\phi) + \eta q \phi_\eta = 0$$

with boundary conditions

$$\kappa(\phi)\phi = q \text{ at } \eta = 0 \text{ at } \kappa(\phi)\phi = \kappa(N^2)N^2 \text{ as } \eta \to -\infty$$

The numerical solution derived for the κ given above is plotted as a function of η in figure 6. The different curves are for different times; thus showing that a similarity solution exists. No analytical similarity solution has as yet been found.

4   Validity and conclusions

4.1   Collapse of the linearity assumption

In deriving the solution for the step function case the advective terms have been neglected. Physically this implies that the advection of heat and momentum are negligible compared to the diffusion terms. Though this assumption could very well be more restrictive in the *transition layer* it is also a stringent condition in the interior and surface Ekman layer. Given solution (22) the collapse of the linear assumption occurs when the advective terms become of the same order of magnitude of the

diffusion terms. This can be evaluated by equating the terms b_t and v_t with their respective advection terms calculated from solutions (22). Thus, the time at which the breakdown of the linear hypothesis occurs in each region and for each equation is given by:

Heat Equation:

Interior:
$$t = \left(\tfrac{1}{R_0}\right)^{2/3} \quad \Rightarrow \quad t = \left(\tfrac{f^2 L^2}{N^2 H^2}\right)^{2/3} \quad \Rightarrow \quad t = 10^8 s$$

Ekman Layer:
$$t = \left(\tfrac{\epsilon\gamma}{R_0}\right)^{2/5} \quad \Rightarrow \quad t = \left(\tfrac{Q f L^2}{N^4 H^4}\right)^{2/5} \quad \Rightarrow \quad t = 3 \times 10^6 s$$

V - Equation:

Interior
$$t = \left(\tfrac{\epsilon}{R_0}\right)^{2/5} \quad \Rightarrow \quad t = \left(\tfrac{Q f^2 L^2}{\kappa N^4 H^2}\right)^{2/5} \quad \Rightarrow \quad t = 10^7 s$$

Ekman Layer
$$t = \left(\tfrac{\epsilon\gamma}{R_0}\right)^{2/5} \quad \Rightarrow \quad t = \left(\tfrac{Q f L^2}{N^4 H^4}\right)^{2/5} \quad \Rightarrow \quad t = 3 \times 10^6 s$$

4.2 Conclusions

Calculations in section 4.1 show that in the Ekman layer the non-linearity assumption does not hold for timescales on the order of those needed for the growth of the chimney to a depth H given a constant heat flux, Q. Moreover the linearity assumptions may not be valid at all at the chimney's boundary, i.e. in the transition layer. This suggests that the next step should involve numerical simulations using the fully non-linear equations.

The analytical solution does nonetheless provide an indication of the processes occuring in the chimney, and that the idea that the chimney is in thermal wind balance is not unreasonable. It also shows that the parametrization introduced in describing the chimney is valid in certain oceanic regimes. Numerical solutions support this hypothesis in the linear regime. In particular the chimney can be thought of a structure which is in continuous geostrophic adjustment, with the vertical circulation trying to maintain thermal wind.

This is to be considered a preliminary attempt to study circulation in a growing chimney. The exact form of κ still remains an open question. Amongst various possibilities one could think of constructing a diffusivity that never actually reaches a constant value in the interior of the chimney, but simply slowly decays to a small value at the boundary.

Acknowledgements

References

Flierl, G.R., Mied, R.P. 1985: Frictionally induced circulations and spin down of a warm core ring. *J. Geophys. Res.,*90, (C5), 8917-8927.

Jones, H., Marshall, J. 1993, Convection with rotation in a neutral ocean: a study of open-ocean deep convection. *J. Phys. Ocean.,* 23, 1009-1039.

Maxworthy, T., Narimousa, S. 1994: Unsteady, turbulent convection into a homogeneous, rotating fluid, with oceanographic applications. *J. Phys. Oceanog.,* 24, 865-887.

Schott, F., Leaman, K.D. 1991:Observations with moored acoustic Doppler current profilers in the convection regime in the Gulf of Lions. *J. Phys.Oceanogr.,* 3, 61-65.
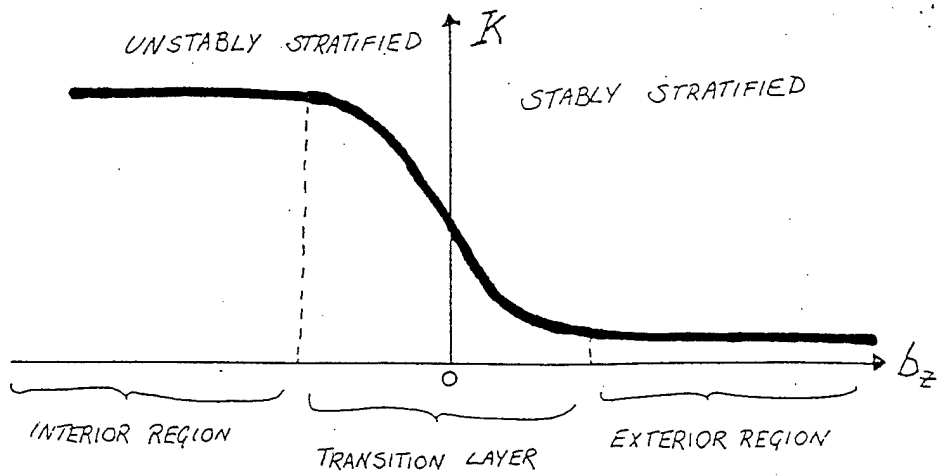
Figure 1a Schematic of the diffusivity, κ, as a function of b_z, where b is the buoyancy.
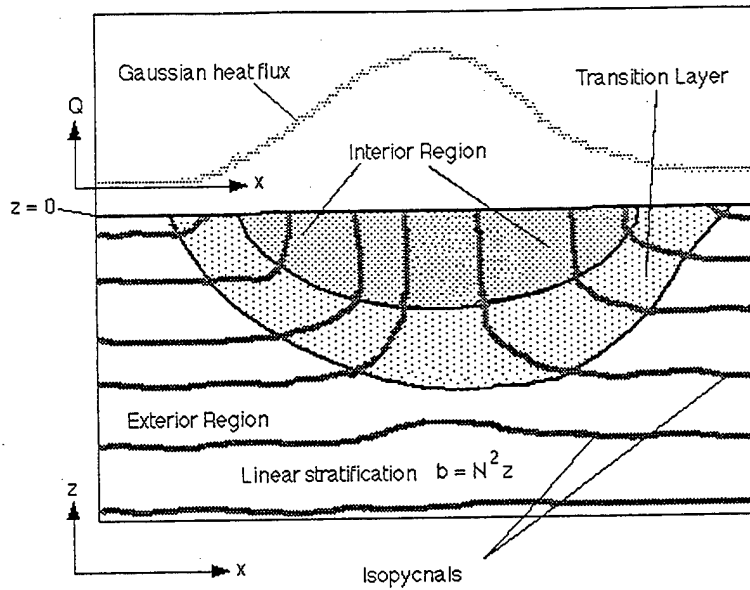
Figure 1b Schematic of the isopycnals in a x-z cross-section of a chimney generated by a Gaussian heat flux applied at the surface.
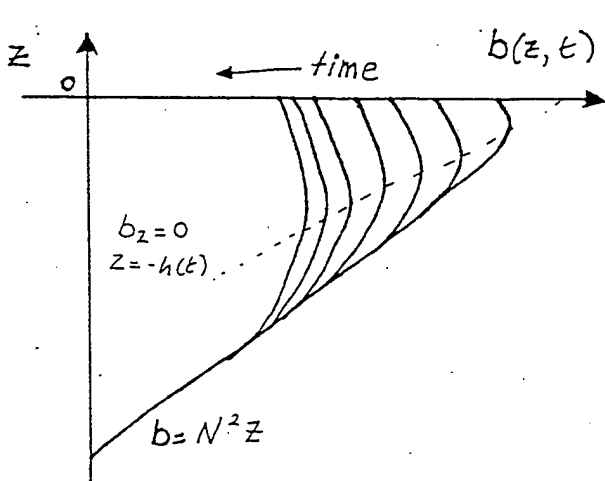
Figure 2 Schematic of the solution found for the 1D model, showing buoyancy as a function of time and depth.
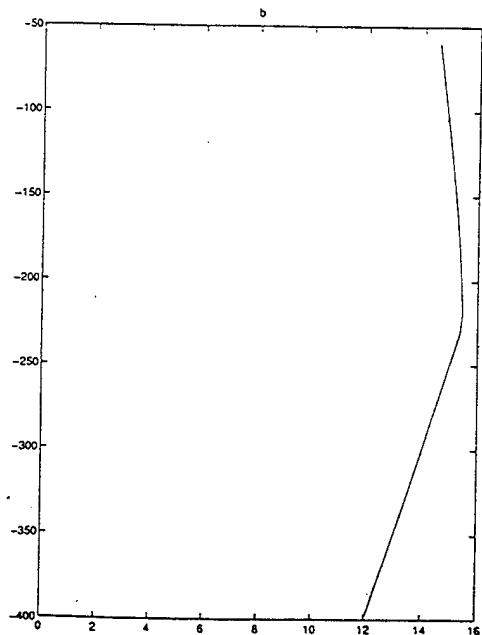
Figure 3 Numerical solution of (1) for κ specified in §3.2.
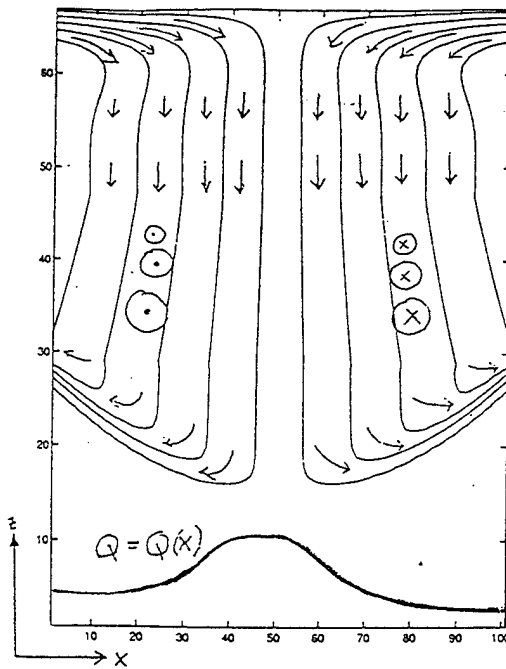
Figure 4 Streamfunction contours of the analytical solution (22) for the 2D chim-
ney. The Ekman layer is expanded, and the transition layer is intended
only as a schematic. Arrows indicate the direction of the flow field, and
the specified heat flux is shown at the bottom.
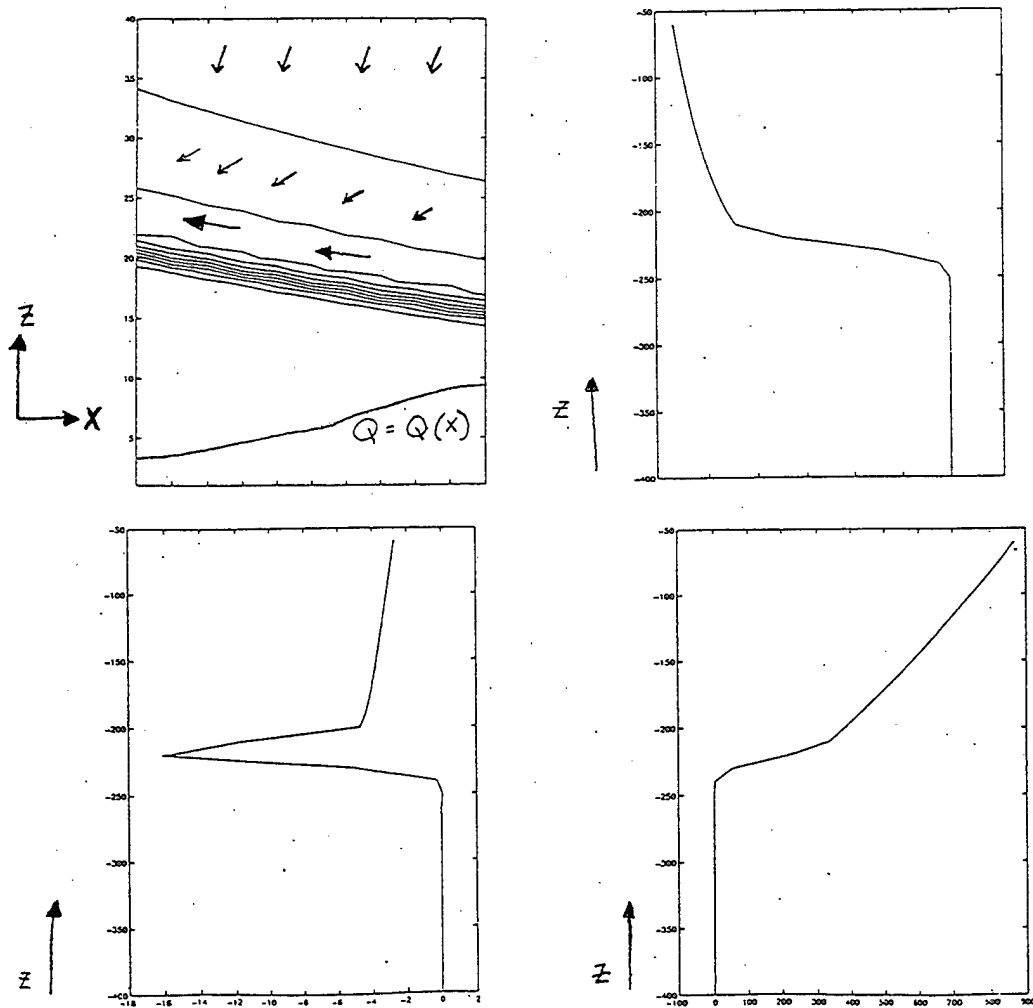
Figure 5 2D numerical solution (§3.2) for a portion of the chimney.
a) Contours of b_z and schematic of the heat flux and flow field.
Vertical profiles for a fixed central x-value. b) b_z c) $u(z)$ d) ψ

Baroclinic Instability at a General Latitude

Stephen Zatman

We consider the linear baroclinic instability of in a frictionless Boussinesq fluid on a plane that is rotating about an axis that is not perpendicular to the plane. We specifically consider the instability of flows which are horizontal and normal to the rotation vector ("zonal"), with a vertical shear. First, we consider purely symmetric instability. The expected result, that instability may occur when the potential vorticity becomes negative, is found. However, the maximum growth rate does not necessarily increase as the potential vorticity becomes more negative. We investigate what happens as the symmetry of the instability is broken, and find that the maximum growth rate for finite longitudinal wavenumber l will have a non-zero zonal wavenumber k. Next, we consider nearly geostrophic baroclinic instability. We find that at high Richardson number, the growth rates of the instability are the same as for the case with a vertical axis of rotation. However, at lower Richardson numbers there is increased instability for small k, and also when the potential vorticity is negative there are lines in the k, l plane where the growth rate becomes infinite (l being a longitudinal wave number), which is consistent with findings of Stone (1966) for non-geostrophic instability near the symmetric ($l = 0$) axis.

1   Introduction

Much of the analysis of baroclinic instability in the ocean (e.g. Pedlosky, 1986) has neglected the horizontal component of the rotation vector. For almost all of the ocean this is reasonable. However, recently there has been some interest in the dynamics of ocean "chimneys", areas around 10^2 kilometers across where cooling events on the surface lead to deep convection. In such chimneys, the potential vorticity is "zapped" until it is close to zero. These chimneys are then thought to be broken up by baroclinic eddies. It is in the instability of such chimneys that we might see the effects of the horizontal component of the rotation vector.

Baroclinic instability on an f plane has been considered by Eady (1949) and others, and on a β plane by Charney (1947) and others. Stone (1969, 1971) considered non geostrophic and non hydrostatic instability on an f plane. We shall consider a problem close to that of the Eady problem: instability on an $f - b$ plane, where $b = 2\Omega \cos\phi$, and ϕ is the co-latitude. In particular, we shall consider instability of a horizontal flow perpendicular to the rotation axis with a vertical shear. Clearly such "zonal" flows are special cases of the sorts of flows one would expect to find in chimneys - we should expect the effect of b to be maximised for such a flow.

In section 2 we shall consider non hydrostatic symmetric instability, i.e. instability with $k = 0$ where k is the zonal wavenumber. Symmetric instability is usually thought

to be unimportant in the ocean as it requires a small Richardson number ($R < 1$), whereas a typical Richardson number in the ocean is very large ($R \sim 10^4$). However, in chimneys the Richardson number may be reduced to $O(1)$ as convection reduces stratification, and indeed one would expect symmetric instability to play a role in setting the potential vorticity to zero. In section 3 we shall look at weakly asymmetric instability by further developing our analysis from section 2. In section 4 we shall consider nearly geostrophic baroclinic instability, through a treatment similar to that of the Eady problem.

2 Symmetric Instability

We assume a Boussinesq adiabatic inviscid fluid on a plane rotating at angular speed Ω about a general axis, with $f = 2\Omega \sin \phi$ the vertical component and $b = 2\Omega \cos \phi$ the vertical component of the planetary vorticity. Gravity is assumed to be normal to the plane. If x, y and z are the zonal, longitudinal and vertical cartesian coordinates, u, v and w the respective components of the velocity, p is the pressure with the mean density term removed and divided by the density, Θ is the specific buoyancy and H is the thickness of the layer, then the governing equations are:

$$\frac{Du}{Dt} - fv + bw + p_x = 0 \tag{1}$$

$$\frac{Dv}{Dt} + fu + p_y = 0 \tag{2}$$

$$\frac{Dw}{Dt} - b\,u + p_z - \Theta = 0 \tag{3}$$

$$\frac{D\Theta}{Dt} = 0 \tag{4}$$

$$u_x + v_y + w_z = 0 \tag{5}$$

$$w = 0 \quad z = 0, H \tag{6}$$

We write $u = \bar{u} + u'$ where $\bar{u}$ is the basic state and u' the perturbation, and similarly $p = \bar{p} + p'$, $\Theta = \overline{\Theta} + \Theta'$, $v = v'$ and $w = w'$. We shall assume the basic state

$$\bar{u} = \frac{u_o\, z}{H} \tag{7}$$

$$\overline{\Theta} = \beta z - \frac{f\, u_o}{H} \tag{8}$$

$$\bar{p} = \frac{1}{2}\left(\beta + \frac{b\, u_o}{H}\right) z^2 - \frac{f\, u_o}{H} yz \tag{9}$$

To nondimensionalise the equations, we use the following scalings: $x \sim y \sim u_o/f$, $t \sim 1/f$, $z \sim H$, $\Theta \sim \beta H$, $p \sim \beta H^2$, $u \sim v \sim u_o$, $w \sim fH$. If we assume perturbations of the form $\exp(i(st + kx + ly))$ and if $L = i(s + kz)$ then equations 1-6 become (dropping the primes):

$$L\,u - v + (1 + B)w + ikRp = 0 \tag{10}$$

$$L\,v + u + ilRp = 0 \tag{11}$$

$$L\,w = \frac{B\,S}{R}u + S\,p_z - S\,\Theta = 0 \tag{12}$$

$$L\,\Theta - \frac{1}{R}v + w = 0 \tag{13}$$

$$iku + ilv + w_z = 0 \tag{14}$$

$$w = 0 \quad z = 0, 1 \tag{15}$$

where we have the following dimensionless numbers: R is the Richardson number $= \beta H^2/u_o^2$, S is a dimensionless stratification $= \beta/f^2$ and $B = bH/u_o$. We expect a typical midlatitude value of B to be of $O(1)$. The hydrostatic limit would be $S \rightarrow \infty$, $B/R \rightarrow 0$. These equations reduce to a single differential equation:

$$(1 + L^2)w_{zz} - 2i\left(\frac{k}{L} - l(1 + B)\right)w_z$$
$$- \left(R(k^2 + l^2)\left(1 + \frac{l^2}{S}\right) + l^2B(1 + B) - 2\frac{(B + 1)lk}{L}\right)w = 0 \tag{16}$$

if $k = 0$ (the "symmetric" limit) then this becomes:

$$(1 + L^2)w_{zz} + 2il(1 + B)W_z - l^2\left(B(1 + B) + R\left(1 + \frac{l^2}{S}\right)\right)w = 0 \tag{17}$$

if $l = 0$ then this becomes:

$$(1 + L^2)w_{zz} - 2i\frac{k}{L}w_z + k^2R\left(1 + \frac{L^2}{S}\right)w = 0 \tag{18}$$

It is interesting to note that in this latter case (which corresponds to $\partial/\partial y = 0$, B does not appear in the equation, and so the effect of the horizontal component of the rotation vector vanishes. If we write $p = p_t + \tilde{p}$ such that terms in $\tilde{p}$ balance terms with B in equations 10 and 12, then:

$$S\,\tilde{p}_z = -B\frac{S}{R}u \tag{19}$$

$$R\,\tilde{p}_x = B\,w \tag{20}$$

$$\Rightarrow \tilde{p}_{zx} = -\frac{B}{R}u_x = \frac{B}{R}w_z \tag{21}$$

If $\partial/\partial y = 0$ then there is no term in p in equation 11, and equation 21 is consistent with equation 14. The effects of b are essentially shorted out through the pressure. This is dependent on the Boussinesq approximation and would not hold for an anelastic approximation, and would not necessarily be true for the atmosphere.

The solution to equation 17 using equation 15 is:

$$w = e^{-Yz}\sin[m\pi z] \tag{22}$$

for integer m, where:

$$Y = il\,\frac{1+B}{1-s^2} \tag{23}$$

$$\frac{l^2}{1-s^2}\left(B(1+B) + R\left(1 - \frac{s^2}{S}\right) - \frac{(1+B)^2}{1-s^2}\right) = -m^2\pi^2 \tag{24}$$

We can define a streamfuction ϕ in the y, z plane such that $\phi_y = w$, $\phi_z = -v$:

$$\phi = -\frac{1}{l}\cos\left[l\left(y - \frac{1+B}{1-s^2}z\right)\right]\sin[m\pi z] \tag{25}$$

The streamlines show that the flow consists of tilted overturning cells. The tilt is not generally the same as that of the rotation vector.

We can use equation 24 to solve for s:

$$s = \pm\left[\chi_a \pm [\chi_b]^{\frac{1}{2}}\right]^{\frac{1}{2}} \tag{26}$$

where:

$$\chi_a = \frac{S\,B(1+B) + R(1+S) + 2S\frac{m^2\pi^2}{l^2}}{2\left(R + S\frac{m^2\pi^2}{l^2}\right)} \tag{27}$$

$$\chi_b = \frac{S^2(B^2 + 4\frac{m^2\pi^2}{l^2}S^2)(1+B)^2 + SBR(6 + 2(S(1+B) + B)) + 4RS + R^2(S-1)^2}{\left(2\left(R + S\frac{m^2\pi^2}{l^2}\right)\right)^2} \tag{28}$$

The condition for instability is $\chi_a > \chi_b^2$, which implies $R < 1 + B$ or, if the shear is reversed ($\overline{u} = -u_o z/H$ in dimensional units), $R < 1 - B$. The dependence on B can not be removed by finding a Richardson number using the component of stratification
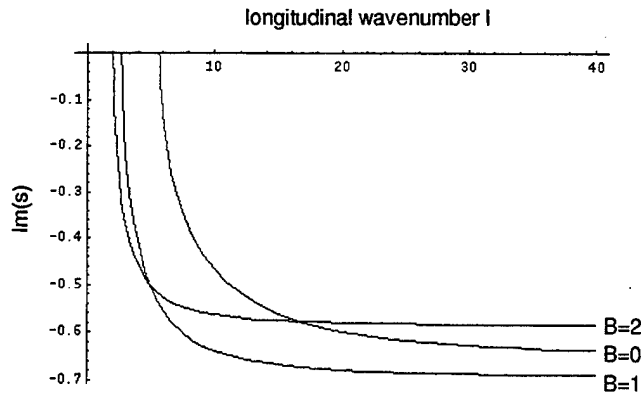
Figure 1: Symmetric instability for $S = 100$ and $R = 0.7$. Negative values of Im(s) indicate growth.

---

parallel to the rotation rather than the vertical, but this condition is equivalent to $Q < 0$, as expected. This implies that if symmetric instability of thermal winds in chimneys takes place, then (in the northern hemisphere) we should expect the south of the chimney to be more unstable than the north.

The maximum instability is for $m = 1, l \rightarrow \infty$. This tends to be increased by B for small values of B, but decreased by B for large values of B. The long wave cut-off, however, is always decreased by B. The magnitude of S has little effect on the results except when $R >> S$.

3 Weakly Asymmetric Instability

We can explore growth rates near the $k = 0$ axis of the k, l plane by performing an expansion about k. We write $w = w_0 + k w_1 + k^2 w_2 + ...$ and $s = s_0 + k s_1 + k^2 s_2 + ...$ and expand equation 16. The first two equations are:

$$M_0 \, w_0 = 0 \tag{29}$$

$$M_0 \, w_1 + M_1 w_0 = 0 \tag{30}$$

where M_0 is the operator on w in equation 17, and M_1 is given by:
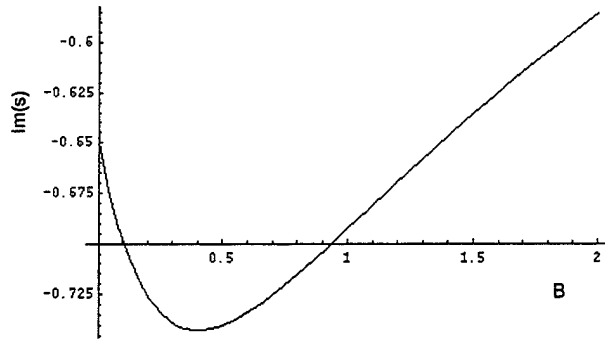
Figure 2: Variation of Im(s) with B for symmetric instability with $S = 100$, $R = 0.7$ and $l \rightarrow \infty$.
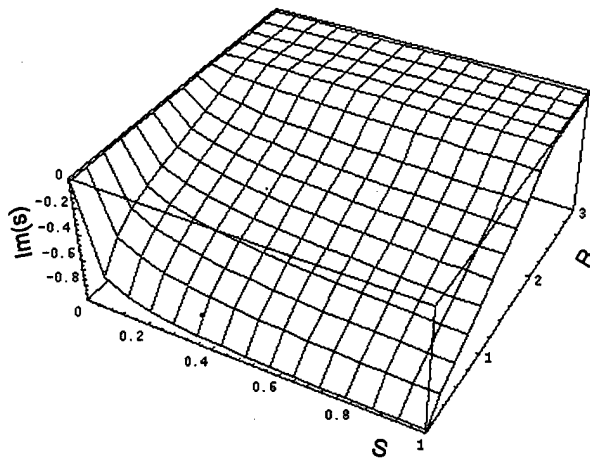
Figure 3: Variation of Im(s) with R and S for symmetric instability with $B = 1$ and $l \rightarrow \infty$.

$$M_1 = 2s_0(s_1 + z)\partial_{zz} + \frac{2}{s_0}\partial_z + \left(-R\,l^2 s_o(s_1 + z) + 2i\frac{l}{s_o}(1 + B)\right) \qquad (31)$$

We know that the boundary conditions of equation 15 apply to all the w_i, and that w_0 is the solution already derived for symmetric instability in section 2. Using the boundary conditions, equation 17 and equation 30 we can find a solvability criterion:

$$\int_0^1 w_0\, e^{\left(\frac{3\gamma_2}{4\gamma_1} + \left[\frac{9\gamma_2^2}{16\gamma_1^2} - \frac{1}{2}\right]^{\frac{1}{2}}\right)z}\, M_1\, w_0\, dz = 0 \qquad (32)$$

$$\gamma_1 = -(1 - s_0^2) \qquad (33)$$

$$\gamma_2 = -2il(1 + B) \qquad (34)$$

$$\gamma_3 = l^2\left(B(1 + B) + R\left(1 - \frac{s_0^2}{S}\right)\right) \qquad (35)$$

We can use this to find a solution for s_1, which is $\partial s/\partial k$ (or part of the wave speed) at $k = 0$. For l greater than the long wave cut-off, the imaginary part of s_1 oscillates both with l and with B, which is peculiar behaviour but which is analogous to the findings of Stone (1966) for non geostrophic instability near the symmetric axis. That study found that the square of the wave speed oscillated between plus and minus infinity as l is increased. The difference may be due to our inclusion of non hydrostatic effects in this case. It should be

4   Nearly Geostrophic Instability

We assume, as commonly done for the Eady problem, that some Rossby number for the system is large and the horizontal velocities are nearly geostrophic, so that we can write $fv = p_x$ and $fu = -p_y$. Aside from the usual requirements of quasigeostrophy, in our case we also require that B as defined in section 2 is of at most $O(1)$. Still, the use of such dynamics is questionable. Our boundary conditions ($w = 0$ at $z = 0, H$) become, through the heat equation:

$$(\partial_t + \overline{u}\partial_x)\Theta' + v'\overline{\Theta}_y = 0 \qquad z = 0, H \qquad (36)$$

using the same notation as in section 2. The vertical momentum equation becomes:

$$p_z + \frac{b}{f}p_y = \Theta \qquad (37)$$

Ignoring terms in w and second order in perturbation variables, we can write the potential vorticity Q as:

Figure 4: Variation of Im(s) with l for weakly asymmetric instability with $R = 0.7$, $S = 100$ and $B = 1$.

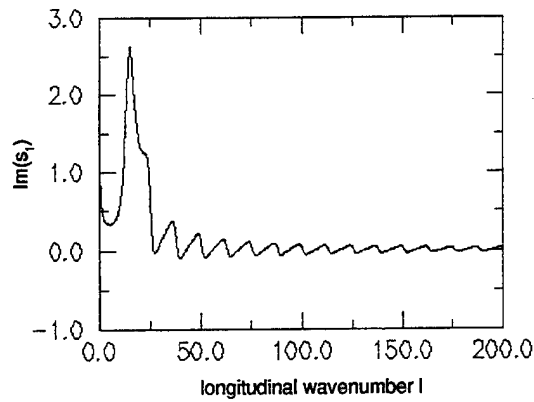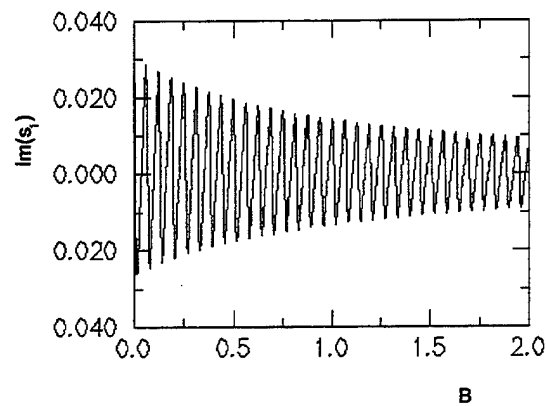Figure 5: Variation of Im(s) with B for weakly asymmetric instability with $R = 0.7$, $S = 100$ and $l = 400$.

$$Q = (f + \overline{\zeta})\overline{\Theta}_z + (b + \overline{\xi})\overline{\Theta}_y + (f + \overline{\zeta})\Theta'_z + \zeta'\overline{\Theta}_z + (b + \overline{\xi})\Theta'_y + \zeta'\overline{\xi}_y \quad (38)$$

$$\zeta = v_x - u_y \quad (39)$$

$$\xi = u_z \quad (40)$$

The first two terms of this are the basic state and hence constant. If we denote the last four terms by q' then, by conservation of potential vorticity, $q' = 0$. Using the same definitions and non-dimensionalisation as in section 2 and dropping the primes, this becomes:

$$p_{zz} + 2il(1 + B)p_z - (R(k^2 + l^2) + B\ l^2(1 + B))p = 0 \quad (41)$$

Solving this, using equation 36 and writing $s = ck$, we can solve for c:

$$c = -\frac{1}{2} - i\Delta_1 \pm \frac{\sqrt{\Delta_2}}{\Delta_3} \quad (42)$$

$$\Delta_1 = \frac{l(1 + 2B)}{R(k^2 + l^2) + B\ l^2(3 + 4B)} \quad (43)$$

$$\Delta_2 = R^2(k^2 + l^2)^2 + Bl^4(3 + 4B)^2 + RBl^2(3 + 4B)(k^2 + l^2) - 4l^2(1 + 2B)^2$$
$$-4\left(R(k^2 + l^2) + Bl^2(3 + 4B)\left(\frac{X}{\tan X} - 1\right)\right) \quad (44)$$

$$\Delta_3 = 2R(k^2 + l^2) + B\ l^2(3 + 4B) \quad (45)$$

$$X = [l^2(1 + B) - R(k^2 + l^2)]^{\frac{1}{2}} \quad (46)$$

The Δ_1 term is zero when $l = 0$ or $R \to \infty$ (for $k \neq 0$). The magnitude is maximum as $k \to 0$, monotonically decreasing with k. This term implies instability at all k (albeit with a growth rate that may be very small).

When $l \to 0$, as expected from the discussion of equation 18, this becomes the standard solution to the Eady problem. If $R \to \infty$ we also arrive back to the standard solution. However, in the case $B \to 0$ but R is not large, our solution is different from the standard solution (due to our inclusion of the horizontal contribution to the potential vorticity).

The major differences between this solution and the standard solution for moderate R are as follows. Except when B is small, Δ_2 becomes positive for smaller k (at which point the two solutions for the imaginary part of c collapse into the one given by the Δ_1 term in equation 42). For B and l sufficiently large Δ_2 may be real for all k, except for sufficiently small R as explained below. Also, for small l the maximum growth rate is for small k (if the Δ_1 is not small compared with $\sqrt{\Delta_2}/\Delta_3$).
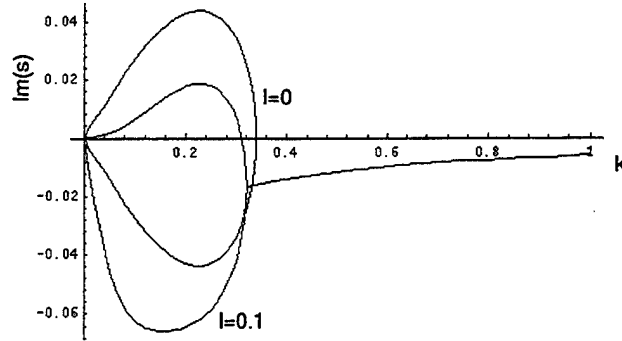
Figure 6: Variation of Im(s) with B for nearly geostrophic instability with R = 50.

For some values of k and l, the X/tan X term in equation 45 → ±∞. This occurs along hyperbolae in the k, l plane given by:

$$k^2 - l^2 \left(\frac{B}{R} + \frac{1}{R} - 1 \right) = -\frac{n^2 \pi^2}{R} \tag{47}$$

where n is an integer other than zero. At these hyperbolae the imaginary part of s becomes infinite. The condition for this to occur is R < 1 + B, i.e. the same as for symmetric instability. These hyperbolae meet the l axis at the same places that the oscillations of c with l at the l = 0 axis found by Stone described in section 3 become singular. The hyperbolae would seem to be a continuation of this feature from the symmetric axis into the k, l plane.

5 Conclusions

The non vertical part of the rotation vector may either stabilise of destabilise a zonal thermal wind with a vertical shear according to the orientation of the wind to symmetric instability, in a way that is consistent with a Q < 0 instability criterion. However, maximum growth rate of the instability decreases with b except when b is small.

For weakly asymmetric instability $\partial Im(s)/\partial k$ for k = 0 oscillates with l, which implies that for finite l the maximum growth rate is not on the l = 0 axis. These are probably

associated with hyperbolae of infinite growth rates in the k, l plane that can be found in the nearly geostrophic limit.

Nearly geostrophic baroclinic instability is most affected by b when the Richardson number is small. In such cases, the maximum growth rate will be at smaller k.

6 Thanks

I would like to thank Rick Salmon for his invaluable help during the program, until he become (unfortunately) preoccupied with fluid experiments of his own. John Marshall was kind to help me in the frantic last days and offered some wonderful insight on baroclinic instability. I appreciated the time Rupert Ford was able to squeeze out of his tight schedule in order to do some scaling. Glenn Flierl's advice was vital. I want to thank Steve Meacham more for his wise words than his abuse of superuser status. George Veronis didn't give up on us, even when half of us turned up to a softball game more hungover than alive. Joe Keller's words on How to Speak were late for the summer but have been priceless since. I wish to thank everybody else I talked to, and all the fellows for a great summer, especially for the inspired demonstration of vodka induced convection by Jon Aurnou. All errors are, of course, entirely my own.

7 References

Charney, J.G., 1947, The dynamics of long waves in a baroclinic westerly current, J. Meteor., 4, 135-163

Eady, E.T., 1949, Long waves and cyclone waves, Tellus, 1, 33-52

Pedlosky, J., 1987, *Geophysical fluid Dynamics*, Springer-Verlag, 710pp

Stone, P.H., 1966, On Non-Geostrophic Baroclinic Stability, J. Atmos. Sci., 23, 390-400

Stone, P.H., 1971, Baroclinic stability under non-hydrostatic conditions, J. Fluid. Mech., 45, 659-671

Stone, P.H., Hess, S., Hadlock, R., and Ray, P., 1969, Preliminary results of experiments with symmetric baroclinic instabilities, J. Atmos. Sci, 26, 991-996

Spectral theory for the Rankine Vortex

N.J. Balmforth

We consider the linear eigenvalue problem for infinitesimal perturbations to ideal, incompressible, two-dimensional vortices. The linear eigenvalue problem contains a singular point for radii at which the mean rotation rate of the vortex matches the rotation frequency of the perturbation. This critical ring introduces an irremovable singularity into the equations for neutral modes and leads to a continuous eigenvalue spectrum. In addition there may also be discrete complex modes of regular form corresponding to growing/decaying conjugate pairs, and discrete neutral modes associated with discontinuities in the distribution of ambient vorticity. In this lecture, we described how to construct a unique set of *singular eigenfunctions* corresponding to the continuum, and established that the complement of eigenfunctions comprised a complete set. Here, we outline these calculations specifically for the Rankine vortex.

The linear equations

In ideal fluid theory, any circular vortex whose rotation rate as a function of radius, r, is $\Omega(r)$, is a possible equilibrium. If we assume dependences on angle, θ, and time, t, of the form $\exp im(\theta - \nu t)$, then infinitesimal perturbations to such basic states satisfy the equations,

$$(\Omega - \nu)\omega = \Delta\psi \tag{1}$$

and

$$\omega = \frac{1}{r}\frac{d}{dr}\left(r\frac{d\psi}{dr}\right) - \frac{m^2}{r^2}\psi \quad, \tag{2}$$

where $\omega(r)$ and $\psi(r)$ are the radially dependent parts of the perturbation to the vorticity and streamfunction, and

$$\Delta = \frac{1}{r}\frac{d}{dr}\left[\frac{1}{r}\frac{d(r^2\Omega)}{dr}\right] \quad. \tag{3}$$

We solve (1) and (2) on the interval $0 \leq r < \infty$, subject to the boundary conditions that ψ vanish at both limits. Equation (1) contains the singular point (radius), $r = r_c$, where $\Omega = \nu$. This equation for the ideal vortex is the analogue of Rayleigh's equation for shear flow in a channel.

The Rankine vortex consists of a rigidly rotating core surrounded by irrotational flow extending to infinite radius. In terms of rotation rate, the vortex is described by

$$\Omega(r) = \begin{cases} \Omega_0 & r < a \\ \Omega_0 a^2/r^2 & r > a, \end{cases} \tag{4}$$

with a the core radius and Ω_0 its rotation rate. For this vortex, $\Omega(r)$ is not twice differentiable, and we must represent Δ by a δ-function:

$$\Delta = -\frac{2\Omega_0}{a}\delta(r - a) \quad. \tag{5}$$

Although this is not a well-behaved function it has the advantage that we may immediately perform any integrals that appear in the problem. Hence we may find explicit solutions for the eigenfunctions.

Discrete modes

We first solve (1) and (2) for the discrete modes of the vortex, which amounts to Kelvin's (1880) original solution. We begin by inverting the Poisson relation (2) between ω and ψ by introducing the Green function, $G(r, r')$, of the Fourier-transformed Laplacian:

$$\psi(r) = \int_0^\infty G(r, r')\omega(r')r'dr' \quad , \tag{6}$$

with

$$G(r, r') = -\frac{1}{2m}\left[\left(\frac{r'}{r}\right)^m H(r - r') + \left(\frac{r}{r'}\right)^m H(r' - r)\right] \quad , \tag{7}$$

where $H(x)$ is the Heaviside function. Hence,

$$\psi(r) = -\frac{2\Omega_0\psi(a)}{\Omega - \nu}G(r, a) \quad . \tag{8}$$

By setting $r = a$, we obtain the dispersion relation,

$$1 = -\frac{2\Omega_0}{\Omega_0 - \nu}G(a, a) = \frac{\Omega_0}{m(\Omega_0 - \nu)} \quad . \tag{9}$$

Thus

$$m\nu = (m - 1)\Omega_0 \quad , \tag{10}$$

and so

$$\psi = -2m\psi(a)G(r, a) = G(r, a) \tag{11}$$

if we set $\psi(a) = G(a, a)$. Finally,

$$\omega = \frac{1}{a}\delta(r - a) \quad . \tag{12}$$

Singular eigenfunctions

To find the eigenfunctions of the continuum we follow Van Kampen's (1955) recipe. We solve (1) by writing

$$\omega(r; r_c) = \mathcal{P}\frac{\Delta\psi}{\Omega - \nu} + C\delta(r - r_c) \quad , \tag{13}$$

with $\mathcal{P}$ meaning the Cauchy principal value, and $\Omega(r_c) = \nu$. We then determine the arbitrary constant, C, by using the normalization,

$$r_c\Xi = \int_0^\infty \omega(r; r_c)rdr = -\frac{2\Omega_0\psi(a; r_c)}{\Omega_0 - \nu} + r_cC \quad , \tag{14}$$

with Ξ an eigenvalue-dependent parameter. Or,

$$C = \Xi + \frac{2\Omega_0\psi(a; r_c)}{r_c(\Omega_0 - \nu)} \quad . \tag{15}$$

If we introduce this value into equation (13) and use (6), we find a relation for the stream-function,

$$\psi(r; r_c) = 2\Omega_0\psi(a; r_c)\frac{r_cG(r, r_c) - aG(r, a)}{a[\Omega_0 - \Omega(r_c)]} + r_c\Xi\, G(r, r_c) \quad . \tag{16}$$

If we select $r = a$, we obtain the algebraic relation,

$$\psi(a; r_c) \left\{ 1 - 2\Omega_0 \frac{r_c G(r, r_c) - aG(r, a)}{a[\Omega_0 - \Omega(r_c)]} \right\} = r_c \Xi \, G(a, r_c) \quad . \tag{17}$$

In order to be able to solve this relation, hence find a solution for ψ for all values of r_c, we must be careful about points for which

$$1 - \frac{\Omega(r)}{\Omega_0} = \frac{1}{m} \left[1 - \left(\frac{r_c}{a} \right)^m H(a - r_c) - \left(\frac{a}{r_c} \right)^m H(r_c - a) \right] \quad . \tag{18}$$

At these points the left-hand side of (17) vanishes and we can only find a solution for $\psi(a; r_c)$ provided we insist $\Xi = 0$. In other words, it is only by choosing a suitable normalization function, $\Xi(r_c)$, that we can find a uniquely prescribed set of singular eigenfunctions. In particular, we choose

$$r_c \Xi = 1 - 2\Omega_0 \frac{r_c G(r, r_c) - aG(r, a)}{a[\Omega_0 - \Omega(r_c)]} \quad , \tag{19}$$

which implies that

$$\psi(a; r_c) = G(a, r_c) \quad . \tag{20}$$

Whence,

$$\psi(r; r_c) = G(r, r_c) - \frac{2\Omega_0}{\Omega_0 - \Omega(r_c)} [G(r_c, a)G(r, a) - G(a, a)G(r, r_c)] \tag{21}$$

and

$$\omega(r; r_c) = \frac{1}{r}\delta(r - r_c) - \frac{2\Omega_0}{\Omega_0 - \Omega(r_c)} \left[\frac{1}{a}G(r_c, a)\delta(r - a) - \frac{1}{r_c}G(a, a)\delta(r - r_c) \right] \quad . \tag{22}$$

Completeness

To establish the completeness of the eigenfunctions, we solve the initial-value problem; we take a superposition of eigenfunctions and represent an arbitrary initial condition in terms of them. The superposition is, on combining an integral over the continuum with the contribution of the discrete mode,

$$Q(r) := \omega(r, t = 0) = \int_0^\infty \Lambda(r_c)\omega(r; r_c) r_c dr_c + \frac{1}{a}\Lambda_d \delta(r - a) \tag{23}$$

$$= \left[1 + \frac{2\Omega_0}{\Omega_0 - \Omega(r)}G(a, a) \right] \Lambda(r) + \frac{1}{a}\delta(r - a) \left[\Lambda_d - 2\Omega_0 \mathcal{P} \int_0^\infty \frac{\Lambda(r_c)G(a, r_c)}{\Omega_0 - \Omega(r_c)} r_c dr_c \right] \quad . \tag{24}$$

The initial condition, Q, we require to be a continuous function. Hence the right-hand side of (24) should not contain any irregular terms like a δ-function. We may eliminate such terms by choosing

$$\Lambda_d = 2\Omega_0 \mathcal{P} \int_0^\infty \frac{\Lambda(r_c)G(a, r_c)}{\Omega_0 - \Omega(r_c)} r_c dr_c \quad . \tag{25}$$

This leaves

$$Q(r) = \left[\frac{\Omega_d - \Omega(r)}{\Omega_0 - \Omega(r)} \right] \Lambda(r) \quad , \tag{26}$$

where $\Omega_d = \Omega(r_d) = (m-1)\Omega_0/m$ is the rotation frequency of the discrete mode.

In general we cannot solve (26) for Λ at the point $r = r_d$ unless that function is not regular there. In fact, we need to set (*cf.* Balmforth & Morrison, 1995)

$$\Lambda(r_c) = \tilde{\Lambda}(r_c) + \mathcal{P}\left[\frac{\Omega_0 - \Omega(r)}{\Omega_d - \Omega(r)}\right]Q_d \quad, \tag{27}$$

where $\tilde{\Lambda}$ is bounded at $r_c = r_d$, and $Q_d = Q(r_d)$. (In principle, we might also include a term $\lambda\delta(r - r_d)$ in (27), but in the current context it does not seem necessary.) Then,

$$\tilde{\Lambda}(r) = \left[\frac{\Omega_0 - \Omega(r)}{\Omega_d - \Omega(r)}\right][Q(r) - Q_d] \quad, \tag{28}$$

which is always solvable. Moreover,

$$\Lambda_d = 2\Omega_0\left[\mathcal{P}\int_0^\infty \frac{\tilde{\Lambda}(r_c)G(a,r_c)}{\Omega_0 - \Omega(r_c)}r_c dr_c + Q_d\mathcal{P}\int_0^\infty \frac{G(a,r_c)}{\Omega_d - \Omega(r_c)}r_c dr_c\right] \tag{29}$$

$$= 2\Omega_0\mathcal{P}\int_0^\infty \frac{Q(r_c)G(a,r_c)}{\Omega_d - \Omega(r_c)}r_c dr_c \quad. \tag{30}$$

Since Λ and Λ_d are now prescribed by Q, we therefore have established completeness.

Temporal evolution

At finite time, the disturbance to the vortex evolves as

$$\omega(r,t) = \int_0^\infty \Lambda(r_c)\omega(r;r_c)e^{-im\Omega(r_c)t}r_c dr_c + \frac{1}{a}\Lambda_d e^{-im\Omega_d t}\delta(r-a) \tag{31}$$

$$= Q(r)e^{-im\Omega(r)t} + \frac{1}{a}\delta(r-a)e^{-im\Omega_d t}\int_0^\infty \frac{G(a,r_c)Q(r_c)}{\Omega_d - \Omega(r_c)}\left\{1 - e^{-im[\Omega_d - \Omega(r_c)]t}\right\}r_c dr_c \tag{32}$$

$$=: \tilde{\omega}(r,t) + \omega_d(t)\delta(r-a) \quad. \tag{33}$$

Hence a δ-function develops immediately in the perturbation. We understand this from a physical perspective by observing that the background vorticity can be written in the form

$$\zeta = \frac{1}{r}(r^2\Omega)' = 2\Omega_0 H(a-r) \quad. \tag{34}$$

If we add the linear perturbation to this basic profile we find

$$\zeta + \sum_{m=1}^\infty \omega_m(r,t)e^{im\theta} = 2\Omega_0 H(a-r) + \sum_{m=1}^\infty [\tilde{\omega}_m(r,t) + \omega_{m,d}(t)\delta(r-a)]e^{im\theta} \quad, \tag{35}$$

where we have restored the dependence of the linear solutions on m and summed over all azimuthal modes. To linear order, equation (35) can be written as

$$\zeta + \sum_{m=1}^\infty \omega_m(r,t)e^{im\theta} = 2\Omega_0 H(r_i - r) + \sum_{m=1}^\infty \tilde{\omega}_m(r,t)e^{im\theta} \quad. \tag{35}$$

with

$$r_i = a + \frac{1}{2\Omega_0} \sum_{m=1}^{\infty} \omega_{m,d}(t)e^{im\theta} \quad . \tag{36}$$

Hence the δ-function piece of the linear solution simply corresponds to the motion of the vorticity interface; at time t, the interface lies at a radius, r_i.

Remarks

In this summary we have described spectral theory exclusively for perturbations to the Rankine vortex. This configuration has the important property that the mean vorticity gradient vanishes everywhere except at the boundary of the core. Hence it becomes possible to directly calculate the eigenfunctions. In the case of a vortex with a general rotation profile, the equations reduce only to an integral Fredholm problem for the streamfunction and we need to invert a singular integral expression to solve the initial-value problem (*cf.* Balmforth & Morrison, 1995).

We also do not need to restrict consideration to incompressible vortices, but we may extend our analysis to study vortices in shallow water or two-dimensional compressible fluid. In these cases, the spectrum also contains an infinite number of discrete modes corresponding to surface gravity waves or acoustic modes. With methods related to those used here we may extricate the compressional modes from the continuum and examine the details of the spectrum.

Once we have establised a complete set of eigenfunctions we can continue on to study the long-time behaviour of the initial-value problem. This usually uncovers algebraic decay of the continuum through phase mixing, but we can also find exponential decay under some circumstances. This proves relevant to recent experiments on electron plasmas that can be magnetically confined in such a way to produce dynamics which approximate that of an ideal two-dimensional fluid (*e.g.* Gould, 1995).

We may also address the issue of vortex stability within the context of Hamiltonian theory. The ideal fluid equations can be recast in the form of a Hamiltonian field theory. The singular eigenfunctions can be used to define a canonical transformation of the Hamiltonian coordinates, which places that theory into canonical, action-angle form (Balmforth & Morrison, 1995). This reveals the amplitudes of the singular eigenfunctions to be some sort of normal coordinates for the fluid. Moreover, we can unambiguously define the energies of the singular modes and predict the existence of negative energy modes, phenomena that have previously been observed in electron plasmas (*e.g.* Gould, 1995).

Finally, once we have a basis set of eigenfunctions for the linear problem, we can advance to consider more general situations in a perturbative context. For example, we can use the eigenfunctions to study the dynamics of weakly dissipative and nonlinear disturbances to the vortex.

References

[1] Balmforth, N. J., & P. J. Morrison, 1995. *Submitted to J. Fluid Mech.*
[2] Gould, R., 1995. *Phys. Plasmas*, **2**, 2151-2163.
[3] Lord Kelvin, 1880. *Phil. Mag.* **10**, 155-168.
[4] Van Kampen, N. G., 1955. *Physica*, **21**, 949-963.

Vorticity Dynamics in Shear Flow

D. del-Castillo-Negrete[*]   W. R. Young[*]   N. J. Balmforth[†]

The dynamics of vorticity in shear flow is an interesting topic in fluid dynamics with important applications in geophysical flows where the generation and persistence of coherent vorticity structures in shear flow is commonly observed. One of the simplest models is the Euler equation:

$$\frac{\partial \nabla^2 \Psi}{\partial t} + \left\{ \Psi, \nabla^2 \Psi \right\} = 0 \ , \tag{1}$$

where the domain is a channel with walls at $y = \pm 1$ and periodic in x, $\{f, g\} := \partial_x f \partial_y g - \partial_x g \partial_y f$, and the velocity field is given by $(u, v) = (-\partial_y \Psi, \partial_x \Psi)$.

The present report has two objectives. The first (Section 1) is to show how, under certain conditions, Eq. (1) can be reduced to the relatively simpler Eqs. (5) and (9) for studying vorticity dynamics in shear flow. The second objective is to study the linear (Section 2), and nonlinear (Sections 3, 4, and 5) dynamics of the reduced equation. To simplify the discussion we will neglect dissipation. However, the results presented can be easily modified to include both viscous dissipation ($\sim \nabla^4 \Psi$) and Ekman dissipation ($\sim \nabla^2 \Psi$). Also, the β effect, which accounts for the variation of Coriolis force with latitude, will been neglected. The incorporation of the β effect in the analysis presented below can be done, but it involves certain technical complications that we prefer not to discuss in this preliminar report.

1 Derivation of the reduced vorticity equation

We begin by decomposing the streamfunction as

$$\Psi = \psi_0(y) + \epsilon^2 \psi(x, y, t) \ . \tag{2}$$

Substituting Eq. (2) into Eq. (1) yields

$$\left(\frac{\partial}{\partial t} + u_0 \frac{\partial}{\partial x} \right) \nabla^2 \psi + \epsilon^2 \left\{ \psi, \nabla^2 \psi \right\} - u_0'' \frac{\partial \psi}{\partial x} = 0 \ , \tag{3}$$

where the primes denote differentiation with respect to y, and $u_0 = -\psi_0'$ is the shear flow velocity profile. The main assumption that we will make is that the shear flow vorticity has the form

$$Z_0 = -u_0' = -1 + \epsilon F(y/\epsilon) \ , \tag{4}$$

[*]Scripps Institution of Oceanography, UCSD La Jolla, CA 92093-0230
[†]Institute for Fusion Studies, UT Austin, TX 78712

where F is a arbitrary function such that $F \to 0$ for $|y| \gg \epsilon$, and ϵ is a small parameter. That is, we are interested in the dynamics of a vorticity band of width and streght of order ϵ, immersed in a constant (order one) vorticity background. In terms of the velocity field, the problem is that of a Couette flow ($u_0 \sim y$) with a "defect" located in a strip of order ϵ around $y = 0$. Some linear stability aspects of this problem have been studied in [1].

The derivation proceeds by a matching asymptotic expansion in the spirit of the theory of critical layers [2, 3]. It is not our intention to present here a detailed derivation (which will be published elsewere); rather, we limit to highlight some of the basic ideas involved. We refer to the $|y| >> \epsilon$ region as the outer region and to the $|y| \sim \epsilon$ region as the inner region.

To study the flow in the inner region, we rescale the time and y coordinates as $t \to \epsilon\, t$ $y \to y/\epsilon$, and propose a solution of the form $\psi_{in} = B(x,t) + \epsilon\, \phi(x,y,t)$, where $\phi(x, y = 0, t) = 0$ and B is an unknown function to be determined. Substituting this expression for ψ_{in} into Eq. (3), and doing the long-wave approximation $\nabla^2 \approx \epsilon^{-2}\, d^2/dy^2$, yields to leading order

$$\frac{\partial Z}{\partial t} + y\,\frac{\partial Z}{\partial x} + \frac{\partial B}{\partial x}\,\frac{\partial Z}{\partial y} = 0 \;, \tag{5}$$

where $Z = \phi'' + F$ is the vorticity in the inner region. That is, in this approximation, the vorticity is simply advected by the streamfunction

$$\psi = -\frac{1}{2}y^2 + B(x,t) \;. \tag{6}$$

The function $B(x,t)$ is determined by considering the outer flow. Rescaling the time as before ($t \to \epsilon\, t$), Eq. (3) for the outer flow reduces to $y\nabla^2\psi_{out} = 0$, which has the general solution $\nabla^2\psi_{out} = -2A(x,t)\delta(y)$, where $\delta(y)$ is the Dirac delta function and $A(x,t)$ is an undetermined function. That is, in this approximation, the outer flow is the superposition of the constant vorticity background and an irrotational flow ψ_{out} driven by the inner flow. The matching of the outer flow across the inner region requires that the velocity jump, $-2A(x,t)$, of the outer flow at $y = 0$ equals the integrated vorticity, $\int Z\, dy$, of the inner flow, that is

$$2A(x,t) = -\int_{-\infty}^{\infty} Z(x,y,t)\, dy \;. \tag{7}$$

The solution of the outer flow equation is given by $\tilde{\psi}_{out}(k,y,t) = \mathcal{G}(k,y)\tilde{A}(k)$, where $\mathcal{G}$ is the Green function, and the tilde denotes Fourier transform. Accordingly, $\tilde{\psi}_{out}(k, y = 0, t) = k^{-1}\tanh k\, \tilde{A}(k,t)$, and therefore to satisfy the matching condition, $\psi_{out}(x, y = 0, t) = \psi_{in}(x, y = 0, t)$, the B function has to satisfy

$$\tilde{B}(k,t) = k^{-1}\tanh(k)\tilde{A}(k,t) \;. \tag{8}$$

Inverting the Fourier transforms in Eq. (8), the relation between B and Z can be written as

$$B(x,t) = -\frac{1}{2}\int dx' \int dy\; \mathcal{K}(x - x')\, Z(x',y,t) \;, \tag{9}$$

where $\mathcal{K}(x) := \pi^{-1} \ln |\coth(\pi x/4)|$. Equation (9), which accounts for the self-consistent modification of the streamfunction in Eq. (6) by the vorticity distribuition, is the analogue of the condition $Z = \nabla^2 \Psi$ in Euler's equation.

The reduced vorticity equation (5), (9) inherits all the conservation laws of Eq. (1); it has the infinite number of vorticity invariants

$$\frac{d}{dt} \int dx \int dy \, \mathcal{C}(Z) = 0, \tag{10}$$

where $\mathcal{C}$ is any function of Z, and the momentum invariant

$$\frac{d}{dt} \int dx \int dy \, yZ = 0 \; . \tag{11}$$

Also, it has the energy invariant

$$\frac{d}{dt} (E_s + E_f) = 0 \; , \tag{12}$$

where E_s is the energy of the inner vortical field or the "shear flow energy", and E_f the energy of the outer irrotational field, defined as

$$E_s = \frac{1}{2} \int dx \int dy \, y^2 Z \; , \quad E_f = \int dx \, AB \; . \tag{13}$$

We conclude this section by pointing out that the reduced vorticity equation is mathematically equivalent to the equation for a one-dimensional electron plasma. Let $f(x, v, t)$ denote the phase space distribution function of a single component plasma, then the evolution of f is governed by the so-called Vlasov equation (see for example [4])

$$\frac{\partial f}{\partial t} + v \frac{\partial f}{\partial x} + \frac{\partial \phi}{\partial x} \frac{\partial f}{\partial y} = 0 \; , \tag{14}$$

where $\phi(x, t)$ is the electrostatic potential which is obtained from $f(x, v, t)$ in a self-consistent way via Poisson equation

$$\frac{\partial^2 \phi}{\partial x^2} = -4\pi \int f(x, v, t) \, dv \; , \tag{15}$$

which can be written as

$$\phi = \int dv \int dx' \, \mathcal{G}(x - x') \, f(x, v', t) \; , \tag{16}$$

where $\mathcal{G}$ is the Green function for the Laplacian in one-dimension. Equations (14) and (16) are equivalent to Eqs. (5) and (9), if we identify the fluid vorticity $Z(x, y, t)$ with the plasma distribution function $f(x, v, t)$, the (x, y) fluid spatial coordinates with the (x, v) plasma phase space coordinates, the fluid outer field $B(x, t)$ with the plasma electrostatic potential $\phi(x, t)$, and the Green's function $\mathcal{G}$ of Poisson equation with the kernel $\mathcal{K}$ in Eq. (9). In this analogy, the shear flow energy E_s corresponds to the kinetic energy of the plasma particles, and the outer flow energy E_f corresponds to the electrostatic energy of the plasma.

2 Linear Stability

To study the linear stability of a vorticity profile $F(y)$ consider

$$Z(x, y, t) = F(y) + Z_1(y)e^{ik(x-ct)} . \tag{17}$$

Substituting Eq. (17) in Eqs. (5) and (9), and neglecting quadratic terms in Z_1, leads directly to the dispersion relation

$$2k \coth(k) = \int_{-\infty}^{\infty} \frac{F'}{y - c} \, dy . \tag{18}$$

This result illustrates the advantages of the reduced system. To get the dispersion relation using the full equation of motion, Eq. (1), one has to solve the eigenvalue problem for Rayleigh equation which is a much harder problem than the evaluation of the integral in Eq. (18).

As a simple example consider the "top-hat" vorticity distribution: $F(y) = \eta$ for $|y| < 1/2$, and $F(y) = 0$ elsewhere, where η is a constant. This vorticity distribution corresponds to a piecewise linear velocity profile. In this case the integral in Eq. (18) is trivial to evaluate and yields to the dispersion relation

$$c^2 = \frac{1}{4} + \frac{\eta}{2} \frac{\tanh k}{k} . \tag{19}$$

For small ϵ (where ϵ is the small parameter used in the derivation of the reduced vorticity equation) this result agrees with Rayleigh's general result.

As another example consider a Lorentzian vorticity profile, $F(y) = \eta/(1 + y^2)$. In this case the integral in Eq. (18) can be evaluated using Cauchy residue theorem and yields the conclusion that normal modes with

$$c = \pm \left(\sqrt{\frac{\pi}{2}|\eta| \frac{\tanh k}{k}} - 1 \right) i , \tag{20}$$

exist in the region of the (k, η) plane defined by the condition $(\pi/2) \, \eta \, \tanh k / k < -1$. Outside this region there is the continuous spectrum in which there is no definite connection between k and c, and the linear problem does not have regular solutions of the form $\sim e^{ik(x-ct)}$.

In addition to providing explicit dispersion relations, the relative simplicity of the linear theory of the reduced vorticity equation allows the derivation of necessary and sufficient conditions for linear instability. These conditions can be obtained using the so-called Nyquist method which has been extensively applied to study the linear stability of Vlasov equation (see for example [4]) which, as we discussed before, is analogous to the reduced vorticity equation.

3   Nonlinear solutions

The Vlasov equation (14), (16) admits a large class of exact nonlinear solutions known as BGK modes (after Bernstein, Greene and Kruskal [5]). In this section we discuss how to construct the analogue of the BGK modes for the reduced vorticity equation. The basic idea is to look for time independent solutions in which the vorticity is a function of the streamfunction.

Let

$$Z(x,y) = \mathcal{Z}(\psi) , \tag{21}$$

where ψ is the streamfunction in Eq.(6). Equation (21) will be an exact solution of Eqs. (5), (7), and (8) for any function $\mathcal{Z}$, provided

$$\int dx' \Lambda(x - x')B(x') = -\frac{1}{2} \int \frac{\mathcal{Z}(\psi)}{\sqrt{2(B - \psi)}} d\psi \tag{22}$$

where $2\pi \Lambda(x) := \int dk\, k \coth k e^{ikx}$. Thus, by selecting appropiate expressions for the function $\mathcal{Z}(\psi)$, exact nonlinear solutions can be found by solving Eq. (22) for $B(x)$. Alternatively, one can assume the function $B(x)$ to be known, and solve Eq. (22) for $\mathcal{Z}(\psi)$. Finding these solutions is complicated due to the integral operator in the left hand side. However, in the long-wave limit the relation between A and B simplifies to $\tilde{B}(k) \approx (1 - k^2/3)\tilde{A}(k)$ and Eq. (22) becomes

$$\frac{d^2 B}{dx^2} = 3B + \frac{3}{2} \int \frac{\mathcal{Z}(\psi)}{\sqrt{2(B - \psi)}} d\psi , \tag{23}$$

which can be rewritten as the potential equation

$$\frac{d^2 B}{dx^2} = -\frac{\partial V}{\partial B} \tag{24}$$

with the potential given by

$$V(B) = -\frac{3}{2}B^2 - \frac{3}{2} \int \mathcal{Z}(\psi)\sqrt{2(B - \psi)} d\psi . \tag{25}$$

Thus, given a function $\mathcal{Z}(\psi)$, a nonlinear solution of the reduced vorticity equation can be obtained by solving Eq. (24), a problem equivalent to finding the trajectories of a one-degree of freedom particle in a potential. Since the potential is time-independent, the solution can easily be reduced to a quadrature. On the other hand, the problem of solving for the function $\mathcal{Z}(\psi)$ assuming the function $B(x)$ is known, is equivalent to the inverse problem of finding the potential of a system knowning its trajectories; under some conditions, this problem has unique solution that can be reduced to a quadrature (see for example [6]). Finding these nonlinear solutions is important because, provided they are stable, they can be used to model the formation and presistence of coherent structures in shear flows

4 Wave-mean flow interaction

A problem of interest in shear flow dynamics is the understanding of how waves change the average properties of the flow. Related to this problem are the problems of marginal stability relaxation and vorticity homogenization. To gain some understanding on these issues we present here the wave-mean flow interaction theory for the reduced voticity equation, and show that the evolution of the average vorticity field is governed by a diffusion-like equation. Let

$$Z(x, y, t) = \bar{Z}(y, t) + Z'(x, y, t) \, , \tag{26}$$

where $\bar{Z} := \int Z dx$, and $\bar{Z}' = 0$. Taking the x-average of Eq. (5) yields

$$\frac{\partial \bar{Z}}{\partial t} = -\frac{\partial}{\partial y} \left(\overline{\frac{\partial}{\partial x} B' \, Z'} \right) \, . \tag{27}$$

The right hand side of Eq.(27) is computed using the linear dynamics

$$\frac{\partial Z'}{\partial t} + y \frac{\partial Z'}{\partial x} + \frac{\partial B'}{\partial x} \frac{\partial \bar{Z}}{\partial y} = 0 \, . \tag{28}$$

Equations (27) and (28) resemble the standard wave-mean flow interaction equations in which the time evolution of the average profile is written in terms of the Reynolds stress which, in turn, is computed using linear theory. However, there is an important difference because, due to the relatively simplicity of the reduced equation, it is possible to obtain an analytic expression for the "Reynolds stress" $\overline{\partial_x B' \, Z'}$ in Eq. (27). As a matter of fact, after some algebra, Eq. (27), can be written as the diffusion equation

$$\frac{\partial \bar{Z}}{\partial t} = \frac{\partial}{\partial y} \left(D \frac{\partial \bar{Z}}{\partial y} \right) \, , \tag{29}$$

with the "diffusion coefficient" given by

$$D = 2 \int_0^\infty \frac{\omega_i \, k \tanh k}{(ky - \omega_r)^2 + \omega_i^2} \, \tilde{\mathcal{E}}(k, t) \, dk \, , \tag{30}$$

where $\omega(k) = \omega_r + i\omega_i$ is the frequency given by the dispersion relation in Eq. (18), and $\tilde{\mathcal{E}}(k, t) \equiv 2\pi \tilde{\mathcal{A}}(k, t) \tilde{\mathcal{B}}(k, t)$ is the spectral energy density of the outer flow which satisfies the equation

$$\frac{\partial \tilde{\mathcal{E}}}{\partial t} = 2 \omega_i \, \tilde{\mathcal{E}} \, . \tag{31}$$

Note that, depending on the sign of ω_i, the diffusion coefficient can be positive or negative.

Equation (29), which is the analogue of the quasilinear equation of plasma physics (see for example [4]), preserves all the invariants Eqs. (10)-(12) of the reduced vorticity equation. We speculate that the waves growing in an unstable vorticity profile tend to mix vorticity so that the average vorticity relaxes to a marginally stable profile by a diffusion-like process during which energy is exchanged between the mean flow and the waves.

5 Numerical integration

To conclude we discuss some results on the numerical integration of the reduced vorticity equation. We used a Fourier pseudospectral method in x, with finite difference in y. The integral in Eq. (7) was evaluated with the trapezoidal rule. For the time-stepping, an Adams-Bashforth-Crank-Nicholson method was used. The y domain (which in the reduced vorticity equation is $(-\infty, \infty)$) was truncated to the interval $(-10, 10)$. For the results reported here, the A, B, and Z fields were neglegible for $|y| > 10$.

We studied the time evolution of initial conditions of the form

$$Z(x, y, t = 0) = \frac{\eta}{1 + y^2} + \frac{\delta}{1 + y^4} \cos x \ . \tag{32}$$

The first term on the right hand side is an unperturbed Lorentzian vorticity profile of amplitude η, which according to Eq. (20) is unstable for $\eta < -2/\pi \approx -0.6366$. The second term is an small perturbation of size δ.

- **Figures 1 (a)-(e): Unstable vorticity profile**

  In this case, $\eta = -2$, and $\delta = 0.1$, and thus the vorticity profile is unstable. Figures (a) and (b) show contour plots of the vorticity field $Z(x, y, t)$ at $t = 0$ and $t = 10$ respectively. As expected, the numerical integration shows growth of the perturbation and vortex formation. Figure (c) shows a cut of the voricity field at $x = \pi$. As the instability grows the mean vorticity profile broadens. Figure (e) shows the evolution of the energy; the solid line is the energy of the outer field $E_f(t) - E_f(0)$, and the dotted line the energy of the shear flow $E_s(t) - E_s(0)$ as defined in Eq.(13). The energy plot shows a tendency towards a saturation stage in which the shear flow and the field energy reach a steady (or possibly oscillatory) state and the interchange of energy between the shear flow and the outer field stops (or oscillates with a small amplitude). This saturation is also observed in the evolution of the $B(x, t)$ field in Fig. (d). Thus, it is plausible that the asymptotic regime in this case can be described by a BGK mode.

- **Figures 2 (a)-(e): Stable vorticity profile**

  In this case, $\eta = -0.5$, and $\delta = 0.025$, and thus the vorticity profile is stable. Figures (a) and (b) show contour plots of the vorticity field $Z(x, y, t)$ at $t = 0$ and $t = 10$ respectively. As expected, there is no growth of the perturbation. As time increases, the vorticity profile, Fig. (c), narrows, and the B field, Fig. (d), becomes smaller. The damping of the outer field $B(x, t)$, and the narrowing of the vorticity profile, is the fluid analogue of the collisionless damping of electrostatic plasma waves known as Landau damping (see for example [4]). Physically, Landau damping can be undestood as an exchange of energy between the plasma particles and the electrostatic wave. That is, the wave damps by transferring its energy to the particles which increase their kinetic energy broadening the distribution function. In an analogous way, the fluid outer

field B damps transferring its energy to the shear flow as is manifest in Fig. (e); at the same time, as shown in Fig. (c), the vorticity profile narrows (the profile narrows instead of broadening because the shear flow energy is negative). Note however that the amplitude of B instead of going to zero saturates in a regime which might be also described by a BGK mode.

References

[1] Gill, A. E., 1965: A mechanism for instability of plane Couette flow and of Poiseuille flow in a pipe, *J. Fluid. Mech.*, **21**, 503-511.

[2] Stewartson, K., 1978: The evolution of the critical layer of a Rossby wave. *Geophys. Astrophys. Fluid. Dyn.*, **9**, 185-200.

[3] Warn, T. and Warn H., 1978: The evolution of a nonlinear critical level, *Stud. Appl. Math.* **59**, 37-71.

[4] Krall, N. A., A. W. Trivelpiece, *Principles of Plasma Physics*, McGraw-Hill, New York, 1973.

[5] Bernstein, I. B., J. M. Greene, and M. D. Kruskal, 1957: Exact nonlinear plasma oscillations, *Phys. Rev.*, **108**, 546-550.

[6] Landau, L. D., and E. M. Lifshitz, *Course of Theoretical Physics, Vol.1 Mechanics*, Pergamon Press, New York, 1976.
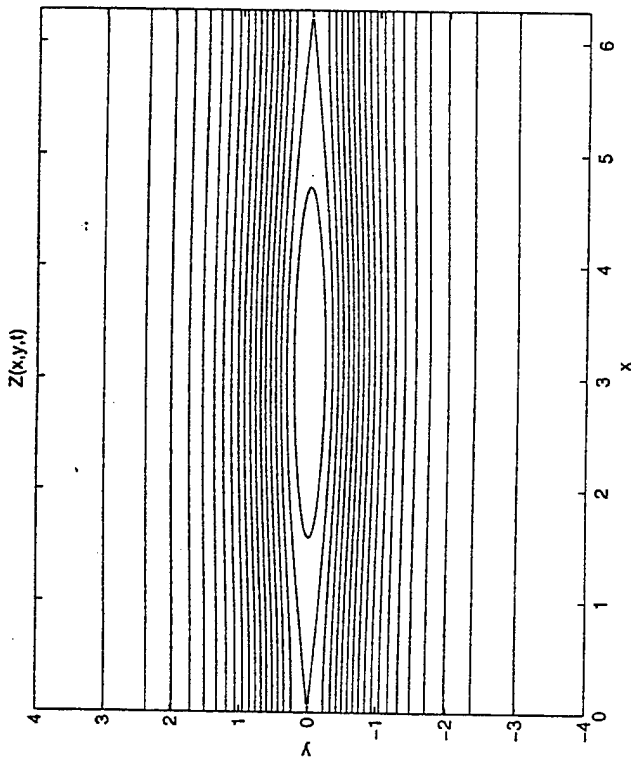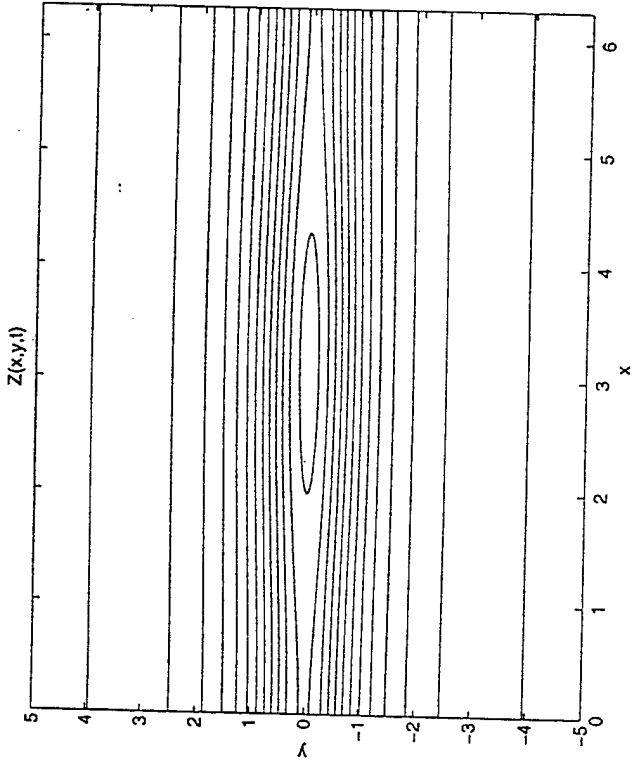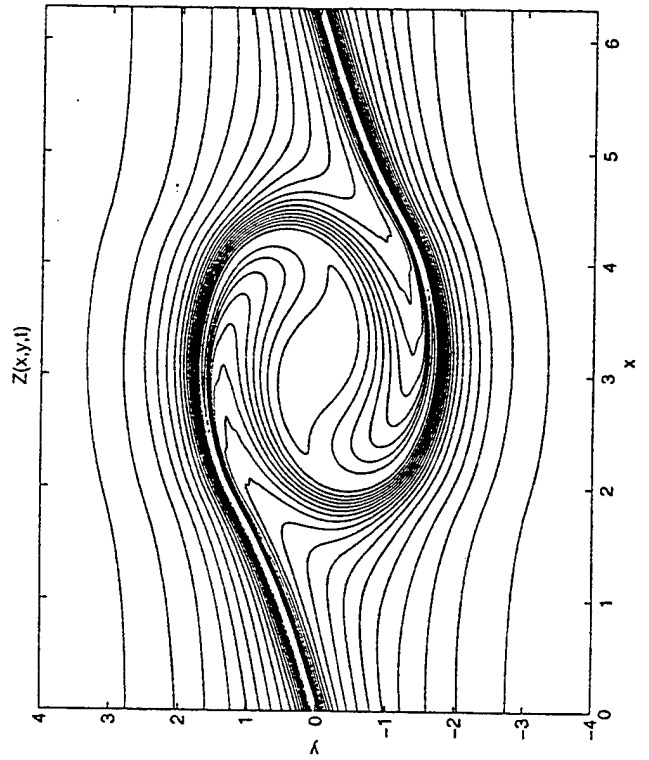
Z(x,y,t)

Fig. 2 (a)
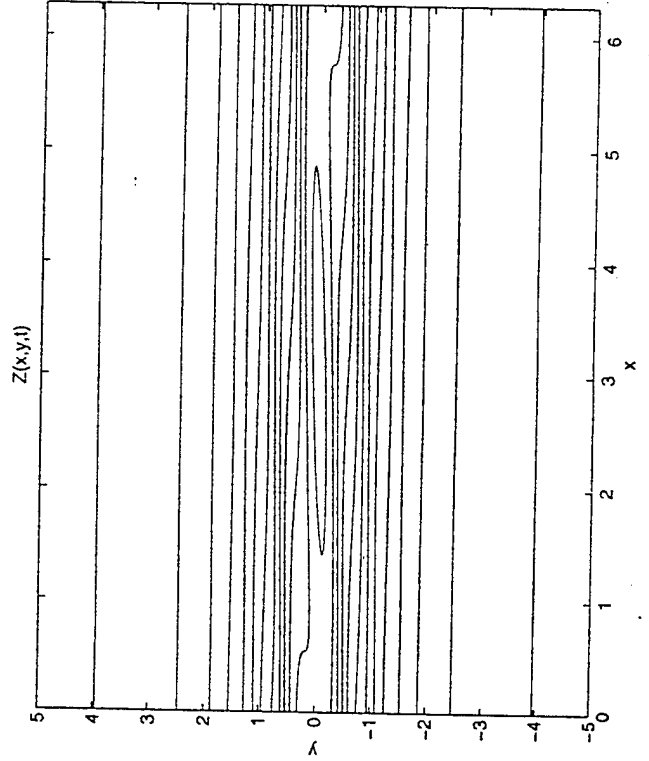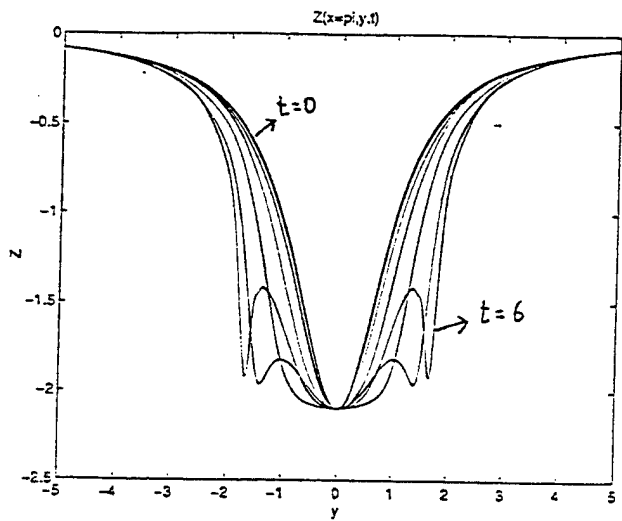

Z(x,y,t)

Fig. 2 (b)

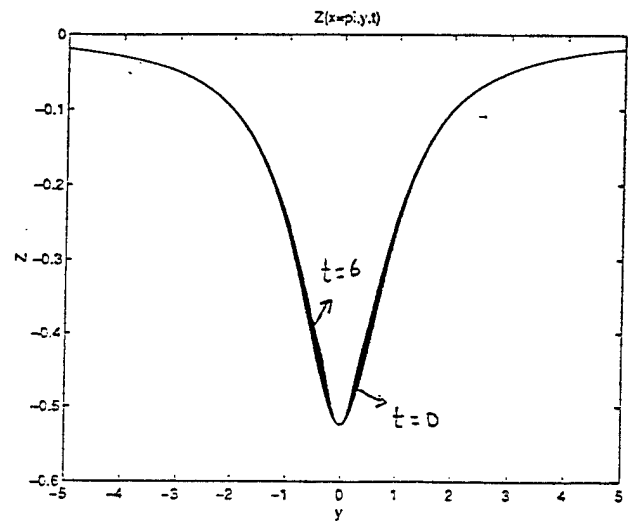
Z(x,y,t)

Fig. 1 (a)

Z(x,y,t)
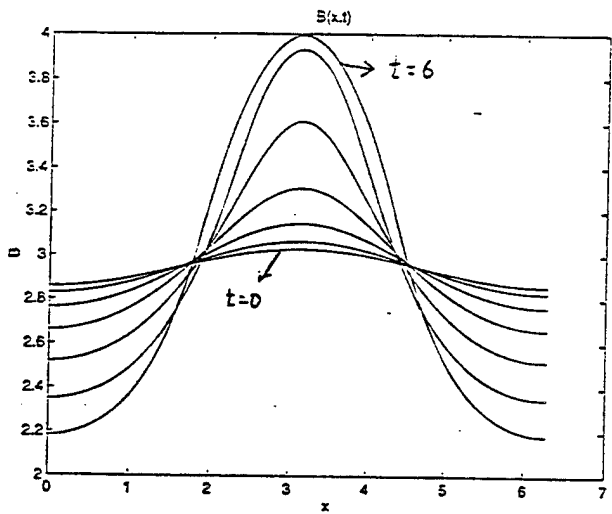
Fig. 1 (b)

Fig. 1 (c)

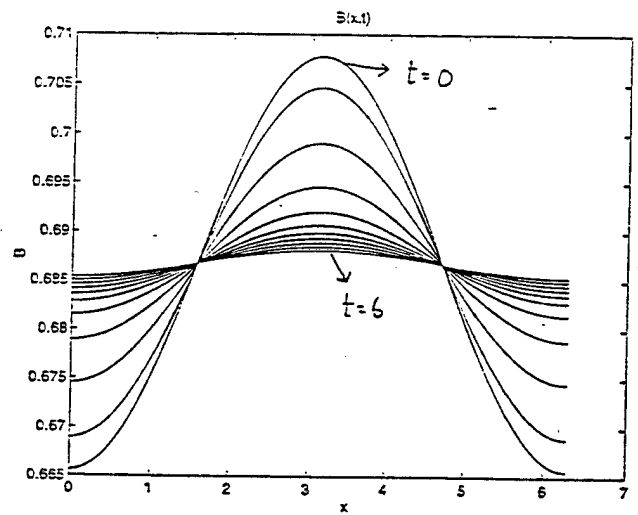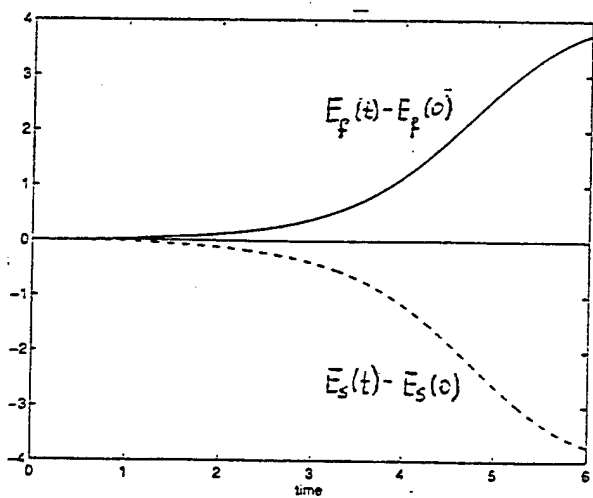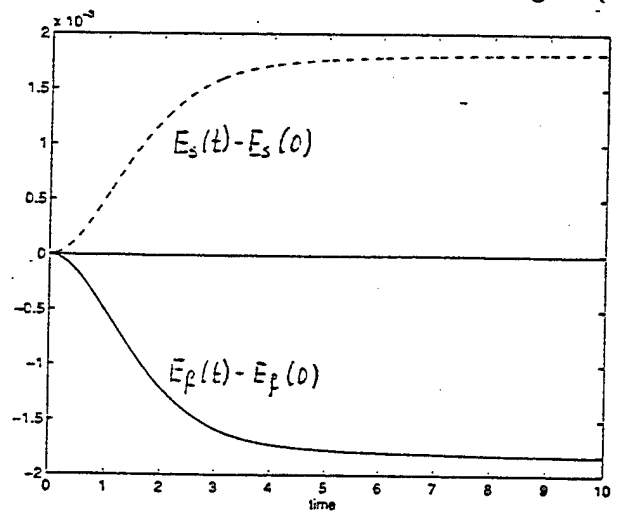
Fig. 2 (c)

Fig. 1 (d)

Fig. 2 (d)

Fig. 1 (e)

Fig. 2 (e)

Ultrasound scattering by turbulent flows

Stéphan Fauve
Ecole Normale Supérieure de Lyon
46, allée d'Italie 69364 Lyon France

1. Sound scattering by velocity gradients

It has been known for a long time that waves can be used to probe a medium which interacts with them. In the case of sound waves, scattering results from density, temperature or velocity fluctuations. This can be easily understood since the three types of perturbations generate local variations of the sound velocity, and the wave equation with a random index of refraction has thus been widely used to study amplitude and phase perturbations of sound waves in turbulent media [1-4]. Although it can be shown that the stochastic wave equation is a reasonable approximation in some limits [5], the hydrodynamic equations describing the interaction of sound waves with turbulent flows cannot be directly put in this form in general. However, the interpretation of many experimental results have been tried in this framework, using empirical models to relate the index of refraction to the statistical properties of the turbulent flow. More formally, the scattering of sound by turbulent inhomogeneities traces back to the coupling between the hydrodynamic modes of a simple fluid, i.e. sound, entropy and vorticity modes [6].

We consider here an incompressible flow and thus neglect its density variations. We also neglect temperature fluctuations. The only scattering mechanism is thus related to fluctuating velocity gradients. This approximation is realistic in the limit of small Mach numbers

$$M \equiv \frac{u_0}{c} \ll 1, \tag{1}$$

and is easily experimentally checked since scattering by density or temperature fluctuations generate a different qualitative behavior of the cross-section versus the scattering angle. We consider that the frequency ω_s of the sound wave is large compared to any characteristic frequency ω_0 of the basic flow,

$$\omega_s \gg \omega_0, \tag{2}$$

which is thus considered frozen, and we assume that viscous dissipation is negligible on the acoustic time scale. Writing $\vec{u} = \vec{u}_0 + \vec{v}_s$ and $\rho = \rho_0 + \rho_s$, where the subscript 0 stands for the basic flow and s for the sound wave, and taking into account the above approximations, we obtain from the conservation equations for momentum and mass

$$\frac{\partial \vec{v}_s}{\partial t} + \frac{1}{\rho_0} \nabla p_s \approx -(\vec{u}_0.\nabla)\vec{v}_s - (\vec{v}_s.\nabla)\vec{u}_0, \tag{3}$$

$$\frac{\partial \rho_s}{\partial t} + \rho_0 \nabla.\vec{v}_s \approx -\vec{u}_0.\nabla\rho_s. \tag{4}$$

The left hand side, with $p_s = c^2\rho_s$, is related to the sound wave alone, and coupling terms with the basic flow on the right hand side of (3, 4) are of respective order, M, $M\lambda_s/l_0$ and M related to the left hand side, where λ_s is the acoustic wavelength and l_0 a characteristic spatial scale of the basic flow. Terms of higher order in M have been omitted and λ_s/l_0 should not be too large in order to ensure the validity of the approximation.

a) The short wavelength limit

In the limit of very high sound frequency or short wavelength, the second term on the right hand side of (3) can be neglected and equations (3, 4) can be put in the form

$$\frac{D^2\rho_s}{Dt^2} \equiv \left(\frac{\partial}{\partial t} + \vec{u}_0.\nabla\right)^2 \rho_s = c^2\nabla^2\rho_s, \tag{5}$$

showing that the sound wave is advected by a locally constant flow. Similar approximations were first used by Obukhov [7] and Blokhintzev [8] to compute scattering of sound waves by turbulence. In the limit of geometrical acoustics, one thus has for the velocity of a point on a wave front

$$\frac{d\vec{r}}{dt} = c\frac{\vec{k}}{k} + \vec{u}_0, \tag{6}$$

where $\vec{k}$ is the local wave vector, and one can compute ray trajectories in the fluid. The refraction of sound by wind has been considered by Rayleigh [9] and geometrical acoustics in moving media has been worked out in details by Blokhinstev [8]. Rudnick considered the refraction of sound at an interface between two perfect fluids moving at different velocities, i.e. a vorticity sheet, [10-12], and Lindsay investigated the case of refraction by a two-dimensional vortex [13]. It can be shown from (6) that a unit vector $\vec{t}$, tangential to an acoustic ray, obeys

$$\frac{d\vec{t}}{dl} \approx -\vec{t} \times \frac{\vec{\omega}_0}{c}, \tag{7}$$

where $\vec{\omega}_0$ is the vorticity field of the flow and dl the element of length along the ray [14]. This formula does not mean that the equiphases of the sound wave are not distorted by a flow without vorticity. Indeed, the flow generally makes the medium anisotropic, and $\vec{t}$ is no longer parallel to the wave vector $\vec{k}$. Phase fluctuations of an acoustic wave propagating in a turbulent medium can be evaluated in the limit of geometrical acoustics [3, 4]. This gives a correct estimation provided that the size of the inhomogeneities l_0 remains large compared to the first Fresnel zone, i.e. up to a propagation distance l given by

$$l \simeq \frac{l_0^2}{\lambda_s}. \tag{8}$$

Note that this condition only implies the size l_0 of the inhomogeneities but not their strength $\delta u_0/c$, where δu_0 is the velocity increment on size l_0, contrary to refraction effects which subsist in the limit of geometrical acoustics.

b) Sound scattering in the small Mach number limit

When the sound wavelength is of the same order than the size of some turbulent eddies, all terms in equations (3, 4) should be kept and, using approximations (1, 2), one obtains

$$\frac{\partial^2 \rho_s}{\partial t^2} - c^2 \Delta \rho_s \approx 2\rho_0 \frac{\partial^2}{\partial x_i \partial x_j}\left(u_{0i} v_{sj}\right). \tag{9}$$

This shows that when the turbulent flow $\vec{u}_0$ is probed by an incident sound wave $(\rho_s^{(0)}, \vec{v}_s^{(0)})$, the source term on the right hand side of (9) generates scattered waves which result from the interaction between the flow and sound velocity fields. It can be observed from equation (9) that the scattered wave is frequency shifted in the case of a time dependent flow $\vec{u}_0$, and also that the interaction term has the same quadrupole distribution than the source term found by Lighthill for aerodynamic noise generation by turbulence at small Mach number [15]. It is thus easy to discriminate scattering by velocity gradients from scattering by temperature fluctuations which leads to a dipolar distribution [16-19]. If the interaction term is small, the total sound field is roughly equal to the incident one and we can replace v_{sj} by $v_{sj}^{(0)}$ i.e. use the Born approximation to compute the scattered wave. This has been done by Kraichnan, who obtained in the far field limit, formulas for the angular and frequency distributions of the scattered wave in terms of the Fourier transforms in space and time of the shear velocity field $\vec{u}_0$.

Although most experiments of sound propagation in turbulent flows concern amplitude and phase fluctuations of the incident wave, there were also a few studies of the

angular distribution of the scattered waves, in atmospheric turbulence by Kallistratova and Tatarskii [16], in grid turbulence in air by Baerg and Schwarz [18] and in a turbulent jet in water by Korman and Beyer [21]. The results obtained by these authors were found to be consistant with Kraichnan's formula, and quantitative differences can be easily explained, in air because of the approximations leading to (9) are not always fulfilled, and for turbulent jets in water because of the possible existence of tiny air bubbles which modify the scattering properties.

Several authors have related the scattered sound to the vorticity $\vec{\omega}_0 = \nabla \times \vec{u}_0$ of the flow, starting from Pitaevskii who calculated the phonon part of the mutual friction force in superfluid helium using the scattering formula for sound by potential vortices [22]. Ferziger considered the case of a Burgers vortex and discussed ultrasound scattering as a possible monitoring system for vorticity [23], and Fabrikant [24], Klimov and Prozorovskii [25] and Lund and Rojas [26] gave compact formulas in the far field approximation, relating the scattering amplitude to the vorticity. One has for the scattering amplitude

$$ f(\vec{k}_1, \vec{k}_2) \propto \frac{1}{\omega_s}(\vec{k}_1 \cdot \vec{k}_2)\left(\vec{k}_1 \cdot \tilde{u}_0(\vec{q})\right) \propto \frac{-i}{\omega_s q^2}(\vec{k}_1 \cdot \vec{k}_2)(\vec{k}_1 \times \vec{k}_2) \cdot \tilde{\omega}_0(\vec{q}), \qquad (10) $$

where $\vec{k}_{1,2}$ are respectively the incident and scattered wave vectors, $\vec{q} \equiv \vec{k}_1 - \vec{k}_2$ is the scattering wave vector, $\tilde{u}_0(\vec{q})$ is the spatial Fourier transform of the vortex flow velocity field and $\tilde{\omega}_0(\vec{q})$ is the spatial Fourier transform of the vorticity. Consequently, only the vorticity component perpendicular to the scattering plane is probed, and the scattered wave vanishes at angles $\pi/2$ and π. The possible divergence of f at small scattering angle is a well known deficiency of the Born approximation. It may be compensated by the q dependence of the $\tilde{\omega}_0(\vec{q})$ if the total vorticity vanishes i.e. if there is no global circulation [24]. However, the Born approximation could not be entirely correct, in particular at small scattering angles, because of the lack of an imaginary part of the scattering amplitude which must exist according to the optical theorem. Corrections to the Born approximation have been evaluated by Klimov and Prozorovskii [25] by taking into account how the incident wave is deformed by the basic flow field.

The expression of the scattering amplitude as a function of the vorticity field may be misleading. It should be considered as a mathematical expression, approximately correct in the Born approximation and in the far field limit, but it would be wrong to deduce that the local scattering mechanism involves only the antisymmetric part of the velocity gradients, i.e. the vorticity. Indeed, it has been shown, using different methods, that irrotational flows do scatter sound waves [7, 27].

However, sound scattering by velocity gradients together with the analysis presented above in the small Mach number and the far field limits, provides a powerful tool to measure directly vorticity dynamics. This has been carefully checked with experiments on model flows such that the von Karman vortex street in the wake of a cylinder; all the results obtained with other experimental techniques on this flow configuration have been confirmed using sound scattering, that has also provided additional results on vorticity dynamics [28-30]. We have used this technique to detect and charaterize vorticity filaments in von Karman turbulent swirling flows generated in the gap between counter-rotating disks.

2. Detection of vorticity filaments in turbulent swirling flows
a) Vorticity filaments

As said above, intense vorticity concentrations have been observed in direct numerical simulations of fully developed turbulence by Siggia [31], and their characteristics have been widely studied [32-35]. The following results are fairly well established so far:
   - vorticity concentrations with the shape of nearly two-dimensional filaments are observed,
   - their core size r_f is in the range between the Taylor and the Kolmogorov lengths, i. e. corresponds to a small spatial scale,
   - their length l_f corresponds to a large spatial scale, probably the integral scale,

- the velocity increment δu_f on their core size is in the large scale range, probably the integral velocity scale u_{rms}.

However, the exact scalings of r_f, l_f and δu_f versus the Reynolds number are not known due to the finite Reynolds number range of the numerical simulations and to possible problems in the filament detection algorithm. The rôle of vorticity filaments, or at least their correlation with the dynamics of turbulence, with the dissipation for instance, is also unclear. It is clear that vorticity filaments violate locally (in time and space) Kolmogorov-41 scaling (as well as isotropy) and it is thus tempting to associate them with intermittency, but no quantitative estimation of their contribution to intermittency is available.

There have been many experimental attempts to visualize coherent vorticity structures in boundary layers or in rotating flows, but only a few in the bulk of fairly homogeneous isotropic flows, i. e. flows for which turbulent fluctuations may be described by the numerical simulations quoted above. Douady et al. studied turbulent flows generated in the gap between two coaxial counter-rotating disks (von Karman swirling flows): visualisation using water seeded with air bubbles, showed that in the median region of the cell, the flow looks rather homogeneous when a turbulent regime is reached. Moreover, intermittent formation of filaments of bubbles was reported, and ascribed to vorticity concentrated on tube-like structures [36]. The detection of these vorticity filaments and the study of their dynamical and statistical properties have been performed via pressure measurements [37-39]. We observed that the pressure drops scale like the square of the integral velocity, thus showing that the characteristic velocity increment on the core of the vortex is of the order of the integral velocity of the turbulent flow [37]. We also studied the statistical properties of the pressure drops [38]: in particular, the waiting time between two successive vorticity filaments sweeping the pressure transducer, displays Poisson statistics at long enough time, but a clear departure from Poisson statistics at short waiting times; the waiting time PDF decays algebraically for short times and exponentially at large times. The cross-over between the two behaviors occurs for an integral time scale, roughly 10 periods of rotation of the disks.

b) Sound scattering by vorticity filaments

The turbulent flow generated in the gap between two coaxial counter-rotating disks has been probed acoustically using pairs of reversible broad band $MATEC$ piezoelectric transducers that are fitted flush with the lateral boundary in the mid-plane between the two disks. A sinusoidal wave is emitted by one transducer; the wave scattered by turbulent fluctuations in the bulk of the flow, is detected using the other transducer at a scattering angle of 60°. The scattering plane is thus horizontal. Thus from (10), the Fourier transform of the vorticity component perpendicular to the scattering plane, i.e. parallel to the axis of the disks, is probed at the scattering wave vector. The incident sound frequency is varied from 1 to 15 MHz; resonant scattering is observed at about 10 MHz in water when the rotation rate of the disks is 1000 RPM, and at smaller frequencies in water-glycerol mixtures or for smaller rotation rates. Away from resonance, the scattered pressure spectrum displays a peak at the incident sound wave frequency, enlarged due to turbulence. In the vicinity of resonant scattering, the additional scattered power occurs in rather sharp peaks in the Fourier spectrum of the scattered pressure which are Doppler-shifted from the incident frequency. They are ascribed to the presence of vorticity filaments crossing the scattering volume with a given velocity. Note that due to the high frequency of the incident wave, the velocity field looks frozen during the measurement time. Resonant scattering occurs when the incident sound wavelength is of the same order of magnitude as the core size r_f of vorticity filaments. Looking at the maximum scattered intensity as a function of the Reynolds number Re, we found that r_f scales like the Taylor microscale of the flow. We also studied in details the statistical properties of vorticity fluctuations and found them in qualitative agreement with pressure statistics (Dernoncourt et al.)[40].

In conclusion, ultrasound scattering is a powerful technique to study turbulent flows and in particular coherent structures. Velocity gradients are probed directly in Fourier space; one does not need to differentiate a signal assuming the Taylor hypothesis, and a whole flow volume can be probed instantaneously at a scale fixed by the scattering

wave vector. Ultrasound scattering is thus much more efficient than conventional hot-wire anemometry to detect coherent structures and study their dynamics and statistical properties.

References

1. Obukhov, A. M., *Izv. Akad. Nauk Seriya Geofiz.* **2**, 155-165 (1953), see *Waves in Random Media* **4**, 9-19 (1994) for an english translation.
2. Obukhov, A. M., *J. Geophys. Research* **64**, 2180-2187 (1959).
3. Chernov, L. A., *Wave propagation in a random medium*, McGraw-Hill (1960).
4. Tatarskii, V. I., *Wave propagation in a turbulent medium*, Dover (1961).
5. Neubert, J. A. and Lumley, J. L., *J. Acoust. Soc. Am.* **48**, 1212-1218 (1970).
6. Chu, B. T. and Kowaznay, L. S. G., *J. Fluid Mech.* **3**, 494- (1958).
7. Obukhov, A. M., *Dokl. Akad. Nauk. SSSR* **30**, 616-620 (1941).
8. Blokhintzev, D., *J. Acoust. Soc. Am.* **18**, 322-334 (1946).
9. Rayleigh, J. W. S. *Theory of sound* Vol. II, chap. 14, Dover (1945).
10. Rudnick, I., *J. Acoust. Soc. Am.* **17**, 245-253 (1946).
11. Keller, J. B., *J. Acoust. Soc. Am.* **27**, 1044-1047 (1955).
12. Miles, J. W., *J. Acoust. Soc. Am.* **29**, 226-228 (1957).
13. Linsay, R. B., *J. Acoust. Soc. Am.* **20**, 89-94 (1948).
14. Landau, L. D. and Lifshitz, E. M., *Fluid mechanics*, 261-262, Pergamon Press (1959).
15. Lighthill, M. J., *Proc. Camb. Phil. Soc.*, **49**, 531-551 (1953).
16. Kallistratova, M. A. and Tatarskii, V. I., *J. Acoust. Soc. Am.* **6**, 503-505 (1960).
17. Monin, A. S., *Sov. Phys. JETP* **7**, 370-373 (1962).
18. Baerg, W. and Schwarz, W., *J. Acoust. Soc. Am.* **39**, 1125-1132 (1966).
19. Contreras, H. and Lund, F., *Phys. Lett.* **149**, 127-130 (1990).
20. Kraichnan, R. H., *J. Acoust. Soc. Am.* **25**, 1096-1109 (1953).
21. Korman, M. S. and Beyer, R. T., *J. Acoust. Soc. Am.* **67**, 1980-1987 (1980).
22. Pitaevskii, L. P., *Sov. Phys. JETP* **8**, 888-890 (1959).
23. Ferziger, J. H., *J. Acoust. Soc. Am.* **56**, 1705-1707 (1974).
24. Fabrikant, A. L., *Sov. Phys. Acoust.* **28**, 410-411 (1982); **29**, 152-154 (1983).
25. Klimov V. V. and Prozorovskii V. L., *Sov. Phys. Acoust.* **33**, 128-131 (1987).
26. Lund, F. and Rojas, C., *Physica* **D 37** 508-514 (1989).
27. Wentzel A. R. and Keller, J. B., *J. Acoust. Soc. Am.* **50**, 911-920 (1971).
28. Gromov, P. R., Ezerskii, A. B. and Fabrikant, A. L., *Sov. Phys. Acoust.* **28**, 452-455 (1982).
29. Baudet, C., Ciliberto, S. and Pinton, J. F., *Phys. Rev. Lett.*, **67**, 193-195 (1991).
30. Pinton, J. F. and Baudet, C., in *Turbulence in spatially extended systems*, Les Houches Series, Basdevant, C., Benzi, R. and Ciliberto, S. editors, Nova Science Publishers (1993).
31. E. D. Siggia, *J. Fluid Mech.* **107**, 375-406 (1981).
32. M. Brachet, *C. R. Acad. Sci. (Paris)* **311**(II), 775-780 (1990).
33. Z.S. She, E. Jackson and S. A. Orszag, *Nature* **344**, 226-228 (1990).
34. A. Vincent and M. Menneguzi, *J. Fluid Mech.* **225**, 1-20 (1991).
35. Jiménez, J., Wray, A. A., Saffmann, P. G. and Rogallo, R., *J. Fluid Mech.* **255**, 65-90 (1993).
36. Douady, S., Couder, Y. and Brachet, M.-E., *Phys. Rev. Lett.* **67**, 983-986 (1991).
37. Fauve, S., Laroche, C. and Castaing, B., *J. Phys. II France* **3**, 271-278 (1993).
38. Abry, P. , Fauve, S., Flandrin, P. and Laroche C., *J. Phys. II France* **4**, 725-733 (1994).
39. Cadot, O., Douady, S. and Couder, Y., *Phys. Fluids* A**7**, 630-646 (1995).
40. Dernoncourt, B., Pinton, J. F. and Fauve, S., "Experimental study of vorticity filaments in turbulent swirling flows", submitted to *J. Physique* (1996).

On diffusion by intelligent movements

Glenn R, Flierl

MIT

Many oceanic organisms have spatial distributions which are much less uniform than tracer quantities; this patchiness presumeably arises from the ability of the animals to regulate their speed or direction based on environmental cues. We wish to understand how patchiness occurs, especially in the presence of turbulent flows, and how it affects interactions with other organisms — grazing and predation. Modelling the dynamics of patchy organisms has close analogies to the theory of gases. The simplest, but computationally overwhelming, approach to the latter is simulating the motions of individual molecules using the rules of Newtonian dynamics and representations of collision processes. Directly equivalent approaches have been taken for organisms. At the opposite end of the spectrum are the Navier–Stokes equations which view the gas as a continuum and introduce viscosity and diffusion to incorporate effects of momentum and energy transfer via collisions. This kind of continuum equation is a very important step if we wish to understand the overall effects of patchiness in larger scale flows/ ecosystems. In between these two approaches lies the Boltzmann equation, which predicts the evolution in space and time of the probability distribution for the molecular velocities. This equation proves crucial in that it forges a direct link between molecular dynamics and continuum mechanics and makes possible direct calculation of the form and coeffients of the viscous/ diffusive terms in the Navier–Stokes equations, as well as an approach to problems where correctins to these are needed.

An analogous equation for organisms should play an equivalent and important role in aiding our understanding of the relationship between the continuum and individual–based models and the limits of validity of the former. We have begun with examples of decision rules for individuals and produced Boltzmann equations for the velocity distribution. Using the Chapman-Enskog procedure, a form of multiple time–scale analysis, we derive an equation for the density of organisms which has biological diffusion and advection (generally *not* non–divergent) terms. Convergent biologically–induced velocities can arise either from directed motions up the gradient in the cue field or from changes in the random swimming movements according to the cue strength. When the cue field is related to the density itself (*e.g.* sensitivity to the number of neighbors within some perception range), the equation becomes nonlinear.

This equations show that a sufficiently dense uniform distribution of animals can become unstable if the organism is attracted to neighbors or slows its random motion as the neighbor density increases, leading to patches. The instability is subcritical, so that concentrations generally vary strongly from within a patch to outside. In the presence of turbulent flows, patches can still form if the shear and strain is not too large. Turbulence does not, however, simply act as an increase in physical diffusion: we have estimated the diffusion coefficient by examining the dispersion of passive particles. If that diffusivity is added to the density equation, patches do not form; in contrast, in the actual turbulent flows, organisms can presumeably take advantage of spots with relatively low strain to build a patch. the patches do tend to be more tranistory, breaking apart and merging as the flow changes around them.

Patchiness can also alter predator–prey dynamics; in the case of patchy prey, the average level increases slightly, while the average predator level decreases. For other parameter ranges, there can be travelling waves or chaotic patches.

Baroclinic Instability of the Oceanic Mixed Layer.

Thomas Haine
Earth, Atmospheric & Planetary Sciences,
MIT, Cambridge, MA

1. INTRODUCTION

We explore the possibility that baroclinic instability, feeding off lateral buoyancy gradients in the oceanic mixed layer, can result in buoyancy fluxes that significantly modify the deepening and shallowing of the layer. In a simple model of the ocean mixed layer, symmetric instability is invoked to set the potential vorticity to zero. The result is a weakly stratified layer susceptible to non-hydrostatic baroclinic instability. A numerical study confirms the simple theory and extends it to a fully non-linear, three dimensional regime.

2. THEORY

Consider the stratified thermocline outcropping in to a mixed-layer as shown in Figure 1. Suppose for a moment that there are no along-channel (x) variations. Then a consideration of the zonal momentum equation (assumed inviscid) on an f-plane tells us that:

$$\frac{DM}{Dt} = 0, \qquad \frac{D\sigma}{Dt} = -\frac{B}{g} \qquad (1),$$

where $M = fy - u$ is the angular momentum, u the zonal velocity, f the Coriolis parameter, y the cross channel coordinate, σ is the potential density, D/Dt is the Lagrangian derivative, B is the buoyancy forcing (induced, for example, by buoyancy loss from the surface) and g is the acceleration due to gravity. If the zonal flow is in thermal wind balance then the Ertel potential vorticity Q of the fluid is:

$$\rho_0 Q = J_{yz}(\sigma, M) \qquad (2),$$

where ρ_0 is a constant reference density. There will be a vertical shear, $\partial u/\partial z$, in the mixed layer if there is a cross-channel density gradient, and so the M surfaces will not be vertical there. Rather they will tilt over. Since the M surfaces are material surfaces, fluid parcels (or rather zonal 'strips', in this thought experiment) will move in slantwise paths.

Now suppose that buoyancy is lost to the atmosphere so that parcels at the surface become dense thereby inducing convection. If the static stability measured along the M surface becomes negative (i.e. the potential vorticity $Q < 0$), then 'slantwise' convection
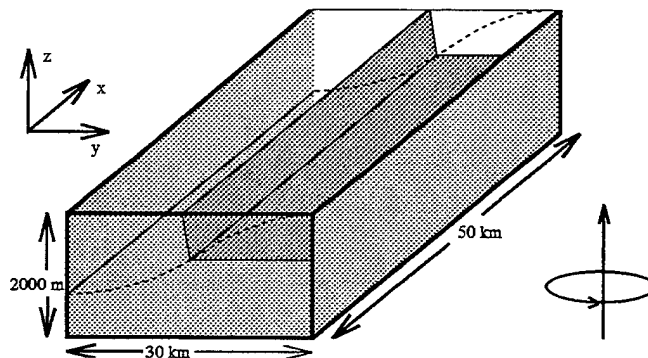

Figure 1. Schematic diagram of an isopycnal outcropping into a mixed layer with a lateral density gradient.

(sometimes called symmetric instability) will occur along the sloping M surfaces. Within a few hours this restores the potential vorticity of the layer to zero. The static stability gradient on the M surfaces vanishes, but because these are tilted over, there is non-zero vertical stratification.

Below we investigate by numerical experiment whether convective overturning of a mixed layer indeed sets the Q of the layer to zero. In the thought experiment above we argued, somewhat unrealistically, that M is conserved in zonal strips. In the fully 3-dimensional numerical experiments presented below no such constraint is imposed. We find that:

(i) the full 3-D Ertel potential vorticity is now set to zero; σ is mixed along the absolute vorticity vector $\hat{k}f + \nabla \times v$, rather than an M surface.

(ii) the resulting 'mixed-layer' is mixed in potential vorticity but vertically stratified in density i.e. $N^2 > 0$.

(iii) the zero potential vorticity layer is susceptible to baroclinic instability; slantwise convection ultimately gives way to non-hydrostatic baroclinic instability (Stone, 1971) as the preferred mechanism of buoyant transport through the mixed layer. Baroclinic eddies transport buoyancy laterally and vertically.

3. MODEL

We use a high resolution numerical model to solve the non-hydrostatic Boussinesq primitive equations in a periodic channel domain which rotates at a constant rate, f, of $10^{-4}s^{-1}$. The fluid is initially resting with a uniform stratification, N, such that everywhere $N/f = 8$. The motion is forced by a steady buoyancy loss through the sea surface. This cooling is independent of x but increases with y following a hyperbolic tangent variation. Thus in the southern third of the channel there is weak surface forcing, in the northern third fairly constant densification equivalent to a heat loss of 800 Wm^{-2}, and there is a sharp transition in between. A linear equation of state is specified dependent on temperature alone.

A key feature of this model is that the fine cell spacing resolves the upright, gravitational, convection. For the first few days a mixed layer of depth H develops according to a simple, non-rotating, one dimensional law which predicts the depth of mixing due to the upright overturning. Namely,
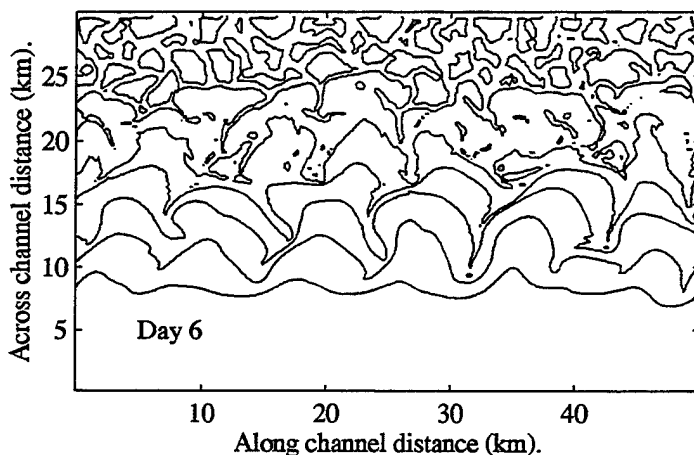

Figure 2. Horizontal section of temperature at 65m depth.

$$H = \frac{\sqrt{2Bt}}{N} \qquad (3),$$

where B is the buoyancy flux across the surface at time t. As a result of the developing density gradient across the channel, a flow adjusts to achieve a thermal wind balance. At the channel centre, the region of highest gradient, the angular momentum surfaces are bent over, and symmetric instability exchanges dense surface water with the underlying fluid along paths which slant to the vertical.

After six days, however, a mode six, finite amplitude, baroclinic instability has grown in the channel centre, and is responsible for exchanging water laterally, from the region of deep mixing, to the unconvected fluid and vice versa (Figure 2). In the north the fine, plume scale elements can be seen drawing the buoyancy from the interior. At later times a field of geostrophic turbulence evolves as the baroclinic waves break. Figure 3a shows that the near surface, mid-channel, fluid has, on average, a weak vertical stratification. There is no evidence of a classic mixed layer with vanishing stratification, except in the region close to the northern wall. The heavy dashed line shows the one dimensional prediction of mixed layer depth (Eq (3)). Figure 3b shows the Ertel potential vorticity at this time, and is much more effective at revealing the "mixed layer" fluid. Across the region of non-vanishing vertical stratification the PV is weak and positive; the signature of symmetric instability. To the south the low PV fluid shows that mixed water has penetrated deeper than the one dimensional prediction, a consequence of the lateral buoyancy flux by baroclinic eddies. To the north the mixed layer is shallower.

4. IMPLICATIONS

We have shown that in a mixed layer with a horizontal density gradient symmetric instability rapidly acts to create a layer with near zero PV and non-vanishing vertical stratification. Furthermore, growing baroclinic waves develop to produce an eddy field which transports buoyancy laterally in the mixed layer. This flux is certainly important on the margins of deep convection chimneys. Our calculations also suggest that it is significant in less extreme mixing regimes. The Gulf Stream, and large areas of the sub-polar North Atlantic show a strong net lateral buoyancy flux. The seasonal cycle modulates these fluxes, giving the greatest power at the time of deepest overturning. Our preliminary results suggest that this lateral mixing mechanism may be ubiquitous and represent an important extra term in traditional one dimensional mixed layer models. It is most significant at the time of subduction, and may be influential in setting the characteristics of newly formed thermocline water.
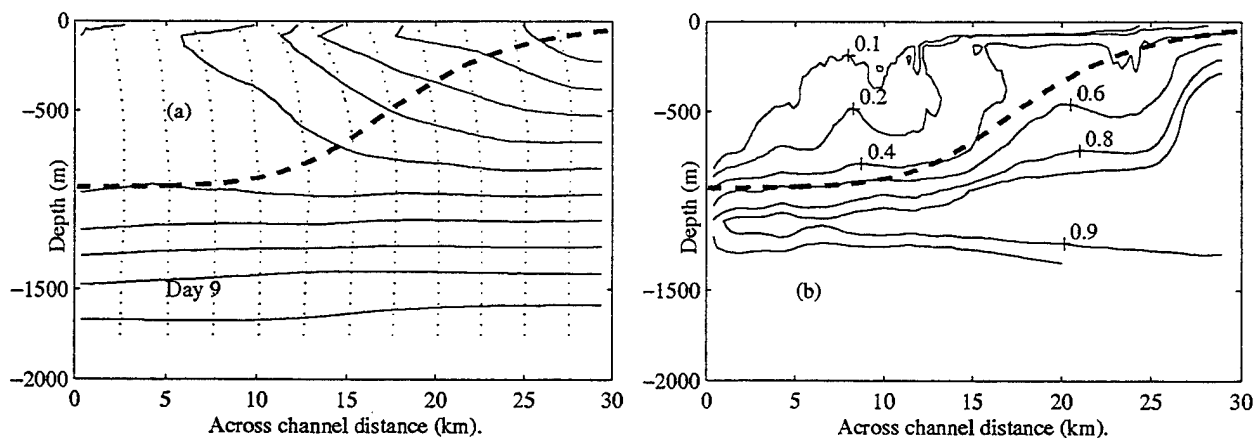

Figure 3. (a) Along-channel mean section of temperature (-), M (..) and 1D mixed layer depth prediction (--), and (b) along-channel mean section of Ertel potential vorticity at day 9.

5. REFERENCES.

Emmanuel, K (1994), Atmospheric Convection, Oxford University Press.
Stone, P (1971), Baroclinic stability under non-hydrostatic conditions, *J. Fluid Mech.*, **45**, 659-671.

Is the Thermocline a Front?
— Symmetries and Conservation Laws in GFD

by Simon Hood
Oceanography Labs., University of Liverpool,
Liverpool, L69 3BX, England

Introduction

In much of the world's oceans there is a surprising characteristic temperature profile: below the mixed layer there is a region of rapid temperature decrease, from the surface value, to a depth of order 1 km (the thermocline) and below this the temperature is almost constant. What physical process (or processes) are responsible for this?

This question, the so-called thermocline problem, has been addressed by many authors and several very different possibilities have been put forward as explanations. Early thermocline work used a similarity approach and two opposing limits were advocated: diffusive control (Robinson and Stommel, 1959) and advective control (Welander, 1959). More recently thermocline studies have made use of layered models. Amongst these Rhines and Young (1982) argue that the role of geostrophic eddies in homogenising properties is important, and Luyten, Pedlosky and Stommel (1983) argue that the thermocline is a consequence of advection of the mixed-layer temperature field down into the ocean interior. There seems little doubt that the upper part of the thermocline is ventilated by this latter proccess, but this does not mean that other physical processes are not at work. (Marshall (1995) advocates one such process.)

The governing equations most often used to model the thermocline are (in non-dimensional form, on a β-plane)

$$yu = -P_y, \qquad yv = P_x, \qquad \theta = P_z, \qquad (1\text{i})$$
$$u_x + v_y + w_z = 0, \qquad u\theta_x + v\theta_y + w\theta_z = \mathcal{F} + \mathcal{D}, \qquad (1\text{ii})$$

and these are, respectively, the geostrophic and hydrostatic approximations to the horizontal and vertical momentum equations, continuity and a thermodynamic equation (salinity is neglected). Here u, v and w are the velocity components, P is pressure and θ is the potential temperature; $\mathcal{F}$ and $\mathcal{D}$ represent forcing and diffusion respectively. Simple scaling arguments (cf. Pedlosky, 1987, Section 6.20) indicate that the effects of horizontal diffusion are much smaller than those of vertical diffusion and assuming no forcing we may write

$$u\theta_x + v\theta_y + w\theta_z = (\kappa(z)\theta_z)_z; \qquad (2)$$

here vertical diffusion is represented by a simple Laplacian scheme which admits variation of diffusivity with depth.

An alternative approach to those more commonly used to determine physical solutions of (1) is to consider the mathematical properties of the equations themselves, in particular their (Lie) symmetries and (materially) conserved quantities. Each of these approaches is considered here.

Lie Symmetries

Lie symmetries of a PDE and their usage are best explained by means of a simple example. Consider Burgers' equation,

$$u_t + uu_x + u_{xx} = 0, \qquad (3)$$

together with the transformation

$$t \longrightarrow \alpha^2 t, \qquad x \longrightarrow \alpha x, \qquad u \longrightarrow \alpha^{-1} u. \qquad (4)$$

Burgers' equation is unchanged by (4) as are the combinations of variables

$$\xi = \frac{x}{t^{1/2}}, \qquad G = t^{1/2} u. \qquad (5)$$

We say that (3) is mapped to itself by (4), and (5) are invariants of the transformation which is a one-parameter (Lie) group. Such invariants may be used to construct a transformation which reduces the number of independent variables in a differential equation. For example, in this case, substituting

$$u(x,t) = t^{-1/2} G(\xi) + \frac{x}{2t} \qquad (6)$$

into (3), we obtain

$$t^{-3/2} \{ G_{\xi\xi} + G G_\xi \} = 0, \qquad (7)$$

i.e., we have reduced Burgers' equation to an ODE.

These ideas are the foundations for an ever growing collection of methods which seek to reduce a PDE to a differential equation in fewer independent variables (or a system of such equations). An accessible introduction to the subject is given by Hill (1992) and a review of several such methods is given in a paper by Olver (1992). The most straightforward of these methods has been applied to the so called thermocline equations, (1), to obtain exact solutions, by Salmon and Hollerbach (1991) and these results have been expanded upon by Hood (1995) and Hood & Williams (1995). The results given in the next section are derived in these latter works.

Results obtained using Lie symmetries

It has been suggested that the dominant process underlying the formation of the thermocline is the formation of a (weak) interior front. The front is supposed to form where water moving downwards due to Ekman convergence at the surface meets hypothesised large scale upwelling and $w \to 0$. (In fact it is only necessary that $w \to 0$; it is not necessary that w change sign. This, however, seems less physical.) Diffusion is important only locally, in the frontal region. (Frontal solutions to PDEs in which characteristics converge in this way are well known in other weakly diffusive systems, such as those represented by Burgers' equation; for example see Kevorkian, 1990.) This explanation of the thermocline is advocated by Salmon (1990).

We can find exact analytic solutions to the thermocline equations which help us to investigate this process by using Lie symmetries. (Frontal solutions are, however, certainly not the only type of solution recoverable by this method: Hood and Williams (1995) include an example of a ventilated thermocline.) To do this we first write the thermocline equations, (1), as

$$M_x M_{zzz} + y(M_{xz} M_{yzz} - M_{yz} M_{xzz}) = y^2 (\kappa M_{zzz})_z, \qquad (8)$$

where

$$u = -\frac{1}{y} M_{yz} \qquad v = \frac{1}{y} M_{xz} \qquad w = \frac{1}{y^2} M_x \qquad \phi = M_z \qquad \theta = M_{zz}, \qquad (9)$$

without loss of generality and then determine transformations like (4) which reduce (8) to a PDE in two independent variables or to an ODE. This is done for transformations which admit diffusivity as an arbitrary function of z by Hood (1995). One such reduction is

$$M(x, y, z) = G(y, z) + x \left[y^2 \kappa_z + \Gamma(y, z) \right], \qquad (10a)$$

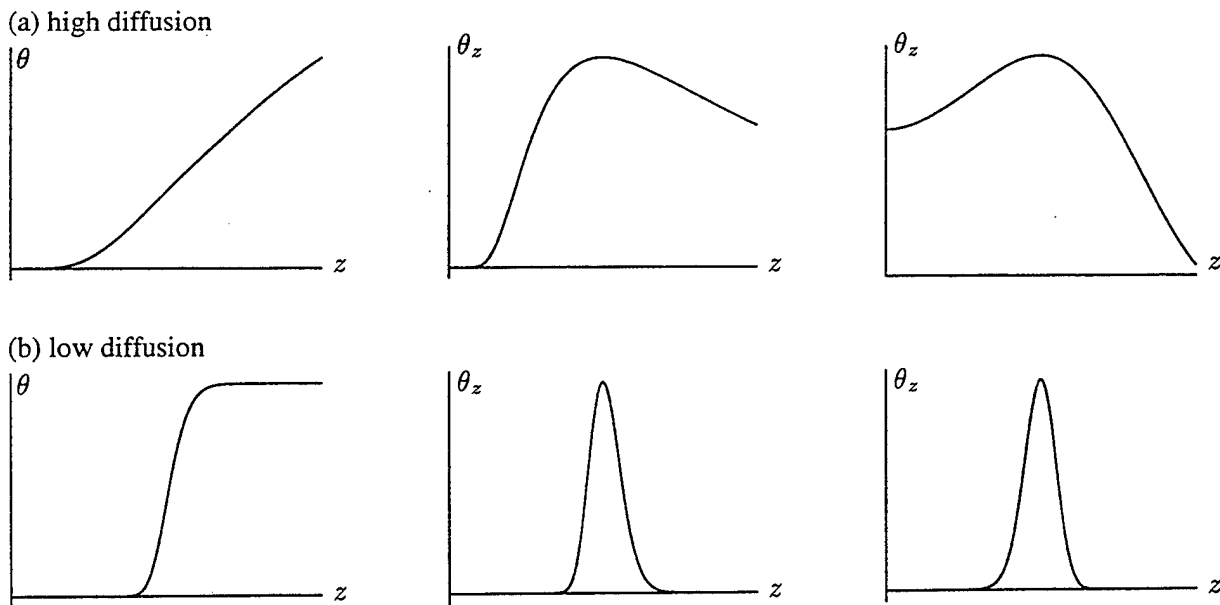Figure 1. The θ and θ_z profiles for a depth-varying diffusivity, $\kappa(z) = \lambda z^3$, are shown in the left-hand and middle columns, respectively. The interior front is clearly seen by the mid-depth maximum in θ_z. The right-hand columns show θ_z profiles for uniform diffusivity, the value chosen being equal to that at the front in the corresponding non-uniform case.

where the unknown functions $G(y, z)$ and $\Gamma(y, z)$ satisfy

$$\Gamma(y, z)G_{zzz} + y\left(y^2\kappa_{zz} + \Gamma_{a,z}\right)G_{yzz} - y\left(y^2\kappa_{zzz} + \Gamma_{a,zz}\right)G_{yz} = y^2\kappa G_{zzzz}, \quad (10b)$$

$$y^2\kappa_{zzzz}\Gamma + \Gamma\Gamma_{zzz} - y^4\kappa\kappa_{zzzzz} - y^2\kappa\Gamma_{zzzz} + y[y^2\kappa_{zz}\Gamma_{yzz}$$
$$+ 2y\kappa_{zzz}\Gamma_z + \Gamma_z\Gamma_{yzz} - 2y\kappa_{zz}\Gamma_{zz} - y^2\kappa_{zzz}\Gamma_{yz} - \Gamma_{yz}\Gamma_{zz}] = 0. \quad (10c)$$

By choosing different w and κ profiles consistent with (10b) and (10c) it is straightforward to investigate front formation. For example, consider Fig. 1. Here the profiles of θ and θ_z are plotted for a diffusivity profile which increases from zero at the ocean bottom and reaches a maximum at the surface (left hand and centre columns). Plots are shown for both high and low diffusivity. An interior front is clearly seen in the latter case. The right hand column shows the θ_z profile for uniform diffusivity profiles. One can clearly see that the front is controlled by the (local) value of κ at the front depth, rather than by, e.g., the depth mean value. Consequently the frontal character of the solutions is robust to changes in diabatic forcing above (and below) the front depth. Corresponding plots of the surface streamlines and isotherms are given in Fig. 2.

Using conserved quantities

It is well known that both density, ρ, and potential vorticity, q, are conserved by flow which satisfies the ideal thermocline equations. Further, assuming that geostrophic eddies homogenise properties on a density surface then

$$q = \widehat{F}(\rho), \quad (11)$$

for some function, $\widehat{F}(\rho)$, i.e., q is constant on a density surface. It is natural to consider (11) in isopycnal coordinates and since $q = y/B_{\rho\rho}$, where B is the Bernoulli function, then integrating we obtain

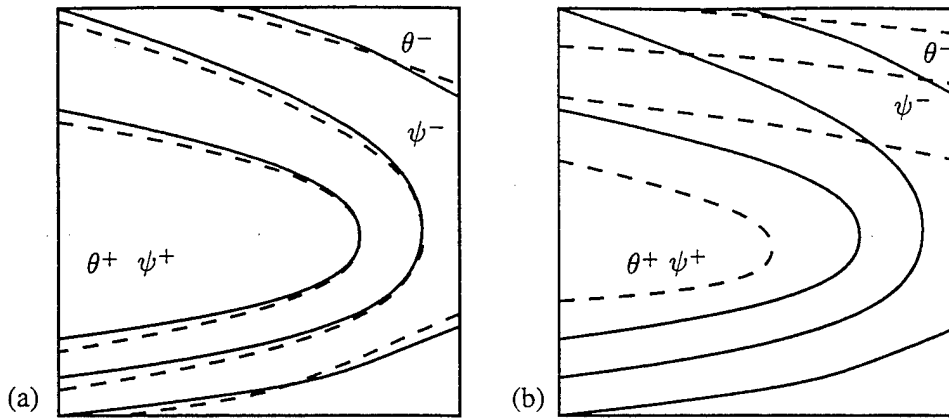$$B(x, t, \rho) = yF(\rho) + \rho b(x, y) + a(x, y), \quad (12)$$

Figure 2. Surface streamlines and isotherms (continuous and dashed respectively) for variable diffusivity, $\kappa(z) = \lambda z^3$, with (a), a low value of λ and (b), a high value. More realistic cross-isothermal flow is seen with higher surface diffusion.

where $a(x,y)$ and $b(x,y)$ are to be determined. Needler (1971), Cushman-Roison (1984) and Salmon (1994) have all considered solutions of this form. However, in current work we propose to assume that (11) is correct only up to $O(1)$.

Solutions of the form (12) are general enough to admit strong boundary conditions at the surface, bottom and (say) the eastern limit of the solution domain, e.g., completely arbitrary Ekman pumping, $w = w_E(x,y)$ at the surface, a level of no motion at depth and prescription of the density profile at some longitude. However, one can use the ansatz, (12), to investigate the effects of different models and parameterisations of "sub-grid-scale" motions, which are neglected by the ideal thermocline equations, on the density profile, and therefore on $F(\rho)$. We therefore choose to impose only a weak (integral) condition on the solution at the eastern boundary — that there is no net flow through a given longitude at all latitudes — and determine $F(\rho)$ by an appeal to $O(\epsilon)$ dynamics. To do this we generalise our ansatz, (12), by admitting slow variation of q with x and y, i.e.,

$$B(x,y,\rho) = yF(\epsilon x, \epsilon y, \rho) + \rho b(x,y) + a(x,y); \tag{13}$$

$O(\epsilon)$ terms in the left-hand side of the thermodynamic equation (cf. (1)) are assumed to balance non-ideal effects, i.e., the sub-grid-scale motions mentioned, e.g., vertical diffusion. In this limit in which $\epsilon \to 0$ a constraint is obtained on $F(\rho)$ from which one can obtain the corresponding density profile.

Given $F(\rho)$ we assume that

$$B(x,y,\rho) = yF(\rho) + \rho b(x,y) + a(x,y) + \epsilon B'(x,y,\rho), \tag{14}$$

where $0 < \epsilon < 1$ and the $O(\epsilon)$ deviation from (12) given by B', which is to be determined, balances non-ideal effects, once more. $O(\epsilon^2)$ terms are neglected and consequently it turns out that we need only solve a first order, linear PDE for $B'_{\rho\rho}$.

By this method it is hoped to investigate the limit in which Ekman pumping and interior dynamical processes control the density/temperature profile, rather than the complementary limit in which the Ekman pumping together with in-flow along some vertical plane is more important.

Preliminary Results

Work to date using these ideas has concentrated on two parameterisations of "sub-grid-scale" motion: (i), Laplacian cross-isopycnal diffusion with uniform diffusivity and (ii), that due to

Gent & McWilliams (1989) in which eddy motion is supposed to have a net advective effect. Density profiles determined in each case are shown in Figure 3.
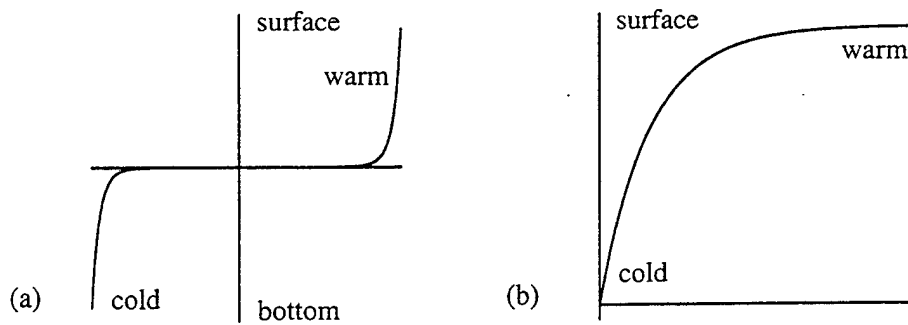

Figure 3. Nondimensional density profiles determined by admitting slow variation of q with x and y (cf. Eq. (13)). In (a) weak cross-isopycnal diffusion leads to a frontal character, whilst in (b) a parametrisation based on that due to Gent & McWilliams leads to an exponential profile.

Discussion

In recent years there appears to have been a move toward layered and numerical models in physical oceanography. Indeed it has even been suggested that the idea of seeking exact (e.g. similarity) solutions to the thermocline equations has had a detrimental effect. There is no question of using exact analytic or perturbation techniques to replace (for example) large scale computer modelling of the ocean with realistic topography. However, exact solutions can and should be used to test computer models. In addition, used as a tool to investigate hypothesised physical processes, by means of thought experiments, these ideas provide an invaluable way to gain insight into ocean dynamics.

References

Cushman-Roison, B., 1984, J. Phys. Oceanogr., **14**, 1179 – 1190.

Gent, P.R. & J.C. McWilliams, 1989, J. Phys. Oceanogr., **20**, 150 – 155.

Hill, J.M., 1992, *"Differential Equations and Group Methods for Engineers and Scientists,"* CRC Press, Boca Raton, Ann Arbor, London and Tokyo.

Hood, S., 1995, submitted to J. Mar. Res.

Hood, S. and R.G. Williams, 1995, submitted to J. Mar. Res.

Kevorkian, J, 1990, *"Partial Differential Equations: Analytical Solution Techniques,"* Wadsworth & Brooks/Cole.

Luyten, J.R., J. Pedlosky and H. Stommel, 1983, J. Phys. Oceanogr., **13**, 292 – 309.

Marshall, J., 1995, coffee-break communication at Woods Hole GFD Summer School.

Needler, 1971, Deep-Sea Res., **18**, 895 – 903.

Olver, P.J., 1992, Appl. Numer. Math., **10**, 307 – 324.

Pedlosky, J., 1987, *"Geophysical Fluid Dynamics,"* Springer-Verlag.

Rhines P.B. and W.R. Young, 1982, J. Mar. Res., **40** suppl., 559 – 595.

Robinson, A.R. and H. Stommel, 1959, Tellus, **11**, 295 – 308.

Salmon R., 1994, J. Mar. Res., **52**, 865 – 908.

Salmon R., 1990, J. Mar. Res., **48**, 437 – 469.

Salmon, R. and R. Hollerbach, 1991, J. Mar. Res., **49**, 249 – 280.

Welander P., 1959, Tellus, **11**, 309 – 318.

Turbulent rotating Rayleigh-Bénard convection II

Keith Julien, NCAR, Boulder, CO 80307-3000

Collaborators: Nic Brummell CU; Sonya Legg & Jim McWilliams, NCAR/UCLA;
Joseph Werne, NCAR.

1 Introduction

Recent numerical simulations of rapidly rotating Rayleigh-Bénard convection (Julien et al. 1995) reveal some rather striking similarities to and differences from the non-rotating case. The most remarkable similarity is the presence of "hard turbulence" where the observed heat transport law between the Nusselt and Rayleigh numbers is given by $Nu \propto Ra^{2/7}$ when the top and bottom boundaries are no-slip (see figure 3 of Werne this proceeding). The existence of this scaling law in rotating convection, which has hitherto only been associated with non-rotating convection (Wu et al. 1988, Werne 1993), suggests the ubiquity of hard turbulent regimes in thermal convection with no-slip top and bottom boundaries. This result is further compounded since the classical 1/3-scaling law (Priestley 1959) is observed when the boundaries are stress-free (see figure 3 of Werne, this proceeding).

Some notable differences are also observed in these simulations of rotating convection. Firstly, a mean unstable thermal stratification is maintained in the bulk of the fluid layer (see figure 2 of Werne, this proceeding). This occurs as a direct consequence of enhanced lateral mixing between buoyant plumes developing out of the unstable thermal boundary layers. Secondly, plumes are topologically adjusted due to Ekman pumping within the thermal boundary layers. Finally, when the top and bottome boundaries are stress-free a high Rayleigh number transition ($Ra \sim 10^8$) from the classical 1/3-law in the heat transport scaling to an as yet undetermined scaling regime exists (see figure 3 of Werne, this proceeding).

In this discussion we attempt to develop a further understanding of the aforementioned characteristics of rotating convection. In particular, we will report on results from two-dimensional numerical simulations that a) demonstrate the importance of lateral mixing in association with the mean thermal stratification, b) deduce the topological adjustment of thermal plumes due to Ekman effects and c) ascertain whether the departure from the 1/3-law at high Rayleigh is a generic consequence of thermal convection with stress-free boundaries or an effect that arises solely due to rotation.

2 Lateral Mixing and Mean Temperature Gradients

The proposed explanation for the existence of an unstable thermal stratification in rotating turbulent convection requires that the thermal plumes be vortical, indeed they are cyclonic as a consequence of conservation of angular momentum during their formation, and that their dynamics be dominated by vortex interactions. The resultant stirring action of the co-rotating plumes and plume mergers laterally mixes fluid in horizontal planes. For example, near the lower boundary, warm plumes interact and are laterally mixed into the surrounding fluid at a given level, thereby raising the ambient temperature. Fewer buoyant elements survive greater distances away from the boundary resulting in a mean unstable stratification with warmer fluid near the
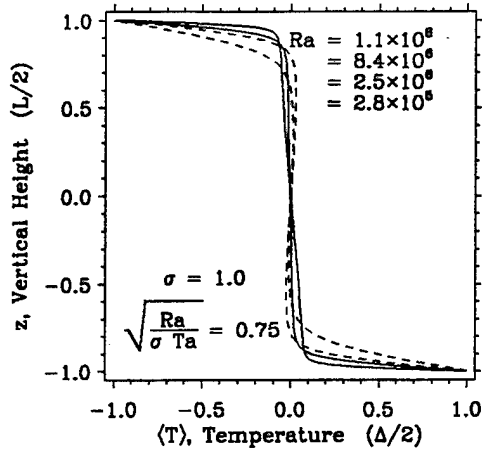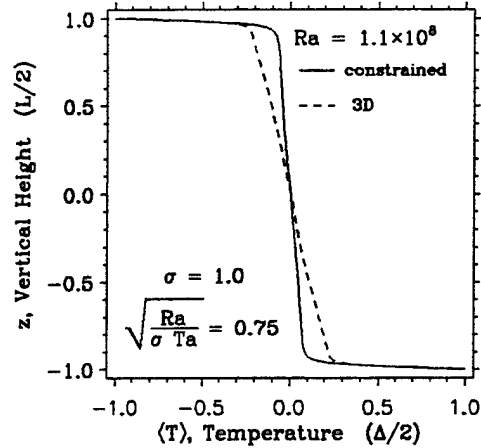
Figure 1: Temperature profiles

Figure 2: Temperature profiles

bottom boundary, and conversely cooler fluid near the top boundary (see figure 2 of Werne, this proceeding).

The following simple model clearly illustrates the importance of lateral mixing (plume-plume interaction) on the thermal stratification: consider rotating convection with fluid motions constrained to be invariant in a selected horizontal direction, *e.g.*, the y-direction with $\partial/\partial y = 0$. This effectively two-dimensional system was first studied by Veronis (1968). Velocities u, v, w and temperature T are made functions of x, z only. With this constraint thermal plumes now become cyclonic vortex sheets as opposed to the more familiar elliptical tube structures observed in the usual (unconstrained) rotating system. Moreover, vortex interactions cannot lead to co-rotating motions but only to (hidden) translations of the vortex sheets in the invariant direction. Lateral mixing due to stirring is therefore suppressed. Figure 1 in fact shows that as the Rayleigh number is increased, at constant convective Rossby number, the thermal stratification in the bulk of the fluid undergoes a transition from a stable (dashed lines) to an unstable (solid lines) profile at $Ra \sim 5 \times 10^6$. Correspondingly, the associated flow changes from cellular to turbulent motions (figures 3). In the cellular regime, plume interactions and therefore lateral mixing are inhibited. The stable stratification results when buoyant fluid elements are advected in an anti-buoyant direction. This effect is particularly enhanced because of the small aspect ratio cellular motions that occur at large rotation rates. In the turbulent regime, shearing motions associated with mergers between plumes originating at the same boundary, and interactions between plumes from opposite boundaries give rise to a lateral mixing that sustains an unstable stratification (figure 1). Note however, that the magnitude of the unstable stratification is not as large as the that found in the unconstrained rotating layer (figure 2), indicating more efficient mixing in the latter.

3 Topological Adjustment of Thermal Plumes due to Ekman Effects

In a rapidly rotating fluid layer, the cyclonic nature of plumes imposes important constraints on the dynamics of the flow near the boundaries. Specifically, Ekman

Ra = 2.5e6   Ta = 4.5e6   Pr = 1.0

Ra = 1.1e8   Ta = 2.0e8   Pr = 1.0

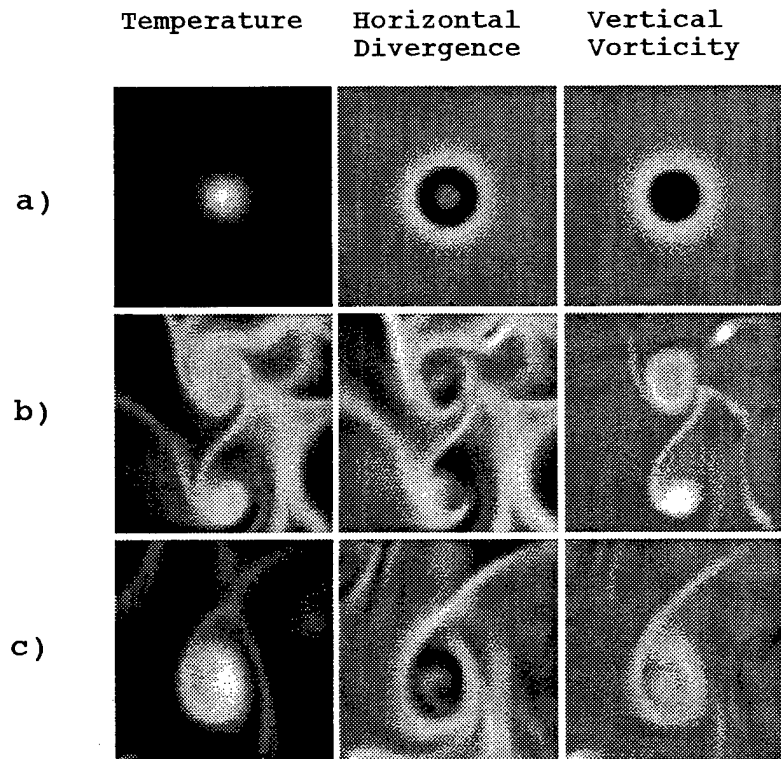Figure 3: Temperature Field; Cellular & Turbulent

| | Temperature | Horizontal Divergence | Vertical Vorticity |

Figure 4: Plume Topology. a) Linear Thermal solution and nonlinear solutions b) Stress-free, c) No-slip.
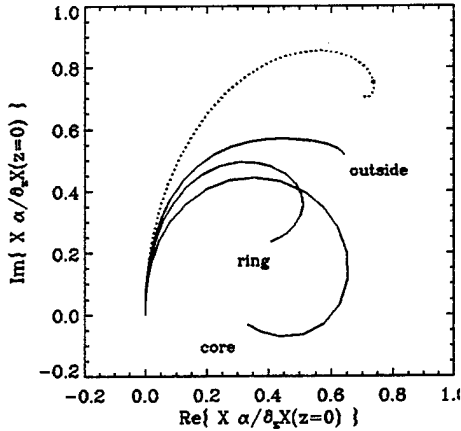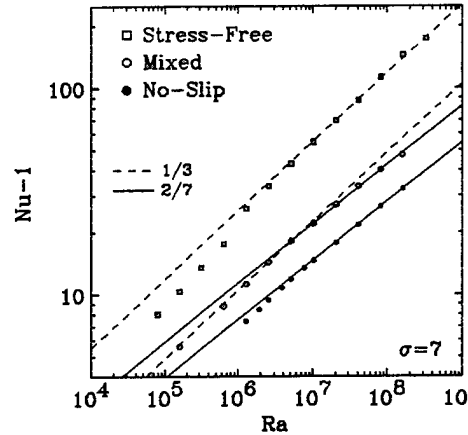
Figure 5: Ekman profiles[2]

Figure 6: Heat Transport

pumping occurs when a vortex tube terminates at a solid no-slip boundary.[1] Evidence for this is illustrated by the observed spirals [$v(z)$ versus $u(z)$ profiles] obtained at various positions within an individual plume in the unconstrained (3D) numerical solutions (figure 5, solid lines). Tighter spirals are found than that given by the classical linear Ekman theory[2] (dashed line) due to the complicated nature of the solutions: the flows are strongly nonlinear, non-hydrostatic, occur in connection with significant buoyancy, and are far from stationary and axisymmetric.

Perhaps the most striking feature arising as a consequence of Ekman effects is the structure of the plume topology. Horizontal cross-sections of thermal plumes in the simulations (figure 4b,c) reveal the development of cyclonic ring-shaped ridges where strong Ekman pumping occurs. This is in contrast to a perhaps more intuitive bump-shape one might expect from Ekman pumping at the core of the plume. The rather unique ring-topology may be explained by the inclusion of thermal (baroclinic) effects into the classical Ekman analysis (Hide 1965, Julien *et al.* 1995). Indeed, horizontal cross-sections of a thermal Ekman layer with a Gaussain profile (intended to represent a developing plume) show the existence of ring structures in the vorticity and horizontal divergence fields (figure 4a). Moreover, the thermal contribution to the linear solution is found to be identical in the presence of both stress-free and no-slip boundaries. However for no-slip boundaries the magnitude of this thermal effect is weak compared to that obtained from the classic viscous effect.

---

[1]For a tube in geostrophic balance (i.e. with the radial pressure gradient balancing centrifugal acceleration), pumping of fluid away from the boundary occurs at the vortex core due to the fact that the fluid velocity (and hence the centrifugal acceleration) vanishes at the wall, creating a pressure imbalance.

[2]The analytic solution for the classic linear Ekman layer has the form $X = q^{-1}\partial_z X(z = 0)(1 - e^{-qz})$, where X is the horizontal velocity in complex notation $X = u + iv$ and q^{-1} is the complex Ekman layer thickness $q = \sqrt{if/\sigma}$. $\partial_z X(z = 0)$ is the surface stress.

4 Departure from the Classical 1/3-Heat Transport Law

A theory for the 1/3-law observed for rotating convection with stress-free boundaries was initially provided by Priestley (1959). This work characterised two distinct regions of heat transport in thermal convection: a turbulent interior, where the heat flux is carried convectively, and thin thermal boundary layers where heat is transported solely by diffusion. Notable departures from this classical scaling, in particular the 2/7 hard-turbulent law, occur when coherent structures in the form of thermal plumes appear in the flow (see Werne, this proceedings for a discussion of scaling theories). These structures serve to communicate information between the thermal boundary layers, either by plumes spanning the depth of the layer thus short-circuiting the convective interior or by transmitting information into the convective interior. Moreover, the different scaling behaviour observed for rotating convection with no-slip and stress-free boundaries implies that boundary conditions in addition to the presence of plumes play a crucial role. However, this conjecture is not clear-cut since these simulations of rotating convection exhibit a transition from the 1/3-law at $Ra \sim 10^8$ in the stress-free case (see figure 3 of Werne, this proceeding). Unfortunately we are currently unable to determine the new scaling exponent due to the computational expense of simulating at higher Rayleigh numbers.

We suggest that the two boundary types (no-slip and stress-free) become indistinguishable at high Rayleigh numbers in rotating convection. This is possible since viscous boundary layers exist adjacent to stress-free boundaries due to the baroclinic Ekman effect (section 3). In support, we find that the transition in scaling for the stress-free case occurs at a Rayleigh number where the thickness of the Ekman boundary layer is equal to that of the thermal boundary layer. This suggests the important role played by the viscous boundary layers in determining the heat transport in thermal convection.

To confirm this conjecture we have performed simulations of non-rotating Rayleigh-Bénard convection in a two-dimensional box with stress-free boundaries. In this case, where no viscous boundary layers can exist, a 1/3-scaling law should prevail. Indeed, figure 6 (squares), shows a 1/3 exponent for Rayleigh numbers up to 10^9 indicating the necessity of viscous boundary layers for departures from the classical scaling law. Furthermore, similar simulations with mixed stress-free and no-slip boundary conditions result in a 2/7 scaling exponent (figure 6, open circles) implying that heat transport is constrained by the presence of any restrictive (no-slip) boundary condition.

Hide 1965 *Tellus* **XVI**, 523.

Julien, Legg, McWilliams & Werne 1995 *J. Fluid Mech.*, submitted.

Priestley 1959 The University of Chicago Press. Chicago & London.

Veronis 1968 *J. Fluid Mech.*, **31**, 113.

Werne 1993 *Phys. Rev. E.* **48**, 1020.

Wu, Castaing, Heslot & Libchaber 1988 In Proceedings in Physics Vol. 32 *Universalities in Condensed Matter*, 208.

Turbulent diffusion in a Gaussian velocity field

Joseph B. Keller*
Departments of Mathematics and Mechanical Engineering
Stanford University
Stanford, CA 94305-2125

1   Introduction

Turbulent diffusion is the process of dispersal of a substance by a fluid in turbulent motion. The velocity of the fluid is represented as a random function of position and time, and then the concentration of the dispersed substance is also a random function. The theory of turbulent diffusion seeks to determine the statistical properties of the concentration in terms of those of the velocity. We shall show how to do this when the Lagrangian velocity of the fluid is Gaussian.

One consequence of this analysis is that the probability density of a diffusing particle satisfies exactly a diffusion equation with a time dependent diffusion coefficient. This and other consequences of the analysis can serve as tests of approximations and of numerical calculations.

To obtain a diffusion process with a finite speed of propagation, it is necessary to assume that the turbulent velocity is bounded rather than unbounded, as in the Gaussian case considered here. Goldstein [1] illustrated this by deriving the telegraph equation, which has a finite propagation speed, for a one dimensional random walk on a lattice. Others have derived analogous equations by approximate analyses of turbulent diffusion.

2 Motion of a single particle

We begin by following Taylor [2]. First we write

$$x(t, x_0, t_0) = x_0 + \int_{t_0}^{t} v(t', x_0, t_0)\, dt' \ . \qquad (2.1)$$

Here $x(t, x_0, t_0)$ is the position at time t of a particle which is at x_0 at time t_0, and $v(t, x_0, t_0)$ is its velocity at time t. Then from (2.1) we obtain the mean $m(t, x_0, t_0) = \langle x(t, x_0, t_0) \rangle$ of x and the covariance $V_{ij}(t, x_0, t_0)$ of the components x_i and x_j:

$$
\begin{aligned}
m(t, x_0, t_0) &= x_0 + \int_{t_0}^{t} \langle v(t', x_0, t_0) \rangle dt', & (2.2) \\
V_{ij}(t, x_0, t_0) &= \langle [x_i(t, x_0, t_0) - m_i(t, x_0, t_0)]\,[x_j(t, x_0, t_0) - m_j(t, x_0, t)] \rangle \\
&= \int_{t_0}^{t} \int_{t_0}^{t} \langle v_i'(t', x_0, t_0)\, v_j'(t'', x_0, t_0) \rangle dt' dt'' \\
&= \int_{t_0}^{t} \int_{t_0}^{t} R_{ij}(t', t'', x_0, t_0)\, dt' dt'' \ . & (2.3)
\end{aligned}
$$

Here angular brackets denote mean or expectation values, $v' = v - \langle v \rangle$ is the fluctuation of v, and $R_{ij}(t', t''; x_0, t_0)$ is the two-time velocity correlation function.

Now we depart from Taylor by assuming that $v(t, x_0, t_0)$ is a Gaussian random function of t. It follows from (2.1) that $x(t, x_0, t_0)$ is also a Gaussian random function of t. Then the probability density of x at time t is given by

$$p(x, t; x_0, t_0) = \frac{1}{(2\pi)^{3/2}(\det V)^{1/2}}\, e^{-\frac{1}{2}(x-m)V^{-1}(x-m)} \ . \qquad (2.4)$$

Here V is the covariance matrix with components given by (2.3), m is the mean (2.2) and $\det V$ is the determinant of V. Similarly, we can consider $x_0(t_0, x, t)$, the position at time t_0 of the particle which arrives at x at time t. It is a Gaussian random function of t_0. The density of x_0 at time t_0, $p(x_0, t_0, x, t)$, is given by (2.4) with x, t and x_0, t_0 interchanged. Examination of (2.2)–(2.4) shows that

$$p(x, t, x_0, t_0) = p(x_0, t_0, x, t) \ . \qquad (2.5)$$

Differentiating (2.4) shows that p satisfies an advection-diffusion equation, which we write in the form

$$p_t + \langle v_i(t, x_0, t_0) \rangle \partial_{x_i} p = D_{ij}(t, x_0, t_0) \partial_{x_i} \partial_{x_j} p \ . \qquad (2.6)$$

In (2.6) repeated indices are to be summed from 1 to 3, $\langle v_i \rangle = \partial_t m_i$ as (2.2) shows, and the time dependent diffusion coefficient tensor is given by

$$D_{ij}(t, x_0, t_0) = -\frac{1}{2} \left[V \left(V^{-1} \right)_t V \right]_{ij} \ . \qquad (2.7)$$

Furthermore (2.3) shows that $V(t_0, x_0, t_0) = 0$, so (2.4) yields

$$p(x, t_0, x_0, t_0) = \delta(x - x_0) \ . \qquad (2.8)$$

Thus p is the unique solution of (2.6) with the initial value (2.8).

By using (2.3) for V in (2.7), we can express D_{ij} in terms of R_{ij}. For example, when v is stationary in time and homogeneous in space, then $R_{ij} = R_{ij}(t' - t'')$ and (2.3) leads to

$$V_{ij}(t, x_0, t_0) = V_{ij}(t - t_0) = 2(t - t_0) \int_0^{t-t_0} R_{ij}(s) ds - 2 \int_0^{t-t_0} s R_{ij}(s) ds \ . \qquad (2.9)$$

We can simplify (2.3) for $t - t_0$ either small or large compared to the correlation time T of v, and we obtain

$$V_{ij}(t - t_0) \sim R_{ij}(0)(t - t_0)^2, \quad t - t_0 \ll T, \qquad (2.10a)$$

$$V_{ij}(t - t_0) \sim 2(t - t_0) \int_0^{t-t_0} R_{ij}(s) ds, \quad t - t_0 \gg T. \qquad (2.10b)$$

Upon using these two results in (2.7) we find

$$D_{ij}(t - t_0) \sim R_{ij}(0)(t - t_0), \quad t - t_0 \ll T, \qquad (2.11)$$

$$D_{ij}(t - t_0) \sim \int_0^{t-t_0} R_{ij}(s) ds, \quad t - t_0 \gg T \ . \qquad (2.12)$$

The expression (2.12), with $t - t_0$ replaced by ∞ is Taylor's result for the diffusion coefficient.

3 Concentration

Now we seek the concentration $c(x, t)$ of a substance dispersed by the fluid motion. Conservation of the substance implies that it satisfies the advection equation

$$c_t(x, t) + \nabla \cdot [u(x, t)c(x, t)] = 0 . \tag{3.1}$$

Here $u(x, t)$ is the random velocity of the fluid. Suppose that initially the concentration is $c_0(x)$:

$$c(x, t_0) = c_0(x) . \tag{3.2}$$

To solve (3.1) and (3.2) we introduce the particle paths $x(t, x_0, t_0)$ defined by

$$\frac{dx}{dt}(t, x_0, t_0) = u[x(t, x_0, t_0), t] , \quad x(t_0, x_0, t_0) = x_0 . \tag{3.3}$$

Then the solution of (3.1) and (3.2) is

$$c[x(t, x_0, t_0), t] = c_0(x_0)/j(t, x_0, t_0) . \tag{3.4}$$

Here $j = |\partial x/\partial x_0|$ is the jacobian of the transformation $x(t, x_0, t_0)$ from x_0 to x. In terms of the inverse transformation $x_0(t_0, x, t)$, (3.4) is

$$c(x, t) = c_0[x_0(t_0, x, t)]/j[t, x_0(t_0, x, t), t_0] . \tag{3.5}$$

When $\nabla \cdot u = 0$ then $j = 1$.

The result (3.5) shows that $c(x, t)$ is a random function. The probability density of the value (3.5) is just $p(x_0, t_0; x, t)$ given by (2.5) and (2.4). Then the mean and variance of c are

$$\langle c(x, t) \rangle = \int \frac{c_0(x_0)}{j(t, x_0, t_0)} \, p(x_0, t_0; x, t) dx_0, \tag{3.6}$$

$$\langle [c(x, t) - \langle c(x, t) \rangle]^2 \rangle = \int \frac{c^2(x_0)}{j^2(t, x_0, t_0)} \, p(x_0, t_0; x, t) dx_0 - \langle c(x, t) \rangle^2. \tag{3.7}$$

Next we consider the two-point two-time covariance of c, defined by

$$\langle [c(x_1, t_1) - \langle c(x_1, t_1) \rangle][c(x_2, t_2) - \langle c(x_2, t_2) \rangle] \rangle = \\ \langle c(x_1, t_1)c(x_2, t_2) \rangle - \langle c(x_1, t_1) \rangle \langle c(x_2, t_2) \rangle . \tag{3.8}$$

To evaluate $\langle c(x_1, t_1)c(x_2, t_2) \rangle$ we need the joint probability density $p(x_0, x_0', t_0; x_1, t_1, x_2, t_2)$ that the particle which arrives at x_1 at time t_1 was

at x_0 at time t_0 and the particle that arrives at x_2 at time t_2 was at x_0' at time t_0. Then we have

$$\langle c(x_1, t_1)c(x_2, t_2)\rangle = \iint \frac{c_0(x_0)c_0(x_0')}{j(t_1, x_0, t_0)j(t_2, x_0', t_0)} \, p(x_0, x_0', t_0; x_1, t_1, x_2, t_2)dx_0 \, dx_0'.$$

(3.9)

In order to determine the two-point probability we write

$$x_1(t_1, x_0, t_0) = x_0 + \int_{t_0}^{t_1} v(t', x_0, t_0)dt',$$

$$x_2(t_2, x_0', t_0) = x_0' + \int_{t_0}^{t_2} v(t', x_0', t_0)dt'.$$

(3.10)

Then we assume that $[v(t, x_0, t_0), v(t, x_0', t_0)]$ is a multivariate Gaussian process. It follows that (x_1, x_2) given by (3.10) is also a multivariate Gaussian. Consequently the probability density p in (3.9) is a Gaussian in the six component vector $y = (x_0, x_0')$:

$$p(x_0, x_0', t_0; x_1, t_1, x_2, t_2) = \frac{1}{(2\pi)^3 \det V} \, e^{-(y-m)V^{-1}(y-m)}.$$

(3.11)

The six component mean m, and the sixth order covariance matrix V are given by expressions like those in (2.2) and (2.3).

It also follows from the Gaussian assumption that the separation $x_1(t, x_0, t_0) - x_2(t, x_0', t_0)$ is a Gaussian random function of t.

References

[1] S. Goldstein, *Quart. Jour. Math. & Appl. Mech.* 4(2), 129–155, 1950.

[2] G.I. Taylor, *Proc. London Math. Soc.* 20, 196–212, 1920.

Bifurcations in Rotating Systems

Edgar Knobloch

Department of Physics, University of California
Berkeley, CA 94720

In the next few pages I would like to make a remark about the use of the "narrow gap" or "straight channel" approximation to model various types of geophysical and laboratory flows. The use of this approximation is common, and is believed to be justified when the scale of the motion is small compared to other scales in the problem, eg., radius of curvature. While this is true it is also misleading in the sense that it obscures certain important qualitative effects which are characteristic of such flows. Consider, for example, convection in a rotating annulus, driven by heating from below. In this system one expects, by analogy with convection in a rotating cylinder (Ecke et al 1992, Goldstein et al 1993), the onset of convection to take the form of travelling waves precessing in the retrograde direction, provided the instability breaks the SO(2) symmetry of the rotating annulus. For sufficiently rapid rotation the unstable mode will take the form of a wall mode, confined to the outer boundary. A similar mode, confined to the inner boundary, will precess in the prograde direction (Kuo and Cross 1993, Herrmann and Busse 1993) but will set in at a higher Rayleigh number. Closely related solutions were found already by Davies-Jones and Gilman (1971) in their study of the onset of convection in a rotating straight channel. However, in contrast to the above expectation, Davies-Jones and Gilman found that the onset of a nonaxisymmetric instability can be *either* via a Hopf bifurcation or a steady state bifurcation, depending on the rotation rate. I show here that the steady state bifurcations found by Davies-Jones and Gilman are a consequence of the fact that their straight channel has O(2) symmetry instead of the expected SO(2) symmetry appropriate to a rotating annulus. The extra reflection symmetry present in their model is a 180° rotation about a vertical axis through the mid-channel and requires that the boundary conditions on the "inner" and "outer" walls be identical. In the annulus this symmetry is broken by the curvature of the walls, even with identical boundary conditions at the sides, and as a result all (nonaxisymmetric) patterns drift.

Convection in an annulus of height h is described by the nondimensionalized equations

$$\frac{1}{\sigma}\left(\frac{\partial}{\partial t} + \mathbf{u}\cdot\nabla\right)\mathbf{u} = -\nabla p + \nabla^2\mathbf{u} + R\Theta\hat{\mathbf{z}} + T\mathbf{u}\times\hat{\mathbf{z}}, \tag{1}$$

$$\left(\frac{\partial}{\partial t} + \mathbf{u}\cdot\nabla\right)\Theta = w + \nabla^2\Theta, \tag{2}$$

$$\nabla\cdot\mathbf{u} = 0, \tag{3}$$

where the quantities $T \equiv 2\Omega h^2/\nu$, $R \equiv g\alpha\Delta T h^3/\kappa\nu$, and $\sigma \equiv \nu/\kappa$ denote, respectively, the square root of the Taylor number, the Rayleigh number, and the Prandtl number. Here Ω is the dimensional angular velocity. However, instead of solving these equations Davies-Jones and Gilman (1971) replace them by the corresponding ones written in locally cartesian

coordinates:

$$\frac{1}{\sigma}\frac{\partial u}{\partial t} = -\frac{\partial p}{\partial x} + \mathcal{T}v + \nabla^2 u, \tag{4}$$

$$\frac{1}{\sigma}\frac{\partial v}{\partial t} = -\frac{\partial p}{\partial y} - \mathcal{T}u + \nabla^2 v, \tag{5}$$

$$\frac{1}{\sigma}\frac{\partial w}{\partial t} = -\frac{\partial p}{\partial z} + R\Theta + \nabla^2 w, \tag{6}$$

$$\frac{\partial \Theta}{\partial t} = w + \nabla^2 \Theta, \tag{7}$$

$$\frac{\partial u}{\partial x} + \frac{\partial v}{\partial y} + \frac{\partial w}{\partial z} = 0, \tag{8}$$

where x, y, z are the radial, azimuthal and vertical coordinates, respectively, defined relative to mid-channel. In this approximation the annulus forms an infinitely long straight channel. These equations are supplemented with stress-free, perfectly conducting boundary conditions at top and bottom,

$$w = \Theta = \frac{\partial u}{\partial z} = \frac{\partial v}{\partial z} = 0 \quad \text{on} \quad z = 0, 1, \tag{9}$$

and no-slip, thermally insulating sidewalls

$$u = v = w = \frac{\partial \Theta}{\partial x} = 0 \quad \text{on} \quad x = \pm a. \tag{10}$$

Here $x = \pm a$ defines the inner and outer radii of the annulus in units of h.

With the boundary conditions (9,10) the resulting system has translation symmetry in the y-direction, a consequence of the rotation invariance of equations (1)-(3). However, equations (4)-(8) possess an additional symmetry not possessed by equations (1)-(3). They are invariant under a 180° rotation about a vertical axis through $x = 0$. That is, if $(u(x,y,z), v(x,y,z), w(x,y,z), \theta(x,y,z), p(x,y,z))$ solves (4)-(8) so does $(-u(-x,-y,z), -v(-x,-y,z), w(-x,-y,z), \theta(-x,-y,z), p(-x,-y,z))$. In the following we denote this rotation by π and note that it is a reflection, $\pi^2 = \text{id}$. As a consequence of this reflection symmetry, the symmetry group of the straight channel with periodic boundary conditions in y is the group O(2), in contrast to the SO(2) symmetry of the annulus. It is this difference in the symmetries of the channel and the annulus that is responsible for the qualitative differences in both their linear stability properties and the nonlinear evolution of the resulting instability.

Consider first a symmetry breaking steady state bifurcation with O(2) symmetry. The temperature eigenfunction takes the form

$$\Theta(x,y,z,t) = v(t)h(x,z)e^{imy} + \text{c.c.}, \qquad m \neq 0, \tag{11}$$

where $h(x,z)$ is the appropriate eigenfunction in the radial and vertical directions. To construct the equations describing the evolution of the complex amplitude $v(t)$ in the nonlinear regime near onset we examine the action of translations $T : \quad y \to y + \alpha$ and reflection $\pi : \quad (x,y) \to (-x,-y)$ on the eigenfunction Θ. Because of the O(2) symmetry of the system a translated or reflected eigenfunction must also be an eigenfunction. As a consequence $h(-x,z) = \pm h^*(x,z)$, i.e., the cross-channel eigenfunction must be either even or odd. Moreover, since the equation for $v(t)$ comes from a system equivariant with respect to translations

and reflection, it must be equivariant with respect to the following action of O(2) on C:

$$T: \quad v \to v e^{im\alpha}, \tag{12}$$

$$\pi: \quad v \to \pm\overline{v}. \tag{13}$$

The most general equation for $v(t)$ therefore takes the form

$$\dot{v} = g(|v|^2, \mu)v = \mu v + a|v|^2 v + O(5), \tag{14}$$

where g is a real-valued function and μ the bifurcation parameter ($\mu = (R - R_c)/R_c$). Note that it is the reflection π that forces g to be real and hence is responsible for the possibility that the initial bifurcation is steady, as assumed. From equation (14) it follows that the bifurcation produces a *circle* of steady states, corresponding to all possible translations of a given steady state. If the reflection symmetry is broken, for example, by the curvature of the annulus, or by imposing different boundary conditions at $x = \pm a$, the function g acquires an imaginary part, and the evolution of $v(t)$ is then governed by

$$\dot{v} = (\mu + i\omega)v + (a + ib)|v|^2 v + O(5). \tag{15}$$

Here μ, ω, a and b are all real. Consequently the bifurcation becomes a Hopf bifurcation, and produces a travelling wave. Note that the direction of precession is given by the sign of ω; the broken reflection symmetry selects a preferred direction. The magnitude of the precession rate is easily estimated as $\omega = \mathcal{O}(\kappa m \mathcal{T})$, where κ denotes the (dimensionless) channel curvature.

A Hopf bifurcation can also exist in the channel problem, as found by Davies-Jones and Gilman (1971). However, because of the O(2) symmetry this bifurcation now leads to two types of solutions simultaneously. These solutions differ in their symmetry properties. A solution we call TW breaks the reflection symmetry; consequently there is a second TW related to the first by the symmetry π. For example, a wall mode travelling clockwise along the outer wall is related to a wall mode travelling counter-clockwise along the inner wall by the symmetry π. In addition to the TW solutions there is a second type of solution called SW. This solution is reflection symmetric, and corresponds to the *simultaneous* presence of both wall modes. It is a simple matter to demonstrate the above results. Instead of (11) we now have

$$\Theta(x, y, z, t) = \{v(t)h_+(x, z) + w(t)h_-(x, z)\}e^{imy} + \text{c.c.}, \qquad m \neq 0, \tag{16}$$

where, at bifurcation, $v(t) \propto e^{i\omega t}$, $w(t) \propto e^{-i\omega t}$. Thus v, w are the amplitudes of waves travelling clockwise and counter-clockwise, respectively, around the annulus. The eigenfunctions $h_+(x, z)$, $h_-(x, z)$ satisfy boundary conditions on the horizontal and vertical walls, and are related by reflection, $h_-(x, z) \equiv h_+^*(-x, z)$. The symmetries T and π act on the amplitudes v and w as follows:

$$T: \quad (v, w) \to (v e^{im\alpha}, w e^{im\alpha}), \tag{17}$$

$$\pi: \quad (v, w) \to (\overline{w}, \overline{v}). \tag{18}$$

This is the standard action of O(2) on $\mathbf{C}^2$. The most general equation equivariant with respect to this action of O(2) was obtained by Knobloch (1986), who showed that the resulting

equations can be simplified by an appropriate near-identity change of variables. The resulting *normal form*, truncated at third order, is

$$\begin{pmatrix} \dot{v} \\ \dot{w} \end{pmatrix} = \begin{pmatrix} \mu + i\omega + a|v|^2 + b|w|^2 & 0 \\ 0 & \mu - i\omega + b^*|v|^2 + a^*|w|^2 \end{pmatrix} \begin{pmatrix} v \\ w \end{pmatrix}. \tag{19}$$

Here v and w are now the transformed amplitudes. The coefficients a and b are complex, and $\mu \in \mathbb{R}$ is the bifurcation parameter. Expressing the amplitudes in terms of polar variables defined by $v = r_+ e^{i\phi_+}$ and $w = r_- e^{i\phi_-}$, and writing $a = a_r + ia_i$ and $b = b_r + ib_i$, we find both travelling wave (TW) and standing wave (SW) solutions to (19):

$$\text{TW} \quad : \quad r_\pm^2 = -\frac{\mu}{a_r}, \quad r_\mp = 0, \quad \dot{\phi}_\pm = \pm\omega \mp \mu\frac{a_i}{a_r} \tag{20}$$

$$\text{SW} \quad : \quad r_+^2 = r_-^2 = -\frac{\mu}{a_r + b_r}, \quad \dot{\phi}_+ = -\dot{\phi}_- = \omega - \mu\frac{a_i + b_i}{a_r + b_r}, \tag{21}$$

subject to the nondegeneracy conditions $a_r \neq 0$ and $a_r \neq \pm b_r$. In addition it is easy to show (Knobloch 1986) that both TW and SW solutions must bifurcate supercritically for either one of them to be stable, and that the solution with the largest amplitude is the stable one. The solution with $r_-(r_+)$ zero corresponds to a travelling wave mode localized on the outer(inner) wall of the annulus and travelling clockwise(counter-clockwise). The SW solution is an equal amplitude superposition of the travelling wave modes localized on both walls and travelling in opposite directions.

In contrast, in the annulus the broken reflection symmetry splits the bifurcation into two successive Hopf bifurcations, with one or other direction of precession preferred. This splitting is dominant at linear order and so is described by the equations

$$\begin{pmatrix} \dot{v} \\ \dot{w} \end{pmatrix} = \begin{pmatrix} \mu + i\omega_1 + a|v|^2 + b|w|^2 & 0 \\ 0 & \mu + \sigma - i\omega_2 + b^*|v|^2 + a^*|w|^2 \end{pmatrix} \begin{pmatrix} v \\ w \end{pmatrix}, \tag{22}$$

where $|\sigma| \ll 1$ and $\omega_1 - \omega_2 = O(\sigma)$. These equations are analyzed by van Gils and Mallet-Paret (1986) and by Crawford and Knobloch (1988). The main conclusions are that the two successive Hopf bifurcations both lead to travelling waves. The counterpart of the SW is now a two-frequency (quasiperiodic) state that bifurcates at finite amplitude from one or other of the primary TW branches. See fig. 1. Note that the observation by Gilman (1973) of stable
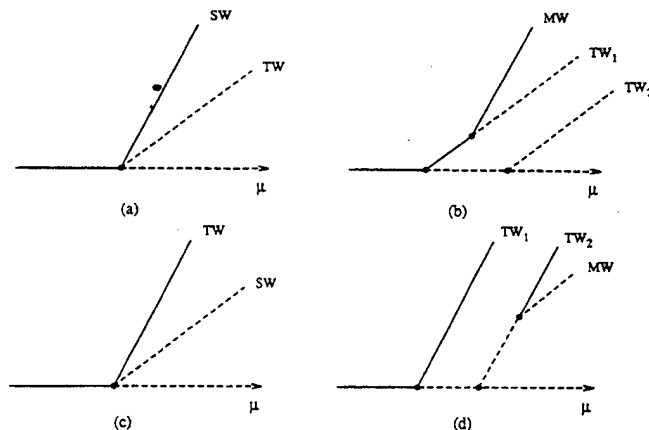

Fig. 1. The effect of curvature on a symmetry-breaking Hopf bifurcation in a rotating channel. Figs. (a,c): $\sigma = 0$; figs. (b,d): $\sigma \neq 0$.

SW in the nonlinear regime implies that in the annulus one should observe stable two frequency waves bifurcating in a secondary bifurcation from a single frequency travelling wave. It is likely, however, that the additional symmetries imposed by Gilman to facilitate his computation prevented him from testing the stability of the SW state with respect to TW perturbations, and that the SW are in fact unstable to TW as in other problems of this type (cf Knobloch et al 1986).

In the O(2) symmetric system the transition from steady to oscillatory solutions takes place via the Takens-Bogdanov bifurcation. Such bifurcation points have been located by Davies-Jones and Gilman, and are characterized by *four* zero eigenvalues. The solution of the linear problem takes the form

$$\Theta = v(t)h(x,z)e^{imy} + \text{c.c.}, \qquad m \neq 0, \tag{23}$$

where

$$\begin{pmatrix} \dot{v} \\ \dot{w} \end{pmatrix} = \begin{pmatrix} 0 & 1 \\ 0 & 0 \end{pmatrix} \begin{pmatrix} v \\ w \end{pmatrix} \tag{24}$$

and $h(-x,z) = \pm h^*(x,z)$, as before. The O(2) symmetry acts on (v,w) as follows

$$T: \quad (v,w) \rightarrow (ve^{im\alpha}, we^{im\alpha}), \tag{25}$$

$$\pi: \quad (v,w) \rightarrow (\overline{v}, \overline{w}). \tag{26}$$

The resulting equation for the evolution of v, truncated at third order, can be written in the form

$$\ddot{v} = \mu v + \nu \dot{v} + A|v|^2 v + B|\dot{v}|^2 v + C(v\overline{\dot{v}} + \dot{v}\overline{v}) + D|v|^2\dot{v}. \tag{27}$$

As before the reflection symmetry π forces all the coefficients to be real. The resulting equation has been analyzed in detail by Dangelmayr and Knobloch (1987), who find a number of different scenarios depending on the sign of the coefficient A and the value of the ratio C/D, including secondary branches of quasiperiodic states. The SW terminate on the branch of steady states in either a global bifurcation ($A > 0$) or in a secondary Hopf bifurcation ($A < 0$). The TW terminate on the branch of steady states in a pitchfork bifurcation; at this bifurcation the precession velocity of the wave vanishes. This is a consequence of the nonlinearity of the equations which can reduce the precession frequency from its value at onset to zero at finite amplitude.

The effect of breaking the reflection symmetry π has not been analyzed in detail, although a few possibilities are sketched in Matthews *et al.* (1992). To determine the possible behavior it is necessary to allow for small imaginary parts in all the coefficients of equations (27). The resulting diagrams include those obtained from equations (15) and (22), and various interconnections between them.

The above discussion provides a qualitative explanation for the linear stability results obtained by Davies-Jones and Gilman (1971) and the nonlinear results obtained by Gilman (1973). In particular Davies-Jones and Gilman found two types of steady modes, corresponding to longitudinal and transverse rolls. These are distinguished by the azimuthal wavenumber minimizing the Rayleigh number, $m_c \leq 1$ for longitudinal rolls, while $m_c = O(\pi/a)$ for transverse rolls, at least for the low rotation rates considered in their paper. For larger rotation rates the bimodal structure of the steady state neutral stability curves persists, but with an intervening interval of oscillations. This curve of Hopf bifurcations terminates at either end in Takens-Bogdanov bifurcations. The appearance of these oscillations can be

understood by analyzing the normal form for a 1:1 spatial resonance with O(2) symmetry, as discussed recently by Julien (1994). Similar behavior was also found in low Prandtl number axisymmetric convection in a rotating cylinder (Goldstein *et al.* 1994). With increasing rotation rate the critical Rayleigh number for the oscillations falls below that for either type of steady rolls and the instability becomes oscillatory. Note that the oscillatory instability will thus have an azimuthal wavenumber that is not as large as that for the steady transverse rolls. These oscillatory modes consist of a minimum of two cells in the radial direction, which (in the language of Davies-Jones and Gilman) propagate with equal speeds in opposite directions along the annulus, (and) have horizontal cell structures that are identical when one is rotated by 180° about the z-direction. In our language this is the description of an SW eigenfunction. Davies-Jones and Gilman did not appreciate, however, that cells travelling along one or other wall are separately eigenfunctions as well. Both TW set in at the same Rayleigh number as a consequence of the reflection symmetry π. For yet larger rotation rates the eigenfunctions are more and more confined to either wall. Recent numerical simulations of compressible convection in an annulus (N. Hurlburt, private communication) verify the existence of these counter-propagating wall states, but because of the SO(2) symmetry of the system the outer wall state sets in before the inner one, and the precession rates of the two wall states are different.

In this note I have tried to point out the dangers of modeling a system using a model with different symmetry properties than the original system. In such circumstances one is guaranteed that the model will lack even the qualitative features of the original system. We have seen that the change of symmetry from SO(2) to O(2) has profound effects both at the linear and nonlinear levels. It allows steady state bifurcations from the conduction state, which evolve, in the nonlinear regime, to convection cells that are slanted with respect to the cross-section due to the Coriolis force but do not drift. With SO(2) symmetry steady state bifurcations are nongeneric and tilted cells must precess. Any physical effect that breaks the symmetry π will have this effect. These include curvature of the walls, differences in the boundary conditions applied at the sidewalls, sloping walls at the top and bottom etc. In fact, as discussed by Knobloch (1994), this is an example of a general phenomenon. For example, in a recent paper Matthews *et al.* (1992) study two-dimensional Boussinesq convection in an oblique magnetic field with periodic boundary conditions in the horizontal. Because of the boundary conditions in the horizontal this system is invariant under SO(2), the tilt of the magnetic field breaking the reflection symmetry in vertical planes. The theory therefore suggests that in the generic case the onset of convection should be through a Hopf bifurcation leading to a pattern drifting preferentially in one or other direction, depending on the tilt of the field. In fact in the Boussinesq case the initial instability is a steady state one and no drifts are found; in the nonlinear regime steady but tilted cells are present. The reason this nongeneric behavior takes place is related, as in the present paper, to the presence of an additional reflection symmetry. This is the reflection in the layer midplane, and is a special property of the Boussinesq formulation. Indeed, Matthews *et al.* find that if the Boussinesq approximation is relaxed, so that this symmetry is lost, the tilted cells begin to drift, as predicted by the analysis of the generic case. An identical explanation accounts for the onset of overstability in rotating compressible convection with or without an imposed axisymmetric magnetic field (Jones *et al.* 1990). In this example the system is treated in the channel approximation with identical boundary conditions at the sidewalls; however, it is the radial stratification that breaks the mid-channel reflection symmetry, leading to precession. Another example arises in the stability of two-dimensional shear flows. With

periodic boundary conditions in the downstream direction such flows have SO(2) symmetry. For generic profiles one therefore expects instability to set in at a Hopf bifurcation, giving rise to waves with a nonzero phase velocity relative to the shear flow. Djordjevic and Redekopp (1990) find that this is indeed so, and point out that if the vorticity profile is symmetric under mid-channel reflection the bifurcation becomes stationary. Additional examples can be found in models of the baroclinic instability, such as the Eady model, or in studies of wavy vortex flow in the Couette-Taylor system using the narrow gap approximation.

References

[1] J.D. Crawford and E. Knobloch, Nonlinearity **1**, 617-652 (1988).

[2] G. Dangelmayr and E. Knobloch, Phil. Trans. R. Soc. London A, **322**, 243-279 (1987).

[3] R.P. Davies-Jones and P.A. Gilman, J. Fluid Mech. **46**, 65-81 (1971).

[4] V.D. Djordjevic and L. Redekopp, Stud. Appl. Math. **83**, 287-317 (1990).

[5] R.E. Ecke, F. Zhong and E. Knobloch, Europhys. Lett. **19**, 177-182 (1992).

[6] P.A. Gilman, J. Fluid Mech. **57**, 381-400 (1973).

[7] H.F. Goldstein, E. Knobloch, I. Mercader and M. Net, J. Fluid Mech. **248**, 583-604 (1993).

[8] H.F. Goldstein, E. Knobloch, I. Mercader and M. Net, J. Fluid Mech. **262**, 293-324 (1994).

[9] J. Herrmann and F.H. Busse, J. Fluid Mech. **255**, 183-194 (1993).

[10] C.A. Jones, P.H. Roberts and D.J. Galloway, Geophys. Astrophys Fluid Dyn. **53**, 145-182 (1990).

[11] K. Julien, Nonlinearity **7**, 1655-1693 (1994).

[12] E. Knobloch, Phys. Rev. A **34**, 1538-1549 (1986).

[13] E. Knobloch, in *Lectures on Solar and Planetary Dynamos*, M.R.E. Proctor and A.D. Gilbert (eds), Cambridge University Press, pp. 331-372 (1994).

[14] E. Knobloch, A.E. Deane, J. Toomre and D.R. Moore, Contemp. Math. **56**, 203-216 (1986).

[15] E.Y. Kuo and M.C. Cross, Phys. Rev. E **47**, R2245-2248 (1993).

[16] P.C. Matthews, N.E. Hurlburt, M.R.E. Proctor and D.P. Brownjohn, J. Fluid Mech. **240**, 559-569 (1992).

[17] S. van Gils and J. Mallet-Paret, Proc. R. Soc. Edinburgh A **104**, 279-307 (1986).

Penetrative convection in rapidly rotating flows

by Sonya Legg
Institute for Geophysics and Planetary Physics, UCLA, Los Angeles, CA 90024-1567
Collaborators: Keith Julien, NCAR; Joe Werne, NCAR; Jim McWilliams, UCLA.

Introduction

Two idealisations of horizontally homogenous convection are commonly studied by numerical simulation and laboratory experiment. **Rayleigh-Benard convection** assumes a constant destabilising temperature difference across the depth of the fluid, resulting in a depth filling, statistically steady convection, convenient for obtaining time-averaged fields and statistics, enabling detailed examination of the dynamics of the plumes, and the transition to turbulence (Heslot et al, 1987; Julien et al, 1995b). However in geophysical convecting layers, the interaction between the convecting plumes and a bounding stably stratified fluid layer is often important; for example in the planetary boundary layers. Hence **penetrative convection**, driven by a destabilising buoyancy flux at one surface (either top or bottom), and bounded at the other side by a stably stratified region, into which the turbulent convective layer is continually deepening, is a more appropriate study scenario. The interface between the convective layer and the stably stratified layer is of particular interest: for example, cold plumes driven by buoyancy loss at the ocean surface may overshoot their neutral buoyancy level, due to kinetic energy aquired in traversing the convective layer, and penetrate into the stably stratified region. The resultant entrainment of denser fluid into the convective layer leads to a reverse buoyancy flux in this interfacial zone (Deardorff et al, 1969), hereafter referred to as the **penetration zone**.

Penetrative and Non-penetrative convection

A distinction is often made between penetrative and non-penetrative convection in the oceanic mixed layer (Turner, 1986). When a surface buoyancy loss results in non-penetrative convection, the upper part of the density profile is assumed well mixed, with no change below. The total buoyancy removed is directly proportional to the shaded area A_1 shown in figure 1, and the mixed layer depth can be estimated from this buoyancy loss: $h_m = \sqrt{(2B_0 t)}/N$ where N is the pre-existing Brunt-Vaisala frequency, and B_0 is the buoyancy flux per unit area (Manins and Turner, 1978). On the other hand, penetrative convection involves entrainment of fluid from below into the mixed layer, leading to an increase in buoyancy (represented by area A_2) in this penetration zone. A greater buoyancy loss in the convective layer (area A_3) than would be balanced by the surface forcing alone and a deeper convective layer ($h_p > h_m$) result. A region of sharp vertical gradients in density, or pycnocline, is formed in the penetration zone as a result of the reverse buoyancy flux. Penetrative convection occurs when the diffusion time necessary to remove the buoyancy anomaly of plumes is much longer than the advection time: *i.e.* the Peclet number $wh/(\kappa)$ is large (Fernando and Little, 1990), where w is a vertical velocity scale, h a vertical length scale and κ the diffusivity.

Features of non-rotating penetrative convection

Numerous studies of non-rotating penetrative convection (eg Deardorff et al, 1980) show a typical resultant density profile as in figure 2a. The density gradients are slightly positive in the upper part, and slightly stable in the lower part of the convective layer (due to upwelling of denser fluid). The buoyancy flux is positive throughout this layer, and negative, about -0.2 the surface value, in the penetration zone below (Figure 2b). Hence in the lower convective layer, there is a counter-gradient flux of buoyancy, indicative of nonlocal transports by depth traversing structures, or plumes, in contrast to mixing by local eddies (Deardorff et al, 1972; Holtslag and Moeng, 1991).

Entrainment: the cause of the negative buoyancy flux

The entrainment of fluid from the stable layer into the convective layer may be caused by any of several mechanisms. A buoyant plume impinging on the interface may cause fluid to be swept up around it, due to the associated ring vortex circulation, and that fluid may then be engulfed into the mixed layer (Linden (1973)). Alternatively, the flattening of the plume against the interface, transfering the motion from the vertical to the horizontal generates a shear layer at the interface, which may be unstable to Kelvin-Helmholtz billows at sufficiently low local Richardson number (Mory, 1990). If the impinging plumes excite internal gravity waves in the stable layer, and these waves remain trapped by the stable layer structure, wave breaking into the convective layer provides another entrainment mechanism (Fernando and Long, 1985). Each mechanism may respond differently to changes in parameters such as the Richardson and Rossby numbers. Some are applicable to vertical mixing driven by surface wind stress, while others apply more specifically to convectively driven mixing characterised by plumes.

The influence of rotation on convection

If we measure the influence of rotation on convection by a convective Rossby number defined as the ratio between the inertial (coriolis) timescale τ_f to the convective timescale τ_w

$$Ro_c = \frac{\tau_f}{\tau_w} = \frac{w^*}{fh} = \left(\frac{B_0}{f^3h^2}\right)^{1/3} = \left(\frac{Ra_f}{Ta^{3/2}\sigma^2}\right)^{1/3} \tag{1}$$

where w^* is the convective velocity, f is the coriolis parameter and h is the depth of the convective layer, and we have substituted $w^* \sim (B_0 h)^{1/3}$ (Deardorff, 1970), we obtain an apriori estimate of the relative influence of rotation on convective motion (Fernando et al, 1991). Ra_f is the flux Raleigh number, Ta is the Taylor number and σ is the Prandtl number. Smaller values of Ro_c correspond to stronger rotational influence so that deep convective layers (large h), are more likely to be influenced by rotation. To investigate the influence of rotation on penetrative convection, we carried out three numerical simulations at identical values of Ra_f or B_0, and identical initial conditions, characterised by a uniform stratification in the lower 2/3 of the volume, and a homogeneous upper 1/3, varying Ro_c from ∞, 0.65 to 0.21. We concentrate our attention on the effect of rotation on entrainment processes, buoyancy

fluxes, and the structure of the pycnocline.

Results

We find that at decreasing Ro, the magnitude of the negative buoyancy flux in the penetration zone also decreases (figure 3a) resulting in less reinforcement of the pycnocline in this region (figure 3b). The mixed layer depths (figure 4a), as estimated from the level at which the density gradient becomes slightly stable, are similar in all three cases, and do not deviate strongly from the non-penetrative estimate, but do have a slightly steeper slope, indicating penetrative convection, with that slope increasing as *Ro* increases. By contrast, the depth of the penetration zone (figure 4b) (measured by the level at which the density gradient approaches the initial stable value) is much deeper for the non-rotating case than for the two rotating cases, although the slope does not appear significantly different from the non-penetrative estimate. Examination of the density anomalies at the penetration zone (see Julien et al 1995a) reveals much smaller, weaker plumes in the strongly rotating case. The predominant entrainment mechanism in the non-rotating case appears to be the splashing of fluid around the plume. The smaller, weaker plumes in the rotating cases are therefore less efficient at this upwelling process, and hence lead to a less penetrative convection.

References

Deardorff, J.W., G.E. Willis, and D.K. Lilly, 1969 Laboratory investigation of non-steady penetrative convection. *J. Fluid Mech.*, **35**, 7-31.

Deardorff, J.W., 1970 Convective Velocity and Temperature Scales for the Unstable Planetary Boundary Layer and for Rayleigh Convection. *J. Atmos. Sci.* **27**, 1211-1213.

Deardorff, J.W., 1972 Theoretical expression for the counter-gradient vertical heat flux, *J. Geophys. Res.*, **77**, 5900-59004.

Deardorff, J.W., G.E.Willis, and B.H.Stockton, 1980 Laboratory studies of the entrainment zone of a convectively mixed layer. *J. Fluid Mech.*, **100**, 41-64.

Fernando, H.J.S., R-R Chen and D.L. Boyer, 1991 Effects of rotation on convective turbulence. *J. Fluid Mech.*, **228**, 513-547.

Fernando, H.J.S. and L.J. Little, 1990 Molecular diffusive effects in penetrative convection. *Phys. Fluids A*, **2**, 1592-1596.

Fernando, H.J.S., and R.R. Long, 1985 On the nature of the entrainment interface of a two-layer fluid subjected to zero-mean shear turbulence. *J. Fluid Mech.*, **151**, 21-53.

Heslot,F., B. Castaing, and A. Libchaber, 1987 Transitions to turbulence in helium gas. *Phys. Rev. A* **36**, 5870-5873.

Holtslag, A.A.M., and C.-H. Moeng, 1991 Eddy diffusivity and countergradient transport in the convective atmospheric boundary layer. *J. Atmos. Sci.*, **48**, 1690-1698.

Julien, K., S. Legg, J. McWilliams, and J. Werne, 1995a Penetrative convection in rapidly rotating flows: preliminary results from numerical simulation. *Dyn. Atmos. Oceans*, in press.

Julien, K., S. Legg, J. McWilliams, and J. Werne, 1995b Rapidly rotating

Rayleigh-Bénard convection. submitted.

Linden, P.F., 1973 The interaction of vortex rings with a sharp density interface: a model for turbulent entrainment. *J. Fluid Mech.*, **60**, 467-480.

Manins and Turner, 1978 The relation between the flux ratio and energy ratio in convectively mixed layers *Q. J. R. Meteorol. Soc.*, **104**, 39-44.

Mory, M., 1990 Models of turbulent mixing at a density interface including the effects of rotation. *J. Fluid Mech.*, **223**, 193-207.

Turner, J.S., 1986 Turbulent entrainment: the development of the entrainment assumption, and its application to geophysical flows. *J. Fluid Mech.*, **173**, 431-471.
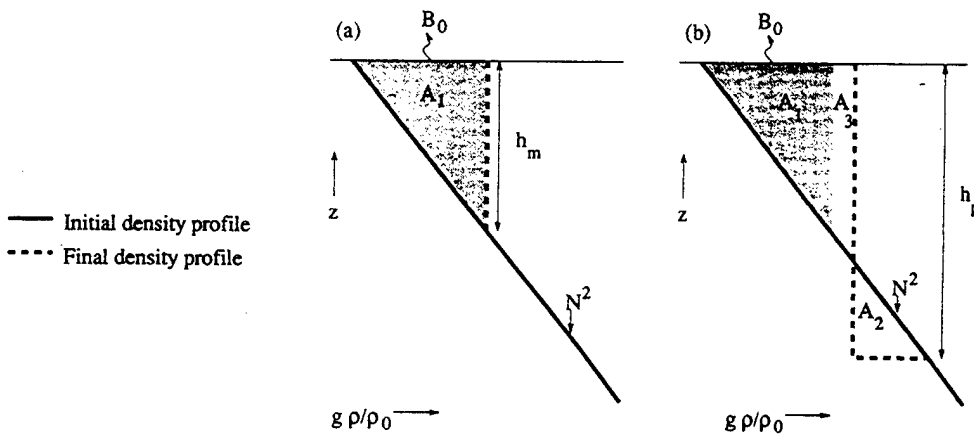
Figure 1: Comparison between the buoyancy budget and final density gradient for (a) non-penetrative and (b) penetrative convection paradigms, given an initial density gradient $(g/\rho_0)(-d\rho/dz) = N^2$, and total surface buoyancy loss $b = B_0 t$, where B_0 is the buoyancy flux. For non-penetrative convection, $b = A_1 = h_m^2 N^2/2$, i.e. $h_m = \sqrt{(2Bt)}/N$. In non-penetrative convection the extra buoyancy gain in the penetration zone (A_2) balances the extra buoyancy loss in the mixed layer (A_3) and the depth of mixing h_p exceeds h_m.
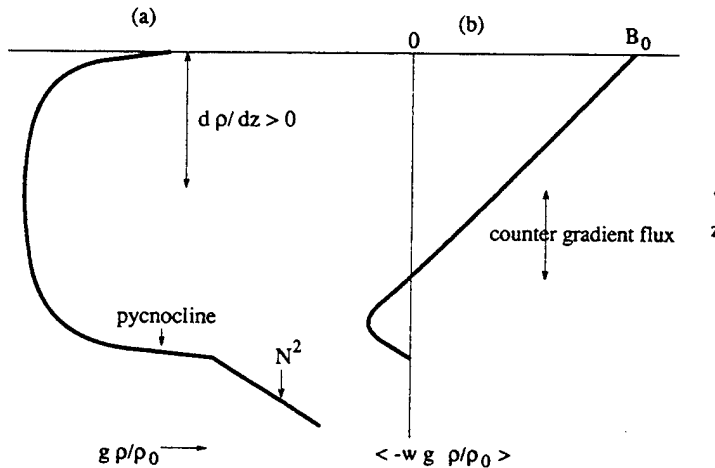

Figure 2: Typical (a) density and (b) buoyancy flux profiles in non-rotating penetrative convection, showing a region of counter-gradient buoyancy fluxes in the lower part of the mixed layer, and pycnocline below.
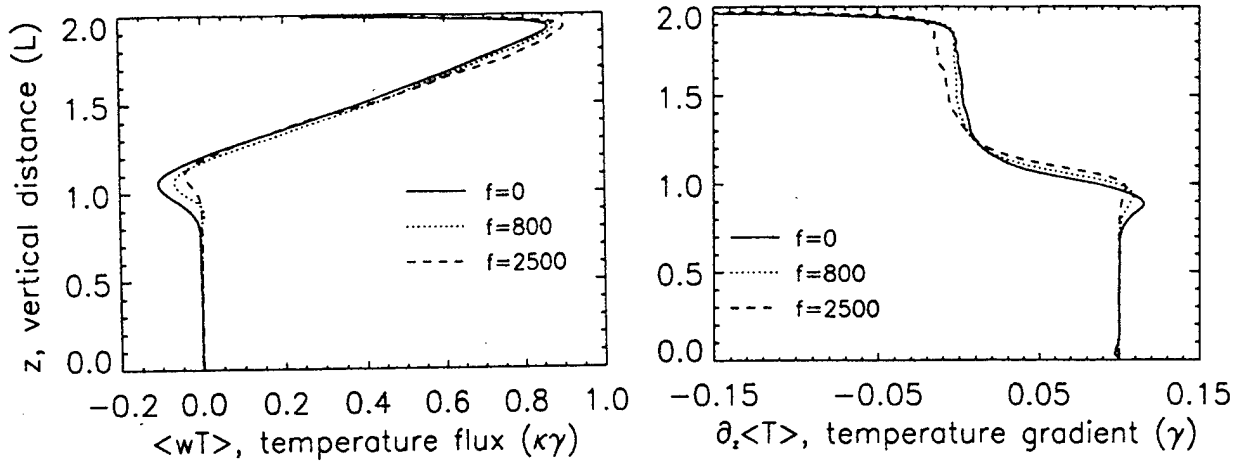
Figure 3: Vertical profiles of (a) temperature flux and (b) temperature gradient for 3 simulations with different values of Ro_c, showing a decrease in magnitude of the negative buoyancy flux in the penetration zone with decreasing Ro_c, and less enhancement of the thermocline.
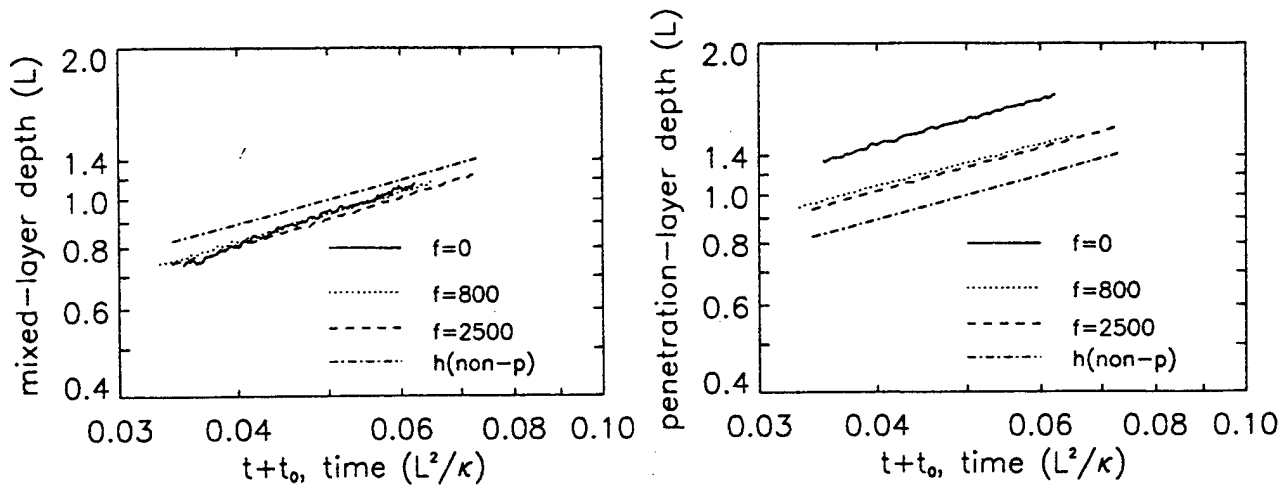

Figure 4: Time development of (a) the mixed layer depth (the depth at which the temperature gradient becomes slightly stable) and (b) the penetration layer depth (the depth at which the temperature gradient tends to the background value), showing the reduction in the width of the penetration zone with increasing rotation.

The Non-hydrostatic Modeling of Large Scale Oceanographic Flows

Amala Mahadevan

Department of Geophysical Sciences, University of Chicago, Chicago, IL 60637

A serious drawback of the hydrostatic model in large scale ocean modeling is that it is ill-posed in domains with open boundaries. Solving the non-hydrostatic equations for large scale flow on the other hand, is wrought with problems of numerical accuracy. An alternate approach that we use is to allow a greater deviation from hydrostatic balance. The approximation preserves the solution accuracy desired, and results in a well-posed model in domains with open or solid boundaries. It is found that by taking advantage of the hydrostatic nature of the problem, one can solve the non-hydrostatic equations at a cost that is not much greater than that of solving the hydrostatic equations.

We consider the equations that describe large scale oceanographic flow, while neglecting viscosity and using the approximation of incompressibility for seawater. We rewrite the total pressure as the sum of a hydrostatic component p and non-hydrostatic component q, where p is defined by

$$p_z + \rho g = 0 \tag{1}$$

and scale the equations in the usual way for the mid-latitudes using the characteristic time scale for advection. The dimensionless form of the equations is then given by

$$Du/Dt + \epsilon^{-1}(p_x + \gamma q_x - fv + \epsilon\delta bw) = 0 \tag{2a}$$

$$Dv/Dt + \epsilon^{-1}(p_y + \gamma q_y + fu) = 0 \tag{2b}$$

$$Dw/Dt + \gamma\epsilon^{-2}\delta^{-2}q_z - \epsilon^{-2}\delta^{-1}bu = 0 \tag{2c}$$

$$u_x + v_y + \epsilon w_z = 0 \tag{2d}$$

where

$$D/Dt \equiv u\partial_x + v\partial_y + \epsilon w\partial_z \tag{3}$$

and x, y, z refer to the eastward, northward and antiparallel to gravity coordinate directions. Here f and b denote the Coriolis parameters due to the normal and tangential to surface components of the earth's angular velocity, ϵ is the Rossby number, δ is the aspect (depth to length) ratio, and γ is a non-hydrostatic parameter that is the ratio of the characteristic magnitudes of non-hydrostatic and hydrostatic pressures. The vertical velocity scales as $\epsilon\delta$ times the horizontal velocity. Our interest is in using the model for mesoscale eddies and currents in the ocean. The value of δ is typically 10^{-2} and ϵ is in the range 10^{-1}–10^{-2} for these situations.

Since all the variables and their derivatives are dimensionless and O(1) in the above equations, it can be seen that in order for no single term in (2c) to be much larger than the others, it must be that

$$\gamma = \delta. \tag{4}$$

Equation (2c) can therefore be rewritten as

$$Dw/Dt + \epsilon^{-2}\delta^{-1}(q_z - bu) = 0. \tag{5}$$

For the large scale flows of interest to us, $\epsilon^{-2}\delta^{-1}$ is in the range 10^4–10^6 and implies that the sum of the vertical pressure gradient and Coriolis term is of the order 10^{-4}–10^{-6}. This sum must be computed to at least 2 digits of accuracy in order to achieve a reasonable accuracy in w and is what makes the numerical solution of these equations intractable. (The problem is even worse if the hydrostatic balance (1) is not subtracted out of the vertical momentum equation.)

By making the hydrostatic approximation, one no longer needs to integrate the vertical momentum equation. The vertical velocity is backed out from (2d), but still suffers from problems of accuracy on account of ϵ being small. Further, the equations are ill-posed when open boundaries are present [*Oliger & Sundstrom* (1978)].

An alternate strategy suggested by *Browning et al.* (1990), is to replace the coefficient $\epsilon^{-2}\delta^{-1}$ in (5) by a much smaller one that we denote by α to give

$$Dw/Dt + \alpha(q_z - bu) = 0. \tag{6}$$

The error made as a result of this approximation can be estimated by forming the error equations (by subtracting the approximate equations from the exact ones), and estimating the order of magnitude of the error variables. It can be shown that the error is $O(\alpha^{-1})$, and thus, with a suitable choice of α, we can retain a desired solution accuracy. Further, it can be shown that the model is well-posed with open or solid boundaries.

The most computationally intensive task in the numerical solution of these equations to find the non-hydrostatic pressure q. To do this, we differentiate (2a),(2b) and (6), and using the incompressibility constraint (2d) construct an elliptic equation of the form

$$q_{xx} + q_{yy} + \epsilon^2 \alpha \gamma^{-1} q_{zz} = rhs. \tag{7}$$

The solution of the linear system arising from the discretization of this elliptic equation can be speeded up immensely by using block relaxation that takes advantage of the fact that $\epsilon^2 \alpha \gamma^{-1} \gg 1$.

As an aside, it is interesting to consider the case when the tangential to surface component of the earth's angular velocity is neglected, or does not exist as in laboratory experiments. The absence of the term bu from (2c) implies that the pressure gradient term can be no larger than the vertical acceleration term. Hence $\gamma \le \epsilon^2 \delta^2$. The consequence of γ being much smaller is that non-hydrostatic effects are negligible and the solution to the non-hydrostatic momentum equations in this case is nearly the same as the solution to the hydrostatic equations.

References

Browning, G.L., Holland, W.R., Kreiss, H-O., & Worley, S.J. 1990. An accurate hyperbolic system for approximately hydrostatic and incompressible oceanographic flows. *Dynamics of Atmospheres and Oceans*, 14, 303–332.

Oliger, Joseph, & Sundstrom, Arne. 1978. Theoretical and practical aspects of some initial boundary value problems in fluid dynamics. *SIAM Journal of Applied Mathematics*, **35**(3), 419–446.

Barotropic, wind-driven circulation in a small basin.

Steve Meacham and Pavel Berloff

Dept. of Oceanography, Florida State University, FL 32306-3048.

1. Introduction

The atmosphere and ocean move on a broad spectrum of length scales. If we consider horizontal scales of motion, it is generally accepted (on physical grounds) that the large (planetary) scale motion is inextricably linked to synoptic scale motion. In the ocean, the synoptic scale is of $O(10-100Km)$. Evidence from observations and numerical simulations generally confirms this. Motion also exists at scales smaller than the synoptic scales. In the ocean it is impractical to make detailed observations of the small scale motion occurring over a region of large horizontal scale, such as an ocean basin. At present, it is also impractical to explicitly resolve motion on scales less than $O(1Km)$ in numerical models of an ocean basin. There are qualitative differences between the dynamics important to small scale motion and those important to synoptic and larger scale flows. For these reasons, numerical models of ocean basins seek to explicitly resolve motion at synoptic and larger scales while parameterising small scale motion with any of a variety of schemes. The similarity between the results of some of the better ocean models and observations, at least in the upper ocean in mid and low latitudes, encourages the use of this approach. Similar considerations apply to the atmosphere, though there the synoptic scale is larger.

Both observations and high-resolution numerical models [1] of the ocean indicate that the flow at synoptic scales is irregular. Ocean currents are frequently dynamically unstable, develop meanders and shed eddies. The interiors of ocean basins contain populations of synoptic scale eddies which move within the basin and interact with each other and with larger scale currents. This makes oceans unpredictable in the conventional sense. Such unpredictability is not confined to the position and strengths of synoptic scale eddies. The interaction of these eddies with large scale flows can lead to transitions in the large scale pattern of flow, as can be seen in, for example, simulations of the Black Sea.

In the atmosphere, lack of predictability was explicitly recognised by Lorenz [2]. An elegant model introduced by Lorenz served to demonstrate that some types of chaotic motion may also contain a geometric simplicity in the form of low-dimensional objects – fractal attractors – that the motion asymptotically approaches when viewed in a dynamical phase space.

Ruelle and Takens [3] proposed that bifurcations from regular behavior to motion on strange attractors might offer a route to certain types of turbulence. At very high Reynolds numbers, shear turbulence appears to be a complicated form of spatio-temporal chaos, but at more moderate degrees of nonlinearity, several types of flows or flow-like phenomena have been found to exhibit low-dimensional dynamical behavior. Examples include Taylor-Couette flow [4] and oscillating chemical reactions of the Belousov-Zhabotinskii type [5].

In the ocean, movement at synoptic scales and larger is constrained by the rotation of the Earth to be quasi-two-dimensional [6]. This offers the prospect that the turbulent character of oceanic flow at these scales may be considerably simpler than high Reynolds number, three-dimensional turbulence.

It seems worthwhile to explore the way in which a simple ocean, driven by wind, becomes turbulent. One conjectures that, as the Reynolds number is decreased, there will be

a series of bifurcations from regular attractors to low-dimensional fractal attractors to progressively higher-dimensional fractal attractors to spatio-temporal chaos. If, at the effective Reynolds numbers produced by the sub-synoptic scale motion, there is a set of attractors each possessing a relatively simple structure, the knowledge of the shape, dimension and probability measure of these attractors may prove useful in determining the probable behavior of such a system. Ideally one would wish to extend such an approach to a coupled ocean-atmosphere system of the type used in studying the dynamics of the Earth's climate. Here we discuss the results of experiments made with a simple two-dimensional ocean model.

2. Model

Our basic dynamical system is a finite-difference numerical model of wind-driven, barotropic flow in a small rectangular basin of uniform depth, H. Since we are not interested in re-solving external gravity waves, we use a rigid-lid approximation. The flow is horizontal and incompressible, the density is uniform and constant. We normalise the density to unity. We use no-slip boundary conditions at the lateral boundaries. The basin is located on a mid-latitude beta-plane [7]. The model is forced by a wind stress τ. The effects of sub-grid scale motion are modelled as a simple diffusion with a uniform diffusivity, ν.

Using a potential vorticity/streamfunction formulation of the problem [8], the governing equation can be expressed in the form

$$\partial_t \nabla^2 \psi + J(\psi, \nabla^2 \psi) + \beta \psi_x = \nu \nabla^4 \psi + \text{curl}(\tau/H) \tag{1}$$

The main dependent variable is, ψ, a streamfunction for the flow. The parameters, ν, H and β (the meridional gradient of the Coriolis parameter) are constant. Letting L_x and L_y be the zonal and meridional dimensions of the basin, we limit our attention to a steady wind-stress of the form $\tau = (\tau_0/L_x)(x - L_x/2)$, which has a uniform, cyclonic curl. (Our original interest was motivated by the behavior of the Black Sea.)

We nondimensionalize as follows. We introduce the Munk frictional boundary layer width, $l = (\nu/\beta)^{1/3}$, and then scale lengths with l, time with $(\beta l)^{-1}$, and streamfunction with βl^3. Eq. (1) becomes

$$\partial_t \nabla^2 \psi + J(\psi, \nabla^2 \psi) + \psi_x = \nabla^4 \psi + \epsilon \tag{2}$$

where

$$\epsilon = \frac{l}{L_x} \frac{\tau_0}{\beta \nu H}.$$

Defining a Reynolds number, Re, a dimensionless basin width, γ^{-1}, and an inertial length scale, L, by

$$Re = \frac{\tau_0}{\beta \nu H}, \qquad \gamma = \frac{l}{L_x}, \qquad L = \frac{\beta \nu H L_x}{\tau_0},$$

we see that $\epsilon = Re\gamma = l/L$ and the problem depends on three dimensionless parameters:

$$\epsilon = \frac{l}{L}, \quad \gamma = \frac{l}{L_x}, \quad \text{and} \quad \delta = \frac{L_y}{L_x}.$$

The last two parameters, γ and δ, come from a consideration of the locations of the basin boundaries. δ is the aspect ratio of the basin. Together with the no-slip boundary conditions adopted here, and in some cases the choice of initial conditions, the specification of ϵ, γ and δ determines the flow field.

Later, when studying the bifurcation properties of the system, we use the dimensional version of the model, fix

$$L_x = 1024 \text{Km}, \quad L_y = 512 \text{Km}, \quad f_0 = 10^{-4} \text{s}^{-1}, \quad \beta = 2 \times 10^{-11} \text{m}^{-1} \text{s}^{-1}, \quad \frac{\tau_0}{f_0^2 HL} = 9.766 \times 10^{-5}$$

and vary ν in the range $100 \text{m}^2 \text{s}^{-1} < \nu < 400 \text{m}^2 \text{s}^{-1}$.

The numerical model of (1) is discretised on a 129×65 grid using a second-order finite difference scheme. An explicit time-stepping scheme is used for all terms in (1) (a second-order Runge-Kutta scheme with a time step of 1800s). The Poisson problem is solved using Hockney's FACR method [9].

Considered as a dynamical system, the "variables" of the system consist of a q value at each of roughly 8000 nodes. This makes it a relatively large dynamical system.

We made a number of calculations that differ by (i) the value of ν used and (ii) the initial condition. Each calculation furnishes one trajectory of the dynamical system in its natural (roughly 8000-dimensional) phase space. Since following the details of this is quite impractical, we chose a diagnostic that represents a spatial integral of the instantaneous state of the system and used the method of delay coordinates [10] to reconstruct low dimensional phase space approximations. The diagnostic that we used was the basin integral of the kinetic energy of the flow, $K(t)$.

An artificial phase space was constructed by defining an artificial phase variable $\boldsymbol{x}(t;\tau) \equiv (x_0, x_1, ..., x_{n-1})$ with

$$x_j = K(t - j\tau)$$

for a fixed delay τ. In the results shown, we have used $n = 3$ and $\tau = 16.67 \text{days}$. Some of the figures below show Poincaré sections constructed as follows. We choose a fixed value of x_0, say C, and consider the plane with coordinates (x_1, x_2) given by $x_0 = C$. Choosing C so that the plane slices through the attractor of interest, we plot the points of intersection of the delay-coordinate phase space trajectory with this plane each time a trajectory passes through it, going from $x_0 < C$ to $x_0 > C$.

3. Results

Before examining the bifurcation structure of this model, we first found the marginal curve in the (ϵ, γ) plane for several different values of the apsect ratio δ (Figure 2). A typical steady solution is shown in Figure 1. In Fig. 2, the steady solution is linearly stable on the large δ/small ϵ side of a marginal curve (upper left side) and linearly unstable on the opposite side. For the case of a square basin ($\delta = 1$), the marginal mode to the left of $\epsilon = 1$ takes the form of an instability of the western boundary current, c.f. Ierley and Young [12], while along the marginal curve to the right of $\epsilon = 1$, the marginal mode appears to be an instability of the standing meander just to the east of the south-western recirculation gyre. Below we study the bifurcations of a $\delta = 0.5$ basin. Along the part of the $\delta = 0.5$ marginal curve shown in Figure 2, the marginal instability always seems to be associated with the standing meander.

We have explored the range $100 \text{m}^2 \text{s}^{-1} \leq \nu \leq 400 \text{m}^2 \text{s}^{-1}$ and identified several families of attractors within this range. For the size of basin and strength of forcing that we have used, the only aymptotic state, when $\nu = 400 \text{m}^2 \text{s}^{-1}$, appears to be a fixed point, corresponding to a steady circulation. At the other end of this range, $\nu = 100 \text{m}^2 \text{s}^{-1}$ is comparable to values of viscosity used in some eddy-resolving ocean simulation studies but larger than in others and larger than the estimates obtained from dye release experiments

(e.g. from the NATRE experiment [11].) Our main reason for stopping at $\nu = 100\text{m}^2\text{s}^{-1}$ is that regions of high dissipation in the flow become very narrow as ν is decreased and are poorly resolved in a model with 8Km resolution when $\nu < 100\text{m}^2\text{s}^{-1}$. Such structures play an important role in determining the flow patterns seen,

We have identified three families of solutions. These are shown in Figure 3 for the range $300 < \nu < 360$. One family is a family of fixed points, stable at sufficiently high ν but losing stability near $\nu = 350$. Lack of convergence in our steady state solver at low values of ν mean that we are unable to continue following this branch of unstable solutions below $\nu = 190\text{m}^2\text{s}^{-1}$, though there seems no reason to believe that this branch of solutions does not continue. We cannot rule out the possibility that, in the vicinity of $\nu = 190\text{m}^2\text{s}^{-1}$, the branch of steady states curves back around to higher values of ν but we have not found any indication of this.

In the vicinity of $\nu = 350\text{m}^2\text{s}^{-1}$, the branch of fixed points undergoes a supercritical Hopf bifurcation, giving rise to a family of unsteady attractors that we can follow down to $\nu = 300\text{m}^2\text{s}^{-1}$. For values of ν close to 350, these take the form of stable limit cycles with periods on the order of 81 days. As ν is reduced, the amplitude of the limit cycles increases. There is also a mild increase in the period of the oscillations. This limit cycle solution appears to undergo a secondary Hopf bifurcation in the vicinity of $\nu = 310\text{m}^2\text{s}^{-1}$ and the stable attractor becomes a 2-torus. After a short interval in ν there appears to be a transition to a chaotic set. This is either stable when it first appears or is attracting in most dimensions and only very weakly unstable. (At $\nu = 300\text{m}^2\text{s}^{-1}$ a Poincare section shows something similar to a chaotic attractor but given the finite integration time it is not possible to rule out that the possibility that what we are seeing is a chaotic transient with a very long time scale.) Below $\nu = 300\text{m}^2\text{s}^{-1}$, the chaotic attractor appears to lose stability. For example at $\nu = 298\text{m}^2\text{s}^{-1}$ and $\nu = 297\text{m}^2\text{s}^{-1}$, a typical trajectory spends a long time in the vicinity of what, from the form of its Poincaré section appears to be a continuation of the chaotic attractor; however, eventually the trajectory is captured by a stable limit cycle belonging to the second family of unsteady solutions discussed next.

A second family of unsteady solutions appears near $\nu = 327.6\text{m}^2\text{s}^{-1}$. This family of unsteady attractors can be traced to below $\nu = 100\text{m}^2\text{s}^{-1}$. At first these attractors take the form of stable limit cycles. Near $\nu = 327\text{m}^2\text{s}^{-1}$ these have periods on the order of 65 days. As ν decreases, the periods of the limit cycles decrease, their amplitudes increase and eventually they undergo a sequence of secondary bifurcations that lead to more complicated attractors. We first see a forward period-doubling bifurcation at around $281\text{m}^2\text{s}^{-1}$ that gives rise to an ν-interval of period 2 oscillations. This eventually ends in a reverse period doubling bifurcation near $\nu = 258\text{m}^2\text{s}^{-1}$. This family continues once more as a series of period 1 limit cycles (with a period of roughly 51 days) until a sequence of two period-doubling bifurcations occurs, leading first to period 2 limit cycles and then to period 4. Examples of these are shown in Figure 4. Between $\nu = 168\text{m}^2\text{s}^{-1}$ and $\nu = 165\text{m}^2\text{s}^{-1}$, the period 4 limit cycle appears to undergo a Hopf bifurcation and we see quasiperiodic solutions on an attracting two-torus. Subsequently there is a bifurcation to what appears, from its Poincaré section to be a chaotic attractor, an example of which, at $\nu = 147\text{m}^2\text{s}^{-1}$, may be seen in Figure 5. The majority of attracting solutions seen at lower values of ν are chaotic and, from their energy values, appear to be continuations of this family. (A narrow band of periodic solutions, first of period 10 and then period 5, was also seen in this range, and there may be other periodic windows that we have failed to detect.) As ν decreases, the chaotic attractor expands and its structure becomes less distinct. (Because of the length of time require to integrate the ocean model, the number of points that we can generate on a Poincaré section is limited.)

4. Discussion

There are several significant aspects of the results sketched out above. We have used a PDE model of a two-dimensional ocean basin, i.e. an infinite dimensional dynamical system. After discretization to reduce the PDE to a numerically integrable form, the system becomes finite-dimensional but its dimension remains very high. We find that for the range of horizontal viscosities consistent with our horizontal grid spacing, the solution asymptotes to a relatively low-dimensional attractor. For example, using a version of a nearest neighbor algorithm [13], we estimate that the dimension of the attractor seen in the Poincaré section for $\nu = 147 \mathrm{m^2 s^{-1}}$ in Figure 5 to be between 2.4 and 2.5. This relatively simplicity is not something that one would immediately anticipate from the visual appearance of the time-dependent physical flow field that corresponds to Figure 5. The physical flow field looks rather complicated and irregular.

In the range we have examined, the chaotic attractor on the higher energy branch of unsteady solutions is gradually changing as ν is decreased. It is spreading out over a larger volume of the delay coordinate phase space and is becoming more diffuse. In addition, its fractal dimension also appears to be slowly increasing. For $\nu = 130 \mathrm{m^2 s^{-1}}$, the nearest neighbor estimate of the fractal dimension lies between 2.8 and 2.9. This gradual increase in dimension makes it difficult to estimate the dimensions of the attractors present at lower values of ν with the limited duration times series that we are able generate.

Since our approach relies heavily on the forward integration of a straighforward evolution model, there may be other attractors that we have missed, nor do we have much information on the sizes of the basins of attraction of the attractors that we did find. The simple-minded approach of integrating forward in time and seeing what happens has the virtue of simplicity but more sophisticated approaches to investigating dynamical systems exist and, if brought to bear on this problem, ought to reveal more of what is going on. The disadvantage of some of the more sophisticated techniques is that, when applied to this rather high-dimensional model, they will require a lot of computational resources.

A direct application of these results to the synoptic and large scale movement of a real ocean basin would clearly be incorrect. We feel that their main significance lies in the fact the we have integrated a system with some of the complexity of the real ocean and found evidence of a relatively simple dynamical behavior. Our numerical model greatly simplifies the dynamics of the ocean, and the parameterization of the effects of sub-grid scale eddies as a simple, constant-coefficient diffusion is rather naive. However, one should not lose sight of the fact that this is still a high-dimensional system. One might also expect to see low-dimensional behavior in more sophisticated ocean models. We are experimenting now with models that include some of the effects of ocean stratification.

The gravest simplification we have made is probably the use of a steady forcing for this model. The true wind forcing of the ocean is of course unsteady. It would be interesting to take a similar approach to a highly simplified climate model containing coupled atmosphere and ocean models. One extension to the current problem that we are attempting is to place the steady wind-forcing with a periodic forcing chosen to represent the seasonal cycle of winds.

Acknowledgements

References and Notes

1. W.R. Holland, *J. Phys. Oceanog.* **8**, 363 (1978).

2. E.N. Lorenz, *J. Atmos. Sci.* **20**, 130 (1963).

3. D. Ruelle and E. Takens, *Commun. Math. Phys.* **50**, 69 (1976).

4. (1) A. Brandstater and H.L. Swinney *Phys. Rev.* **A 35**, 2207 (1987), (2) A. Brandstater, J. Swift, H.L. Swinney, A. Wolf, J.D. Farmer, E. Jen and P.J. Crutchfield *Phys. Rev. Lett.* **51**, 1442 (1983).

5. (1) R.H. Simoyi, A. Wolf and H.L. Swinney *Phys. Rev. Lett.* **49**, 245 (1982), (2) J.-C. Roux, R.H. Simoyi and H.L. Swinney *Physica* **8D**, 257 (1983).

6. (1) J. Pedlosky, *Geophysical Fluid Dynamics*, 2nd edn, Springer-Verlag (1987), (2) P.B. Rhines, *J. Fluid Mech.* **69**, 1975).

7. J. Pedlosky, *op. cit.*

8. P.J. Roache, *Computational Fluid Dynamics*, Hermosa, Albuquerque, (1982).

9. R.W. Hockney, *Method of Comp. Phys.* **9**, 135 (1970).

10. (1) F. Takens, in *Lecture Notes in Mathematics*, eds. D.A¿ Rand and L.-S. Young, Springer-verlag (1981); (2) N.H. Packard, J.P. Crutchfield, J.D. Farmer and R.S. Shaw, *Phys. Rev. Lett.* **45**, 712 (1980); (3)J.-C. Roux, R.H. Simoyi and H.L. Swinney, *op. cit.*

11. J.R. Ledwell, A.J. Watson and C.S. Law, *Nature*, **364**, 701 (1993).

12. G.R. Ierley and W.R. Young, J. Phys. Oceang.. **22**, xxx (1992).

13. The estimates of fractal (Hausdorff) dimension quoted in the text were obtained using a program written by E.J. Kostelich that implements a nearest-neighbor algorithm. References on this approach can be found in (1) J.D. Farmer, E. Ott and J.A.Yorke, *Physica* **7D**, 153 (1983) and (2) E.J. Kostelich and H.L. Swinney in *Chaos and Related Nonlinear Phenomena*, eds. I. Procaccia and M. Shapiro, Plenum, New York. (1986).
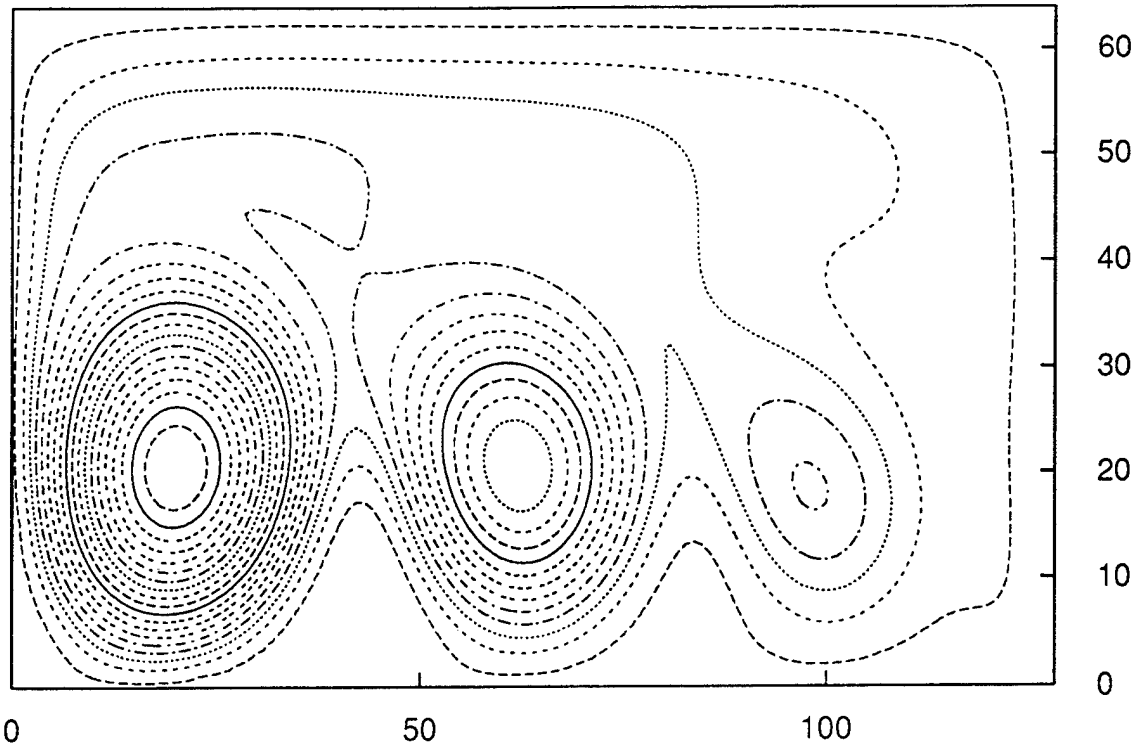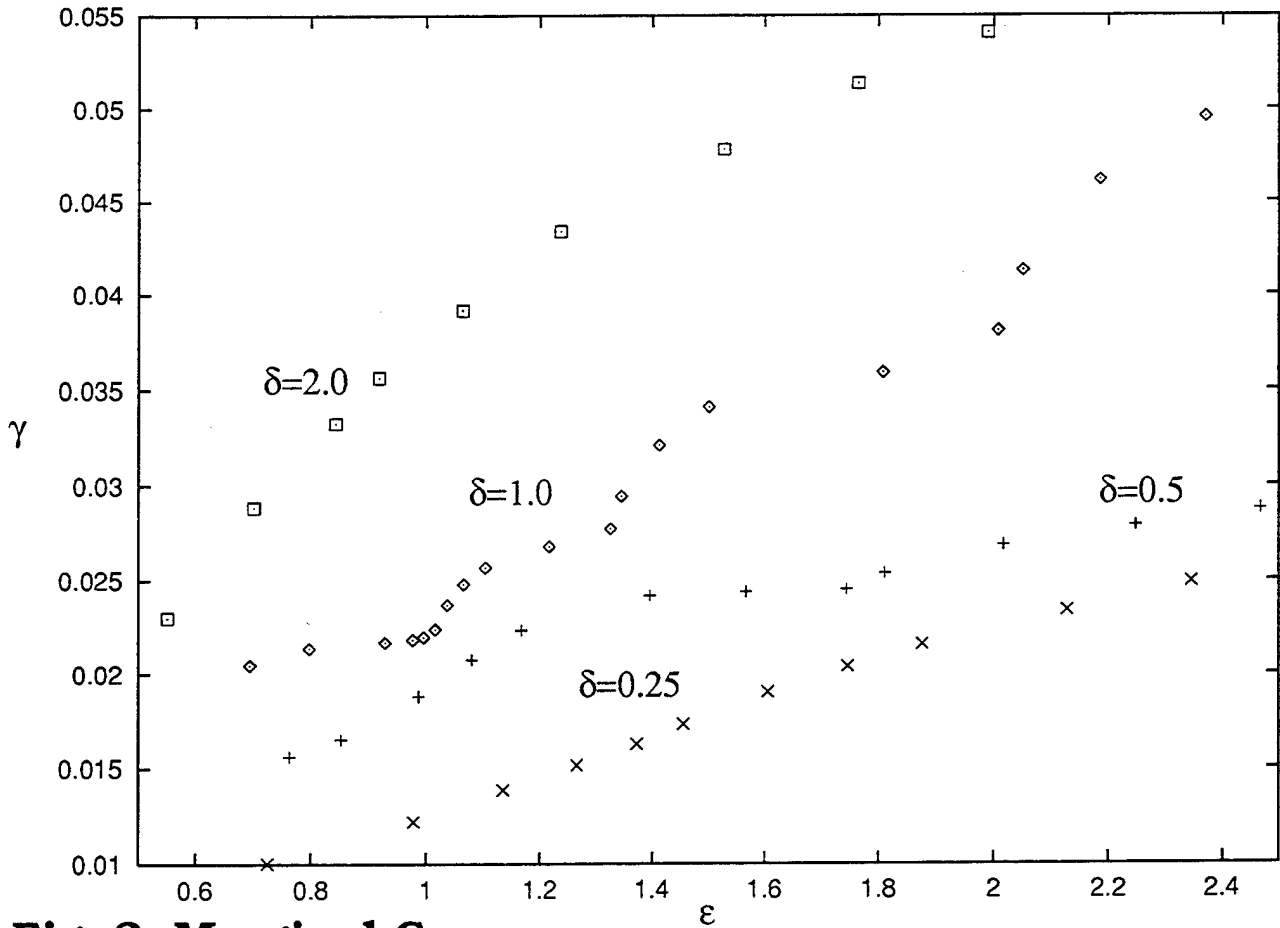
Fig. 1. Streamfunction for a typical steady state
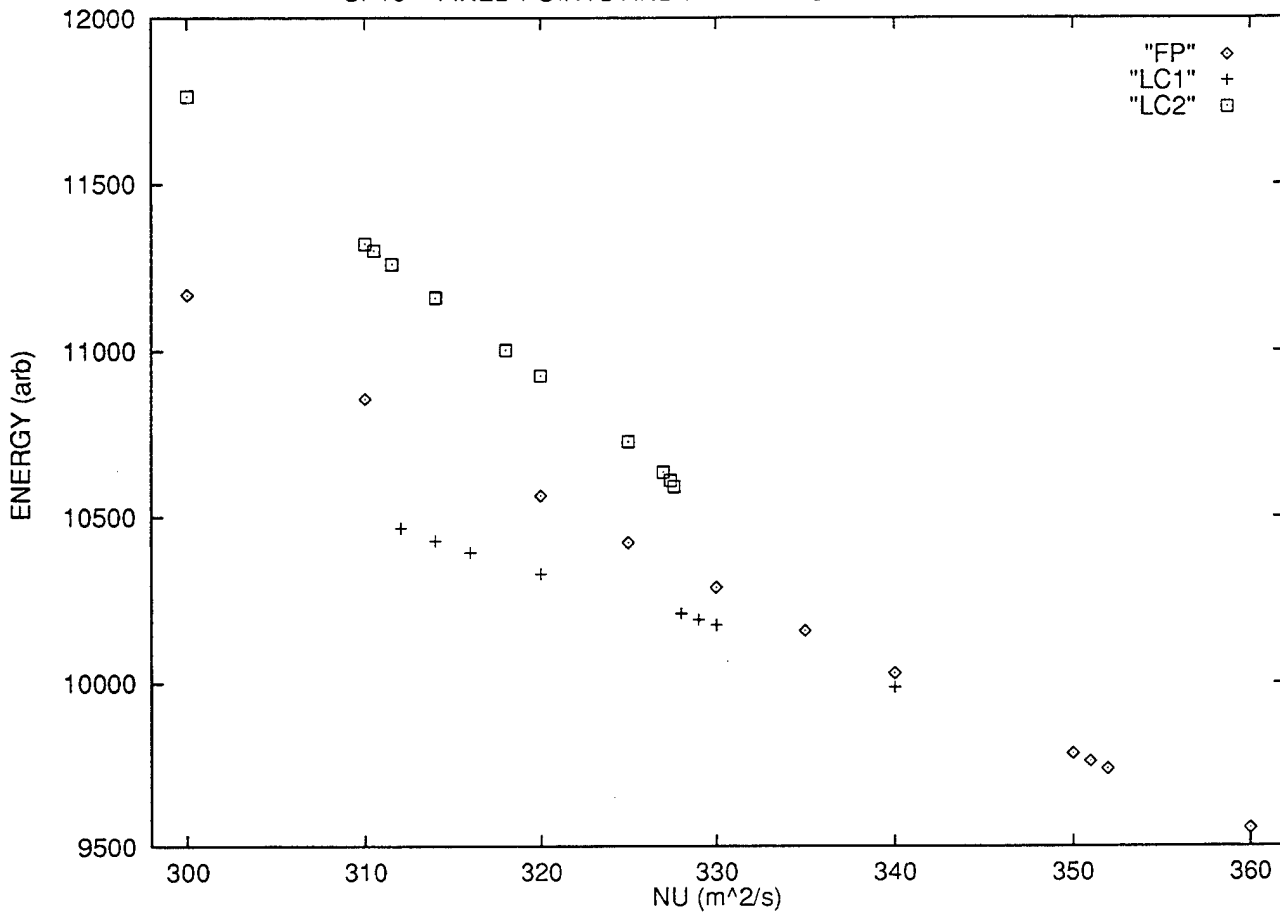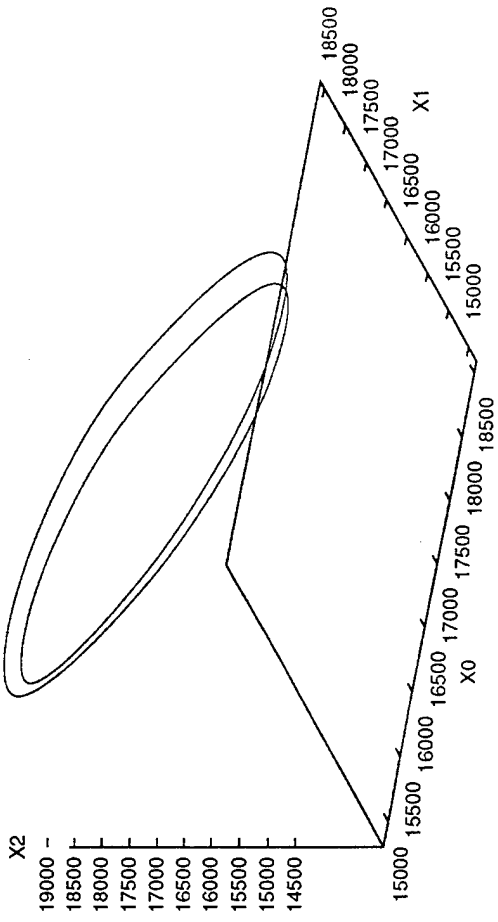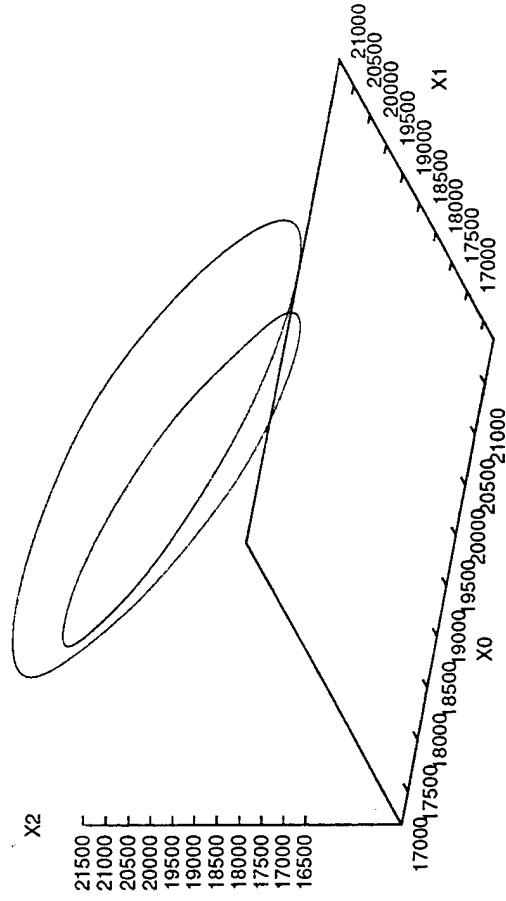

Fig. 2. Marginal Curves

Fig. 3. Examples of 3 branches of solutions:
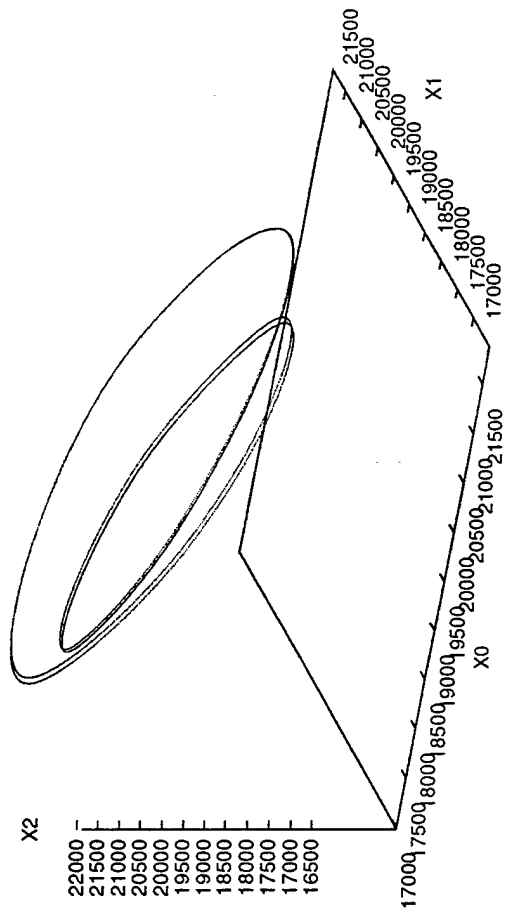FP = fixed points, LC1 & LC2 = two branches of limit cycles.
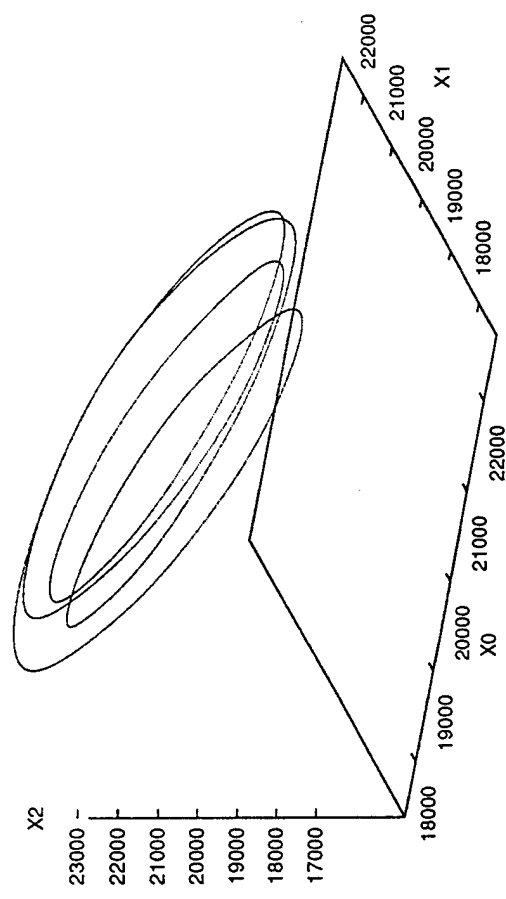
SP10.116 210

sp10.23 180

SP10.24 176

SP10.28c 168
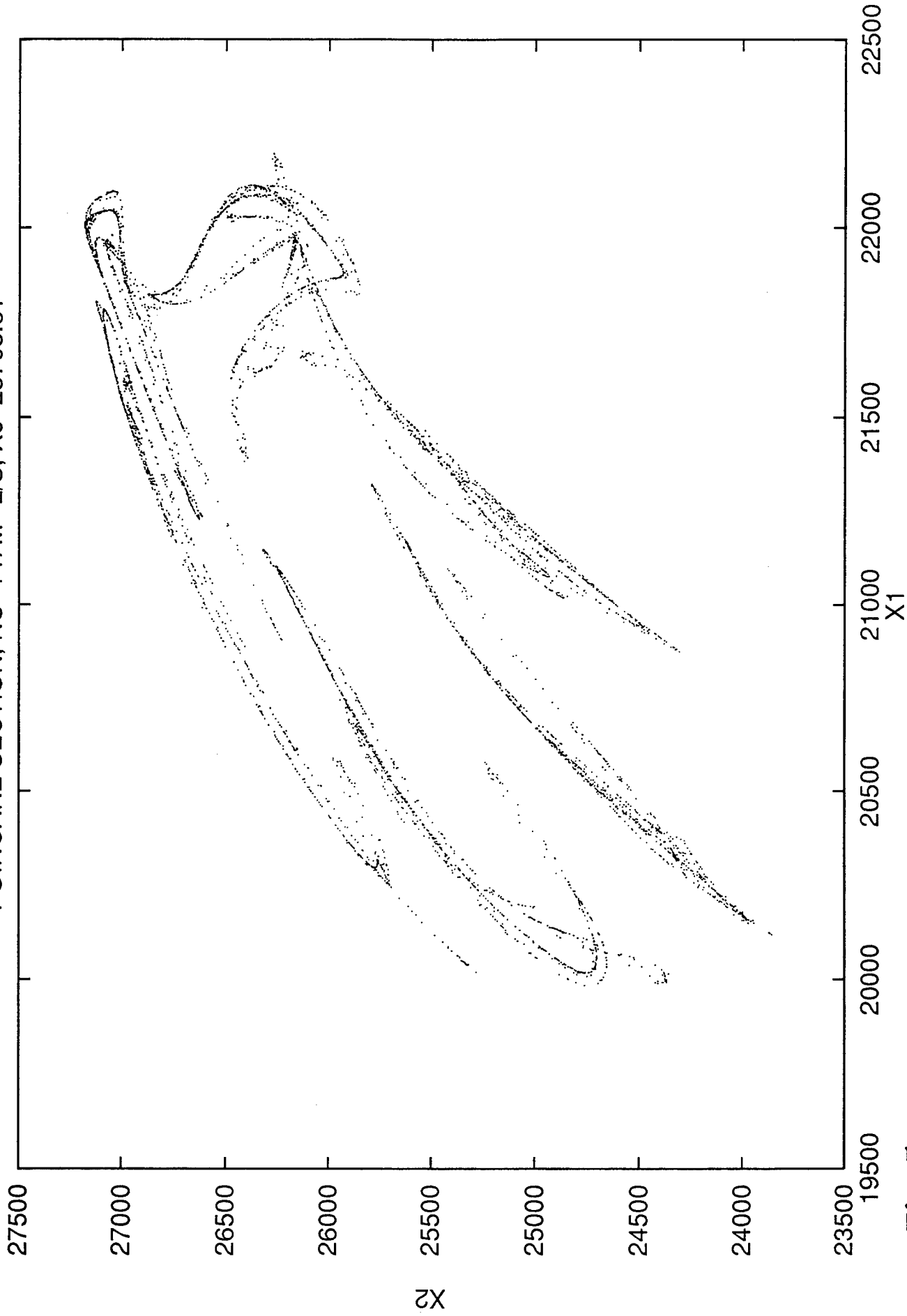

Fig. 4

POINCARE SECTION, NU=147M**2/S, X0=23708.61

Fig. 5

Rayleigh-Bénard Convection in Compressed Gases

Brendan B. Plapp and Eberhard Bodenschatz
Department of Physics, Cornell University

Recently, experiments in Rayleigh-Bénard convection[1] revealed a complex, time-dependent state in which targets, single- and multi-armed spirals were continually created, annihilated and advected throughout the fluid layer. This state, termed "spiral defect chaos" (SDC), was found to occur where the Busse balloon stability boundaries would predict a stationary pattern of straight rolls. Although SDC was later observed in theoretical simulations of the Boussinesq equations,[2] the nature of SDC is still not understood. Recent theoretical work has sought to explain the spatio-temporal chaos via the concept of an "invasive defect".[3]
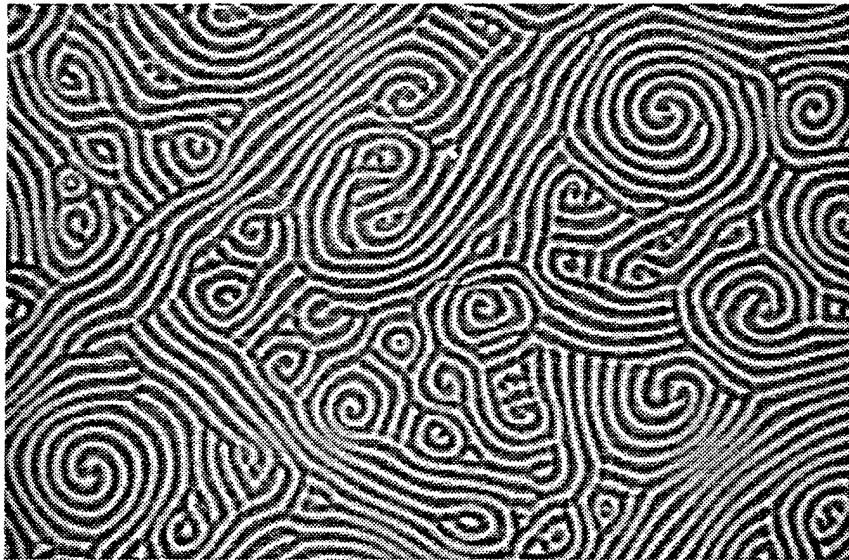

Figure 1: Shadowgraph image of Spiral Defect Chaos at $\varepsilon = (Ra - Ra_c)/Ra_c \approx 1$ in pressurized CO_2. White indicates cold downflow; dark represents warm upflow.

While individual spirals have been studied in biological and chemical systems, nothing is known about spirals in Rayleigh-Bénard convection. To characterize this fundamental coherent structure of SDC, we have experimentally investigated the dynamics of individual spirals.

By using CO_2 pressurized to 50 atm, we could produce convection in a very shallow layer and thereby achieve a large lateral to vertical aspect ratio. Six cells of different aspect ratios were then simultaneously investigated, as shown in figure 2. Forcing sidewalls were constructed to select circular patterns, and the modes of formation and destruction for target patterns, 1-, 2-, 3- and 4-armed spirals were observed. Each spiral arm extended from a central core tip out to a trailing defect which revolved around the center at a constant radius. Between the defect and the sidewalls were concentric circular rolls.

1. S. W. Morris, E. Bodenschatz, D. S. Cannell, and G. Ahlers, Phys. Rev. Lett. 71, 2026 (1993).
2. W. Decker, W. Pesch, and A. Weber, Phys. Rev. Lett. 73, 648 (1994).
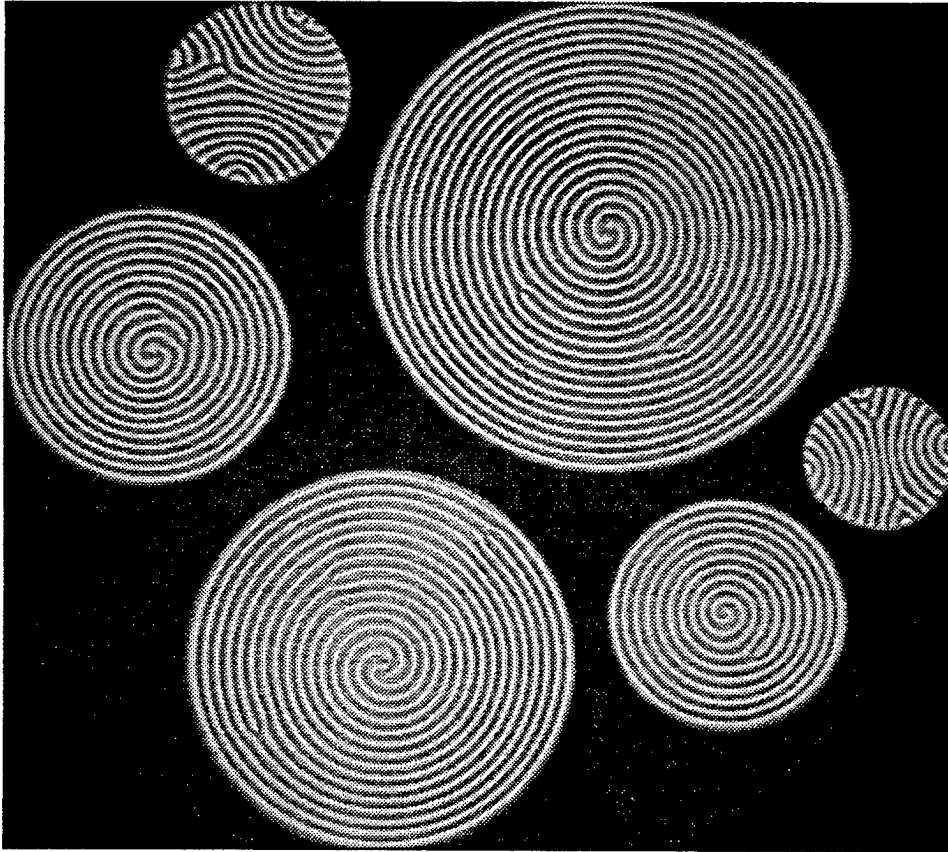3. M. C. Cross and Y. Tu, Phys. Rev. Lett. 75, 834 (1995).

Figure 2: Shadowgraph image of six cells at $\varepsilon = 0.7$; note 1-, 2- and 3- armed spirals in the four largest cells and Pan Am patterns in the two smallest. Largest cell is 4.3 cm in diameter, smallest is 1.3 cm. Layer thickness is 430 μm.

The 1-armed spirals' frequencies of rotation were measured and found to increase with the applied temperature difference. This trend reversed when the spiral core moved off-center in a manner similar to the focus instability.[4] Although the outer tip speed increased in the compressed region, the slowing of the tip in the expanded region was so great that the average rotation rate decreased.

The drift of the spiral off-center also presaged the occurrence of one or more skewed-varicose instabilities, which form the high wavenumber boundary in the Busse balloon for stable rolls for our Prandtl number of 1.4. In a skewed-varicose event, a roll pair is torn, causing the pattern to relax to a smaller wavenumber. The low wavenumber boundary for stable rolls (at Prandtl number 1.4) is the cross-roll instability, in which a significant dilation between nominally parallel rolls causes perpendicular rolls to grow in the gap. We have compared the wavenumbers at which the instabilities occurred to those predicted by theory. Further results and theoretical comparisons will be described elsewhere.[5]

---

4. A. C. Newell, T. Passot, and M. Souli, Eur. J. Mech., B/Fluids, 10, no. 2 - Suppl., 151, (1991).
5. B. B. Plapp, E. Bodenschatz, W. Bäuml, and W. Pesch, in preparation.

Spin-offs of the North Atlantic Current

by T. Rossby
Graduate School of Oceanography
University of Rhode Island
Kingston, RI 02881

The North Atlantic Current (NAC) has the distinction of reaching much farther poleward than any other western boundary current. As the continuation of the Gulf Stream after it curves around the SE Newfoundland Rise near 40°N, 50°W, the NAC flows northeast past Flemish Cap to the Northwest Corner before turning sharply to the east towards northern Europe. While these notes focus on the northward flow of the current, it is intriguing to speculate on why the Gulf Stream, unlike its cousin in the Pacific, the Kuroshio Extension Current, turns north at all. The most obvious reason is that the thermohaline or meridional overturning cell 'draws' the waters poleward. But this begs the question why the current turns north in the west: Why not continue to the east as a zonal jet and then turn north? But other possibilities come to mind. To mention one: the eastward flowing Gulf Stream 'locks onto' the southern flank of the Southeast Newfoundland Rise. As the isobaths turn to the north and northwest, so does the current. If so, what would happen if the SE Newfoundland Rise did not exist?! Would the Gulf Stream continue eastward as does the Kuroshio? It might be interesting to test this with a numerical model of the North Atlantic Circulation. Fig.1 shows Iselin's (1936) map of the depth of the 10°C isotherm in the NW Atlantic.
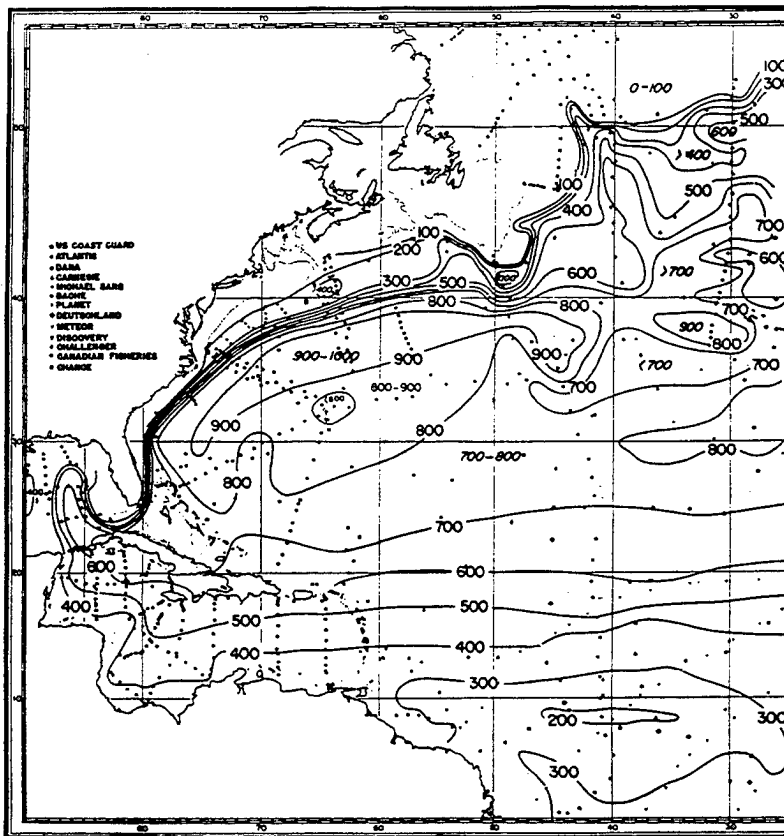

Fig. 1. The depth of the 10°C isotherm in the NW Atlantic according to Iselin (1936).

Studies of the NAC region have been hampered by the persistent cloud coverage and lack of ground stations nearby that can receive AVHRR imagery on a routine basis. We recently concluded a study of the region using isopycnal rafos floats. Lagrangian techniques for studying currents can be very helpful for the float trajectories provide a substantial amount of spatial information. A major focus of this project was to elucidate the structure of the current, and to determine to what extent it acts as a barrier between the warm subtropical waters of the Newfoundland Basin and the cold subpolar waters flowing south in the Labrador Current (LC) inshore of the NAC. The isopycnal contrast between waters of the NAC and LC is enormous, and can exceed 10° on shallow density surfaces. Starting in summer 1993, we have on three separate occasions deployed floats on two specific volume anomaly surfaces corresponding to the 27.2 and 27.5 sigma-t surfaces. The majority of float missions lasted ten months. Some were deployed in the NAC, and others to either side of the current. The field program ended in June 1995 and the remaining float data will have been processed by the end of the year. From the trajectories of the first ~60 floats we have constructed a cartoon, Fig. 2, of the mean path of the current (Rossby, 1995).
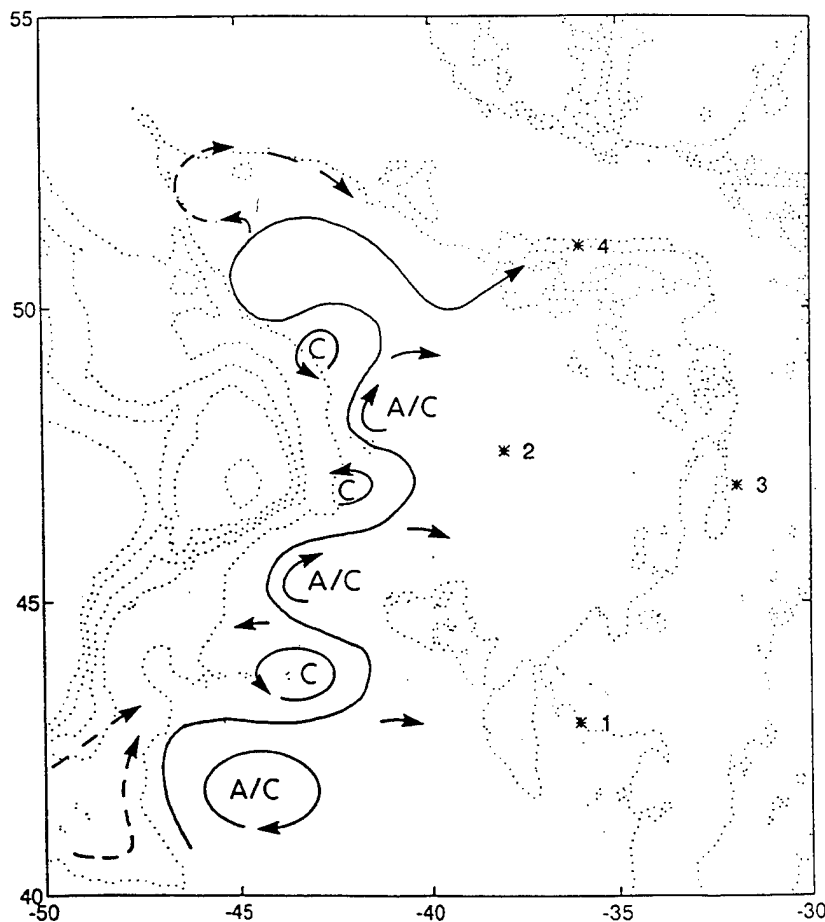
Fig. 2. Cartoon of the path of the NAC and adjacent recirculation cells. The arrows indicate probable pathways and directions of exchange between the NAC and surrounding waters. The dashed lines indicate possible inshore pathways from the Gulf Stream. The dashed line in the north indicates an additional meander that appears in some of the deeper float trajectories. The four stars mark the positions of the sound sources providing the acoustic navigation for the rafos floats.

The most striking aspect of the current must surely be its highly convoluted path: the meanders are short and steep. Further, where there are crests, troughs are rarely if ever observed, and vice versa. Unlike the Gulf Stream where meanders propagate eastward, these meanders are stationary and locked, we believe, to the bathymetry. This will be quantified when all of the float data have been processed. We have found little evidence for zonal jets emanating from the NAC. After the NAC turns east near 52°N, it retains a jet-like structure for only a short distance. From the float data available thus far, it appears that the NAC changes its character from a narrow jet to a broad eastward flow with perhaps eddy- or topographically induced transient jets superimposed.

As a result of the semi-permanent meanders, strong recirculations develop within the 'bights' of the meanders. Two floats illustrate this: float 277 shows the shedding of an anti-cyclonic eddy at the northwest corner, Fig. 3.
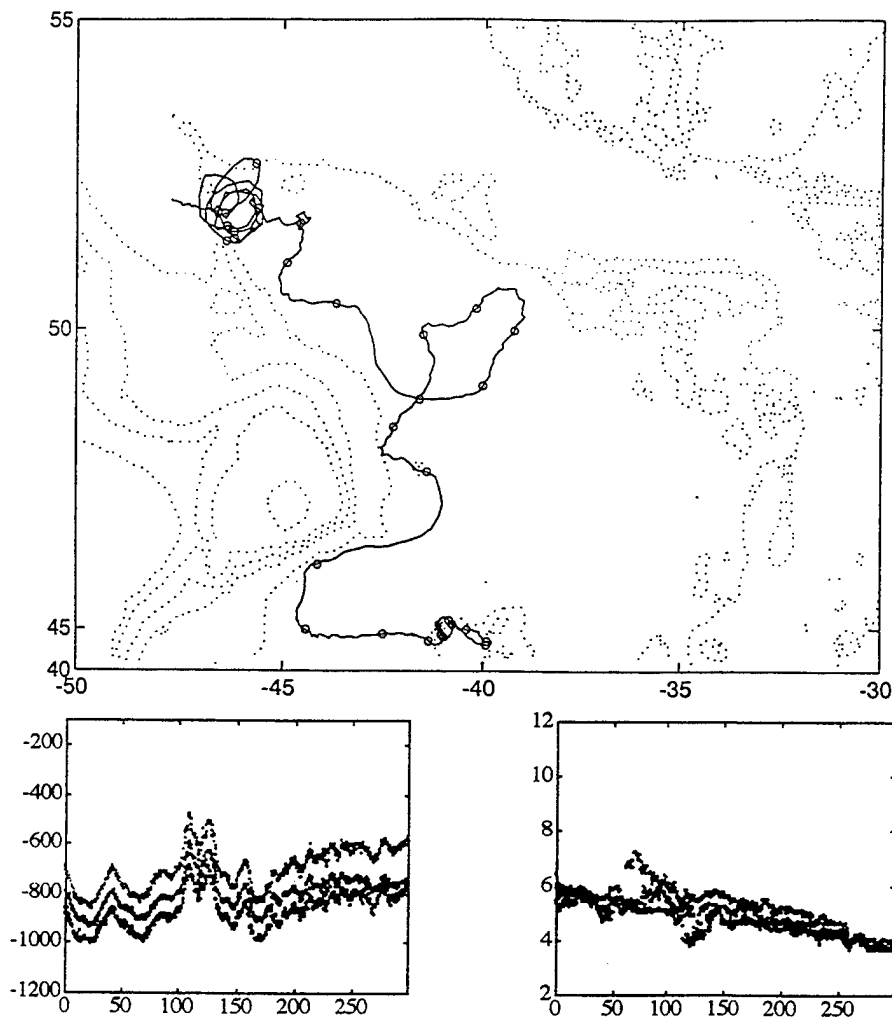
Fig. 3. The top panel shows the trajectory, the lower panels show the temperatures and pressures at the depth of the float and the density surfaces 0.1 σ-units below and above. (The float is programmed to float up and down to these neighboring density surfaces twice a day.) Note the decrease/increase in stratification in the upper/lower half-layers with time.

The interesting feature to note is the cooling of the eddy after it breaks away, and the increasing layer thickness. The maximum cooling rate occurs during the late winter months, so it is tempting to assume that the float is at the bottom of a deepening mixed layer, but the anticyclonic orbiting of the float indicates that it is within a baroclinic pool of water, so we can't exclude the possibility of lateral cooling by the surrounding Labrador Waters as well.

The second eddy is effectively a permanent feature of the North Atlantic. We call it the Mann eddy after Cedric Mann (Mann, 1967). One of the floats remained trapped in it for its entire 10 month mission, Fig. 4.

Fig. 4. The trajectory of float 260 trapped in the pycnocline undr the Mann eddy for 10 months. The gradual cooling (not shown) suggests lateral mixing. A Gaussian estimate of the eddy's relative vorticity is -0.14f, comparable to the NAC's negative shear vorticity.

The temperature record indicates a cooling trend the entire time, but the float's great depth and the high stratification preclude contact with the overlying mixed layer. Assuming the float was not leaking (which we need to ascertain) and hence sinking into colder waters, the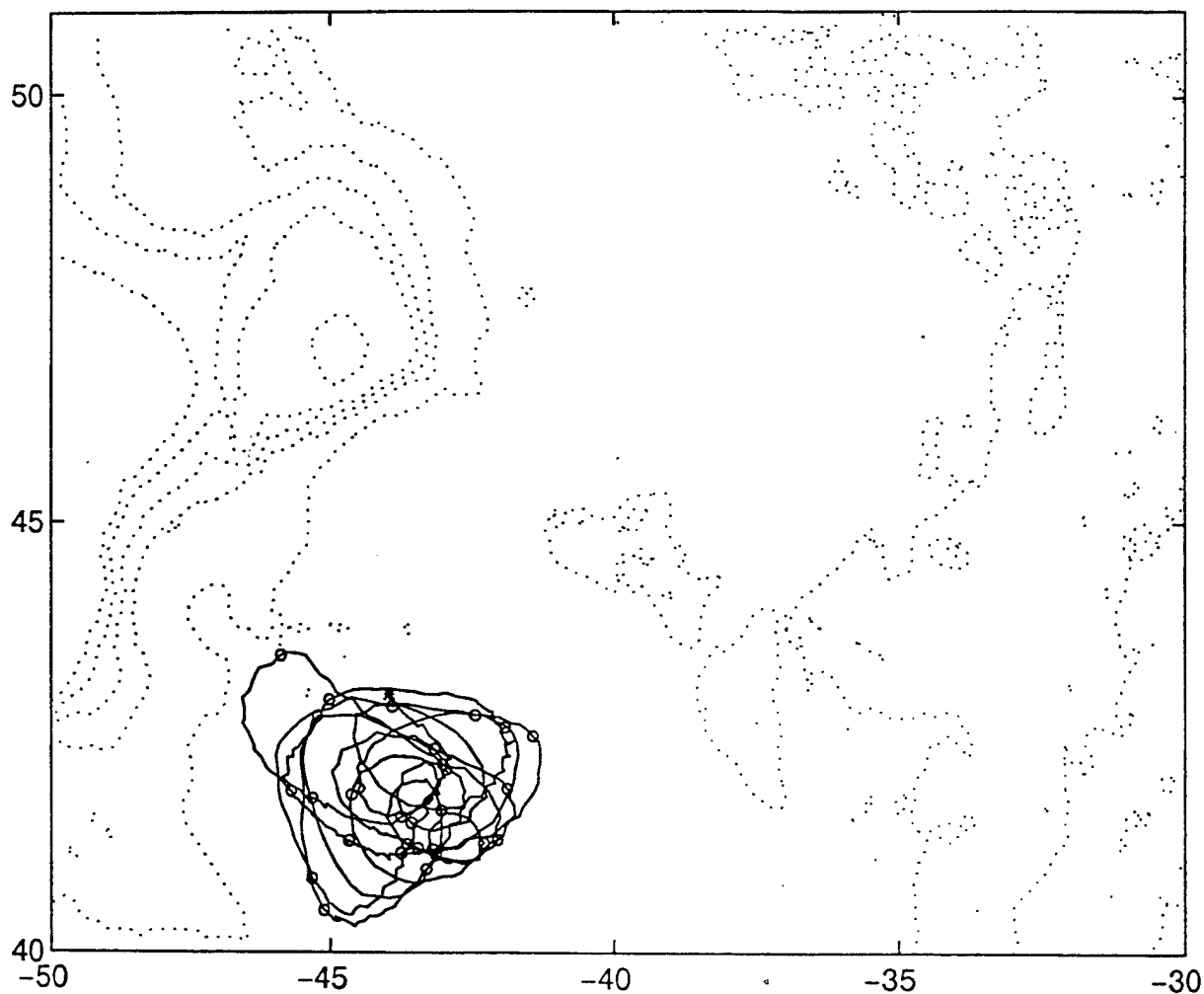 only mechanism available would appear to be lateral (isopycnal) mixing with cold waters of Labrador Sea origin along the meander perimeter. The temperatures are within an allowable range for this to be possible, but since the cooling cannot continue forever, the waters will have to be flushed out at some point. The thermocline in this eddy is several hundred meters deeper than in the Newfoundland Basin (Mann, 1967). This represents a substantial reservoir of eddy potential energy which the curved flow of the meander crest somehow maintains. As a consequence of the deep thermocline, a layer of low stratification can always be found above it, Fig. 5. It is very difficult to believe that these layers retain such uniformity for months after the cessation of winter time cooling. Perhaps some kind of slantwise convection or cabbeling mechanism might be involved in suppressing restratification. A careful look at the float track in Fig. 4 will show strong inertial motion.
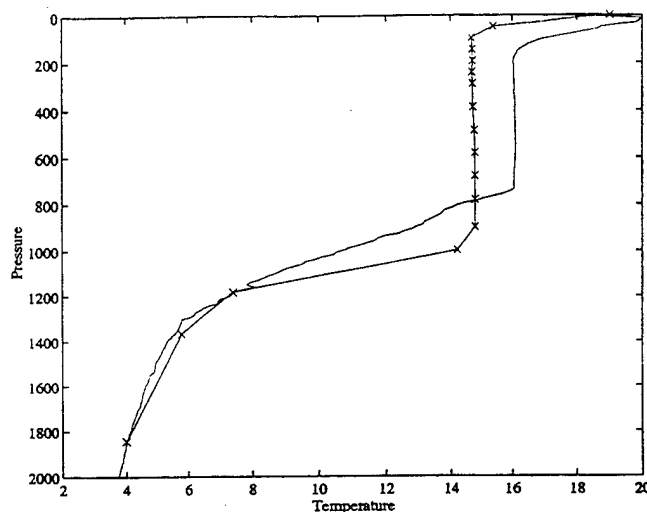
Fig. 5. Temperature profiles from the Mann (x) eddy (Mann, 1967) and a recent CTD cast.

Addendum: The sharp meandering of the current and the expulsion of anticyclonic vorticity in the form of tight recirculations and separated eddies means that the eastward flowing NAC, i.e. after it leaves the western boundary, is transporting less relative a/c vorticity than the NAC advected into the region at the southern end. The apparent broadening of the NAC after it turns east would be consistent with this hypothesis since the advection of vorticity (for a homogeneous flow on a local f-plane) is proportional to the inverse square of the width of the current. The difference in transport would have to be dissipated in the standing meanders or removed in the form of discrete eddies. Perhaps eddy shedding is an intrinsic part of the dissipation process: eddies spin-up and break away making room for the next one since the meanders alone apparently can't dissipate the vorticity. When all of the data are ready, we will attempt to construct a potential vorticity budget for the NAC region. This will hopefully include estimates of eddy formation rates and perhaps export from the area.

References:
Iselin, C. O'D, 1936. A study of the circulation of the western North Atlantic. Pap. Phys. Oceanogr. Meteor.,4,101 pp.
Mann, C. R., 1967. The termination of the Gulf Stream and the Beginning of the North Atlantic Current. Deep-Sea Res.,14,337-359.
Rossby, T., 1995. The North Atlantic current and Surrounding Waters 'At the Crossroads'. Rev. Geophys. Submitted Feb. 1995

Large-scale aspects of convection: observations, vertical transports, and implications

Uwe Send

Oceanic deep convection is an important process in the large-scale and global thermohaline circulation system. It must be this process which generates the deep water masses, since they can only acquire their low temperatures and high densities through surface contact in regions where corresponding surface conditions are found in winter. It is well known now from direct observations as well as numerical and lab modelling studies that convection in the ocean takes place in the form of vertical cells, with typical diameters of order $1km$. Within these cells (sometimes also referred to as *plumes*), appreciable vertical velocities of up to $10cm/s$ may be found (see Schott et al. 1994 for an overview of observations). Scaling relations based entirely on external parameters (buoyancy flux B, rotation f, depth H) are quite successful at predicting the various properties of plumes. There is still some controversy regarding the choice of rotating versus non-rotating scalings, but for typical ocean conditions these yield rather similar sizes and vertical velocities for the plumes. Some of these scaling relations can be found in Jones and Marshall (1993), Maxworthy and Narimousa (1994), Coates et al. (1994).

An important topic also is the large-scale (or *integral*) net effect of the ensemble of all the plumes in a convection region. Send and Marshall (1995) investigated the mean downward transport (area integral of w) in a convection regime. Using several different approaches, they demonstrate that convection must be essentially a *mixing process* with negligible vertical transport. For example, any oceanographically significant mean w would induce unrealistically large relative vorticity. Observed density structures and numerical model analyses also supported this *mixing element* concept of convection plumes. Send and Marshall went on to introduce a vertical mixing timescale $t_{mix} = H/w_{plume}$, based on which successful scaling relations for a number of large-scale properties of the convection region were derived. Good agreement between predictions from these and numerical model simulations were obtained for the temporal evolution of the density anomaly, for the magnitude and width of the *rim current* circulating around the (denser water of the) convection region, and the instability time-scale and wavenumber of this rim current.

The success of the mixing concept of convection suggests that also in numerical models, it ought to be possible to represent and thus parameterize the plume activity by a suitable mixing scheme. A quantitative scaling for a vertical diffusivity to be used during active convection had been put forward in Send and Marshall (1995) and this was then rigorously tested via twin experiments in Klinger et al. (1995). The net results was that during the first days after the onset of convection, it was important to use a mixing scheme (e.g. a diffusivity) with the correct t_{mix}. However, in the long run all parameterization tried, even convective adjustment, yielded water mass properties and volumes close to the runs with resolved plume activity.

One question immediately arises from the above results: If there is no mean downward transport during the active convection period (the plume phase), how then is the volume of deep water replenished that is observed to exit the convection basins in the thermohaline system ? Let us idealize the end state of the deep mixing phase by a density field as sketched in figure 1. It is clear then that convection has generated an additional volume $A \times H/2$ of water with deep water

densities (hatched in fig. 1), compared to the 'climatological' mean state (A is the surface area of the convection region). If one assumes that, in the long run, this water somehow settles into the deep-water pool, the extra volume of deep water generated is just given by $A \times H/2$. This is how the water mass generation in terms of volume should be calculated. Note that this is different from the volume mixed and e.g. enriched with tracers, which would be $A \times H$.
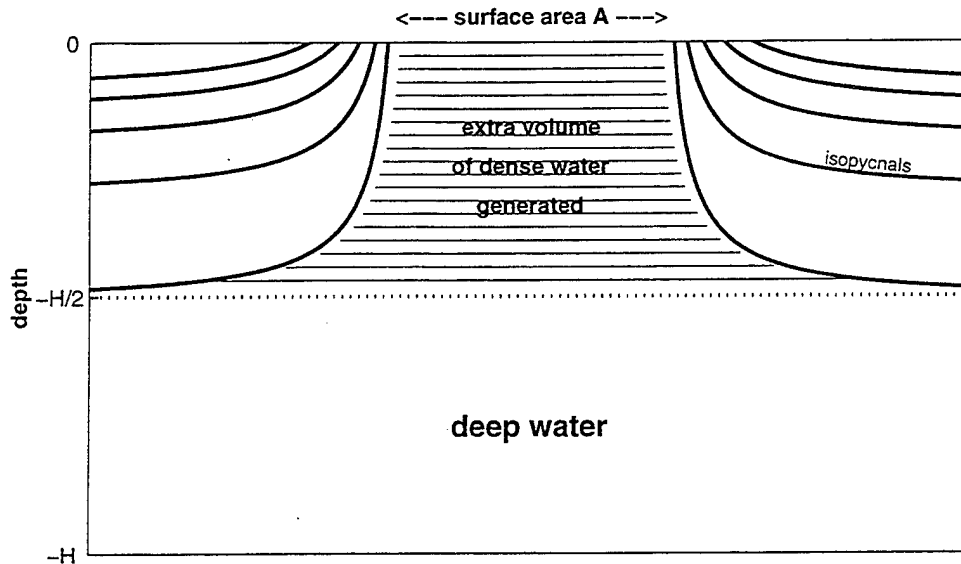

Figure 1: *Cartoon of the large-scale density field after the active deep convection phase.*

In a rotating system, the dense water reaching up to the surface in figure 1 cannot simply sink. Possible mechanisms to extract the available potential energy from such a state are baroclinic instability, frictional spin-down, and draining of the water in a deep boundary current. Another possibility that cannot be neglected, however, is that the dense water is mainly removed and/or mixed away horizontally (e.g. through instability eddies), without appreciable vertical transport. These various mechanisms will be re-visited in subsequent sections.

Large-scale observations

In the winter of 1991/92 an experiment (*THETIS*) was conducted in the northwestern Mediterranean convection regime in the *Gulf of Lions* (THETIS Group, 1994). Apart from small-scale observations with moored ADCP instruments and temperature/salinity sensors, the project included an acoustic tomography array, designed to sample the integral properties of the whole convection region. The evolution of the area-averaged heat content determined in this way gives insight into the large-scale fluxes (Send et al. 1995). During the months of December and January, the upper-layer stratification is gradually eroded by the seasonal cooling (and evaporation), until typically in February a short final burst of buoyancy loss is sufficient to generate convection to large depths (here $1000-2000m$). During these 2 months of so-called *preconditioning*, the large-scale tomography data show that approximately 85-90% of the surface heat loss remains trapped in the convection region, which implies a residence time of about 2 months for the water occupying the upper 500m

in the area. This is believed to be a major factor in determining the sites where convection can happen (Send et al. 1996b), since water needs to be confined in the region with high buoyancy loss long enough for the surface fluxes to act. We have some evidence that wind-forced circulations are responsible for this trapping, instead of it being a self-preserving mechanism where the stratification from previous years induces the trapping necessary for the next convection season. As a result of the small exchange with the surroundings during the months leading up to the deep convection, mixed-layer models driven by the surface buoyancy fluxes are quite successful at reproducing the time-evolution of the convective mixing (depth, water mass properties) (Mertens 1994, Send et al. 1995).

Such 1-dimensional model simulations can then be used for a further test of the mechanisms which determine the localization of convection areas. For the above *THETIS* experiment each hydrographic station from November/December was used to initialize a local 1-D mixed-layer run, thus yielding a spatial distribution of mixing depth at the time of the main convection event (February). The area with predicted convection depths exceeding $1000m$ agreed approximately in size and location (but not in its detailed shape) with the observations. Simulations with spatially uniform and spatially varying surface forcing gave very similar results, which shows that the convection site is less set by the surface flux distribution than by the pre-existing stratification (if the water remains trapped there sufficiently long). As a result, the initial stratification and the total buoyancy loss during the season are sufficient to make approximate predictions about the convection depth and also about the horizontal extent in such regions with sufficient residence time. This can roughly yield the new volume available for the deep water each year, according to figure 1. Further refinements are possible by accounting for the limited horizontal exchange through instability eddy activity (the 'lost' 10-15% buoyancy deficit quoted above), using e.g. the parameterization suggested by Visbeck et al. (1995) (see also Visbeck/Marshall, this volume).

When a tomography array is moored in a convection regime, it allows to monitor directly the extent of the upper-layer mixed region sketched in figure 1. For the *THETIS* experiment this yielded a volume which translates into approximately 0.3Sv annual volume addition for the deep water pool (assuming the dense water eventually manages to settle into deep-water layers) (Send et al. 1995). After the deep convection phase, our observations reveal two stages of large-scale removal of the dense water from the region. Initially, most of the area is very quickly capped over with a very shallow, $O(50m)$ deep, stratified layer within a few days. The restratification of the remainder of the upper/intermediate water levels appears to take place on a 40-day time scale. Which processes are responsible for this, cannot be deduced with the available type of observations. However, it is clear that instability eddies must play a significant role, at least for the horizontal export of dense water and possibly also for lowering its center of mass by extracting potential energy. Quantitative estimates for this in comparison with the observations are still under way.

Acoustic tomography can also be used to estimate area-averaged relative vorticity by closing a circulation-integral path around the convection region. This is a rather noisy measurements for the size of the signal and for our instruments. In *THETIS* averaging over a period of several days before the deep convection and again afterwards revealed, however, that any average vorticity generated in the process was much smaller than would be expected from significant vertical transports. This is another confirmation of the mixing concept of convection.

New observational evidence of one process removing the dense water formed during convection was

recently obtained with a single deep mooring some $100km$ downstream from the Mediterranean convection region (Send et al. 1996a). This mooring had been deployed in the deep boundary current, with current meters and temperature sensors, in order to test if a direct draining of the dense convection water from the *Gulf of Lions* into a deep boundary current occurred. Approximately 1 month after the convection phase, a cold anomaly was observed at that mooring. The timing, amplitude and vertical structure of this signal is consistent with it originating from convectively generated water which is advected past the mooring. The time scale of the event was about 40 days. The exact agreement with the restratification time-scale deduced from tomography above is certainly fortuitous, but it is worth noting that the order magnitude is the same. The typical scales of the deep boundary current imply then that up to one half of the convectively generated extra volume of dense water (as in fig. 1) could have been removed by a direct bleeding into the boundary current.

Implications

The Mediterranean has served as a convenient test basin for observing many of the thermohaline processes which are important on a global scale. Both from the observations there and from the theoretical studies summarized above, we have gained insight into a number of the large-scale properties and processes in convection regions. Most of the questions of interest are related to the topics of how much water is *transformed* (i.e. has its water mass properties changed) and how much new volume of deep water is *generated*, and how this water feeds into the thermohaline circulation (or even affects it). We can now move to the subpolar North Atlantic and apply some of the results to the convection there which generates one of the main water masses of the North Atlantic Deep Water (NADW), the Labrador Sea Water (LSW).

In numerical model simulations of the CME type (Böning et al. 1995), a rather surprising result was recently noted. While the model generates a reasonable equivalent of the convection in the Labrador Sea and of the spreading of this water in the deep boundary current throughout the Atlantic, only very small vertical transports were found in the Labrador Sea in the annual average. It is clear that several Sverdrups of water with LSW properties are exported from the subpolar gyre, so this water has to be fed into the system somewhere. Since the inflow in the thermohaline system is in the surface layers, somewhere there has to be a downward transport in the subpolar gyre. Model analyses have shown that the sinking in this type of model usually takes place in the northern sponge (or buffer) zones and just south of overflow areas. Regardless of whether this is a model artefact or not, a relevant question is *"Is it a physically reasonably possibility to have convective mixing in one place and downward transports in another ?"*.

We have seen in the previous sections that during the active convection phase, downward transports are negligible. In the subsequent stages, i.e. after the creation of a state that was sketched in fig. 1, the first-order process appears to be a *horizontal* exchange due to eddy activity. Evidence for a sinking or vertical draining is not available at the moment (unless convection happens into a deep boundary current or near a boundary). Therefore, the observed water mass properties in e.g. the LSW flowing out of the subpolar gyre, could very well be set by starting with water that has sunk in regions upstream of the convection sites (e.g. near the overflows) and then acquires some of the LSW properties through horizontal exchange as it circulates around the Labrador Sea. The actual

fraction of convectively modified water (e.g. enriched with oxygen or tracers) in the water exiting the region would be rather small in such a scenario. This is in agreement with the small values for this fraction determined from freon observation further south in the Atlantic.

If the convection does not feed any water volume into the thermohaline system, but only sets some of the deep water mass properties, one would expect a rather small sensitivity of the thermohaline circulation to the convection processes. This is in contrast to current results of coarse-resolution coupled climate models, which exhibit strong dependence on the presence and location of convection activity. Thus, the sensitivity of climatically relevant thermohaline fluctuations to convection activity remains an open question.

References

Böning, C.W., F.O.Bryan, W.R.Holland, R.Döscher, 1995: *Deep water formation and meridional overturning in a high-resolution model of the North Atlantic.* J.Phys. Oceanogr. (submitted).

Coates, M.J., G.N. Ivey and J.R. Taylor, 1994: *Unsteady, turbulent convection into a rotating stratified fluid modelling deep convection.* J. Phys. Oceanogr. , (submitted).

Jones, H., and J.Marshall, 1993: *Convection with rotation in a neutral ocean; A study of open ocean deep convection.* J. Phys. Oceanogr., 23 (6), 1009-1039

Klinger, B., J. Marshall and U. Send, 1995: *Representation and Parameterization of deep convective plumes by mixing.* J. Geophys. Res. (submitted).

Maxworthy, T. and S. Narimousa, 1994: *Unsteady, turbulent convection into a homogeneous, rotating fluid, with Oceanographic Applications.* J. Phys. Ocean., 24, 865–887

Mertens, C., 1994: *Winterliche Deckschichtentwicklung und ihre zwischenjährliche Variabilität im nordwestlichen Mittelmeer.* Diploma Thesis, Institut fr Meereskunde, Kiel.

Schott,F., M.Visbeck, U.Send, 1994: *Open Ocean Deep Convection, Mediterranean and Greenland Seas.* In: P.Malanotte-Rizzoli and A.Robinson (eds.): Ocean processes in Climate Dynamics. Kluwer

Send ,U. and J.Marshall, 1995: *Integral effects of deep convection.* J.Phys.Oceangr. 25 (5), 855–872.

Send, U., F.Schott, F.Gaillard and Y.Desaubies, 1995: *Observation of a deep convection regime with acoustic tomography.* J.Geophys.Res. ,100 (C4), 6927-6941.

Send, U., J. Font und C. Mertens, 1996a: *A convective signature observed in an oceanic deep boundary current.* EOS (in print)

Send, U., M. Visbeck, C. Mertens, and M. Crepon, 1996b: *The Localization of Convective Regions,* in preparation for J. Geophys. Res.

THETIS Group, 1994: *Open-Ocean Deep Convection Explored in the Mediterranean.* EOS, 75 (19), 217, 219-221.

Visbeck, M., J. Marshall and H. Jones, 1995: *On the dynamics of convective "chimneys" in the ocean.* J. Phys. Oceanogr. (submitted)

Observations of Convective 'Plumes' in the Ocean

Martin Visbeck[1]

Center for Meteorology and Physical Oceanography, MIT, Cambridge, MA 02139-4307
e-mail: visbeck@ldeo.columbia.edu

1. Introduction

Oceanic deep convection was firstly studied in the western Mediterranean Sea during the MEDOC experiment in the winter of 1969 [*MEDOC group*, 1970] and three phases of the deep convective process were outlined; which as a concept should be applicable to other sites of open ocean convection:

- **Preconditioning:** Deep convective regions are found to have minimal stratification throughout the year and are areas of maximum winter buoyancy loss. A cyclonic circulation, which is usually wind driven reduces the buoyancy in the interior by bending isopycnal towards the oceans surface in the center. The associated circulation pattern traps the water masses at its center where buoyancy loss to the atmosphere can accumulate over the winter period. Usually it takes most of the winter to remove the upper stratification until during February and March the mixed layer density is very close to that of the deep water.

- **Violent mixing:** Once the stratification is weak strong buoyancy loss during cold air outbreaks will initiate deep convection. It is assumed that an ensemble of small scale 'plumes' mix the water column and thereby efficiently transfer properties to great depth. Severe weather conditions during times of large buoyancy loss will, however, obstruct shipboard operations. Therefore other platforms such as neutrally buoyant floats or moored instruments are much better suited to document dynamical processes during the violent mixing phase. *Voorhis and Webb* [1970] firstly reported strong down welling events of several centimeters per second which they deduced from neutrally buoyant float trajectories. More recently acoustically measured velocity profiles [*Schott and Leaman*, 1991; *Schott et al.*, 1993, 1994, 1996] showed similarly strong down welling events that lasted only a few hours

at a fixed location.

- **Spreading:** Once an ensemble of 'plumes' has processed and mixed the ocean a pool of dense and essentially unstratified water is left behind which has become known as a 'chimney'. Those chimneys will be 50-200 km wide and only 1-3 km deep. From theory we know that such chimneys will have a baroclinically unstable 'rim-current' around their margins [*Herman and Owens*, 1993; *Legg and Marshall*, 1993; *Jones and Marshall*, 1993]. Baroclinic eddies with about the theoretically expected properties have been observed in the periphery of convective regions [*Gascard*, 1978; *Gascard and Clarke*, 1983]. Such eddies will break the chimney apart and spread convected fluid laterally and thereby facilitate a lateral transfer of buoyancy [*Jones and Marshall*, 1993; *Maxworthy and Narimousa*, 1994; *Visbeck et al.*, 1996]. Furthermore, rapid restratification was observed in the upper layer which can not be accounted for by air-sea interaction [*Send et al.*, 1995]. At depth, the spreading of convected water was documented by many studies [e.g. *Sankey*, 1973; *Rhein*, 1995]. *Visbeck et al.* [1996] propose that baroclinic eddies are responsible for both, the fast inward transfer of stratified water at the surface and the slow spreading at depth.

In the following we turn out attention to the violent mixing phase which occurs in late winter usually between January and April. We will inspect observations of the vertical velocity structures during periods of deep convection that were obtained by acoustic Doppler current profilers (ADCPs) which measure profiles of vertical and horizontal velocities at a fixed location with an accuracy of about 1 cm s^{-1}. Those time series of vertical velocities together with some knowledge about the larger scale mean flow can be used to estimate the width of convection cells [*Schott and Leaman*, 1991; *Schott et al.*, 1993, 1994, 1996]. Motivated by these observations of strong down welling of more than 10 cm s^{-1} and an estimated plume diameter of less than 1 km, laboratory [*Maxworthy and Narimousa*, 1991, 1994] and numerical ex-

---

[1]now at Lamont-Doherty Earth Observatory of Columbia University, Palisades, NY 10964-8000

periments [*Jones and Marshall*, 1993; *Paluszkiewicz et al.*, 1994] were employed to gain dynamical understanding of the deep convective process in the ocean. *Fernando et al.* [1991]; *Maxworthy and Narimousa* [1994] and *Jones and Marshall* [1993] presented scaling laws for the turbulence structures at high Rayleigh numbers in a rotating unstratified fluid subject to buoyancy loss at the surface. The velocity and length scales are found to be unaware of molecular viscosity and depend only on external parameters such as the surface buoyancy loss B_0, the depth of convection H, and the rate of rotation f. A nondimensional number Ro^* was constructed, which has become known as the 'natural' or 'convective' Rossby number [see *Marshall et al.*, 1994, for a review]:

$$Ro^* = \frac{U}{fL} = \frac{B_0^{1/2}}{f^{3/2}H} = \frac{l_{rot}}{H} \qquad . \qquad (1)$$

The length scale l_{rot} can be interpreted as a critical depth

$$z_c \sim l_{rot} = \frac{B_0^{1/2}}{f^{3/2}} \qquad (2)$$

at which the plumes are significantly affected by rotational forces. For small values of R_0^* when the mixing depth (H) is deeper than the critical depth (z_c), plumes become aware of and their width is controlled by rotation. However, if the mixing is shallower than z_c isentropic three dimensional turbulence prevails with plume diameter of the order of the depth scale. For isentropic turbulent convection a velocity scale is given by [e.g. *Turner*, 1973]:

$$U_{3d} \sim (B_0 H)^{1/3} \qquad ; \qquad (3)$$

if, however, rotation is important then this scaling law modifies to:

$$U_{rot} \sim \left(\frac{B_0}{f}\right)^{1/2} \qquad . \qquad (4)$$

Which of the two regimes is appropriate for deep convection in the ocean? Typical values for the convective Rossby number R_0^* (1) as a function of penetration depth and heat loss (for a thermal expansion coefficient $\alpha = 1 \times 10^{-4\circ}C^{-1}$ and $f = 1 \times 10^{-4}s^{-1}$) are given in figure 1 and show that for deep convection in the ocean ($Q = 1000$ W m^{-2}, $H = 2000$ m) rotation might matter.

Figure 1. Convective Rossby number R_0^* as a function of surface heat loss Q and mixing depth H.
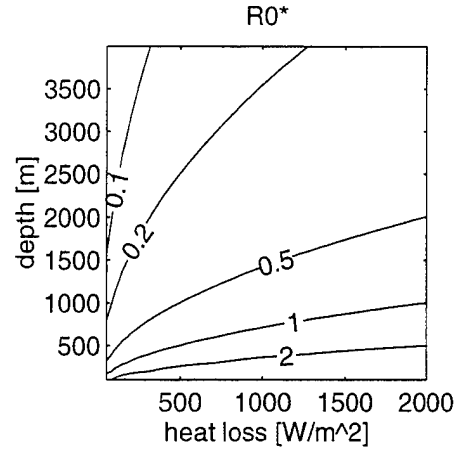
2. Observations of vertical velocities during deep convection

Western Mediterranean Sea

The first ADCP observations of deep convection were obtained during the winter of 1987. A cooling episode between February 15-23 gave rise to strong vertical velocities and convection reached down to the bottom at 2500m depth [*Schott and Leaman*, 1991; *Leaman and Schott*, 1991].

During a later experiment in winter 1992 a small scale mooring triangle with a side length of about 2 km (roughly corresponding to the water depth) was deployed and each mooring was equipped with at least one ADCP [*Schott et al.*, 1996]. The mooring triangle was embedded in a gyre scale tomographic array that monitored the heat content of the convective region and documented aspects of the large scale circulation [*THETIS group*, 1994; *Send et al.*, 1995]. All phases of the convective process were observed, however, convection penetrated only down to 1500 m depth during a moderately strong cooling period between February 18-24 [*Schott et al.*, 1996]. The central mooring was equipped with two ADCPs, one looking upward and the other downward from a depth of 300 m. Together they have documented the vertical velocity structure of convection events from 100 to 600 m depth (Fig. 2). Several of those events were captured by all ADCPs of the mooring triangle, however, uncorrelated in time among the instruments. We can immediately conclude that the plume width was smaller than 2 km, the distance between the moorings.

Figure 2. Deep convection observed in the north western Mediterranean Sea: a) Bathymetric map of the region with mean surface currents (gray arrows) and the region of deep mixing (gray shaded) included. b) Contour section of vertical velocity versus depth and time in hours during a convection event (19. Feb. 1992). c) Time series of vertical velocity at 350 m depth. d) Time series of temperature above (depth 300 m) and below (depth 1000 m) the ADCP velocity record (c).
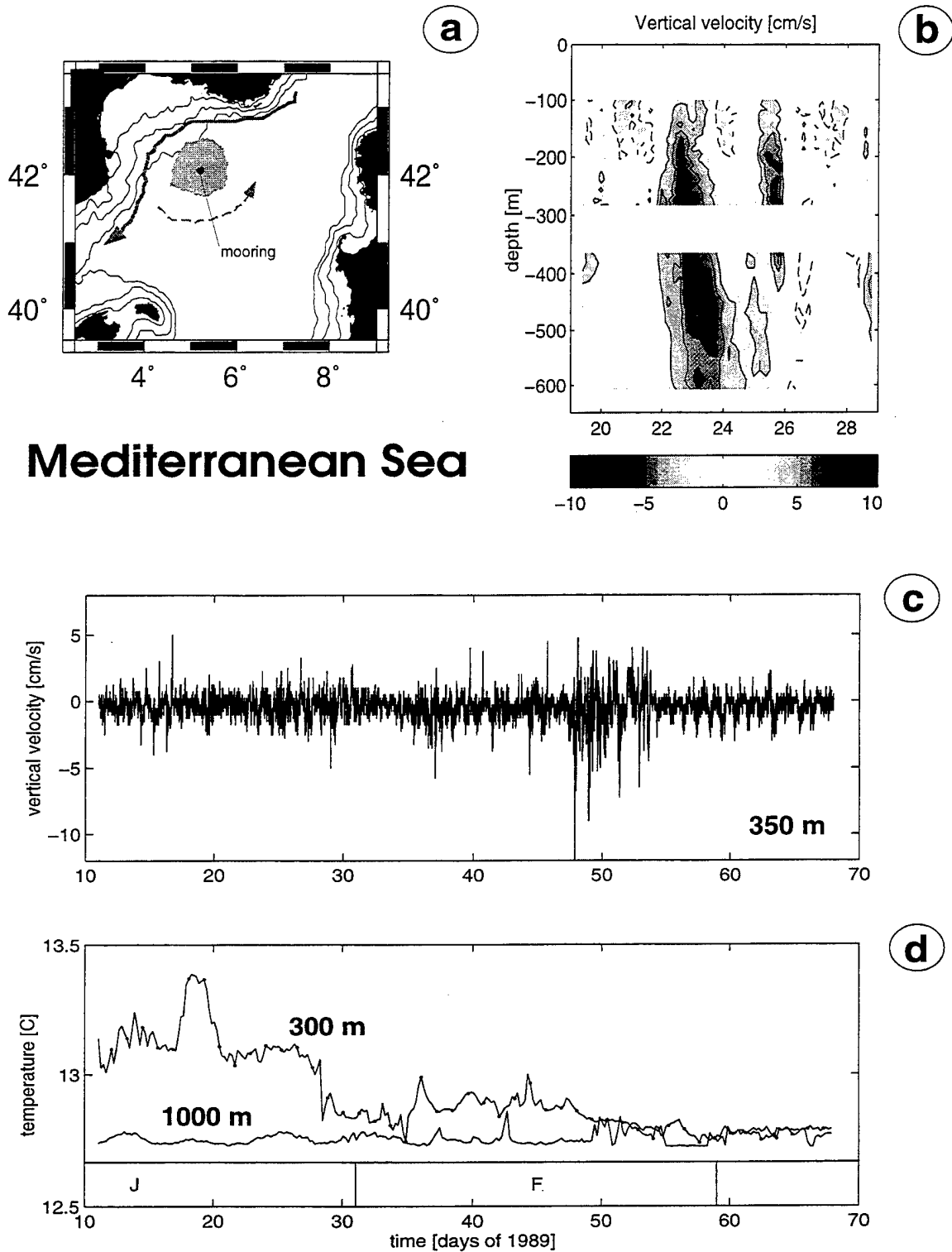
Figure 3. Deep convection observed in the central Greenland Sea: a) Bathymetric map of the region with mean surface currents (gray arrows) and the region of deep mixing (gray shaded) included. b) Contour section of vertical velocity versus depth and time in hours during a convection event (16. March 1989) d) Time series of temperature above (depth 200 m) and below (depth 1400 m) the ADCP velocity record (c).
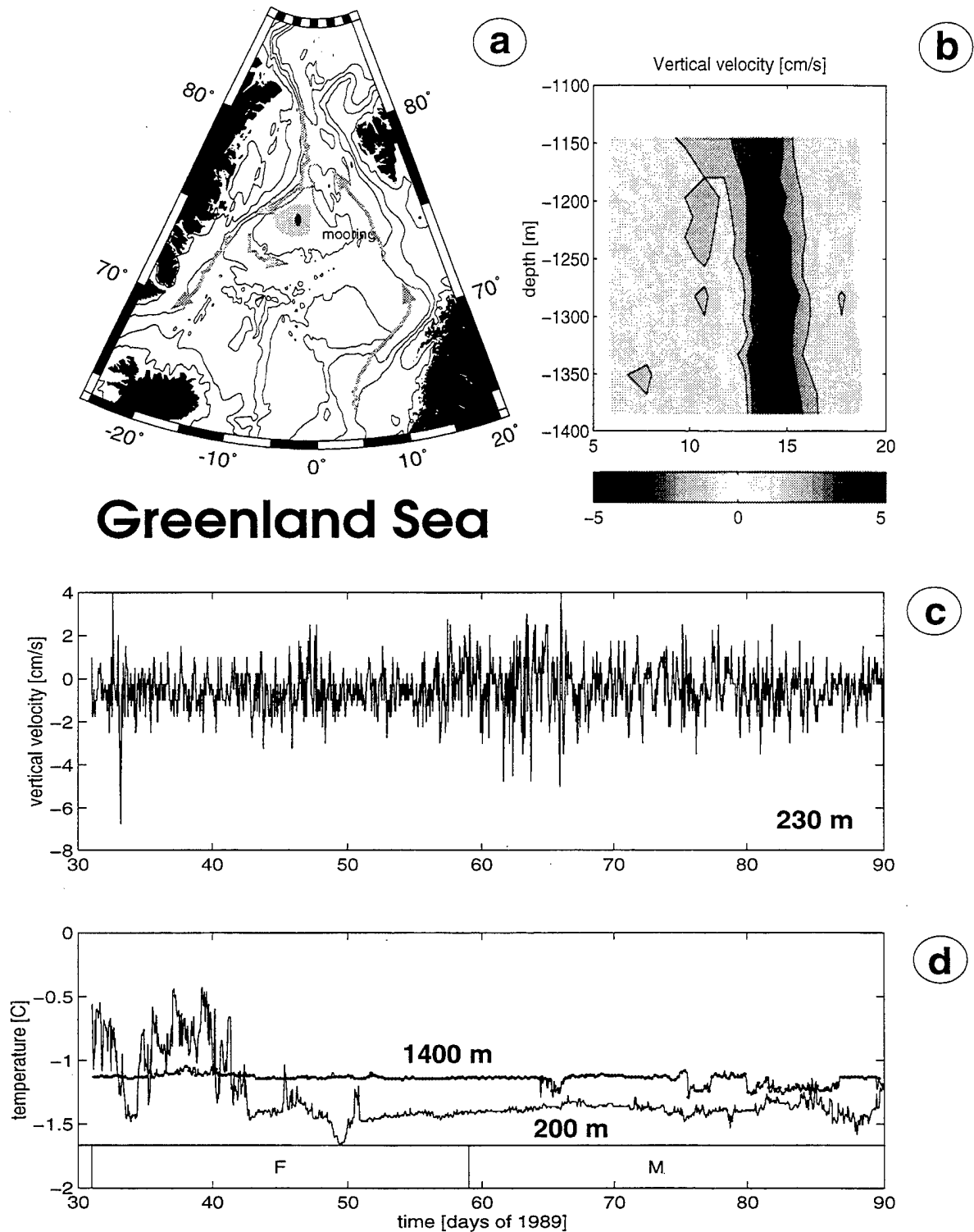
Central Greenland Sea

An international convection experiment was carried out in the Greenland Sea during the winter 1988/89 in the framework of the Greenland Sea Project [*GSP group*, 1990]. Four moorings were equipped with AD-CPs at several location within the central Greenland Sea [*Schott et al.*, 1993], and some of which were part of a tomographic array deployed jointly by Scripps and Woods Hole oceanographic institutions [*Greenland Sea Tomography Group*, 1993; *Pawlowicz et al.*, 1995]. In the Greenland Sea the situation is complicated due to the presence of sea ice which has a significant effect on air-sea interactions [*Visbeck et al.*, 1995]. During ice formation salt enriched brine is released from the ice which significantly increases the mixed-layer density. On the other hand ice melt will decrease the mixed-layer density and depth dramatically. Moreover, a closed ice cover will reduce the air-sea fluxes due to the insulating effect of sea ice. Therefore sea ice processes are crucial during the pre-conditioning phase. However, in March 1989 convection reaching down to 1500m depth occured in an ice free bay and a plume was observed between 1100 and 1400 m depth on March 16 (Fig. 3).

Central Labrador Sea

Preliminary data from a mooring deployment in the central Labrador Sea close the former weather ship station 'BRAVO' are displayed in figure 4. The mooring is part of a monitoring effort in the central Labrador Sea initiated by Rhines (UW, Seattle) and Lazier (BIO, Halifax). In the same region a major ocean convection experiment will take place in the winters of 1997 and 1998 [see *D'Asaro*, 1994, for an outline].

In conclusion the small scale plumes show a striking similarity among the three sites with strong downward motion occuring only a few times during the winter and each of a duration of only a few hours. In the following we will compare the maximum plume velocity and plume diameter from all sites to theoretical scaling arguments.

3. Plume observations and scaling laws

3.1. Vertical velocity scale

The maximum downward velocities is easily diagnosed from the ADCP records and was therefore chosen as a velocity reference scale. The errors should be about 1 cm s^{-1} plus some uncertainty weather ac-

tually the center of a plume was 'seen' by the instrument.

3.2. Estimating plume diameter from Eulerian time series

One way to estimate plume diameter from Eulerian time series of vertical velocities is to assume that convection cells are advected by the mooring as a 'frozen' structure [*Schott and Leaman*, 1991, Fig. 5]. Then the time it takes for a plume to drift by the observer divided by the mean advection speed gives the plume diameter, which is defined here as the maximum distance between zero contours of the vertical velocity.

3.3. Plume scales and their relation to external forcing

Inspecting many 'plumes' like the ones shown in figures 2-4 gave plume diameter which are summarized in table 1.

In order to test the observations against theoretical scaling laws we need to know the buoyancy loss at the surface. For some experiments air-sea fluxes were measured from research vessels, for others we used fluxes from meteorological weather forecast models. Typical atmospheric and oceanic parameter and the estimated fluxes using bulk formulae for a period of a few days duration are summarized in table 2.

It was a surprise to us that the total heat loss is quite similar in all three convection sites, however, the distribution among the individual heat flux components is different with dominant sensible heat loss in the arctic regions. Moreover, the surface buoyancy flux, taken here as the sum of heat (Q) and fresh water flux ($E - P$):

$$B_0 = \frac{g}{\rho}\left(\frac{\alpha}{c_p}Q + \beta S(E-P)\right) \quad , \quad (5)$$

with the appropriate oceanic heat capacity (c_p), and thermal (α) and haline (β) expansion coefficients, showed large differences between the regions and only minor contribution from the freshwater fluxes. The differences are mainly due to variations of the thermal expansion coefficient, $\alpha = -(\partial\rho)/(\rho_0 \ \partial T)$, which strongly depends on temperature and is a factor of 8 smaller in the cold waters of the central Greenland Sea compared to the Mediterranean Sea.

Given the buoyancy flux at the surface (B_0) the depth of convection (H) and the vertical component of the earth's rotation (f) we can now estimate the expected vertical velocities and turbulent length

Figure 4. Deep convection observed in the central Labrador Sea: a) Bathymetric map of the region with mean surface currents (gray arrows) and the region of deep mixing (gray shaded) included. b) Contour section of vertical velocity versus depth and time in hours during a convection event (7. March 1995). c) Time series of vertical velocity at 450 m depth. d) Time series of temperature above (depth 260 m) and below (depth 510 m) the ADCP velocity record (c).
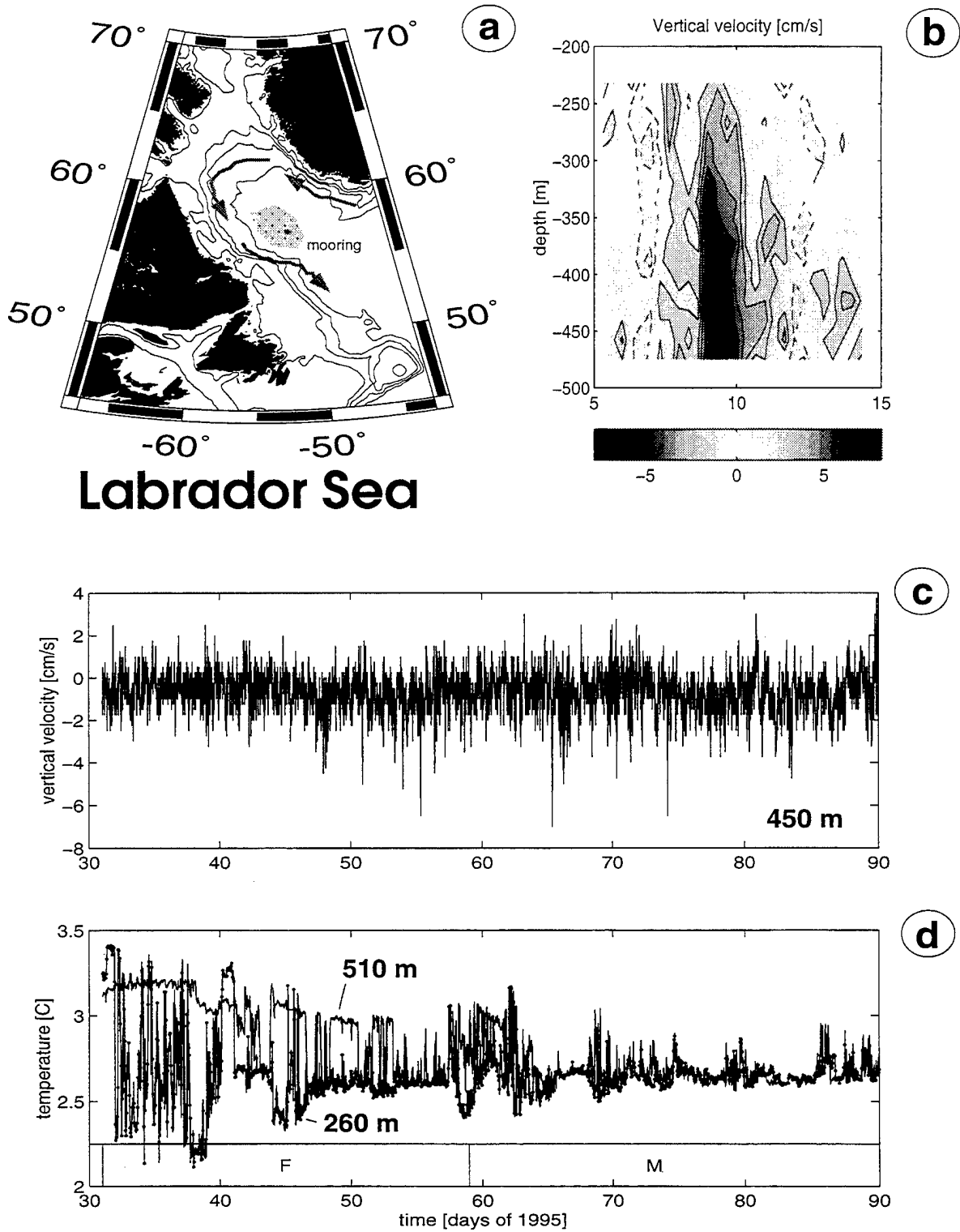
Figure 5. Sketch of a convection cell with downward motion shaded and parcel displacements indicated by dots.

Table 1. Observed length and velocity scales of convection cells.

parameter	units	Mediterranean	Labrador Sea	Greenland Sea
date		18-22 Feb	20 Feb - 30 Mar	15 Feb - 15 Mar
depth of convection	m	1100-1500	~ 2200	800-1500
max. downward velocity	cm s^{-1}	12	8	6
plume diameter	m	800-1000	1000-1500	600-1000

Table 2. Meteorological conditions during a convection period of a few days duration in late winter.

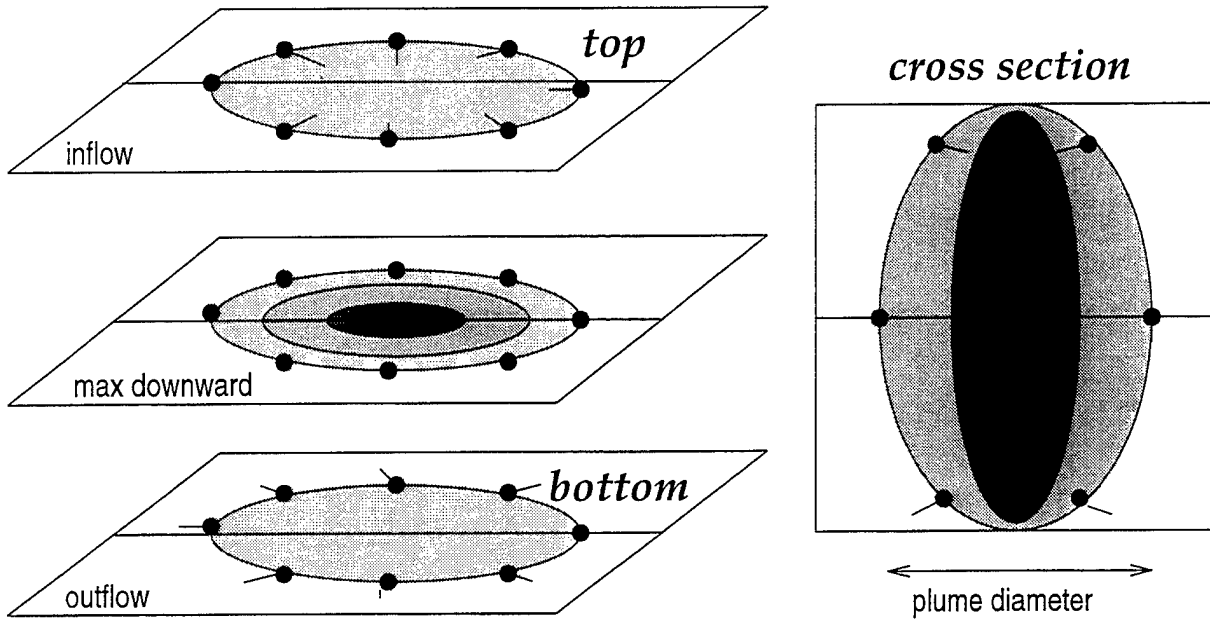| parameter	units	Mediterranean	Labrador Sea	Greenland Sea
SST	°C	12.9	2.9	-1.4
salinity		38.5	34.4	34.9
air temperature dry	°C	8	-9	-14
air temperature wet	°C	5	-7	-13
wind speed (u_{10})	m s^{-1}	15	13	13
cloud cover	%	40	60	60
precipitation	mm day^{-1}	?	?	?
surface heat flux				
sensible heat flux	W m^{-2}	-150	-370	-400
latent heat flux	W m^{-2}	-400	-140	-140
short wave radiation	W m^{-2}	120	80	40
long wave radiation	W m^{-2}	-80	-60	-30
total heat flux	W m^{-2}	-500	-490	-530
evaporation	mm day^{-1}	13	6	4
thermal expansion	°C^{-1}	1.9×10^{-4}	1.0×10^{-4}	0.3×10^{-4}
surface buoyancy flux				
thermal buoy. flux	m^{2}s^{-3}	2.5×10^{-6}	1.0×10^{-6}	0.5×10^{-6}
haline buoy. flux	m^{2}s^{-3}	0.5×10^{-6}	0.2×10^{-6}	0.1×10^{-6}
total buoyancy flux	m^{2}s^{-3}	3.0×10^{-6}	1.2×10^{-6}	0.6×10^{-6}

Table 3. Comparing observed length and velocity scales from ADCP observations to turbulence theory.

parameter	units	Mediterranean	Labrador Sea	Greenland Sea
depth of convection	m	1100-1500	1800-2200	800-1500
buoyancy flux	m^{2}s^{-3}	3.0×10^{-6}	1.2×10^{-6}	0.6×10^{-6}
Coriolis parameter	s^{-1}	0.98×10^{-4}	1.2×10^{-4}	1.4×10^{-4}
$R_o^* = B_0^{1/2}/(f^{3/2}H)$		0.4	0.1	0.1
isentropic turbulence regime				
$w = (B_0 H)^{1/3}$	cm s^{-1}	7.7	6.4	4.5
$l = H$	m	1300	2000	1200
rotational regime				
$w_{rot} = (B_0/f)^{1/2}$	cm s^{-1}	5.5	3.2	2.1
$l_{rot} = (B_0/f^3)^{1/2}$	m	560	260	150
observations				
w_{max}	cm s^{-1}	10	8	6
plume diameter	m	800-1000	1000-1500	600-1000

scales for each region and compare them to the observations (Tab. 3). We find the correct order of magnitude for both the rotational and non rotational scaling arguments and a convective Rossby number slightly smaller than unity. However, the non rotational scaling laws seem to match the estimated plume diameter somewhat better. We conclude that the observations are consistent with plumes of aspect ratio one and maximum vertical velocities given by $w = 1.5 \, (B_0 H)^{1/3}$.

4. Discussion

It was shown that vertical velocity time series are a convenient quantity in order to measure scales of deep convective 'plumes' in the ocean. The observed maximum vertical velocities and diagnosed diameter are consistent with scaling arguments for both the rotational and non rotational turbulence. This implies that deep convective plumes in the three open ocean convection regions might be affected by the earth's rotation. The uncertainties in the estimates do not allow a stronger conclusion. As shown by *Visbeck* [1993] there is no unambiguous information in the velocity time series that allows to confirm weather plumes themselves rotate or not. The observations are consistent with the assumption that plumes are efficient mixing agents without a significant mean vertical transport [*Schott et al.*, 1994; *Send and Marshall*, 1995]. Their mixing time scale can be estimated by:

$$t_{mix} = \frac{H}{W_{plume}} \sim \frac{H^{2/3}}{B_0^{1/3}} \qquad (6)$$

and typically is on the order of a few hours. A vertical 'plume' mixing coefficient would then be:

$$k_{mix} = W_{plume} H \sim B_0^{1/3} H^{4/3} \qquad (7)$$

and typically be of the order of 100 m^2 s^{-1}. It seems that representing convective plumes by a fast mixing process is reasonable. However, care has to be taken when the equation of state is strongly nonlinear, as it is the case for water temperatures near the freezing point. Then thermobaric effects might enhance the penetration of individual plumes [*McDougall*, 1987; *Garwood et al.*, 1994]. More observations are needed to settle the issue about the importance of rotation and maybe Lagrangian float trajectories provide new insights. Further, the interaction of plume dynamics with the mesoscale eddy field deserves more attention since both process occur together in all of the investigated sites of deep water formation.

References

D'Asaro, E., Measuring deep convection. A workshop report, Applied Physics Lab. UW, Seattle, 1994.

Fernando, H., R. Chen, and D. Boyer, Effects of rotation on convective turbulence., *J. Fluid. Mech.*, *228*, 513–547, 1991.

Fischer, J., and M. Visbeck, Seasonal variations of the daily zooplankton migration in the Greenland Sea., *Deep-Sea Res.*, *40*, 1547–1557, 1993.

Garwood, R. J., S. Isakari, and P. Gallacher, Thermobaric convection., in *Deep Convection and Deep Water Formation in the Oceans*, edited by O. Johannessen, R. Muench, and J. Overland. AGU Monograph, 1994.

Gascard, J., Mediterranean deep water formation, baroclinic instabilities and oceanic eddies., *Oceanol. Acta*, *1*, 315–330., 1978.

Gascard, J., and A. R. Clarke, The formation of Labrador Sea Water, Part II — Mesoscale and smallerscale processes., *J. Phys. Oceanogr.*, *13*, 1779–1797., 1983.

Greenland Sea Tomography Group, Ocean acoustic tomography in the Greenland Sea., *Geophys. Res. Let.*, *20*, 2211–2214, 1993.

GSP group, The Greenland Sea Project - a venture towards understanding of the oceans role in climate., *EOS*, *71*, 750–755., 1990.

Herman, A., and B. Owens, Energetics of gravitational adjustment for mesoscale chimneys., *J. Phys. Oceanogr.*, *23*, 346–371, 1993.

Jones, H., and J. Marshall, Convection with rotation in a neutral ocean: A study of open-ocean deep convection., *J. Phys. Oceanogr.*, *23*, 1009–1039, 1993.

Leaman, K., and F. Schott, Hydrographic structure of the convection regime in the Gulf of Lions: Winter 1987., *J. Phys. Oceanogr.*, *21*, 573–596., 1991.

Legg, S., and J. Marshall, A heton model of the spreading phase of open-ocean deep convection., *J. Phys. Oceanogr.*, *23*, 1040–1056, 1993.

Marshall, J., J. Whitehead, and T. Yates, Laboratory and numerical experiments in ocean convection., in *Ocean Processes in Climate Dynamics: Global and*

Mediterranean Examples, edited by P. Malanotte-Rizzoli, and A. Robinson, pp. 173–201. Kluwer, 1994.

Maxworthy, T., and S. Narimousa, Vortex generation by convection in a rotating fluid., *Ocean Modeling, (unpubl. manuscr.)*, *92*, 1991.

Maxworthy, T., and S. Narimousa, Unsteady, turbulent convection into a homogeneous, rotating fluid, with oceanographic applications., *J. Phys. Oceanogr.*, *24*, 865–887, 1994.

McDougall, T., Thermobaricity, cabbeling, and watermass conversion., *J. Goephys. Res.*, *92*, 5448–5464., 1987.

MEDOC group, Observation of formation of deep water in the Mediterranean Sea., *Nature*, *227*, 1037–1040., 1970.

Paluszkiewicz, T., R. Garwood, and D. Denbo, Deep convective plumes in the ocean., *Oceanography*, *7*, 37–44, 1994.

Pawlowicz, R., J. Lynch, W. Owens, P. Worcester, W. Morawitz, and P. Sutton, Thermal evolution of the Greenland Sea gyre in 1988-89., *J. Geophys. Res.*, *100*, 4727–4750, 1995.

Rhein, M., Deep water formation in the western mediterranean., *J. Geophys. Res.*, *100*, 6943–6960, 1995.

Sankey, T., The formation of deep water in the northwestern Mediterranean., *Progress in Oceanography, vol. 6*, 159–179., 1973.

Schott, F., and K. Leaman, Observations with Moored Acoustic Doppler Current Profilers in the Convection Regime in the Golfe du Lion., *J. Phys. Oceanogr.*, *21*, 558–574., 1991.

Schott, F., M. Visbeck, and J. Fischer, Observations of vertical currents and convection in the central Greenland Sea during the winter of 1988/89., *J. Geophys. Res.*, *98*, 14,401–14,421, 1993.

Schott, F., M. Visbeck, and U. Send, Open ocean deep convection, Mediterranean and Greenland seas., in *Ocean Processes in Climate Dynamics: Global and Mediterranean Examples*, edited by P. Malanotte-Rizzoli, and A. Robinson, pp. 203–225. Kluwer, 1994.

Schott, F., M. Visbeck, U. Send, J. Fischer, L. Stramma, and Y. Desaubies, Observations of deep convection in the Gulf of Lions, northern Mediterranrean, during the winter of 1992/93., *J. Geophys. Res.*, p. in press, 1996.

Send, U., and J. Marshall, Integral effects of deep convection., *J. Phys. Oceanogr.*, *25*, 855–872, 1995.

Send, U., F. Schott, F. Galliard, and Y. Desaubies, Observations of a deep convective regime with acoustic tomography., *J. Geophys. Res.*, *100*, 6927–6942, 1995.

THETIS group, Open-ocean deep convection explored in the Mediterranean., *EOS*, *75*, 217–221, 1994.

Turner, J., *Buoyancy Effects in Fluids.* Cambridge University Press, 1973.

Vaughan, S., and K. Leaman, The role of small-scale cells in the mediterranean convection process., *J. Phys. Oceanogr.*, *25*, 2423–2436, 1995.

Visbeck, M., Konvektion im offenen Ozean. Interpretation von Beobachtungen aus der Grönlandsee und dem westlichen Mittelmeer. Dissertation, Tech. Rep. 237, Inst. f. Meereskunde, Kiel, 1993.

Visbeck, M., J. Fischer, and F. Schott, Preconditioning the Greanland Sea for deep convection: Ice formation and ice drift., *J. Geophys. Res.*, *100*, 18,484–18,502, 1995.

Visbeck, M., J. Marshall, and H. Jones, On the dynamics of isolated convective regions in the ocean., *J. Phys. Oceanogr.*, p. to appear, 1996.

Voorhis, A., and D. C. Webb, Large vertical currents observed in a western sinking region of the northwestern Mediterranean., *Cah. Océanogr.*, *22*, 571–580., 1970.

Turbulent rotating Rayleigh-Bénard convection (with comments on $\frac{2}{7}$)

Joseph Werne, NCAR, Boulder, CO 80307-3000

Collaborators: Keith Julien, NCAR; Sonya Legg & Jim McWilliams, UCLA

1 Introduction

Consider a uniformly rotating Boussinesq fluid confined between horizontal plates. If the lower plate is hotter than that above, the fluid in between will experience a buoyant force that may drive it to convective motion. For a sufficiently large temperature drop between the plates, intense plumes (which themselves generate shear and its associated turbulence) spontaneously develop. The ensuing dynamics of these plumes, their mutual interaction, and global transport properties are all affected directly, or indirectly, by the rate of rotation of the fluid layer. My discussion will concentrate on these effects, and will report numerical solutions which illuminate similarities to and differences from non-rotating convection.

2 Non-rotating turbulent convection

2.1 Experimental findings

Non-rotating Rayleigh-Bénard convection is a classic problem experiencing a resurgence recently due to experimental observation of some remarkable and unexpected collective behavior of its plumes. A fundamental question involves the heat transport through the layer for a specified temperature drop. Heslot, Castaing & Libchaber (1987) reported the stabilization (*i.e.*, consistent circulation in a particular direction) and reduced heat transport of a single convection cell once thermal plumes appear, while Krishnamurti (1995) discusses the generation of mean shearing motions by plumes which cluster together and march in "soldier-row" formation across a large (40 × 40 × 1) experimental cell. Krishnamurti's large-scale turbulent patterns exhibit an even more drastic reduction in the heat transport than that seen by Heslot *et al.*

With these new observations comes the theoretical challenge of explaining the reduction in the heat transport due to the presence of plumes (Castaing *et al.* 1989; She 1989; Shraiman & Siggia 1990; Yakhot 1992). I will review two of four existing theories which attempt to explain the fundamental physical behavior of laboratory plumey convection, which in recent years has acquired the name "hard turbulence:" Castaing *et al.* 1989 and Shraiman & Siggia 1990. In particular, these theories strive to derive the observed heat-transport law, $Nu \propto Ra^{2/7}$. Here $Nu = H/(\kappa\Delta/L)$ is the Nusselt number or normalized heat flux H, and $Ra = g\alpha\Delta L^3/(\nu\kappa)$ is the Rayleigh number or normalized temperature drop Δ. g and α are the local acceleration due to gravity and the fluid's thermal expansion coefficient. L is the layer depth.[1]

---

[1] While Libchaber's group repeatedly observes the 2/7-law for turbulent convection in both small ($A = 1$) and large ($A = 6.7$) containers — A is the width-to-height or aspect ratio — Krishnamurti's recent results favor a 1/4-law. Aside from geometry (K's apparatus is rectilinear while L's is cylindrical), the major difference between the experiments is the fluid: liquid water ($\sigma \approx 7$) for K and Helium gas ($\sigma \approx 0.7$) for L, where the Prandtl number $\sigma = \nu/\kappa$ is the ratio of fluid viscosity ν to thermal diffusivity κ. The much shorter diffusion time, and hence the effectively longer experimental run-time for water (and/or the value of σ) may play a role in establishing K's clustered rows of plumes. As yet no turbulent heat-transport theory attempts to explain K's observed 1/4-law.

2.2 Heat-transport theories

The first of these theories extends earlier notions of Priestley (1959) (also Malkus 1963; Howard 1966) which characterize turbulent convection as efficient and advective in the bulk, but solely diffusive near the boundaries where the velocity is zero. The thin "boundary layers" each span half of the temperature drop Δ, giving $H = \kappa\Delta/(2\lambda) \rightarrow Nu = L/(2\lambda)$ where λ is the boundary-layer thickness. Priestley's remaining assumption is a depth L (or equivalently Ra) sufficiently large that $\lambda \neq \lambda(L)$, resulting in $Nu \propto Ra^{1/3}$ which has actually been observed for Ra below that at which the 2/7-law emerges (Wu $et\ al.$ 1988). Nevertheless, the large range over which the 2/7-law has been observed opens an ever-widening gap from the 1/3-law, the ratio of the two laws exceeding 2.4 at $Ra = 10^{15}$. The contribution by Castaing $et\ al.$ was to conjecture a "mixing zone" where plumes grow out of the boundary layers, then mix through turbulent agitation before merging with the bulk fluid. They propose 1) that plume dynamics is dominated by viscous drag $\nu u_c/\lambda^2 \approx g\alpha\Delta$, and 2) that turbulent convective motions are as Prandtl (1932) suggests, advective $H = u_c\Delta_c$ with kinetic energy of the dominant eddies gained at the expense of buoyancy work as they traverse the layer $u_c^2/2 \approx g\alpha\Delta_c L$. Here u_c and Δ_c are the characteristic velocity and temperature contrast of the dominant turbulent eddies; $\Delta/2$, u_c, and λ are estimates of a plume's temperature, final velocity, and thickness. By solving this system of four equations for the four unknowns (H, λ, u_c, and Δ_c), $Nu \propto Ra^{2/7}$, as well as other scaling laws, is obtained.

Shraiman & Siggia also derive the 2/7-law, but now using only the one feature of hard turbulence absent from the picture proposed by Castaing $et\ al.$: the stable large-scale circulation. In fact, Shraiman & Siggia propose the 2/7-law emerges precisely when the dominant circulation is sufficiently fast to produce shear-flow turbulence near the boundaries. They estimate the dissipation in the layer as $\epsilon \approx u_*^3/L$, where $u_* = \sqrt{\nu(\partial U/\partial z)_{wall}}$ is the "friction velocity," U being the mean velocity parallel to the boundary (wall) and z the normal direction. By suggesting a thermal boundary layer λ thinner than the viscous sub-layer adjacent to the wall, where the mean velocity profile is linear $U = z\,(\partial U/\partial z)_{wall}$, the heat equation can be simplified and the result $Nu \propto (\partial U/\partial z)_{wall}^{1/3}$ obtained. Employing the exact relation $\epsilon L^4/\kappa^3 = \sigma\,Nu\,(Ra - 1)$, the scaling laws $Nu \propto Ra^{2/7}$ and $(\partial U/\partial z)_{wall} \propto Ra^{6/7}$ result. Though the role of plumes appears secondary within Shraiman & Siggia's boundary-layer analysis, it is actually the collective action of the plumes as they establish the large-scale circulation which makes the turbulent shear possible. In addition, in the bulk fluid the plumes carry practically all of the heat flux.

The stark contrast between these two approaches points to the caution with which one must digest scaling theories for turbulent fluids: derivation of a known result does not guarantee the underlying assumptions sufficient to realize the behavior in nature. Even greater care is required when an $unverified$ scaling law is "derived" through simple scaling arguments — but this is not the case here.

3 Rotating turbulent convection

Rotating the fluid layer alters the dynamics of plumes dramatically. For experiments or simulations with rotation rates Ω comparable to (or greater than) the convective velocity divided by L, individual plumes approximately conserve angular momentum as they move from the boundaries, amplifying cyclonic vorticity while contracting horizontally. In this way, buoyancy and vortex stretching share a mutual feedback, producing a flow-field dominated by strongly cyclonic plumes. Experiments by Rossby (1969) and Zhong, Ecke & Steinberg (1993) indicate that increased rotation enhances the heat transport slightly; they propose Ekman pumping as a possible cause.[2] Another important difference between rotating and non-rotating convection is the decrease in inter-plume spacing resulting from external rotation. Figure 1 shows the development of the flow field (temperature T and vertical vorticity ω) as Ra is increased while fixing the layer's convective Rossby number $Ro = \sqrt{Ra/(\sigma\,Ta)}$; $Ta = (2\Omega L^2/\nu)^2$ is the Taylor number.[3] This figure appears in Julien, Legg, McWilliams & Werne (1995); it depicts numerical solutions of rotating Rayleigh-Bénard convection with no-slip top and bottom and periodic side boundaries. The domain aspect ratio is $2 \times 2 \times 1$.[4] The line marked at the bottom of each column indicates the horizontal scale of convection predicted by linear stability (Chandrasekhar 1961). As Ra and Ta are increased, chaotic roll-convection gives way to isolated vortex/plumes with decreasing horizontal scale. At high Ra, plume-plume (or equivalently, vortex-vortex) interactions become increasingly likely, given higher plume-vorticity and shortened distances between neighbors. Because the plumes are primarily aligned vertically, the vortical interactions which ensue involve the co-rotation of cyclonic vorticity, with plumes circulating about each other in horizontal planes. The result is lateral stirring tending to mix the thermal content of a plume with its surrounding fluid, thus weakening the plume and intensifying the temperature of the background. The result is a mean temperature gradient not present for non-rotating convection. Figure 2 depicts this gradient which persists for increasing Ra at fixed Ro. (Note the thinning boundary layers near $z = \pm 1$.)

Despite these marked differences between rotating and non-rotating convection (vortical interactions, mean thermal gradient, Ekman pumping, *etc.*), the 2/7-law remains for simulations with no-slip vertical boundaries (figure 3). Stress-free boundaries, on the other hand, exhibit Priestley's 1/3-law. Conclusions then are 1) the detailed dynamics of plumes are relatively unimportant to establishing the 2/7-law, and 2) boundary details are crucial. Both of these conclusions are consistent with Shraiman & Siggia (1990), and the second casts doubt on the fundamental nature of

---

[2]Ekman pumping occurs when a vortex tube terminates at a solid boundary. For a tube in geostrophic balance (*i.e.*, with the radial pressure gradient balancing centrifugal acceleration), pumping of fluid away from the boundary occurs at the vortex core due to the fact that the fluid velocity (and hence the centrifugal acceleration) vanishes at the wall, creating a pressure imbalance.

[3]Ro is the ratio of the rotation timescale $(2\Omega)^{-1}$ to the convective timescale $\sqrt{L/(g\alpha\Delta)}$. For a given value of Ro, the influence of rotation on convection should be roughly constant.

[4]Simulations are conducted using a pseudo-spectral, Fourier-Chebyshev "tau"-method. The influence-matrix with tau-corrections is employed (Kleiser & Schumann 1980; Werne 1995). All simulations resolve the Kolmogorov length-scale for the turbulence.
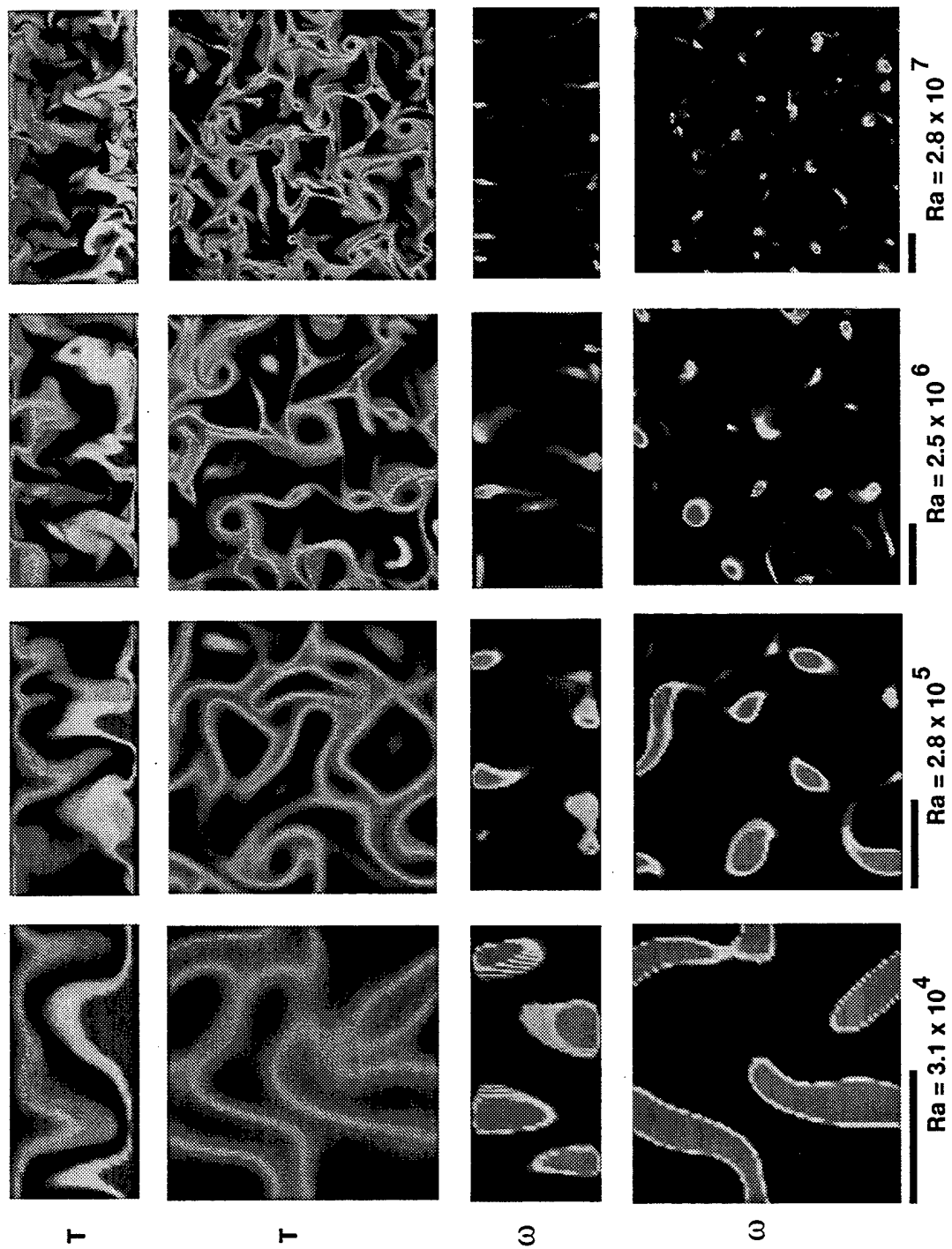
Figure 1: Temperature & vertical vorticity. Sideviews (rows 1 & 3) and horizontal planes (rows 2 & 4).
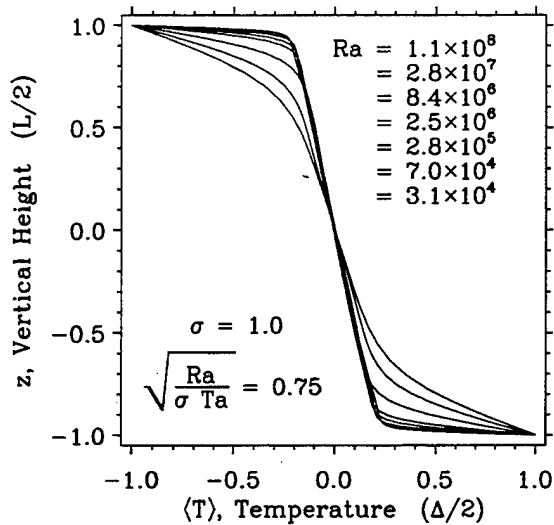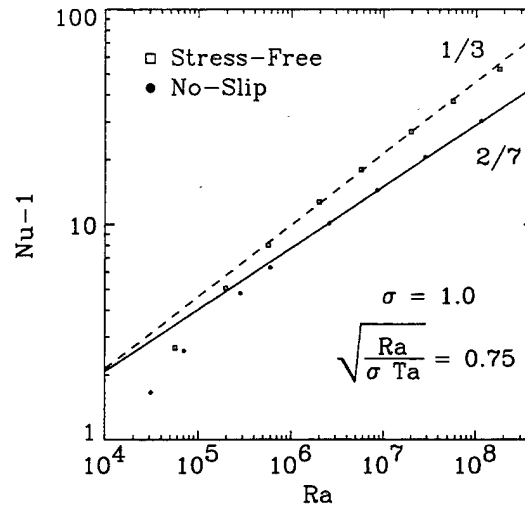
Figure 2: Temperature profiles.

Figure 3: Heat transfer versus Ra.

Castaing et al. (1989), since that theory cannot distinguish stress-free from no-slip boundaries. The key point is that the majority of the heat transport through the boundaries takes place in strong shear regions between plumes, not at plume-sites. This is consistent with earlier findings (Werne 1993).

Castaing et al. 1989 J. Fluid Mech. **204**, 1.

Chandrasekhar 1961 Hydrodynamic and Hydromagnetic Stability. Oxford University Press.

Heslot, Castaing & Libchaber 1987 Phys. Rev. A **36**, 5870.

Howard 1966 In Proc. of the 11th Int. Congr. of Appl. Mech. Munich (Germany) (ed. H. Gortler). p. 1109. Springer, Berlin.

Julien, Legg, McWilliams & Werne 1995 J. Fluid Mech., submitted.

Kleiser & Schumann 1980 In Proc. 3rd GAMM Conf. Numerical Methods in Fluid Mechanics, (ed. E. H. Hirschel). p. 165. Vieweg, Braunschweig.

Krishnamurti 1995 Preprint.

Malkus 1963 In Theory and Fundamental Research in Heat Transfer, (ed. J. A. Clark). Pergamon Press, Tarrytown.

Prandtl 1932 Beitr. Physik fr. Atmos. **19**, 188.

Priestley 1959 The University of Chicago Press. Chicago & London.

Rossby 1969 J. Fluid Mech., **36**, 309.

She 1989 Phys. Fluids A **1**, 911.

Shraiman & Siggia 1990 Phys. Rev. A **42**, 3650.

Werne 1993 Phys. Rev. E. **48**, 1020.

Werne 1995 J. Comput. Phys., in press.

Wu, Castaing, Heslot & Libchaber 1988 In Proceedings in Physics Vol. 32 Universalities in Condensed Matter, 208.

Yakhot 1992 Phys. Rev. Lett. **69**, 769.

Zhong, Ecke & Steinberg 1993 J. Fluid Mech. **249**, 135.

Intermittent mixing: the Zappa model

by

W.R.Young & Mahdi Ben Jelloul
Scripps institution of Oceanography
University of California at San Diego
La Jolla, CA 92093-0230
USA

Consider the dispersion of some tracer (concentration $c(c, z, t)$) in the shallow channel. Our notation is explained in the sketch below and the mathematical model is

$$c_t + uc_x = \text{mix}_n, \tag{1}$$

where "mix" indicates some model of mixing that tries to vertically homogenize the tracer.
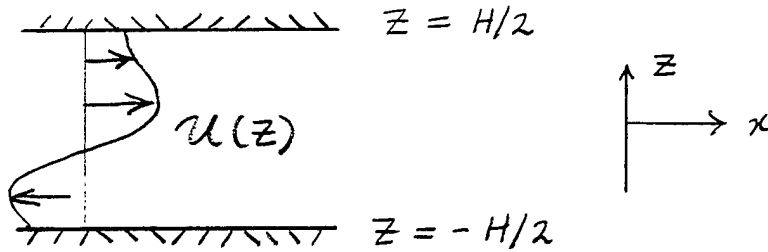

FIGURE 1 Definition sketch: the tracer is contained in a channel $H/2 > z > -H/2$.

We compare three different models of mixing and show that they all lead more or less to the same conclusion. The three models are

$$\text{mix}_1 = Dc_{zz},$$
$$\text{mix}_2 = \tau^{-1}(\bar{c} - c), \tag{2a, b, c}$$
$$\text{mix}_3 = \text{zapping at intervals of } \tau.$$

In (2b) the vertical average over the layer is denoted by

$$\bar{c}(x, t) = \frac{1}{H} \int_{-H/2}^{H/2} c(x, z, t)\, dz. \tag{3}$$

The Zappa model in (2c) works by letting the tracer advect for a time τ (that is, the right hand side of (1) is zero) and then instantaneously vertically homogenizing the tracer. Thus at the time $t = n\tau$, $c(x, z, t) \to \bar{c}(x, t)$. This might model some sort of event driven mixing, such as the passage of a storm, or mixing which occurs only at some point in a tidal cycle.

Our conclusion is that in the long term the dispersion of the tracer can be described by an effective diffusion equation for $\bar{c}(x, t)$:

$$\bar{c}_t + \bar{u}\bar{c}_x = D_{\text{eff}}\bar{c}_{xx}. \tag{4}$$

The effective diffusivity in (4) is given by $D_{\text{eff}} = cU^2 T_{\text{mix}}$ where c is a dimensionless constant, U is the scale of $u(z)$, and T_{mix} is the vertical homogenization time. For example, using the model in (2a), $T_{\text{mix}} = H^2/D$ and then the result above is Taylor's (1953) shear dispersion result. For the other two models $T_{\text{mix}} = \tau$.

The point is that the details of the mixing model on the RHS of (1) are not that important: one expects that the combination of the sheared velocity field, $u(z)$, and the vertical mixing will always produce an effective diffusion coefficient in the vertically averaged tracer equation in (4). One is usually interested only in gross questions such as: where is most of the tracer? how long does it take the width of a slug of tracer to double? In this case it doesn't pay to get too exercised about which of the models in (2) is "better". All three models are plausible representations of small scale mixing processes and all three models result in an effective diffusion equation which describes the dispersion of tracer on large scales and long times.

There are many ways of deriving (4): we take a simple and instructive route, and use the Zappa model in (2c). Without any loss of generality we can take $\bar{u} = 0$ — otherwise we can change frame so that the vertically averaged velocity is zero. Now imagine that one is maintaining a uniform gradient of tracer, Γ, and that at $t = 0^+$ a zap has just occured so that:

$$c(x, z, 0^+) = \Gamma x. \tag{5}$$

Then, in the interval before the next zap, the tracer is advected by the $u(z)$ so that

$$c(x, z, t) = \Gamma[x - u(z)t] \qquad \text{when} \qquad 0 < t < \tau. \tag{6}$$

The result in (6) is the solution of (1), with zero RHS, and (5) as an initial condition. Now at $t = \tau$ the tracer is zapped again and, since $\bar{u} = 0$, the post-zap tracer is again given by (5). It looks like nothing has happened as a result of all this advection and zapping. But the interesting point is that there has been a flux of tracer during the interval between zaps and it is easy to calculate how much tracer has been advected down the channel during this period:

$$F(x, t) = \int_{-H/2}^{H/2} u(z)\Gamma[x - u(z)t]\, dz,$$
$$= -H\overline{u^2}\Gamma t, \qquad \text{when} \qquad 0 < t < \tau. \tag{7a, b}$$

Thus the flux as a function of time has the sawtooth pattern shown below: after the most recent zap the flux starts at zero and then grows linearly with time till the next zap homogenzies the tracer and knocks the flux back down to zero.
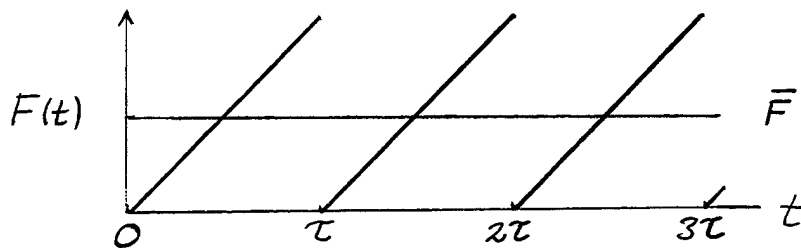

FIGURE 2: The flux as a function of time is a "sawtooth".

The final step is to note that the averaged flux (averaged over both the interval between the zaps and the depth of the channel) is just

$$\bar{F} = -\frac{1}{2}\overline{u^2}\tau\Gamma. \tag{8}$$

the expression in (8) is the flux-gradient relation which is typical of a diffusive process: the diffusivity is $D_{\text{eff}} = \overline{u^2}\tau/2$.

It is educational to repeat the calculation above for the other two mixing models in (2): in both cases one looks for a steady solution of the from $c(x, z, t) = \Gamma x + c'(z)$. Substitution gives an easy equation for $c'(z)$ and then the final step is to calculate the vertically averaged flux and identify the constant of proportionality in the flux–gradient relation as the effective diffusivity. All three models have the property that weaker vertical mixing (i.e., larger T_{mix}) produces stronger horizontal dispersion. At first sight this seems curious, but the sawtooth graph of $F(t)$ in the figure above shows clearly where this inverse dependence comes from: the sheared velocity field "unmixes" the tracer and the horizontal flux grows as this "unmixing" proceeds.

There are several other embellishments of the Zappa model which serve as good homework exercises for students. Suppose that the interval between zaps is a random variable so that after a zap occurs the time to the next zap is determined by selecting τ from a probability distribution with probability density function $\mathcal{P}(\tau)$. What is the effective diffusivity in this case? The answer is mildly interesting because it involves the first two moments of τ i.e., $\int_0^\infty \tau^n \mathcal{P}(\tau)\, dt$ with $n = 1$ and 2. A second suggestion is to use the Zappa model and the particular velocity $u = sy$ to solve an initial value problem with $c(x, z, 0) = \exp(ikx)$. The goal is to show that the evolution of long waves ($kH \ll 1$) is governed by the effective advection-diffusion equation in (4), and that the effective diffusivity is the same as that which is found by considering the flux–gradient relationship. This exercise is interesting because the evolution of not–so–long waves is not diffusive, and students then appreciate some of the approximations involved in (4).

Now let us turn to a problem in which the tracer is dynamically active rather than passive. Consider a stratified fluid, use the Boussinesq approximation and write the density as $\rho = \rho_0 \left[1 - g^{-1}b(x, z, t)\right]$ where $b(x, z, t)$ is the "buoyancy". The equations of motion are then

$$\frac{Du}{Dt} = -p_x + \text{zap}, \qquad \frac{Dw}{Dt} = -p_z + b, \qquad u_x + w_z = 0, \qquad \frac{Db}{Dt} = \text{zap}, \tag{9}$$

where "zap" indicates that we use the Zappa model of mixing and apply this instantaneous homogenization to both momentum and buoyancy. Suppose that at $t = 0^+$ a zap has just occured and the buoyancy is $b(x, z, 0) = \Gamma x$ while $(u, w) = (0, 0)$. There is an exact solution of (9) which illustrates how dense fluid flows under light and so releases the potential energy stored in the stratification:

$$u = -\Gamma z t, \qquad p = \Gamma \left[xz + \Gamma z^2 \frac{t^2}{4}\right], \qquad w = 0, \qquad b = \Gamma \left[x + \Gamma z \frac{t^2}{2}\right] \qquad \text{when} \qquad 0 < t < \tau. \tag{10}$$

Notice that we have assumed that there is no vertically integrated transport, $\bar{u} = 0$. This condition, which might be enforced by distant vertical sidewalls, is used to determine the constant of integration which arises when one determines the pressure by integrating the hydrostatic relation.

We now compute the buoyancy flux which occurs during the interval between zaps:

$$F = \int_{-H/2}^{H/2} ub\,dz = -\frac{1}{24}H^2 t^3 \Gamma^3 \qquad \text{when} \qquad 0 < t < \tau. \tag{11}$$

The solution in (11) shows that the gravitational slumping produces an accelerating velocity and this in turn is responsible for the t^3 growth of the buoyancy flux which occurs in between the zaps. The final step is to calculate how much buoyancy is transported by integrating (11) in time, and then averaging over many such zapping cycles. One finds that the analog of (8) is

$$\bar{F} = -\frac{1}{96}H^2 \tau^3 \Gamma^3 \tag{12}$$

so that the flux of buoyancy is proportional to the cube of the buoyancy gradient.

We can use the result in (13) to make a heuritic argument that in a "slowly varying configuration" the vertically averaged buoyancy satisfies the nonlinear diffusion equation:

$$\bar{b}_t = \frac{1}{96}H^2 \tau^3 \left(\bar{b}_x^3\right)_x. \tag{13}$$

To understand the meaning of "slowly varying", observe that in the time between zaps fluid travels through a distance of order $\ell \sim b_x H\tau^2$. If the buoyancy gradient "looks" uniform over this distance then we expect the solution in (10) to apply locally. The obvious length associated with the variation of the buoyancy gradient is b_x/b_{xx}. Requiring that this length scale be less than ℓ shows that "slowly varying" means that the nondimensional number $b_{xx}H\tau^2$ is small.

The nonlinear diffusion equation (13) was first obtained by Erdogan & Chatwin (1967) using molecular diffusion and viscosity as a mixing model †. Once again, it is comforting to see that alternative assumptions about how mixing works do not alter the final form of the answer: it is instructive to return to (9) and figure out where the three powers of Γ came from. One realizes quickly that the alternative mixing models in (2a) and (2b) will not change the processes responsible for the various powers of Γ.

Simpson & Linden (1989) have given an interesting theoretical and experimental discussion of the role of buoyancy curvature, b_{xx}, in driving frontogenesis. In the simple solution, (10), there is no frontogenesis: the b–surfaces tilt over and maintain equal spacing; the horizontal buoyancy gradient is constant. But if the initial condition has some buoyancy curvature then Simpson & Linden show that the buoyancy gradient can increase. If there is no mixing then one suspects that b_x will become infinite in a finite time: this singularity is frontogenesis. The interesting point is then that if we use the Zappa model there is a race between the zap and the singularity formation: given an initial condition which happens first? Since the time to singularity formation is scales like $1/\sqrt{b_{xx}H}$ this race is decided by the same nondimensional parameter that we identified in the discussion of the validity of (13).

† Because Erdogan & Chatwin used molecular diffusivity, rather than zapping, the analog of τ in (13) is H^2/D. This implies that the diffusivity in the analog of (13) is proportional to the eighth power of the layer depth!

We followed Simpson & Linden and had some frontogenetic fun by considering the solution of (9) with the initial condition $b(x, z, 0) = B(x)$: we use $B = B_0 \tanh(kx)$ as a concrete illustration. If $kH \ll 1$ then one can use the hydrostatic approximation and then it is not too hard to develop a Taylor series in t for solution of (10). With the aid of MAPLE one finds that

$$b(x, z, t) = B(x) + \frac{z}{2} B'^2 t^2 + \left(\frac{39z^2 + 5}{144} \right) B'^2 B'' t^4$$
$$+ \left[\left(\frac{4z^3 + 7z}{432} \right) B''' B'^4 + \left(\frac{453z^3 + 247z}{4320} \right) B'^3 B''^2 \right] t^6 + O(t^8). \tag{14}$$

The first two terms of (14) agree with the exact solution in (11) but thereafter the buoyancy curvature, B_{xx}, and higher spatial derivatives becomes important. Of course the expansion in (14) becomes invalid close to the putative singularity, but a charitable reader might concede that the figure below shows the birth of a front.
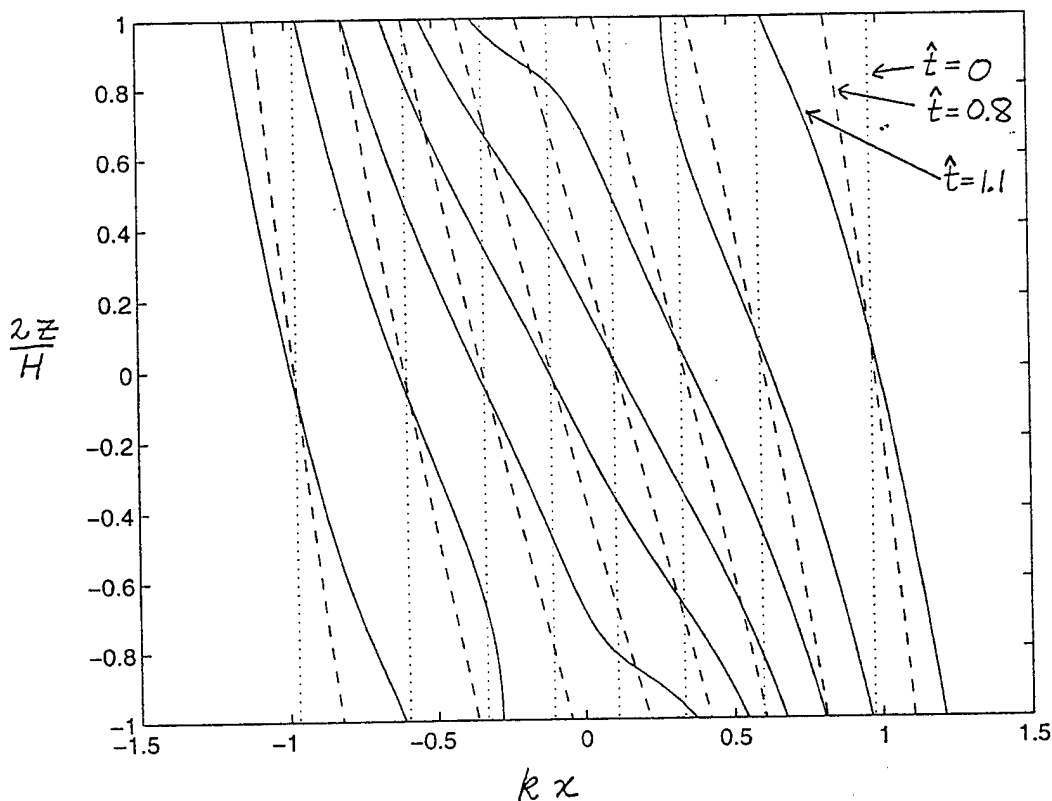
FIGURE 3: The solution in (14) with $B = B_0 \tanh(kx)$ and the scaled time is $\hat{t} = t\sqrt{2/k^2 H B_0}$. At $\hat{t} = 0$ the buoyancy surfaces are vertical. At $\hat{t} = 0.8$ the tilting has begun but there is no indication of frontogenesis yet. At $\hat{t} = 1.1$ the singularity has begun to form on the boundaries at $z = \pm H/2$.

References

Erdogan, M. E. & P.C. Chatwin, 1967. *J. Fluid Mech.* **29**, 465.

Simpson, J. E. and P.F. Linden, 1989. *J. Fluid Mech.* **202**, 1.

Taylor, G. I., 1953. *Proc. Roy. Soc. A* **219**, 186.

NUMERICAL SIMULATIONS OF
ROTATING AND THERMALLY-STRATIFIED TURBULENCE

Olivier MÉTAIS

Laboratoire de Écoulements Géophysiques et Industriels de Grenoble, URA CNRS 1509
Institut de Mécanique de Grenoble
Institut National Polytechnique et Université Joseph Fourier
BP 53X, 38041 Grenoble Cédex, France

1   Introduction

Rotation and stable density stratification modify the turbulence dynamics in many geophysical situations and on a large range of scales. We here summarize the results of numerical simulations aimed at investigating the effects of stably-stratified turbulence and/or solid-body rotation on turbulence and coherent vortices. In a first part, we consider the dynamics of coherent vortices present in free and wall-bounded (barotropic) shear flows submitted to solid-body rotation. The second part will be devoted to the effects of solid-body rotation on stably-stratified homogeneous turbulence.

2   Coherent vortices in rotating shear flows

Turbulent or transitional shear flows in a rotating frame have been extensively studied due to their importance in many geophysical and engineering applications. Within these flows, the local Rossby number, which characterizes the relative importance of inertial and Coriolis forces, can vary significantly. Typical values of the Rossby number are on the order of 0.05 in mesoscale oceanic eddies and in Jupiter's Great Red Spot, 0.3 for large synoptic-scale atmospheric perturbations, and 2.5 for the atmospheric wake of a small island. Turbulence in rotating fluids finds numerous industrial applications in turbo-machinery; e.g., the turbulent characteristics of the flow in blade passages of radial pumps and compressor impellers determine the efficiency of these devices. Turbulence is also of great importance for the cooling by the fluid inside the blades. Depending upon the magnitude of the radial velocity, the Rossby number within rotating machines can range from values close to unity to very small ones (of the order 0.05).

Laboratory experiments, theoretical works, numerical simulations and atmospheric and oceanic observations show that they are three basic effects associated with rotating bounded- or free-shear flows. (i) If the shear vorticity is parallel and of same sign as the rotation vector (cyclonic rotation), the flow is made more two-dimensional. (ii) If the two vectors are anti-parallel (anticyclonic rotation), destabilization is observed at moderate rotation rates (high Rossby numbers), while (iii) two-dimensionalization is recovered for fast rotation. It is easy to show that the asymmetry between the cyclonic and anticyclonic cases can only be explained by considering the influence of rotation on the growth of three-dimensional perturbations.

2.1 Linear-stability analysis

In order to describe the early stage of the development, Yanase *et al.* (1993) have performed a three-dimensional, viscous, linear-stability analysis of two planar free-shear flows subject to rigid-body rotation oriented along the span: the mixing layer and the plane wake. The mean ambient velocity is oriented in the longitudinal direction x and varies with y, $[\bar{u}(y), 0, 0]$. The rotation vector is the spanwise direction z, $\vec{\Omega} = (0, 0, \Omega)$. The Rossby number is here based upon the maximum ambient vorticity of the basic profile, that is, the vorticity at the inflexion point(s), $-(d\bar{u}/dy)_i$, i.e.,

$$R_o = -(d\bar{u}/dy)_i/2\Omega \quad . \tag{1}$$

In the mixing layer, R_o is positive for cyclonic rotation and negative for anticyclonic rotation. For the wake, one considers the modulus $|R_o|$ of the Rossby number. From the linearized governing equations, it is shown that cyclonic rotation prevents the growth of three-dimensional perturbations and two-dimensionalization is observed. For strong anticyclonic rotation ($R_o > -1$) the effect is similar. For moderate anticyclonic rotation ($R_o < -1$), however, the flow stability is dramatically modified. In this regime, a new instability appears along the k_z-axis ($k_x = 0$), corresponding to a purely streamwise instability: the shear/Coriolis instability. For both the mixing layer and the wake, this shear/Coriolis instability has larger amplification rates than the co-existing Kelvin-Helmholtz instability for roughly the range $-8 < R_o < -1.5$, and its effect is maximum for $R_o \simeq -2.5$. Yanase *et al.* (1993) have also shown that, for purely longitudinal modes ($k_x = 0$), and if the stability problem is reduced to perturbations such that $k_x = 0$, a necessary and sufficient conditions for inviscid instability is that the local Rossby number $R_o(y) = -d\bar{u}/dy/2\Omega$ should be smaller than -1 somewhere in the layer. Notice that, for a purely longitudinal perturbation, the eigenvalue equation is similar to the one governing the radial velocity when studying the inviscid linear centrifugal instability in the limit of axisymmetric disturbances.

Further insight into the shear/Coriolis instability can be obtained by examining the vorticity dynamics. We note $\underline{\omega}'(x, y, z, t) = (\omega'_x, \omega'_y, \omega'_z)$, the relative vorticity perturbation about the basic shear. Under simplifying assumptions, such as neglecting viscous effects, assuming $\partial/\partial x(\cdot) = 0$ (the shear/Coriolis instability), the following equations can be obtained (see Métais *et al.*, 1995b, for details)

$$\frac{\bar{d}\omega'_x}{dt} = 2\Omega\omega'_y \tag{2}$$

$$\frac{\bar{d}\omega'_y}{dt} = -\left(2\Omega - \frac{d\bar{u}}{dy}\right)\omega'_x \quad . \tag{3}$$

where $\bar{d}$ stands now for the substantial derivative following the basic flow. These can also be recovered by considering an exact solution of Euler's equations, in terms of sheets of fluid moving idependently (Métais *et al.*, 1992). It reduces to the following equation for ω'_x:

$$\frac{d^2\omega'_x}{dt^2} = -2\Omega(-\frac{d\bar{u}}{dy} + 2\Omega)\omega'_x \quad . \tag{4}$$

This indicates, that, in the linear regime, the longitudinal vorticity component grows exponentially in the regions such that $R_o < -1$, in agreement with the results of the linear stability analysis. Furthermore, for a given ambiant vorticity $-\frac{d\bar{u}}{dy}$ and varying Ω, maximum amplification is achieved for $R_o = -2$. In this case, the same amplification rate is achieved for ω'_x and ω'_y:

$$\frac{1}{\omega'_x}\frac{d\omega'_x}{dt} = \frac{1}{\omega'_y}\frac{d\omega'_y}{dt} \tag{5}$$

For $\omega'_x(0) \approx \omega'_y(0)$, this yields to the formation of vortex filaments oriented at 45° with respect to the x-direction.

2.2 The non-linear regime

The previous analysis allows to describe the early linear stage of the perturbations growth. Further insight in the nonlinear regime, can be obtained, firstly by examining the vorticity stretching mechanisms, and secondly by performing three-dimensional simulations of the full Navier-Stokes equation.

In a former study (Lesieur *et al.*, 1991) have emphasized the importance of considering the absolute vorticity, and not just the relative vorticity, since Kelvin's circulation theorem directly applies to the absolute vorticity. For example, if the relative vorticity is written as the sum of the ambient $-(d\bar{u}/dy)\underline{z}$ and fluctuating $\underline{\omega}'$ components. The absolute vorticity then writes $(2\Omega - d\bar{u}/dy)\underline{z} + \underline{\omega}'$. If the flow is locally cyclonic (i.e., Ω and $-(d\bar{u}/dy)$ have the same sign), then the absolute vortex lines are closer to the spanwise direction than the corresponding relative ones. Therefore, as compared to the non-rotating case, the effectiveness of vortex turning and stretching is reduced. Conversely, if the flow is locally anticyclonic, especially for the regions where 2Ω has a value close to $d\bar{u}/dy$ (weak absolute spanwise vorticity), absolute vortex lines are very convoluted, and will be very rapidly stretched out all over the flow, as a dye would do. It was thus predicted that in rotating shear flows, the vortex filaments of Rossby number -1 (hence anticyclonic) would be stretched into longitudinal alternate vortices. This phenomenological argument will be referred to as the weak-absolute vorticity stretching principle.

2.3 Numerical simulations of rotating free-shear flows

We here concentrate on the rotating mixing layer case and we will show, through numerical simulations, how the rotation modifies the three-dimensional flow topology. The reader can
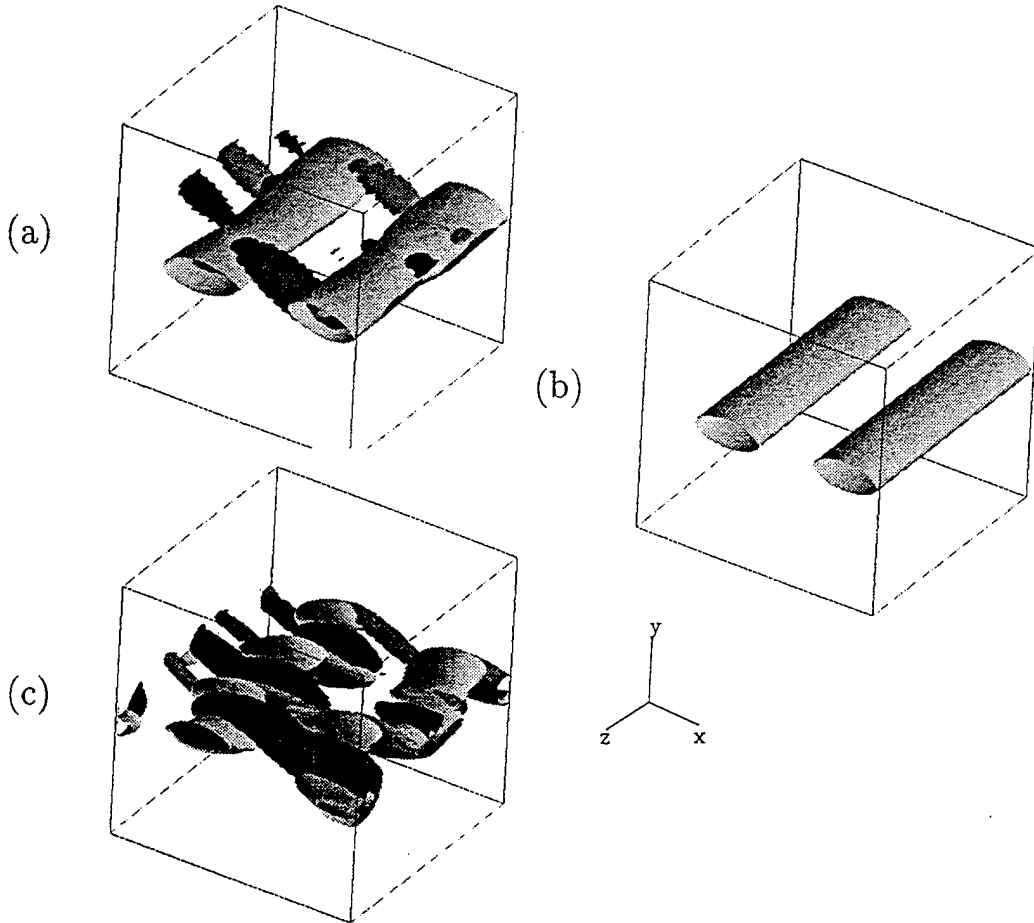
Figure 1: Mixing layer. Relative vorticity isosurfaces at $t = 17.8\delta_i/|U_0|$. a) nonrotating case: $\omega_z = 45\%$ of $|\omega_{2D}^{(i)}|$ (vorticity maximum associated with the initial mean profile), light gray; $\omega_l = 4.5\%$ of $|\omega_{2D}^{(i)}|$ coloured by the sign of ω_x, black $\omega_x < 0$, dark gray $\omega_x > 0$. b) $R_o^{(i)} = -1$. $\omega_z = 45\%$ of $|\omega_{2D}^{(i)}|$, light gray. c) $R_o^{(i)} = -5$. $\omega_z = 45\%$ of $|\omega_{2D}^{(i)}|$, light gray; $\omega_l = 22.5\%$ of $|\omega_{2D}^{(i)}|$ coloured by the sign of ω_x, black $\omega_x < 0$, dark gray $\omega_x > 0$ (from Métais et al., 1995b).

refer to Lesieur et al. (1991), Métais et al. (1992), and Métais et al. (1995b) for more details. Temporal shear flows are considered with periocity in the streamwise direction. We consider a mixing layer associated with an hyperbolic-tangent mean-velocity profile: $\bar{u}(y) = U_0 \tanh y/\delta$ where $2U_0$ is the velocity difference accross the layer, and $\delta = \delta_i/2$, with δ_i initial vorticity thickness. We define the Rossby number as, $R_o^{(i)} = -U_0/2\Omega\delta$. $R_o^{(i)}$ is positive for cyclonic rotation (U_0 and Ω of opposite sign) and negative for anticyclonic rotation. The Reynolds number $Re^{(i)} = |U_0|\delta/\nu$ is here taken equal to 50. Initially, a low-amplitude random noise is superposed upon the ambient velocity profiles. Two different types of perturbations are considered. Firstly, a quasi-two-dimensional one consisting of the superposition of a purely two-dimensional perturbation (z independent) of kinetic energy $\epsilon_{2D}U_0^2$ and a three-dimensional perturbation of energy $\epsilon_{3D}U_0^2$, with $\epsilon_{2D} = 10\epsilon_{3D} = 10^{-4}$. The perturbation peaks at the fondamental Kelvin-Helmholtz mode. This case will be referred to as the "forced transition" case. The second type of perturbations which has been considered is purely three-dimensional,

with $\epsilon_{3D} = 10^{-4}$ and $\epsilon_{2D} = 0$. The noise is now a white-noise which does not favour any mode, and the most amplified one can freely emerge: this case will be called the "natural transition" case.

We will show that the simulations have confirmed the global trends observed in the experiments and predicted by the linear-stability analysis: the Kelvin-Helmholtz vortices are two-dimensionalized by the rotation when these are cyclonic; this is also true for rapid anticyclonic rotation. Conversely, a moderate anti-cyclonic rotation disrupts the primary vortices. The latter are stretched into intense longitudinal alternate vortices of Rossby number -1, as predicted by the weak absolute vorticity stretching principle.
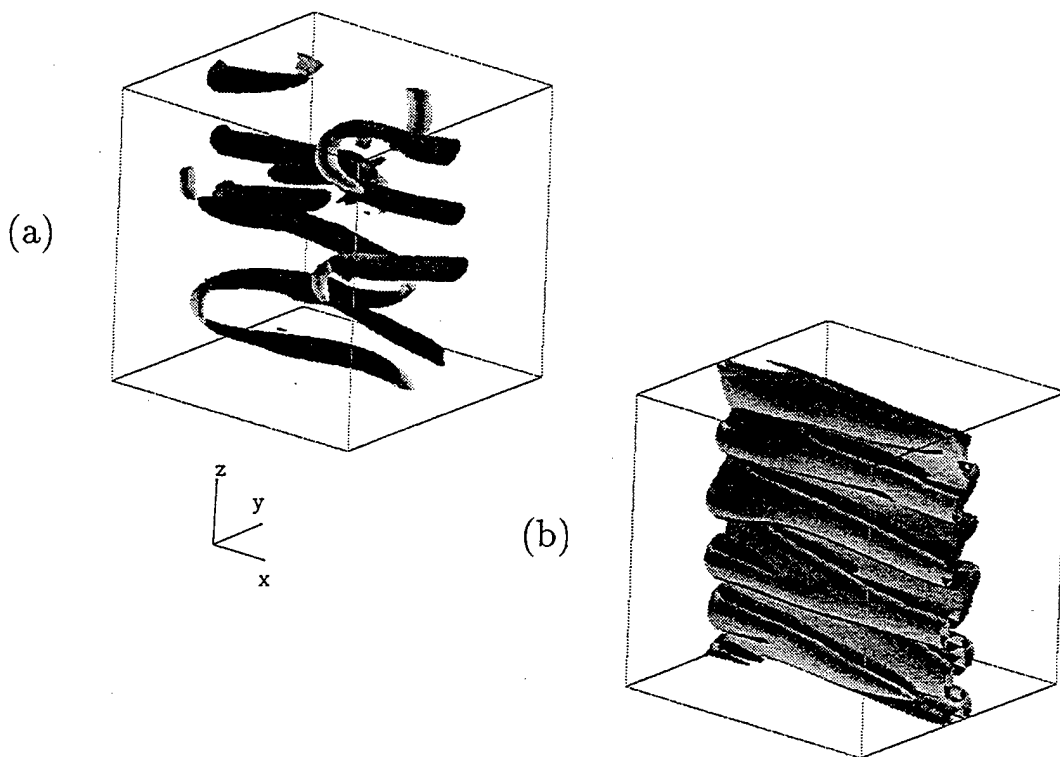

Figure 2: Mixing layer. Relative vorticity isosurfaces at $t = 26.8\delta_i/|U_0|$. (a) forced-transition; (b) natural transition. ω_z, light gray; ω_l (longitudinal vorticity) coloured by the sign of ω_x, black $\omega_x < 0$, dark gray $\omega_x > 0$ (from Métais et al., 1995b).

In the early stage of the development, the results have corroborated the linear-stability predictions for quantities such as the critical Rossby for maximum destabilization, found to be ≈ -2. In the present paper, a special care is given to the coherent-vortex dynamics. Now we look at the three-dimensional flow structure, in the forced transition case. We focus on the relative vorticity iso-surfaces at $t = 17.8\delta_i/|U_0|$ obtained in the non-rotating case ($R_o^{(i)} = \infty$), and for anticyclonic rotation at $R_o^{(i)} = -5$ and $R_o^{(i)} = -1$.

(1) $R_o^{(i)} = \infty$ (Figure 1a). Here, one observes quasi-two-dimensional Kelvin-Helmholtz billows, slightly distorted in the spanwise direction. Weak longitudinal vortices are stretched between the primary rolls: those are identified through isosurfaces of weak longitudinal vorticity.

(2) $R_o^{(i)} = -1$ (Figure 1b) displays the spanwise vorticity field with the same iso-contour value than in the non-rotating case. Anticyclonic and cyclonic flows are similar at this Rossby number, and a strong two-dimensionalization is observed in both cases. The longitudinal vortices have disappeared. Furthermore, the two-dimensionalization tendency can be observed in the cyclonic case even for large positive $R_o^{(i)}$. This agrees well with both the predictions of the linear stability analysis by Yanase *et al.* (1993) and the phenomelogical theory proposed by Lesieur *et al.* (1991).

(3) $R_o^{(i)} = -5$ (Figure 1c). The Kelvin-Helmholtz vortices are now highly distorted and exhibit strong oscillations along the spanwise direction. The longitudinal vorticity is much higher than in the non-rotating case: we observe the simultaneous formation of Kelvin-Helmholtz vortices and longitudinal hairpin vortices which are stretched inbetween. As time goes on, this produces an important increase of the longitudinal vorticity component: by the end of the run the longitudinal vorticity is approximately twice the one associated with the initial mean velocity profile. By the end of the run (Figure 2a), the Kelvin-Helmholtz vortices have been totally dislocated and the flow is entirely composed of hairpin-shaped longitudinal vortices. A similar sequence had been proposed in this case by Lesieur *et al.* (1991), using the weak absolute vorticity stretching mechanism: weak absolute vorticity in the stagnation region between the Kelvin-Helmholtz rollers would be stretched longitudinally between the latter, yielding longitudinal alternate vortices which should destroy the primary vortices. It is worth noting that these vorticity structures originate from the growth of the longitudinal mode predicted by the linear stability analysis (see Yanase *et al.* 1993).

In the case of natural transition, we observe the rapid formation of purely longitudinal structures corresponding to regions of high *relative* vorticity (Figure 2b). These exhibit some analogies with the Görtler vortices observed in the boundary layer over a concave wall. These structures have a spanwise wavelength λ_s corresponding to the fastest shear/Coriolis mode predicted by the linear-stability analysis of Yanase *et al.* (1993). Close examination of the time evolution of the *absolute* vortex lines shows that the flow undergoes very distinct stages. In the first stage, the vorticity dynamics are dominated by quasi-linear mechanisms yielding absolute vortex lines inclined at 45° with respect to the horizontal plane. These are in phase in the longitudinal direction. We have checked that maximum longitudinal vorticity stretching is achieved in the flow regions with a local Rossby number of approximately -2.8. In a second stage, nonlinear stretching mechanisms yield quasi-horizontal longitudinal hairpins of absolute vorticity. As in the forced-transition case, these absolute vortex tubes correspond to local Rossby number ≈ -1. The ω_x stretching terms become larger than for ω_y, and those terms are found to be maximum within the legs of the vortices. The dynamics are then dominated by a strong quasi-horizontal stretching of longitudinal *absolute* spanwise vorticity. During that stage, we observe that the ambient velocity profile exhibits a long range of nearly constant shear whose vorticity exactly compensates the solid-body rotation vorticity. Both in the forced and natural transition cases, the eventual states are in agreement with the phenomenological theory proposed by Lesieur *et al.* (1991). Thus a very efficient mechanism to create intense longitudinal vortices in rotating anticyclonic shear layers is provided, thanks to a linear longitudinal instability followed by a vigorous stretching of absolute vorticity. It would be interesting to look for the existence of these longitudinal vortices in laboratory experiments studying rotating

mixing layers and wakes. We know show that the same holds for other types of shear flows submitted to solid-body rotation. We here concentrate on the rotating turbulent channel flow.

2.4 Numerical simulations of rotating channel flow

We here investigate, via three-dimensional direct numerical simulations, the influence of spanwise rotation on the vortex topology in turbulent channel flow (see Lamballais *et al.*, 1995; for further details). Let $|R_o^{(i)}|$ be the Rossby number associated with the vorticity maxima of the initial basic velocity profile. We now compare the non-rotating and rotating turbulent flow in a channel at $Re = 3750$ (based upon the centerline velocity of the initial laminar velocity profile and the half-channel height). The initial conditions consist in a field issued from a non-rotating calculation on which we impose a spanwise rotation corresponding to $|R_o^{(i)}| = 6$. We then integrate till the flow has reached a statistically steady state. After a short transient, the turbulence intensity is amplified on the anticyclonic side while relaminarization occurs on the cyclonic side. We have checked that the statistical results agree well with the simulations performed by Kristoffersen & Andersson (1993).

We particularly examine how the instantaneous vorticity field differs from the non-rotating case. Comparison of the isosurface of the relative vorticity modulus (Figure 3) shows clearly a change of vortex topology when rotation is applied. Near the cyclonic wall, the iso-vorticity surfaces are nearly flat indicating a weak growth of the perturbation. On the anticyclonic side, the increase of the turbulence level is associated with the longitudinal vorticity intensification.
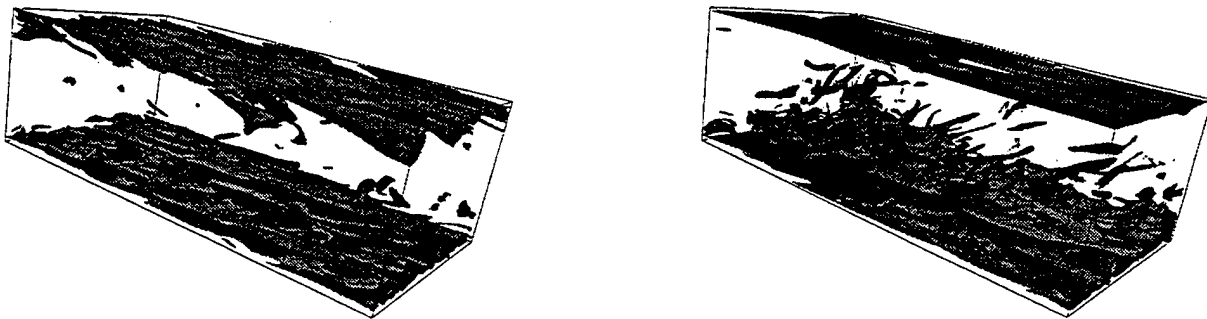

Figure 3: Isosurface of the vorticity modulus $\omega = 3$ at $|R_o^{(i)}| = \infty$ (left) and $|R_o^{(i)}| = 6$ (right), $Re = 3750$ (from Lamballais *et al.*, 1995).

We have checked that the vortex topology is strongly affected by the rotation. The enhancement of the anticyclonic perturbations level is associated with hairpin vortices which are much more inclined (30° to the wall) than in the non-rotating case (45°). These extend till the channel center. Superposed on these structures, we also observe large-scale longitudinal rolls (Taylor-Görtler-like vortices) as in the laboratory experiments of Johnston *et al.* (1972) and the direct numerical simulations of Kristoffersen & Andersson (1993).

The mean velocity profile exhibits a characteristic linear region of slope 2Ω (see Figure 4). It is associated with a local Rossby number $R_o(y) = -1$, where $R_o(y) = -(d\bar{u}(y)/dy)/2\Omega$.
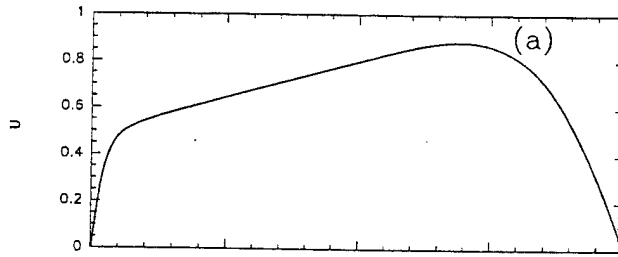
Figure 4: Mean velocity profile $\bar{u}(y)$ ($|Ro^{(i)}| = 6, Re = 3750$; from Lamballais *et al.*, 1995). The anticyclonic wall corresponds to the left of the figure; the cyclonic wall to the right.

The analysis of the different terms involved in the equations for the mean square (absolute) vorticity fluctuations shows that the stretching mechanisms play a major role. These are much more important than the transport processes. This is in agreement with the phenomenological arguments proposed by Lesieur *et al.* (1991).

3   Stably-stratified rotating turbulence

Bartello *et al.* (1994) have performed calculations of rotating homogeneous turbulence from isotropic 3D initial conditions characterizing fully-developed non-rotating turbulence. They demonstrate that rotation acts to organize cyclonic regions (i.e. with $\vec{\omega} \cdot \vec{\Omega} > 0$) into quasi 2D coherent structures, while anticyclonic regions show no such tendency when $R_o^{(i)} = [\vec{\omega} \cdot \vec{\Omega}]_{rms}/2\Omega^2 \approx 1$. The situation bears a resemblance to the rotating turbulence experiments of Hopfinger *et al.* (1982), where 3D structures generated by an oscillating grid at the bottom of their tank two-dimensionalized towards the top, where the Rossby number was smaller. In this experiment, the quasi-two-dimensional vortices were all cyclones.

This shows that a solid-body rotation when applied to three-dimensional turbulence tends to generate vertical coherence in some regions of the flow. As opposed to rotation, stable density stratification may induce a very pronounced flow vertical variability. Indeed, Riley *et al.* (1981) and Lilly (1983) have suggested that, in the limit of small Froude numbers, stably-stratified turbulence could obey a two-dimensional turbulence dynamics. However, the numerical studies by Herring and Métais (1989) and Métais and Herring (1989) have shown that the horizontal motion dominates in a strongly stably-stratified environment, but the flow develops a strong vertical variability and reorganizes itself into decoupled horizontal layers. The shear of the horizontal velocity at the interface between the layers leads to energy dissipation, and prevents the turbulence from exhibiting the characteristics of two-dimensional turbulence.

We here numerically investigate the effects of solid-body rotation on stably-stratified turbulence with energy injection at small scales. Freely-decaying computations are reported elsewhere (see Bartello, 1995 ; Métais *et al.*, 1995a). The three-dimensional Navier-Stokes equations within the Boussinesq approximation are simulated and homogeneous turbulence is considered. We focus on the small Froude number (F_r) régime when the Rossby number (R_o) ranges from large (slow rotation) to small (rapid rotation) values. The Brünt-Vaissälä frequency N is assumed to be constant. In order to reduce the dissipative and diffusive ranges extension, the

Laplacian operator in the viscous term is replaced with an iterated Laplacian (see Basdevant and Sadourny, 1983). The computational domain is a cubic periodic box, the resolution is 64^3 collocation points, and pseudo-spectral numerical methods are used. The results are presented in details in (Métais *et al.*, 1994, 1995a).

3.1   Turbulence and waves

When solid-body rotation and stable density stratification are simultaneously present, one must find a simple way of discrimating between the turbulent part of the motion and the component associated with non-linearily interacting inertial-gravity waves. One may use the fact that inertial gravity waves have no potential vorticity, and extract the turbulent component of the velocity field which is associated with the potential vorticity. This can be done in the limit of small Froude and Rossby numbers corresponding to Charney's (1971) geostrophic turbulence. Hydrostatic and geostrophic balances then imply that the (normalized) conserved potential vorticity ζ can be expressed in terms of a stream function ψ (Charney, 1971, see also Lesieur, 1990):

$$\zeta = N^2 \left[\nabla_H^2 \psi + \left(\frac{f}{N} \right)^2 \frac{\partial^2 \psi}{\partial z^2} \right] \tag{6}$$

(N is the Brünt-Vaissälä frequency; $f = 2\Omega$ is the Coriolis parameter; H denotes the horizontal and z the vertical direction). Therefore, from the potential vorticity, one can derive ψ through (6). The *geostrophic* turbulent part of the horizontal velocity and (normalized) density fields can then be deduced in the following way:

$$u_G = \frac{\partial \psi}{\partial y}, \quad v_G = -\frac{\partial \psi}{\partial x}, \quad \Theta_G = f \frac{\partial \psi}{\partial z} \ . \tag{7}$$

E_G^x and E_G^y will designate the two-components of the *geostrophic* kinetic energy and E_G^z the *geostrophic* available potential energy respectively associated to $u_G; v_G$ and Θ_G.

As a first order approximation, one can consider that all the vertical velocity is associated with the wave motion: $w_w = w$ (where the w index stands for wave). The wave density field can be easily derived from:

$$\frac{\partial \Theta_w}{\partial t} = -i\omega \Theta_w = N^2 w \tag{8}$$

with $\omega^2 = \left(N^2 k_H^2 + f^2 k_z^2 \right) / \left(k_H^2 + k_z^2 \right)$. The facts that the wave field has no potential vorticity and also that the velocity field is non-divergent lead to:

$$\nabla_H^2 u_w = -\frac{\partial^2 w}{\partial z \partial x} - \frac{f}{N^2} \frac{\partial^2 \Theta_w}{\partial z \partial y} \ , \quad \nabla_H^2 v_w = -\frac{\partial^2 w}{\partial z \partial y} + \frac{f}{N^2} \frac{\partial^2 \Theta_w}{\partial z \partial x} \tag{9}$$

These expressions were previously derived by Müller *et al.* (1986) and Lelong (1990).

Notice that for $f = 0$, one recovers the classical decomposition of the horizontal velocity field into rotational and divergent components. It is equivalent to Craya's (1958) decomposition, which has been used to discriminate between stratified turbulence and internal gravity

waves (Riley *et al.*, 1981; Métais and Herring, 1989). Subsequently, we call vortical mode the rotational component of the horizontal velocity field:

$$u_v = \frac{\partial \psi}{\partial y}; \quad v_v = -\frac{\partial \psi}{\partial x} \; , \; with \; \omega_z = -\nabla_H^2 \psi \quad , \tag{10}$$

where ω_z is the vertical vorticity component.

3.2 Numerical simulations

For the present runs, the flow is forced at small scale: the forcing is random in space and Markovian in time, and acts on a wavenumber band ($k_B = 10 < k < 12 = k_T$). We define $k_f = [k_B + k_T]/2$ to be the centroid of the forcing wavenumber band. These conditions are analogous to those chosen by Herring and Métais (1989). The forcing is three-dimensional and acts equally on the three velocity components u, v, w (no density forcing). The intensity of buoyancy and rotation effects will be characterized by a Froude number F_r, and a Rossby number respectively defined as:

$$F_r = \frac{\sqrt{1/2 \left\langle \omega_x^2 + \omega_y^2 \right\rangle}}{N}; \quad R_o = \frac{\sqrt{\langle \omega_z^2 \rangle}}{f} \tag{11}$$

where ω_x, ω_y and ω_z are the relative vorticity components, and the angular brackets stand for a spatial average. $\tilde{\Omega}$ and the mean stratification are both oriented along the vertical direction. We here focus on the small Froude number régime when the Rossby number ranges from large (slow rotation) to small (rapid rotation) values. We concentrate on the energy transfer from the injection scales to the large scales.

In Figure 5a, we display, for various cases, the three-dimensional wavenumber spectrum of the vortical kinetic energy (c.f. eq. 10) when the system has reached an equilibrium. In the absence of rotation and stratification, for k smaller than the forcing wavenumber the energy is equipartitioned between the modes: this yields a k^2 spectrum. One may notice that, for $k > k_f$, the spectral shape closely corresponds to a $k^{-5/3}$ Kolmogorov energy cascade. In the non-rotating strongly-stratified case ($\Omega = 0; N = 4\pi; F_r \approx 0.2$), the vortical energy transfer towards the large scales is more efficient than in the non-stratified case and the spectrum is shallower than k^2. The buoyancy effects are still dominant when a weak rotation ($\Omega = 2\pi/10$; $N/f = 10$, $R_o \approx 1$) is imposed: the spectral behaviour remains almost unchanged. A complete change is observed for strong rotation ($\Omega = 2\pi$; $N/f = 1$, $R_o \approx 0.1$): the spectrum now follows a $k^{-5/3}$ law for $k < k_f$ and the spectral slope is increased for $k > k_f$.

As pointed out by Charney (1971), for geostrophic turbulence, both the total energy, and the potential enstrophy are conserved by the non-linear terms of the equations. One can write:

$$E_G = \int_0^\infty E(k)dk; D_p = \int_0^\infty k^2 E(k)dk \quad . \tag{12}$$

This double conservation property is analogous to two-dimensional turbulence, the difference being that $E(k)$ is here a three-dimensional spectrum. Furthermore, the energy possesses three components: two kinetic and one potential. Nevertheless, this constraint should prevent the
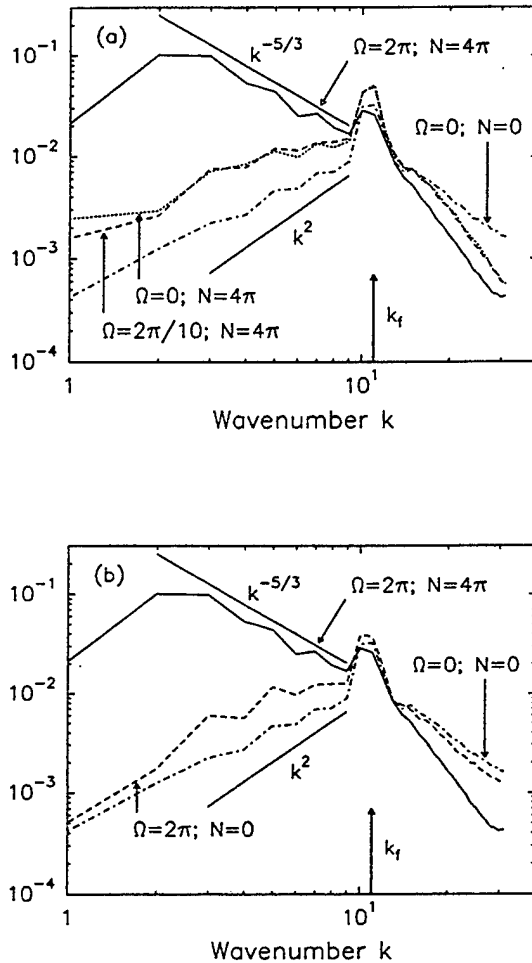
Figure 5: Three-dimensional wavenumber spectrum of the vortical kinetic energy for various values of Ω and N (from Métais *et al.*, 1995a).

energy injected at a wave-number k_f from cascading towards larger k and it should be uniformly transferred to lower wavenumbers along a $k^{-5/3}$ spectrum similar to the two-dimensional turbulence energy cascade proposed by Kraichnan (1967). The numerically observed $k^{-5/3}$ behaviour for small k could therefore be a manifestation of geostrophic turbulence dynamics. This will be confirmed by the subsequently presented results.

Figure 5b is the analogue of Figure 5a. Here, the vortical kinetic energy spectra of the isotropic (no rotation, no stratification) and the strongly-stratified, rapidly-rotating cases are compared to the one obtained when only fast rotation is applied without any stratification ($\Omega = 2\pi$; $N = 0$). We have checked that the large-scale flow exhibits quasi-two-dimensional vortices composed of both cyclones and anticyclones are present. However, although the flow contains these highly-anisotropic structures, the slope of the vortical kinetic energy spectrum for small k remains close to the isotropic k^2 spectrum (see Figure 5b).

A particular attention is now given to the strongly-stratified, rapidly-rotating regime. Due to the nature of the forcing, energy is injected in the inertio-gravity wave as well as in the geostrophic part of the motion. Figure 6a compares the three-dimensional wave-number spectrum of the total kinetic energy (KE_{total}) to the analogous spectra for the geostrophic kinetic energy ($KE_{geo} = E_G^x + E_G^y$) and the inertio-gravity wave kinetic energy (KE_{wave}) constructed with the velocity field u_w, v_w and w_w defined by (9). Due to the combined effects of rotation and stratification, the two kinds of motions are segregated: the geostrophic energy dominates the $k^{-5/3}$ inverse cascade and reaches larger and larger scales. By contrast, the wave energy cascades towards the scales smaller than the injection scales and is therefore submitted to a strong dissipation. A similar picture can be drawn for the geostrophic and wave part of the available potential energy.

Charney (1971) concentrated on the potential enstrophy cascade and argued that the dynamics of quasi-geostrophic flow lead, at small scales, to an equipartition of energy among the x and y components of the kinetic energy and the available potential energy. Here, the geostrophy energy is equipartitioned among its three components E_G^x, E_G^y and E_G^z over almost the whole spectrum including in the large-scale inverse cascade (see Figure 6b).

3.3 Discussion

The observed atmospheric mesoscale spectra (see Gage and Nastrom 1986, for a review) exhibit several features in common with the present numerical results: $k^{-5/3}$ inverse cascades for both velocity and temperature spectra with equipartitioning between each of the two components of horizontal and potential energy. These similarities might lead to believe that the mesoscale spectra do correspond to geostrophic turbulence propagating towards the large scales. However, the variation of the Rossby number as a function of the scale of motion L, or the corresponding wavenumber $k = 2\pi/L$, can be evaluated as $R_o(k) = \omega(k)/f$. $\omega(k)$ is here a measure of the characteristic relative vorticity at wavenumber k. It can be estimated through the kinetic energy spectrum $E(k)$:

$$R_o(k) \propto \frac{\sqrt{k^3 E(k)}}{f} \tag{13}$$

This shows that for $E(k) \sim k^{-5/3}$ then $R_o(k) \sim k^{2/3}$. Using Gage and Nastrom (1986) data, we find a Rossby number ≈ 1 around the injection scales of $10km$ and then ≈ 0.2 at $100km$ (inverse cascade). This is at variance with the present computations for which the Rossby number at the injection scales is small (≈ 0.2). Higher resolution computations should therefore be performed for more precise comparisons.

4 References

- Bartello, P., 1995. Geostrophic adjustement and inverse cascade in rotating stratified turbulence, *J. Atmos. Sci., in press.*

- Bartello, P., Métais, O. & et LESIEUR, M., 1994, "Coherent structures in rotating three-dimensional turbulence", *J. Fluid Mech.*, **273**, pp 1-29.

- Basdevant, C. and Sadourny, R., 1983. Modélisation des échelles virtuelles dans la simulation numérique des écoulements bidimensionnels. *J. Mec. Theor. et Appl.*, Numéro Spécial, pp. 243-269.

- Charney, J.G., 1971. Geostrophic turbulence. *J. Atmos. Sci.*, **28**, pp. 1087-1095.

- Craya, A., 1958. Contribution à l'analyse de la turbulence associée à des vitesses moyennes. P. S. T. Ministère de l'Air, Paris, 345 pp.

- Gage, K.S. and Nastrom, G.D., 1986. Theoretical interpretation of atmospheric wavenumber spectra of wind and temperature observed by commercial aircraft during GASP. *J. Atmos. Sci.*, **43**, pp. 729-740.

- Herring, J.R. and Métais, O., 1989. Numerical experiments in forced stably stratified turbulence. *J. Fluid Mech.*, **202**, pp. 97-115.

- Hopfinger, E.J., Browand F.K., & Gagne, Y., 1982. Turbulence and Waves in a Rotating Tank. *J. Fluid Mech.*, **25**, pp. 505-534.

- Johnston, J.P., Halleen, R.M., & Lezius, D.K., 1972. Effects of spanwise rotation on the structure of two-dimnesional fully developped turbulent channel flow. *J.Fluid Mech.*, **56**, pp. 533-557.

- Kraichnan, R.H., 1967. Inertial ranges in two-dimensional turbulence. *Phys. Fluids*, **10**, pp. 1417-1423.

- Kristoffersen, R. & Andersson, H.I., 1993. Direct simulations of low-Reynolds-number turbulent flow in a rotating channel. *J. Fluid Mech.*, **256**, pp. 163-197.

- Lamballais, E., Lesieur, M. & Métais, O., 1995. Effects of spnawise rotation on the vorticity stretching in transitional and turbulent channel flow. *Selected Proceedings* of the Tenth Symposium on *Turbulent Shear Flows, International Journal of Heat and Fluid Flow*.

- Lelong, M.-P., 1990. Weakly non-linear internal wave-vortical mode interaction in stably stratified flows. PhD Thesis, University of Washington.

- Lesieur M. 1990. *Turbulence in Fluids* (second revised edition), Kluwer Academic Publisher, 412 pp.

- Lesieur, M., Yanase, S. & Métais, O., 1991. Stabilizing and destabilizing effects of a solid-body rotation upon quasi-two-dimensional shear layers. *Phys. Fluids A*, **3**, pp. 403-407.

- Lilly, D.K., 1983. Stratified turbulence and the mesoscale variability of the atmosphere. *J. Atmos. Sci.*, **40**, pp. 749-761.

- Métais, O., Bartello, P., Garnier, E., Riley, J.J. & Lesieur, M., 1995a. Inverse cascade in stably-stratified rotating turbulence. *Dynamics of Atmospheres and Oceans, sous presse.*

- Métais, O., Flores, C., Yanase, S., Riley, J.J. & Lesieur, M., 1995b. Rotating free-shear flows. Part 2: numerical simulations. *J. Fluid Mech.*, **293**, pp. 47-80.

- Métais, O. & Herring, J.R., 1989. Numerical simulations of freely evolving turbulence in stably stratified fluids. *J. Fluid Mech.*, **202**, pp. 117-148.

- Métais, O., Riley, J.J., & Lesieur, M., 1994. Numerical simulations of stably-stratified rotating turbulence. In *Stably-stratified flows- flow and dispersion over topography*, I.P. Castro and N.J. Rockliff eds., Oxford University Press, pp. 139-151.

- Métais, O., Yanase, S., Flores, C., Bartello, P. & Lesieur, M., 1992. Reorganization of coherent vortices in shear layers under the action of solid-body rotation. Selected proceedings of the *Turbulent Shear Flows VIII*, Springer-Verlag, pp.415-430

- Müller, P, Holloway, G., Henyey, F. & Pomphrey, N., 1986. Nonlinear interactions among internal gravity waves. *Reviews of Geophysics*, **24**(3), pp. 493-536.

- Riley, J.J., Metcalfe, R.W. & Weissman, M.A. (1981). Direct numerical simulations of homogeneous turbulence in density stratified fluids. In: B.J. West (Editor), AIP Conf. Proc. N° 76, New York, Nonlinear Properties of Internal Waves, pp. 79-112.

- Yanase, S., Flores, C., Métais, O., & Riley, J.J. 1993 Rotating free shear flows Part 1: Linear stability analysis, *Phys. of Fluids. A.* **5** (11), 2725-2737.
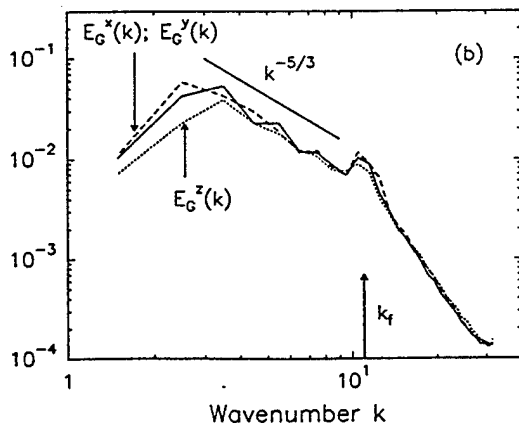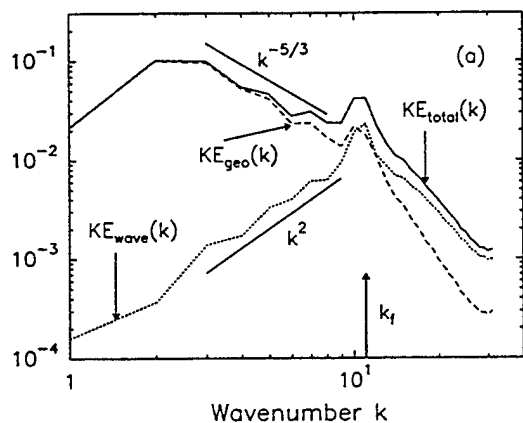
Figure 6: $\Omega = 2\pi$; $N = 4\pi$: a) three-dimensional wave-number spectrum of the total kinetic energy (KE_{total}) to the analogous spectra for the geostrophic kinetic energy ($KE_{geo} = E_G^x + E_G^y$) and the inertio-gravity wave kinetic energy (KE_{wave}) ; b) three-dimensional spectra of the geostrophy energy components E_G^x, E_G^y and E_G^z (from Métais *et al.*, 1995a).

DOCUMENT LIBRARY

Distribution List for Technical Report Exchange – May 1995

University of California, San Diego
SIO Library 0175C
9500 Gilman Drive
La Jolla, CA 92093-0175

Hancock Library of Biology & Oceanography
Alan Hancock Laboratory
University of Southern California
University Park
Los Angeles, CA 90089-0371

Gifts & Exchanges
Library
Bedford Institute of Oceanography
P.O. Box 1006
Dartmouth, NS, B2Y 4A2, CANADA

Commander
International Ice Patrol
1082 Shennecossett Road
Groton, CT 06340-6095

NOAA/EDIS Miami Library Center
4301 Rickenbacker Causeway
Miami, FL 33149

Research Library
U.S. Army Corps of Engineers
Waterways Experiment Station
3909 Halls Ferry Road
Vicksburg, MS 39180-6199

Institute of Geophysics
University of Hawaii
Library Room 252
2525 Correa Road
Honolulu, HI 96822

Marine Resources Information Center
Building E38-320
MIT
Cambridge, MA 02139

Library
Lamont-Doherty Geological Observatory
Columbia University
Palisades, NY z10964

Library
Serials Department
Oregon State University
Corvallis, OR 97331

Pell Marine Science Library
University of Rhode Island
Narragansett Bay Campus
Narragansett, RI 02882

Working Collection
Texas A&M University
Dept. of Oceanography
College Station, TX 77843

Fisheries-Oceanography Library
151 Oceanography Teaching Bldg.
University of Washington
Seattle, WA 98195

Library
R.S.M.A.S.
University of Miami
4600 Rickenbacker Causeway
Miami, FL 33149

Maury Oceanographic Library
Naval Oceanographic Office
Building 1003 South
1002 Balch Blvd.
Stennis Space Center, MS, 39522-5001

Library
Institute of Ocean Sciences
P.O. Box 6000
Sidney, B.C. V8L 4B2
CANADA

National Oceanographic Library
Southampton Oceanography Centre
European Way
Southampton SO14 3ZH
UK

The Librarian
CSIRO Marine Laboratories
G.P.O. Box 1538
Hobart, Tasmania
AUSTRALIA 7001

Library
Proudman Oceanographic Laboratory
Bidston Observatory
Birkenhead
Merseyside L43 7 RA
UNITED KINGDOM

IFREMER
Centre de Brest
Service Documentation - Publications
BP 70 29280 PLOUZANE
FRANCE

50272-101

REPORT DOCUMENTATION PAGE	1. REPORT NO. WHOI-96-09	2.	3. Recipient's Accession No.

4. Title and Subtitle	5. Report Date
"Rotating Convection" 1995 Summer Study Program in Geophysical Fluid Dynamics	July 1996
	6.

7. Author(s) Rick Salmon, Glen Flierl and Lee Anne Campbell	8. Performing Organization Rept. No. WHOI-96-09

9. Performing Organization Name and Address	10. Project/Task/Work Unit No.
Woods Hole Oceanographic Institution Woods Hole, Massachusetts 02543	11. Contract(C) or Grant(G) No. (C) OCE-8901012 (G)

12. Sponsoring Organization Name and Address	13. Type of Report & Period Covered
National Science Foundation	Technical Report
	14.

15. Supplementary Notes

This report should be cited as: Woods Hole Oceanog. Inst. Tech. Rept., WHOI-96-09.

16. Abstract (Limit: 200 words)

The 1995 program in Geophysical Fluid Dynamics addressed "Rotating Convection," with particular emphasis on high-Rayleigh-number convection and on convection in the ocean.

17. Document Analysis   a. Descriptors

rotating convection
heat transport
geophysical fluid dynamics

b. Identifiers/Open-Ended Terms

c. COSATI Field/Group

18. Availability Statement	19. Security Class (This Report) UNCLASSIFIED	21. No. of Pages 322
Approved for public release; distribution unlimited.	20. Security Class (This Page)	22. Price

(See ANSI-Z39.18)	See Instructions on Reverse	OPTIONAL FORM 272 (4-77) (Formerly NTIS-35) Department of Commerce